Transactions of the ASME®

Journal of Fluids Engineering

FLUIDS ENGINEERING DIVISION
Technical Editor
DEMETRI P. TELIONIS (1995)
Executive Secretary
PAT WHITE (1995)
Technical Editor's Office
SAAD A. RAGAB
Calendar Editor
M. F. ACKERSON

Associate Technical Editors
R. K. AGARWAL (1994)
R. E. A. ARNDT (1996)
O. BAYSAL (1995)
DENNIS M. BUSHNELL (1993)
N. A. CUMPSTY (1995)
M. GHARIB (1995)
A. F. GHONIEM (1995)
CHIH-MING HO (1993)
THOMAS T. HUANG (1993)
J. A. C. HUMPHREY (1994)
O. C. JONES (1995)
G. KARNIADAKIS (1995)
R. W. METCALFE (1995)
L. NELIK (1995)
WING-FAI NG (1996)
R. L. PANTON (1995)
ANDREA PROSPERETTI (1993)
M. W. REEKS (1995)
W. S. SARIC (1996)

BOARD ON COMMUNICATIONS
Chairman and Vice-President
R. D. ROCKE

Members-at-Large
T. BARLOW, T. DEAR, L. KEER, J. KITTO, W. MORGAN, E. M. PATTON, S. PATULSKI, R. E. REDER, R. SHAH, A. VAN DER SLUYS, F. M. WHITE, J. WHITEHEAD

OFFICERS OF THE ASME
President, **J. H. FERNANDES**
Exec. Dir.
D. L. BELDEN
Treasurer,
R. A. BENNETT

PUBLISHING STAFF
Mng. Dir., Publ.,
CHARLES W. BEARDSLEY
Managing Editor,
CORNELIA MONAHAN
Production Asstistant, **MARISOL ANDINO**

Transactions of the ASME, Journal of Fluids Engineering (ISSN 0098-2202) is published quarterly (Mar., June, Sept., Dec.) for $130.00 per year by The American Society of Mechanical Engineers, 345 East 47th Street, New York, NY 10017. Second class postage paid at New York, NY and additional mailing offices. POSTMASTER: Send address changes to Transactions of the ASME, Journal of Fluids Engineering, c/o THE AMERICAN SOCIETY OF MECHANICAL ENGINEERS, 22 Law Drive, Box 2300, Fairfield, NJ 07007-2300. **CHANGES OF ADDRESS** must be received at Society headquarters seven weeks before they are to be effective. Please send old label and new address. **PRICES:** To members, $40.00, annually: to nonmembers, $130.00. Add $24.00 for postage to countries outside the United States and Canada. **STATEMENT** from By-Laws. The Society shall not be responsible for statements or opinions advanced in papers or . . . printed in its publications (B7.1, Par. 3).

COPYRIGHT © 1993 by The American Society of Mechanical Engineers. Authorization to photocopy material for internal or personal use under circumstances not falling within the fair use provisions of the Copyright Act is granted by ASME to libraries and other users registered with the Copyright Clearance Center (CCC) Transactional Reporting Service provided that the base fee of $3.00 per article is paid directly to CCC, 27 Congress St., Salem, MA 01970. Request for special permission or bulk copying should be addressed to Reprints/Permission Department.

INDEXED by Applied Mechanics Reviews and Engineering Information, Inc.
Canadian Goods & Services Tax Registration #126148048

Published Quarterly by The American Society of Mechanical Engineers

VOLUME 115 • NUMBER 3 • SEPTEMBER 1993

Technical Briefs

(Contents continued on page 344)

Downloaded 03 Jun 2010 to 171.66.16.159. Redistribution subject to ASME license or copyright; see http://www.asme.org/terms/Terms_Use.cfm

Contents (continued)

Announcements and Special Notices

Journal of
Fluids
Engineering

Editorial

The continued advancements in high performance computing, both in hardware and software, and the cost competitive advantage of numerical simulations over laboratory experiments have made computational fluid dynamics an integral tool in the study of science and engineering problems. However, unlike experimental methods for which a large body of knowledge and techniques exist for the evaluation of experimental error and uncertainty (and are widely accepted), equivalent techniques for the evaluation of numerical error and uncertainty are less well developed and accepted. A recent article in the *Journal of Fluids Engineering* (Celik, 1993) highlighted this point and identified possible reasons for both the lack of interest in this topic and lack of accepted methods for the evaluation of uncertainty by the computational science community. Celik went on to identify three major topics of relevance to the issue of numerical accuracy and uncertainty. These are: (i) the separation of numerical errors from modeling errors; (ii) the identification, estimation, and reduction of numerical errors; and (iii) the assessment of codes and computational schemes with respect to numerical uncertainty through benchmarking. As Celik indicated, there is the need to improve the quality of the large number of papers being published today in computational fluid dynamics, and thus there is an urgent need for implementing a policy regarding numerical uncertainty analysis or quantitative error estimation.

The Fluids Engineering Division (FED) of the ASME, through the Coordinating Group on Computational Fluid Dynamics (CGCFD), has taken on the task of leading the computational fluid dynamics community and focusing their attention on the formulation of reasonable measures for numerical accuracy. The CGCFD has by charter the responsibility to promote discussion and interest in research into all areas of computational fluid dynamics and principal among these are methods for the evaluation of numerical accuracy. The CGCFD has performed its function by conducting symposia, forums, and panel discussions addressing this complex topic. The objective here is to delineate standard practices by which computational studies may be performed and the standards by which archival publications will be gauged. As a result of these meetings and discussions a new level of standards for the evaluation of journal publications has been promulgated for the *Journal of Fluids Engineering*.

The *Journal of Fluids Engineering* has had the policy that it: *will not accept for publication any paper reporting the numerical solution of a fluids engineering problem that fails to address the task of systematic truncation error testing and accuracy estimation.* This policy statement, originally presented in Roache, Ghia, and White (1986), was the first of its kind and provided a very general standard for evaluating journal publications. In the seven years since this policy's implementation, significant advances in computer hardware and computational software have occurred such that CFD is no longer in its infancy, but is a full-fledged tool in engineering and scientific problem solving. As Roache, Ghia, and White (1986) point out, fifteen years before the publication of their editorial, any successful calculation was of interest, and much of this exploratory work deserved publication. But even in their time it was recognized that this practice was outmoded. Therefore, it seems only logical and scientifically correct that the CFD community meet higher standards for evaluation of accuracy, standards on par with those required of the experimental community. What follows below then, are refinements and enhancements to the Journal's original statement on numerical accuracy, which attempt to elucidate the criteria by which Journal papers will be judged.

Finally, it is not the intent of this new policy statement to eliminate a class of simulations which some have referred to as ''practical engineering project simulations.'' The justification by these individuals for performing a single grid simulation has been that budget constraints, schedule constraints, or computer resource constraints prevent a systematic analysis of accuracy from being performed. It is assumed that in performing CFD analyses for ''practical engineering projects,'' for which experimental data is usually not available, that one must perform, in the natural course of the project, an evaluation of the accuracy of the simulation results in order to determine the validity of these particular calculations. Without such an effort there is no clear justification for presenting a simulation as representative of the physical phenomena. Therefore, it would seem only natural, even in the solution of practical engineering problems, that the items addressed here, be used to validate a simulation.

The author wishes to acknowledge the comments and suggestions to this new policy statement from Prof. B. P. Leonard (University of Akron), Dr. P. J. Roache (Ecodynamics), Dr. Ramesh Agarwal (McDonnell Douglas), Prof. Oktay Baysal (Old Dominion University), and Prof Demetri Telionis (Virginia Polytechnic Institute and State University).

The guidelines on the following page have been approved by the FED Coordinating Group on Computational Fluid Mechanics and the Editorial Board of the Journal.

Dr. Christopher J. Freitas
Chairman of the Coordinating
Group on Computational
Fluid Dynamics

Journal of Fluids Engineering Editorial Policy Statement on the Control of Numerical Accuracy

Although no standard method for evaluating numerical uncertainty is currently accepted by the CFD community, there are numerous methods and techniques available to the user to accomplish this task. The following is a list of guidelines, enumerating the criteria to be considered for archival publication of computational results in the *Journal of Fluids Engineering*

1. Authors must be precise in describing the numerical method used; this includes an assessment of the formal order of accuracy of the truncation error introduced by individual terms in the governing equations, such as diffusive terms, source terms, and most importantly, the convective terms. It is not enough to state, for example, that the method is based on a "conservative finite-volume formulation," giving then a reference to a general CFD textbook.
2. The numerical method used must be at least formally second-order accurate in space (based on a Taylor series expansion) for nodes in the interior of the computational grid. The computational expense of second, third, and higher order methods are more expensive (per grid point) than first order schemes, but the computational efficiency of these higher order methods (accuracy per overall cost) is much greater. And, it has been demonstrated many times that, for first order methods, the effect of numerical diffusion on the solution accuracy is devastating.
3. Methods using a blending or switching strategy between first and second order methods (in particular, the well-known "hybrid," "power-law," and related exponential schemes) will be viewed as first-order methods, unless it can be demonstrated that their inherent numerical diffusion does not swamp or replace important modelled physical diffusion terms. A similar policy applies to methods invoking significant amounts of explicitly added artificial viscosity or diffusivity.
4. Solutions over a range of significantly different grid resolutions should be presented to demonstrate grid-independent or grid-convergent results. This criterion specifically addresses the use of improved grid resolution to systematically evaluate trucation error and accuracy. The use of error estimates based on methods such as Richardson extrapolation or those techniques now used in adaptive grid methods, may also be used to demonstrate solution accuracy.
5. Stopping criteria for iterative calculations need to be precisely explained. Estimates must be given for the corresponding convergence error.
6. In time-dependent solutions, temporal accuracy must be demonstrated so that the spurious effects of phase error are shown to be limited. In particular, it should be demonstrated that unphysical oscillations due to numerical dispersion are significantly smaller in amplitude than captured short-wavelength (in time) features of the flow.
7. Clear statements defining the methods used to implement boundary and initial conditions must be presented. Typically, the overall accuracy of a simulation is strongly affected by the implementation and order of the boundary conditions. When appropriate, particular attention should be paid to the treatment of inflow and outflow boundary conditions.
8. In the presentation of an existing algorithm or code, all pertinent references or other publications must be cited in the paper, thus aiding the reader in evaluating the code and its method without the need to redefine details of the methods in the current paper. However, basic features of the code must be outlined according to Item 1, above.
9. Comparison to appropriate analytical or well-established numerical benchmark solutions may be used to demonstrate accuracy for another class of problems. However, in general this does not demonstrate accuracy for another class of problems, especially if any adjustable parameters are involved, as in turbulence modelling.
10. Comparison with reliable experimental results is appropriate, provided experimental uncertainty is established. However, "reasonable agreement" with experimental data alone will not be enough to justify a given single-grid calculation, especially if adjustable parameters are involved.

These ten items lay down a set of criteria by which the editors and reviewers of this Journal will judge the archival quality of publications dealing with computational studies for the *Journal of Fluids Engineering*. We recognize that the effort to perform a thorough study of numerical accuracy may be great and that many practical engineering calculations will continue to be performed by first order methods, on a single fixed grid. However, such analyses would not be appropriate for presentation in this archival journal. With the gains in performance of low-end workstations, it is now reasonable to require papers on solutions by CFD to meet these fundamental criteria for archiving of a publication.

With the details of these ten criteria now presented, a shortened statement will appear in each volume of the journal. This statement will appear as follows:

The Journal of Fluids Engineering will not consider any paper reporting the numerical solution of a fluids engineering problem that fails to address the task of systèmatic truncation error testing and accuracy estimation. Authors should address the following criteria for assessing numerical uncertainty.

1. The basic features of the method including formal truncation error of individual terms in the governing numerical equations must be described.
2. Methods must be at least second order accurate in space.
3. Inherent or explicit artificial viscosity (or diffusivity) must be assessed and minimized.
4. Grid independence or convergence must be established.
5. When appropriate, iterative convergence must be addressed.
6. In transient calculations, phase error must be assessed and minimized.
7. The accuracy and implementation of boundary and initial conditions must be fully explained.
8. An existing code must be fully cited in easily available references.
9. Benchmark solutions may be used for validation for a specific class of problems.
10. Reliable experimental results may be used to validate a solution.

References

Celik, I., 1993, "Numerical Uncertainty in Fluid Flow Calculations: Needs for Future Research," ASME Journal of Fluids Engineering, Vol. 115, June 1993, pp. 194-195.

Roache, P. J., Ghia, K. N., and White, F. M., 1986, "Editorial Policy Statement on the Control of Numerical Accuracy," ASME Journal of Fluids Engineering, Vol. 108, Mar. 1986, pp. 2.

Journal of Fluids Engineering
Technical Forum

Research Needs in Fluids Engineering

Basic Research Needs in Fluid-Solid Multiphase Flows

by C. T. Crowe[1]

The flows of liquid-solid and gas-solid mixtures have been important to industrial processes for many years. The complexity of these flows has necessitated the use of empiricism in design, often leading to non-optimal and expensive systems. The development of more sophisticated experimental techniques and the availability of high speed computational capability now provide the tools to improve the physical understanding of such flows. The ultimate goal is the development of reliable, predictive models to complement design and accurate, robust instruments to optimize performance of engineering systems.

There are numerous basic research needs in the flow of liquid-solid flows which are encountered in a variety of applications from the food to the mining industry. A relevant application in the metals processing industry is the application of abrasive water jets for high-speed, closely controlled cutting. The conventional approach has been to use a rheological model, such as a Bingham plastic or a power-law fluid, with empirical coefficients which may be valid only for limited conditions. One of the problems in the experimental studies of slurries has been the measurement of flow properties because of the opacity of the slurry mixture. Velocity and concentration measurements have been made with probes inserted in the flow but the effect of the probes on the flow properties is not well established. There is a need to develop techniques that provide non-intrusive in-situ measurements of the concentration and velocity profiles. These techniques may involve tracking tracer particles using neutron magnetic resonance or some other technique. Another approach may be the development of transparent particles in liquids (preferably water) which would enable conventional PIV or LDA techniques. These is also a need to develop a model which accounts for the particle-particle interaction and the interaction of the particles and the fluid in a thick slurry mixture and which can be used to predict the rheological behavior at arbitrary solid loadings and strain rates.

There are also basic research needs in the flows of gas-particle and gas-droplet mixtures in applications from energy conversion to materials processing. The access to high-speed computational facilities has enabled the development of numerical models which now show promise of predictive capability for complex gas-particle (droplet) flows. There are, however, fundamental research issues that have to be resolved for continued model development.

Although significant progress has been made in understanding particle mixing due to turbulence, new insights have shown that the standard time-averaged approach in quantative descriptions are misleading. Studies have shown, that under certain conditions, particles will tend to concentrate in regions of high strain and not mix uniformly throughout the fluid. There is a need to better quantify particle mixing in turbulent flows.

Another basic research need is to establish the effect of the dispersed phase on the turbulence of the carrier phase, known as turbulence modulation. The generation or suppression of turbulence in the fluid has a profound effect on mixing effectiveness, particle dispersion and pressure loss in a flowing system. This is a very difficult problem because of the complex nature of turbulence itself. There is a need for a complementary numerical (analytic) and experimental effort to resolve these issues. Experimental studies of the turbulence intensity and length scales, together with measurements of particle velocity fluctuations, are needed at high loadings. Under these conditions the measurements are seriously encumbered by the opacity of a highly loaded mixture. Some progress has been made in numerical studies using sophisticated models for the turbulence field such as large eddy simulation and direct numerical simulations. Still considerably more work is needed for systems with non negligible condensed phase volume fraction.

Another research need is to improve understanding of particle-particle (or droplet-droplet) interaction in dense sprays. The particle-wall and particle-particle interaction is the primary mechanism for transfer of momentum from a surface to the dispersed-phase flow field. Detailed measurements are needed on the momentum lost due to wall collisions and the relationship between particle properties before and after collision. These data are dependent on many variables such as wall roughness, material properties of the particle and wall material and particle shape. The measurements are difficult because of the problems associated with using LDA and PIV techniques close to a surface.

Droplet-droplet interaction and the resulting coalescence or breakup is a very important research topic because droplet size is a key parameter in any gas-droplet flow. In many atomization systems, the droplet size is significantly affected by droplet-droplet collisions in the dense portion of the spray. A developing area strongly affected by atomization is spray casting and forming. In this application metal is atomized and sprayed on a substrate. The rapid cooling of the small droplets

---

[1] Mechanical and Materials Engineering, Washington State University, Pullman, WA 99164-2920.

results in improved material properties. Measurements of droplet mechanics and droplet size are difficult in the dense regions of a developing spray.

Another area where fundamental research on gas-particle flows could benefit an industrial process is plasma arc coating. In this process a plasma with temperatures as high as 20,000 K is developed. Particles are injected into the plasma, melt and are deposited on a surface. The conditions in the plasma plume are such that the particles are in the free molecule or slip flow regimes. Some important research issues are the drag and heat transfer on a particle in a plasma. There is also the need to understand the dynamics of a plasma plume which exhausts into air at standard conditions. Experimental measurements are very difficult because of the high temperatures. Also the high density difference between the plume and the surroundings renders the development of a viable numerical model a difficult task.

Another merging area which is a challenge to the fluid dynamicist is the generation of nanocluster materials. These materials are nanometers in size and have interesting material properties because of the large fraction of molecules on the surface. These clusters can be generated by the supersonic expansion of a metal vapor in which the metal nucleates to form clusters. The problem is the design of systems to remove the clusters from the flow stream. The application of thermophoresis represents one technique. The nanoclusters are much smaller than the mean free path of the gas molecules so continuum mechanics is no longer applicable.

The experimental measurements and numerical simulations of fluid-particle flows is becoming more feasible because of the availability of more sophisticated experimental and numerical techniques. Still there is considerably more work to be done before one can use the information available to improve and optimize the design of fluid-particle systems.

Questions in Fluid Mechanics

Flow-Driven Particle Impact Erosion: Asking the Right Questions

By Joseph A. C. Humphrey[1]

This column is dedicated to exposing significant questions of high potential interest to the fluid mechanics community. Here I wish to focus on asking questions in a specific subject area of great concern to a large number of industrial processes and equipment where flow-driven particle impact erosion (PIE) is a costly problem. How costly? Lumping together plant shutdowns, the replacement of worn equipment, decreased process efficiencies, product loss or contamination, over-design practices and the implementation of safety factors, the cost is in the hundreds of millions of dollars annually.

There are essentially two ways to reduce undesirable PIE. One is to select appropriate materials to maximize resistance to wear. This solution is generally expensive and often restricted to specialized or critical applications where exotic, highly resistant superalloy or ceramic materials can be justified. The other solution, of concern here, is to alter the conditions affecting the behavior of erosive particle-fluid suspensions including particle size, shape, concentration, impact speed, impact angle and impact location. Of these conditions, the last four can be strongly determined by the flow field driving particle motion.

A major challenge in understanding, possibly avoiding and, hopefully, controlling PIE is its inter-disciplinary nature; see the extensive review by Humphrey (1990). At the most fundamental level, PIE is a highly complex particle-surface interaction problem and considerable effort has been expended researching the materials-related aspects of this form of wear. To date, however, theoretical attempts to model the complicated exchanges of mass, momentum and energy that take place between high speed particles and the surfaces they erode by impaction have met with, at most, modest success and are of little generality. This is because much of the theory is highly phenomenological in content, relying on experimental data (to provide closure) which are obtained under such idealized or specialized conditions that the practical predictive value of the theory is minimal.

Notwithstanding, semi-empirical deterministic relations describing the PIE of ductile and brittle materials have been derived and put to predictive use. The relations are of the form $E=kV_i^n f(\beta_i)$ where E is the mass of surface eroded per total mass of impacting particles, k and n are "constants" assumed to depend on the pair of materials involved, V_i and β_i are the particle impact speed and angle with respect to the surface, and f is a function of β_i. Note that the relatively early recognition given to V_i and β_i, as critical parameters affecting erosion, was strictly within the context of a materials interaction point of view with the result that most studies and interpretations of observations were rigidly fixed in this mold.

For example, the unusually large range (from 2 to 4, approximately) in the value of n in the above expression for E was originally attributed to variations in particle/surface material properties among experiments, and the question asked for years was: "How does the exponent n in the expression for E depend on material properties?" In his pioneering study, Laitone (1979) asked the equivalent of the following, very different, question: "Does the exponent n in the expression for E depend on the flow field?" In a detailed analysis of particle motion up to the instant of impact, Laitone showed that all values of n exceeding 2 could be explained exclusively in terms of fluid mechanics effects. Clearly, Laitone asked (and answered) the *right* question.

Primarily because of the enormous costs involved, PIE continues to be a scientific-engineering subject of tremendous national importance. Typically, much equipment and many processes involve particles with momentum equilibration numbers ranging from 0.1 to 10 so that the associated flow fields can strongly influence the speed, angle and location of particle impact. As a result, the *fluid mechanics* aspects of PIE are receiving increasingly more (justly deserved and long overdue) attention. In this regard, better designed and more carefully

---

[1] Department of Mechanical Engineering, University of California at Berkeley, Berkeley, CA 94720.

results in improved material properties. Measurements of droplet mechanics and droplet size are difficult in the dense regions of a developing spray.

Another area where fundamental research on gas-particle flows could benefit an industrial process is plasma arc coating. In this process a plasma with temperatures as high as 20,000 K is developed. Particles are injected into the plasma, melt and are deposited on a surface. The conditions in the plasma plume are such that the particles are in the free molecule or slip flow regimes. Some important research issues are the drag and heat transfer on a particle in a plasma. There is also the need to understand the dynamics of a plasma plume which exhausts into air at standard conditions. Experimental measurements are very difficult because of the high temperatures. Also the high density difference between the plume and the surroundings renders the development of a viable numerical model a difficult task.

Another merging area which is a challenge to the fluid dynamicist is the generation of nanocluster materials. These materials are nanometers in size and have interesting material properties because of the large fraction of molecules on the surface. These clusters can be generated by the supersonic expansion of a metal vapor in which the metal nucleates to form clusters. The problem is the design of systems to remove the clusters from the flow stream. The application of thermophoresis represents one technique. The nanoclusters are much smaller than the mean free path of the gas molecules so continuum mechanics is no longer applicable.

The experimental measurements and numerical simulations of fluid-particle flows is becoming more feasible because of the availability of more sophisticated experimental and numerical techniques. Still there is considerably more work to be done before one can use the information available to improve and optimize the design of fluid-particle systems.

Questions in Fluid Mechanics

Flow-Driven Particle Impact Erosion: Asking the Right Questions

By Joseph A. C. Humphrey[1]

This column is dedicated to exposing significant questions of high potential interest to the fluid mechanics community. Here I wish to focus on asking questions in a specific subject area of great concern to a large number of industrial processes and equipment where flow-driven particle impact erosion (PIE) is a costly problem. How costly? Lumping together plant shutdowns, the replacement of worn equipment, decreased process efficiencies, product loss or contamination, over-design practices and the implementation of safety factors, the cost is in the hundreds of millions of dollars annually.

There are essentially two ways to reduce undesirable PIE. One is to select appropriate materials to maximize resistance to wear. This solution is generally expensive and often restricted to specialized or critical applications where exotic, highly resistant superalloy or ceramic materials can be justified. The other solution, of concern here, is to alter the conditions affecting the behavior of erosive particle-fluid suspensions including particle size, shape, concentration, impact speed, impact angle and impact location. Of these conditions, the last four can be strongly determined by the flow field driving particle motion.

A major challenge in understanding, possibly avoiding and, hopefully, controlling PIE is its inter-disciplinary nature; see the extensive review by Humphrey (1990). At the most fundamental level, PIE is a highly complex particle-surface interaction problem and considerable effort has been expended researching the materials-related aspects of this form of wear. To date, however, theoretical attempts to model the complicated exchanges of mass, momentum and energy that take place between high speed particles and the surfaces they erode by impaction have met with, at most, modest success and are of little generality. This is because much of the theory is highly phenomenological in content, relying on experimental data (to provide closure) which are obtained under such idealized or specialized conditions that the practical predictive value of the theory is minimal.

Notwithstanding, semi-empirical deterministic relations describing the PIE of ductile and brittle materials have been derived and put to predictive use. The relations are of the form $E = kV_i^n f(\beta_i)$ where E is the mass of surface eroded per total mass of impacting particles, k and n are "constants" assumed to depend on the pair of materials involved, V_i and β_i are the particle impact speed and angle with respect to the surface, and f is a function of β_i. Note that the relatively early recognition given to V_i and β_i, as critical parameters affecting erosion, was strictly within the context of a materials interaction point of view with the result that most studies and interpretations of observations were rigidly fixed in this mold.

For example, the unusually large range (from 2 to 4, approximately) in the value of n in the above expression for E was originally attributed to variations in particle/surface material properties among experiments, and the question asked for years was: "How does the exponent n in the expression for E depend on material properties?" In his pioneering study, Laitone (1979) asked the equivalent of the following, very different, question: "Does the exponent n in the expression for E depend on the flow field?" In a detailed analysis of particle motion up to the instant of impact, Laitone showed that all values of n exceeding 2 could be explained exclusively in terms of fluid mechanics effects. Clearly, Laitone asked (and answered) the *right* question.

Primarily because of the enormous costs involved, PIE continues to be a scientific-engineering subject of tremendous national importance. Typically, much equipment and many processes involve particles with momentum equilibration numbers ranging from 0.1 to 10 so that the associated flow fields can strongly influence the speed, angle and location of particle impact. As a result, the *fluid mechanics* aspects of PIE are receiving increasingly more (justly deserved and long overdue) attention. In this regard, better designed and more carefully

---

[1] Department of Mechanical Engineering, University of California at Berkeley, Berkeley, CA 94720.

controlled fluid mechanics experiments should be performed, and more realistic descriptions of particle motion and universal models of erosion should be developed. These studies should include adequate discussions of experimental and/or numerical model uncertainties.

Understandably, in a field as complex as PIE, progress is slow and major issues remain to be solved. I believe that the following are among the most difficult and pressing questions yet to be satisfactorily addressed.

1. Even though PIE is a stochastic phenomenon, it continues to be attacked primarily via approaches that are entirely deterministic at most (if not all) levels of inquiry, ranging from the motion of a particle towards a solid surface to its interactions with that surface. *What are the universal limitations inherent to all deterministic approaches and how can the stochastic nature of PIE be properly accounted for?*
2. A discrete (Lagrangian) description of particle motion is intuitively appealing. However, in concentrated systems with significant particle-particle interactions the associated momentum balance force terms are not well understood or readily modelled, especially near solid surfaces. This lack of knowledge of detailed particle-particle interactions can be "exchanged" for equivalent ignorance in a continuous (Eulerian) description of particle motion, by postulating particle-particle constitutive relations that are also unknown. *With PIE applications in mind, what are the merits and demerits of the two approaches and is there a clear-cut way to go?*
3. In a theory of flow-driven particle motion, it is important to account for the effects of random fluid velocity fluctuations, especially near solid surfaces, for PIE applications. *How do particles with large momentum equilibrium numbers "filter out" the effects of the turbulent flow field acting upon them, and what are the pratical implications for PIE?*
4. *Do appropriate experimental or theoretical relations exist for predicting the drag, Magnus and Saffman forces acting on particles immersed in highly unsteady turbulent flows near solid surfaces? In this regard, what are the current major experimental limitations in PIE, especially in relation to fluid mechanics effects?*
5. *What are the conditions for which particle-particle interactions near a solid surface must be properly accounted for in a theory purporting to model PIE at high particle concentrations, and how do these conditions change as a function of distance from the surface?*
6. Under repeated impaction the topography of an eroding solid surface evolves randomly with time. This affects the motions of fluid and particles near the surface as well as the dynamics of particle-particle and particle-surface interactions. *Given the stochastic nature of this phenomenon, could fractal theory be usefully applied to describe the time evolution of an eroding surface?*
7. Experimentally determined particle restitution coefficients currently play an important role in, for example, predicting erosion in turbomachinery equipment. *Given that these coefficients are highly dependent on the material pairs involved and that they cannot be determined with high accuracy or precision, especially when particle fragmentation takes place, how accurate and generally applicable are the models that are based on the use of these coefficients?*
8. *How do temperature gradients near solid surfaces affect particle motion and, therefore, PIE?*

These few questions are submitted in the hope of stimulating further thought and technical advances in this very important subject area.

References

Humphrey, J. A. C., 1990, "REVIEW—Fundamentals of Fluid Motion in Erosion by Solid Particle Impact," *Int. J. Heat and Fluid Flow*, Vol. 11, pp. 170–195.

Laitone, J. A., 1979, "Aerodynamic Effects in the Erosion Process," *Wear*, Vol. 56, pp. 239–246.

U.S. Competitiveness: A Fluid Engineer's Viewpoint

Column 4—What Government Studies Indicate and Some Suggestions

by D. M. Bushnell[1]

National industrial competitiveness is the historical artifact of a large number of parameters, i.e., national monetary/fiscal/regulatory policies, quantity and quality of capital equipment, quality of management, worker effectiveness [education, motivation, union regulations], worker standard of living/labor rate, foreign competition [technology level, labor rate, governmental policies] and the rate of technological change/innovation.

The present remarks will focus upon the latter issue namely, technological change in the civilian sector, a subject of direct interest to the engineering community. It should be stressed that although technological change, often termed the "fuel of a nation's economic engine," is a major element in the competitiveness equation, it is only one such element. Technology advances can be utilized to enhance product quality, features/characteristics and production efficiency.

Technological advances in the marketplace are a result of: (*a*) basic and applied product research, (*b*) process [e.g., production technology] research, and (*c*) the application of this research to product design and production thereof. During the nearly half century subsumed by the cold war, the primary focus of advanced research in the U.S. was military in nature. Also much of the U.S. civilian-related research tended to focus upon product rather than upon improvements in process/production technology. These trends are the reverse of those in nations, such as Japan, which are considered to be highly competitive. That is, much of their research is related to civilian products and their production technology.

It should be noted that a necessary key to the success of such an approach is the exploitation of "offshore" [out of country] product-related research to the maximum extent pos-

---

[1] NASA Langley Research Center, Hampton, VA 23665.

controlled fluid mechanics experiments should be performed, and more realistic descriptions of particle motion and universal models of erosion should be developed. These studies should include adequate discussions of experimental and/or numerical model uncertainties.

Understandably, in a field as complex as PIE, progress is slow and major issues remain to be solved. I believe that the following are among the most difficult and pressing questions yet to be satisfactorily addressed.

1. Even though PIE is a stochastic phenomenon, it continues to be attacked primarily via approaches that are entirely deterministic at most (if not all) levels of inquiry, ranging from the motion of a particle towards a solid surface to its interactions with that surface. *What are the universal limitations inherent to all deterministic approaches and how can the stochastic nature of PIE be properly accounted for?*
2. A discrete (Lagrangian) description of particle motion is intuitively appealing. However, in concentrated systems with significant particle-particle interactions the associated momentum balance force terms are not well understood or readily modelled, especially near solid surfaces. This lack of knowledge of detailed particle-particle interactions can be "exchanged" for equivalent ignorance in a continuous (Eulerian) description of particle motion, by postulating particle-particle constitutive relations that are also unknown. *With PIE applications in mind, what are the merits and demerits of the two approaches and is there a clear-cut way to go?*
3. In a theory of flow-driven particle motion, it is important to account for the effects of random fluid velocity fluctuations, especially near solid surfaces, for PIE applications. *How do particles with large momentum equilibrium numbers "filter out" the effects of the turbulent flow field acting upon them, and what are the pratical implications for PIE?*
4. *Do appropriate experimental or theoretical relations exist for predicting the drag, Magnus and Saffman forces acting on particles immersed in highly unsteady turbulent flows near solid surfaces? In this regard, what are the current major experimental limitations in PIE, especially in relation to fluid mechanics effects?*
5. *What are the conditions for which particle-particle interactions near a solid surface must be properly accounted for in a theory purporting to model PIE at high particle concentrations, and how do these conditions change as a function of distance from the surface?*
6. Under repeated impaction the topography of an eroding solid surface evolves randomly with time. This affects the motions of fluid and particles near the surface as well as the dynamics of particle-particle and particle-surface interactions. *Given the stochastic nature of this phenomenon, could fractal theory be usefully applied to describe the time evolution of an eroding surface?*
7. Experimentally determined particle restitution coefficients currently play an important role in, for example, predicting erosion in turbomachinery equipment. *Given that these coefficients are highly dependent on the material pairs involved and that they cannot be determined with high accuracy or precision, especially when particle fragmentation takes place, how accurate and generally applicable are the models that are based on the use of these coefficients?*
8. *How do temperature gradients near solid surfaces affect particle motion and, therefore, PIE?*

These few questions are submitted in the hope of stimulating further thought and technical advances in this very important subject area.

References

Humphrey, J. A. C., 1990, "REVIEW—Fundamentals of Fluid Motion in Erosion by Solid Particle Impact," *Int. J. Heat and Fluid Flow*, Vol. 11, pp. 170-195.

Laitone, J. A., 1979, "Aerodynamic Effects in the Erosion Process," *Wear*, Vol. 56, pp. 239-246.

U.S. Competitiveness: A Fluid Engineer's Viewpoint

Column 4—What Government Studies Indicate and Some Suggestions

by D. M. Bushnell[1]

National industrial competitiveness is the historical artifact of a large number of parameters, i.e., national monetary/fiscal/regulatory policies, quantity and quality of capital equipment, quality of management, worker effectiveness [education, motivation, union regulations], worker standard of living/labor rate, foreign competition [technology level, labor rate, governmental policies] and the rate of technological change/innovation.

The present remarks will focus upon the latter issue namely, technological change in the civilian sector, a subject of direct interest to the engineering community. It should be stressed that although technological change, often termed the "fuel of a nation's economic engine," is a major element in the competitiveness equation, it is only one such element. Technology advances can be utilized to enhance product quality, features/characteristics and production efficiency.

Technological advances in the marketplace are a result of: (*a*) basic and applied product research, (*b*) process [e.g., production technology] research, and (*c*) the application of this research to product design and production thereof. During the nearly half century subsumed by the cold war, the primary focus of advanced research in the U.S. was military in nature. Also much of the U.S. civilian-related research tended to focus upon product rather than upon improvements in process/production technology. These trends are the reverse of those in nations, such as Japan, which are considered to be highly competitive. That is, much of their research is related to civilian products and their production technology.

It should be noted that a necessary key to the success of such an approach is the exploitation of "offshore" [out of country] product-related research to the maximum extent pos-

---

[1] NASA Langley Research Center, Hampton, VA 23665.

sible. Currently, two-thirds of the planet's R&D of all types is conducted outside the U.S., therefore it is in our best interests to utilize this out-of-country research far more than we have thus far. There are several obvious examples such as the VCR where the basic product research was conducted in one country [e.g., in this case the U.S.] and innovated [produced/marketed] via process research and development in another country [e.g., Japan].

A contributory factor as to whether a nation is strong in basic or applied [product and/or process] research is the research value system of the university community. Historically, in the U.S. since the 50's much of university engineering research has been government-supported and usually dealt with basic issues connected with product rather than process. Several of the "competitive" countries tend to promote industrial or combined government/industrial funding of university research with an emphasis upon process/innovation/engineering as opposed to basic science/research.

Another technological competitiveness issue concerns the spectrum of research [both product and process related] in terms of "great leaps forward" on the one hand and evolutionary, step-by-step improvements on the other. Obviously research should be conducted across the entire spectrum. The U.S. has in the past tended toward trying to take "leaps," sometimes to the detriment of more evolutionary activities. The U.S. is attempting, with the aid of "Total Quality Management," to address the need for an increased emphasis on evolutionary activities.

What then can a nation do to increase the contributions which its technology makes to the national [economic] competitive position? Information available thus far indicates that the answer to this question is multi-faceted and involves a balanced set of civilian-related research activities which include:

1. University and national laboratory research, funded by industry/government consortia, which covers the spectrum from basic research through production/application, for both product and process along with a workable system to "protect" the results.
2. Maximum utilization of offshore, out-of-country research.
3. Inclusion of the spectrum of activities from near term, evolutionary innovative product and process improvement [including quality enhancement] to further term, "great leaps forward."

In the current information age, basic research results, which are usually not "protected," are very rapidly communicated across the globe and therefore seldom provide competitive advantage to the originating country. Major advantages accrue from product and process advances which provide improvements in quality and reduced production costs. Such advances can be patented and become "intellectual property" which will then be protected. However, such protection will be only transitory. A technological culture is required which emphasizes a continuous striving for improvement in what is becoming a very competitive world economy to the extent that the term "economic warfare" is sometimes utilized. As stated previously, technology level [product and process] is only one of the elements which must be worked to improve a nation's competitive posture, but it is an area upon which we as engineers can have a direct impact.

Fluid Dynamics of Sprays—1992 Freeman Scholar Lecture

William A. Sirignano
Department of Mechanical
and Aerospace Engineering,
University of California, Irvine,
Irvine, CA 92717-2700

Various theoretical and computational aspects of the fluid dynamics of sprays are reviewed. Emphasis is given to rapidly vaporizing sprays on account of the richness of the scientific phenomena and the several, often disparate, time scales. Attention is given to the behavior of individual droplets including the effects of forced convection due to relative droplet-gas motion, Stefan convection due to the vaporization or condensation of the liquid, internal circulation of the liquid, interactions with neighboring droplets, and interactions with vortical eddies. Flow field details in the gas boundary layer and wake and in the liquid droplet interior are examined. Also, the determinations of droplet lift and drag coefficients and Nusselt and Sherwood numbers and their relationships with Reynolds number, transfer number, Prandtl and Schmidt numbers, and spacing between neighboring droplets are extensively discussed. The spray equations are examined from several aspects; in particular, two-continua, multi-continua, discrete-particle, and probabilistic formulations are given. The choice of Eulerian or Lagrangian representation of the liquid-phase equations within these formulations is discussed including important computational issues and the relationship between the Lagrangian method and the method of characteristics. Topics for future research are suggested.

1 Introduction

A spray is one type of two-phase flow. It involves a liquid as the dispersed or discrete phase in the form of droplets or ligaments and a gas as the continuous phase. There are many occurrences of spray phenomena in power and propulsion applications, industrial applications, and nature. A dusty flow is very similar to a spray except that the discrete phase is solid rather than liquid. Bubbly flow is the opposite kind of two-phase flow wherein the gas forms the discrete phase and the liquid is the continuous phase. Generally, the liquid density is considerably larger than the gas density, so bubble motion involves lower kinematic inertia, higher drag force, and different behavior under gravity force than droplet motion.

The fluid dynamics of sprays is a rapidly developing field of broad importance. There are many interesting applications of spray theory related to power, propulsion, heat exchange, and materials processing. Important and intellectually challenging fluid dynamic phenomena can occur in many different ways with sprays. On the scale of an individual droplet in a spray, boundary layers and wakes appear due to relative motion between the droplet center and the ambient gas. Other complicated and coupled fluid dynamic factors are abundant: shear-driven internal circulation of the liquid in the droplet, Stefan flow due to vaporization or condensation, flow modifications due to closely neighboring droplets in the spray, hydrodynamic interfacial instabilities leading to droplet shape distortion and perhaps droplet shattering, and droplet interactions with vortical structures in the gas flow (e.g., turbulence). On a much larger and coarser scale, we have the complexities of the integrated exchanges of mass, momentum, and energy of many droplets in some subvolume of interest with the gas flow in the same subvolume. The problem is further complicated by the strong coupling of the phenomena on the different scales; one cannot describe the mass, momentum, and energy exchanges on the large scale without detailed knowledge of the fine-scale phenomena. Note that in some practical applications, these scales can differ by several orders of magnitude so that a challenging subgrid modeling problem results.

The author's research interests have focused on the theoretical and computational aspects of the spray problem. Therefore, this review will emphasize those aspects. Major, but not total attention, will be given to the research of the author and his co-workers. Also, detailed consideration will be given to applications where the mass vaporization rate is very large since this is the most complex situation and therefore its coverage leads to the most general formulation of the theory. In particular, as the vaporization rate increases, the coupling between the two phases becomes stronger and, as the droplet lifetime becomes as small as some of the other characteristic times, the transient or dynamic character of the problem emerges in a dominant manner.

The fast vaporization rate is especially prominent in situations where the ambient gas is at very high temperatures (of the order of 1000 K or higher). Combustion with liquid fuels is the most notable example here. The spray combustion regime is a most interesting limiting case of the more general field of

---

Contributed by the Fluids Engineering Division for publication in the JOURNAL OF FLUIDS ENGINEERING. Manuscript received by the Fluids Engineering Division November 20, 1992; revised manuscript received February 18, 1993. Associate Technical Editor: D. P. Telionis.

thermal and dynamic behavior of sprays. In the high temperature domain, rapid vaporization causes droplet lifetimes to be as short as the time for a droplet to heat throughout its interior. It can be shorter than the time for liquid-phase mass diffusion to result in the mixing of various components in a multicomponent liquid. The combustion limit is inherently transient from the perspective of the droplet, richer in terms of scientific issues, and more challenging analytically and numerically than low temperature spray problems.

The spray problem is complicated by the presence of spatial temperature and concentration gradients and internal circulation in the liquid. Interaction amongst droplets is another complication to be treated.

There is a great disparity in the magnitudes of the scales. Liquid-phase mass diffusion is slower than liquid-phase heat diffusion which, in turn, is much slower than the diffusion of vorticity in the liquid. Transport in the gas is faster than transport in the liquid. Droplet diameters are typically of the order of a few tens of microns to a few hundreds of microns in diameter. Resolution of internal droplet gradients can imply resolution on the scale of microns or even on a submicron scale. Combustor or flow chamber dimensions can be five or six orders of magnitude greater than the required minimum resolution. Clearly, subgrid droplet vaporization models are required to make progress on this problem.

Experiments have been successful primarily in resolving the global characteristics of sprays. The submillimeter scales associated with the spray problem have made detailed experimental measurements very difficult. If an attempt is made to increase droplet size, similarity is lost; droplet Reynolds number can be kept constant by decreasing velocity but the Grashof number grows implying that buoyancy becomes relatively more important. Also, Weber number decreases as droplet size increases; surface tension becomes relatively less important and the droplet is more likely to acquire a nonspherical shape. Modern nonintrusive laser diagnostics have made resolution possible on a scale less than one hundred microns so that, in recent years, more experimental information has been appearing. Nevertheless, theory and computation have led experiment in terms of resolving the fluid dynamical characteristics of spray flows.

In Section 2, we shall discuss the vaporization of individual droplets and study the phenomenon on the scale of the droplet diameter. The theoretical models and correlations of computational results for individual droplets can be used to describe exchanges of mass, momentum, and energy between the phases in a spray flow. The spray with its many droplets is examined in Section 3. Much of the results presented in Sections 2 and 3 can be helpful in engineering practice. Some of the information already appears in computational codes; modification of the codes to address more recent advances should not be difficult. One shortcoming, of course, is the limited experimental verification as previously discussed. Interactions amongst a few droplets and their effects on the modification of the theory are discussed in Section 4. Turbulence-droplet interactions are briefly surveyed in Section 5. Concluding remarks are stated in Section 6. The spray discussion of Section 3 precedes the topics of Sections 4 and 5 because droplet-droplet interactions and turbulence-droplet interactions have not yet been fully integrated into a comprehensive spray theory. These interaction studies are still active research domains and, so far, little application to engineering practice has occurred. Due to length limitations on this article, several important areas of spray phenomena are not discussed. Excluded examples are primary and secondary atomization, slurry sprays, and radiation-droplet interactions.

2 Theory of Isolated Droplet Vaporization, Heating and Acceleration

The vaporizing droplet problem is a challenging, multidisciplinary issue. It can involve heat and mass transport, fluid dynamics and chemical kinetics. In general, there is a relative motion between a droplet and its ambient gas. Here, the general aerodynamic characteristics of pressure gradients, viscous boundary layers, separated flows, and wakes can appear for the gas flow over the droplet. Reynolds number based upon the relative velocity, droplet diameter, and gas-phase properties is a very important descriptor of the gaseous flow field. Internal liquid circulation, driven by surface shear forces, is another important fluid dynamic feature of the droplet problem.

These flow features have critical impact on the exchanges of mass, momentum, and energy between the gas and liquid phases. They are important for both vaporizing and nonvaporizing situations. The vaporizing case is complicated by regressing interfaces and boundary layer blowing.

Nomenclature

a = droplet acceleration
a = constant of curvature in stagnation point flow
a, b = parameters in Section 2.2, Eq. (50)
A = constant in Section 2.2
$\tilde{A}$ = liquid vortex strength
B = transfer number
C_D, C_L = drag and lift coefficients
c_ℓ = liquid specific heat
c_p = specific heat at constant pressure
d = droplet diameter
D = mass diffusivity, droplet center-to-center spacing
e = thermal energy
e = error
e = unit vector
g_1, g_2 = functions defined in Section 2.2, Eqs. (46)–(47)
f = Blasius function
f = droplet distribution functions (probability density function)
F = drag force per unit mass on droplet
F, G = functions defined in Section 2.2, Eqs. (46)–(47)
h = enthalpy
k = nondimensional constant in Section 2.2, also turbulence wavenumber
L = latent heat of vaporization
L = differential operator
Le = Lewis number
m = droplet mass
$\dot{m}$ = droplet mass vaporization rate
$\dot{M}$ = mass source term
n = droplet number density
Nu = Nusselt number
p = pressure
Pr = Prandtl number
$\dot{q}$ = heat flux
Q = energy per unit mass of fuel
r = spherical radial coordinate
$\tilde{r}$ = cylindrical radial coordinate
r_f = flame radius
R = droplet radius
R_2 = droplet radii ratio
R = gas constant
Re = Reynolds number
s = nondimensional radius
S = weighted area in numerical interpolation schemes
Sh = Sherwood number
Sc = Schmidt number
t = time
T = temperature
u, v = velocity
U = free stream velocity
v = velocity in the argument of distribution function
V = volume in eight-dimensional phase space

There is interest in the droplet vaporization problem from two different aspects. First, we wish to understand the fluid dynamic and transport phenomena associated with the transient heating and vaporization of a droplet. Second, but just as important, we must develop models for droplet heating, vaporization, and acceleration that are sufficiently accurate and simple to use in a spray analysis involving very many droplets. The first goal can be met by examining both approximate analyses and finite-difference analyses of the governing Navier-Stokes equations. The second goal can only be addressed at this time with approximate analyses since Navier-Stokes resolution for the detailed flow field around each droplet is too costly in a practical spray problem. However, correlations from Navier-Stokes solutions provide useful inputs into approximate analyses.

Introductory descriptions of vaporizing droplet behavior can be found in Chigier (1981), Clift et al. (1978), Glassman (1987), Kanury (1975), Kuo (1986), Lefebvre (1989), and Williams (1985). Useful research reviews are given by Faeth (1983), Law (1982), and Sirignano (1983).

In developing the study of the gas flow field surrounding the droplet and of the liquid flow in the droplet, certain assumptions are employed. Small Mach number is considered so that kinetic energy and viscous dissipation are negligible. Gravity effects, droplet deformation, radiation, Dufour energy flux, and mass diffusion due to pressure and temperature gradients are all neglected. (Note, however, that thermophoresis can affect the transport rates for submicron particles: e.g., soot.) The multicomponent gas-phase mixture is assumed to behave as an ideal gas. Phase equilibrium is stated at the droplet-gas interface. Gas-phase density and thermophysical parameters are generally considered variable, unless otherwise stated. Liquid-phase viscosity is generally taken as variable in the finite-difference calculations but density and other properties are typically taken to be constant. The basic equations governing the gas flow are the Navier-Stokes equations for a viscous, variable density, and variable properties multicomponent mixture. The liquid-phase primitive equations are the incompressible Navier-Stokes equations; however, the stream-function, vorticity axisymmetric formulation is typically employed. These equations are described in general form by Williams (1985) and in boundary layer form by Chung (1965). Useful descriptions of the Navier-Stokes equations for single component (variable density and constant density) flow can be found in many reference books. Landau and Lifshitz (1987), Howarth (1964), Sherman (1990), and White (1991) are recommended. The formulation for the gas and the liquid phases of the axisymmetric droplet problem complete with boundary, interface, and initial conditions can be found in Chiang (1990).

In the limiting case where there is no relative motion between the droplet and the gas, a spherically symmetric field exists for the gas field surrounding the droplet and for the liquid field. If a small relative velocity occurs, the droplet acceleration becomes so large that the relative velocity between the droplet and the surrounding gas immediately goes to zero. Therefore, in this limit, relative velocity remains negligible even as the gas velocity varies. Here, the fluid motion is reduced to a Stefan convection in the radial direction. Although our major interest will be in the forced convection case, it is helpful to discuss briefly this spherically symmetric case. All of the important issues in this case will also appear in the more general case.

2.1 Spherically-Symmetric Droplet Vaporization and Heating. Consider the case where a spherical droplet vaporizes with a radial flow field in the gas-phase. The vapor from the droplet convects and diffuses away from the droplet surface. Heat conducts radially against the convection toward the droplet interface. At the droplet surface, the heat from the gas partially accommodates the phase change and the remainder conducts into the liquid interior, raising the liquid temperature at the surface and in the interior of the droplet. This type of convection is named Stefan convection. In case of condensation, the Stefan convective flux becomes negative.

In some cases, the reactant vapor, diffusing away from the vaporizing droplet, can mix in the gas film with the other reactant, diffusing from the ambient gas, and react in an exothermic manner. The energy source enhances the droplet heating and vaporization. This can happen with a fuel droplet vaporizing in an oxidizing environment if the reaction time is not longer than the film diffusion time; otherwise, a flame must envelop many droplets if it is to occur. See Sirignano (1983).

The liquid does not move relative to the droplet center in this spherically symmetric case. Rather, the surface regresses into the liquid as vaporization occurs. Therefore, heat and mass transfer in the liquid occur due only to diffusion with a

Nomenclature (cont.)

V = liquid volume
$\dot{w}$ = chemical reaction rate
W = molecular weight
x = spatial coordinate
y = normal coordinate in boundary layer
Y = mass fraction
z = spatial coordinate

Greek Symbols

α = thermal diffusivity
β = Shvab Zeldovich variables
δ = distance ratio in Section 3
$\bar{\delta}$ = upstream distance for application of boundary condition
ϵ = species flux fraction
ϵ = correction in Section 3 for application of ambient conditions
η = Blasius coordinate
θ = void volume fraction
λ = thermal conductivity
μ = dynamic viscosity
ν = stoichiometric coefficient (mass of fuel per mass of oxygen)
ρ = density
τ = nondimensional time
τ_H = droplet heating time
τ_L = droplet lifetime
τ^* = droplet heating time with uniform temperature
ϕ = normalized streamfunction
φ = generic variable
χ = ratio of effective thermal diffusivity to thermal diffusivity
ψ = liquid volume fraction
Ψ = stream function
ω = velocity

Subscripts

0 = initial condition
∞ = conduction at infinity
eff = effective value
F = vapor or fuel vapor
H = related to thermal transfer
i = index for vectorial component, index for species component
j = index for vectorial component
e = edge of boundary layer
L = lift
ℓ = liquid
M = related to mass transfer
n, p = integers for numerical mesh points
N = nitrogen
O = oxygen
p = particle
P = product
s = droplet surface condition
wb = wet bulb

Superscript

k = index for droplet group

moving boundary but without convection. Here, we present the spherically symmetric isolated droplet equations. A quasi-steady assumption is made for the gas phase because diffusion of heat and mass in the gas is relatively fast compared to the liquid; this assumption weakens as we approach the critical pressure.

Continuity

$$\frac{\partial}{\partial r}(\rho u r^2) = 0 \quad \text{or} \quad \rho u r^2 = \text{constant} = \frac{\dot{m}}{4\pi} \tag{1}$$

Energy

$$\frac{\partial}{\partial r}(\rho u r^2 h) - \frac{\partial}{\partial r}\left(\lambda r^2 \frac{\partial T}{\partial r}\right) = -\rho r^2 Q \dot{w}_F \tag{2}$$

Vapor Species Conservation

$$L(Y_F) = \frac{\partial}{\partial r}(\rho u r^2 Y_F) - \frac{\partial}{\partial r}\left(\rho D r^2 \frac{\partial Y_F}{\partial r}\right) = \rho r^2 \dot{w}_F \tag{3}$$

Oxygen Species Conservation

$$L(Y_{\mathrm{O}}) = \rho r^2 \dot{w}_{\mathrm{O}} = \rho r^2 \dot{w}_F / \nu \tag{4}$$

Nitrogen Species Conservation

$$L(Y_{\mathrm{N}}) = 0 \tag{5}$$

Product Species Conservation

$$L(Y_P) = -\rho r^2 \dot{w}_F \left(\frac{\nu + 1}{\nu}\right) \quad \text{or} \quad Y_F + Y_{\mathrm{O}} + Y_{\mathrm{N}} + Y_P = 1 \tag{6}$$

In these equations, we assume very low Mach number (and therefore uniform pressure) and neglect Soret and Dufour effects and radiation. Also, we assume Fickian mass diffusion, Fourier heat conduction, and one-step chemical kinetics. In the limit of no chemical reaction, $Y_P = 0$ and $\dot{w}_F = 0$. Equations of state for ρ and h are also prescribed; in particular, a perfect gas is usually considered.

Typically, ambient conditions at $r = \infty$ are prescribed for Y_{O}, Y_{N}, Y_F, Y_P, and T. Interface conditions are also prescribed at the droplet surface. Temperature is assumed to be continuous across the interface. Phase equilibrium is assumed at the interface typically by the use of the Clausius-Clapeyron relation. Mass balance at the interface is imposed for each species.

$$\left.\frac{\dot{m}}{4\pi} Y_{i_s} - \rho D R^2 \frac{\partial Y_i}{\partial r}\right)_s = \frac{\dot{m}}{4\pi}\delta_{iF}, \quad i = \mathrm{O}, F, \mathrm{N}, P \tag{7}$$

where δ_{iF} is the Kronecker delta function.
For nonvaporizing species, radial convection and diffusion cancel each other. The right-hand side is nonzero only for the vaporizing species.

The energy balance at the interface equates the difference in conductive fluxes to the energy required to vaporize the liquid at the surface.

$$\left.\lambda R^2 \frac{\partial T}{\partial r}\right)_s = \left.\lambda_\ell R^2 \frac{\partial T}{\partial r}\right)_{\ell s} + \frac{\dot{m}}{4\pi} L = \frac{\dot{m}}{4\pi} L_{\mathrm{eff}} \tag{8}$$

where L_{eff} is an effective latent heat of vaporization.

In considering Eqs. (1) through (6), it should be realized that density is immediately related to temperature through an equation of state. Therefore, Eq. (1) can be considered to govern the radial gas velocity. Equations (2) through (6) are the second-order differential equations governing five quantities: temperature and the four mass fractions. Ten boundary or matching conditions would normally be required. We have a total of twelve conditions: five ambient conditions for the five quantities, five interface conditions given by Eqs. (7) and (8), a phase equilibrium condition at the interface, and a continuous temperature condition at the interface. Apparently, two extra conditions are presented that are needed because the problem has an eigenvalue character. The vaporization rate $\dot{m}$ and the heat entering the liquid phase $4\pi\lambda_\ell R^2 \, (\partial T/\partial r)_{\ell,s}$ are unknown a priori. This means that, if T_s were known, the gas-phase problem could readily be solved without examining the details of the liquid phase. Another valid viewpoint is that, if the heating rate of the liquid were known, the gas-phase problem including the interface temperature could be readily determined without consideration of the liquid-phase details. However, in the general problem, neither the surface temperature nor the liquid heating rate are known a priori. An analysis of heat diffusion in the liquid phase is required in order to provide an additional relationship between the liquid heating rate and the interface temperature.

In the special case of very fast chemistry, constant specific heat and unitary Lewis number ($\rho D = \lambda / c_p$) for the gas-phase, the gas-phase equations can be reduced to certain algebraic relations.

$$\dot{m} = 4\pi \left[\int_R^\infty \frac{dr}{\rho D r^2}\right]^{-1} \log(1 + B) \tag{9}$$

where

$$B \equiv \frac{h_\infty - h_s + \nu Q Y_{\mathrm{O}\infty}}{L_{\mathrm{eff}}} = \frac{\nu Y_{\mathrm{O}\infty} + Y_{Fs}}{1 - Y_{Fs}} \tag{10}$$

Note that Y_{Fs} is a function of T_s through the phase equilibrium relation. Therefore, Eqs. (8) and (10) relate interface temperature to liquid heating rate. When heating rate becomes zero, $L_{\mathrm{eff}} = L$, and Eq. (10) yields the wet bulb temperature for the droplet.

In the special case under consideration, it is convenient to present the solution in terms of Shvab-Zeldovich variables β which satisfy $L(\beta) = 0$. In particular, we have

$$\beta_1 \equiv Y_{\mathrm{O}} - Y_F/\nu; \quad \beta_2 \equiv Y_{\mathrm{O}} + Y_P/(1 + \nu);$$
$$\beta_3 = Y_{\mathrm{O}} + h/\nu Q; \quad \beta_4 = Y_{\mathrm{N}} \tag{11}$$

It is found that Eqs. (2) through (6) yield

$$\beta - \beta_\infty \sim \exp\left[-\frac{m}{4\pi}\int_r^\infty \frac{dr'}{\rho D (r')^2}\right] - 1 \tag{12}$$

In the limit of negligible Stefan convection, the first derivative terms in Eqs. (2) through (6) can be neglected yielding

$$\beta - \beta_\infty \sim -\frac{\dot{m}}{4\pi}\int_r^\infty \frac{dr'}{\rho D (r')^2} \tag{13}$$

Note that the same result can be found by a series expansion of Eq. (12) whereby the first term in the expansion gives the results with neglected Stefan flow. The constants of proportionality in Eqs. (12) and (13) are different for each of the four β functions and are determined from the interface conditions.

Equation (12) indicates a monotonic behavior with radius for the β functions. In the case where no exothermic reaction occurs in the gas film, a monotonic behavior for temperature and vapor mass fraction results. With chemical reaction, we have a peak in temperature and in product concentration occurring at the flame position. An infinitesimally thin flame assumption leads to certain simplifications in the determination of the profile in the reaction case. Without the thin flame assumption, the reacting case requires the integration of Eq. (4) coupled with Eqs. (11) and (12).

For very fast oxidation chemical kinetics, the reaction zone reaches the limit of zero thickness. Then $\beta_1 = Y_{\mathrm{O}}$ and $Y_F = 0$ outside of the flame zone while $\beta_1 = -Y_F/\nu$ and $Y_{\mathrm{O}} = 0$ inside the flame zone and $Y_F = Y_{\mathrm{O}} = 0$ at the flame zone. Now, determinations of Y_P and T from Eqs. (11) and (12) readily follow once the surface temperature is determined from the coupled liquid-phase solution.

The position of the flame zone can be determined for the thin flame case as

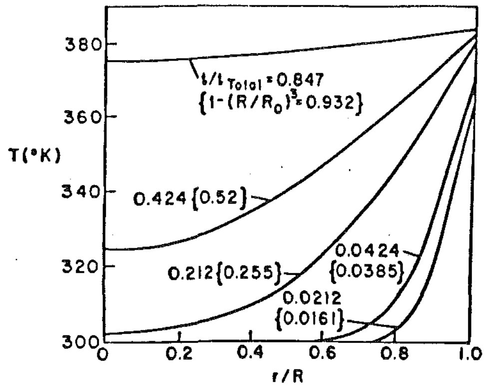

Fig. 1 Temporal and spatial variations of liquid temperature for spherically symmetric droplet vaporization. Temperature versus nondimensional radial coordinate for fixed fraction of droplet lifetime (or fixed vaporized fraction of original mass).

$$\frac{r_f}{R}=\frac{\log\left(\dfrac{1+\nu Y_{O\infty}}{1-Y_{Fs}}\right)}{\log(1+Y_{O\infty})} \tag{14}$$

Now, the solution of the equation for heat diffusion through the liquid phase can be considered to provide the necessary relation between the interface temperature and the liquid heating rate. That equation is written in spherically symmetric form

$$\frac{\partial T_\ell}{\partial t}=\alpha_\ell\left(\frac{\partial^2 T_\ell}{\partial r^2}+\frac{2}{r}\frac{\partial T_\ell}{\partial r}\right) \tag{15}$$

The time derivative is considered in the liquid phase although it is neglected in the gas phase because the liquid thermal diffusivity at subcritical conditions is much smaller than the gas-phase diffusivity. Gas-phase time derivatives are retained at near critical and supercritical conditions. In the most general case, Eq. (15) can be solved by finite-difference techniques although approximate techniques (Law and Sirignano, 1977; Sirignano, 1983) have been employed. The coupled solutions of Eqs. (11), (12), and (15) yield the final results.

The liquid heating time τ_H is defined as the time required for a thermal diffusion wave to penetrate from the droplet surface to its center and is of the order of $R_0^2/\alpha_\ell=\rho_\ell c_\ell R_0^2/\lambda_\ell$. From Eq. (9) with a constant value of ρD and from a relationship between the initial liquid droplet mass and its initial radius, the droplet lifetime τ_L can be estimated as $\rho_\ell R_0^2/[2\rho D\log(1+B)]$. The ratio of heating time τ_H to lifetime τ_L is estimated by

$$\frac{\tau_H}{\tau_L}=\frac{2\rho D c_\ell}{\lambda_\ell}\log(1+B)=2\frac{\lambda}{\lambda_\ell}\frac{c_\ell}{c_p}\log(1+B) \tag{16}$$

The most interesting effect appears through the temperature dependence of the parameter B. The transient behavior is found to persist over a large portion of the droplet lifetime when the ambient temperatures are high, especially for higher molecular weight liquids.

Typical results from Law and Sirignano (1977) for the liquid-phase temperature are found in Fig. 1 which portrays a thermal wave diffusing from the droplet surface toward its center. The surface regression is shown in Fig. 2.

There are several special cases of interest. In the first case, we consider that the droplet heating time is short compared to the lifetime. This implies that the droplet interior is quickly heated since a thermal wave diffuses from the droplet surface to its center in a short time compared to the lifetime. As a consequence, a nearly uniform liquid temperature is established quickly. Many authors have employed the simplifications of this case, sometimes beyond its range of validity. See Law (1976) and El-Wakil et al. (1956), for example. Equation (16) shows that this case can occur if $\lambda \ll \lambda_\ell$, $c_\ell \ll c_p$, or B is small. Ambient temperatures of a few hundred degrees centrigrade can lead to a small B value.

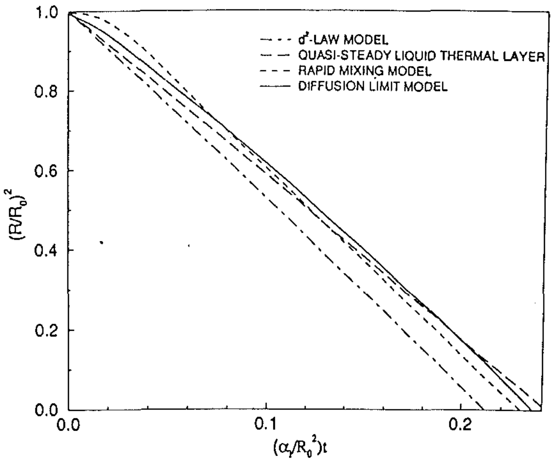

Fig. 2 Comparison of four models for spherically symmetric droplet vaporization. Nondimensional radius squared versus nondimensional time.

For this case, further classification can be made with regard to the temporal behavior of the liquid temperature. Equation (15) can be integrated over the droplet volume accounting for the zero gradient at the droplet center and for the regressing surface. Furthermore, it can be assumed in this case that surface temperature is approximately equal to the volumetric average liquid temperature. As a result, we have that the heat flux entering the liquid is

$$\dot{q}_\ell=mc_\ell\frac{dT_\ell}{dt} \tag{17}$$

where m is the instantaneous droplet mass, T_ℓ is the average liquid temperature, and $\dot{q}_\ell=4\pi R^2\lambda_\ell\,(\partial T/\partial r)_{\ell,s}$. This indicates that the liquid temperature would continue to rise until the heat flux $\dot{q}_\ell$ became zero, i.e., the wet bulb temperature T_{wb} is reached. The characteristic time τ^* for this heating depends upon the magnitudes of the thermal inertia mc_ℓ and the heat flux q_ℓ. There can be shown to be two possibilities; either $\tau^*<\tau_H$ or $\tau^*>\tau_H$ for Eq. (17). However, if $\tau^*<\tau_H$, Eq. (17) is not valid because the temperature remains nonuniform on that time scale. Equation (17) is only valid and interesting if $\tau^*>\tau_H$.

An estimate for τ^* can be obtained by using Eqs. (8) and (10) to yield $\dot{q}_\ell$ which is then substituted in Eq. (17). In particular, $\dot{q}_\ell$ is represented by a truncated Taylor series expansion about the wet bulb temperature point. The result is

$$\frac{\tau^*}{\tau_H}=\frac{1}{3}\frac{\lambda_\ell}{\lambda}\left[\frac{1}{\log\dfrac{1+\nu Y_{O\infty}}{1-Y_{Fs}}}\right]\times\left[\frac{\nu Y_{O\infty}+Y_{Fs}}{1-Y_{Fs}+\dfrac{L^2}{c_pR}\dfrac{Y_{Fs}}{T_S^2}\left(\dfrac{1+\nu Y_{O\infty}}{1-Y_{Fs}}\right)}\right] \tag{18}$$

where Y_{Fs} is evaluated at the wet bulb temperature. A Clausius-Clapeyron relationship has been assumed to describe phase equilibrium. Furthermore, it can be shown from Eqs. (8) and (10) that, at the wet bulb temperature,

$$Y_{Fs}=\frac{\dfrac{h_\infty-h_{wb}+\nu QY_{O\infty}}{L}-\nu Y_{O\infty}}{1+\dfrac{h_\infty-h_{wb}+\nu QY_{O\infty}}{L}} \tag{19}$$

which can be substituted above.

It can be concluded that the characteristic time τ^* is bounded below by a quantity of order τ_H. Therefore, this case can be divided into two subcases. In one situation, the wet bulb temperature is reached in a time of the same order of magnitude as the heating time which is very short compared to the lifetime. Here, liquid temperature can be considered constant with $L_{\text{eff}} = L$. Then, Eqs. (9) and (10) and the phase equilibrium relation for $Y_{Fs}(T_s)$ immediately yield the vaporization rate $\dot{m}$ and the droplet temperature $T_s = T_{wb}$. When ρD is constant, integration of Eq. (9), where $m = 4\pi R^3 \rho_\ell / 3$, yields the well-known d^2 law. That is,

$$(R/R_0)^2 = 1 - t/\tau_L \tag{20}$$

Note that the previously given estimate for τ_L is exact here with B calculated using $L_{\text{eff}} = L$.

The second subcase involves a characteristic time τ^* substantially larger than τ_H and perhaps comparable to τ_L. This requires the integration of Eq. (17) (coupled with Eq. (10) that relates $\dot{q}_L$ to $T_\ell = T_s$). The results for such an integration are shown in Fig. 2. The use of an average temperature tends to underestimate the surface temperature during the early vaporization period because the thermal energy is artificially distributed over the droplet interior. As a result, the early vaporization rate for this subcase is less than found in the general case by solving the diffusion equation (15). However, because the surface temperature is artificially low at first, more heat enters the droplet and ultimately it vaporizes faster than the general case as shown in Fig. 2.

Another interesting case occurs when the heating time is much longer than the lifetime. Then, a thin thermal layer is maintained in the liquid near the surface; the regression rate is too large for the thermal wave to penetrate faster than the regressing surface. This case can occur if λ_ℓ is small or if c_ℓ or B is large. Very large ambient temperatures of a few thousand degrees Kelvin can lead to this situation. The thin thermal layer can be considered quasi-steady so that the conductive heat flux through the surface balances the liquid convective rate toward the surface. (Convection here is measured relative to the regressing surface.) We have therefore the approximation that

$$\left.\lambda_\ell \frac{\partial T_\ell}{\partial r}\right)_s = \rho_\ell U_\ell c_\ell (T_s - T_{\ell 0}) \quad \text{or} \quad L_{\text{eff}} = L + c_\ell (T_s - T_{\ell 0}) \tag{21}$$

Equations (10) and (21) together with the phase equilibrium relation yield T_s (which here is constant with time). Then Eq. (9) yields $\dot{m}$ and subsequently $R(t)$. Since L_{eff} is here a constant with larger positive value than L, another d^2 relationship results but with a lower absolute value of the slope on a time plot. Equation (17) can be employed with τ_L now calculated using Eq. (18).

The two d^2-law results are also plotted in Fig. 2 for the purpose of comparison with the general case. The general case is the only one of the three cases discussed so far that considers an initial transient. The first (well-known) d^2-law neglects the initial thermal diffusion across the droplet interior while the other d^2-law neglects the initial diffusion across the thin layer.

Note that the droplet lifetimes vary little from model to model in Fig. 2. However, the local slope of the curves (related to instantaneous vaporization rates) do vary more significantly. This variation implies that the vaporization rate as a function of spacial position for a droplet moving through a volume can depend significantly upon the particular model.

There are various complications that occur when a multicomponent liquid is considered (Landis and Mills, 1974 and Sirignano and Law, 1978). Different components vaporize at different rates, creating concentration gradients in the liquid phase and causing a liquid-phase mass diffusion. The theory requires the coupled solutions of liquid-phase species continuity equations, multicomponent phase equilibrium relations (typically Raoult's law), and the gas-phase multicomponent energy and species continuity equations. Liquid-phase mass diffusion is commonly much slower than liquid-phase heat diffusion so that thin diffusion layers can occur near the surface especially at high ambient temperatures where the surface regression rate is large. The more volatile substances tend to vaporize faster at first until their surface concentrations values are diminished and further vaporization of those quantities becomes liquid-phase-mass-diffusion controlled.

Liquid-phase mass diffusion also becomes important at pressures near or above the critical pressure of the liquid even if it initially is a pure component. Ambient gases dissolve in the liquid to a significant extent as the critical pressure is approached; then mass diffusion occurs in the liquid phase. It is noteworthy that the actual critical pressure and temperature vary spatially with composition. Typically, the dependence on composition is very nonlinear and the critical pressure for a mixture can be greater than the critical pressure of any component. Therefore, subcritical conditions can exist at an interface with a distinct discontinuity between liquid and gas even if the pressure is above the critical pressure of the original pure component in the droplet. See Sheun et al. (1992) and Delplanque and Sirignano (1993) for detailed analyses of these problems.

The spherically symmetric droplet problem introduces many fundamental physical issues that remain in the problem as the flow field becomes more complex due to the relative motion between the gas and the droplet. The effects of transient heat conduction and mass diffusion, phase equilibrium at the interface, and the regressing liquid surface remain as the relative flow is introduced. The effects of relative motion are discussed in the following subsection.

2.2 Convective Droplet Vaporization. In most applications, droplets in a spray will be moving at some relative velocity to the surrounding. The Reynolds number based upon the relative velocity, droplet radius, and gas properties can be as large as the order of one hundred. Convective boundary layers and separated near wakes can therefore surround the droplet. For a liquid-gas (or liquid-liquid) interface, shear stress and tangential velocity do not generally become zero at the same point; the separation point is defined as the zero velocity point where the streamline actually leaves the surface. The boundary layer enhances the heat and mass transport rates over the values for the spherically symmetric droplet. Furthermore, the shear force on the liquid surface causes an internal circulation that enhances the heating of the liquid. As a result, vaporization rate increases with increasing Reynolds number.

One commonly used empirical result is the Ranz and Marshall (1952) correlation that corrects the spherically symmetric vaporization rate $\dot{m}_{ss}$ as follows:

$$\dot{m} = \dot{m}_{ss}(1 + 0.3\text{Pr}^{1/3}\text{Re}^{1/2})$$

This formula is based upon certain quasi-steady, constant radius, porous wetted sphere experiments. A similar correlation is reported by Frossling (1938). Those experiments do not account for transient heating, regressing interface, and internal circulation. There is a need for more fundamental experimental and theoretical analyses.

The calculations for a vaporizing droplet that is moving through a gas require the solution of a complex set of nonlinear coupled partial differential equations. The problem is inherently unsteady since droplet size is continually changing due to vaporization; relative velocity is also changing due to droplet drag; and temperatures are varying on account of droplet heating. The problem can be considered to be axisymmetric for a spherical droplet. Since the boundary is moving due to droplet vaporization, adaptive gridding is required for finite-difference computations.

The configuration to be studied for an isolated droplet is an axisymmetric flow as depicted in Fig. 3. Droplet can turn in a flow or the gas flow can change direction but typically

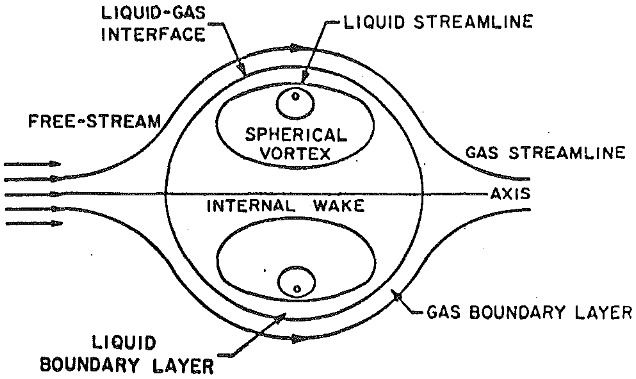

Fig. 3 Vaporizing droplet with relative gas-droplet motion and internal circulation

the characteristic time for a change of vectorial direction of the relative velocity is long compared to the residence time for an element of gas to flow past the droplet. Therefore, axisymmetry is a very good approximation. The droplet still retains a spherical shape provided that the Weber number remains of order unity or less.

The evaluations of the vaporization rate and heating rate have been performed by both approximate analyses and exact solution of the coupled gas and liquid flow equations by finite-difference calculations. These analyses and their results will be discussed in the following sections.

Approximate Analyses for Gas-Phase Boundary Layer. There exist various analyses that describe the behavior of a quasi-steady, laminar, gas-phase boundary layer that exists at the interface of a droplet with Reynolds number (based upon relative velocity) that is larger than unity. The earliest studies were performed by Prakash and Sirignano (1978, 1980) for single component liquids and Lara-Urbaneja and Sirignano (1981) and Law et al. (1977) for multicomponent liquids. Prakash and Sirignano (1978, 1980) and Lara-Urbaneja and Sirignano (1981) used integral boundary layer techniques to analyze the gaseous flow over a vaporizing droplet surface. These works were the first to identify the essential physics of the convective droplet vaporization problem. The analyses were made earlier to those to be described in this subsection and also were more complex without offering clear advantages. They were not yielding as complete and as detailed information as the finite-difference solution of the Navier-Stokes elliptic flow equations. At the same time, the integral techniques were too complex to incorporate into extensive spray computations.

Later analyses that will be examined more closely here were developed by Sirignano (1979), Tong and Sirignano (1982a, 1982b, 1983, 1986a, 1986b), and Abramzon and Sirignano (1989). These analyses are strictly limited to boundary layers and do not predict the behavior in the near wake. Some of the analyses can predict the point of separation on the droplet surface. They use either integral techniques or local similarity assumptions for the analysis. Since most of the heat and mass transport for the Reynolds number range of interest (order one hundred and less) occurs before the point of separation, vaporization, and droplet heating rates can be well predicted. However, since form drag is competitive in magnitude with friction drag, and drag coefficient cannot even be approximated by these analyses; input is needed for these values.

Under the assumption that the droplet Reynolds number is large compared to unity (but not so large that instability or turbulence occurs), a thin, gas-phase boundary layer exists on the surface of the droplet. In our application, we can reasonably neglect kinetic energy and viscous dissipation. Also, $\mathrm{Pr}=\mathrm{Sc}=1$ and one-step chemistry can be assumed following Tong and Sirignano. The x, y coordinates are tangent and normal to the droplet surface, respectively, with r representing the distance from the axis of symmetry. The governing equations in quasi-steady form are

Continuity

$$\frac{\partial(\rho u r)}{\partial x}+\frac{\partial(\rho v r)}{\partial y}=\mathrm{O} \tag{22}$$

x-Momentum

$$L\left(\frac{u}{u_e}\right)=\rho u\frac{\partial}{\partial x}\left(\frac{u}{u_e}\right)+\rho v\frac{\partial}{\partial y}\left(\frac{u}{u_e}\right)-\frac{\partial}{\partial y}\left(\mu\frac{\partial}{\partial y}\left(\frac{u}{u_e}\right)\right)$$
$$=\Bigg[\frac{\rho_e}{\rho}-\frac{u}{u_e}\Bigg)^2\Bigg]\rho\frac{du_e}{d_x}\quad\text{where}\quad\frac{dp_e}{dx}=\rho_e u_e\frac{du_e}{dx}. \tag{23}$$

Note that $u_e(x)$ is the potential flow velocity immediately external to the boundary layer. The y-momentum equation states that pressure gradients in the y direction are negligible.

Energy

$$L(h)=-Q\dot{w}_F \tag{24}$$

Species Conservation

$$L(Y_i)=\dot{w}_i\quad i=\mathrm{O},F,P,\mathrm{N} \tag{25}$$

The x-momentum equation can be further simplified as the ambient temperature is much higher than the surface temperature and the ambient velocity is much higher than the tangential surface velocity. The right-hand side of Eq. (23) goes to zero at the outer edge of the boundary layer; also, it becomes very small at the droplet surface. The ad hoc assumption can be made following Lees (1956) that the right-hand side is everywhere zero because the quantity in square brackets is negligibly small. Note that the pressure gradient can still be nonzero; it is the transverse variation of the dynamic pressure that is small.

Two interesting cases are readily studied: the stagnation point flow ($r=x$ and $u_e=ax$) and the shoulder region ($\theta=\pi/2$, $r=R$, $u_e=(3/2)U_\infty$) where the pressure gradient is zero and the flow locally behaves like a flat plate flow. That is, because the right-hand side of Eq. (23) is negligible, local similarity is believed to be a very good approximation. The well-known similarity solution

$$u=u_e(x)\frac{df}{d\eta}(\eta)\equiv u_e(x)f'(\eta)$$

is found where $f(\eta)$ satisfies the Blasius equation and

$$\eta=\frac{ru_e\int_0^y\rho dy'}{\left[\int_0^x\rho_e\mu_e u_e r^2 dx'\right]^{1/2}}$$

The vaporization rate per unit area is given by

$$\rho v)_s=-Af(0) \tag{26}$$

Note that $A=(2a\rho_e\mu_e)^{1/2}$ for the stagnation point and $\rho_e\mu_e[u_e/2\int_0^x\rho_e\mu_e dx']^{1/2}$ for the shoulder region.

Two of the three boundary conditions for the third-order, nonlinear ordinary different equation governing $f(\eta)$ are

$$\frac{df}{d\eta}(0)=u_s/u_e;\quad\frac{df}{d\eta}(\infty)=1 \tag{27}$$

The third boundary condition will be developed from Eq. (26) and requires a coupling with the solution of the energy equation.

The definitions given in Eq. (11) can be used to solve Eqs. (24) and (25) for the case of rapid chemical kinetics. With the simplified version of Eq. (23) discussed above, it can be shown that for all of the β functions

$$\beta=\beta_s+\frac{u-u_s}{u_e-u_s}(\beta_e-\beta_s)=\beta_s+\frac{f'(\eta)-f'(0)}{1-f'(0)}(\beta_e-\beta_s) \tag{28}$$

Equations (24) and (25) are second-order partial differential equations normally associated with five boundary conditions at the outer edge of the boundary layer and five boundary conditions at the droplet surface. The ambient conditions for temperature (or enthalpy) and mass fractions are provided. Five boundary conditions at the droplet surface are given by conservation of energy and species mass flux as follows

$$\lambda \frac{\partial T}{\partial y}\Big)_{g,s} = \lambda_\ell \frac{\partial T}{\partial y}\Big)_{\ell,s} + \rho v)_s L \equiv \rho v)_s L_{\text{eff}} \tag{29}$$

$$\rho v)_s Y_{Fs} - \rho D \frac{\partial Y_F}{\partial y}\Big)_s = \rho v)_s \tag{30}$$

and

$$\rho v)_s Y_{i,s} - \rho D \frac{\partial Y_i}{\partial y}\Big)_s = 0; \quad i = \mathrm{O}, P, \mathrm{N} \tag{31}$$

In addition, we have a phase equilibrium relation and a continuity condition on the temperature at the interface. The extra two conditions are required because the vaporization rate (per unit area) $\rho v)_s$ and the liquid heating rate (per unit area) $\lambda_\ell (\partial T/\partial y)_s$ are not given a priori. They are eigenvalues of the problem. Complete determination requires the coupling with the heat transport problem in the liquid phase.

From these boundary conditions, Eq. (28), and Eq. (10), we can develop the third boundary condition for the Blasius differential equation. We find that

$$\frac{f''(0)}{[f(0)][1-f'(0)]} = \frac{1}{B} \tag{32}$$

Actually, the Blasius function depends upon η, B, and u_s/u_e since B and u_s/u_e appear in the boundary conditions (27) and (32). So $f(0)$ implies $f(0, B, u_s/u_e)$. Furthermore, $f(0)$ is negative for the vaporization conditions. It can also be shown that

$$\lambda_\ell \frac{\partial T}{\partial y}\Big)_{\ell,s} = -Af(0)\left[\frac{h_e - h_s + Q\nu Y_{O\infty}}{\dfrac{1+\nu Y_{O\infty}}{1-Y_{Fs}} - 1} - L\right] \tag{33}$$

An interesting comparison is made between this convective case and the spherically symmetric case. Equations (26), (29), and (33) can be combined to reproduce an equation exactly like Eq. (10) except that h_e appears instead of h_∞. This demonstrates a great similarity in the physics of the two cases. Furthermore, the same formula for the wet bulb temperature results in the spherically symmetric case and for the stagnation point and shoulder region under similarity conditions.

The flow is expected to separate shortly after the point of zero pressure gradient. Therefore, most of the heat and mass transport occurs on the forward side or the "shoulders" of the droplet; little occurs on the downstream side. The above analyses for the stagnation region and for the shoulder region can be used to construct a reasonable estimate for the global liquid heating rate and vaporization rate.

From this analysis, Sirignano (1979) has shown that the Nusselt number Nu follows a certain relationship. In particular,

$$\mathrm{Nu} = \frac{k[-f(0)]}{B} \mathrm{Re}^{1/2} \tag{34}$$

where k is a positive nondimensional coefficient of order unity which is determined by averaging the heat flux over the droplet surface in an approximate manner (based upon the two local solutions discussed above). Again, $f(0)$ is negative with vaporization. Also, we have the global vaporization rate via a similar averaging process

$$\dot{m} = \mu_e R[-f(0)]\mathrm{Re}^{1/2} \tag{35}$$

The results (34) and (35) are based upon an analysis limited to high droplet Reynolds number. There exists an important domain between the spherically symmetric case (zero Reynolds number case) and the thin laminar boundary layer case (high Reynolds number case). A more robust vaporization model that covers a wide range of Reynolds number is needed. This is especially important since a given droplet can experience a range of Reynolds number during its lifetime. Typically, the droplet Reynolds number will decrease with time as the droplet diameter and the relative velocity decrease. There are exceptions to the monotonic behavior; e.g., oscillatory ambient flow where large fluctuations of relative velocity (including change in direction) can occur.

One ad hoc method for developing a more robust model was presented by Abramzon and Sirignano (1989). The Nusselt number and the vaporization rate are each given by a composite of two asymptotes (zero Reynolds number limit and large Reynolds number limit). We have that

$$\mathrm{Nu} = \frac{2\log(1+B)}{B}\left[1 + \frac{k}{2}\frac{[-f(0)]}{2\log(1+B)}\mathrm{Re}^{1/2}\right] \tag{36}$$

$$\dot{m} = 4\pi\rho D R \log(1+B)\left[1 + \frac{k}{2}\frac{[-f(0)]}{\log(1+B)}\mathrm{Re}^{1/2}\right] \tag{37}$$

Note that $f(0) = f(0, u_s/u_e, B)$ reaches a finite limit as B becomes large. The above results therefore disagree strongly with the Ranz-Marshall or Frossling correlations. The problems with those correlations are that they were developed for only a very narrow range of B values.

Abramzon and Sirignano actually made two further extensions. First, they considered general values for Schmidt, Prandtl, and Lewis numbers, relaxing the unitary conditions and allowing for variable properties. Second, they considered a range of Falkner-Skan solutions to develop the average transport rates across the gas boundary layer on the droplet surface. With the definitions

$$B_H = \frac{h_e - h_s}{L_{\text{eff}}} \quad \text{and} \quad B_M = \frac{Y_{Fs} - Y_{F\infty}}{1 - Y_{Fs}} \tag{38}$$

they demonstrated that

$$\mathrm{Nu} = 2\frac{\log(1+B_H)}{B_H}\left[1 + \frac{k}{2}\frac{\mathrm{Pr}^{1/3}\mathrm{Re}^{1/2}}{F(B_H)}\right];$$

$$\mathrm{Sh} = 2\frac{\log(1+B_M)}{B_M}\left[1 + \frac{k}{2}\frac{\mathrm{Sc}^{1/3}\mathrm{Re}^{1/2}}{F(B_M)}\right]$$

$$\dot{m} = 4\pi\frac{\lambda R}{c_p}\log(1+B_H)\left[1 + \frac{k}{2}\frac{\mathrm{Pr}^{1/3}\mathrm{Re}^{1/2}}{F(B_H)}\right]$$

$$= 4\pi\rho D R \log(1+B_M)\left[1 + \frac{k}{2}\frac{\mathrm{Sc}^{1/3}\mathrm{Re}^{1/2}}{F(B_M)}\right] \tag{39}$$

Note that, when $\mathrm{Pr} = \mathrm{Sc} = 1$, we have that $B_M = B_H$. Otherwise,

$$B_H = (1+B_M)^a - 1 \quad \text{where} \quad a \equiv \frac{c_{pF}}{c_p}\frac{1}{\mathrm{Le}}\,\frac{1 + \dfrac{k}{2}\dfrac{\mathrm{Re}^{1/2}}{F(B_M)}}{1 + \dfrac{k}{2}\dfrac{\mathrm{Re}^{1/2}}{F(B_H)}} \tag{40}$$

A correlation of numerical results shows that

$$F(B) = (1+B)^{0.7}\frac{\ln(1+B)}{B}$$

$$\text{for } 0 \le B_H,\ B_M \le 20 \text{ and } 1 \le \mathrm{Pr},\ \mathrm{Sc} \le 3. \tag{41}$$

Other approximate or asymptotic techniques have been utilized to solve related problems. Hadamard (1911) and Rybczynski (1911) solved for the creeping flow around a nonvaporizing liquid droplet. Acrivos and Taylor (1962) and Acrivos and Goddard (1965) analyzed the heat transfer for this type of flow and estimated the Nusselt number. Harper and Moore (1968) and Harper (1970) solved the high Reynolds number nonvaporizing droplet; boundary layers on both sides of the droplet interface were analyzed. Rangel and Fernandez-Pello (1984) studied the high Reynolds number vaporizing droplet with an isothermal liquid assumption. Chung et al. (1984a, 1984b) and Sundararajan and Ayyaswamy (1984) studied condensing droplets by perturbation and numerical methods.

In the case where many components exist in the liquid phase, it is necessary to track the vapor components individually as the species advect and diffuse through the gas phase. If there are n vaporizing components in the liquid, an additional $n-1$ field equations of the form of Eq. (25) and an additional $n-1$ boundary conditions of the form of Eq. (30) must be added to the system. Also, a phase equilibrium relationship is required for each component and the chemical source term in the energy equation (24) must be modified.

The gas-phase equations are strongly coupled to the liquid-phase equations through the continuity of velocity and temperature and the balances of mass, force, and energy. See, for example, Eqs. (27), (29), (30), and (32).

Liquid-Phase Flows. The jump in shear stress across a liquid-gas interface equals the gradient of surface tension (Levich, 1962). Sirignano (1983) argues that generally, the temperature and composition variations along the surface of a droplet are too small to cause a significant gradient of surface tension. Therefore, we consider a continuity of shear stress across the interface.

The liquid-phase responds to the viscous shear force at the interface by circulating within the droplet. Toroidal stream surfaces in the liquid result with low velocities. Due to the larger liquid density, the Reynolds number for the internal circulation (based upon droplet diameter, maximum liquid velocity, and liquid properties) can be of the same order of magnitude as or higher than the Reynolds number for the gas flow over the droplet. Peclet numbers are even higher in the liquid because of the large Prandtl and Schmidt numbers. Heat and mass transport in the liquid will therefore behave in a highly dissimilar fashion to the transport of momentum or vorticity. The analysis of the hydrodynamics in the approximate models differs substantially from the analyses of heat and mass transport on account of the large Prandtl and Schmidt numbers.

It is convenient to address the incompressible, liquid-phase hydrodynamics by the use of the vorticity-stream-function formulation. The vorticity equation can be developed by taking the curl of the momentum equation. For an incompressible fluid, we have

$$\frac{D\omega}{Dt}=\omega\cdot\nabla\mathbf{u}+\nu\nabla^2\omega \tag{42}$$

In a planar flow, ω and $\mathbf{u}$ are orthogonal. So, the first term on the right-hand side becomes zero in that case. Therefore, in the inviscid limit, the vorticity vector, ω, is constant along a particle path. In the case of a non-swirling axisymmetric flow, ω is always directed in the local θ direction. Then, it can be shown that

$$\omega\cdot\nabla\mathbf{u}=\frac{\omega v}{\tilde{r}}\mathbf{e}_\theta \tag{43}$$

where v is the radial component of velocity and $\tilde{r}$ is the radial coordinate in cylindrical coordinates. In the inviscid limit, it follows that $\omega/\tilde{r}$ is constant along a particle path with magnitude of $\omega/\tilde{r}$. In the steady (or quasi-steady) liquid flow, the particle path is a closed streamline so that $\omega/\tilde{r}$ is a function of the streamfunction ψ. Note that the Prandtl number and the Schmidt number for a typical liquid are large compared to unity. Diffusion of heat and mass are slow, therefore, compared to diffusion of vorticity in the liquid. A quasi-steady hydrodynamic behavior is established in a short time compared to the transient time for heating or mixing. It is also assumed that the transient time is sufficiently short so that the hydrodynamics instantaneously adjusts to droplet diameter changes resulting from vaporization. In our simplified models, quasi-steady hydrodynamic behavior is assumed, while transient heating is allowed.

The Hill's spherical vortex (Lamb, 1945; Batchelor, 1990) is a well-known solution of Eqs. (42) and (43) in the inviscid limit that also satisfies matching interface conditions with an external potential flow. In this special case, $\omega/\tilde{r}$ has the same constant value for all values of the stream function. It has been shown that

$$\omega=5\tilde{A}r\sin\theta=5\tilde{A}\tilde{r} \tag{44}$$

$$\psi=-\frac{1}{2}\tilde{A}r^2(R^2-r^2)\sin^2\theta=-\frac{1}{2}\tilde{A}\tilde{r}^2(R^2-(\tilde{r}^2+z^2)) \tag{45}$$

$$=-\frac{3}{4}U\frac{\tilde{r}^2}{R^2}(R^2-\tilde{r}^2-z^2) \tag{46}$$

Note that U is the instantaneous relative velocity between the droplet and the ambient gas. The maximum potential flow velocity at the interface is 3/2 times that value. We will not assume in our analysis that a potential flow exists immediately near the surface; rather, allowance is made for a viscous boundary layer. So, we consider $\tilde{A}$ to be the liquid vortex strength and relate it simply to the maximum velocity at the liquid surface which can be an order of magnitude less (depending upon density and viscosity) than the extrapolated potential flow velocity value. In particular,

$$\tilde{A}=U_{\max}/R \tag{47}$$

Therefore, Eq. (46) is neglected when the viscous boundary layer is considered. Rather, Eqs. (45) and (47) are employed.

It is convenient to define the nondimensional variables $\phi=(8\psi\tilde{A}R^4)+1$ and $s=r/R$. Then

$$\phi=1-4s^2(1-s^2)\sin^2\theta \tag{48}$$

Note that $\phi=1$ at the interface ($s=1$) and at the center of the internal wake ($\theta=0$, $\theta=\pi$) and that $\phi=0$ at the vortex center ($s=1/\sqrt{2}$ and $\theta=\pi/2$).

The above solution has been established effectively as a high Reynolds number limiting behavior. That is, the viscous term has been neglected in the derivation so that an inviscid solution for the internal liquid flow results. The low Reynolds number quasi-steady limiting behavior is given by the Hadamard-Rybczynski solution (Hadamard, 1911; Rybczynski, 1911; Batchelor, 1990; Lamb, 1945). There, the inertial term in both the surrounding gas and the interior liquid is neglected. The remaining linear system is solved by separation of variables. The solution in external phase differs significantly from the high Reynolds number solution. The most interesting result is that the Hill's spherical vortex solution given by Eqs. (44), (45) or (48), and (47) applies for the Hadamard-Rybczynski low Reynolds number solution. This can be explained by the fact that the vector $\omega=\omega\mathbf{e}_\theta=5\tilde{A}\tilde{r}\mathbf{e}_\theta$ actually satisfies Laplace's equation, so that the viscous term in Eq. (42) goes to zero without assuming zero viscosity. (Note the scalar ω is not harmonic, however.) Viscosity only affects the value of the constant $\tilde{A}$ through the interface matching process. Hill's spherical vortex solution actually applies over a wide range of Reynolds number; in the vorticity equation, both the inertial (nonlinear) terms and the diffusion (viscous) term are individually equal to zero. In the original momentum equation, the viscous term balances exactly the pressure gradient term and the inertial (nonlinear) terms are identically zero. This fortuitous character is shared with Couette and Poiseuille flows. This low Reynolds solution has not been extended to the case of vaporizing droplets where it might provide the basis for an interesting perturbation on the spherically symmetric vaporization case.

In a large Peclet number situation, heat and mass transport within the droplet will involve a strong convective transfer along the streamline with conduction primarily normal to the stream surface. In the limit of zero Peclet number, only conduction occurs. Over the full range of Peclet number, the heat and mass transport problems are axisymmetric and unsteady. With a certain coordinate transformation, the large Peclet number problem can be cast as a one-dimensional, unsteady problem.

In place of the spherical coordinates r and θ, we can use the streamfunction ψ (a measure of distance normal to the streamsurface) and ξ (a measure of distance in the local flow direction). The azimuthal coordinate η is maintained in the transformation. There is no variation in the η direction due to the axisymmetric and, for rapid circulation (high Peclet number), the variation in the ξ direction is negligible. The only variation therefore comes due to conduction in the ψ direction. Transforming the coordinates and averaging temperature along the streamsurface, we find that the liquid-phase energy equation becomes

$$F(\psi)\frac{\partial T}{\partial t}=\alpha_\ell\frac{\partial}{\partial\psi}\left(G(\psi)\frac{\partial T}{\partial\psi}\right) \tag{49}$$

where the following definitions have been made for integrals over the closed fluid path.

$$F(\psi)=\oint\frac{h_\xi d\xi}{u_\ell}=\frac{8}{\tilde{A}R}g_1(\phi)\text{ and }G(\psi)=\oint\frac{h_\eta h_\xi}{h_\psi}d\xi=\frac{\tilde{A}R^5}{8}g_2(\phi) \tag{50}$$

Note that h_η, h_ξ, and h_ψ are scale factors of the transformation and $u_1(\psi, \xi)$ is the local velocity which is tangential to the stream surface (Prakash and Sirignano, 1978, 1980). The differential $h_\xi d\xi$ is an element of length along the streamline and $(h_\xi/u_\ell)d\xi$ is a differential Lagrangian time; the cyclic integral $F(\psi)$ is therefore the circulation time. It can be shown that

$$V(\psi)=2\pi\int_0^\psi F(\psi')d\psi' \quad\text{and}$$

$$V(\phi, t)=2\pi R^3(t)\int_0^\phi g_1(\phi')d\phi' \tag{51}$$

gives the volume enclosed by the stream surface ψ. Note that here ψ is referenced to the vortex center where its value is set to zero, with the maximum value at the droplet surface. Using ϕ as defined by Eq. (48), we can state that

$$V(\psi)=V(R(t), \phi)=V(t, \phi)\quad\text{and}\quad\left.\frac{\partial\phi}{\partial t}\right)_\psi=-\frac{\left.\frac{\partial V}{\partial t}\right)_\phi}{\left.\frac{\partial V}{\partial\phi}\right)_t}$$

It follows that

$$\left.\frac{\partial T}{\partial t}\right)_\psi=\left.\frac{\partial T}{\partial t}\right)_\phi-\frac{\left.\frac{\partial V}{\partial t}\right)_\phi}{\left.\frac{\partial V}{\partial\phi}\right)_t}\frac{\partial T}{\partial\phi} \tag{52}$$

Combination of Eqs. (49), (50), and (52) leads to the following one-dimensional form of the diffusion equation

$$\frac{\partial T}{\partial\tau}=a(\phi, \tau)\frac{\partial^2T}{\partial\phi^2}+b(\phi, \tau)\frac{\partial T}{\partial\phi} \tag{53}$$

where

$$\tau=\alpha_\ell t/R_0^2;\quad a(\phi, \tau)=(R_0/R)^2g_2(\phi)/g_1(\phi)$$

and

$$b(\phi, \tau)=(R_0/R)^2g_2'(\phi)/g_1(\phi)+(3/R)(dR/dt)\int_0^\phi g_1(\phi')d\phi'/g_1(\phi)$$

where $g_2'(\phi)$ is the derivative and ϕ' is a dummy variable.

Then Eq. (53) can be solved with proper matching conditions at the interface, i.e., Eqs. (30), (31), and (33) plus the phase-equilibrium condition and continuity of temperature. A boundary condition at $\phi=0$, the vortex center, prescribes that the heat flux goes to zero there.

The liquid transient heating phenomenon with internal circulation then involves unsteady heat conduction from $\phi=1$ (the warm droplet surface and the warm axis of symmetry) toward $\phi=0$ (the relatively cool vortex center). Temperature is a monotonically increasing function of ϕ with the gradient diminishing with time. The limit of uniform but time-varying temperature results as the liquid thermal diffusivity goes to infinity. Contrary to earlier beliefs by some investigators, the *uniform temperature limit does not result from infinitely rapid* internal circulation. As shown above, infinitely fast circulation or infinite liquid Peclet number results in the finite temperature gradients becoming oriented normal to the stream surfaces. Note that the averaging of the temperature over the stream surface eliminated the convection term from Eq. (53); only conduction is represented therein. Furthermore, the transformation from ψ to ϕ modified the vaporizing droplet problem from a moving boundary problem to a fixed boundary problem. The effect of the regressing interface appears in the coefficient of that diffusion equation.

It has been shown by Tong and Sirignano (1982a, 1982b, 1983, 1985, 1986) and Sirignano (1993) that the liquid-phase heat diffusion equation (53) and its counterpart mass diffusion equation can be simplified when the change in droplet radius due to vaporization occurs slowly compared to changes in liquid temperature. Under that assumption, the nonlinearities introduced by the coefficients in Eq. (53) can be modified to give an approximate piecewise linear behavior for the equation. A Green's function analysis reduces the equation to an integral form whereby a quadrature gives the liquid temperature at any point as a function of the surface heat flux. An integral equation results that relates surface temperature to surface heat flux. The Green's function (which is the kernel function in the integral equation) is obtained as an eigenvalue expansion. Tong and Sirignano (1986b) showed that the problem could be reduced to a system of ordinary differential equations, thereby improving computational efficiency at a given accuracy.

An alternative approach to the analysis of the liquid-phase heat diffusion was proposed by Abramzon and Sirignano (1989). In particular, an effective thermal diffusivity $\alpha_{\ell_{\text{eff}}}$ was employed wherein

$$\alpha_{\ell_{\text{eff}}}=\chi\alpha_\ell\quad\text{and}\quad\chi=1.86+0.86\tanh[2.225\log_{10}(\text{Pe}_\ell/30)] \tag{54}$$

Equation (54) results from the fitting of numerical results by Johns and Beckmann (1966) for mass transfer between a droplet with internal circulation and a moving external immiscible liquid. The liquid-phase Peclet number, Pe_ℓ, depends upon liquid properties, droplet radius, and the maximum liquid velocity. Here, a "spherically symmetric" pseudo-temperature field is solved using the diffusion equation

$$\frac{\partial T}{\partial t}=\frac{\alpha_{\ell_{\text{eff}}}}{r^2}\frac{\partial}{\partial r}\left(r^2\frac{\partial T}{\partial r}\right) \tag{55}$$

The use of the effective thermal diffusivity presents an accurate description of the characteristic heating time and thermal inertia of the liquid. Via Eq. (54), the effective diffusivity monotonically increases with the maximum liquid velocity. It is bounded below by the molecular diffusivity and above by 2.72 times that finite value. It is expected therefore that the surface

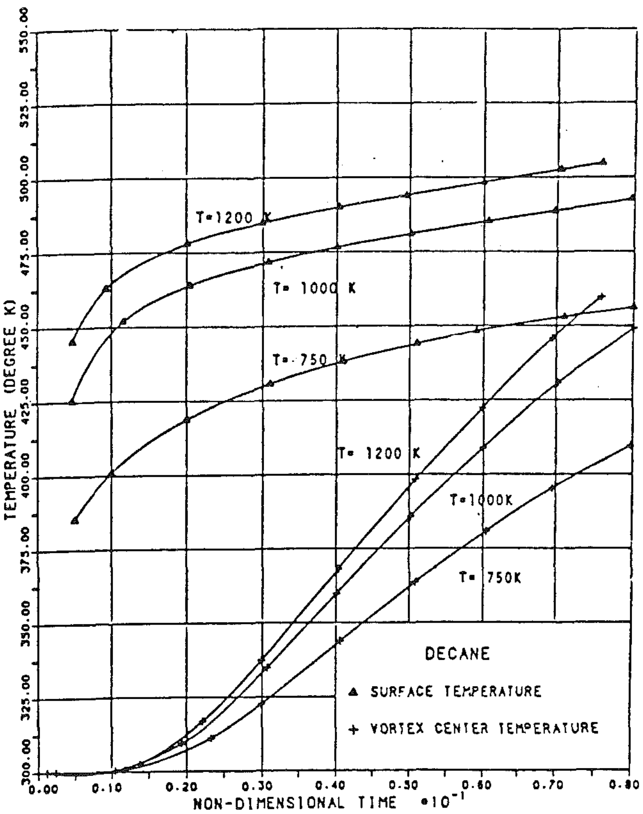

Fig. 4 Surface and vortex center temperature variation for decane liquid droplet at droplet Re = 100 and various ambient temperatures

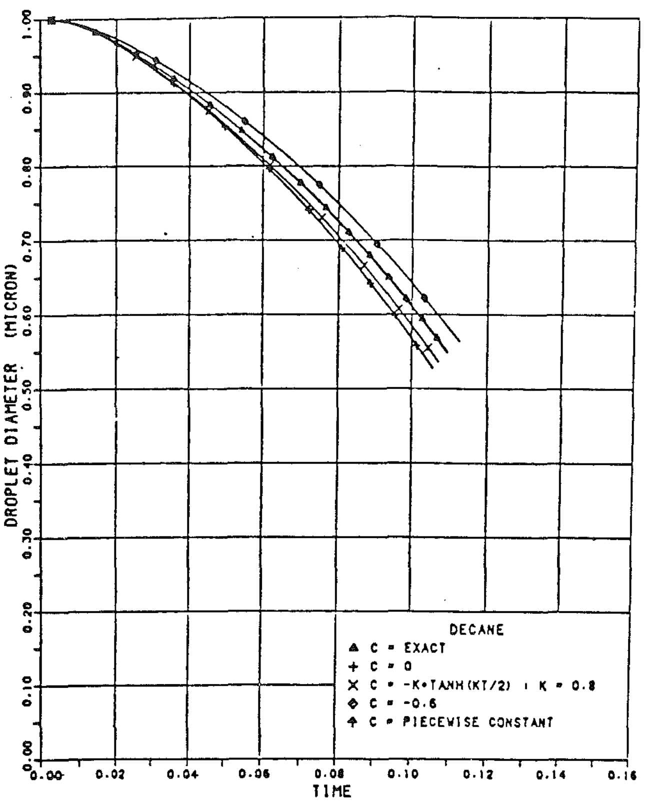

Fig. 5 Droplet diameter versus time for decane. *C* is a parameter describing surface regression rate.

temperature history will be portrayed with only a small error by this ad hoc analysis. The details of the internal temperature field can be grossly in error. For example, the pseudo-temperature will be a minimum at the center of the droplet while the actual temperature is a minimum at the vortical center.

In the case of a multicomponent liquid fuel, mass diffusion in the liquid phase becomes important. As the more volatile substance is vaporized faster from the surface, more of that substance will diffuse from the interior of the droplet to the surface to vaporize. For n liquid components, $n-1$ liquid-phase mass diffusion equations must be solved for $n-1$ mass fractions; the other mass fraction can immediately be deduced since the mass fractions sum to unity. The mass diffusion equations can be placed in forms equivalent to Eq. (49) or Eq. (53). These equations have been solved by approximate and exact methods (Lara-Urbaneja and Sirignano, 1981; Tong and Sirignano, 1986a, 1986b; Continillo and Sirignano, 1988, 1991; and Megaridis and Sirignano, 1991, 1992). The problem is especially interesting and challenging because the liquid mass diffusivity is typically an order of magnitude smaller than the liquid thermal diffusivity so that a new time scale and a greater degree of "stiffness" are created.

Results From Approximate Analyses. The high Reynolds number, quasi-steady, gas-phase boundary-layer analysis coupled with the model of heat diffusion in the internal vortical flow gives a reasonable representation of the quantitative behavior of the velocity and thermal fields in the gas boundary layer and in the liquid. Figure 4 shows results by Tong and Sirignano for surface temperature versus time and for temperature at the vortical center versus time. Spatial variations in the liquid temperature are seen to occur. The surface temperature gradually increases with time toward the wet bulb temperature while the lower vortical center temperature increases at a faster rate, thereby decreasing the spatial variance. Figure 5 shows that the rate of change of the radius (which is related to the vaporization) is slower at first and later increases, giving a clear indication of important transient effects.

The gas-film model coupled with the effective liquid conductivity allows for coverage of a much wider range of Reynolds number. This ability makes the model of Abramzon and Sirignano more practical for use in a spray calculation, where even the droplets that begin with a large relative velocity and large Reynolds number witness a deceleration that eventually gives them lower values of the relative velocity and Reynolds number. Figures 6 and 7 show typical variations of the gas-phase Reynolds number, liquid-phase Reynolds number, and liquid-phase Peclet number with time. The Peclet number strongly influences the effective conductivity through Eq. (54); it is seen that it can vary over several orders of magnitude in the droplet lifetime. The high Peclet number assumption that leads to the establishment of Eqs. (49) and (53) and the high gas-phase Reynolds number assumption that allows for thin boundary layers are not valid over the complete lifetime of the droplet.

Figures 8, 9, and 10 compare droplet radius, surface temperature, and vaporization rate variations during the droplet lifetime for several liquid-phase models. The most accurate model is the "extended" model which yields the solution for the liquid-phase axisymmetric energy equation with the velocity field determined by the Hill's spherical vortex solution. See Abramzon and Sirignano (1989) for details. The effective conductivity model is seen to agree very well in terms of these results which are sufficient to give a useful coupling with the gas phase in spray calculations. The Abramzon and Sirignano model does provide a uniformly good description of the internal liquid temperature; it is better at very small Peclet numbers where its spherically symmetric structure is closer to the real situation. Figures 8, 9, and 10 show that the effective thermal conductivity model results and the actual thermal con-

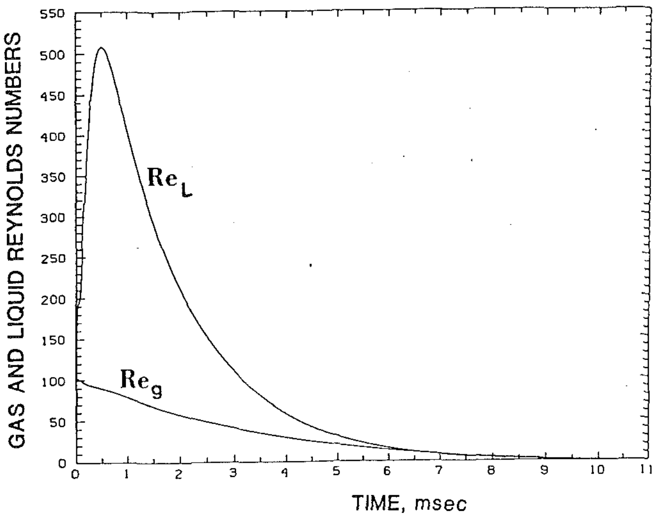

Fig. 6 Gas-phase Reynolds number, Re_g, and liquid-phase Reynolds number, Re_L versus time

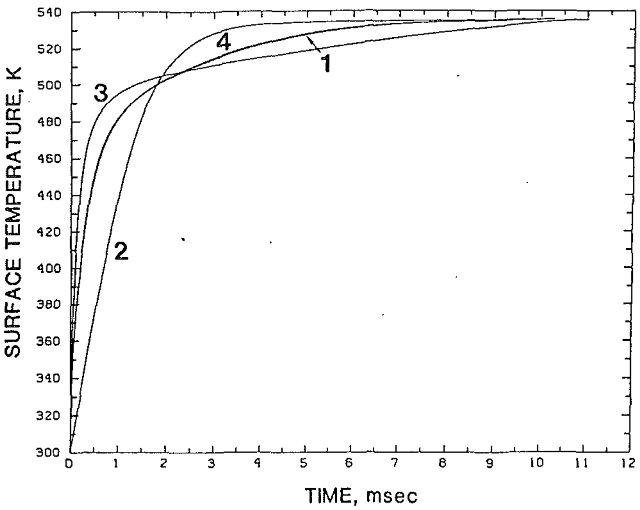

Fig. 9 Surface temperature (K) versus time: various models

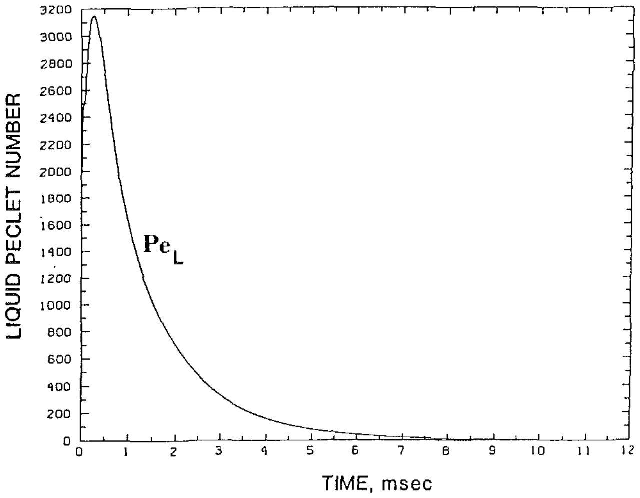

Fig. 7 Liquid-phase Peclet number versus time

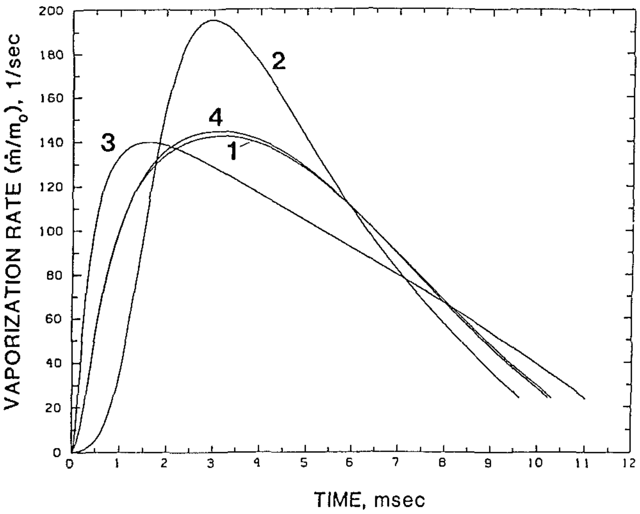

Fig. 10 Vaporization rate versus time: various models

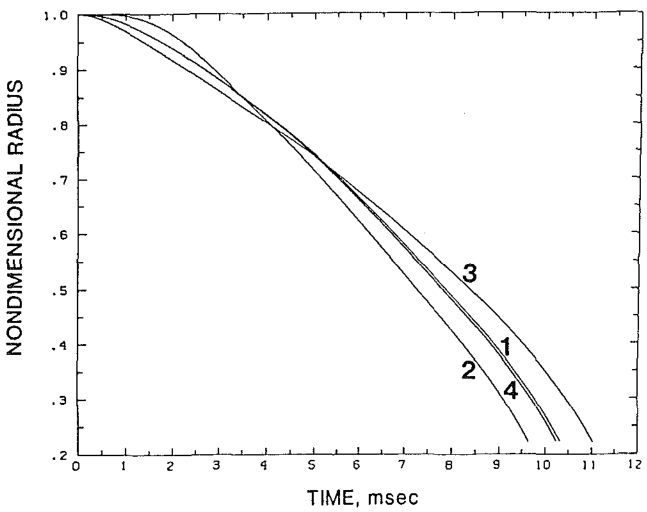

Fig. 8 Nondimensional droplet radius versus time: extended model (curve 1), infinite conductivity model (curve 2), finite conductivity model (curve 3), and effective conductivity model (curve 4)

ductivity model results are significantly different, implying that internal liquid convection is very important. The infinite conductivity model also produces very different results. It is noteworthy that small differences in the droplet radius and surface temperature curves of Figs. 8 and 9 relate to much larger differences in vaporization rate as shown in Fig. 10. Talley and Yao (1986) developed a semi-empirical effective conductivity model that produced good agreement with experiments. Furthermore, it predicted faster liquid-phase mixing than the Tong and Sirignano model.

None of these approximate models addresses the separated, elliptic flow region. Typically, heat and mass transfer are substantially reduced in that region for the Reynolds number range of interest, so that the droplet heating rate and vaporization rate can still be predicted satisfactorily. The pressure or form drag is a major portion of the total droplet drag at velocities above the creeping flow range. Therefore, drag coefficients cannot be predicted well by these models. Either correlations for the drag coefficients obtained from experiment or correlations obtained from finite difference computations can be utilized in principle as inputs to these approximate models. Experiments have generally only yielded correlations that do not account for vaporization (blowing); it is known that solid sphere data, for example, results in overprediction of the drag if employed for vaporizing droplets. One exception is the experimental work of Renksizbulut and Yuen (1983) where the influence of transfer number was determined. In the next subsection, computational solution of the Navier-Stokes equation and derived correlations are discussed. The correlation for the drag coefficient can be employed in the simplified model although the first uses of these models preceded the availability of the correlation.

Both Tong and Sirignano (1989) and Abramzon and Sirignano (1989) studied the convecting vaporizing droplet under ambient oscillatory conditions. The major conclusion is that oscillations of the vaporization rate have sufficiently large amplitude and sufficiently small phase lag with the pressure to be a plausible mechanism for combustion instability in rockets and ramjets.

Exact Analyses for Gas-Phase and Liquid-Phase Flow. Exact analyses for gaseous flows over liquid droplets and internal liquid flows have been performed by several investigators. These Navier-Stokes computations resolve the inviscid flow outside of the boundary layer and wake, as well as the viscous, thermal, and diffusive layers, the recirculating near wake and part of the far wake. The shear-driven internal liquid circulation and transient heating are also resolved. Therefore, elliptic flow regions as well as the hyperbolic and parabolic regions are analyzed in detail. In addition to the global and local heat and mass exchange between the gas and liquid (which is primarily determined by the solution of the parabolic flow regions), these computations yield the drag force on the droplet (which requires resolution of the elliptic near wake as well as the other flow regions).

Exact calculations of the flow around and within vaporizing droplets serve several purposes. First, they provide detailed insight to the phenomena of heat, mass, and momentum transport for the droplet field. Second, these calculations provide a basis for comparison and verification of the simplified models that can be employed in spray calculations. Finally, the calculations can be made for a range of parameters yielding correlations for lift coefficient, drag coefficient, Nusselt numbers, Sherwood numbers, and other similarity parameters that can be employed in the simplified models.

Generally, implicit finite difference techniques are employed and the gas-phase primitive variables (velocity components, temperature, pressure, and mass fractions) are calculated directly, without transformation to other variables. The axisymmetric, unsteady form of the governing equations is solved with stiff upstream boundary conditions and zero-derivative downstream boundary conditions. The liquid and gas flows are coupled at the spherical droplet surface by conditions of continuity on temperature, species and global normal mass fluxes and tangential shear force and balance of normal momentum and normal heat flux. The stream-function-vorticity method is typically employed for the incompressible liquid. Chiang (1990) provides details of the most recent numerical methodology with adaptive nonuniform numerical grids.

Conner and Elghobashi (1987) considered the Navier-Stokes solution for laminar flow past a solid sphere with surface mass transfer. Dwyer and Sanders (1984a,b,c) performed finite-difference calculations assuming constant properties and constant density. Patnaik et al. (1986) relaxed the density assumption in their calculations but considered other properties to be constant. These calculations were made for a hydrocarbon fuel droplet vaporizing in high temperature air so that the heating and vaporization were highly transient. Haywood and Renksizbulut (1986), Renksizbulut and Haywood (1988), and Haywood et al. (1989) solved the problem of a fuel droplet vaporizing into a fuel vapor environment at moderate temperature and the problem of a fuel droplet vaporizing in air at 800 K and one atmosphere of pressure. They considered variable properties and variable density. Chiang et al. (1992) extended the computational theory to high temperature and high pressure air environments with fuel droplets allowing for variable properties and variable density with multicomponent gaseous mixtures. They showed by comparison that the constant property calculations of Raju and Sirignano (1990) and Patnaik et al. (1986) could overpredict drag coefficients by as much as 20 percent. Of course, appropriate averaging of the properties (between free stream values and droplet interface values) to determine the constant property for the calculation could reduce the error. They also calculated the deceleration of the droplet accounting for the noninertial frame of reference.

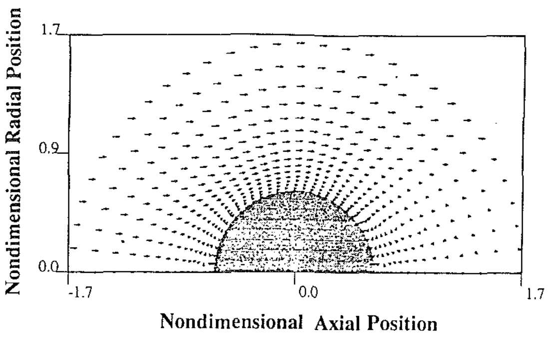

Fig. 11 Gas-phase velocity vectors at nondimensional time of 25.0 and Reynolds number of 23.88

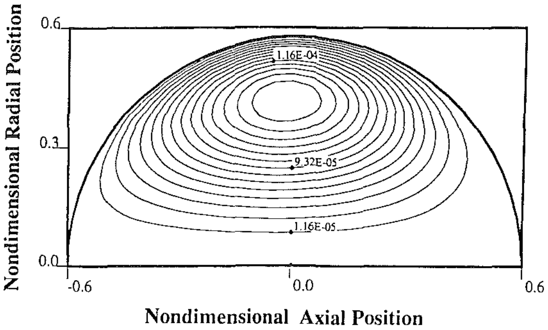

Fig. 12 Liquid-phase stream function contours at nondimensional time of 25.0 and Reynolds number of 23.88. Contour interval: 1.16×10^{-5}

The results of Chiang (1990) and Chiang et al. (1992) are shown in Figs. 11 through 17. Figures 11 and 12 show the instantaneous gas-phase velocity field and the liquid-phase streamlines, respectively, at a time when the Reynolds number is 23.88. The decrease in relative droplet-gas velocity due to drag and the decrease in droplet radius due to vaporization imply that the droplet Reynolds number is decreasing with time. Features such as the near-wake separation and recirculation and the internal liquid circulation are clearly seen. Figure 13 shows the liquid-phase isotherms at three points in time as the droplet decelerates from an initial Reynolds number of 100. High Peclet number behavior dominates in the early period but later conduction in the streamwise direction competes with convection. Figures 14 and 15 provide typical results for the drag coefficient and Nusselt number. Figure 16 shows the drag coefficient as a function of instantaneous Reynolds number which is decreasing with time. The drag coefficient is not monotonically decreasing with increasing Reynolds number because of the dependence upon the transfer number. There is a weak sensitivity to the initial liquid temperature but a strong sensitivity to the model for droplet heating and vaporization. These nondimensional numbers are reduced substantially below the values for nonvaporizing spheres due to the blowing effect in the boundary layer. The contributions of the

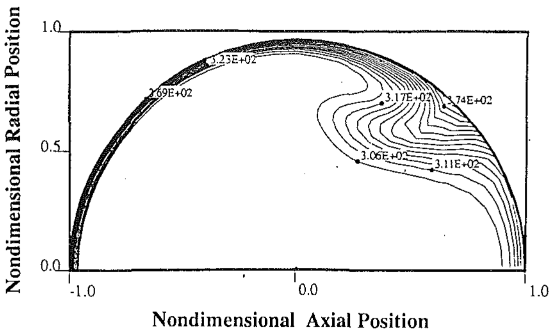

Fig. 13(*a*)

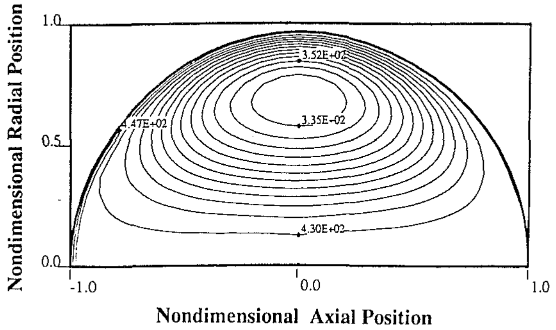

Fig. 13(*b*)

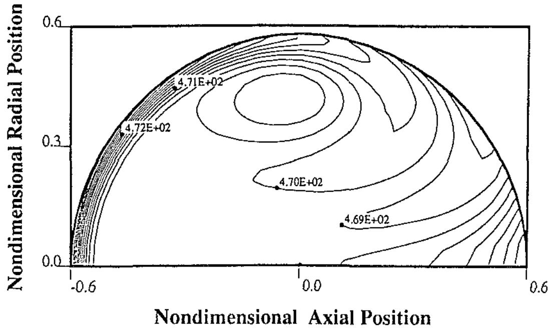

Fig. 13(*c*)

Fig. 13 Transient history of droplet heating. Liquid-phase isotherms at three nondimensional times and corresponding instantaneous Reynolds number: (*a*) time = 0.50 and Re = 96.45; (*b*) time = 5.00 and Re = 76.06; (*c*) time = 25.00 and Re = 23.88

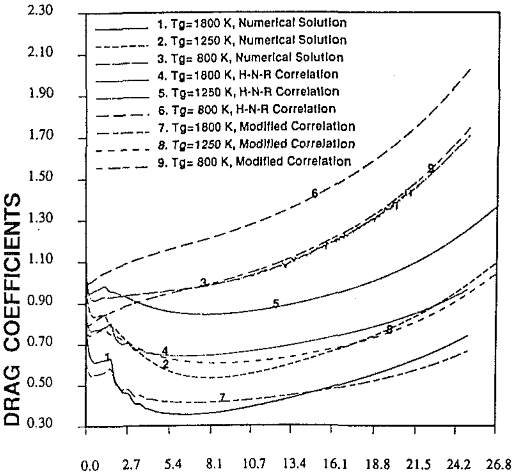

Fig. 14 Drag coefficients versus nondimensional time for different ambient temperatures: numerical results and correlations

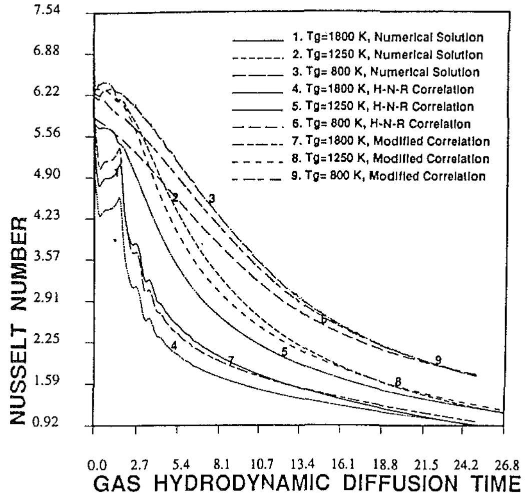

Fig. 15 Nusselt number versus nondimensional time for different ambient temperatures: numerical results and correlations

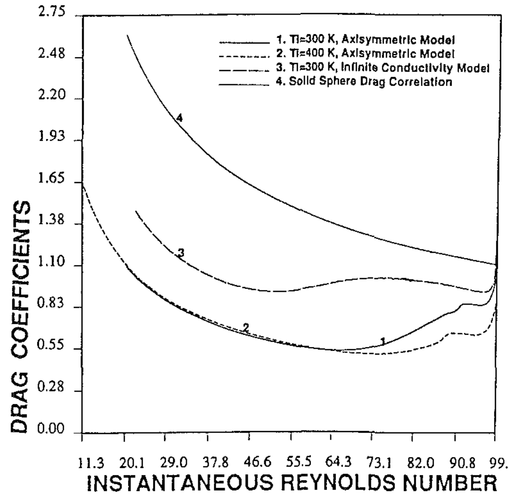

Fig. 16 Drag coefficient versus instantaneous Reynolds number: different models and initial liquid temperature

friction drag, pressure drag, and thrust (due to vaporization) are compared to each other in Fig. 17. Clearly, friction drag is affected the most by ambient temperature and heating rate through the modification of the vaporization (blowing) rate. The impact of blowing rate (through the ambient temperature variation), displayed by Figs. 14 and 15, is observed to be very strong.

Correlations of the numerical results have been obtained by Chiang et al. (1992) relating these nondimensional groupings to the instantaneous Reynolds number and transfer number *B*. They are:

$$C_D = (1+B_H)^{-0.27}\frac{24.432}{\mathrm{Re}_m^{0.721}};$$

$$\mathrm{Nu} = 1.275(1+B_H)^{-0.678}\mathrm{Re}_m^{0.438}\mathrm{Pr}_m^{0.619}$$

$$\mathrm{Sh} = 1.224(1+B_M)^{-0.568}\mathrm{Re}_m^{0.385}\mathrm{Sc}_m^{0.492} \qquad (56)$$

where Re_m, Pr_m, and Sc_m are based upon average gas film values (except for the use of free-stream density in Re_m) and varied from 30 to 200, 0.7 to 1.0, and 0.4 to 2.2, respectively. Also, B_H and B_M are given by Eq. (38) and cover the ranges 0.4 to 13 and 0.2 to 6.5, respectively. These correlations are shown by Figs. 14 and 15 to fit the high temperature, multicomponent gas situation much better than the previously de-

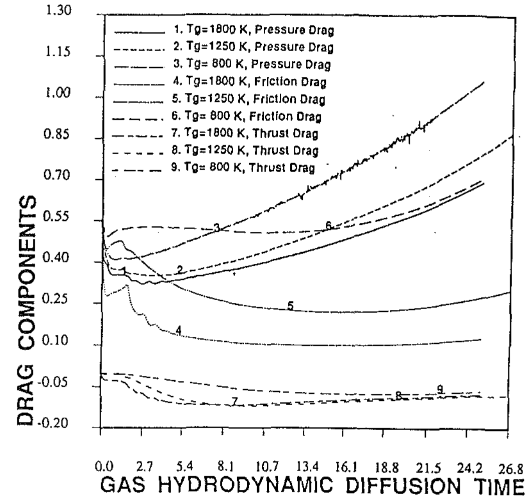

Fig. 17 Three drag coefficient components versus time for different ambient temperatures

veloped (*H-N-R*) correlations of Haywood et al. (1989). The Chiang et al. correlations can be employed for gas film model development without use of any of the models previously discussed. Note that vaporization rate can be readily related to Sherwood number. Model development for the liquid phase is still necessary since many parameters in the correlations introduce surface values. An alternate approach would be to use only the drag coefficient correlation with the approximate model. Under the implied condition of quasi-steady behavior in the gas film, the correlations describe the exchanges of mass, momentum, and energy between the two phases. The transient heating of the liquid phase must be analyzed in the simplified model in order to obtain the surface temperature and liquid heating rate for input to the transfer number which appears in the correlations.

In some recent calculations for droplets near the critical temperature, liquid density variations are taken into account. Specifically, Chiang and Sirignano (1991) replaced the liquid-phase stream function and vorticity calculations with a velocity and pressure calculation. In current research, a cubic equation of state is applied for the liquid and gas. Also, dissolving and diffusion of the ambient gas components in the liquid are considered near the critical point.

3 Spray Equations

We will focus here on the formulation of the describing equations for the dynamics of a spray, considering the discrete phase to be strictly a liquid and the continuous phase to be strictly a gas. Of course, it is simple to generalize the formulation to include dusty flows and bubbly flows.

The spray equations will be presented in three different but related constructions: the two-continua or multicontinua formulation, the discrete particle formulation, and the probabilistic formulation. Both Lagrangian and Eulerian methods will be examined. The relationships amongst these various formulations and methods will be emphasized and will be a major contribution here. Previous research on the multicontinua formulation is reported by Sirignano (1972, 1986, 1993), Crowe et al. (1977), Crowe (1978, 1982), and Ducowicz (1980). The discrete particle method is discussed by Sirignano (1986, 1993) while the probabilistic formulation is discussed by Williams (1985) and Sirignano (1986, 1993). The extensions of the current treatise beyond those previous formulations will be identified as we proceed.

In developing the spray equations, it is convenient to define various density functions. Let ρ be the material density of the gas which is the mass per unit volume in a volume that includes only gas. $\bar{\rho}$ is the gas bulk density which is the mass of the gas in a volume that includes both gas and liquid. Similarly, ρ_ℓ and $\bar{\rho}_\ell$ are the material density and the bulk density of the liquid. Furthermore, θ is defined as the void fraction of the gas which is the ratio of the equivalent volume of gas to a given volume of a gas and liquid mixture. Obviously, $1-\theta$ is the void fraction of liquid. In our terminology, void fraction simply means θ.

It follows that

$$\bar{\rho}=\theta\rho \quad \text{and} \quad \bar{\rho}_\ell=(1-\theta)\rho_\ell$$

For very dilute sprays, $\theta \rightarrow 1$ and $\bar{\rho}\approx\rho$. However, because $\rho_\ell \gg \rho$ in typical cases, it could be poor in that limit to declare that $\bar{\rho}_\ell$ is negligible compared to ρ. Note that ρ_ℓ will be considered to be constant although $\bar{\rho}_\ell$ can vary spatially and temporally.

There are various types of spray calculations that can be of interest. A most important issue involves the length scale of resolution. First, there is the question of whether droplets can be viewed as point sources with respect to gas-phase consideration. This can be a valid approximation in a domain if the collective volume of all liquid droplets and of all of their immediate gas films in that domain is small compared to the total gas volume in that same domain. The approximation can fail locally in regions of dense spray even if the above criteria is met globally. Only in the limiting case of a spherically symmetric transport field around the droplet does the point source approximation give the exact influence on the far gas field. We almost always make the point source approximation.

Another issue concerns the desired resolution compared to the average spacing between droplets. If the resolution is smaller than that spacing, we must account for each droplet physically present in the flow. This clearly limits the total number of droplets that can be considered. Since droplets are considered here as discrete particles, a numerical method that uses an Eulerian scheme for the gas phase and a Lagrangian scheme for the liquid phase is utilized.

If resolution on a scale larger than the droplet spacing is sufficient, only average droplets in each neighborhood need to be considered. Then, we can obviously consider domains that include a much larger number of droplets. Eulerian calculations are employed for the gas phase and either an Eulerian or Lagrangian scheme can be used for the dispersed liquid phase. The Lagrangian scheme is preferred because it reduces numerical error due to artificial diffusion.

3.1 Two-Continua and Multicontinua Formulations.

Let us develop the governing equations beginning with the conservation of mass statement. Each dependent variable at any spatial point is an instantaneous average value over a neighborhood (of that point) that includes both liquid and gas. Therefore, both liquid properties and gas properties exist at a point regardless of whether that point is actually in a gas or in a liquid at that instant. This method is a two-continua approach since both a continuum of gas properties and a continuum of liquid properties are defined. The gas-phase continuity equation is

$$\frac{\partial\bar{\rho}}{\partial t}+\frac{\partial}{\partial x_j}(\bar{\rho}u_j)=\dot{M} \tag{57}$$

while the liquid-phase continuity equation is

$$\frac{\partial\bar{\rho}_\ell}{\partial t}+\frac{\partial}{\partial u_j}(\bar{\rho}_\ell u_{\ell j})=-\dot{M} \tag{58}$$

where $\dot{M}$ is the mass vaporization rate per unit volume. Models for evaluating the vaporization rate are discussed in other sections.

The mixture continuity equation is given by

$$\frac{\partial(\bar{\rho}+\bar{\rho}_\ell)}{\partial t}+\frac{\partial}{\partial x_j}(\bar{\rho}u_j+\bar{\rho}_\ell u_{\ell j})=0 \tag{59}$$

The above equations can be obtained by a control volume approach under the assumption that, as the volume shrinks to zero, the limiting value of the volume void fraction θ is identical to the limiting value of the void fraction of the bounding surface area. Clearly, only two of the three above equations are independent.

Equation (58) can be recast as an equation governing θ instead of $\bar{\rho}_\ell$. It becomes

$$\frac{\partial \theta}{\partial t}+\frac{\partial}{\partial x_j}(\theta u_{\ell j})=\frac{\dot{M}}{\rho_\ell}+\frac{\partial u_{\ell j}}{\partial x_j} \tag{60}$$

The nonzero right-hand side indicates that θ is not conserved for two reasons: (1) vaporization (or condensation) changes the liquid volume and (2) droplet trajectories diverge (or converge) thereby increasing (or decreasing) the distances between droplets.

Often, it is convenient to divide the droplets into many classes according to initial values of velocity, position, diameter, and/or composition. Then, our two-continua approach is expanded to a multicontinua approach. In such a case, it is not usually convenient to solve Eqs. (58) or (60) for $\bar{\rho}_\ell$ or θ. Rather, we distinguish each class of droplets according to an integer value k and set

$$n=\sum_k n^{(k)};\quad \dot{M}=\sum_k \dot{M}^{(k)}=\sum_k \dot{m}^{(k)}n^{(k)} \tag{61}$$

where $\dot{m}^{(k)}$ is the vaporization rate of an average droplet in the kth class, $n^{(k)}$ is the number density of droplets in that kth class, and n in the global droplet number density. The methods discussed in Section 2 can be employed to determine $\dot{m}^{(k)}$. The determination of $n^{(k)}$ will be discussed later in this section. In the limit of a very large number of different droplet classes, the summation of Eq. (61) can be replaced by an integral. This extension to a multicontinua approach was first suggested by Ducowicz (1980) and pursued by Sirignano (1986); it allows for better resolution of the variations amongst the many droplets that can be present in a spray calculation. Note that while Ducowicz (1980) refers to his method as a discrete particle method, it does not meet the discrete particle definition employed here. It is a multicontinua method.

We can define $\psi^{(k)}$ as the liquid volume fraction of the kth class of droplets and $\bar{\rho}_\ell^{(k)}$ as the bulk liquid density of that class. Then

$$1-\theta=\sum_k \psi^{(k)};\quad \bar{\rho}_\ell^{(k)}=\psi^{(k)}\rho_\ell^{(k)}=n^{(k)}\frac{4\pi}{3}(R^{(k)})^3\rho_\ell^{(k)} \tag{62}$$

Note that we are allowing for the possibility that different droplet classes can possess different material densities. The effects of different liquid material densities and the effect of void volume were considered by Ducowicz (1980) but not contained in the original presentations by Sirignano (1972, 1986, 1993). Crowe (1977) did consider the effect of void volume but did not consider separate classes of droplets.

It follows that

$$\frac{\partial \bar{\rho}_\ell^{(k)}}{\partial t}+\frac{\partial}{\partial x_j}(\bar{\rho}_\ell^{(k)}u_{\ell j}^{(k)})=-n^{(k)}\dot{m}^{(k)}=-\dot{M}^{(k)} \tag{63}$$

where

$$u_{\ell j}=\sum_k \frac{\bar{\rho}_\ell^{(k)}}{\bar{\rho}_\ell}u_{\ell j}^{(k)}$$

is a mass-weighted average liquid droplet velocity. When the material density is the same for all droplet classes, it also becomes a volume-weighted average velocity. Furthermore, we have

$$\frac{\partial \psi^{(k)}}{\partial t}+\frac{\partial}{\partial x_j}(\psi^{(k)}u_{\ell j}^{(k)})=-\frac{\dot{M}^{(k)}}{\rho_\ell^{(k)}} \tag{64}$$

We can solve either Eq. (63) or (64) simultaneously with other equations to be discussed later in this section and then use Eq. (62) to get both $\psi^{(k)}$ and $\bar{\rho}^{(k)}$. However, we still require either $n^{(k)}$ or $R^{(k)}$ to determine the right-hand side of Eq. (63) or (64). Realizing that

$$\dot{m}^{(k)}=-\frac{4\pi}{3}\rho_\ell^{(k)}\frac{d}{dt}(R^{(k)})^3$$

where the time derivative is taken in the Lagrangian sense following the droplet, we can manipulate Eqs. (62) and (63) to obtain

$$\frac{\partial n^{(k)}}{\partial t}+\frac{\partial}{\partial x_j}(n^{(k)}u_{\ell j}^{(k)})=0 \tag{65}$$

which is a conservation equation for droplet number for each class. A global conservation equation is obtained by summing Eq. (65) over all classes. Then

$$\frac{\partial n}{\partial t}+\frac{\partial}{\partial x_j}(n\tilde{u}_{\ell j})=0 \tag{66}$$

where

$$\tilde{u}_{\ell j}=\sum_k \frac{n^{(k)}u_{\ell j}^{(k)}}{n}$$

is a number-weighted average velocity.

It is now seen that the two Eqs. (62), Eq. (63) [or (64)], and Eq. (65) provide four (two differential plus two algebraic) equations that will yield $\bar{\rho}_\ell^{(k)}$, $\psi^{(k)}$, $n^{(k)}$, and $R^{(k)}$. Necessary inputs are $u_{\ell i}^{(k)}$ which will come from the solution of the momentum equation and a mathematical model for the vaporization rate $\dot{m}^{(k)}$.

Consider now the species conservation equations for the gas. The integer index m represents the particular species. The mass fraction Y_m is prescribed by

$$\frac{\partial}{\partial t}(\bar{\rho}Y_m)+\frac{\partial}{\partial x_j}(\bar{\rho}u_jY_m)-\frac{\partial}{\partial x_j}\left(\bar{\rho}D\frac{\partial Y_m}{\partial x_j}\right)=\dot{M}_m+\bar{\rho}\dot{w}_m=\sum_k n^{(k)}\dot{m}^{(k)}+\bar{\rho}\dot{w}_m \tag{67}$$

where

$$\dot{M}=\sum_m \dot{M}_m=\sum_m \epsilon_m\dot{M};\quad \dot{m}^{(k)}=\sum_k \dot{m}_m^{(k)};\quad \sum_m \dot{w}_m=0$$

In Eq. (67), the mass diffusivity is assumed to be the same for all species. ϵ_m is a species flux fraction. Obviously,

$$\sum_m \epsilon_m=1.$$

Summation over all components in Eq. (67) yields the continuity Eq. (57). Therefore, if we have N different species, only $N-1$ species conservation equations need to be solved together with Eq. (57). Note that Eqs. (57) and (67) can be combined to yield a nonconservative form

$$\bar{\rho}\left[\frac{\partial Y_m}{\partial t}+u_j\frac{\partial Y_m}{\partial x_j}\right]-\frac{\partial}{\partial x_j}\left(\bar{\rho}D\frac{\partial Y_m}{\partial x_j}\right)=(\epsilon_m-Y_m)\dot{M}+\bar{\rho}\dot{w}_m \tag{68}$$

Generally, the conservative form of the equations are preferred for computation. Note that here the "conservative" Eq. (11) still has source terms.

Now, let us consider the gas-phase momentum equation.

$$\frac{\partial}{\partial t}(\bar{\rho}u_i)+\frac{\partial}{\partial x_j}(\bar{\rho}u_ju_i)+\frac{\partial p}{\partial x_i}-\frac{\partial}{\partial x_j}(\theta\tau_{ij})-\frac{\partial}{\partial x_j}[(1-\theta)\tau_{\ell ij}]=\sum_k n^{(k)}\dot{m}^{(k)}u_{\ell i}^{(k)}-F_{Di}+\bar{\rho}g_i \tag{69}$$

where

$$F_{Di}=\sum_k n^{(k)}F_{Di}^{(k)} \quad \text{and} \quad \tau_{ij}=\mu\left(\frac{\partial u_i}{\partial x_j}+\frac{\partial u_j}{\partial x_i}\right)-\frac{2}{3}\delta_{ij}\frac{\partial u_i}{\partial x_j}$$

The assumption is made in the momentum equation that the gradient of the pressure force is continuous across liquid-gas interfaces, but differences are allowed in the viscous stress imposed on the mixture through the different phases. The above equation was derived with the same control volume and bounding surface as described for the continuity equation. In this momentum equation, we first note the uncertainty created by a lack of rigor. On the one hand, we are averaging gas and liquid properties over many droplet spacings so that both liquid and gas properties exist at any point. On the other hand, we shrink the control volume to zero in our calculus and, in that limit, we attempt to distinguish between gas and liquid boundary forces. The statement that the volume void fractions serve as weighting factors for liquid viscous stress and gaseous viscous stress is no better than a reasonable assumption since clarity in the limit of shrinking the volume to zero is really lost in the averaging process. The above equation also includes momentum sources and sinks due to droplet vapor mass sources, reaction to droplet drag, and body forces on the gas.

Combination of Eqs. (57) and (69) yields another nonconservative form of the momentum equation

$$\bar{\rho}\left[\frac{\partial u_i}{\partial t}+u_j\frac{\partial u_i}{\partial x_j}\right]+\frac{\partial p}{\partial x_i}-\frac{\partial}{\partial x_j}[\theta\tau_{ij}+(1-\theta)\tau_{\ell ij}]$$
$$=\sum_k n^{(k)}\dot{m}^{(k)}(u_{\ell i}^{(k)}-u_i)-F_{Di}+\bar{\rho}g_i \qquad (70)$$

The liquid-phase momentum equation can be written as

$$\frac{\partial}{\partial t}(\bar{\rho}_\ell u_{\ell i})+\frac{\partial}{\partial x_j}(\bar{\rho}_\ell u_{\ell j}u_{\ell i})=-\sum_k n^{(k)}\dot{m}^{(k)}u_{\ell i}^{(k)}+F_{Di}+\bar{\rho}_\ell g_i \qquad (71)$$

Actually, it is preferably to avoid Eq. (71) and to use a separate momentum equation for each class of droplets. In particular, we have

$$\frac{\partial}{\partial t}(\bar{\rho}_\ell u_{\ell i}^{(k)})+\frac{\partial}{\partial x_j}(\bar{\rho}_\ell^{(k)}u_{\ell j}^{(k)}u_{\ell i}^{(k)})$$
$$=-n^{(k)}\dot{m}^{(k)}u_{\ell i}^{(k)}+n^{(k)}F_{Di}^{(k)}+\bar{\rho}_\ell g_i \qquad (72)$$

or, combining with Eq. (58), we obtain

$$\bar{\rho}_\ell^{(k)}\left[\frac{\partial u_{\ell i}^{(k)}}{\partial t}+u_{\ell,j}^{(k)}\frac{\partial u_{\ell i}^{(k)}}{\partial x_j}\right]=n^{(k)}F_{Di}^{(k)}+\bar{\rho}_\ell^{(k)}g_i \qquad (73)$$

Note that Eqs. (69) and (71) could be added to yield a mixture momentum equation that eliminates all right-hand-side source terms except for the body forces.

In the development of the energy equation, only low Mach number equations are considered so that kinetic energy and viscous dissipation terms are neglected in the formation. Note that the perfect gas law yields

$$\theta p=\bar{\rho}RT \quad \text{and} \quad \bar{\rho}e=\bar{\rho}h-\theta p \qquad (74)$$

Then the energy equation can be written as

$$\frac{\partial}{\partial t}(\bar{\rho}h)+\frac{\partial}{\partial x_j}\bar{\rho}u_jh)-\frac{\partial}{\partial x_j}\left(\theta\lambda\frac{\partial T}{\partial x_j}\right)$$
$$-\frac{\partial}{\partial x_j}\left[(1-\theta)\lambda_\ell\frac{\partial T}{\partial x_j}\right]-\frac{\partial}{\partial x_j}\left(\sum_m\bar{\rho}h_mD\frac{\partial Y_m}{\partial x_j}\right)=\frac{d}{dt}(\theta p)$$
$$+\sum_m\bar{\rho}\dot{w}_mQ_m-\sum_k n^{(k)}m^{(k)}L_{\text{eff}}^{(k)}+\sum_k n^{(k)}\dot{m}^{(k)}h_s^{(k)} \qquad (75)$$

It can be noted that

$$h=\int_{T_{\text{ref}}}^{T}c_pdT'=\int_{T_{\text{ref}}}^{T}\left(\sum_m Y_mc_{pm}(T')\right)dT'$$

Furthermore, we can combine the continuity equation (57) with (75) to obtain a nonconservative form

$$\bar{\rho}\left[\frac{\partial h}{\partial t}+u_j\frac{\partial h}{\partial x_j}\right]-\frac{\partial}{\partial x_j}\left(\theta\frac{\lambda}{C_p}\frac{\partial h}{\partial x_j}\right)$$
$$+\frac{\partial}{\partial x_j}\left[\bar{\rho}D(\text{Le}-1)\sum_m h_m\frac{\partial Y_m}{\partial x_j}\right]-\frac{\partial}{\partial x_j}\left[(1-\theta)\lambda_\ell\frac{\partial T}{\partial x_j}\right]$$
$$=\frac{d(\theta p)}{dt}+\sum\bar{\rho}\dot{w}_mQ_m-\sum_k n^{(k)}\dot{m}^{(k)}(h-h_s^{(k)}+L_{\text{eff}}^{(k)}) \qquad (76)$$

Note that the chemical source terms would be eliminated from Eqs. (75) and (76) if the enthalpy were redefined to include the summation of the mass fraction times the heat of formation over all species.

The liquid-phase temperature will generally vary spatially and temporally within the liquid droplet. A Navier-Stokes solver or some approximate algorithms as described in Section 2 by Eqs. (49) and (53) can be employed to determine the temperature field in the droplet including the surface temperature. In the special case of a uniform but time varying liquid temperature in the droplet, an equation for the thermal energy contained in the droplet can be useful. If e_ℓ is the liquid internal energy per unit mass, then $\bar{\rho}e_\ell$ is the liquid internal energy per unit volume of mixture. In the case where a spatial variation of temperature occurs in the droplet, e_ℓ could be considered as the average over the droplet. However, an equation for e_ℓ would not be so useful here since the difference between the average value and the surface value is not specified but yet the results are most sensitive to the surface temperature. The liquid energy equation can be rewritten for each class of droplets

$$\frac{\partial}{\partial t}(\bar{\rho}_\ell^{(k)}e_\ell^{(k)})+\frac{\partial}{\partial x_j}(\bar{\rho}_\ell^{(k)}u_{\ell j}^{(k)}e_\ell^{(k)})$$
$$=n^{(k)}\dot{q}_\ell^{(k)}-n^{(k)}\dot{m}^{(k)}e_{\ell s}^{(k)} \qquad (77)$$

This equation can be combined with Eq. (63) to yield an alternative form

$$\bar{\rho}_\ell^{(k)}\left[\frac{\partial e_\ell^{(k)}}{\partial t}+u_{\ell j}^{(k)}\frac{\partial e_\ell^{(k)}}{\partial x_j}\right]=n^{(k)}\dot{m}^{(k)}\left(e_\ell^{(k)}-e_{\ell s}^{(k)}+\frac{\dot{q}_\ell^{(k)}}{\dot{m}^{(k)}}\right) \qquad (78)$$

where $\dot{q}_\ell^{(k)}$ is the conductive heat flux from the liquid interface of a droplet toward its interior. Note that during droplet heating, we expect that $e_\ell^{(k)}-e_{\ell s}^{(k)}$ is negative (maximum liquid temperature is at the interface) or zero so that energy is lost from the liquid phase on account of this effect.

The liquid-phase equations form a hyperbolic subsystem of partial differential equations. In particular, we define the operation

$$\frac{d^{(k)}}{dt}=\frac{\partial}{\partial t}+u_{\ell j}^{(k)}\frac{\partial}{\partial x_j}$$

This is a Lagrangian time derivative following an average droplet in the *k*th droplet class. Then mass conservation states that the droplet radius is described by

$$\frac{d^{(k)}R^{(k)}}{dt}=-\frac{\dot{m}^{(k)}}{4\pi\rho_\ell^{(k)}(R^{(k)})^2} \qquad (79)$$

The droplet position is governed by

$$\frac{d^{(k)}x_i^{(k)}}{dt}=u_{\ell i}^{(k)} \qquad (80)$$

while Eq. (73) governs the droplet velocity

$$\bar{\rho}_\ell^{(k)}\frac{d^{(k)}u_{\ell i}^{(k)}}{dt}=n^{(k)}F_{Di}^{(k)}+\bar{\rho}_\ell^{(k)}g_i \qquad (81)$$

The energy Eq. (78) can be written as

$$\bar{\rho}_\ell^{(k)} \frac{de_\ell^{(k)}}{dt} = n^{(k)} \dot{m}^{(k)} \left(e_\ell^{(k)} - e_{\ell s}^{(k)} + \frac{\dot{q}_\ell^{(k)}}{\dot{m}^{(k)}} \right) \tag{82}$$

Equations (81) and (82) are the characteristic equations for the hyperbolic partial differential equations (72) and (78). Equation (80) describes the characteristic lines through space for those hyperbolic equations. The Lagrangian method for the averaged liquid properties is therefore fully equivalent to the method of characteristics as explained by Sirignano (1986, 1993). The Ducowicz (1980) analysis is actually a method of characteristic approach to the multicontinua formulation rather than the type of discrete-particle formulation discussed in the next subsection. This method of characteristics allows the partial differential equations to be converted to ordinary differential equations that are solved more readily with a reduction in the numerical error due to integration. Specifically, the solution of the partial differential equations can produce artificial diffusion through the difference equation approximation; this type of error does not occur with the differencing of the ordinary differential equations.

These equations are solved simultaneously with the gas-phase equations (57), (67) or (68), (69) or (70), and (75) or (76) together with the equation of state (74). These gas-phase equations are typically solved by finite-difference methods on an Eulerian mesh that is either fixed or defined through some adaptive grid scheme. The terms representing exchanges of mass, momentum, and energy between the two phases appear as source and sink terms in both the gas-phase and liquid-phase equations. They provide the mathematical coupling between the two subsystems of equations representing the two phases. The liquid Lagrangian equations are effectively solved on a different grid from the gas-phase equations so that interpolation is continually used in the evaluation of the source and sink terms. Care must be taken in avoiding other numerical errors of the same order as the artificial diffusion that has been eliminated; these other errors can be created by a low order interpolation scheme. Details about the method and analyses of its performance can be found in Aggarwal et al. (1981, 1983, 1985).

The Lagrangian or characteristic path is the trajectory of an average droplet that represents a group of droplets that (at least initially) are in the same neighborhood. The droplet number density can vary along this path but the number of droplets represented remains fixed (in the absence of droplet shattering or coalescence).

In this two-continua method, two distinct characteristic lines (from the same or different droplet classes) can intersect without implication of a collision. The characteristic lines or trajectories represent the paths of average droplets; each average droplet represents a beam or moving cloud of droplets. If average spacing between neighboring droplets is sufficiently large, two beams can pass through each other without any collisions. An important implication here is that multivalued liquid properties can occur; at a given point in space and time, more than one value of a liquid property for a given class of droplets can exist. Note that the direct solution of hyperbolic partial differential equations for the liquid properties will smear any multivalued solutions upon numerical integration. In this regard, the Lagrangian method is substantially more powerful and reliable.

In the Lagrangian method, we bypass the use of Eq. (65) for the droplet number conservation. We must still evaluate the droplet number density which appears in source and sink terms in Eqs. (57), (58), (60), (63), (64), (67) through (73), (75), and (76) through (78). Typically, we determine number density locally in a two-continua finite-difference computation by: (i) determining the number of average droplets for each droplet class in each computational cell at each temporal point in the calculation, (ii) determining, based upon the initial condition for each average droplet, the total number of actual droplets of each class present in the computational cell, and (iii) dividing this total number by the volume of the computational cell to obtain the number density.

The gas-phase and liquid-phase equations described in this section can be applied to turbulent flows, but first, Reynolds averaging or Favre averaging of the equations should be performed. Also, some approximations are required to close the equations. As a result of this process, averaged forms of the previous equations plus additional equations for the turbulent kinetic energy and other second-order quantities result. See Elghobashi and coworkers (1983, 1984, 1991, 1992) for details on these turbulent spray analyses.

Initial conditions are required for the solution of the unsteady form of the equations. Often, the unsteady form is employed even when we wish to obtain the steady-state solution. For example, if the system of differential equations (57), (67), (69), (75), (79), (80), (81), and (82) were to be solved, initial conditions would be required for the gas-phase velocity, density, mass fractions, and enthalpy and for the velocities, positions, radii, and thermal energies of the average droplets in each class.

Boundary conditions are also required. Equations (67), (69), and (75) have elliptic spatial operators so that, for velocity, mass fractions, and enthalpy, conditions on the quantities or their gradients are required for every boundary point. Equation (57) is a first-order hyperbolic equation so that density needs to be specified only at the inflow boundaries. Boundary conditions on Eqs. (79), (80), (81), and (82) for the average droplet properties are only required for inflow. When the droplet passes through an open boundary, we discontinue the calculation for that particular droplet. When a droplet strikes a solid wall, there are several options: (i) the wall can be assumed to be so cold that the droplet sticks to the wall and no further vaporization occurs (effectively removing the droplet from the field of computation), (ii) the wall is so hot that the droplet immediately vaporizes providing a local gaseous mass source, and (iii) the droplet rebounds, perhaps shattering into a number of small droplets. Clearly, the last condition is the most difficult to implement in a calculation. Naber and Reitz (1988) have claimed that better agreement with experimental data can be obtained for some calculations if the droplet is assumed to flow along the wall with the local gas velocity near the wall.

3.2 Discrete-Particle Formulation. The two-continua or multicontinua approach allows resolution only on a scale larger than the average spacing between neighboring droplets. Often, however, we must resolve a spray behavior on a finer scale. In combustion applications, ignition and flame structure are examples where that level of resolution is required. An alternative to the two-continua approach is the discrete particle approach that serves the purpose of higher resolution. This method follows each individual droplet and resolves the liquid field within each droplet and the gas field surrounding each droplet. Obviously, it is limited to a smaller number of droplets and to a smaller volume of mixture than the two-continua approach. Since the discrete phase is being resolved here, only gas properties or only liquid properties exist at a given point in space or time. The hyperbolic partial differential equations or their characteristic differential equations have no meaning in this approach. Although the droplet trajectories are not characteristic lines in this approach, certain ordinary differential equations are still written along these trajectory lines so that we have a Lagrangian method here, albeit of another type than previously discussed. Here, we do not distinguish droplets by class because, obviously, each droplet forms its own class.

The governing equations for each droplet are

$$\frac{dR}{dt} = \frac{\dot{m}}{4\pi\rho_\ell R^2} \tag{83}$$

$$\frac{dx_i}{dt}=u_{\ell i} \tag{84}$$

$$\frac{du_{\ell i}}{dt}=\frac{3\bar{F}_{Di}}{4\pi\rho_\ell R^3}+g_i \tag{85}$$

and

$$\frac{de_\ell}{dt}=\frac{3\dot{m}}{4\pi\rho_\ell R^3}\left(e_\ell-e_{\ell s}+\frac{\dot{q}_\ell}{\dot{m}}\right) \tag{86}$$

Often, Eq. (86) is replaced by the energy function for the liquid which governs diffusion and convection in the droplet.

The gas-phase equations must be solved simultaneously with the above droplet equations. The discrete-particle approach is only sensible when resolution is finer than the spacing between neighboring droplets. Therefore, the computational mesh size must be significantly smaller (by at least an order of magnitude) than the spacing. In the dilute (or nondense) sprays, this interdroplet spacing is also much greater than the average droplet diameter so therefore we expect the computational mesh size to be comparable to or greater than the droplet diameter. Here, we expect most computational cells will not contain a droplet but only gas; only a small fraction of the cells will contain a droplet, and typically only one droplet each, since average spacing is so large. Equations (57), (67) or (68), (69) or (70), (74), and (75) or (76) describe the gas phase and can be placed into finite-difference form. Here, $\theta=1$ and $\bar{\rho}=\rho$ is taken. Also, the source terms representing exchanges of mass, momentum and energy between phases go to zero in those equations for these cells. This is definitely accurate for the great majority of cells which do not contain any droplet. In the cells containing droplets, we can allow θ to deviate from unity to account for the droplet volume. Whenever the droplet diameter is small compared to the mesh size, θ can be assumed to be unity neglecting droplet volume from the perspective of the coupling with the gas phase.

3.3 Computational Issues. The analyses for the discrete particle method and for the two-continua (or multi-continua) method as outlined herein are built on the premise that subgrid modeling of the behaviors of the liquid in the droplet interior and of the gas in the boundary layer and wake of the droplet will be employed. These subgrid models are discussed in Section 2. This is sensible when the droplet diameter is much smaller than the interdroplet spacing and smaller than or comparable to the mesh size needed to resolve the gas phase. Then, the subgrid modeling avoids the costly solution of complex equations on a grid size smaller than the droplet diameter. In the case of a dense spray, the droplet diameter becomes comparable to the spacing and, therefore, resolution of the gas phase and resolution of the liquid phase are just as costly. It makes much less sense to use the discrete-particle method with its inherent sub-grid modeling for these dense sprays. If fine resolution is required, solution of the Navier-Stokes equations with account for phase boundaries is suggested. Complexity of the problem will limit the total volume of mixture that can be treated. If average properties were sufficient, the two-continua method can be used for these dense sprays. Note that the equations formulated in this section do not account for collisions that might occur in very dense sprays.

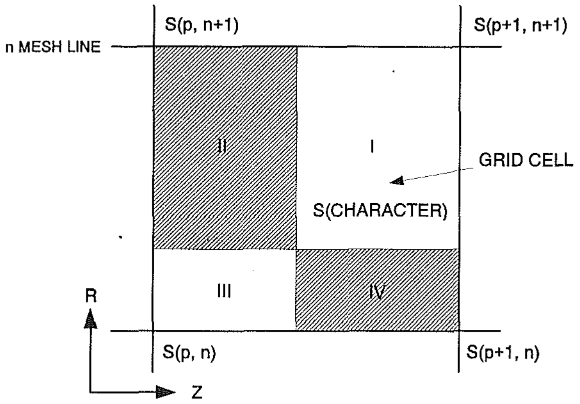

Fig. 18 Graphical display of weighting factors for two dimensional Eulerian-Lagrangian spray calculations

In both the multicontinua method and the discrete-particle method, a phase-exchange source term value for the gas phase is generally not immediately given at a gas-phase mesh point. Rather, it is presented at the instantaneous position of the droplet. Its value must be extrapolated to the mesh points. The lowest-order approximation involves simply transferring the value from the droplet location to the nearest mesh point. This produces numerical errors of the same first order as numerical diffusion errors that are avoided for the liquid phase by the Lagrangian method. It is superior therefore to distribute the source term in a weighted manner to the neighboring mesh points. There will be two, four, or eight neighboring mesh points depending upon whether we have a one, two, or three-dimensional calculation. The droplet or average droplet under consideration is within a rectangle defined by the corners at the four mesh points (p, n), $(p+1, n)$, $(p+1, n+1)$, and $(p, n+1)$. Consider that the nearest mesh point is (p, n). The lowest-order approximation merely transfers the source term S to the mesh point (p, n) with resulting first-order accuracy. The second-order scheme divides the source term S into four parts, each associated with a mesh point and weighted inversely to proximity of that mesh point to the droplet position. Namely

$$S_{p,n}=\frac{A_{p,n}}{A}S;\quad S_{p+1,n}=\frac{A_{p+1,n}}{A}S;$$

$$S_{p+1,n+1}=\frac{A_{p+1,n+1}}{A}S;\quad S_{p,n+1}=\frac{A_{p,n+1}}{A}S$$

where A is the area of the original rectangle and $A_{p,n}$, etc., are the areas of the subdivided rectangles shown in Figure 18. Note that the extension to three dimensions involves eight subdivided rectangular volumes.

Note that the source point is taken as the center of the droplet. Furthermore, in the multicontinua approach, many droplets can be represented by each average droplet. Also, any given mesh point can be a corner point for several cells (four in two dimensions), each of which can contain droplets and transfer portions of the source terms to the mesh point. These source contributions from various droplets are simply additive. Finally, note that the same geometrical weighting factors should be employed to evaluate gas properties at the droplet position (for input as source terms to the liquid-phase equations) given the properties at the neighboring mesh points.

In the discrete-particle method, we must present ambient gas conditions for the droplet in order to determine the droplet vaporization rate, heating rate, drag, and trajectory. In a finite difference scheme, the gas properties at immediately neighboring mesh points to the instantaneous droplet position are employed as the ambient conditions on the subgrid droplet model. Theoretically, these ambient conditions should exist at the edge of the gas film (boundary layer and wake) surrounding the droplet; in practice, however, the neighboring mesh points might be in the gas film leading therefore to errors in the matching of the subgrid droplet model to the gas phase. These errors and their corrections were addressed by Rangel and Sirignano (1989b) and Sirignano (1993).

The surprising result is that as the gas-phase grid is refined, the error increases; the neighboring mesh points to the droplet actually move closer to the droplet and into the surrounding gas film. In the case where the droplet moves with the surrounding gas, we can assume that the gas film is spherically symmetric with respect to the droplet center. In that case, Rangel and Sirignano have shown that mass vaporization rate given by Eq. (9) should be multiplied by the factor $1+\epsilon$ to correct for the error in application of the ambient boundary condition on the droplet model. For the case where the gas-phase grid size is smaller than the droplet radius, it is found that

$$\epsilon = -\frac{1}{1+\delta}$$

where δ is the ratio of the distance between the mesh point (where ambient conditions are applied) and the droplet center to the droplet radius. This analytical solution of Rangel and Sirignano considers the ambient gas conditions as given and only addresses errors associated with the location of the application of these conditions. It does not address the compounding of this error in a coupled gas-liquid calculation by the modification of the ambient values because of the modified vaporization rate; it is assumed that, as one problem is corrected, the other problem is automatically corrected in the coupled calculation.

It should be noted that, for this case where the relative velocity between the droplet and the ambient gas is zero, the droplet can be accurately considered as a point source from the gas perspective. That is, the point-source approximation has been shown by Rangel and Sirignano (1989b) to predict exactly the gas film properties surrounding the droplet. While the droplet size affects the vaporization rate, the ambient gas is only affected by the vaporization rate and, in other ways, it is not affected by the droplet size. This simplification does not apply exactly to the case where a finite relative velocity exists.

Rangel and Sirignano (1989b) have shown for the convective case that a point-source approximation plus a free stream does not provide an accurate velocity field around the droplet (even in the inviscid limit). A point-source, doublet, and free stream combination provides a much more accurate description. In this case, the flow field around the droplet depends upon both the vaporization rate and the droplet diameter. There are still inaccuracies besides the viscous effects on the velocity field. For example, with the point source approximation, the vaporization mass flux is assumed to be uniform over the droplet surface, which is not accurate.

The gas film or boundary layer thickness in the convective case will decrease as the droplet Reynolds number increases. The strategy proposed by Rangel and Sirignano is that the ambient conditions are applied at a position upstream of the droplet by a distance $\bar{\delta}$ given by

$$\frac{\bar{\delta}}{R} = \left(1+\frac{5}{\mathrm{Re}^{0.6}}\right)(1+B_M)^{0.17}$$

The upstream direction is determined by the relative velocity vector between the gas and the liquid; the value of $\bar{\delta}$ then determines the position where the ambient conditions are applied. The values at the neighboring mesh points (that form the corners of a cell in which the determined point lies) are averaged, in a weighted manner, to provide the ambient conditions. The transfer number B_M above is calculated using the ambient conditions at this point. Errors are significantly reduced by evaluating the transfer number at this upstream position versus evaluating it at the droplet position. At large grid size to droplet diameter ratio, the error decreases as droplet Reynolds number increases or as the grid size to droplet diameter ratio increases.

Certain studies have been performed to address the issue of optimizing the numerical calculations for sprays. Axisymmetric sprays were studied by Aggarwal et al. (1985) and Sirignano (1993). Laminar, nonreacting situations were considered. Turbulence and chemical reactions would modify characteristic length and time scales, thereby affecting the optimal numerical scheme. Two problems were considered: (i) an axisymmetric, steady jet flow and (ii) an unsteady, axisymmetric confined model flow.

In both cases, an Eulerian mesh was used for the parabolic gas-phase equations. Note that in the model problem, the spatial differential operator is elliptic. A Lagrangian scheme was used for the hyperbolic equations describing the vaporizing liquid phase. All hydrodynamic and thermal interactions between the two phases were considered. Generally, with one exception, consistent second-order-accurate numerical schemes were considered.

In the first problem, the subset of gas-phase equations has been attacked by four numerical methods: a predictor-corrector explicit method, a sequential implicit method, a block implicit method, and a symmetric operator-splitting method. The computations predicted the hydrodynamics and transport in the gas phase as well as the droplet trajectories. The size, temperature, and velocity of each droplet group were also predicted. Time for computation as a function of the error bound was determined. At low error tolerances, the sequential implicit method gave the best results; at large error tolerances, the explicit and operator-splitting methods gave better results. The block implicit scheme was least effective at all accuracies. Further information can be found in Aggarwal et al. (1985) and Sirignano (1993).

In the second problem, a set of model equations was studied but the technique applies very well to a more general and more physically-accurate set of equations as well. The integration scheme and the scheme for interpolation between the Lagrangian and Eulerian meshes were demonstrated to be second-order accurate. Effects of mesh size, number of droplet characteristic, time step, and the injection pulse time were determined via a parametric study. The results indicated slightly more sensitivity to grid spacing than to the number of droplet characteristics. Still further information is given in Aggarwal et al. (1983) and Sirignano (1993).

3.4 Applications. The spray equations have been studied and solved for many applications: single-component and multicomponent liquids, high temperature and low temperature gas environments, monodisperse and polydisperse droplet size distributions, steady and unsteady flows, one-dimensional flows, laminar and turbulent regimes, and recirculating (strongly elliptical) and nonrecirculating (hyperbolic, parabolic, or weakly elliptic) flows. The references cited here will not be totally inclusive of all of the interesting analyses that have been performed; rather, only a selection will be presented here. Overviews of the relationships between the developments of the subgrid vaporization models and the spray calculations can be found in Sirignano (1985a, 1988).

Some of the earlier research employed an Eulerian description of the two-continua formulation. For example, Seth et al. (1978) and Aggarwal and Sirignano (1984) performed one-dimensional analyses of flames propagating through fuel sprays. They did not resolve flame structure to a scale smaller than the average spacing between droplets and suffered some artificial diffusion associated with the Eulerian formulation. Sirignano (1985b) considered a very simple vaporizing spray to develop integral solutions. Other research has addressed the two-continua problem with a Lagrangian description. Aggarwal et al. (1981, 1983, 1985) studied axisymmetric idealized two-continua problems to establish some of the computational foundations and performance analyses for the Lagrangian method. They determined the trade-offs between computational time and accuracy. Among other issues, some guidance is given concerning the number of characteristics (or, equivalently, average particles) that should be selected to yield consistent accuracy with the Eulerian mesh selection for the gas-phase equations. Bhatia and Sirignano (1991) considered oscillatory vaporization and combustion in a one-dimensional simulation of a ramjet combustor.

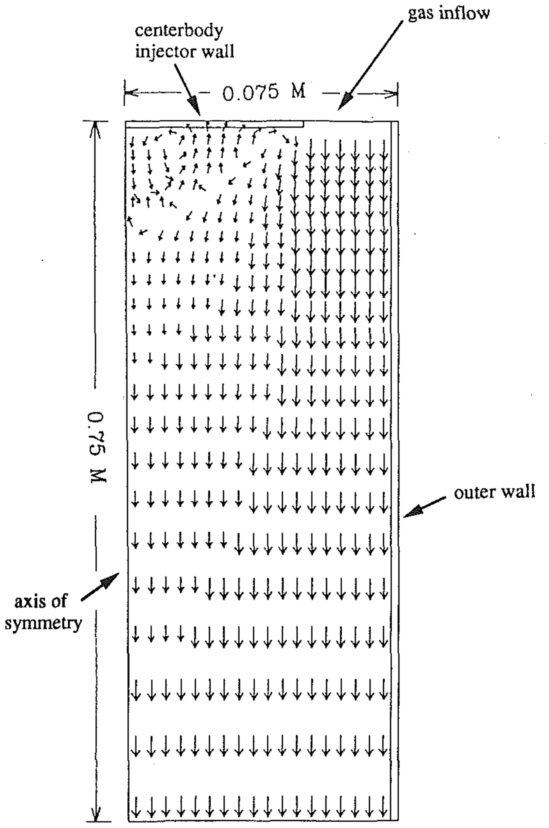

Fig. 19 Gas velocity vectors for centerbody injector configuration. Schematic of axisymmetric chamber showing outer wall, centerbody wall, gas inflow, and axis of symmetry

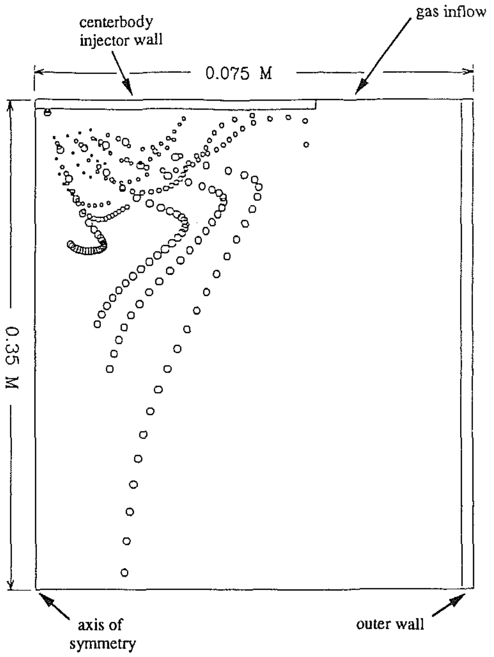

Fig. 20 Droplet trajectories and sizes for polydisperse spray with centerbody injector configuration shown in Fig. 19

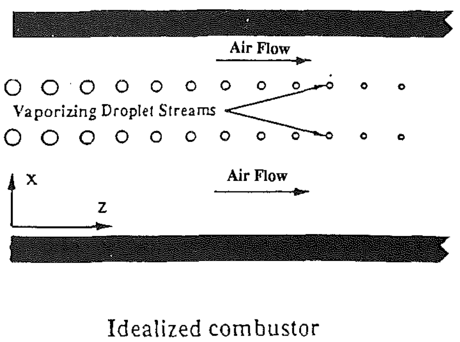

Fig. 21 Two-dimensional, planar, parallel droplet stream configuration

The multicontinua formulation has been extended to turbulent domains with the works of Raju and Sirignano (1989, 1990) and of Molavi and Sirignano (1988). Here, the gas-phase equations accounted for the averaged effects of turbulent fluctuations of the gas field but no fluctuations in the droplet behavior were considered. A development of the theory with coupled gas and liquid fluctuations made by Elghobashi and co-workers (1983, 1984, 1985, 1989, and 1991) will be discussed in Section 5. Raju and Sirignano and Molavi and Sirignano considered axisymmetric and planar two-dimensional idealized configurations related to center-body and dump combustors. Single component and multicomponent fuels were considered. Gas velocity directions in Fig. 19 indicate a recirculating flow field near the centerbody injector. Figure 20 shows some vaporizing droplet trajectories and sizes calculated by Raju and Sirignano for a polydisperse spray; the larger droplets are seen to penetrate further than the smaller droplets. Smaller droplets are more likely to become entrained in the recirculating flow field.

One-dimensional, planar unsteady spray configurations have been studied extensively using the discrete particle Lagrangian methodology. Various subgrid vaporization models were studied by Aggarwal et al. (1984) who found that substantial global differences in the two-phase flow can result from different vaporization models; it is clear that accurate subgrid modeling of vaporization is required. Other one-dimensional planar studies based upon the discrete particle formulation include Aggarwal and Sirignano (1985a,b, 1986). They found that ignition delays for sprays could be less than for gas mixtures at the same stoichiometric ratio. Similarly, spray flame speeds could exceed the premixed flame speed at the same stoichiometry. Continillo and Sirignano (1988) extended the study to a spherically symmetric spray configuration. Aggarwal (1987, 1988) and Continillo and Sirignano (1991) considered multicomponent liquid sprays in one-dimensional, planar and spherically symmetric configurations. Generally, vaporization rates, ignition delays, and flame propagation rates were predicted.

Studies have been performed on two-dimensional planar flows with parallel streams of droplets. The basic configuration is displayed in Fig. 21. Steady-state calculations that approximate the droplet streams to be continuous liquid streams have been performed by Rangel and Sirignano (1986, 1988b, 1989a). The continuity and momentum equations for the gas flow are not solved in these analyses; rather, the pressure and gas velocity are assumed to be uniform. The droplet velocities are determined by conservation of momentum principles. These studies actually lie between two-continua formulations and discrete-particle formulations. They resolve the flow in one transverse direction on a scale smaller than the spacing between droplets; however, the properties are not resolved on the scale of the droplet spacing in the liquid-stream direction. Averaging of liquid properties occurs in one of the two spacial directions thereby yielding a steady flow result that integrates implicitly over time to remove the effect of the inherent intermittency associated with the spacing between the droplets in the stream. (Averaging in the third direction is implicit since the problem *ab initio* was reduced to a two-dimensional statement.) Certain important phenomena can still be identified even though properties are smoothed to eliminate the intermittency. Figure 22

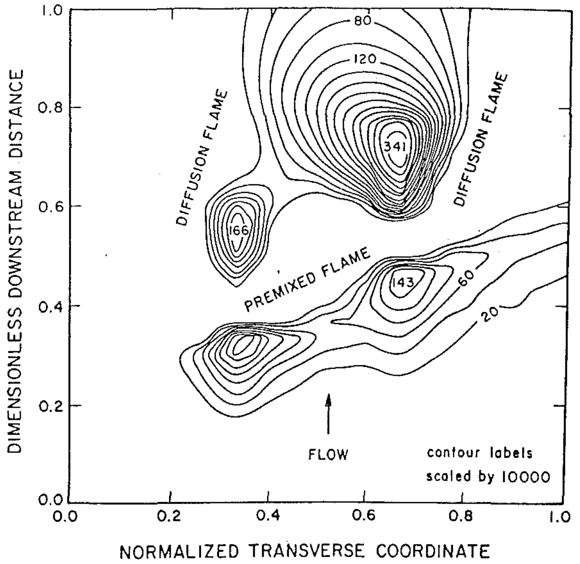

Fig. 22 Fuel vapor mass fractions in the two parallel droplet stream configuration

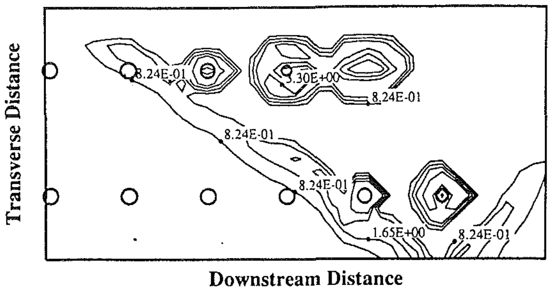

Fig. 23(*a*)

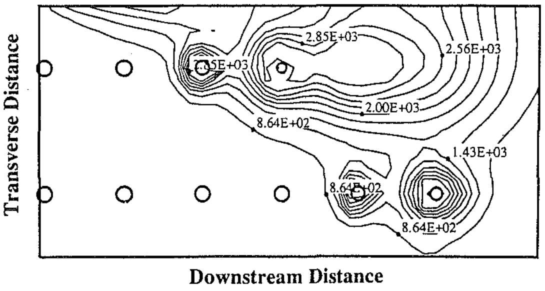

Fig. 23(*b*)

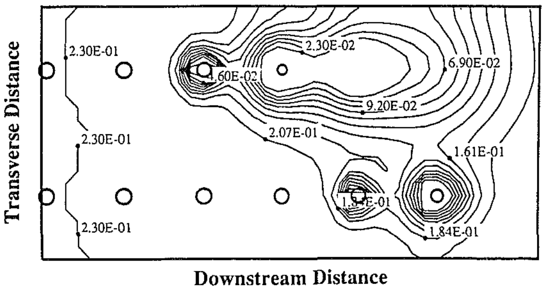

Fig. 23(*c*)

Fig. 23 Unsteady, two parallel droplet stream configuration contour plots at nondimensional time = 0.016: (*a*) reaction rate with contour intervals of 0.824, (*b*) gas temperature with contour intervals of 283 K, and (*c*) oxygen mass fraction with contour intervals of 0.023

shows fuel vapor mass fraction in a two-droplet-stream configuration. A multiple flame is portrayed since regions of large fuel vapor mass fraction are separated. Early vaporization and mixing of the fuel vapor with the air together with the introduction of an ignition source allow a premixed flame to occur. The droplets penetrate the premixed flame before complete vaporization has occurred; therefore, continued vaporization in the presence of a hot gas with excess air is sustained. This causes diffusion flames to be established around each stream of droplets. Delplanque and Rangel (1991) performed a related analysis for one stream of droplets flowing through the gaseous viscous boundary layer near a hot wall. They include the important effect of gaseous thermal expansion which created a gas motion and droplet drag that moved the droplet stream away from the wall as it flowed downstream.

The intermittent effects have been addressed in the unsteady analyses of Delplanque et al. (1990) and Rangel and Sirignano (1988a, 1991). These studies are fully in the domain of discrete particle formulations (with the understanding that any two-dimensional representation involves averaging in the third dimension). The inclusion of the intermittent effects yields results that support the general conclusions of the steady-state analyses. Figure 23 shows that both diffusion-flame and premixed-flame structures exist. Furthermore, it is seen that the diffusion flame can envelop more than one droplet. Delplanque et al. also studied the effect of the point source approximation correction discussed in Section 3.3. Figure 24 shows the importance of the correction for the prediction of droplet temperature and droplet mass in the regions where those quantities are rapidly varying with time.

Continillo and Sirignano (1990) studied a counterflow spray problem using a two-continua formulation. They considered two opposed air streams with normal octane liquid droplets injected with the left-hand-side stream. Figure 25 shows that two flames occur in the stagnation region. They are primarily fed by fuel vapor diffusing from vaporizing droplets that have penetrated to the zone between the two flames. Some vaporization occurs before the droplets penetrate the left-hand flame; therefore, that flame has a combined premixed and diffusion character. Figure 25 also shows the effect of varying strain on the behavior of the flow. Increasing the strain results in narrowing the two reaction zones and causing them to approach each other and the stagnation plane. Ultimately, the increasing strain rate causes the two reaction zones to merge and only one temperature peak is seen in Fig. 25(c). Other recent studies

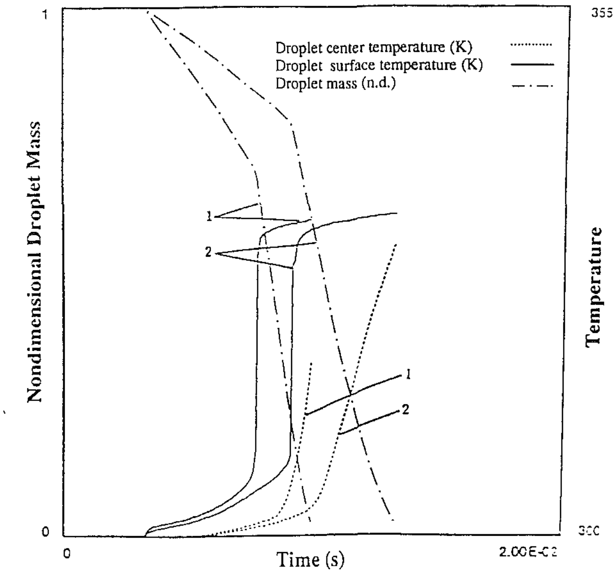

Fig. 24 Droplet temperature and mass versus time for the second droplet in the stream nearest the ignition source in a parallel stream configuration. Point source approximation correction for Curve 1. No correction for Curve 2.

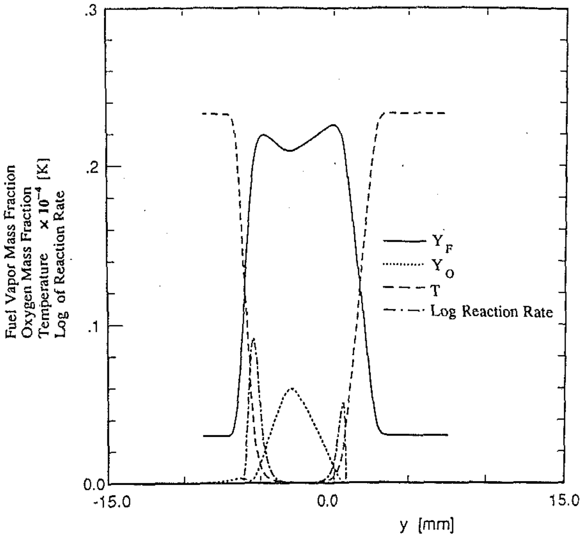

Fig. 25(*a*)

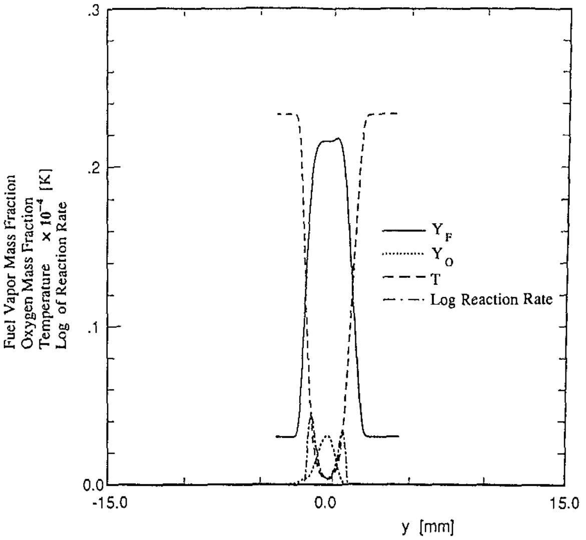

Fig. 25(*b*)

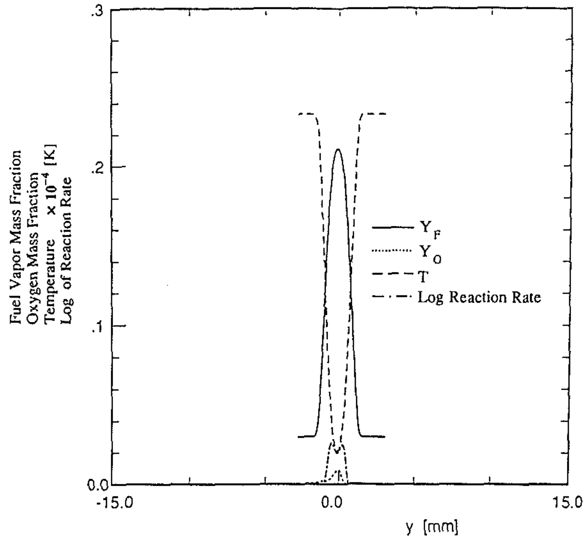

Fig. 25(*c*)

Fig. 25 Counterflow spray: influence of the strain rate. Profiles of temperature (solid line), fuel vapor mass fraction (dotted line), oxygen mass fraction (dashed line), and log of reaction rate (dot-dash line). Initial droplet diameter = 50 μm. Strain rate = (*a*) 100 s^{-1}, (*b*) 300 s^{-1}, and (*c*) 500 s^{-1}.

on counterflow spray flames include an experimental study by Chen et al. (1988) and theoretical/experimental study by Li et al. (1992). The study by Li et al. predicts the locations of the vaporization zone and the reaction zone as a function of the strain rate for heptane and methanol sprays transported in a nitrogen stream and mixing with a counterflowing oxygen/nitrogen stream. Extinction conditions are also predicted.

The subgrid vaporization models used in these above-maintained spray studies have evolved over the years. Originally, spherically symmetric models with Ranz-Marshall corrections were employed. During the middle 1980's, the Tong and Sirignano model came into use. More recently, the Abramzon and Sirignano model has been employed. Also, experimental drag coefficients such as those of Ingebo (1956) and Renksizbulut and Yuen (1983) have been replaced by computational correlations such as those of Haywood et al. (1989) and Chiang et al. (1992) for input to spray models.

The general conclusions of the one-dimensional planar, two-dimensional planar, and spherically symmetric studies are that: (i) resolution on the scale of the spacing between droplet is important in the determination of ignition phenomena and flame structure, (ii) more than one flame zone can exist at any instant with spray combustion, (iii) an inherent unsteadiness results for the flame structure, (iv) diffusion-like or premixed-like flames can occur, (v) ignition and flame propagation for sprays can sometimes be faster than for gaseous mixtures of identical stoichiometry, and (vi) droplets tend to burn in a cloud or group rather than individually.

3.5 Probabilistic Formulation. It is sometimes convenient to employ a probabilistic formulation for the spray analysis. Whenever we have spacial resolution on a scale comparable to or smaller than the averaging spacing between droplets, a given computation cell has a significant probability of not containing any droplet at any particular instant of time. Furthermore, in dealing with a very large number of droplets in a spray, there is no practical way to know exactly where each droplet is located at each instant; a probabilistic formulation is practical therefore in a high resolution analysis.

A probability density function can be defined as $f(t, x_i, R, u_{\ell i}, e_\ell)$ and an infinitesimal hyper-volume in eight-dimensional space is given by

$$dV = dx_1\, dx_2 dx_3 du_{\ell 1} du_{\ell 2} du_{\ell 3} dR\, de_\ell$$

Then, fdV is the probability of finding a droplet in the hyper-volume dV at a particular instant of time. Note that for very fine resolution fdV is less than unity. However, for very coarse resolution, that product can become much larger than unity since many droplets can be in the hyper-volume; in that case, f is more commonly named a distribution function. Williams (1985) discusses the distribution function. Sirignano (1986, 1993) extends the independent variable space, relates the probability density function to the distribution function, and separates droplets by class according to initial values.

We can separate the droplets into distinct classes depending upon their initial size, velocity, or composition. Then, a probability density function or a distribution function can be defined for each class of the droplets. Conservation of droplet numbers (neglecting shattering or coalescence) leads to the following equation which governs the probability density function $f^{(k)}$ for the kth class of droplets

$$\frac{\partial f^{(k)}}{\partial t}+\frac{\partial}{\partial x_j}(u_{\ell j}f^{(k)}) + \frac{\partial}{\partial u_{\ell j}}(a_{\ell j}f^{(k)})+\frac{\partial}{\partial R}(\dot{R}f^{(k)})+\frac{\partial}{\partial e_\ell}(\dot{e}_\ell f^{(k)})=0 \qquad (87)$$

where

$$a_{\ell i}\equiv\frac{\tilde{F}_{Di}}{\frac{4}{3}\pi\rho_\ell R^3}+g_i$$

is the droplet acceleration. Note that Eq. (87) is equivalent to the statement that fdV is a constant.

The characteristics of the hyperbolic partial differential equation (87) are given by

$$\frac{d^{(k)}x_i}{dt}=u_{\ell i};\quad \frac{d^{(k)}u_{\ell i}}{dt}=a_{\ell i};\quad \frac{d^{(k)}R}{dt}=\dot{R}=-\frac{\dot{m}}{4\pi\rho_\ell R^2}$$

$$\frac{d^{(k)}e_\ell}{dt}=\dot{e}_\ell=\frac{\dot{m}}{\frac{4\pi}{3}\rho_\ell R^3}\left[e_\ell-e_{\ell s}+\frac{\dot{q}}{\dot{m}}\right] \tag{88}$$

These characteristics define particle paths or probable particle paths for each class of droplet.

Integration of the distribution function gives the averaged values used in the multi-continua approach. The droplet number density $n^{(k)}$ is given by the five-dimensional integral

$$n^{(k)}=\int f^{(k)}du_{\ell i}dR\,de_\ell \tag{89}$$

Any of the variables $\varphi=u_{\ell i}$, $a_{\ell i}$, R, $\dot{R}$, e_ℓ, or $\dot{e}_\ell$ can be integrated to give the average quantity

$$\varphi^{(k)}=\left[\int f^{(k)}\varphi\,du_{\ell i}dR\,de_\ell\right]\Big/n^{(k)} \tag{90}$$

where $\varphi^{(k)}$ represents $u_{\ell i}^{(k)}$, $a_{\ell i}^{(k)}$, $R^{(k)}$, $\dot{R}^{(k)}$, $e_\ell^{(k)}$, or $\dot{e}_\ell^{(k)}$.

Integration of the divergence form of the equation governing $f^{(k)}$, namely Eq. (87), leads to the Eq. (65) for conservation of droplet number which governs droplet number density. Note that, since both $u_{\ell i}$ and x_i are independent variables in Eq. (87), the second term in that equation can be simplified. In particular, within that term, $u_{\ell i}$ can be brought forward of the derivative sign.

Equation (87) can be multiplied by φ (term-by-term), rearranged, and integrated over the five-dimensional volume. Here, it is assumed that $f^{(k)}$ goes to zero as $u_{\ell i}$ or R becomes infinite. Also, $\dot{R}$ becomes zero when $R=0$. Finally, with respect to the averaged quantities defined by Eq. (90), it is assumed that the average of a product of two quantities equals the product of the averages of the two quantities. The error in this assumption reduces as the band of the independent variables ($u_{\ell i}$, R, e_ℓ) for a nonzero probability density function in a given class k is reduced. When $\varphi=1$, Eq. (65) is reproduced by this process and when $\varphi=u_{\ell i}$, Eq. (73) is reproduced. With modest effort, use of $\varphi=R$ and $\varphi=e_\ell$ can yield Eqs. (58) and (78), respectively.

The probabilistic formulation or, equivalently, the distribution function formulation is of primary value, because it strengthens the theoretical foundations of the spray equations. In the case where coarse resolution is sought, both gas-phase and liquid-phase properties are averaged over a neighborhood containing many droplets. Then, any uncertainty associated with the precise locations of individual droplets is removed from the final analytical form by the averaging process. In the fine resolution case, uncertainty in droplet position remains a factor; the probability density function describes this uncertainty. There is also an uncertainty in the gas-phase values here on account of the coupling between the phases. For very dilute sprays, the uncertainty in the gas-phase properties can be neglected. In denser sprays, these uncertainties in the gas-phase properties appear in high resolution practical spray problems; theory has not yet fully addressed this interesting problem. Aggarwal and Sirignano (1985a) discuss the uncertainty in ignition delay associated with the uncertain distance of the nearest droplet to the ignition source.

4 Interactions Amongst Droplets

There are three levels of interaction amongst neighboring droplets in a spray. If droplets are sufficiently far apart, the only impact is that neighboring droplets (through their exchanges of mass, momentum, and energy with the surrounding gas) will affect the ambient conditions of the gas field surrounding a given droplet. As the distance between droplets becomes larger, the influence of neighboring droplets becomes smaller and tends toward zero ultimately. At this first level of interaction, the geometrical configuration of the (mass, momentum, and energy) exchanges between a droplet and its surrounding gas is not affected by the neighboring droplets. In particular, the Nusselt number, Sherwood number, and lift and drag coefficients are identical in values to those for an isolated droplet. This type of interaction has been fully discussed in Section 3.

At the next level of interaction, droplets are closer to each other, on average, and the geometrical configurations of the exchanges with the surrounding gas are modified. In addition to modification of the ambient conditions, the Nusselt number, Sherwood number, and the lift and drag coefficients are modified. Here, a droplet cannot be treated as if it were an isolated droplet; the neighboring droplet(s) are within the gas film or wake of the droplet. In a convective situation, a droplet can influence a second droplet at substantial distances of many tens of droplet radii if the latter is in its wake. If the droplets are placed side by side in a convective situation, significant influence occurs only over short distances of a few droplet radii. This type of interaction will be the major subject of discussion for this section.

The third level of interaction amongst droplets involves collisions whereby the liquids of the different droplets actually make contact with each other. Here, the droplets might coalesce into one droplet or emerge from the collision as two or more droplets. Some discussion of this subject will be made later in this section.

From another perspective, Sirignano (1983) classified interactive droplet studies into three categories: droplet arrays, droplet groups, and sprays. Arrays involved a few interaction droplets with ambient gaseous conditions specified. There are many droplets in a group but gaseous conditions far from the cloud are specified and are not coupled with the droplet calculations. The spray differs from the group in that the total gas field calculation in the domain is strongly coupled to the droplet calculation. In the spray, either the droplets penetrate to the boundaries of the gas or, while the droplets may not penetrate, the impact of the exchanges of mass, momentum, and energy extends throughout the gas. A useful review on droplet interactive processes can be found in Annamalai and Ryan (1992). Note that unpublished information from Annamalai and Ryan indicates that radiative transfer between droplets can be significant even if the separation distance is ten diameters or greater.

The earliest work on droplets that were interactive at the second level was performed for vaporizing droplet arrays without forced convection. Twardus and Brzustowski (1977) considered two vaporizing and burning fuel droplets of equal size with spacing between their centers as a parameter. The vaporization rate decreased monotonically as the spacing decreased. At very large spacing, the droplets achieved the maximum vaporization rate equal to the isolated droplet value for each droplet. When the spacing decreased to the minimum value with the spherical droplet surfaces in contact, the vaporization rate and the Nusselt number were reduced by approximately 31 percent from the isolated droplet values. Clearly, the proximity of another droplet in this stagnant situation inhibited the exchange of mass and energy between the droplet and the gas. Labowsky (1978, 1980) considered several interactive vaporizing droplets in a stagnant domain and found similar reductions in transport rates. More recently, Umemura et al. (1981a, 1981b) have studied this interactive problem. Xiong et al. (1985) argue that diffusion analyses without consideration of natural or forced convection leads to overprediction of the effect of droplet interactions.

Low Reynolds number flow for interacting particles has been studied by Happel and Brenner (1965), Batchelor and Green (1972), and Jeffrey and Onishi (1984). Nonvaporizing arrays with forced convection at intermediate Reynolds number were studied by Tal and Sirignano (1982) and Tal et al. (1983, 1984a, 1984b). Spherical particles were aligned both in tandem and side-by-side with the gas flowing past them. Relative velocity was held fixed and steady-state solutions were obtained. A cylindrical-cell approach was employed to allow axisymmetric Navier-Stokes calculations to give approximate descriptions of the three-dimensional phenomena. These calculations showed that drag coefficients and Nusselt number decreased for the downstream droplets as the spacing between tandem droplets decreased. In other words, the downstream droplets were partially shielded by the wake of the forward droplet. As spacing between side-by-side droplets decreased, the local relative gas velocity and Reynolds number increases leading to an increase in convective transport and in friction drag. Therefore, the Nusselt number and drag coefficient increase beyond the isolated droplet values as the spacing between side-by-side droplets decreases. Note that surface regression (due to vaporization) and internal circulation were not considered so that the droplets here are essentially equivalent to solid particles. The studies of Tal et al. have considered up to four particles or droplets in tandem. In the case where there are no side-by-side particles and only tandem particles, the drag coefficient and Nusselt number of the first or upstream particle are generally approximately equal to the isolated particle values. In all cases, the downstream particles experience reduced drag coefficient and Nusselt number from the first particle; furthermore, little difference occurs in the values for the second, third, and fourth particles in tandem.

Studies on group vaporization have generally addressed only the first level of interaction. See, for example, Chiu and Liu (1971), Labowsky and Rosner (1978), Chiu et al. (1983), Suzaki and Chiu (1971), and Bellan and Cuffel (1983). Bellan and Harstad (1987, 1988) studied a cluster of droplets in a convective flow focussing on the build-up of fuel vapor and cooling of the gas. The work of Ryan et al. (1990) is an exception wherein correction factors accounted for the second level of interaction. Similarly the spray calculations, such as those addressed in Section 3, have considered only the first level of interaction. A novel approach employing numerical simulations with a cellular automaton for dense sprays was recently introduced by Borghi and Loison (1992).

Patnaik and Sirignano (1986) extended the work of Patnaik et al. (1986) to consider two droplets moving in tandem at constant spacing. The solution of the first droplet was calculated as if that droplet were isolated. Then, that solution for the wake was used as a free stream input to the downstream droplet. The weaknesses of this model are the omission of variation in spacing and upstream influence of the second droplet. Tong and Chen (1988) extended the cylindrical-cell model of Tal and Sirignano (1982) to include vaporization. A three-droplet linear (tandem) array was studied to obtain correlations for the Nusselt number. Kleinstreuer et al. (1989) employed a finite element analysis of the linear array to yield the drag coefficients of interacting spheres. Also, they used a boundary layer analysis for vaporizing droplets to simulate coupled transfer processes for three droplets in tandem. The analysis involves individual computations for the three spheres with coupling only through the determination of an effective temperature for the gas flow approaching the downstream droplets. Tsai and Sterling (1990) determined Nusselt number and drag coefficients for steady flow past a linear array of non-vaporizing spheres. They obtained results that were in qualitative agreement with Tal et al. (1983) and Tong and Chen (1988). All of the above analyses take advantage of axisymmetric flow.

Raju and Sirignano (1990b) developed a transient axisymmetric finite difference analysis with a grid generation scheme for two vaporizing droplets moving in tandem. They considered variable density but otherwise constant thermophysical properties in similar fashion to Patnaik et al. (1986). The extension beyond other studies for tandem droplets involves transient behavior (including unequal regression rates of the two droplet surfaces and temporal variation in droplet spacing due to differences in droplet drag and mass), fully coupled Navier-Stokes solution (allowing for complete coupling of internal liquid flow and gas flow and for complete elliptic behavior with upstream influence), and different initial sizes for the upstream and downstream droplets. They studied a limited range of initial values for Reynolds number, droplet spacing, and droplet radii ratio. The most interesting result was that there exists a critical ratio of the two initial droplet diameters below which droplet collision does not occur. If the ratio of the downstream droplet initial diameter to the upstream initial diameter is larger than the critical ratio, the reduced drag coefficient of the downstream droplet causes less deceleration and greater relative velocity with the gas for the downstream droplet. Therefore, collision is likely since the spacing decreases with time. Below the initial ratio, the reduced inertia of the downstream droplet causes the spacing to increase. The critical ratio is found to be less than unity and very weakly dependent upon initial Reynolds number. Recall, however, that Chiang et al. (1992) showed that constant thermophysical properties could lead to errors in the detailed prediction of the drag coefficients. These errors, of course, make the precise determination of the critical ratio questionable.

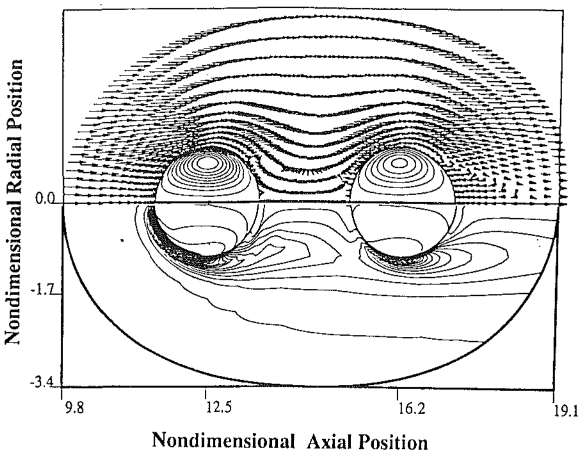

Fig. 26 Two-tandem droplet case: gas-phase velocity vector and liquid-phase stream function (on top), and vorticity contours for both phases (on bottom). Time = 3.00, $Re_1 = 80.31$, $Re_2 = 85.84$, $R_1 = 1.00$, $R_2 = 1.00$, nondimensional spacing = 3.71.

More recently, Chiang and Sirignano (1993a) and Chiang (1990) have extended the two-tandem-droplet calculation of Raju and Sirignano (1990b) to account for variable thermophysical properties. A wider range of initial values for Reynolds number, droplet spacing, and droplet radii ratio were considered. Also, correlations of the numerical results for drag coefficient, Nusselt number, and Sherwood number with Reynolds number, transfer number, spacing, and radii ratio were obtained. Furthermore, Chiang and Sirignano (1993b) have extended the analysis to three droplets moving in tandem.

The two-droplet results of Chiang and Sirignano are in qualitative agreement with the findings of Raju and Sirignano. Figure 26 shows gas-phase velocity vector, liquid-phase stream function, and vorticity contours for both phases. The downstream sphere is seen to be within the wake of the upstream sphere. Hence, the effective Reynolds number for the downstream sphere is less than the Reynolds number for the upstream sphere. The strength of the liquid-phase vortex and transport rates on the forward side are less for the downstream droplet than for the upstream droplet. Transport rates on the

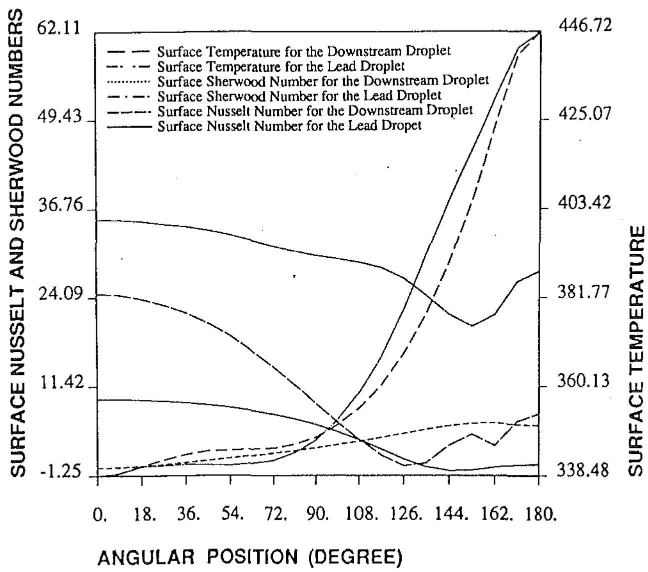

Fig. 27 Surface temperatures, Nusselt number, and Sherwood number versus position on droplet surface for the two-tandom-droplet case. N-decane liquid, 1000 K ambient temperature, 300 K initial droplet temperature, 100 initial Reynolds number, 1.00 initial R_1 and R_2, 8.0 initial spacing.

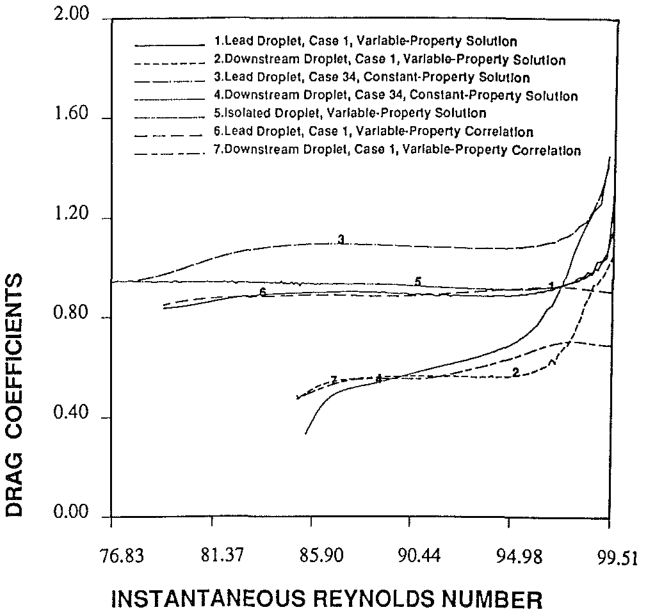

Fig. 28 Drag coefficient versus instantaneous Reynolds number for two-tandem-droplet case

aft side of the droplet are greater for the downstream droplet than for the upstream droplet as shown by Fig. 27.

The drag coefficient is displayed as a function of instantaneous Reynolds number in Fig. 28. The reduction of the drag coefficient for the downstream droplet and the general overprediction of the constant-property solution are shown. The similarity between the drag coefficient of an isolated droplet and that of the lead droplet are shown also. Center-to-center spacing as a function of time is shown in Fig. 29 for various initial spacings D and various initial droplet radii ratio R_2. The prediction of strong influence upon the downstream droplet at a spacing of sixteen droplet radii is consistent with the experimental findings of Temkin and Ecker (1989) who found influences up to thirty radii spacing. It is seen that a critical value of R_2 can exist that distinguishes between increasing spacing and decreasing spacing with time.

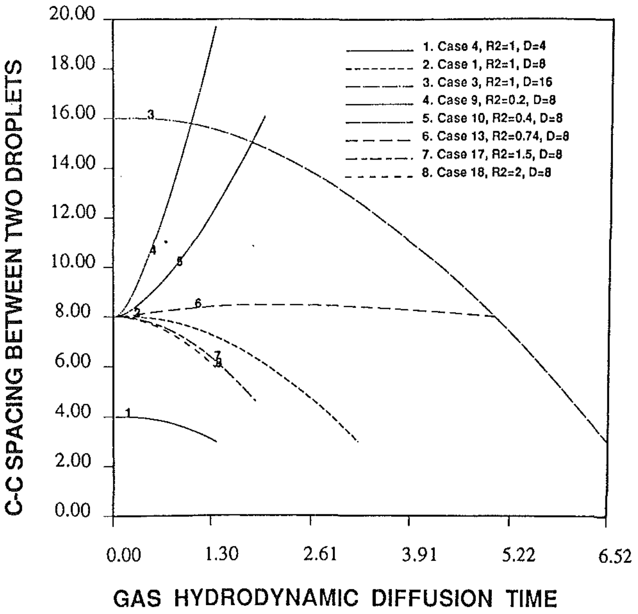

Fig. 29 Center-to-center droplet spacing versus nondimensional time for various initial values for spacing D and radii ratio R_2

Chiang and Sirignano (1993a) obtained correlations for drag coefficients from their computational results as shown in Fig. 28; also, correlations for Nusselt number and Sherwood number were obtained. A linear regression model was employed to fit over 3000 data points. The correlations are normalized by the isolated droplet correlations given by Eq. (56) of Section 2. The correlations for each of the droplets follow.

For the lead droplet:

$$\frac{C_{D1}}{C_{D\mathrm{iso}}}=0.877\,\mathrm{Re}_m^{0.003}(1+B_H)^{-0.040}D^{0.048}(R_2)^{-0.098}$$

$$\frac{\mathrm{Nu}_1}{\mathrm{Nu}_{\mathrm{iso}}}=1.245\,\mathrm{Re}_m^{-0.073}\mathrm{Pr}_m^{0.150}(1+B_H)^{-0.122}D^{0.013}(R_2)^{-0.056}$$

$$\frac{\mathrm{Sh}_1}{\mathrm{Sh}_{\mathrm{iso}}}=0.367\,\mathrm{Re}_m^{0.048}\mathrm{Sc}_m^{0.730}(1+B_M)^{0.709}D^{0.057}(R_2)^{-0.018} \tag{91}$$

where

$$0.\le B_H\le 1.06;\ 0.\le B_M\le 1.29;\ 11\le \mathrm{Re}_m\le 160;$$
$$0.68\le \mathrm{Pr}_m\le 0.91;\ 1.47\le \mathrm{Sc}_m\le 2.50;\ 2.5\le D\le 32;$$
$$0.17\le R_2\le 2.0$$

For the downstream droplet:

$$\frac{C_{D2}}{C_{D\mathrm{iso}}}=0.549\,Re_m^{-0.098}(1+B_H)^{0.132}D^{0.275}(R_2)^{0.521}$$

$$\frac{\mathrm{Nu}_2}{\mathrm{Nu}_{\mathrm{iso}}}=0.528\,\mathrm{Re}_m^{-0.146}\mathrm{Pr}_m^{-0.768}(1+B_H)^{0.356}D^{0.262}(R_2)^{0.147}$$

$$\frac{\mathrm{Sh}_2}{\mathrm{Sh}_{\mathrm{iso}}}=0.974\,\mathrm{Re}_m^{0.127}\mathrm{Sc}_m^{-0.318}(1+B_M)^{-0.363}D^{-0.064}(R_2)^{0.857} \tag{92}$$

where

$$0.\le B_H\le 2.52;\ 0.\le B_M< 1.27;\ 11\le \mathrm{Re}_m\le 254;$$
$$0.68\le \mathrm{Pr}_m< 0.91;\ 1.48\le \mathrm{Sc}_m\le 2.44$$

Chiang and Sirignano (1993b) considered three tandem vaporizing droplets of equal initial diameters. The qualitative conclusions of the two-droplet study generally apply to the behavior of the first two droplets. The drag coefficients and transport rates for the second and third droplets are significantly reduced below the lead droplet values which remain close to the isolated droplet values. The transport rates of the

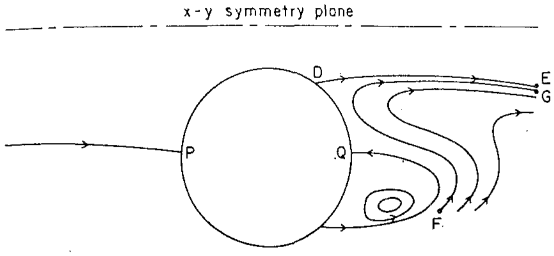

Fig. 30 **Streamlines in symmetry plane for flow past two side-by-side spheres**

second and third droplets differ by a very small amount in general; however, the second droplet has a slightly lower drag coefficient than the third droplet. Correlations are reported in the paper.

The two-tandem and three-tandem-vaporizing-droplet computational results are consistent with the non-vaporizing sphere results of Tal et al. who found little difference in drag coefficient for downstream particles in a tandem stream. Also, many experimental investigators have found that, in a long stream of equi-sized droplets moving in tandem with uniform initial spacing amongst the droplets, the spacing remains constant with time, implying equal drag coefficients. (Sangiovanni and Kesten, 1976; Nguyen et al., 1991; and Nguyen and Dunn-Rankin, 1992).

Asano et al. (1988) analyzed two tandem spheres in a steady flow with constant properties. The interactions are described in a simple manner using geometric factors. Nguyen et al. (1991) performed a computational and experimental study of droplets moving in tandem. Vaporization was not significant in their experiment due to low ambient temperatures and saturated vapors in the droplet stream vicinity. They found that a lead droplet and a trailing droplet of equal size will collide for small initial spacings which agrees with theoretical predictions including their own prediction. Further experimental studies on drag reduction and collisions for a small number of droplets moving in tandem are reported by Nguyen and Dunn-Rankin (1992).

The interaction of two spheres moving side-by-side in parallel, or approximately in parallel, is a three-dimensional phenomenon. Only a limited number of three-dimensional flow calculations for individual spheres have been made. Dandy and Dwyer (1989) considered steady, uniform shear flow past a heated sphere. Tomboulides et al. (1991) considered flow past a sphere with an unsteady wake.

More recently, Kim et al. (1993) have studied three-dimensional flow over two identical spheres moving in parallel at constant velocity. The separation distance between the two sphere centers is held constant and the line connecting the centers is normal to the free stream velocity vector. Both liquid and solid spheres were considered at Reynolds numbers between 50 and 150. The transient finite-difference calculations were made in one quadrant of the flow field, taking advantage of the two perpendicular planes of symmetry. The asymptotic results yielded the steady flow results.

Figure 30 shows streamlines in the plane of symmetry containing the two sphere centers. In this case, the separation distance is small. It is seen that the flow through the gap between the neighboring spheres has a jetlike character and entrains the outer flow. On the foreside of the sphere in Fig. 30, the stagnation point is perturbed from its position in an axisymmetric flow. As a result, the flow on the side closer to the neighboring sphere has a lower velocity and higher pressure than the axisymmetric case; on the other side, the velocity is higher and the pressure is lower than the axisymmetric reference. On account of asymmetric deviations of pressure and surface friction, the spheres experience lift and torque as well as a modification of the drag due to the mutual interaction.

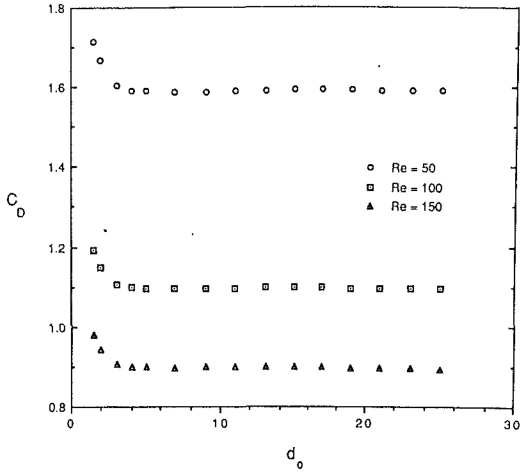

Fig. 31 **Drag coefficients versus separation distance at several Reynolds numbers for flow past two side-by-side spheres**

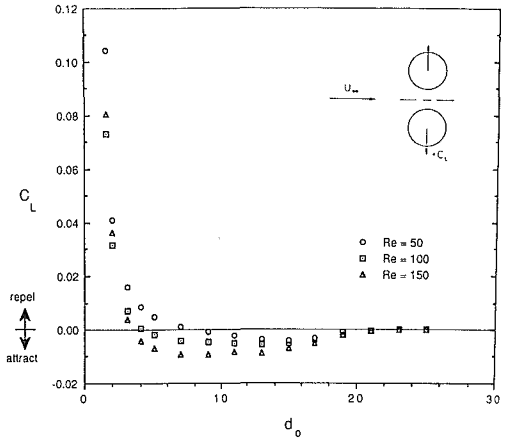

Fig. 32 **Lift coefficients versus separation distance at several Reynolds numbers for flow past two side-by-side spheres**

The lift forces on the spheres result in a weak attraction at large separation distances and a strong repulsion at small separation distances. The drag coefficient increases as the separation decreases. Figures 31 and 32 display drag and lift coefficients for liquid spheres.

In another recent study, Kim et al. (1992) have considered the effects of drag and lift on the trajectories of two droplets of equal size and equal and parallel initial velocity. At large initial separation, the two droplets move slightly closer while, at small initial separation, the deflection due to repulsion was more significant. In both cases, the translation of the two droplets were nearly parallel.

A general conclusion from the several studies is that collisions amongst droplets seem to have a low probability in a spray where the droplets are moving in a parallel direction or along divergent paths. The stability of droplets in a linear stream and the repulsive lift forces of nearby droplets moving in parallel tend to support this conclusion.

Various types of collisions between two droplets are possible in a spray environment. Weak collisions such as grazing collisions can occur. We can have stronger "head-on" collisions, as determined by relative velocity (i.e., both droplets can be moving in any absolute direction). The stronger collisions can lead to one of several phenomena: permanent coalescence, coalescence with a vibration that leads to separation into two other droplets, coalescence and vibration with separation into two droplets plus smaller satellite droplets, shattering into many smaller droplets, or bouncing. An interesting experimental study of two colliding (water and normal-alkane) droplets has been made by Jiang et al. (1992). The three-droplet collision is less interesting on account of its lower probability of occurrence.

Arguments are given by O'Rouke and Bracco (1980) that coalescence is an important factor in the dense spray region near the injection point. They developed an elaborate spray model accounting for collision and coalescence of droplets. Bracco (1985) and Reitz (1987) also discuss and employ this model. The model predicts increasing average droplet size with downstream distance from the injector; some experimental evidence of growing droplet size with distance is also cited. This reviewer is, however, rather skeptical because no fundamental experimental study resolving the phenomena on the scale of the droplets within a spray context has been made. The work of Jiang et al. (1992), for example, involved only two droplets deliberately aimed at each other. Several other mechanisms could cause increasing average droplet size with downstream distance: (1) smaller droplets vaporize faster leaving the larger droplets; (2) condensation occurs in the cold, vapor-rich, dense spray region near the injector; and (3) the longer wavelength disturbances on the jet will take a longer Lagrangian time to grow and to yield the larger droplets.

5 Droplet Interactions With Turbulence and Vortical Structures

The interactions of a spray with a turbulent gas flow is very important in many applications (e.g., most power and propulsion applications). Two types of studies exist. In one type, the global and statistical properties associated with a cloud or spray with turbulent field are considered. In the other type, detailed attention is given to how an individual particle behaves in a turbulent field. Some studies consider both perspectives. Most of the research work in the field has been performed on the former type of study. Faeth (1987) and Crowe et al. (1988) give helpful reviews of this type of research.

5.1 Turbulent Spray Flows. The interactive turbulent fields can be separated into homogeneous turbulent fields and free shear flows (e.g., jets and mixing layers). In some theoretical studies, two-dimensional vortical structures interacting with a spray have been examined. Most of the studies deal with situations where the contribution of the spray to the generation of the turbulence field is secondary. That is, there exists a forced gas flow whose mass flux and kinetic energy flux substantially exceeds the flux values for the liquid component of the dilute flow. The turbulence kinetic energy flux of the gas flow is much less than the mean kinetic energy flux of the gas flow and is comparable to the mean kinetic energy of the liquid flow. Therefore, the turbulent field is much more likely in this situation to receive kinetic energy transferred from the mean gas flow than kinetic energy transferred from the mean liquid flow. An exception to this situation would be a liquid-propellant rocket motor where all of the forced flow is initially in liquid form. In this case, the turbulent kinetic energy appears directly or indirectly through transfer from the mean kinetic energy of the liquid. The direct transfer is defined to be the type where turbulent fluctuations in the liquid flow or boundary layer and wake instabilities in the gas flow past the liquid (e.g., vortex shedding over droplets) cause the gas-phase turbulent fluctuations. Indirect transfer is the case whereby vaporization causes the mean kinetic energy of the liquid to be transformed into mean kinetic energy of the vapor which in turn gets partially transferred to turbulent kinetic energy of the gas.

Dispersion of particles or droplets in a turbulent field has been a subject of major research interest over the past few decades. Hinze (1975) discusses the rudimentary aspects of fluid and particle dispersion. According to Hinze (1975), the first analytical work on particle motion in a turbulent field was performed by Tchen who took the equation for particle motion derived by Basset, Boussinesq and Oseen and applied it to a particle in a homogeneous turbulent field. Stokes drag, pressure gradient force, virtual mass, and the Basset correction were considered in the analysis. The equation of particle motion will be discussed later in this section. Implicitly, the analysis is limited to low droplet Reynolds number, to cases where the turbulent eddy is large compared to the particle size, and to cases where the particle remains in the same eddy for its lifetime. Hinze explains how others have relaxed the last restriction. Based upon the works discussed in Sections 2 and 3 of this paper, we know how to extend the prediction of droplet or particle motion to higher Reynolds number. The second restriction is a major one; there are practical situations where the droplet or particle size is comparable to the smallest (Kolmogorov) scale of turbulence. Therefore, the droplet experiences not only a temporal variation in its local free stream but nonuniformity as well.

Faeth (1987) has compared three types of two-phase models for turbulent flows: locally homogeneous flow (LHF), deterministic separated flow (DSF), and stochastic separated flow (SSF). He prefers SSF for practical dilute sprays; that model considers finite interphase transport rates and uses random-walk computations to simulate turbulent dispersion for the dispersed phase.

Crowe et al. (1988) review both time-averaged and time-dependent free shear flows of two phases. The time-dependent methods capture the instantaneous flow and can better calculate particle trajectories. In the time-averaged method, a steady flow with gradient diffusion is usually considered.

Elghobashi and Abou-Arab (1983) developed a two-equation turbulence model for two-phase flows that eliminated much of the ad hoc character of simulating the character of the interaction between the two phases in a turbulent flow. While the formulation is derived from continuity and momentum equations, modeling at third order is necessary to achieve closure. The resulting equations describe the turbulent kinetic energy and the dissipation of the turbulent kinetic energy for the continuous phase. Elghobashi et al. (1984) applied the two-equation model to a particle-laden jet calculation and demonstrated respectable agreement with experiment. They showed that additional dissipation of the flow results in this two-phase case. Mostafa and Elghobashi (1985a,b) extended the model to account for vaporization. Rizk and Elghobashi (1985) studied the motion of a spherical particle near a wall accounting for the effects of lift and the modification of drag. Rizk and Elghobashi (1989) extended the two-phase, two-equation turbulence model to account for confined flows with wall effects.

The above mentioned research by Elghobashi and coworkers has employed Eulerian formulations for both the dispersed and continuous phases. Gosman and Ioannides (1981), Mostafa and Mongia (1988), Mostafa et al. (1989), and Berlemont et al. (1991) have employed a stochastic Lagrangian method for the dispersed phase, together with a two-equation turbulence model for the continuous phase. The first study did not account for the modification of the two-equation turbulence model due to the presence of the second phase. MacInnes and Bracco (1992a) have examined stochastic dispersion models for non-vaporizing sprays. They considered several cases of homogeneous turbulence and of shear flows. Concerns were raised about many existing models that predicted eventual non-uniform distribution of particles in a flow that initially possessed a uniform distribution. An approximate correction is derived. The work is extended to include the effects of finite particle response time by MacInnes and Bracco (1992b).

Squires and Eaton (1989, 1991), Elghobashi (1991), and Elghobashi and Truesdell (1991, 1992, 1993) have analyzed two-phase flows by direct numerical simulation (DNS) of isotropic homogeneous turbulent flows. Squires and Eaton used only Stokes drag as the force on the particle and considered both one-way and two-way couplings of the two phases with

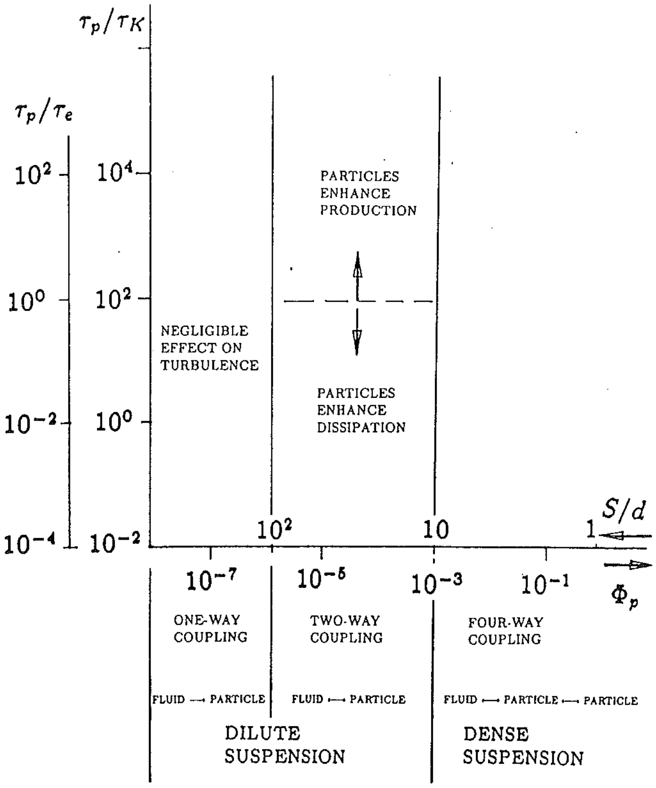

Fig. 33 Map of flow regimes in turbulent particle-laden flows from Elghobashi (1991)

regard to the turbulent field. Figure 33 from Elghobashi (1991) shows the domains of various types of coupling between the phases. The three parameters in the map are the ratio of the droplet kinematic response time to the Kolmogorov time scale, the ratio of the droplet response time to the integral time scale for turbulence, and the ratio of the average distance between neighboring droplets to the droplet diameter. The two time ratios are plotted on the ordinate while the length ratio is plotted on the abscissa. Volume fraction which is immediately determined from the length ratio is also shown. Elghobashi and Truesdell considered viscous and pressure drag, pressure gradient and viscous stress forces on the particle, Basset correction, gravity, and virtual mass. One-way coupling was considered by Elghobashi and Truesdell (1992) while two-way coupling was considered in their other papers (1991, 1993); the particles did not modify the turbulent field substantially for dilute flows. Lagrangian methods were employed to calculate particle trajectories. At zero gravity and short dispersion times, inertia caused particle diffusivity to exceed the fluid diffusivity. Both gravity and inertia reduced lateral dispersion. At low frequencies, particle energy remains higher than the fluid energy. Particle energy is lower than fluid energy in the mid-to-high frequency range. Drag and gravity tended to be the dominant forces. The Basset correction was the next largest force term but generally an order of magnitude smaller.

Some theoretical studies have been performed on time-dependent behavior within mixing layers and jets laden with particles or droplets. Generally, inviscid vortex methods for the dispersed phase are employed. Coupling between the hydrodynamics of the two phases is assumed to be one-way only. Chein and Chung (1987) emphasized the effects of vortex pairing in a mixing layer. The pairing was found to enhance the entrainment and dispersion of the particles. They found optimal dispersion in the mid-range of the Stokes number (ratio of particle aerodynamic response time to the flow characteristic time). Chung and Troutt (1988) extended the method to jet flows. They noted the importance of the large-scale component of turbulence in the dispersion process.

Interesting experimental work on particle dispersion in mixing layers has been performed by Lazaro and Lasheras (1989, 1992a, 1992b) for flows with and without acoustic forcing. In the unforced case, a similarity for particle dispersion independent of particle size is found if the coordinates are normalized by a length proportioned to a density ratio times a Reynolds number times a diameter. Both experimental and theoretical evidence from Lazaro and Lasheras (1989), Chung and Troutt (1988), Chein and Chung (1988), and others indicates that the dispersion of particles with high inertia can exceed that of passive scalars. This agrees with the previously cited DNS results for homogeneous turbulence.

Rangel (1990, 1992) extended the vortex method to consider heat transfer and vaporization of the droplets as well as dispersion. Vortex pairing was also considered in a planar, temporal mixing layer with one-way coupling. The larger droplets tended to be less sensitive to the vortical structure on account of their higher inertia. The smaller droplets were more easily entrained but tended to vaporize completely before vortex pairing had a significant effect. The gas temperature and vapor mass fraction fields were determined by finite-difference Eulerian computations with the droplets serving as sources and sinks. Vortex-dynamical methods were employed to calculate gas velocity while the droplet properties were calculated by Lagrangian discrete-particle methodology. The effects of droplet kinematic inertia were carefully examined. Figure 34 demonstrates the droplet motion and the vapor mass fraction contours in a case where three initially parallel droplet streams are moving through a temporally developing, two-dimensional mixing layer. Droplet and gas properties are averaged in the third dimension. Rangel and Continillo (1992) considered vaporization and ignition for the two-dimensional interaction of a viscous line vortex with a fuel droplet ring or cloud. The effects of chemical kinetic and vaporization parameters on the ignition delay time were determined. Bellan and Harstad (1992) recently modeled a cluster of droplets embedded in a vortical structure. The cluster and the vortex were assumed to convect together which differs from the previous studies. Centrifugal effects caused fuel vapor to accumulate in the vortex core.

In general, much remains to be determined about the modulation of both the mean flow and the turbulent fluctuations or vortical structures by the spray of droplets or cloud of particles. In different situations, the presence of droplets or particles can either enhance or reduce turbulence. More analyses with two-way coupling are necessary.

5.2 Individual Droplet Behavior in a Turbulent Flow. Relatively little research has been performed on the interaction of turbulent eddies with individual droplets or particles. An important parameter is the ratio of the turbulent length scale to the droplet diameter. Existing theories typically assume that the droplet is much smaller than the turbulent length scale; i.e., $Rk \ll 1$ for all values of the wavenumber k in the turbulence spectrum. In this limit, a quasi-uniform free stream is experienced by the droplet. Of course, temporal changes can still occur in the free stream. However, it can be shown that, for many flow devices that operate at high Reynolds number, the Kolmogorov scale actually becomes of the order of 100 microns and compares with the droplet size.

A second important parameter is the ratio of the characteristic time for change in the velocity fluctuation to the residence time for the gas (continuous phase) flow past the droplet. If U is the mean relative droplet velocity and u' is the velocity fluctuation of the gas, this ratio is given by $U/u'Rk$. For values of order unity or smaller, the flow over the droplet is unsteady. Only when the ratio is large compared to unity can the quasi-steady flow assumption be made. In that case and with $Rk \ll 1$, the values of the drag and lift coefficients and the Nusselt and Sherwood numbers are not affected by the tur-

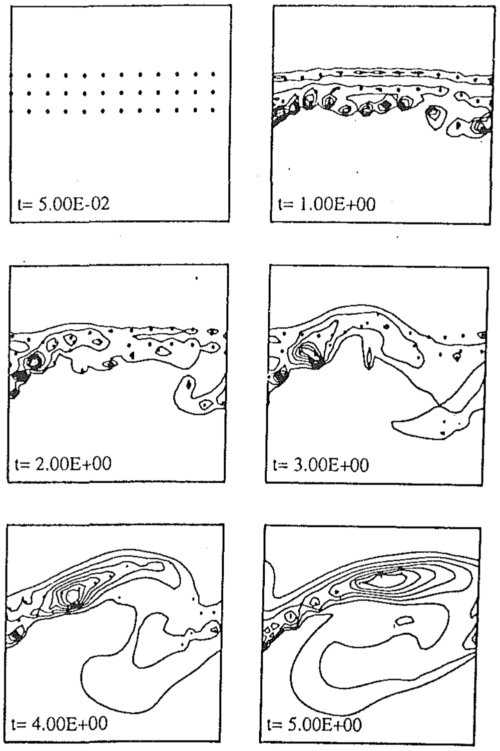

Fig. 34 Temporal development of vapor mass fraction contours and droplet position with three droplet streams moving through a temporally developing two-dimensional mixing layer

bulent flow. (Note that the aerodynamic forces and the transport rates would still be affected by the turbulent fluctuations.)

The conventional practice is to use certain corrections on the drag force for unsteadiness in the relative droplet velocity. Neglecting gravity, we can write

$$\frac{4\pi}{3}\rho_\ell R^3\frac{du_p}{dt}=6\pi\mu R(u-u_p)+\frac{2}{3}\pi\rho R^3\left(\frac{du}{dt}-\frac{du_p}{dt}\right)+6R^2\sqrt{\pi\rho\mu}\int_{t_0}^{t}\frac{\left(\frac{du}{dt}-\frac{du_p}{dt}\right)}{\sqrt{t-t'}}dt' \qquad (93)$$

The second term is the apparent mass term that accounts for the inertia of the gas in the boundary layer and wake of the droplet. It is negligible when the gas density is much smaller than the liquid density (which is usually the case). The third term is the Basset correction force; within the context of a low Reynolds number flow, it corrects for temporal variations in the relative velocity. It can be shown by an order of magnitude argument that this correction is negligible if the second (time ratio) parameter mentioned above is large compared to unity.

Equation (93) is seriously flawed for application to sprays in turbulent flows in spite of its extensive use. It does not account for situations with high wavenumber where Rk is of order unity or larger. It also requires correction for higher Reynolds number, correction for effects of vaporization and Stefan flow, and corrections for the proximity of other droplets. In the quasi-steady and quasi-uniform limit, these corrections have been discussed in Sections 2, 3, and 4. If values of both the first and second parameters are large, a nonuniform but quasi-steady flow is obtained. As discussed in Section 4, some studies of these three-dimensional flows have been made. However, in general, substantially more research is required here.

It should be understood that some velocity fluctuations in the wavenumber range where Rk is of order unity will be generated at sufficiently high droplet Reynolds number. We can expect that vortex shedding of the flow over a droplet can occur producing eddies of a size of the same order of magnitude as the droplet.

Little research has been performed on convective heat and mass transport in turbulent spray flows. On account of its relevance to combustion instability in liquid-fueled and liquid-propellant systems, a substantial amount of research has been performed on the impact of long wavelength ($Rk \ll 1$) fluctuations on a spray (Strahle, 1964, 1965a, 1965b, 1966; Priem, 1963; Priem and Heidmann, 1960; Heidmann and Wieber, 1965, 1966; Harrje and Reardon, 1972; Tong and Sirignano, 1989). The fluctuations of transport rates in this case with uniform but temporally varying free streams approaching the droplet has been found to be significant. Extension of these analyses to the high wavenumber domain is necessary to understand fully the behavior of sprays involved in heat and mass exchange with a turbulent flow.

6 Concluding Remarks

Engineering design can benefit from the advances of the past decade discussed in this review. For example, the models for droplet vaporization, heating, and acceleration can be added to existing codes. While droplet lifetimes do not vary substantially from one model to the next, the instantaneous vaporization and heating rates and the acceleration do vary significantly. Therefore, the trajectories and vapor concentration as a function of time and position within a flow chamber or flow field can vary substantially depending on the particular model. The accuracy of the model becomes more important in situations where multicomponent liquids are present, local heat losses to the walls must be predicted, or flammability limits in a combustion chamber must be predicted.

The spray formulations discussed in Section 3 provide mechanisms for developing scientific insight and for improvements in engineering analysis and design. Numerical errors can be diminished following the guidelines. Also, resolution can be optimized with consideration given to the various trade-offs. It still remains for issues of droplet interactions in dense sprays and of turbulence-droplet interactions to be completely included in the spray analysis. It is expected that, in the not-too-distant future, a fuller spectrum of these types of interactions can be addressed in the formulations of the spray equations to be used in practice.

The behavior of a spray flow has been shown to be complex and to involve many length and time scales. There are many distinct subdomains in the flow and many challenging analytical and computational issues. The topic of spray flow still requires more research. Some comments and suggestions on these needs follow.

There is a glaring lack of experimental data that resolves the flow in the boundary layer, wake, and internal liquid of a droplet. One promising development is the laser based technique (Melton and Winter, 1990) that demonstrates qualitatively the presence of the internal circulation of the droplets. It can provide the basis for further experimental developments. Recently, interesting non-intrusive liquid interior temperature measurements have been made by Wells and Melton (1990), Hanlon and Melton (1992), and Zhang and Melton (1993). There is qualitative agreement between theory and experiment on these measurements.

In all analyses and calculations to date, only spherical droplets have been considered. The more realistic situation is that the larger droplets (more precisely droplets with large Weber numbers) will distort and the solution requires the determination of the interface shape and location. Droplet distortion and possible break-up into smaller droplets is a problem of major practical importance, demanding substantial advances in computational methodologies. Droplet distortion results when the surface-tension force becomes smaller than the pressure and shear forces on the droplet surface. The issue of the determination of the liquid-gas interface is one of the major analytical challenges in the field of nonlinear mechanics. In the extreme of droplet distortion, the issue of the droplet breakup into smaller droplets becomes important.

Another challenge concerns droplet vaporization at near-critical and supercritical pressures. The critical point for a mixture depends strongly upon the composition and critical pressure values can be greater for a mixture than for any of its components. Therefore, certain portions of the field can be supercritical while other portions are subcritical even when the pressure is uniform. Droplets can exist therefore even if the pressure is higher than the critical pressure for any of the gas or liquid components. These calculations are very sensitive to the approximations employed for the equation of state and for the thermodynamic properties. A limited number of studies at spherically symmetric conditions exist but extensive study of the axisymmetric droplet and of the spray situation are needed.

The surface tension becomes greatly reduced as the critical point is approached; therefore, the near-critical behavior is complicated by the distortion of the droplet shape. Also, ambient gases more readily dissolve in the liquid as the critical point is reached. The liquid phase becomes multicomponent and liquid-phase mass diffusion becomes important.

More than one species can be present in the liquid phase either on account of initial conditions or due to absorption from the gas phase. In such cases, the liquid-phase mass diffusion must be considered through species-continuity equations for the liquid. In addition, a phase-equilibrium interface condition is required for each liquid component. The major computational complication is not the addition of another equation but rather the addition of a new and longer characteristic time. The Lewis number for a common liquid is typically greater than ten. Therefore, finer spatial and temporal resolution is required for the liquid phase when mass diffusion becomes important there.

One of the computational challenges before us involves the study of split operators that will expedite these spray calculations wherein the liquid-phase characteristic time can be much larger than the gas-phase times. The liquid-phase calculations could be performed with larger time steps than for the gas-phase calculations.

Another challenge relates to the nucleation of vapor within the droplet. This internal gasification becomes possible with a multicomponent mixture when the phase equilibrium at some internal point yields a vapor pressure (for a given local temperature and liquid composition) that exceeds the total pressure at the point of nucleation. This gasification, at the extreme, could result in a destruction of the droplet into smaller droplets. In order to analyze this gasification and microexplosion, the ability to treat moving nonspherical boundaries must be developed. Even then, the phenomenon might occur on such a fine scale that subgrid modeling is required.

Another interesting challenge involves slurry droplets wherein solid particles exist in the liquid. Often, small metal or coal particles are mixed with liquid fuels to obtain very high energy densities. These particles have kinematic and thermal inertias so that momentum and energy exchanges with the liquid are nontrivial.

One important need is to address further corrections with the point-source approximation. First, correction is needed in the dense spray situation where total liquid volume in a given domain is not negligible compared to the gas volume. Second, the correct application of the ambient conditions for the subgrid droplet model must be pursued.

The full two-way coupling of turbulent gas flows with the spray must be studied further. Only limited studies of this important interaction have been made. Another key problem in certain applications involves the distortion, shattering, or coalescence of droplets. Spray calculation methodology should be developed to treat this phenomenon. While some studies of radiative heating of a spray have been performed, there is a need for further study.

Other interesting extensions involve three-dimensional configurations and highly compressible (including supersonic) gas behavior. Little or nothing has been analyzed for sprays in these situations.

Typically, liquid is injected as a jet to form the spray. Our current analytical capability allows only for the prescription of some upstream boundary conditions giving initial droplet sizes and velocities. There is a major need to develop a predictive capability for the primary atomization process. This would allow for the analysis of the spray formation processes.

Another major challenge involves our capability to determine spacing between neighboring droplets in a computationally efficient manner. Currently, the only clear option is to scan the positions of all droplets in a calculation and, thereby, tediously determine minimum distances. This tedious route has not been followed in practice. The need exists in a dense spray to determine these spacings since the droplet drag, lift, torque, heating rate, and vaporization rate will depend upon this spacing.

Acknowledgments

Interactions over the past two decades with ten postdoctoral associates and fourteen graduate students on the subject of sprays have been very productive, stimulating, and instructive. Nearly all of these junior collaborators are identified in the references. Exciting interactions with senior collaborators are also recognized; Drs. H. A. Dwyer, S. E. Elghobashi, G. J. Fix, B. R. Sanders, E. Suuberg, and S. C. Yao are identified here. Several federal funding agencies and industrial organizations have been supportive of my spray research; special recognition for continuing support goes to Dr. Julian Tishkoff of AFOSR and Dr. Gabriel Roy of ONR. Ms. Sue Kanda and Ms. Lisa Rehbaum are acknowledged for their outstanding word processing efforts. Finally, the ASME Fluids Engineering Division and the Freeman Scholar Award Committee are thanked for their support of the exercise that resulted in this review paper.

References

Abramzon, B., and Sirignano, W. A., 1989, "Droplet Vaporization Model for Spray Combustion Calculations," *International Journal of Heat and Mass Transfer*, Vol. 32, pp. 1605-1618.

Acrivos, A., and Taylor, T. D., 1962, "Heat and Mass Transfer from Single Spheres in Stokes Flow," *Physics of Fluids*, Vol. 5, pp. 387-394.

Acrivos, A., and Goddard, J., 1965, "Asymptotic Expansion for Laminar Forced Convection Heat and Mass Transfer," *Journal of Fluid Mechanics*, Vol. 23, pp. 273-291.

Aggarwal, S. K., Lee, D. N., Fix, G. J., and Sirignano, W. A., 1981, "Numerical Computation of Fuel Air Mixing in a Two-Phase Axisymmetric Coaxial Free Jet Flow," *Proceedings Fourth IMACS Intl. Symposium on Computer Methods for Partial Differential Equations*, IMACS.

Aggarwal, S. K., Fix, G. J., Lee, D. N., and Sirignano, W. A., 1983, "Numerical Optimization Studies of Axisymmetric Unsteady Sprays," *Journal of Computational Physics*, Vol. 50, pp. 101-115.

Aggarwal, S. K., and Sirignano, W. A., 1984, "Numerical Modeling of One-Dimensional Enclosed Homogeneous and Heterogeneous Deflagrations," *Computer and Fluids*, Vol. 12, pp. 145-158.

Aggarwal, S. K., Tong, A. Y., and Sirignano, W. A., 1984, "A Comparison of Vaporization Models in Spray Calculations," *AIAA Journal*, Vol. 22, pp. 1448-1457.

Aggarwal, S. K., Fix, G. J., and Sirignano, W. A., 1985, "Two-Phase Laminar Axisymmetric Jet Flow: Explicit, Implicit, and Split-Operator Approximations," *Numerical Methods in Partial Differential Equations*, Vol. 1, pp. 279-294.

Aggarwal, S. K., and Sirignano, W. A., 1985a, "Ignition of Fuel Sprays: Deterministic Calculations for Idealized Droplet Arrays," *Twentieth Symposium (International) on Combustion*, The Combustion Institute, pp. 1773-1780.

Aggarwal, S. K., and Sirignano, W. A., 1985b, "Unsteady Spray Flame Propagation in a Closed Volume," *Combustion and Flame*, Vol. 62, pp. 69-84.

Aggarwal, S. K., and Sirignano, W. A., 1986, "An Ignition Study of Polydisperse Sprays," *Combustion Science and Technology*, Vol. 46, pp. 289-300.

Aggarwal, S. K., 1987, "Modeling of Multicomponent Fuel Spray Vaporization," *International Journal of Heat and Mass Transfer*, Vol. 30, pp. 1949-1961.

Aggarwal, S. K., 1988, "Ignition Behavior of a Dilute Multicomponent Fuel Spray," AIAA 26th Aerospace Sciences Meeting, Paper 88-0635.

Annamalai, K., and Ryan, W., 1992, "Interactive Processes in Gasification and Combustion. Part I: Liquid Drop Arrays and Clouds," *Progress in Energy Combustion and Science*, Vol. 18, pp. 221-295.

Asano, K., Taniguchi, I., and Kawahara, T., 1988, "Numerical and Experimental Approaches to Simultaneous Vaporization of Two Adjacent Volatile Drops," *Proceedings of the 4th International Conference on Liquid Atomization and Sprays*, pp. 411-418.

Batchelor, G. K., and Green, J. T., 1972, "The Hydrodynamic Interaction of Two Small Freely-moving Spheres in a Linear Flow Field," *Journal of Fluid Mechanics*, Vol. 56, pp. 375-400.

Batchelor, G. K., 1990, *An Introduction to Fluid Dynamics*, Cambridge University Press.

Bellan, J., and Cuffel, R., 1983, "A Theory of Non-dilute Spray Evaporation Based Upon Multiple Drop Interactions," *Combustion and Flame*, Vol. 51, pp. 55-67.

Bellan, J., and Harstad, K., 1987, "Analysis of the Convective Evaporation of Non-dilute Clusters of Drops," *International Journal of Heat and Mass Transfer*, Vol. 30, pp. 125-136.

Bellan, J., and Harstad, K., 1988, "Turbulence Effects During Evaporation of Drops in Clusters," *International Journal of Heat and Mass Transfer*, Vol. 31, pp. 1655-1668.

Bellan, J., and Harstad, K., 1992, "Evaporation of Steadily Injected, Identical Clusters of Drops Embedded in Jet Vortices," *Twenty-Fourth Symposium (International) on Combustion*, Poster Session.

Berlemont, A., Grancher, M., and Gousebet, G., 1991, "On the Lagrangian Simulation of Turbulence Influence on Droplet Evaporation," *International Journal of Heat and Mass Transfer*, Vol. 34, pp. 2805-2812.

Bhatia, R., and Sirignano, W. A., 1991, "A One-Dimensional Analysis of Liquid-Fueled Combustion Instability," *Journal of Propulsion and Power*, Vol. 7, pp. 953-961.

Borghi, R., and Loison, S., 1992, "Studies of Dense Sprays Combustion by Numerical Simulation with a Cellular Automaton," *Twenty-Fourth Symposium (International) on Combustion*, The Combustion Institute, in press.

Bracco, F. V., 1985, "Modeling of Engine Sprays," SAE Preprint 850394.

Chein, R., and Chung, J. N., 1987, "Effects of Vortex Pairing on Particle Dispersion in Turbulent Shear Flows," *International Journal of Multiphase Flow*, Vol. 13, pp. 785-802.

Chein, R., and Chung, J. N., 1988, "Simulation of Particle Dispersion in a Two-Dimensional Mixing Layer," *AIChE Journal*, Vol. 34, pp. 946-954.

Chen, Z. H., Lin, T. H., and Sohrab, S. H., 1988, "Combustion of Liquid Fuel Sprays in Stagnation-Point Flow," *Combustion Science and Technology*, Vol. 60, pp. 63-77.

Chiang, C. H., 1990, "Isolated and Interacting, Vaporizing Fuel Droplets: Field Calculation with Variable Properties," Ph.D. dissertation, University of California, Irvine.

Chiang, C. H., and Sirignano, W. A., 1991, "Axisymmetric Vaporizing Oxygen Droplet Computations," Preprint 91-0281, AIAA 29th Aerospace Sciences Meeting, Reno, NV.

Chiang, C. H., Raju, M. S., and Sirignano, W. A., 1992, "Numerical Analysis of Convecting, Vaporizing Fuel Droplet with Variable Properties," *International Journal of Heat and Mass Transfer*, Vol. 35, pp. 1307-1324.

Chiang, C. H., and Sirignano, W. A., 1993a, "Interacting, Convecting, Vaporizing Fuel Droplets with Variable Properties," *International Journal of Heat and Mass Transfer*, in press.

Chiang, C. H., and Sirignano, W. A., 1993b, "Axisymmetric Calculations of Three-Droplet Interactions," *Atomization and Sprays*, Vol. 3, pp. 91-107.

Chigier, N. A., 1981, *Energy, Combustion, and Environment*, McGraw-Hill, New York.

Chiu, H. H., and Liu, T. M., 1971, "Group Combustion of Liquid Droplets," *Combustion Science and Technology*, Vol. 17, pp. 127-131.

Chiu, H. H., Kim, H. Y., and Croke, E. J., 1983, "Internal Group Combustion of Liquid Droplets," *Nineteenth Symposium (Intl.) on Combustion*, The Combustion Institute, pp. 971-980.

Chung, P. M., 1965, "Chemically Reacting Nonequilibrium Boundary Layers," *Advances in Heat Transfer*, Vol. 2, Hartnett, J. P., and Irvine, T. F., eds., Academic Press.

Chung, J. N., Ayyaswamy, P. S., and Sadhal, S. S., 1984a, "Laminar Condensation on a Moving Drop. Part I. Singular Perturbation Technique," *Journal of Fluid Mechanics*, Vol. 139, pp. 105-130.

Chung, J. N., Ayyaswamy, P. S., and Sadhal, S. S., 1984b, "Laminar Condensation on a Moving Drop. Part 2. Numerical Solutions," *Journal of Fluid Mechanics*, Vol. 139, pp. 131-144.

Chung, J. N., and Troutt, T. R., 1988, "Simulation of Particle Dispersion in an Axisymmetric Jet," *Journal of Fluid Mechanics*, Vol. 186, pp. 199-227.

Clift, R., Grace, J. R., and Weber, M. E., 1978, *Bubbles, Drops, and Particles*, Academic Press.

Conner, J. M., and Elghobashi, S. E., 1987, "Numerical Solution of Laminar Flow Past a Sphere with Surface Mass Transfer," *Numerical Heat Transfer*, Vol. 122, pp. 57-82.

Continillo, G., and Sirignano, W. A., 1988, "Numerical Study of Multicomponent Fuel Spray Flame Propagation in a Spherical Closed Volume," *Twenty-Second Symposium (International) on Combustion*, The Combustion Institute, pp. 1941-1949.

Continillo, G., and Sirignano, W. A., 1990, "Counterflow Spray Combustion Modelling," *Combustion and Flame*, Vol. 81, pp. 325-340.

Continillo, G., and Sirignano, W. A., 1991, "Unsteady, Spherically Symmetric Flame Propagation Through Multicomponent Fuel Spray Clouds," *Modern Research Topics in Aerospace Propulsion*, G. Angelino, L. DeLuca, and W. A. Sirignano, eds., Springer-Verlag.

Crowe, C. T., Sharma, M. P., and Stock, D. E., 1977, "The Particle-Source-in Cell (PSI-CELL) Model for Gas-Droplet Flows," ASME Journal of Fluids Engineering, Vol. 99, p. 325.

Crowe, C. T., Chung, J. N., and Troutt, T. R., 1988, "Particle Mixing in Free Shear Flows," *Progress in Energy and Combustion Science*, Vol. 14, pp. 171-199.

Crowe, C. T., 1978, "On the Vapor Droplet Flows Including Boundary Droplet Effects," *Two-Phase Transport and Reactor Safety*, Vol. 1, pp. 385-405.

Crowe, C. T., 1982, "Numerical Models for Dilute Gas-Particle Flows," ASME Journal of Fluids Engineering, Vol. 104, pp. 297-301.

Dandy, D. S., and Dwyer, H. H., 1990, "A Sphere in Shear Flow at Finite Reynolds Number: Effect of Shear on Particle Lift, Drag, and Heat Transfer," *Journal of Fluid Mechanics*, Vol. 216, pp. 381-410.

Delplanque, J.-P., Rangel, R. H., and Sirignano, W. A., 1990, "Liquid-Waste Incineration in a Parallel-Stream Configuration: Effect of Auxiliary Fuel," *Dynamics of Deflagrations and Reactive Systems: Heterogeneous Combustion, Progress in Astronautics and Aeronautics*, Vol. 132, AIAA, pp. 164-186.

Delplanque, J.-P., and Rangel, R. H., 1991, "Droplet Stream Combustion in the Steady Boundary Layer Near a Wall," *Combustion Science and Technology*, Vol. 78, pp. 97-115.

Delplanque, J.-P., and Sirignano, W. A., 1993, "Numerical Study of the Transient Vaporization of an Oxygen Droplet at Sub- and Super-critical Conditions," *International Journal of Heat and Mass Transfer*, in press.

Dukowicz, J. K., 1980, "A Particle-Fluid Numerical Model for Liquid Sprays," *Journal of Computational Physics*, Vol. 35, pp. 229-253.

Dwyer, H. A., and Sanders, B. R., 1984a, "Detailed Computation of Unsteady Droplet Dynamics," *Twentieth Symposium (International) on Combustion*, The Combustion Institute, pp. 1743-1749.

Dwyer, H. A., and Sanders, B. R., 1984b, "Comparative Study of Droplet Heating and Vaporization at High Reynolds and Peclet Numbers," *Dynamics of Flames and Reactive Systems, Progress in Astronautics and Aeronautics*, Vol. 95, AIAA, pp. 464-483.

Dwyer, H. A., and Sanders, B. R., 1984c, "Droplet Dynamics and Vaporization with Pressure as a Parameter," ASME Winter Annual Meeting, paper 84-WA/HT-20.

El-Wakil, M. M., Priem, R. J., Brikowski, H. J., Meyer, P. S., and Uyehara, O. A., 1956, "Experimental and Calculated Temperature and Mass Histories of Vaporizing Fuel Drop," NACA TN 2490.

Elghobashi, S. E., and Abou-Arab, T. W., 1983, "A Two-Equation Turbulence Model for Two-Phase Flows," *The Physics of Fluids*, Vol. 26, pp. 931-938.

Elghobashi, S. E., Abou-Arab, T., Rizk, M., and Mostafa, A., 1984, "Prediction of the Particle-Laden Jet with a Two-Equation Turbulence Model," *International Journal of Multiphase Flow*, Vol. 10, pp. 697-710.

Elghobashi, S. E., and Truesdell, G. C., 1991, "On the Interaction Between Solid Particles and Decaying Turbulence," *Eighth Symposium on Turbulent Shear Flows*, Munich.

Elghobashi, S. E., 1991, "Particle-Laden Turbulent Flows: Direct Simulation and Closure Models," *Applied Scientific Research*, Vol. 48, pp. 301-314.

Elghobashi, S. E., and Truesdell, G. C., 1992, "Direct Simulation of Particle Dispersion in a Decaying Isotropic Turbulence," *Journal of Fluid Mechanics*, Vol. 242, pp. 655-706.

Elghobashi, S. E., and Truesdell, G. C., 1993, "On the Two-Way Interaction Between Homogeneous Turbulence and Dispersed Solid Particles: Part I: Turbulence Modification," to appear in *Physics of Fluids*, Vol. A5.

Faeth, G. M., 1983, "Evaporation and Combustion of Sprays," *Progress in Energy Combustion Science*, Vol. 9, pp. 1-76.

Faeth, G. M., 1987, "Mixing, Transport, and Combustion in Sprays," *Progress in Energy and Combustion Science*, Vol. 13, pp. 293-345.

Frossling, N., 1938, "Evaporation of Falling Drops," *Gerlands Beitr. Geophys*, Vol. 52, p. 170.

Glassman, I., 1987, *Combustion*, 2nd edition, Academic Press.

Gosman, A. D., and Ioannides, E., 1981, "Aspects of Computer Simulation of Liquid-fuelled Combustors," AIAA Preprint 81-0323.

Hadamard, J. S., 1911, "Mouvement Permanent Lent d'une Sphere Liquide et Visqueuse dans Une Liquid Visquese," *C. R. Acad. Sci.*, Vol. 152, pp. 1735-1738.

Hanlon, T. R., and Melton, L. A., 1992, "Exciplex Fluorescence Thermometry of Falling Hexadecane Droplets," ASME *Journal of Heat Transfer*, Vol. 114, pp. 450-457.

Happel, J., and Brenner, H., 1965, *Low Reynolds Number Hydrodynamics*, Prentice Hall.

Harper, J. F., and Moore, D. W., 1968, "The Motion of a Spherical Liquid Drop at High Reynolds Number," *Journal of Fluid Mechanics*, pp. 367-391.

Harper, J. F., 1970, "Viscous Drag in Steady Potential Flow Past a Bubble," *Chemical Engineering Science*, Vol. 25, pp. 342-343.

Harrje, D. T., and Reardon, F. H., editors, 1972, *Liquid Propellant Rocket Combustion Instability*, NASA SP194, Government Printing Office.

Haywood, R. J., and Renksizbulut, M., 1986, "On Variable Property, Blowing and Transient Effects in Convective Droplet Evaporation with Internal Circulation," *Proceedings of the Eighth International Heat Transfer Conference*, pp. 1861-1866.

Haywood, R. J., Nafziger, N., and Renksizbulut, M., 1989, "A Detailed Examination of Gas and Liquid Phase Transient Processes in Convective Droplet Evaporation," ASME *Journal of Heat Transfer*, Vol. 111, pp. 495-502.

Heidmann, M. F., and Wieber, P. R., 1965, "Analysis of n-heptane Vaporization in Unstable Combustor with Travelling Transverse Oscillations," NASA TN-3424.

Heidmann, M. F., and Wieber, P. R., 1966, "Analysis of Frequency Response Characteristics of Propellant Vaporization," NASA TM-X-52195.

Hinze, J. O., 1972, "Turbulent and Fluid Particle Interaction," *Progress in Heat and Mass Transfer*, Vol. 6, pp. 433-452.

Hinze, J. O., 1975, *Turbulence*, McGraw-Hill.

Howarth, L. (ed.), 1964, *Modern Developments in Fluid Dynamics-High Speed Flow*, Vol. 1, Clarendon Press.

Ingebo, R. D., 1956, "Drag Coefficients for Droplets and Solid Spheres in Clouds Accelerating in Airstreams," NACA Technical Note 3762.

Jeffrey, D. J., and Onishi, Y., 1984, "Calculation of the Resistance and Mobility Functions for Two Unequal Rigid Spheres in Low Reynolds Flow," *Journal of Fluid Mechanics*, Vol. 139, pp. 261-290.

Jiang, Y. J., Umemura, A., and Law, C. K., 1992, "An Experimental Investigation on the Collision Behaviour of Hydrocarbon Droplets," *Journal of Fluid Mechanics*, Vol. 234, pp. 171-190.

Johns, L. E., and Beckman, R. B., 1966, "Mechanism of Dispersed-Phase Mass Transfer in Viscous, Single-Drop Extraction System," *AIChE Journal*, Vol. 12, pp. 10-16.

Kanury, A. M., 1975, *Introduction to Combustion Phenomena*, Gordon and Breach, New York.

Kim, I., Elghobashi, S. E., and Sirignano, W. A., 1992, "Three-Dimensional Flow Computation for Two Interacting, Moving Droplets," Preprint 92-0343, AIAA 30th Aerospace Sciences Meeting, Reno, NV.

Kim, I., Elghobashi, S. E., and Sirignano, W. A., 1993, "Three-Dimensional Flow Over Two Spheres Placed Side-by-Side," *Journal of Fluid Mechanics*, Vol. 246, pp. 465-488.

Kleinstreuer, C., Chiang, H., and Wang, Y. Y., 1989, "Mathematical Modelling of Interacting Vaporizing Fuel Droplets," *Heat Transfer Phenomena in Radiation, Combustion and Fire*, Vol. 106, ASME Heat Transfer Division, pp. 469-477.

Kuo, K. K., 1986, *Principles of Combustion*, John Wiley and Sons.

Labowsky, M., 1978, "A Formalism for Calculating the Evaporation Rates of Rapidly Evaporating Interacting Particles," *Combustion Science and Technology*, Vol. 18, pp. 145-151.

Labowsky, M., and Rosner, D. C., 1978, "Group Combustion of Droplets in Fuel Clouds, I. Quasi-steady Predictions," *Evaporation-Combustion of Fuels*, J. T. Zung, ed., *Advances in Chemistry Series*, Vol. 166, pp. 63-79.

Labowsky, M., 1980, "Calculation of Burning Rates of Interacting Fuel Droplets," *Combustion Science and Technology*, Vol. 22, pp. 217-226.

Landau, L. D., and Lifshitz, E. M., 1987, *Fluid Mechanics*, 2nd Edition, Pergamon Press.

Lamb, Sir H., 1945, *Hydrodynamics*, Dover.

Landis, R. B., and Mills, A. F., 1974, "Effects of Internal Diffusional Resistance on the Vaporization of Binary Droplets," Paper B7.9, *Fifth Int. Heat Transfer Conf.*, Tokyo, Japan.

Lara-Urbaneja, P., and Sirignano, W. A., 1981, "Theory of Transient Multicomponent Droplet Vaporization in a Convective Field," *Eighteenth Symposium (Intl.) on Combustion*, The Combustion Institute, pp. 1365-1374.

Law, C. K., 1976, "Unsteady Droplet Combustion with Droplet Heating," *Combustion and Flame*, Vol. 26, pp. 17-22.

Law, C. K., Prakash, S., and Sirignano, W. A., 1977, "Theory of Convective, Transient, Multicomponent Droplet Vaporization," *Sixteenth Symposium (Intl.) Combust.*, The Combustion Institute, pp. 605-617.

Law, C. K., and Sirignano, W. A., 1977, "Unsteady Droplet Combustion With Droplet Heating II: Conduction Limit," *Combustion and Flame*, Vol. 28, pp. 175-186.

Law, C. K., 1982, "Recent Advances in Droplet Vaporization and Combustion," *Progress Energy Combustion Science*, Vol. 8, pp. 171-201.

Lazaro, B. J., and Lasheras, J. C., 1989, "Particle Dispersion in a Turbulent, Plane, Free Shear Layer," *Physics of Fluids*, Vol. A1, pp. 1035-1044.

Lazaro, B. J., and Lasheras, J. C., 1992a, "Particle Dispersion in the Developing Free Shear Layer. Part 1. Unforced Flow," *Journal of Fluid Mechanics*, Vol. 235, pp. 143-178.

Lazaro, B. J., and Lasheras, J. C., 1992b, "Particle Dispersion in the Developing Free Shear Layer. Part 2. Forced Flow," *Journal of Fluid Mechanics*, Vol. 235, pp. 179-221.

Lefebvre, A. H., 1989, *Atomization and Sprays*, Hemisphere.

Lees, L., 1956, "Laminar Heat Transfer Over Blunt-Nosed Bodies at Hypersonic Flight Speeds," *Jet Propulsion*, Vol. 26, pp. 259-269.

Levich, V. G., 1962, *Physicochemical Hydrodynamics*, Prentice Hall.

Li, S. C., Libby, P. A., and Williams, F. A., 1992, "Experimental and Theoretical Studies of Counterflow Spray Diffusion Flames," *Twenty-Fourth Symposium (International) on Combustion*, The Combustion Institute, in press.

MacInnes, J. M., and Bracco, F. V., 1992a, "Stochastic Particle Dispersion Modelling and the Tracer-Particle Limit," *Physics of Fluids, A* (in press).

MacInnes, J. M., and Bracco, F. V., 1992b, "A Stochastic Model of Turbulent Drop Dispersion in Dilute Sprays," ILASS-Europe Conference, Amsterdam.

Megaridis, C. M., and Sirignano, W. A., 1991, "Numerical Modelling of a Vaporizing Multicomponent Droplet," *Twenty-Third Symposium (International) on Combustion*, The Combustion Institute, pp. 1413-1421.

Megaridis, C. M., and Sirignano, W. A., 1992, "Multicomponent Droplet Vaporization in a Laminar Convecting Environment," *Combustion Science and Technology*, Vol. 87, pp. 27-44.

Melton, L. A., and Winter, M., 1990, "Measurement of Internal Circulation in Droplets Using Laser-Induced Fluorescence," *Applied Optics*, Vol. 29, pp. 4574-4577.

Molavi, K., and Sirignano, W. A., 1988, "Computational Analysis of Acoustic Instabilities in Dump Combustor Configurations," Preprint 88-2856, AIAA/ASME 24th Joint Propulsion Conference, Boston, MA.

Mostafa, A. A., and Elghobashi, S. E., 1985a, "A Two-Equation Turbulence Model for Jet Flows Laden with Vaporizing Droplets," *International Journal of Multiphase Flow*, Vol. 11, pp. 515-533.

Mostafa, A. A., and Elghobashi, S. E., 1985b, "A Study of the Motion of Vaporizing Droplets in a Turbulent Flow," *Dynamics of Flames and Reactive Systems, Progress in Astronautics and Aeronautics*, Vol. 95, J. R. Bowen, N. Mason, A. K. Oppenheim, R. I. Soloukhin, eds., pp. 513-529.

Mostafa, A. A., and Mongia, H. C., 1988, "On the Interaction of Particles and Turbulent Fluid Flow," *International Journal of Heat and Mass Transfer*, Vol. 31, pp. 2063-2075.

Mostafa, A. A., Mongia, H. C., McDonell, V. G., and Samuelsen, G. S., 1989, "Evolution of Particle Laden Jet Flows: A Theoretical and Experimental Study," *AIAA Journal*, Vol. 27, pp. 167-183.

Naber, J. D., and Reitz, R. D., 1988, "Modelling Engine Spray/Wall Impingement," Preprint 88-0107, SAE Congress and Exposition, Detroit, Feb. 29-Mar. 4.

Nguyen, Q. V., and Dunn-Rankin, D., 1992, "Experiments Examining Drag in Linear Droplet Packets," *Experiments in Fluids*, Vol. 12, pp. 157-165.

Nguyen, Q. V., Rangel, R. H., and Dunn-Rankin, D., 1991, "Measurement and Prediction of Trajectories and Collision of Droplets," *International Journal of Multiphase Flow*, Vol. 17, pp. 159-177.

O'Rourke, P. J., and Bracco, F. V., 1980, "Modeling of Drop Interactions in Thick Sprays and a Comparison with Experiments," Stratified Charge Automotive Engines Conference, The Institution of Mechanical Engineers.

Patnaik, G., Sirignano, W. A., Dwyer, H. A., and Sanders, B. R., 1986, "A Numerical Technique for the Solution of a Vaporizing Fuel Droplet," *Dynamics of Reactive Systems, Progress in Astronautics and Aeronautics*, Vol. 105, AIAA, pp. 253-266.

Patnaik, G., and Sirignano, W. A., 1986, "Axisymmetric, Transient Calculation for Two Vaporizing Fuel Droplets," Western States Section/Combustion Institute Technical Meeting, Banff, Alberta, Canada.

Prakash, S., and Sirignano, W. A., 1978, "Liquid Fuel Droplet Heating with Internal Circulation," *International Journal of Heat and Mass Transfer*, Vol. 21, pp. 885-895.

Prakash, S., and Sirignano, W. A., 1980, "Theory of Convective Droplet Vaporization with Unsteady Heat Transfer in the Circulating Liquid Phase," *International Journal of Heat and Mass Transfer*, Vol. 23, pp. 253-268.

Priem, R. J., and Heidmann, M. F., 1960, "Propellant Vaporization as a Design Criterion for Rocket Engine Combustion Chambers," NASA Report TR-R67.

Priem, R. J., 1963, "Theoretical and Experimental Models of Unstable Rocket Combustors," *Ninth Symposium (International) on Combustion*, The Combustion Institute, pp. 982-992.

Raju, M. S., and Sirignano, W. A., 1989, "Spray Computations in a Centerbody Combustor," ASME *Journal of Engineering for Gas Turbines and Power*, Vol. 111, pp. 710-718.

Raju, M. S., and Sirignano, W. A., 1990a, "Multicomponent Spray Computations in a Modified Centerbody Combustor," *Journal of Propulsion and Power*, Vol. 6, pp. 97-105.

Raju, M. S., and Sirignano, W. A., 1990b, "Interaction Between Two Vaporizing Droplets in an Intermediate-Reynolds-Number-Flow," *Physics of Fluids*, Vol. 2, pp. 1780-1796.

Rangel, R. H., and Fernandez-Pello, A. C., 1984, "Mixed Convective Droplet Combustion with Internal Circulation," *Combustion Science and Technology*, Vol. 42, pp. 47-65.

Rangel, R. H., and Sirignano, W. A., 1986, "Rapid Vaporization and Heating of Two Parallel Fuel Droplet Streams," *Twenty-First Symposium (International) on Combustion*, The Combustion Institute, pp. 617-624.

Rangel, R. H., and Sirignano, W. A., 1988a, "Unsteady Flame Propagation in a Spray with Transient Droplet Vaporization," *Twenty-Second Symposium (International) on Combustion*, The Combustion Institute, pp. 1931-1939.

Rangel, R. H., and Sirignano, W. A., 1988b, "Two-Dimensional Modeling of Flame Propagation in Fuel Stream Arrangements," *Dynamics of Reactive Systems Part II: Heterogeneous Combustion and Applications*, A. L. Kuhl, J. R. Bowen, J. S. Leyer and A. Borisov, eds., *Progress in Astronautics and Aeronautics*, Vol. 113, AIAA, pp. 128-150.

Rangel, R. H., and Sirignano, W. A., 1989a, "Combustion of Parallel Fuel Droplet Streams," *Combustion and Flame*, Vol. 75, pp. 241-254.

Rangel, R. H., and Sirignano, W. A., 1989b, "An Evaluation of the Point-Source Approximation in Spray Calculations," *Numerical Heat Transfer*, Part A, Vol. 16, pp. 37-57.

Rangel, R. H., 1990, "Spray Entrainment and Mixing in a Temporally-Growing Shear Layer," ASME Winter Annual Meeting, HTD 148, pp. 11-18.

Rangel, R. H., and Sirignano, W. A., 1991, "Spray Combustion in Idealized Configurations: Parallel Droplet Streams," *Numerical Approaches to Com-*

bustion Modeling, Progress in Astronautics and Aeronautics, Vol. 135, E. S. Oran and J. P. Boris, eds., pp. 585–613.

Rangel, R. H., 1992, "Heat Transfer in Vortically Enhanced Mixing of Vaporizing Droplet Sprays," *Annual Review of Heat Transfer*, Vol. 4, C. L. Tien, ed., Hemisphere, pp. 331–362.

Rangel, R. H., and Continillo, G., 1992, "Theory of Vaporization and Ignition of a Droplet Cloud in the Field of a Vortex," *Twenty-Fourth Symposium (International) on Combustion*, The Combustion Institute (in press).

Ranz, W. E., and Marshall, W. R., 1952, "Evaporation from Drops," *Chemical Engineering Progress*, Vol. 48, pp. 141–146 and pp. 173–180.

Reitz, R. D., 1987, "Modeling Atomization Processes in High-Pressure Vaporizing Sprays," *Atomisation and Spray Technology*, Vol. 3, pp. 309–337.

Renksizbulut, M., and Haywood, R. J., 1988, "Transient Droplet Evaporation With Variable Properties and Internal Circulation at Intermediate Reynolds Numbers," *International Journal of Multiphase Flow*, Vol. 14, pp. 189–202.

Renksizbulut, M., and Yuen, M. C., 1983, "Experimental Study of Droplet Evaporation in High Temperature Air Stream," ASME *Journal of Heat Transfer*, Vol. 105, pp. 384–388.

Rizk, M. A., and Elghobashi, S. E., 1985, "The Motion of a Spherical Particle Suspended in a Turbulent Flow Near a Plane Wall," *The Physics of Fluids*, Vol. 28, pp. 806–817.

Rizk, M. A., and Elghobashi, S. E., 1989, "A Two-Equation Turbulence Model for Dispersoid Dilute Confined Two-Phase Flows," *International Journal of Multiphase Flow*, Vol. 15, pp. 119–133.

Ryan, W., Annamalai, K., and Caton, J., 1990, "Relation Between Group Combustion and Drop Array Studies," *Combustion and Flame*, Vol. 80, pp. 313–321.

Rybczynski, W., 1911, "On the Translatory Motion of a Fluid Sphere in a Viscous Medium," *Bull. Int. Acad. Pol. Sci., Lett. A. Sci. Math. Natur. Series A*, pp. 40–46.

Sangiovanni, J. J., and Kesten, A. S., 1976, "Effect of Droplet Interaction on Ignition in Monodispersed Droplet Streams," *Sixteenth Symposium (International) on Combustion*, The Combustion Institute, pp. 577–592.

Seth, B., Aggarwal, S. K., and Sirignano, W. A., 1978, "Flame Propagation Through an Air-Fuel Spray with Transient Droplet Vaporization," *Combustion and Flame*, Vol. 32, pp. 257–270.

Sherman, F. S., 1990, *Viscous Flow*, McGraw-Hill.

Shuen, J. S., Yang, V., and Hsiao, C. C., 1992, "Combustion of Liquid Fuel Droplets in Supercritical Conditions," *Combustions and Flame*, Vol. 89, pp. 299–319.

Sirignano, W. A., 1972, "Introduction to Analytical Models of High Frequency Combustion Instability," *Liquid Propellant Rocket Combustion Instability*, D. T. Harrje and F. H. Reardon, eds., NASA SP194, U.S. Government Printing Office.

Sirignano, W. A., and Law, C. K., 1978, "Transient Heating and Liquid Phase Mass Diffusion in Droplet Vaporization," *Evaporation-Combustion of Fuels*, J. T. Zung, ed., *Adv. in Chemistry Series 166*, ACS, pp. 1–26.

Sirignano, W. A., 1979, "Theory of Multicomponent Fuel Droplet Vaporization," *Archives of Thermodynamics and Combustion*, Vol. 9, pp. 235–251.

Sirignano, W. A., 1983, "Fuel Droplet Vaporization and Spray Combustion," *Progress Energy Combustion Science*, Vol. 9, pp. 291–322.

Sirignano, W. A., 1985a, "Spray Combustion Simulation," *Numerical Simulation Combustion Phenomena*, R. Glowinski, B. Larrouturou, and R. Teman, eds., Springer-Verlag, Heidelburg.

Sirignano, W. A., 1985b, "Linear Model of Convective Heat Transfer in a Spray," *Recent Advances in Aerospace Science*, C. Casci, ed., Plenum Press.

Sirignano, W. A., 1986, "The Formulation of Spray Combustion Models: Resolution Compared to Droplet Spacing," ASME *Journal of Heat Trnasfer*, Vol. 108, pp. 633–639.

Sirignano, W. A., 1988, "An Integrated Approach to Spray Combustion Model Development," *Combustion Science and Technology*, Vol. 58, No. 1–3, pp. 231–251.

Sirignano, W. A., 1993, "Computational Spray Combustion," *Numerical Modeling in Combustion*, T. J. Chung, ed., Hemisphere Publications, in press.

Squires, K. D., and Eaton, J. K., 1989, "Study of the Effects of Particle Loading on Homogeneous Turbulence Using Direct Numerical Simulation," *Proceedings International Symposium on Turbulence Modification in Dispersed Multiphase Flows*, San Diego, CA.

Squires, K. D., and Eaton, J. K., 1991, "Preferential Concentration of Particles by Turbulence," *Physics of Fluids A*, Vol. 3, pp. 1169–1178.

Strahle, W. C., 1964, "Periodic Solutions to a Convective Droplet Burning Problem: the Stagnation Point," *Tenth Symposium (International) on Combustion*, The Combustion Institute, pp. 1315–1325.

Strahle, W. C., 1965a, "Unsteady Reacting Boundary Layer on a Vaporizing Flat Plate," *AIAA Journal*, Vol. 3, pp. 1195–1198.

Strahle, W. C., 1965b, "Unsteady Laminar Jet Flames at Large Frequencies of Oscillation," *AIAA Journal*, Vol. 3, pp. 957–960.

Strahle, W. C., 1966, "High Frequency Behavior of the Laminar Jet Flame Subjected to Transverse Sound Waves," *Eleventh Symposium (International) on Combustion*, The Combustion Institute, pp. 747–754.

Sundararajan, T., and Ayyaswamy, P. S., 1984, "Hydrodynamics and Heat Transfer Associated with Condensation on a Moving Drop: Solutions for Intermediate Reynolds Number," *Journal of Fluid Mechanics*, Vol. 149, pp. 33–58.

Suzaki, T., and Chiu, H. H., 1971, "Multi Droplet Combustion on Liquid Propellants," *Proc. Ninth International Symposium on Space Technology and Science*, AGNE Publishing Co., Tokyo, Japan, pp. 145–154.

Tal, R., and Sirignano, W. A., 1982, "Cylindrical Cell Model for the Hydrodynamics of Particle Assemblages at Intermediate Reynolds Numbers," *AIChE Journal*, Vol. 28, pp. 233–237.

Tal, R., Lee, D. M., and Sirignano, W. A., 1983, "Hydrodynamics and Heat Transfer in Sphere Assemblages-Cylindrical Cell Models," *International Journal of Heat and Mass Transfer*, Vol. 26, pp. 1265–1273.

Tal, R., Lee, D. N., and Sirignano, W. A., 1984a, "Periodic Solutions of Heat Transfer for Flow Through a Periodic Assemblage of Spheres," *International Journal of Heat and Mass Transfer*, Vol. 27, pp. 1414–1417.

Tal, R., Lee, D. A., and Sirignano, W. A., 1984b, "Heat and Momentum Transfer Around a Pair of Spheres in Viscous Flow," *International Journal of Heat and Mass Transfer*, Vol. 27, pp. 1953–1962.

Talley, D. G., and Yao, S. C., 1986, "A Semi-Empirical Approach to Thermal and Composition Transients Inside Vaporizing Fuel Droplets," *Twenty-First Symposium (International) on Combustion*, The Combustion Institute, pp. 609–616.

Temkin, S., and Ecker, G. Z., 1989, "Droplet Pair Interactions in a Shockwave Flow Field," *Journal of Fluid Mechanics*, Vol. 202, pp. 467–497.

Tomboulides, A. G., Orszag, S. A., and Karniadakis, G. E., 1991, "Three-dimensional Simulation of Flow Past a Sphere," *ISOPE Proceedings*, Edinburgh.

Tong, A. Y., and Sirignano, W. A., 1982a, "Transient Thermal Boundary Layer in Heating of Droplet with Internal Circulation: Evaluation of Assumptions," *Combustion Science and Technology*, Vol. 11, pp. 87–94.

Tong, A. Y., and Sirignano, W. A., 1982b, "Analytical Solution for Diffusion and Circulation in a Vaporizing Droplet," *Nineteenth Symposium (International) on Combustion*, The Combustion Institute, pp. 1007–1020.

Tong, A. Y., and Sirignano, W. A., 1983, "Analysis of Vaporizing Droplet with Slip, Internal Circulation, and Unsteady Liquid-Phase and Quasi-Steady Gas-Phase Heat Transfer," ASME-JSME Thermal Joint Engineering Conference.

Tong, A. Y., and Sirignano, W. A., 1986a, "Multicomponent Droplet Vaporization in a High Temperature Gas," *Combustion and Flame*, Vol. 66, pp. 221–235.

Tong, A. Y., and Sirignano, W. A., 1986b, "Multicomponent Transient Droplet Vaporization with Internal Circulation: Integral Equation Formulation and Approximate Solution," *Numerical Heat Transfer*, Vol. 10, pp. 253–278.

Tong, A. Y., and Chen, S. J., 1988, "Heat Transfer Correlations for Vaporizing Liquid Droplet Arrays in a High Temperature Gas at Intermediate Reynolds Number," *International Journal of Heat and Fluid Flow*, Vol. 9, pp. 118–130.

Tong, A., and Sirignano, W. A., 1989, "Oscillatory Vaporization Fuel Droplets in Unstable Combustor," *Journal of Propulsion and Power*, Vol. 5, pp. 257–261.

Tsai, J. S., and Sterling, A. M., 1990, "The Application of an Embedded Grid to the Solution of Heat and Momentum Transfer for Spheres in a Linear Array," *International Journal of Heat and Mass Transfer*, Vol. 33, pp. 2491–2502.

Twardus, E. M., and Brzustowski, T. A., 1977, "The Interaction Between Two Burning Fuel Droplets," *Archiwum Processor Spalania*, Vol. 8, pp. 347–358.

Umemura, A., Ogawa, A., and Oshiwa, N., 1981a, "Analysis of the Interaction Between Two Burning Droplets," *Combustion and Flame*, Vol. 41, pp. 45–55.

Umemura, A., Ogawa, A., and Oshiwa, N., 1981b, "Analysis of the Interaction Between Two Burning Droplets with Different Sizes," *Combustion and Flame*, Vol. 43, pp. 111–119.

Wells, M. R., and Melton, L. A., 1990, "Temperature Measurements of Falling Droplets," ASME *Journal of Heat Transfer*, Vol. 112, pp. 1008–1013.

Williams, F. A., 1985, *Combustion Theory; The Fundamental Theory of Chemically Reacting Flow Systems*, Second Edition, Benjamin/Cummings, Menlo Park, CA.

White, F. M., 1991, *Viscous Fluid Flow*, McGraw-Hill.

Xiong, T. Y., Law, C. K., and Miyasaka, K., 1985, "Interactive Vaporization and Combustion of Binary Droplet System," *Twentieth Symposium (International) on Combustion*, The Combustion Institute, pp. 1781–1787.

Zhang, J., and Melton, L. A., 1993, "Potential System Errors in Droplet Temperatures Obtained by Fluorescence Methods," ASME *Journal of Heat Transfer*, in press.

R. P. Taylor

J. K. Taylor

Thermal & Fluid Dynamics Laboratory,
Mechanical and Nuclear Engineering
Department,
Mississippi State University,
Mississippi State, MS 39762

M. H. Hosni

Department of Mechanical Engineering,
Kansas State University,
Manhattan, KS 66506

H. W. Coleman

Propulsion Research Center,
Mechanical Engineering Department,
University of Alabama in Huntsville,
Huntsville, AL 35899

Relaxation of the Turbulent Boundary Layer After an Abrupt Change From Rough to Smooth Wall

(Data Bank Contribution*)

Measurements of velocity and turbulence intensity profiles and skin friction coefficient are presented for turbulent flat-plate boundary layer flow over a test surface with a rough-to-smooth step change in surface roughness. The first 0.9 m length of the test surface is roughened with 1.27 mm diameter hemispheres spaced 2 base diameters apart in a uniform staggered array, and the remaining 1.5 m length is smooth. The profiles are compared with previous data for all-rough cases under closely matched conditions in the same facility. The skin friction data are compared with previous data for both all-rough and all-smooth cases.

Introduction

The results of fluid mechanics measurements in the turbulent boundary layer over a flat plate with the first 0.9 m length roughened with 1.27 mm diameter hemispheres and the remaining 1.5 m length smooth are reported. Measurements of velocity and turbulence intensity profiles and skin friction coefficient distributions are presented for turbulent boundary layer flow over a test surface with a rough-to-smooth step change in surface roughness. Engineering applications where surfaces have a wide variation in the size and character of the roughness are inservice turbine blades and atmospheric boundary layers. R. P. Taylor (1990) measured the surface roughness on inservice aeroengine turbine blades and found the roughness height to vary as much as an order of magnitude around the blades. In addition, the statistical character of the roughness was found to vary greatly. There are many applications in the atmospheric boundary layer where the surface is part rough and part smooth. The land-sea interface is an often named example.

Because of the wide array of applications and fundamental interest, there have been several extensive experimental studies of turbulent flow over surfaces that were part rough and part smooth, and the basic character of such flows is understood. The measurements presented here were taken in support of convective heat transfer experiments which were motivated by concern over the use of smooth heat flux gages to measure the heat transfer rate on otherwise rough gas turbine blades. Of particular interest for this work were the Space Shuttle Main Engine fuel pump turbine blades, which have rough coatings with an rms height of about 15 μm. This is very rough considering that the boundary layer thickness is about 0.5 mm. Heat transfer tests on these components are often conducted by installing small (about 1 mm diameter) heat flux gages. These gages usually are much smoother than the surrounding surface.

The fluid mechanics measurements presented here for all-smooth, all-rough, and rough-to-smooth cases were taken in the same facility, with the same roughness, and with the same instruments and, therefore, comparisons can be made directly with a high degree of confidence. The roughness is a well defined three-dimensional distributed roughness and complements the previous laboratory experiments which were taken with sand or two-dimensional rib roughness.

A good recent review of the literature is given by Smits and Wood (1985). A previous review was given by Tani (1968). A review article on turbulent flow over rough surfaces in general is given by Raupach et al. (1991). The companion heat transfer data from the present experiments have been presented in part as R. P. Taylor et al. (1991a, 1991b).

Experimental Apparatus and Measurements

The experiments were performed in the Turbulent Heat Transfer Test Facility (THTTF). Complete descriptions of the facility and its qualification are presented in Coleman et al. (1988) and Hosni et al. (1991). This facility is a closed-loop wind tunnel with a free-stream velocity range of 6 to 67 m/s.

---

*Data have been deposited to the JFE Data Bank. To access the file for this paper, see instructions on p. 542 of this issue.

Contributed by the Fluids Engineering Division for publication in the JOURNAL OF FLUIDS ENGINEERING. Manuscript received by the Fluids Engineering Division August 8, 1991; revised manuscript received October 27, 1992. Associate Technical Editor: D. M. Bushnell.

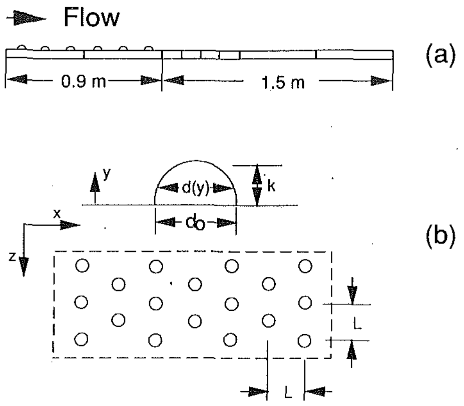

Fig. 1 Descriptions of the rough-to-smooth test surface and the roughness shape for the hemisphere roughened surface

The temperature of the circulating air is controlled with an air to water heat exchanger and a cooling water loop. Following the heat exchanger the air flow is conditioned by a system of honeycomb and screens.

The bottom wall of the nominally 2.4 m long by 0.5 m wide by 0.1 m high test section consists of 24 electrically heated flat plates which are abutted together to form a continuous flat surface. The plates are assembled using dowels to form a continuous flat test surface with an allowable vertical mismatch at the joint between two plates of 0.013 mm. Figure 1 shows a schematic diagram for the test surface used in these experiments. The first 0.9 m of the test section was roughened with 1.27 mm diameter hemispheres, and the remaining 1.5 m length was smooth. The roughness elements were spaced 2 base diameters apart in a staggered array as shown in the figure.

The top wall can be adjusted to maintain a constant freestream velocity. An inclined water manometer with resolution of 0.06 mm is used to measure the pressure gradient during top wall adjustment. Static pressure taps are located in the side wall adjacent to each plate. The pressure tap located at the second plate is used as a reference, and the pressure difference between it and each other tap is minimized. For example, the maximum pressure difference for the 43 m/s case was 0.30 mm of water.

The boundary layer is tripped at the exit of the 19:1 area ratio nozzle with a 1 mm × 12 mm wooden strip. This trip location is immediately in front of the test surface.

Profile Measurements. The profiles of mean velocity, u, and longitudinal velocity fluction, $\overline{u'^2}$, were taken with a DANTEC 55P02 horizontal hot-wire. At each measurement position, 1000 instantaneous anemometer output voltage readings were taken 0.01 second apart and converted into velocities using a fourth order least squares calibration equation. The mean of the 1000 velocities was used as the mean velocity at that location, and the variance was taken as $\overline{u'^2}$. According to Coleman et al. (1988) the overall uncertainties are ±2 per= cent for u and ±5 percent for $\overline{u'^2}$. Near the wall the high turbulence intensity results in large pitch and yaw angles. The uncertainty in the hot-wire measurements near the wall are, therefore, greater than those quoted above.

All velocity and turbulence measurements were made in the region above the roughness elements. For these three-dimensional roughness elements, the turbulent mixing is very vigorous and spacial variations are mixed out at the profile locations. No distinction could be made between element crests and valleys at the profile level.

Skin Friction Coefficient Measurement. The skin friction coefficients, C_f, over the smooth-wall surface were determined using a 1.6 mm inside diameter, 3.2 mm outside diameter Preston tube. The difference between the total pressure at the Preston tube and the undisturbed static pressure at a tap in the sidewall at the same x-location was measured with calibrated pressure transducers. This difference in pressure was used with Patel's (1965) calibration equation to solve for the skin friction coefficient.

The Preston tube method of determining the skin friction coefficient is valid only for smooth-wall turbulent boundary layer flows. The technique depends upon the assumption of a universal law of the wall common to smooth wall turbulent boundary layer flows. The region just downstream of the step change in surface roughness does not have a well developed smooth-wall inner layer. Therefore, an additional uncertainty for the Preston tube measurements of skin friction coefficient made in this region exists. However, as shown in J. K. Taylor et al. (1991), the inner layer develops quickly for this experiments, and all of the Preston tube measurements, with the exception of those made at the first smooth plate, are considered to be valid determinations with uncertainties of ±6 percent (Coleman et al., 1988).

Results

All of the fluid mechanics results presented below are for zero pressure gradient, isothermal, incompressible boundary layer flow of air with a free-stream velocity of 12 m/s. These data are compared with data from all-rough, Hosni et al. (1989), and all-smooth, Coleman et al. (1988), experiments which were collected in the same apparatus using the same instruments. The complete discussion is given in J. K. Taylor et al. (1991) along with data for a freesteam velocity of 58 m/s.

The abrupt change in roughness is often scaled in terms of the factor $M = \ln(z_{01}/z_{02})$ where z_{01} is the term in the rough-wall logarithmic velocity profile

$$\mathbf{u}^+ = \frac{1}{\kappa} \ln \left(\frac{y - \Delta z}{z_{01}} \right) \tag{1}$$

Nomenclature

C_f = skin friction coefficient
d_0 = roughness element base diameter
$d(y)$ = local roughness element diameter
k = roughness element height
L = roughness element spacing
M = change in roughness factor, $\ln(z_{01}/z_{02})$
u = mean longitudinal velocity
u^* = friction velocity, $U_\infty(C_f/2)^{1/2}$
u' = longitudinal velocity fluctuation
u^+ = nondimensional u, u/u^*)
U_∞ = freestream velocity
x = axial distance from nozzle exit
y = coordinate normal to the wall surface
y^+ = nondimensional y, yu^*/ν
z = transverse coordinate
z_{01} = term in rough-wall logarithmic velocity profile, Eq. (1)
z_{02} = term in smooth-wall logarithmic velocity profile
Δz = apparent origin of rough-wall velocity profile
κ = constant in logarithmic law of the wall—taken as 0.41
ν = kinematic viscosity

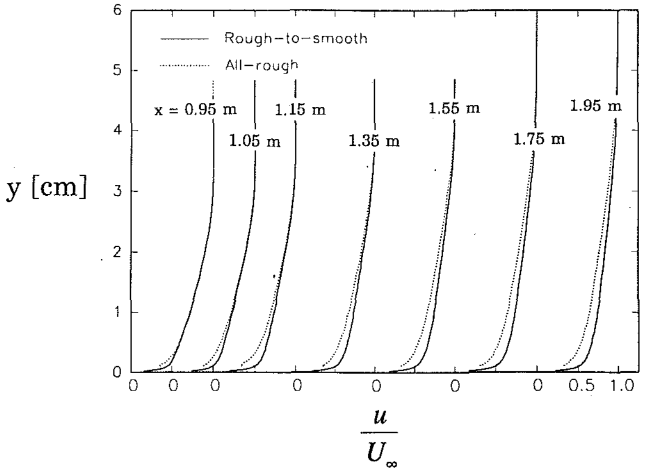

Fig. 2 Composite plot of y versus u/U_∞ for the rough-to-smooth and all-rough surfaces for $U_\infty = 12$ m/s

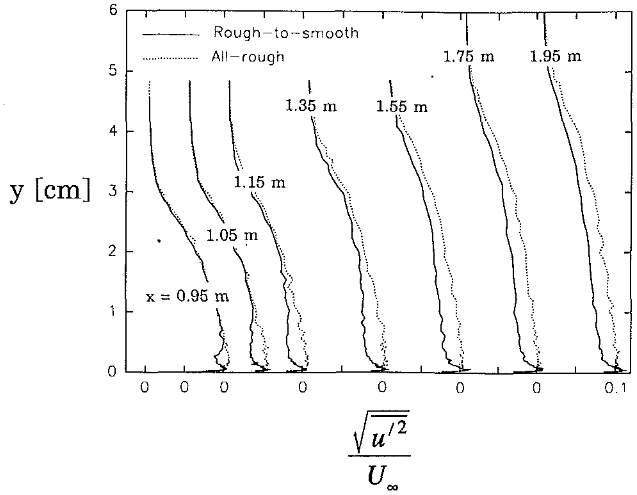

Fig. 4 Axial turbulence intensity profiles for the rough-to-smooth and all-rough test surfaces at increasing x-locations plotted on a shifted axis for $U_\infty = 12$ m/s

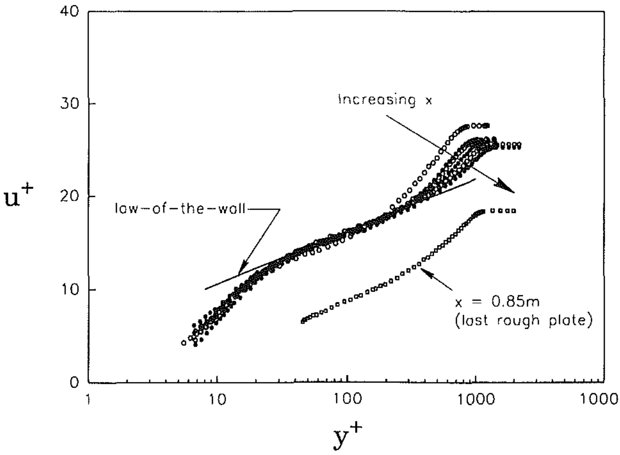

Fig. 3 Mean velocity profiles for the rough-to-smooth surface compared with the smooth wall law of the wall for $U_\infty = 12$ m/s

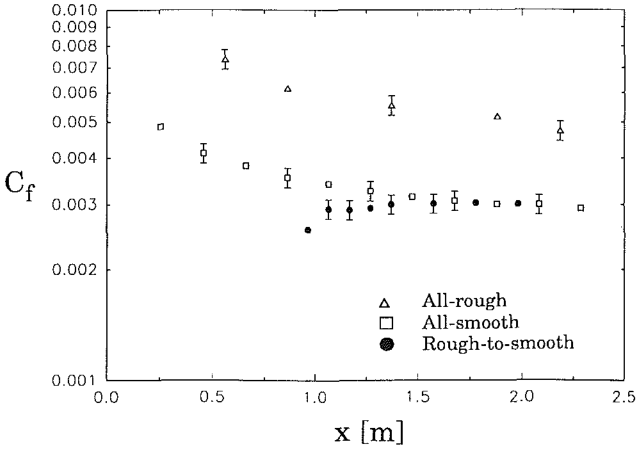

Fig. 5 Comparison of skin friction coefficient versus x for the rough-to-smooth, all-rough, and all-smooth surfaces for $U_\infty = 12$ m/s

with Δz being the apparent origin of the rough-wall velocity profile and where z_{02} is the equivalent term in the smooth-wall velocity profile. Using a velocity profile from the region just upstream of the rough-to-smooth intersection, Δz is determined by finding the value that gives a constant value of

$$z_{01} = (y - \Delta z)\exp(-\kappa u^+) \tag{2}$$

in the logarithmic region of the velocity profile. For the 12 m/s case in this paper, this value was $\Delta z = 0.15$ mm. This gives a z_{01} value of 0.00315 mm. Using the smooth-wall law of the wall velocity profile, the value of z_{02} is computed at the same Reynolds number. This gives a ratio of $z_{01}/z_{02} = 23.3$ and a value of $M = \ln(z_{01}/z_{02}) = 3.15$.

Figure 2 shows a composite plot of the boundary layer mean velocity profiles plotted in y versus u/U_∞ coordinates. These profiles are measured at locations 0.95, 1.05, 1.35, 1.55, 1.75, and 1.95 m downstream of the test section leading edge with the rough-to-smooth interface at 0.90 *m*. The u/U_∞ abscissa is plotted with a multiple origin to show the progression of the velocity profiles downstream of the rough-to-smooth interface. The plot also shows the corresponding rough-wall velocity profiles under carefully matched flow conditions for the identical locations. The origin for the y coordinate in the rough-wall profiles is the base smooth wall between the roughness elements as shown in Fig. 1. Figure 3 shows the rough-to-smooth velocity profiles in inner region coordinates $\mathbf{u}^+ = \mathbf{u}/(\mathbf{U}_\infty \sqrt{\mathbf{C}_f/2})$ and $\mathbf{y}^+ = \mathbf{y}\mathbf{U}_\infty \sqrt{\mathbf{C}_f/2}/\nu$. These figures show that after the interface, the velocity profile is quick to deviate from the rough-wall profile near the wall, however, there is quite a distance before the fully smooth wall profile is obtained.

Figure 4 shows the turbulence intensity profiles plotted in coordinates y versus $\sqrt{\mathbf{u}'^2}/\mathbf{U}_\infty$ on a multiple origin plot. The sharp near-wall peak typical for smooth-wall profiles is seen for all x locations after the step. Also shown on this plot are the rough-wall profiles for the same x-locations. The near-wall regions for the rough-to-smooth case quickly deviate from the all-rough scheme. However, the flow still has the rough-wall characteristics further out in the wake region for a considerable distance downstream.

Local skin friction coefficients were determined along the smooth-wall portion of the test surface using Preston tube measurements. Figure 5 shows the skin friction coefficient distribution for the rough-to-smooth surface at a freestream velocity of 12 m/s. Also shown on the plot are the all-rough data from Hosni et al. (1989) and the all-smooth wall data from Coleman et al. (1988). Hosni's rough-wall data have an uncertainty of ±10 percent. The values of C_f determined from the Preston tube method have an uncertainty of ±6 percent except for the value at the first smooth plate, as discussed above. The values of C_f fall below the smooth-wall values immediately after the rough-to-smooth interface and then rise back to the smooth-wall values. Schofield (1981) found similar trends in his compilation of the available data. Data at 58 m/s in the THTTF showed a similar trend.

Summary and Conclusions

A step change in surface roughness from rough to smooth has been shown to have a dramatic effect on the turbulent boundary layer. After the step change in roughness the skin fricition coefficient falls below the all-smooth wall values at the equivalent *x*-location and then gradually increases approaching the all-smooth values far downstream of the interface. Mean velocity and turbulence intensity profiles show the flow to rapidly assume smooth-wall-like behavior near the wall while requiring more distance to assume a complete smooth-wall behavior.

JFE Data Bank Contributions

The experimental data for the velocity and turbulence intensity profiles and for the skin friction coefficient distributions presented in this paper are being added to the *Journal of Fluids Engineering*, Data Bank.

Acknowledgment

This research was supported by the NASA Lewis Research Center, grant NAG 3 1116. The authors gratefully acknowledge the interest and encouragement of Mr. Kestutis Civinskas of Lewis Research Center.

References

Coleman, H. W., Hosni, M. H., Taylor, R. P., and Brown, G. B., 1988, "Smooth Wall Qualification of a Turbulent Heat Transfer Test Facility," Report TFD-88-2, Mechanical and Nuclear Engineering Deparment, Mississippi State University.

Hosni, M. H., Coleman, H. W., and Taylor, R. P., 1989, "Measurement and Calculation of Surface Roughness Effects on Turbulent Flow and Heat Transfer," Report TFD-89-1, Mechanical and Nuclear Engineering Department, Mississippi State University.

Hosni, M. H., Coleman, H. W., and Taylor, R. P., 1991 "Measurements and Calculations of Rough-Wall Heat Transfer in the Turbulent Boundary Layer," *International Journal of Heat and Mass Transfer*, Vol. 34, No. 4/5, pp. 1067-1082.

Patel, V. C., 1965, "Calibration of the Preston Tube and Limitations on Its Use in Pressure Gradients," *Journal of Fluid Mechanics*, Vol. 23, No. 1, pp. 185-208.

Raupach, M. R., Antonia, R. A., and Rajagopalan, S., 1991, "Rough-Wall Turbulent Boundary Layers," *Applied Mechanics Reviews*, Vol. 44, No. 1, pp. 1-25.

Schofield, W. H., 1981, "Turbulent Shear Flows Over a Step Change in Surface Roughness," *Journal of Fluids Engineering*, Vol. 103, pp. 344-351.

Smits, A. J., and Wood, D. H., 1985, The Response of Turbulent Boundary Layers to Sudden Perturbations," *Annual Review of Fluid Mechanics*, Vol. 17, pp. 321-358.

Tani, I., 1968, "Review of Some Experimental Results on the Response of a Turbulent Boundary Layer to Sudden Perturbations," *Proceedings Computation of Turbulent Boundary Layers*—1968 AFOSR-IFP-Stanford Conference, Stanford University, CA, Aug. 18-25, pp. 483-495.

Taylor, J. K., Taylor, R. P., Hosni, M. H., and Coleman, H. W., 1991, "An Investigation of the Influence of a Step Change in Surface Roughness on Turbulent Flow and Heat Transfer," Report TFD-91-1, Mechanical and Nuclear Engineering Department, Mississippi State University.

Taylor, R. P., 1990, "Surface Roughness Measurements on Gas Turbine Blades," *Journal of Turbomachinery*, Vol. 112, pp. 175-180.

Taylor, R. P., Taylor, J. K., Hosni, M. H., and Coleman, H. W., 1991a, "Heat Transfer in the Turbulent Boundary Layer with a Step Change in Surface Roughness," ASME Paper No. 91-GT-266.

Taylor, R. P., Taylor, J. K., Hosni, M. H., and Coleman, H. W. (1991b), "Investigations of Surface Alignment Effects on Turbulent Boundary Layer Heat Transfer for a Step Change in Surface Roughness," presented at the ASME National Heat Transfer Conference, Minneapolis, July 28-31, *Mixed Convective Heat Transfer*, Pepper, D. W., Armaly, B. F., Ebadian, M. A., and Oosthuizen, P. H., eds., ASME HTD-Vol. 163, pp. 103-109.

Measurement and Calculation of Fluid Dynamic Characteristics of Rough-Wall Turbulent Boundary-Layer Flows

M. H. Hosni
Department of Mechanical Engineering,
Kansas State University,
Manhattan, KS 66506-5106

H. W. Coleman
Mechanical Engineering Department,
University of Alabama in Huntsville,
Huntsville, AL 35899

R. P. Taylor
Thermal & Fluid Dynamics Laboratory,
Mechanical and Nuclear Engineering
Department,
Mississippi State University,
Mississippi State, MS 39762

Experimental measurements of profiles of mean velocity and distributions of boundary-layer thickness and skin friction coefficient from aerodynamically smooth, transitionally rough, and fully rough turbulent boundary-layer flows are presented for four surfaces—three rough and one smooth. The rough surfaces are composed of 1.27 mm diameter hemispheres spaced in staggered arrays 2, 4, and 10 base diameters apart, respectively, on otherwise smooth walls. The current incompressible turbulent boundary-layer rough-wall air flow data are compared with previously published results on another, similar rough surface. It is shown that fully rough mean velocity profiles collapse together when scaled as a function of momentum thickness, as was reported previously. However, this similarity cannot be used to distinguish roughness flow regimes, since a similar degree of collapse is observed in the transitionally rough data. Observation of the new data shows that scaling on the momentum thickness alone is not sufficient to produce similar velocity profiles for flows over surfaces of different roughness character. The skin friction coefficient data versus the ratio of the momentum thickness to roughness height collapse within the data uncertainty, irrespective of roughness flow regime, with the data for each rough surface collapsing to a different curve. Calculations made using the previously published discrete element prediction method are compared with data from the rough surfaces with well-defined roughness elements, and it is shown that the calculations are in good agreement with the data.

Introduction and Background

Both the fluid dynamics and thermal characteristics of a flow field are affected by the shape and surface condition of a solid wall. Many surfaces of engineering interest such as reentry vehicles, missiles, ship hulls, heat exchangers, and piping systems are rough in the aerodynamic sense. Both skin friction and heat transfer can be significantly larger for a turbulent flow over a rough surface compared with an equivalent turbulent flow over a smooth surface. In light of the broad applicability and importance of the effects of surface roughness, there is significant engineering interest in detailed studies concerning the performance and structural features of turbulent flows over rough surfaces. Also development of accurate predictive models for fluid mechanics and heat transfer in turbulent flow over rough surfaces are of interest. Such efforts require experimental data for a range of roughness conditions.

The work reported herein is concerned with experimental mean velocity profiles and boundary-layer thickness and skin friction coefficient distributions in aerodynamically smooth, transitionally rough, and fully rough flow regimes. Experiments are reported for incompressible flow of air over three rough surfaces for a range of free-stream velocities which gives x-Reynolds numbers up to 9,000,000. The three rough surfaces are composed of 1.27 mm diameter hemispherical elements spaced 2, 4, and 10 diameters apart, respectively, in staggered arrays on otherwise smooth walls. The data are discussed and compared with previously published rough surface data.

Due to the importance of the effects of surface roughness and the wide array of applications, there have been many experimental studies of turbulent flow over various types of rough surfaces and the basic character of rough wall flows is understood. However, the majority of the previous works deal with the sandgrain type roughness and data on well-defined rough surfaces required for accurate predictive models are limited. Also, many of the reported data sets are for fully developed flows and only few data sets are available for developing flows. The measurements presented here are for well-defined three-dimensional distributed roughnesses in developing flows. These data sets were taken in support of convective heat transfer experiments and are significant in that they complement the heat transfer sets taken in the same facility with deliberately matched flow conditions (Hosni et al., 1991)

Contributed by the Fluids Engineering Division for publication in the JOURNAL OF FLUIDS ENGINEERING. Manuscript received by the Fluids Engineering Division October 21, 1991; revised manuscript received February 8, 1993. Associate Technical Editor: T. T. Huang.

and extended the data and conclusions reported for a similar surface from a series of experiments at Stanford university.

A detailed discussion of previous research is presented in Hosni et al. (1989) and will not be reported here. A good recent review article on turbulent flow over rough surfaces in general is given by Raupach et al. (1991).

Reports from a series of experimental studies at Stanford University on a well-defined rough surface (Healzer, 1974 and Pimenta, 1975) presented experimental results for developing flows. These data sets are for a single rough surface comprised of spheres of a single size (1.27 mm diameter) packed in the most dense array. (This surface hereafter is referred to as the Stanford surface.)

Pimenta (1975) studied the effects of roughness on the structure of rough-wall turbulent boundary layers using the Stanford surface. For classification of the state (aerodynamically smooth, transitionally rough, or fully rough) of the boundary-layer flow over rough surfaces he suggested an alternative approach independent of the roughness Reynolds number limits which had traditionally been used based on fully developed pipe flow results. He identified the flow regimes based on certain similarity characteristics of the flow. He concluded that for this surface the skin friction coefficient was independent of Reynolds number in the fully rough flow regime, so that $C_f = g(\delta_2/r)$, where r is the radius of the spherical roughness elements, and δ_2 is momentum thickness. He concluded that his skin friction coefficient data versus momentum thickness for the fully rough state collapsed to a single curve. He observed similar behavior from his Stanton number data versus enthalpy thickness in the fully rough flow regime. Pimenta's conclusions supported the previous observations reported by Healzer (1974).

Predictions for the skin friction results are presented using the previously reported discrete element prediction approach. Details of this technique and the previous works are presented elsewhere (Taylor et al., 1985; Scaggs et al., 1988) and will not be repeated here.

Experimental Apparatus and Measurement Procedures

The experiments were performed in the Turbulent Heat Transfer Test Facility (THTTF). Complete descriptions of the facility and its qualification are presented in Coleman et al. (1988) and Hosni et al. (1989). This facility is a closed-loop wind tunnel with a free-stream velocity range of 6 to 67 m/s. The temperature of the circulation air is controlled with an air to water heat exchanger and a cooling water loop. Following the heat exchanger, the air flow is conditioned by a system of honeycomb and screens and then enters a three-dimensional, 20 to 1 contraction ratio, fiberglass nozzle which was designed to smoothly accelerate the flow without separation at the nozzle inlet or outlet. The boundary layer is tripped at the exit of the nozzle with a 1 × 12 mm wooden strip. This trip is immediately in front of the first test plate. Measurements at free-stream air velocities of 12 and 58 m/s indicated that the axial velocity in the nozzle exit plane is uniform within about ±0.5 percent. Free-stream turbulence intensities measured 4 cm downstream of the nozzle exit were less than 0.3 percent for free-stream velocities from 61 m/s to 6 m/s and less than 0.4 percent at 3 m/s. Measurements 1.1 m downstream of the nozzle exit showed the spanwise variation of momentum thickness to be less than ±5 percent.

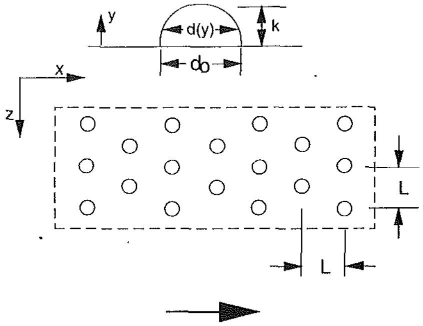

Fig. 1 Surface roughness description and nomenclature

The bottom wall of the nominally 2.4 m long by 0.5 m wide by 0.1 m high test section consists of 24 flat plates which are abutted together to form a continuous flat surface. The smooth surface plates used in the baseline tests have a surface finish with centerline average roughness, Ra, measured as less than 0.5 micrometers. The three sets of precision machined rough test plates considered here have 1.27 mm diameter hemispherical elements spaced 2, 4, and 10 base diameters in staggered arrays as shown in Fig. 1. The rough plates with $L/d_o = 10$ have an average roughness on the "smooth wall" portion of the plates between the roughness elements of $Ra < 4.3$ micrometers. The rough plates with $L/d_o = 4$ have an average roughness on the "smooth-wall" portion of $Ra < 1.6$ micrometers. The average roughness of the smooth-wall portion of the surface with $L/d_o = 2$ could not be measured because of the physical size of the profilometer; however, visually they appeared to be equal to or better than the $L/d_o = 4$ plates. The plates are assembled using dowels to form a continuous flat test surface with an allowable mismatch at the joint between two plates of 0.013 mm.

For the hot-wire anemometry technique, a TSI-100-2 Intelligent Flow Analyzer System with two constant temperature anemometer units and two hot-wire probes were used. Probes were: a DISA 55P05 horizontal, boundary-layer type probe and a DISA 55P02 45 deg slant probe both, of 5 microndiameter platinum plated tungsten wire with gold plated ends. Each of the two anemometer units in the flow analyzer was dedicated to either the horizontal or slanted probe. The probes were the same models used by Pimenta (1975) in his investigation using the Stanford Surface. The horizontal hot-wire was used to measure the profiles of mean velocity and the fluctuating longitudinal velocity component $(\overline{u'^2})$. The slant hot-wire was used to determine the other Reynolds stresses $(\overline{v'^2}, \overline{w'^2}$, and $\overline{u'v'})$.

The overall uncertainties associated with the hot wire measurements are (Coleman et al., 1988): u, ±2 percent; $\overline{u'^2}$, ±5 percent; $\overline{v'^2}$, ±15 percent; $\overline{w'^2}$, ±10 percent; and $\overline{u'v'}$, ±10 percent.

Nomenclature

C_D = roughness element drag coefficient
C_f = skin friction coefficient $(2\tau_w/\rho U_\infty^2)$
d_o = roughness element base diameter
$d(y)$ = local roughness element diameter
k = roughness element height
L = roughness elements spacing
Re_{δ_2} = momentum thickness Reynolds number $(\rho U_\infty \delta_2/\mu)$
u = mean longitudinal velocity
u^* = friction velocity $(U_\infty \sqrt{C_f/2})$
u^+ = nondimensional velocity (u/u^*)
$\overline{u'v'}$ = Reynolds shear stress factor
U_∞ = free-stream velocity
x = axial distance from nozzle exit
y = coordinate normal to surface
y^+ = nondimensional y (yu^*/ν)
δ = boundary-layer thickness
δ_2 = momentum thickness
ν = kinematic viscosity
ρ = density

All friction coefficient determinations for rough walls were performed using hot-wire anemometry. The local skin friction coefficient was determined using the measured quantities and the continuity and momentum equations integrated from the plate surface to a position Y_1 in the boundary layer

$$\frac{C_f}{2}=\frac{\nu}{U_\infty^2}\frac{\partial u}{\partial y}\bigg|_{Y_1}-\frac{\overline{u'v'}}{U_\infty^2}\bigg|_{Y_1}-\frac{d}{dx}\left[\int_0^{Y_1}\left(\frac{u}{U_\infty}\right)^2 dy\right]+\frac{u_{Y_1}}{U_\infty}\frac{d}{dx}\left[\int_0^{Y_1}\left(\frac{u}{U_\infty}\right)dy\right] \quad (1)$$

The position Y_1 was always 3.3 mm for the smooth surface and 3.6 mm for the rough surfaces, since the rotatable slant hot-wire probe was limited to $Y > 3.2$ mm. The x-derivatives were determined using a first-order finite difference approximation and velocity profiles measured at adjacent x-stations. Since the Reynolds stress term in Eq. (1) is about 95 percent of C_f for the situations measured, any uncertainties in determination of other terms contribute very little to the uncertainty in the value of C_f determined using this equation. Distributions of the local skin friction coefficient along the smooth wall test surface were determined with both hot-wire anemometry and the Preston tube (Preston, 1954) method with the calibration of Patel (1965). The estimated uncertainty (Coleman et al., 1988) in the hot wire determined skin friction coefficients in this study is about ±10–12 percent, and the uncertainty in the Preston tube skin friction coefficients is about ±6 percent. Comparisons of data from these techniques with previously reported data are discussed later when Fig. 6 is presented.

Discussion of Results

Experimental profiles of mean velocity and distributions of boundary-layer thickness and skin friction coefficient obtained in the THTTF for turbulent boundary-layer flows over three well-defined rough surfaces are presented for a range of free-stream velocities. The smooth wall data sets from this experimental facility serve as the baseline data for comparisons with the rough walls results. All of the THTTF data are for zero pressure gradient, incompressible, turbulent boundary-layer flow of air.

Calculations made using the discrete element prediction method are compared with data taken on the three rough surfaces in the THTTF and the data from the Stanford single rough surface. The Stanford surface and the THTTF surfaces can be considered to be in the same family of rough surfaces if one assumes that surfaces of 1.27 mm diameter hemispheres and 1.27 mm diameter spheres spaced in the most dense array appear similar to a turbulent boundary layer.

Mean Velocity Profiles. Figure 2 shows the boundary-layer mean velocity profiles taken with the horizontal hot-wire at a nominal free-stream velocity of 12 m/s for the rough surfaces and the smooth surface plotted in inner variable (u^+ versus y^+) coordinates with y measured from the base smooth wall. The friction velocity used in u^+ and y^+ for each profile was that determined by the hot-wire method for corresponding positions. This figure shows the expected distinct velocity shift between the smooth and the rough surface flows. It is also apparent that the nondimensional velocity profiles for flows over the $L/d_o = 10$ rough surface and the smooth surface are equivalent. Similar plots showed that the trends of the velocity shifts for each of the higher free-stream velocities were analogous to the 12 m/s runs.

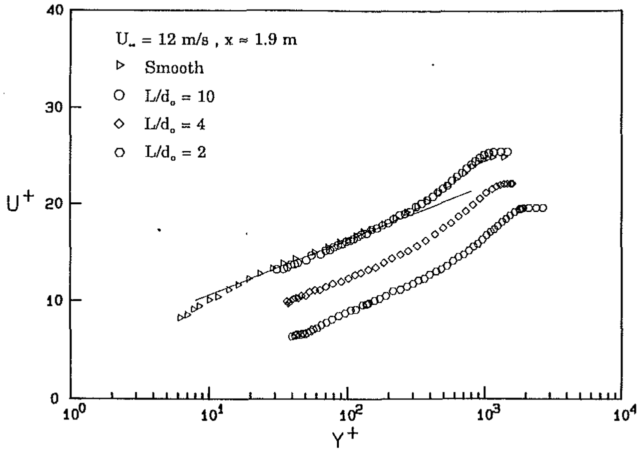

Fig. 2 Mean velocity profiles for the smooth and the three rough surfaces compared with the smooth wall law of the wall

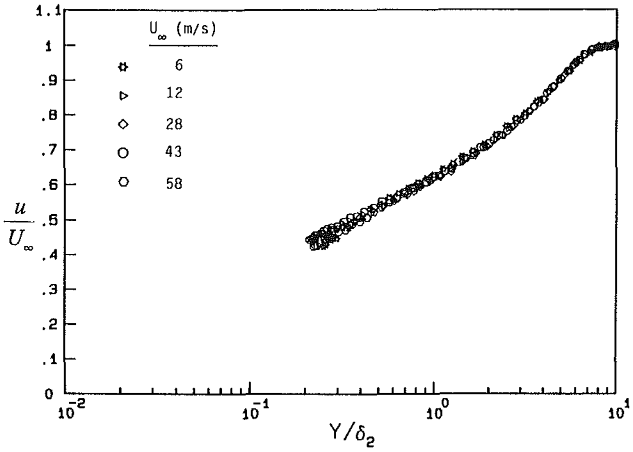

Fig. 3 Mean velocity profiles for the $L/d_o = 4$ rough surface illustrating similarity in u/U_∞ versus y/δ_2 coordinates

Pimenta (1975), for the Stanford rough surface, concluded that the rough-wall skin friction coefficients for the fully rough regime were dependent only on the momentum thickness $C_f/2 = f(\delta_2)$ and suggested that the y/δ_2 coordinate might be more appropriate than y^+ for presentation of fully rough velocity profiles. Figure 3 shows the velocity profiles for nominal free-stream velocities of 6, 12, 28, 43, and 58 m/s plotted in u/U_∞ versus y/δ_2 coordinates for the $L/d_o = 4$ rough surfaces. This figure shows that the scaling of the velocity profiles based on the momentum thickness is appropriate, as Pimenta suggested. Furthermore, this figure shows that in these coordinates the velocity profiles taken on the same rough surface are essentially independent of free-stream velocity and, consequently, of roughness flow regimes. Thus, the data shown in Fig. 3 illustrate that "collapse" of experimentally determined velocity profiles in these coordinates cannot be used to distinguish roughness flow regimes.

The same u/U_∞ versus y/δ_2 coordinates are used in Fig. 4 to compare velocity profiles from flows over the three rough surfaces and the smooth surface for a free-stream velocity of 12 m/s. This figure shows that scaling on the momentum thickness alone is not sufficient to produce similar velocity profiles for different rough surfaces. These coordinates were also used to compare the profile data taken on the surfaces at higher free-stream velocities, and this same trend was observed in each case.

Boundary-Layer Thicknesses. The boundary-layer thickness, δ, was taken as the distance above the plate at which the boundary-layer mean velocity was within 1 percent of the free-stream velocity. A fourth-order interpolation polynomial was applied to the velocity profile data obtained with the horizontal hot-wire to determine the boundary-layer thickness at each profile station.

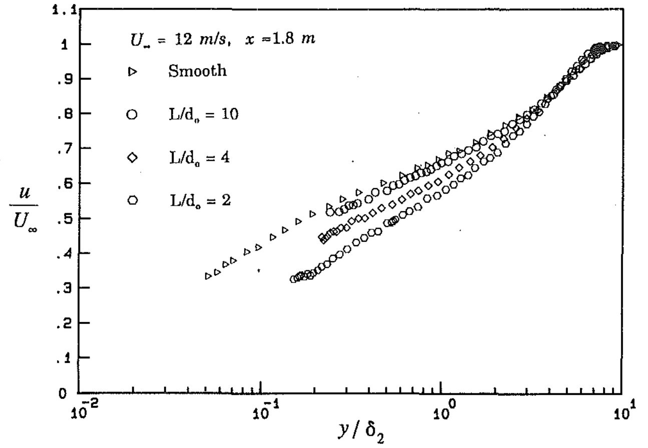

Fig. 4 Comparison of mean velocity profiles for the smooth and the three rough surfaces plotted in u/U_∞ versus y/δ_2 coordinates

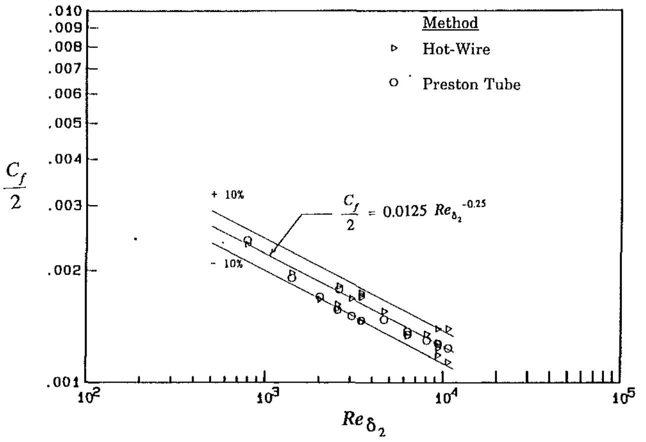

Fig. 6 Composite plot of the smooth wall skin friction coefficient distributions compared with the Re_{δ_2} correlation

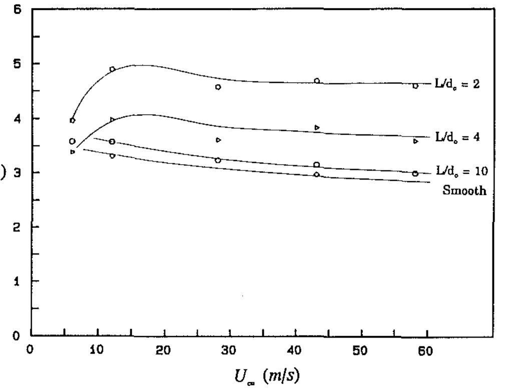

Fig. 5 Influence of increasing free-stream velocity on the behavior of boundary-layer thickness for the smooth and the rough surfaces

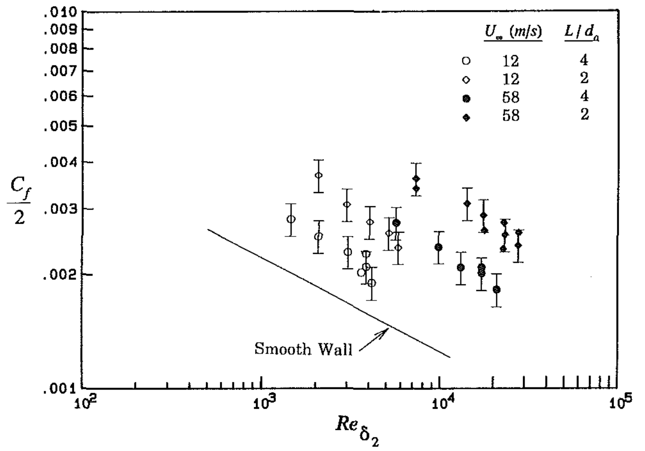

Fig. 7 Comparison of the skin friction coefficient distributions for the $L/d_0=4$ and $L/d_0=2$ surfaces in Re_{δ_2} coordinates

Figure 5 shows the behavior of boundary-layer thickness at $x \approx 1.7$ m with increasing free-stream velocity for the smooth surface and the three THTTF rough surfaces. For zero pressure gradient boundary-layer flow over a smooth surface, boundary-layer thickness at a fixed distance x from the origin, decreases as the free-stream velocity increases. However, the boundary layer over a rough surface is influenced by additional factors such as the size, shape, and density of the roughness elements, and as the free-stream velocity is increased, the flow regime may move from aerodynamically smooth to transitionally rough and finally to fully rough. In such a case, the boundary-layer thickness is initially mostly controlled by the viscosity (Reynolds number), then viscosity and roughness, and then roughness, respectively. Flows over the surface with $L/d_0 = 10$, which are classified as transitionally rough in all cases, behave much like the smooth surface flows but with slightly larger boundary-layer thickness. In flows over the other two rough surfaces, the boundary-layer thicknesses increase rapidly with increasing velocity, then seem to level off as fully rough conditions become firmly established. The boundary-layer and momentum thicknesses for the smooth surface flows are quite different from those of the rough surface flows for equivalent free-stream conditions. As an example, at $x \approx 1.7$ m for a free-stream velocity of 43 m/s δ and δ_2 are, respectively, 58 and 86 percent larger in the flow over the $L/d_0=2$ rough surface as in the smooth wall flow.

Skin Friction Coefficient. Skin friction coefficient data were determined with an uncertainty of ±10–12 percent from Reynolds shear stress and boundary-layer velocity profiles measured using hot-wire anemometry as described by Hosni et al. (1989). Since the hot-wire technique is the only method used in determining the skin friction coefficient distributions for rough surfaces, the correctness of the instrumentation, data collection and data reduction procedures were verified by performing qualification tests using smooth flat test plates. The THTTF smooth wall skin friction data obtained using the hot-wire method are compared in Fig. 6 with both the local skin friction data determined with the Preston tube method and an accepted smooth wall skin friction correlation (Kays and Crawford, 1980) plotted with ±10 percent bands. The smooth wall skin friction data obtained with the hot-wire method are in excellent agreement with the data obtained using the Preston tube method and the accepted smooth wall skin friction correlation.

Not shown in this paper but presented in Hosni et al. (1989), the skin friction coefficient data for the $L/d_0=10$ rough surface at various free-stream velocities fall within the scatter of the smooth wall data and approximately within the ±10 percent range of the smooth wall correlation. Considering the data uncertainties, then, there is no discernable difference in the skin friction coefficient data on the smooth and $L/d_0=10$ rough surface.

Figure 7 presents the skin friction coefficients for the $L/d_0=4$ and $L/d_0=2$ rough surfaces for nominal free-stream velocities of 12 and 58 m/s. Also shown for reference is the smooth wall correlation. This figure clearly exhibits the influence of the roughness on the friction coefficients and shows

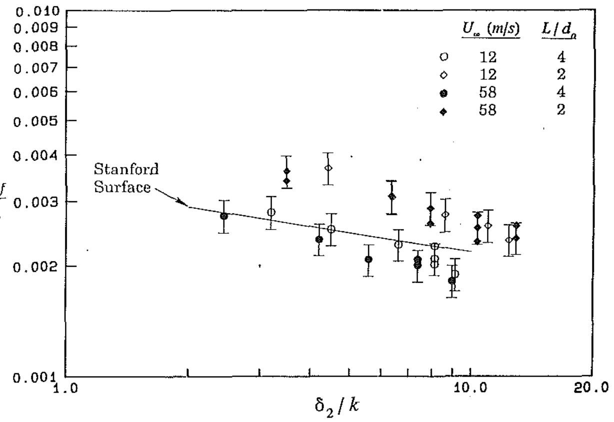

Fig. 8 Comparison of the skin friction coefficient distributions for the $L/d_o=4$ and $L/d_o=2$ surfaces in δ_2/k coordinates

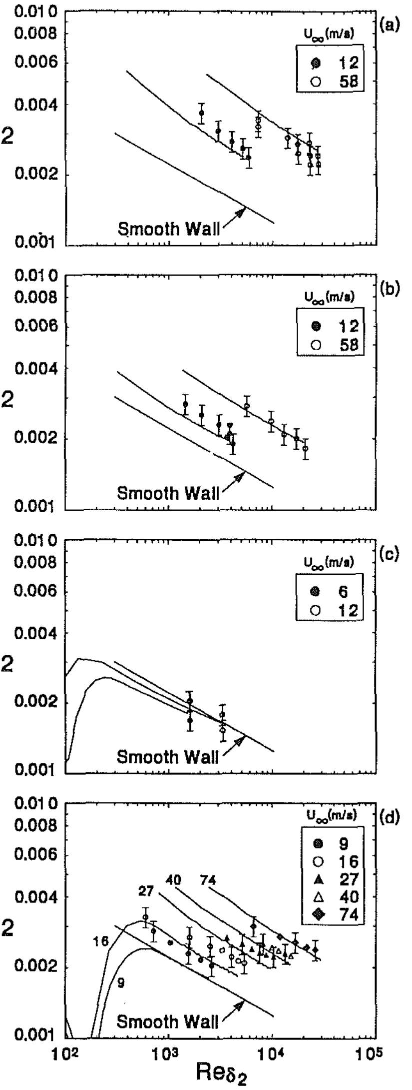

Fig. 9 Comparison of C_f data with the discrete element predictions for the rough surfaces. (*a*) $L/d_o=2$; (*b*) $L/d_o=4$; (*c*) $L/d_o=10$; (*d*) Stanford surface (Healzer, 1974; Pimenta, 1975).

that as the surface becomes rougher, the skin friction coefficient increases. The skin friction coefficient, C_f, at an Re_{δ_2} of about 13,000 is 0.00234 for the smooth wall and for the $L/d_o=4$ rough surface is 0.00418, which corresponds to a 78 percent increase. The skin friction coefficient for the roughest surface ($L/d_o=2$) at about the same Re_{δ_2} is 0.00620. This corresponds to a significant increase of about 165 percent with respect to the smooth wall skin friction coefficient.

These same rough-wall skin friction coefficient data are plotted against the ratio of momentum thickness to roughness height in Fig. 8. These coordinates were first suggested by Healzer (1974) as the most appropriate coordinates for presenting rough-wall skin friction coefficient data. Using the Stanford rough surface, he measured turbulent boundary layer mean velocity profiles, calculated momentum thicknesses, and subsequently obtained skin friction coefficients based on the momentum integral equation. Due to the data uncertainty, he could not make a firm assessment on any free-stream velocity dependence of his data. Pimenta (1975) obtained skin friction distributions over the same rough surface using hot-wire anemometry and stated that in the fully rough state of the boundary layer, friction coefficient $C_f/2$ is independent of Reynolds number and a function only of local momentum thickness. He observed that his fully rough skin friction distributions plotted versus momentum thickness normalized by roughness height collapsed together and the one transitionally rough data set appeared to be a little lower. The curve labeled "Stanford surface" represents Pimenta's fully rough data.

As shown in Fig. 8 the THTTF skin friction coefficient data for each of the $L/d_o=4$ and $L/d_o=2$ surfaces collapse within the data uncertainty, irrespective of transitionally rough or fully rough regime. Also, it is apparent that for each rough surface, the data collapse to a different curve. In these coordinates, our $L/d_o=2$ surface is "roughest," followed by the Stanford surface, then by our $L/d_o=4$ surface.

Prediction Results. Results obtained using the discrete element prediction method are compared with data taken on the rough surfaces in the THTTF and the data from the Stanford single rough surface in Fig. 9. The predictions presented in the following are true predictions and no fluid mechanics data from measurements were used in the predictions.

Skin friction coefficient distributions are plotted versus momentum thickness Reynolds number in this figure and curves are used to depict the predictions and the smooth wall correlation. Comparison of the THTTF data and predictions, Fig. 9(*a*,*b*,*c*), shows that the agreement is excellent, with the predictions matching the data within the estimated ±10 percent uncertainty. These comparisons essentially cover the aerodynamically smooth, transitionally rough, and fully rough flow regimes.

In Fig. 9(*d*), the zero pressure gradient skin friction coefficient distributions for the Stanford rough surface (Healzer, 1974; Pimenta, 1975) are compared with the calculations made with the discrete element method. Since this surface was composed of spheres packed in the most dense array and did not have a solid base smooth wall, an effective base wall location 0.2 sphere diameters below the crests of the elements as determined by Taylor et al. (1985) was used. The uncertainty bands represent the estimated ±10 percent uncertainty in reported C_f data. The predictions for every run fall either within or just outside the data uncertainty bands, indicating agreement with the data within 10–12 percent. However, the $U_\infty=9$ m/s case is predicted to be aerodynamically smooth, which is not indicated by the data.

Summary and Conclusions

As a result of this experimental investigation, profiles of mean velocity and Reynolds stress components (not presented in this paper) and distributions of boundary-layer thickness and skin friction coefficient from aerodynamically smooth, transitionally rough, and fully rough turbulent boundary-layer flows are now available for the three well-defined THTTF rough surfaces ($L/d_o = 2$, 4, and 10) in addition to the previously reported data for the somewhat similar Stanford rough surface. These data sets are significant in that they complement the previously reported Stanford data sets since the data have been taken in a similar facility using similar data reduction procedures and the probe types and specifications (i.e., sensor length and diameter) were the same. These additional data sets allow observations and conclusions about the characteristics of rough-wall turbulent boundary-layer flows to be made which were not apparent in the data from the single Stanford surface.

It appears that for a given surface, the scaling of the mean velocity profiles based on momentum thickness is appropriate to produce similar velocity profiles, as Pimenta (1975) suggested. The present data illustrate that "collapse" of experimentally determined velocity profiles in these coordinates cannot be used to distinguish roughness flow regimes. Also scaling on the momentum thickness alone is not sufficient to produce similar velocity profiles for flows over surfaces of different roughness character.

The boundary-layer thicknesses for the rough surface flows are quite different than those of smooth surface flows for equivalent free-stream conditions. For zero pressure gradient boundary-layer flow over a smooth surface, the boundary-layer thickness, at a fixed distance x from the origin, decreases as the free-stream velocity increases. In flows over the $L/d_o = 2$ and 4 rough surfaces, boundary-layer thickness at a fixed distance x increases rapidly with increasing free-stream velocity, then seems to level off as the fully rough condition become firmly established. In general, the boundary-layer thickness at a fixed distance x from the origin was larger for a rough surface than the smooth surface for equivalent free-stream conditions.

The THTTF skin friction coefficient data for each of the $L/d_o = 4$ and $L/d_o = 2$ rough surfaces plotted in $C_f/2$ versus the ratio of momentum thickness to roughness height, δ_2/k, collapse within the data uncertainty, irrespective of transitionally rough or fully rough regime. However, it is apparent that for each rough surface, the data collapse to a different curve. Therefore, the conclusion based on the Stanford data that $C_f = f(\delta_2/k)$ must be limited to a particular rough surface.

The results of comparisons of the skin friction data with the corresponding predictions using the discrete element method are very encouraging, with the predictions within the ±10–12 percent data uncertainty bands.

Acknowledgment

This work was supported by the U.S. Air Force Office of Scientific Research (Research Grant AFOSR-86-0178); the experimental apparatus was acquired under grant AFOSR-85-0075. The authors gratefully acknowledge the interest and encouragement of Capt. Hank Helin and Dr. Jim McMichael of AFOSR.

References

Coleman, H. W., Hosni, M. H., Taylor, R. P., and Brown, G. B., 1988, "Smooth Wall Qualification of a Turbulent Heat Transfer Test Facility," Report TFD-88-2, Mechanical and Nuclear Engineering Department, Mississippi State University.

Healzer, J. M., 1974, "The Turbulent Boundary Layer on a Rough, Porous Plate: Experimental Heat Transfer with Uniform Blowing," Ph.D dissertation, Mechanical Engineering Department, Stanford University. (Also report HMT-18).

Hosni, M. H., Coleman H. W., and Taylor, R. P., 1989, "Measurement and Calculation of Surface Roughness Effects on Turbulent Flow and Heat Transfer," Report TFD-89-1, Mechanical and Nuclear Engineering Department, Mississippi State University.

Hosni, M. H., Coleman H. W., and Taylor, R. P., 1991, "Measurement and Calculations of Rough-Wall Heat Transfer in the Turbulent Boundary Layer," *International Journal of Heat and Mass Transfer*, Vol. 34, pp. 1067–1082.

Kays, W. M., and Crawford, M. E., 1980, *Convective Heat and Mass Transfer*, 2nd ed., McGraw-Hill.

Patel, V. C., 1965, "Calibration of the Preston Tube and Limitations on Its Use in Pressure Gradients," *Journal of Fluid Mechanics*, Vol. 23, pp. 185–208.

Pimenta, M. M. 1975, "The Turbulent Boundary Layer: A Experimental Study of the Transport of Momentum and Heat with the Effect of Roughness," Ph.D. dissertation, Mechanical Engineering Department, Stanford University. (Also Report HMT-21).

Preston, J. H., 1954, "The Determination of Turbulent Skin Friction of Means of Pitot Tubes," *Journal of the Royal Aeronautical Society*, Vol. 58, pp. 109–121.

Raupach, M. R., Antonia, R. A., and Rajagopalan, S., 1991, "Rough-Wall Turbulent Boundary Layers," *Applied Mechanics Reviews*, Vol. 44, pp. 1–25.

Scaggs, W. F., Taylor, R. P., and Coleman, H. W., 1988, "Measurement and Prediction of Rough Wall Effects of Friction Factor—Uniform Roughness Results," ASME JOURNAL OF FLUIDS ENGINEERING, Vol. 110, pp. 385–391.

Taylor, R. P., Coleman, H. W., and Hodge, B. K., 1985, "Prediction of Turbulent Rough-Wall Skin Friction Using a Discrete Element Approach," ASME JOURNAL OF FLUIDS ENGINEERING, Vol. 107, pp. 251–257.

Effects of a Large Eddy Breakup Device on the Fluctuating Wall Pressure Field

(Data Bank Contribution*)

W. L. Keith
Mem. ASME

J. J. Barclay

Submarine Sonar Department,
Naval Undersea Warfare Center Detachment,
New London, CT 06320

Wall pressure spectra and mean velocity profiles were measured with and without a large eddy breakup device (LEBU) located upstream in high R_θ turbulent boundary layers. Changes of the order of 5 percent occurred in the mean wall shear stress. The wall pressure spectra of the manipulated flow did not show the existence of any highly energized coherent structures, but rather moderate changes occurring over broad frequency ranges. Reductions in the wall pressure autospectra occurred at lower frequencies associated with turbulence activity in the outer layer and the outer portion of the log law layer. Increases occurred at higher frequencies associated with the inner portion of the log law layer. The changes in the wall pressure coherence levels were similar, but generally more complex with greater spatial persistence. The changes in both the autospectra and coherence indicate a conversion of energy from lower to higher convective wavenumbers.

Introduction

Large eddy breakup devices (LEBUs) have been shown to be effective for passive drag reduction. In particular cases, the reduction in the drag due to skin friction downstream of the LEBU exceeds the increased drag due to the LEBU itself, leading to net drag reductions of 5 to 10 percent. Wilkinson et al. (1987), Anders and Watson (1985), and Anders (1989) measured reductions in the mean wall shear stress τ over significant distances downstream from a LEBU. Saville and Mumford (1988) concluded that in addition to the breakup of the larger scale turbulent structures in the outer layer, vorticity introduced from the wake of the LEBU which migrates into the inner layer was an important mechanism for reducing τ. Anders (1989) has shown that the effectiveness of LEBUs for drag reduction diminishes at higher Reynolds numbers. A decoupling of the inner and outer boundary layer scales was suggested as a possible mechanism for this effect. Testing at moderate to high R_θ values is therefore desirable, as results from lower R_θ experiments cannot be readily scaled to higher values.

Passive control of flow-induced vibration and noise constitutes an additional application for LEBUs. Beeler (1986) measured the wall pressure autospectra in a wind tunnel at an equilibrium R_θ of 6,490. The pressure measurement location was 70δ downstream from tandem LEBUs which were mounted at a height H/δ of 0.8. The spectral levels were increased at nondimensional frequencies $\omega\nu/u^{*2}$ greater than approximately .5, and reduced at lower frequencies. A reduction of 12.5 percent in the wall pressure rms occurred, as well as a 25 percent reduction in τ. Savill and Mumford (1988) discussed the reduction in the lower convective wavenumber streamwise velocity fluctuations behind a single LEBU that were observed by Savill (1984, 1986). These reductions were found to be accompanied by a conversion of energy from the larger to the smaller eddies. Corke et al. (1982) also measured the spectra of the streamwise velocity and found the turbulent energy to be reduced at low convective wavenumbers and enhanced at higher ones. The changes in the velocity spectra observed by Corke et al. (1982) and Savill (1984, 1986) are qualitatively consistent with the changes in the wall pressure spectra measured by Beeler. Farabee (1986) gave a comprehensive review of investigations of wall pressure fluctuations in equilibrium and perturbed boundary layers, and discussed relationships between the wall pressure and velocity fluctuations for those cases.

The effects of a LEBU on the mean velocity profiles, the mean wall shear stress, and the fluctuating wall pressure field were investigated here. The approach involved measuring these quantities in an equilibrium boundary layer at a particular streamwise location, and repeating the measurements at the same free stream velocities with a LEBU installed upstream.

---

*Data have been deposited to the JFE Data Bank. To access the file for this paper, see instructions on p. 542 of this issue.

Contributed by the Fluids Engineering Division for publication in the JOURNAL OF FLUIDS ENGINEERING. Manuscript received by the Fluids Engineering Division July 21, 1992; revised manuscript received December 4, 1992. Associate Technical Editor: D. M. Bushnell.

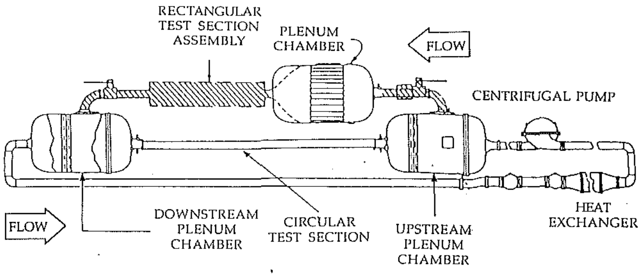

Fig. 1 Water tunnel components and flow schematic

The experiments were conducted in an acoustically quiet water tunnel at the New London Laboratory, shown schematically in Fig. 1. This facility has recently been used by Keith (1989) to measure the effect of riblets on wall pressure fluctuations and also by Keith and Bennett (1991) to measure the turbulent wall pressure and wall shear stress fluctuations.

Experimental Setup

The water tunnel was designed with acoustic isolation provided by rubber hoses between the major components to minimize transmission of acoustic energy. The 30 in. diameter plenum chamber consists of an inlet diffuser section, followed by a 0.37 in. cell aluminum honeycomb section 18 in. long, followed by two stainless steel 20 by 20 mesh screens each with a 67.2 percent open area. The flow converges into the rectangular test section through a nozzle with an area contraction ratio of 8.2. The nozzle was designed by Aerolab Corporation to minimize the generation of vorticity and the free stream turbulence intensity. Transition occurs at the inlet region of the nozzle, and fully turbulent boundary layers exist on the channel walls at the start of the test section.

The interior of the rectangular test section is 83 in. long, 12 in. wide, and increases in height linearly from 4.00 in. at the start to 4.41 in. at the exit. This divergence in height compensates for the growth of the boundary layers on the channels walls, such that the change in dynamic head is within 1 percent. The measured increase in δ over the length of the test section was consistent with the results of Schlichting (1979) for smooth flat plate boundary layers at zero pressure gradient.

Measurements of the streamwise velocities were made with a TSI Model 9100 Laser Doppler Velocimetry (LDV) system, configured for a single velocity component in the backscatter mode using the green beam. A 500 (mm) focal length lens was used with a 2.27 × beam expander. The resulting measurement volume was an ellipsoid with a diameter of 0.006 in. and a length (spanwise to the flow) of 0.12 in. The 2 watt argon-ion laser was operated at 1.0 to 1.25 watts. Data analysis was accomplished using a TSI Model 1900 counter processor, microcomputer, and modified TSI software.

The piezoelectric sensors used for the wall pressure measurements were end-capped, air-filled cylinders fabricated at the New London Laboratory. The sensors were calibrated in air and displayed a flat response over the frequency ranges investigated here. The sensing areas had a 0.08 in. diameter. Three of the sensors were flush mounted in the spanwise center on the bottom wall, at a location approximately 62 in. from the start of the test section. The sensor streamwise spacings were 0.6 in., 1.0 in., and 1.6 in.

The analog voltage signals from the sensor were amplified 20 dB with Ithaco model 143 N low noise preamplifiers and an additional 40 dB with Ithaco highpass filter amplifiers set at 10 Hz. The signals were then recorded with a TEAK model XR-7000, 21 channel analog tape recorder. The record speed was 15 in/sec, providing a record bandwidth of 0 to 5000 Hz. The analog signals from the tape recorder were filtered with Wavetek Model 630 bandpass filters with a roll-off of 6 dB per octave. A Hewlett Packard Model 3562 spectrum analyzer with 800 lines of spectral resolution was used to compute the spectra and correlation functions. An analyzer bandwith of 2000 Hz was used, resulting in binwidths of 2.5 Hz.

To assess the background acoustic noise in the rectangular test section, the coherence was measured between a pressure sensor flush mounted on the top wall and one flush mounted directly below on the bottom wall. Contributions from convected turbulence in the boundary layers on the top and bottom walls were not coherent, such that coherence levels $\gamma^2(\omega)$ were approximately .02 for frequencies greater than 25 Hz. Discrete tonals at 25 Hz and lower were due to acoustic waves in the fluid which radiated from the centrifugal pump. Autospectral and coherence data at frequencies lower than 25 Hz will therefore not be presented in this paper, since the measured levels due not represent contributions solely from convected turbulence.

The LEBU geometry and dimensions as shown in Fig. 2, were chosen based upon the work of Savill and Mumford (1988) and Anders (1989). Efforts were not made to minimize the LEBU form drag. Preliminary tests made using a ribbon type LEBU with rectangular cross section and rounded leading and trailing edges, showed results qualitatively similar to those presented here. As a sharp trailing edge is believed to enhance the reduction in τ, the upper surface of the LEBU was tapered from the leading to trailing edge. The bottom surface was parallel with the bottom wall of the test section. The thickness of the rounded leading edge was chosen as 0.1 in. to minimize flow induced vibrations. The LEBU was mounted in tension on vertical struts positioned near the channel side walls, as

Nomenclature

k = streamwise wavenumber (rad/ft)
$p(x, t)$ = fluctuating wall pressure (μPa)
$R(\Gamma, \xi)$ = $<p(x, t)\, p(x+\xi, t+\Gamma)>/\{<p(x, t)^2>\ <p(x+\xi, t+\Gamma)^2>\}^{1/2}$, correlation function (normalized)
R_θ = $U_o\theta/\nu$ momentum thickness Reynolds number ($R_\theta \equiv R_1, R_2, R_3, R_4$ respectively)
U_o = free-stream velocity (ft/sec)
$U_c(\omega)$ = wall pressure convection velocity (ft/s)
$u(y)$ = mean streamwise velocity (ft/s)
u^* = $(\tau/\rho)^{1/2}$ friction velocity (ft/s)
x = distance from the LEBU leading edge (in)
$\gamma^2(\omega)$ = wall pressure coherence (normalized)
δ = boundary layer thickness (in)
ξ = pressure sensor separation (in)
θ = boundary layer momentum thickness (in)
ρ = fluid density (lbf-s^2/ft^4)
τ = mean wall shear stress (psi)
ν = fluid kinematic viscosity (ft^2/s)
$\Phi(\omega) = \tilde{\Phi}(f)/2\pi$ = single-sided autospectrum (μPa^2/(rad/s))
$\Phi(\omega, \xi) = \tilde{\Phi}(f, \xi)/2\pi$ = single-sided cross-spectrum (μPa^2/(rad/s))
$\Phi(k, \omega)$ = wavenumber-frequency spectrum (μPa^2/(rad^2/s-ft))

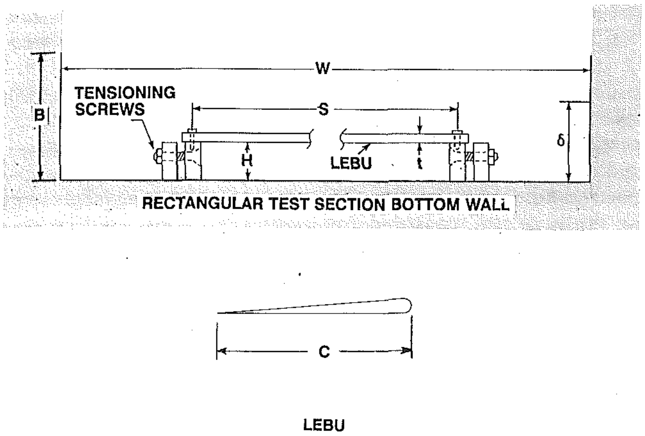

Fig. 2 LEBU details (in): $W = 12$, $H = .6$, $B = 2.1$ (1/2 channel ht.), $S = 7.6$, $t = .1$, $\delta = 1.3$, $C = 1.3$

Table 1 Equilibrium boundary layer parameters

U_o (ft/s)	δ (in.)	θ (in).	R_θ	u^*/U_o	u^*/U_o (Coles)	ν/u^* (in.)
05	1.31	0.15	$R_1 = 6{,}250$	0.038	0.037	0.00063
10	1.29	0.14	$R_2 = 11.667$	0.036	0.035	0.00033
15	1.37	0.15	$R_3 = 18{,}750$	0.034	0.034	0.00023
20	1.31	0.13	$R_4 = 21{,}667$	0.034	0.033	0.00018

shown in Fig. 2. The use of struts was required since the LEBU could not penetrate or be attached to the side walls of the test section. Velocity and wall pressure measurements were made with only the struts in place. No changes were observed with respect to the equilibruim flows.

The frequency of vibration for the fundamental transverse mode of the LEBU was determined as 250 (Hz) by treating the LEBU as a simply supported finite elastic beam, following Junger and Feit (1986). No discrete tonals or coherent acoustic energy was measured with flow past the LEBU at the Reynolds numbers investigated. Preliminary tests were also made with LEBUs 0.05 in. thick and less. For these cases discrete tonals in the pressure spectra were observed at the fundamental frequencies.

Mean Velocity and Wall Shear Stress Measurements

Velocity measurements in the equilibrium boundary layer and free stream were made at a streamwise location 62 in. downstream from the start of the test section. The random error (the ratio of the standard deviation to the expected value) in the mean velocity data was 0.5 percent. The free stream turbulence intensity was 1 percent. Velocity measurements in the viscous sublayer within 10 viscous lengths from the wall were not possible due to the very small viscous length scales ν/u^* as listed in Table 1. Values for u^* were therefore determined using values for $u(y)$ measured in the log law layer. For each $u(y)$ in the log law layer, a value of u_i^* was found such that Clauser's (1956) expression

$$u(y)/u^* = 2.44\ \ln(u^*y/\nu) + 4.9 \tag{1}$$

was satisfied. The u_i^* were then averaged to determine u^* and τ. The random error in u^* determined from the standard deviation of the u_i^* about u^* was found to be 2 percent. The corresponding error in τ was 4 percent. This error reflects the random error in the velocity data as well as the error resulting from the accuracy of Eq. (1) for this particular boundary layer. The 4 percent error in the absolute value of τ is comparable to stated errors from other investigations where similar indirect methods were used to determine τ.

The resulting values for u^*/U_o at each Reynolds number agreed well with Cole's (1953) results for an ideal boundary layer, as shown in Table 1. The velocity measurements scaled on inner variables as well as Eq. (1) are shown in Fig. 3.

Velocity measurements were repeated at the same location in the test section at the same free-steam velocities with the LEBU positioned upstream at $x = 10\delta$ (or 13.2 in). and also at $x = 14\delta$ (or 18.2 in). The ratio H/δ_L of the LEBU height H to the local boundary layer thickness δ_L was approximately .5 at all free-stream velocities for the first location at $x = 10\delta$. The decrease in δ_L from the first to the second LEBU location was approximately 5 percent. Based upon preliminary measurements made with the LEBU at varying heights above the wall, we concluded that a 5 percent difference in the relative height of the LEBU in the boundary layer was not significant.

Lemay et al. (1985) found that a universal law of the wall held for boundary layers manipulated with LEBUs for $x > 10\delta$. Values for u^* and τ were therefore determined as in the equilibrium case. The results support the existence of a well defined log law layer for the manipulated flow, as shown in Fig. 3. The changes in τ are tabulated in Table 2. The trend is an increase in τ for $x = 10\delta$ followed by a decrease for $x = 14\delta$, as shown in Fig. 4. A similar trend of an increase followed by a decrease in τ was observed by Anders (1989). At comparable values of R_θ, Anders (1989) found reductions in τ of 5 percent (on average) at downstream locations $20 < x/\delta < 75$, with increases in τ occurring for x/δ closer to the LEBU.

The magnitude of the changes in τ are comparable to our stated random error of 4 percent in the absolute value of τ.

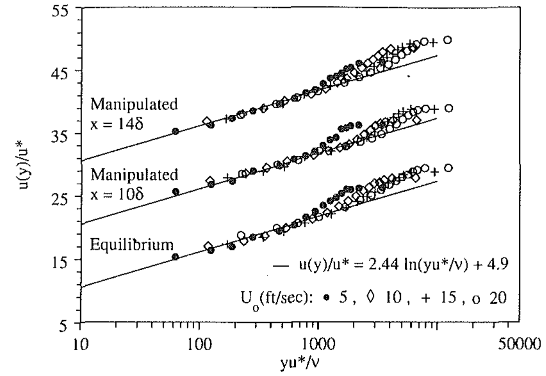

Fig. 3 Velocities scaled on inner variables (vertical axis offset by 10 and 20 units for the manipulated data with the LEBU located at $x = 10\delta$ and 14δ, respectively)

Table 2 Mean wall shear stress values

U_o (ft/s)	Equilibrium flows τ (psi)	Manipulated flows $x = 10\delta$ τ (psi)	$x = 14\delta$ τ(psi)
05	.000476	.000491	.000481
10	.001746	.001894	.001660
15	.003587	.003601	.003545
20	.006321	.006470	.006111

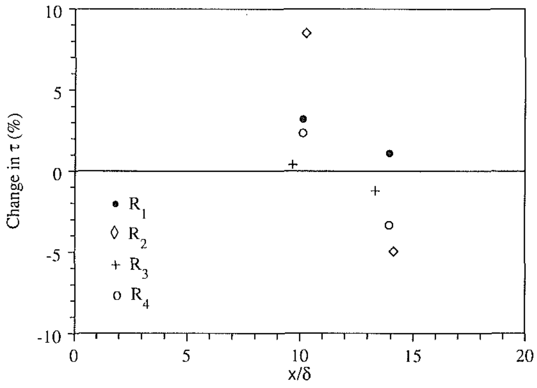

Fig. 4 Percent change in the mean wall shear stress, LEBU located at x/δ upstream

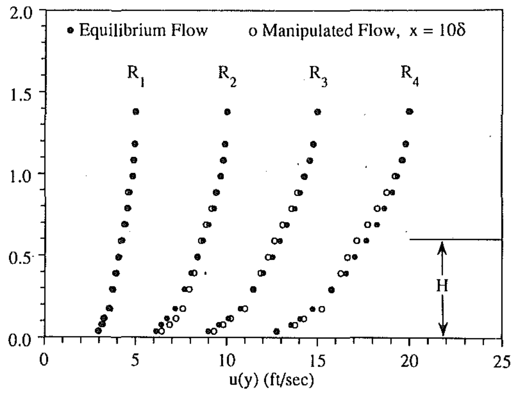

Fig. 5 Equilibrium and manipulated velocities, LEBU located at $x = 10\delta$

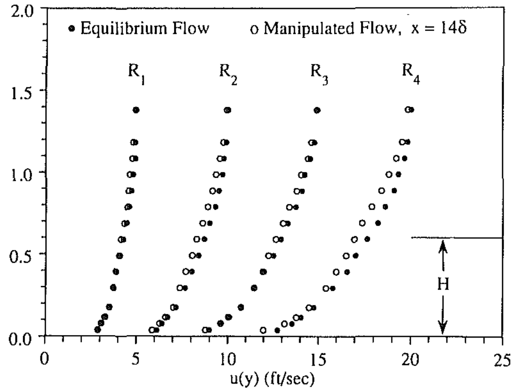

Fig. 6 Equilibrium and manipulated velocities, LEBU located at $x = 14\delta$

We therefore determined values for u^* and τ using a number of velocity data points repeatedly taken at one fixed y (or y^+) location in the log law layer. Values for u^* and τ were obtained from Eq. (1) as previously described. The values obtained for τ agreed with those obtained using the former approach. Using this method, the random error in τ was 1 percent, and was primarily due to the random error of 0.5 percent in the measurements of $u(y)$. The larger 4 percent random error obtained with the former approach reflects both the scatter of the velocity data $u(y)$ about Eq. (1) and the error in the measurements of $u(y)$. The scatter of the velocity data about Eq. (1) is comparable for the equilibrium and manipulated flows, as shown in Fig. 3. A random error in τ of 1 percent is therefore more accurate for purposes of comparing the equilibrium and manipulated flows. However, this does not imply that the error in the estimation of the absolute value of τ for any particular case is 1 percent. All values of τ were obtained with the former approach using a number of data points $u(y)$ in the log law layer.

The effect of the LEBU on the dimensional mean velocity profiles is apparent, as shown in Figs. 5 and 6. With the LEBU at $x = 10\delta$, increases in $u(y)$ occurred near the wall, leading to increases in τ. Velocity deficits existed in the outer layer near the LEBU at $y = H$. The magnitude of these deficits increased with increasing free-stream velocity. With the LEBU at $x = 14\delta$, the decreases in $u(y)$ near the wall leading to decreases in τ are also apparent. The velocity deficits near the LEBU are increased with respect to the $x = 10\delta$ data, indicating that the outer layer was still departing from equilibrium at this location.

Wall Pressure Autospectra Measurements

The wall pressure autospectra and coherence measurements at equilibrium R_θ values of R_2 and R_4 will first be analyzed. The spectral data obtained at R_1 was limited in frequency due to the low signal to noise ratio, and the data at R_3 showed consistent trends with respect to the R_2 and R_4 cases. All autospectra and coherence functions were computed from 500 ensemble averages. The measured autospectra were repeatable to within $+/-.5$ dB at all frequencies. For clarity in presentation, a fifth order polynomial curve was fit to the autospectra and coherence data. These curves accurately represent the shape of the measured functions. The scatter of the autospectral data about the curves was within $+/-$ .5 dB, with an average scatter of .2 dB.

Farabee and Casarella (1991) recently established nondimensional frequency ranges over which particular scaling laws held for equilibrium wall pressure autospectra. They also established the location of the turbulent sources in the boundary layer which contribute to the wall pressure for the various frequency ranges. Here, we offer a brief summary of their results. Our autospectra will then be presented in both nondimensional and dimensional forms. The nondimensional forms are required in order to utilize the results of Farabee and Casarella (1991). The dimensional forms are useful for accurately comparing the equilibrium and manipulated spectra, since the errors resulting from the measured scaling parameters do not appear.

To nondimensionalize their spectra, Farabee and Casarella (1991) used an outer variable scaling given by

$$\Phi(\omega)u^*/\tau^2\delta \text{ versus } \omega\delta/u^*, \tag{2}$$

and an inner variable scaling given by

$$\Phi(\omega)u^{*2}/\tau^2\nu \text{ versus } \omega\nu/u^{*2}. \tag{3}$$

Motivation for this particular outer scaling is also discussed by Panton and Linebarger (1974). The inner variable scaling has been used by various investigators in the past. A "low" frequency range was defined by $\omega\delta/u^* < 5$. Farabee and Casarella (1991) found that cancellation of acoustic noise using signal processing was required to obtain spectral data in this range. Here, noise cancellation techniques were not pursued, and the 25 (Hz) background noise limit precluded spectral measurements in the "low" frequency range.

A "mid" frequency range was defined by $5 < \omega\delta/u^* < 100$, with contributions resulting from turbulent sources in the outer layer. Farabee and Casarella (1991) found that the spectral scaling given by (2) held here. Our measurements extended over the higher portion of this frequency range, as shown in Fig. 7. An "overlap" frequency range was defined by $100 < \omega\delta/u^* < 0.30\,R_\tau$, where the ratio of the outer to inner length scale is defined as $R_\tau = u^*\delta/\nu$. Spectral contributions result from turbulent sources in the log law layer. Farabee and Casarella (1991) found that the spectral scalings given by (2) and (3) both held here, consistent with the existence of an overlap layer. Our measurements covered most of this frequency range, as shown in Fig. 7.

A "high" frequency range was defined by $0.30\,R_\tau < \omega\delta/u^*$ and $\omega\nu/u^{*2} > 0.3$. Contributions at these frequencies result from turbulent sources in the buffer layer. Our measurements did not extend over these frequencies. Sensors sufficiently small to resolve these very small inner scales and suitable for use in water are not presented available. We note that Farabee and Casarella (1991) used pin-hole sensors in air having values of ru^*/ν ranging from 16 to 33.

A reasonable collapse of our spectral data for the two equilibrium Reynolds numbers occurs over the entire frequency range with the outer scaling given by (2), as shown in Fig. 7. However, the effectiveness of any particular scaling for collapsing autospectral data sets cannot be determined without considering that spatial resolution of the pressure sensor at each Reynolds number, as discussed by Keith et al. (1992). In the case of the outer scaling, for $\omega\delta/u^* > 300$, our measured

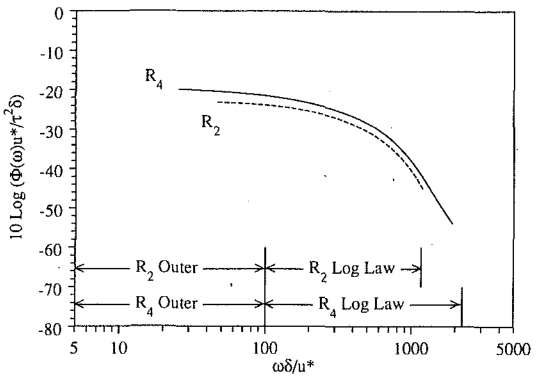

Fig. 7 Equilibrium wall pressure autospectra scaled with outer variables

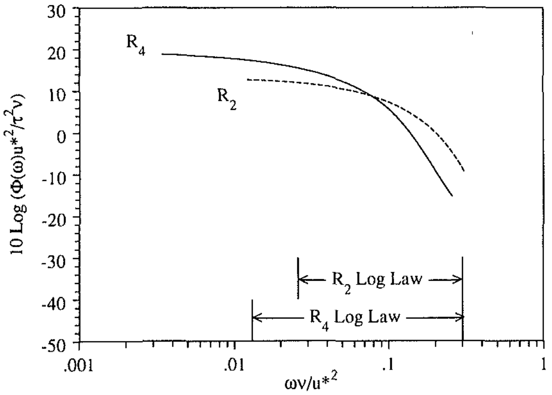

Fig. 8 Equilibrium wall pressure autospectra scaled with inner variables

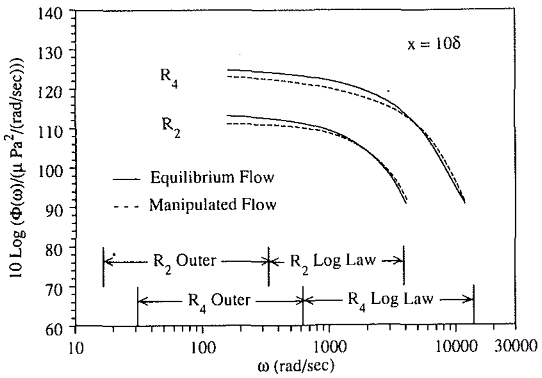

Fig. 9 Equilibrium and manipulated dimensional wall pressure autospectra, LEBU located at $x=10\delta$

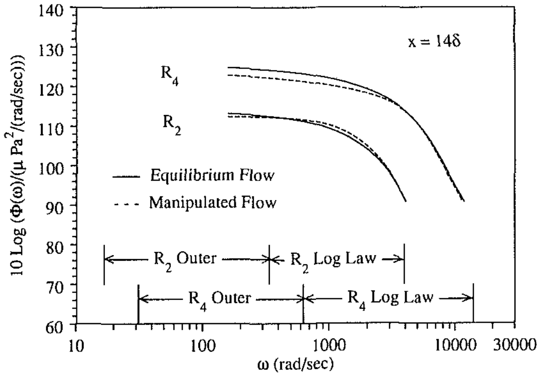

Fig. 10 Equilibrium and manipulated dimensional wall pressure autospectra, LEBU located at $x=14\delta$

spectral levels at both Reynolds numbers were lower than the true levels, due to inadequate sensor spatial resolution. In order to account for this effect, we use the results of Corcos (1963).

Using a particular model for the wall pressure field, Corcos (1963) showed that the ratio of the measured spectral level to the true spectral level at any frequency ω_0 depends only upon the quantity $\omega_0 r/U_c$. Here, r is the radius of the pressure sensor and $U_c = U_c(\omega_0)$ is the convection velocity of a pressure disturbance. The dimensionless quantity $\omega_0 r/U_c$ may be interpreted as the ratio $2\pi r/\lambda$ of the sensor radius to a convected wavelength corresponding to ω_0. This interpretation emphasizes that although the measurement error appears in the frequency domain, the error is due to the spatial and not the temporal response of the sensor.

For spectra which have been nondimensionalized, the quantity $\omega_0 r/U_c$ must be expressed in terms of the particular frequency scaling used. For the outer scaling of (2), we have

$$\omega_0 r/U_c = (\omega_0\delta/u^*)(u^*/U_c)(r/\delta). \tag{4}$$

For any particular nondimensional frequency $\omega_0\delta/u^*$, the quantity (u^*/U_c) (r/δ) determines the effect of the measurement error on the nondimensional pressure spectra. Here, the quantity (u^*/U_c) (r/δ) decreased by 7 percent as R_θ increased from R_2 to R_4. This change was primarily due to the decrease in u^*/U_c (or essentially u^*/U_o) as R_θ increased, since δ did not change significantly. We conclude that the collapse of our spectral data scaled with outer variables is therefore not significantly influenced by the measurement errors due to the spatial resolution of the pressure sensor. The collapse of the spectral data therefore does not vary significantly with frequency, as shown in Fig. 7.

The spectra scaled with the inner variables given by (3) do not collapse well over the log law frequency ranges, as shown in Fig. 8. For frequencies $\omega\nu/u^{*2} > 0.04$, measurement errors occur due to sensor spatial resolution. For the inner frequency scaling we have

$$\omega_0 r/U_c = (\omega_0\nu/u^{*2})(u^*/U_c)(ru^*/\nu). \tag{5}$$

For a particular nondimensional frequency $\omega_0\nu/u^{*2}$, the quantity (u^*/U_c) (ru^*/ν) determines the effect of the measurement error on the spectra. This quantity increased by 77 percent as R_θ increased from R_2 to R_4. The was primarily due to the change in the inner length scale ν/u^*. The quantity ru^*/ν therefore increased from 121 at R_2 to 222 at R_4. As a result, the effect of the measurement error at a particular nondimensional frequency $\omega_0\nu/u^{*2}$ is significantly greater at R_4 than at R_2, as shown by the more rapid roll-off of the R_4 data in Fig. 8. Conclusions as to the effectiveness of the inner scaling for collapsing the data over the log law frequency range are therefore not possible.

The manipulated pressure spectra are compared to the equilibrium spectra in Figs. 9 and 10. The dimensional frequency ranges related to the outer and log law lawyers were determined using the equilibrium boundary layer length and time scales. With the LEBU located at $x=10\delta$, the spectral levels were decreased over frequencies related to the outer layer and the outer portion of the log law layer. Slight increases occurred at the higher frequencies related to the log law layer, as shown in Fig. 9. The trend is indicative of a conversion of energy from the lower to higher convective wavenumbers, or outer to inner layers. The dominant effect is the reduction of energy at the lower frequencies and lower convective wavenumbers. The changes in the spectra agree qualitatively with those measured by Beeler (1986).

At the lower free-stream velocity with the LEBU located at $x=14\delta$, the manipulated spectra relaxed to equilibrium over

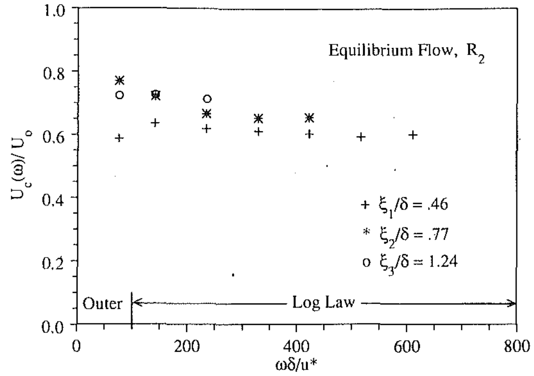

Fig. 11 Equilibrium wall pressure convection velocities, $U_o = 10$ (ft/s), $R_\theta = 11{,}667$

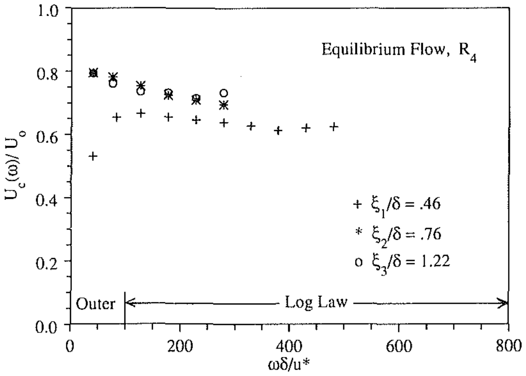

Fig. 12 Equilibrium wall pressure convection velocities, $U_o = 20$ (ft/s), $R_\theta = 21{,}667$

the entire frequency range. At the higher free stream velocity reductions persisted at lower frequencies, as shown in Fig. 10. The decoupling of the inner and outer length scales suggested by Anders (1989) may cause this Reynolds number effect. For the equilibrium flow, R_τ increased by a factor of approximately 2 from R_2 to R_4. As the inner layer relaxed to equilibrium downstream of the LEBU, its influence on the outer layer was therefore less at the higher free stream velocity. The outer layer of the manipulated flow therefore relaxed to equilibrium more slowly at the higher free stream velocity. This effect will be discussed further in conjunction with the coherence measurements.

Wall Pressure Convection Velocity and Coherence Measurements

The convection velocities of the wall pressure field were determined from two point measurements of the correlation function $R(\Gamma, \xi)$. The relationship $U_c(\omega_0) = \xi/\Gamma_m$ was used, where Γ_m is the temporal delay corresponding to the maximum value of $R(\Gamma, \xi)$, and ω_0 denotes the center of the 50 Hz narrow frequency band. The random error in $U_c(\omega)/U_o$ was within 1 percent for all cases.

The convection velocities obtained using the smallest sensor spacing are lower at all frequencies than for the larger spacings, as shown in Figs. 11 and 12. At a frequency ω_0, contributions to $U_c(\omega_0)$ result from a range of wavenumbers convecting at slightly different speeds. The measured value of $U_c(\omega_0)$ therefore represents an average over these wavenumbers as well as the 50 Hz frequency band. The variation in $U_c(\omega_0)$ with sensor spacing results from the varying spatial correlations associated with these various wavenumbers. The larger sensor spacing discriminates in favor of the lower convective wavenumbers having greater spatial correlations. The convection velocities of the lower convective wavenumbers are slightly higher due to the mean spatial location of these sources in the boundary layer.

The convection velocities measured with the larger sensor spacings increase as the frequency decreases. This trend reflects the higher convection velocities of the lower convective wavenumbers contributing at the lower frequencies. The data for the smallest sensor spacing displays a decrease over the same low frequency range. This trend reflects contributions from sources with lower spatial correlations which convect at lower speeds. These sources will be discussed further in conjunction with the coherence measurements.

At both free stream velocities and all sensor separations, the measured convection velocities $U_c(\omega)$ for the manipulated flow agreed with the equilibrium results to within 1 percent. The changes in the manipulated mean velocity profiles were generally of the order of 5 percent or less throughout the boundary layer. Changes in the measured convection velocities would therefore be expected to be quite small, particularly in view of the averaging over frequency and wavenumber inherent to the measurement process.

The Corcos (1963) model of the streamwise cross-spectra of the wall pressure field may be expressed as

$$\Phi(\omega, \xi) = \Phi(\omega) A(\omega\xi/U_c) e^{-i\omega\xi/U_c}. \tag{6}$$

The function $A(\omega\xi/U_c)$ may be interpreted as the magnitude of the normalized cross-spectra expressed as a function of the similarity variable $\omega\xi/U_c$, where $U_c = U_c(\omega)$. In addition, the function $A(\omega\xi/U_c)$ may be equated to $\gamma(\omega\xi/U_c)$ where $\gamma^2(\omega\xi/U_c)$ is defined as the coherence. For each fixed separation ξ we generated the function $A(\omega\xi/U_c)$ by scaling the coherence with the measured convection velocities. The resulting functions $A(\omega\xi/U_c)$ were repeatable to within $+/-.05$ at all frequencies. The scatter of the data about the fitted curves was within $+/-.05$ in all cases, with an average scatter of .03. Corcos (1963) showed that the effects of sensor spatial resolution on the measured function $A(\omega\xi/U_c)$ are very small in comparison to the effects on the autospectra. Our results will be shown to support this conclusion.

The data for both equilibrium Reynolds numbers and the three separations collapses very well at the higher values of the similarity variable $\omega\xi/U_c$, as shown in Figs. 13 and 14. This collapse implies the convective wavenumbers in this range experience the same loss of coherence as they convect one wavelength. The frequency range over which this collapse occurs is associated with the log law layer. Here, an exponential decay constant of $-.125$, consistent with Corcos (1963) and Farabee and Casarella (1991), was found to provide the best exponential curve fit for the function $A(\omega\xi/U_c)$. However, the data deviates form a purely exponential form, as shown. There is no theoretical or physical justification for the purely exponential form. Farabee and Casarella (1991) noted that the exponential decay constant reported from various investigations varies from $-.10$ to $-.19$, and is a function of various flow parameters. A value of $-.125$ implies that a wavenumber experiences a 90 percent loss of coherence as it convects approximately three wavelengths.

At the lower values of $\omega\xi/U_c$, the data from the two larger spatial separations departs from the similarity scaling, reaches a maximum value, and rolls off. The convective wavenumbers in this range are characterized by a rapid loss of spatial coherence and lower convection velocities. This trend of departure from the similarity scaling was also measured by Farabee and Casarella (1991) and Corriveau and Berman (1986). Farabee and Casarella (1991) used the maximum value of the function $A(\omega\xi/U_c)$ to define a cut-off $\omega_0\xi/U_c$ for the similarity region. An associated convective wavenumber cut-off $k_0 = \omega_0\xi/U_c$ defined the wavenumbers governed by the similarity scaling. Their nondimensional wavenumber cut-off $k_0\delta$ was 2.3 for their

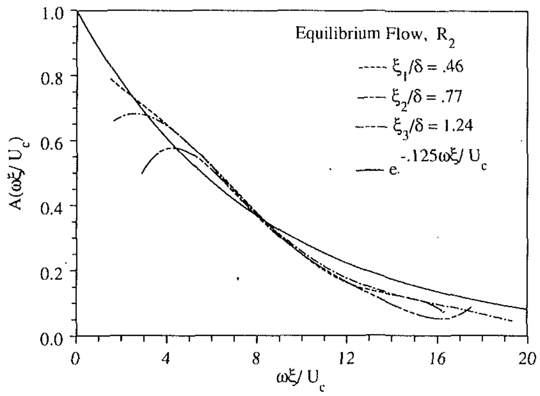

Fig. 13 Equilibrium wall pressure function $A(\omega\xi/U_c)$, $U_o = 10$ (ft/s), $R_\theta = 11{,}667$

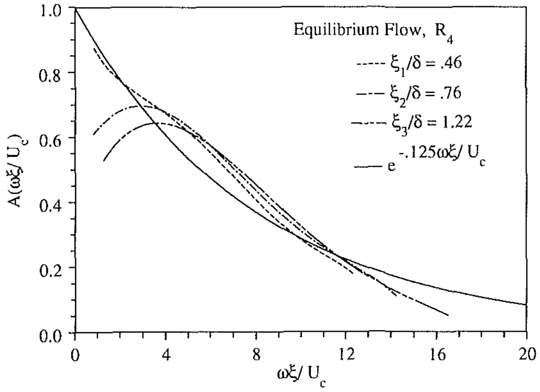

Fig. 14 Equilibrium wall pressure function $A(\omega\xi/U_c)$, $U_o = 20$ (ft/s), $R_\theta = 21{,}667$

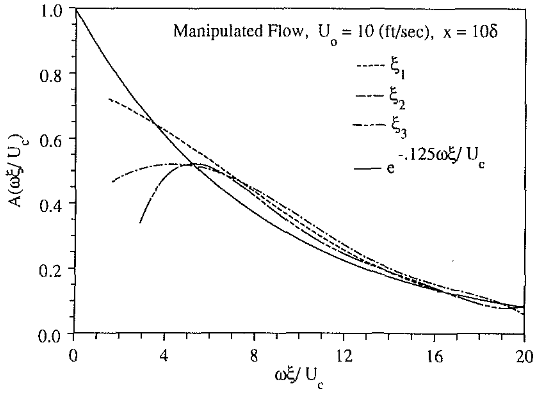

Fig. 15 Manipulated wall pressure function $A(\omega\xi/U_c)$, $U_o = 10$ (ft/s), LEBU located at $x = 10\delta$

minimum separation $\xi/\delta = 0.21$, and 1.3 for their maximum separation $\xi/\delta = 5.0$. Here, at R_2 a value of 3.3 for $k_0\delta$ was obtained at both $\xi/\delta = 0.77$ and $\xi/\delta = 1.24$. At R_4, $k_0\delta$ was 3.7 at $\xi/\delta = 0.76$ and 3.0 at $\xi/\delta = 1.22$.

At the higher Reynolds number the trend of decreasing $k_0\delta$ with increasing separation was consistent with the results of Farabee and Casarella (1991). However, our values for $k_0\delta$ were consistently higher. Here, wavelenths greater than approximately 2δ suffer a rapid loss of spatial coherence as compared to 5δ for Farabee and Casarella (1991). Free-stream disturbances related to our higher turbulence intensity may cause the longer wavelength sources in the outer portion of the boundary layers to experience a more rapid loss of spatial coherence. Measurements of the velocity fluctuations in the outer layer are required to further investigate these effects. We now compare the functions $A(\omega\xi/U_c)$ for the manipulated flow with the equilibrium results. Since the convection velocities were unchanged in the manipulated flow, changes in the functions $A(\omega\xi/U_c)$ were due to changes in the coherence levels themselves.

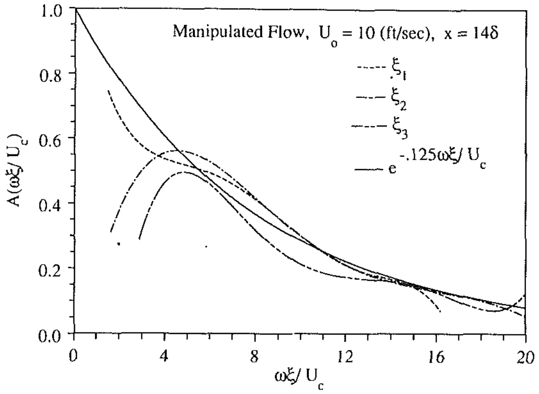

Fig. 16 Manipulated wall pressure function $A(\omega\xi/U_c)$, $U_o = 10$ (ft/s), LEBU located at $x = 14\delta$

At the lower free-stream velocity with the LEBU located at $x = 10\delta$, a similarity region exists, as shown in Fig. 15. The cut-off $\omega_0\xi/U_c$ defining the similarity region is greater than for the equilibrium flow. In this region the coherence levels are greater, and the data for different separations ξ does not collapse as well as in the equilibrium case. At lower values of $\omega\xi/U_c$ the departure from the similarity scaling is greater, with decreased coherence levels with respect to the equilibrium flow.

The same general trends exist with the LEBU located at $x = 14\delta$, as shown in Fig. 16. However, the data for the largest spatial separation does not collapse as well under the similarity scaling, and the loss of spatial coherence at lower values of $\omega\xi/U_c$ is greater. We note that the autospectra for this case had relaxed to equilibrium.

At the higher free-stream velocity the changes in the coherence are more complex. A similarity region is apparent with the LEBU located at $x = 10\delta$, but less well defined for $x = 14\delta$, as shown in Figs. 17 and 18. Increased loss of spatial coherence occurs at lower values of $\omega\xi/U_c$, although distinct trends with sensor separation are not apparent. A cut-off value $\omega_0\xi/U_c$ for the similarity region is not well defined. The changes in the coherence at the higher free-stream velocity are generally greater than at the lower, consistent with the Reynolds number effect seen in the autospectra.

Overall, the presence of the LEBU led to increased spatial coherence in the similarity region, decreased spatial coherence at lower values of $\omega\xi/U_c$, and increases in the cut-off $\omega_0\xi/U_c$ defining the similarity region. These effects are indicative of a breakup of the eddies in the outer layer and a conversion of coherent energy to the higher wavenumbers (or smaller wavelengths) in the log law layer.

Changes in the coherence persisted in cases where the autospectra had relaxed to equilibrium. This implies a redistribution of energy in the wavenumber frequency spectra. For a particular frequency ω_0, the wavenumber spectra $\Phi(k, \omega_0)$ may be expressed as the spatial Fourier transform of the cross-spectra given by

$$\Phi(k, \omega_0) = 1/2\pi \int_{-\infty}^{\infty} \Phi(\omega_0, \xi) e^{-ik\xi} d\xi. \qquad (7)$$

From Eq. (6),

$$\Phi(k, \omega_0) = 1/2\pi \int_{-\infty}^{\infty} \Phi(\omega_0) A(\omega_0\xi/U_c) e^{-i\xi(\omega_0/U_c + k)} d\xi. \qquad (8)$$

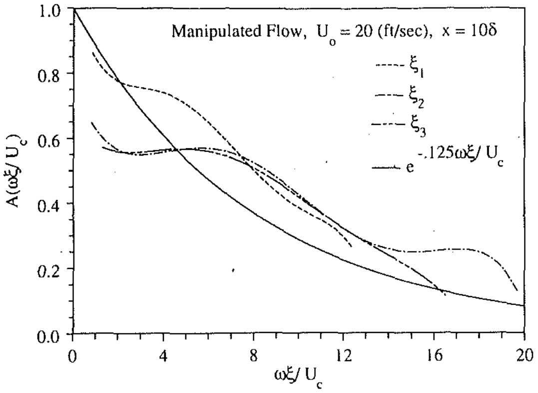

Fig. 17 Manipulated wall pressure function $A(\omega\xi/U_c)$, $U_o = 20$ (ft/s), LEBU located at $x = 10\delta$

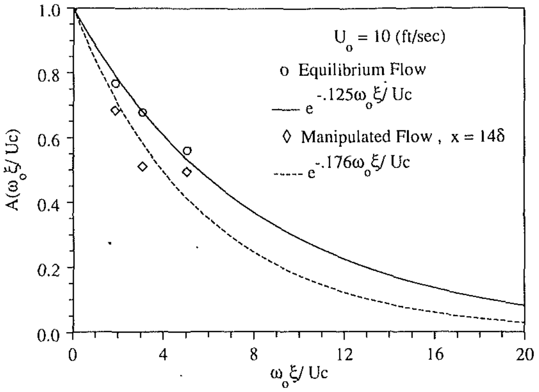

Fig. 19 Equilibrium and manipulated wall pressure function $A(\omega_0\xi/U_c)$, $\omega_0/U_c = 37.5$ (rad/ft), $U_o = 10$ (ft/s), LEBU located at $x = 14\delta$

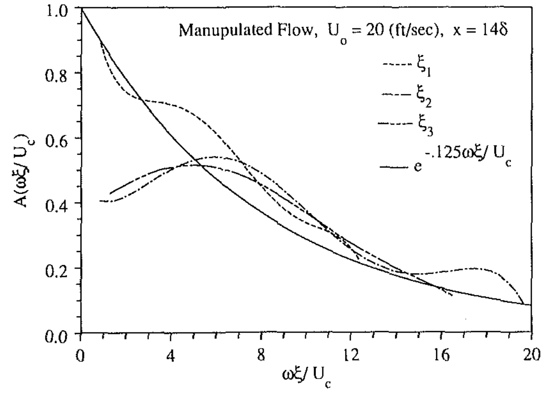

Fig. 18 Manipulated wall pressure function $A(\omega\xi/U_c)$, $U_o = 20$ (ft/s), LEBU located at $x = 14\delta$

The autospectra $\Phi(\omega_0)$ may be expressed as

$$\Phi(\omega_0) = \int_{-\infty}^{\infty} \Phi(k, \omega_0)dk. \tag{9}$$

For the case where $\Phi(\omega_0)$ has returned to equilibrium and the function $A(\omega_0\xi/U_c)$ has not, Eq. (8) implies $\Phi(k, \omega_0)$ will be perturbed from equilibrium. From Eq. (9) it is clear that the autospectra $\Phi(\omega_0)$ may relax to equilibrium although a redistribution of energy with wavenumber persists.

In principle, $\Phi(k, \omega_0)$ may be determined from Eq. (8), if the quantity $A(\omega_0\xi/U_c)$ is known. For a fixed ω_0, we have four values of $A(\omega_0\xi/U_c)$ corresponding to the three sensor spacings and also the $\xi = 0$ case. Therefore $\Phi(k, \omega_0)$ cannot be determined to a high degree of accuracy. However, an estimate of the effect of the LEBU on $\Phi(k, \omega_0)$ may be obtained as follows. Following Willmarth and Roos (1965), the function $A(\omega_0\xi/U_c)$ is taken to be of the form

$$A(\omega_0\xi/U_c) = a_1 e^{a_2|\omega_0\xi/U_c|}. \tag{10}$$

An exact solution for $\Phi(k, \omega)$ may be determined by combining Eq. (10) with Eq. (8) and evaluating the integral to obtain

$$\Phi(k, \omega_0) = (\Phi(\omega_0)/k_c)(-2a_1a_2/(2\pi(a_2^2 + (k/k_c + 1)^2))), \tag{11}$$

where the convective wavenumber $k_c = \omega_0/U_c(\omega_0)$. In evaluating the integral in Eq. (8), the convection velocity $U_c(\omega_0)$ is treated as constant, and the variation of $U_c(\omega_0)$ with ξ as shown in Figs. 11 and 12 is not taken into account. We also note that the form of $A(\omega_0\xi/U_c)$ given by Eq. (10) is approximate, since the behavior of $A(\omega_0\xi/U_c)$ as ξ approaches zero cannot be determined experimentally due to the finite size of wall pressure sensors. The expression for $\Phi(k, \omega_0)$ given by Eq. (11) is therefore approximate in nature.

A normalized form of the wavenumber spectrum $\Phi(k, \omega_0)$ may be defined as

$$\Phi^*(k^*, \omega_0) = \Phi(k, \omega_0)(k_c/\Phi(\omega_0)), \tag{12}$$

and from Eq. (11)

$$\Phi^*(k^*, \omega_0) = -2a_1a_2/(2\pi(a_2^2 + (k^* + 1)^2)), \tag{13}$$

where $k^* = k/k_c$.

In order to evaluate Eq. (13), a value of 274 (rad/s) was chosen for ω_0, such that k_c was 37.5 rad/ft. The resulting value of $k_c\delta$ was 4.0, such that k_c lies in the higher wavenumber region in which the similarity scaling holds. A value of 1 was chosen for a_1 such that $\Phi(\omega_0, 0) = \Phi(\omega_0)$, consistent with Eq. (6).

For the case of the lower free stream velocity with the LEBU located at $x = 14\delta$, an exponential curve fit was used to determine values for a_2. For the equilibrium flow, a value of $-.125$ was found, which is consistent with our previous results. For the manipulated flow, a value of $-.176$ was found for a_2. The scatter of the data about the exponential curves was greater for the manipulated flow, as shown in Fig. 19. Using these values for a_2, the function $\Phi^*(k^*, \omega_0)$ was determined for the equilibrium and manipulated flows from Eq. (13).

A slightly broader convective ridge exists for the manipulated flow, with a reduction of energy near the peak, as shown in Fig. 20. The broader convective ridge may imply a larger range of convected eddies contributed to the spectra at this frequency ω_0. We note that comparison of the normalized wavenumber spectra $\Phi^*(k^*, \omega_0)$ for the two cases is equivalent to comparing the dimensional spectra $\Phi(k, \omega_0)$, since $\Phi(\omega_0)$ was unchanged, and k_c was approximately constant. The effect of the LEBU on $\Phi^*(k, \omega_0)$ at other frequencies ω_0 may be significantly different, in view of the complex changes in the coherence. Although these estimates of the wavenumber spectra are somewhat qualitative, they emphasize the importance of the spatial domain for investigating changes in the structure of turbulent boundary layers.

Conclusions

The effects of a LEBU on the energy content of the fluctuating wall pressure field were determined. There was no evidence of highly energized coherent structures convecting downstream of the LEBU. Near the LEBU, the autospectra displayed moderate changes occurring over broad frequency ranges, leading to a reduction of energy. A conversion of energy from the lower convective wavenumbers in the outer layer to the higher wavenumbers in the log law layer also occurred. These effects are not highly correlated with the small changes which occurred in the mean wall shear stress.

The spatial coherence measurements indicated changes per-

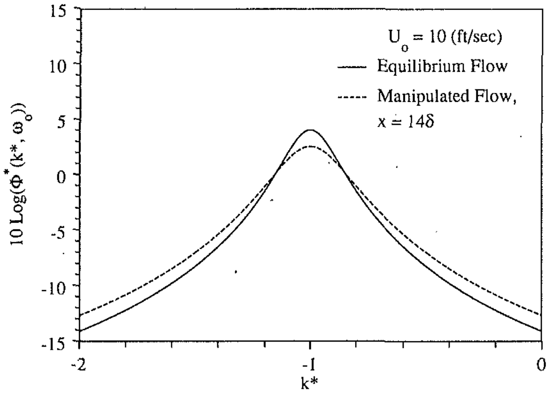

Fig. 20 Equilibrium and manipulated normalized wall pressure wavenumber spectra, $\omega_o/U_c = k_c = 37.5$ (rad/ft), LEBU located at $x = 14\delta$

sisted after the frequency spectra had relaxed to equilibrium. The changes induced in the spatial turbulence structure which would be reflected in the wavenumber spectra were therefore not always apparent in the frequency spectra. Direct measurements of the wavenumber spectra made with arrays of pressure sensors are required to further investigate these effects.

The effectiveness of LEBUs of this type for drag reductions over this range of R_θ values appear to be minimal. The reductions in the wall pressure spectral levels at low frequencies are favorable for passive control of flow induced vibration and noise. The redistribution of energy in the wavenumber spectra which persists farther downstream might also prove to be beneficial.

JFE Data Bank Contributions

The data presented in Figs. 3 through 20, which include mean velocities, wall pressure spectra, and wall pressure convection velocities, have been deposited on the JFE Data Bank. All of the data is in the same form as it appears in the respective figures. To access the file for this paper, see the instructions on p. 542 of this issue.

Acknowledgments

The authors are grateful to Dr. T. Farabee of Carderock Division Naval Surface Warfare Center and Dr. J. B. Anders of NASA Langley Research Center for helpful discussions. Funding was provided by the Office of Naval Research Applied Hydrodynamics Program, Program Manager Mr. James Fein, and the IR/IED Program at NUWC, Program Manager Dr. K. Lima.

References

Anders, J. B., 1989, "LEBU Drag Reduction in high Reynolds Number Boundary Layers," *AIAA Paper*, AIAA-89-1011.

Anders, J. B., and Watson, R. D., 1985, "Airfoil Large-Eddy Breakup Devices for Turbulent Drag Reduction," *AIAA Paper*, AIAA-85-0520.

Beeler, G. B., 1986, "Turbulent Boundary Layer Wall Pressure Fluctuations Downstream of a Tandem LEBU," *Journal of the AIAA*, Vol. 24, Apr. pp. 689-691.

Clauser, F. H., 1956, "The Turbulent Boundary Layer," *Advances in Applied Mechanics*, Vol. 4, No. 1, Academic Press, New York, NY, pp. 1-51.

Coles, D., 1953, "Measurements in the Boundary Layer on a Smooth Flat Plate in Supersonic Flow, Pt. 1, The Problem of the Turbulent Boundary Layer," *Report No. 20-69*, JPL, CIT, Pasadena.

Corcos, G. M., 1963, "Resolution of Pressure in Turbulence," *Journal of the Acoustical Society of America*, Vol. 35.

Corke, T. C., Nagib, H. M., and Guezennec, Y. G., 1982, "A New View on Origin, Role, and Manipulation of Large Scales in Turbulent Boundary Layers," Ill. Inst. Tech., NASA CR-165861.

Corriveau, P., and Berman, C. H., 1986, "Wavenumber Spectra Derived from Turbulent Surface Pressure Measurements," AIAA Paper 86-1859.

Farabee, T. M., 1986, "An Experimental Investigation of Wall Pressure Fluctuations Beneath Non-Equilibrium Turbulent Flows," *Report No. DTNSRDC-86/047*, David Taylor Naval Ship R&D Ctr., Bethesda, MD, May.

Farabee, T. M., and Casarella, M. J., 1991, "Spectral Features of Wall Pressure Fluctuations Beneath Turbulent Boundary Layers," *Physics of Fluids*, Vol. A No. 3, p. 10, Oct.

Junger, M. C., and Feit, D., 1986, *Sound, Structures, and Their Interaction*, MIT Press, Cambridge, MA, pp. 206-209.

Keith, W. L., 1989, "Spectral Measurements of Pressure Fluctuations on Riblets," *Journal of the AIAA*, Vol. 27, No. 12, Dec. pp. 1822-1824.

Keith, W. L., and Bennett, J. C., 1991, "Low Frequency Spectra of the Wall Shear Stress and Wall Pressure in a Turbulent Boundary Layer," *Journal of the AIAA*, Vol. 29, No. 4, Apr. pp. 526-530.

Keith, W. L., Hurdis, D. A., and Abraham, B. M., 1992, "A Comparison of Turbulent Boundary Layer Wall Pressure Spectra," ASME JOURNAL OF FLUIDS ENGINEERING, Vol. 114, No. 3, September, pp. 338-347.

Lemay, J., Provencal, D., Gourdeau, R., Nguyen, V. D., and Dickinson, J., 1985, "More Detailed Measurements Behind Turbulence Manipulators Including Tandem Devices Using Servo-Controlled Balances," *AIAA Paper*, 85-0521, Mar.

Panton, R. L., and Linebarger, J. H., 1974, "Wall Pressure Spectra Calculations for Equilibrium Boundary Layers," *Journal of Fluid Mechanics*, Vol. 30, pp. 261-287.

Savill, A. M., 1984, "The Skin Friction Reduction Mechanisms of Flat Plate Turbulence Manipulators," Abstr., *Euromech 181*.

Savill, A. M., 1986, "On the Manner in Which Outer Layer Disturbances Affect Turbulent Boundary Layer Skin Friction," *Advances in Turbulence: Proceedings of the European Turbulence Conference*, Lyon, Springer, pp. 533-545.

Savill, A. M., and Mumford, J. C., 1988, "Manipulation of Turbulent Boundary Layers by Outer Layer Devices: Skin Friction and Flow Visualization Results," *Journal of Fluid Mechanics*, Vol. 191, pp. 389-418.

Schlichting, H. S., 1979, *Boundary Layer Theory*, McGraw-Hill, New York, NY, pp. 636-638.

Wilkinson, S. P., Anders, J. B., Lazos, B. S., and Bushnell, D. M., 1987, "Turbulent Drag Reduction Research at NASA Langley-Progress and Plans," *Proceedings of the Royal Aeronautical Society, Turbulent Drag Reduction by Passive Means*, Vol. 1, London, pp. 1-32.

Willmarth, W. W., and Roos, F. W., 1965, "Resolution and Structure of the Wall Pressure Field Beneath a Turbulent Boundary Layer," *Journal of Fluid Mechanics*, Vol. 22.

Ventilated Flow in the Unobstructed Space Between Corotating Disks in a Cylindrical Enclosure

D. Gor

J. A. C. Humphrey

R. Greif

Department of Mechanical Engineering,
Computer Mechanics Laboratory,
University of California at Berkeley,
Berkeley, CA 94720

An experimental investigation has been performed for the ventilated flow of air in the unobstructed space between the center pair of four disks corotating in a fixed cylindrical enclosure. This configuration is of fundamental interest and considerable practical utility in the computer industry. Time-resolved and time-averaged measurements of the circumferential velocity component were obtained using a laser-Doppler velocimeter in back-scatter mode. The data were collected along the radial coordinate direction on the midplane between the disks ($Z = 0$) and along the axial coordinate at two radial locations ($R = 0.71$ and 0.86). Three values of the Reynolds number ($Re = 2.73 \times 10^3$, 2.22×10^4, and 2.66×10^5) were investigated for a limited but significant range of the Rossby number ($|Ro| < 0.85$), including air sucked radially inward ($Ro < 0$) and air blown radially outward ($Ro > 0$). The experimental data present a challenging target for numerical procedures purporting to predict this class of flows. In agreement with earlier preliminary calculations performed by Humphrey et al. (1992), the imposition of a radial ventilation condition in the experiments is observed to have a pronounced effect on the inter-disk flow characteristics. However, the predicted results were found to depend strongly on the boundary conditions imposed and present measurements show the importance of knowing these accurately. These and related findings are discussed with special consideration given to their potential impact on the improved design of ventilated disk storage systems.

1 Introduction

1.1 The Problem of Interest. Flows induced by rotating disks are of considerable fundamental interest because of the richness of the physical phenomena they encompass, including three-dimensionality, unsteadiness, and turbulence under the influence of centrifugal and Coriolis forces. Rotating disk configurations are especially important in the computer industry where hard disk drives, consisting of one or more corotating disks, are used as data storage units. Numerous technological improvements, such as better magnetic read/write head designs and increased track density, have improved the reliability and storage capacity of disk storage systems. However, miniaturization trends in the computer industry, leading to smaller disk drives rotating at higher speeds, require a better understanding of the thermofluids aspects of the inter-disk flows. Smaller dimensions and higher speeds of rotation magnify three problems which can seriously disrupt accurate electromagnetic data transfer. These are: (i) the presence of foreign particles; (ii) flow-induced mechanical instabilities; and (iii) uneven temperature distributions. In order to improve the reliability and performance of current disk drives while providing a basis for the improved design of future devices, it is necessary to advance the understanding of the fluid motion in the inter-disk spaces. In this regard, it is especially interesting to consider how the imposition of a net radial throughflow, or "ventilation" condition, affects this motion. The present study advances upon prior work performed in the absence of ventilation as well as limited work in the presence of a positive radial outflow in the inter-disk space. The configuration of interest, shown in Fig. 1, involves the unobstructed flow in the space between the center pair of four, centrally clamped, disks corotating in a fixed cylindrical enclosure.

1.2 Literature Review. Because of their geometrical simplicity and practical importance, rotating disk configurations have been the subject of continuous fundamental and applied research for nearly a century. For extensive reviews of the literature available on coaxial, corotating disk geometries, Kreith (1968), Greenspan (1968), and Humphrey et al. (1991) are useful references. The last review is concerned with configurations especially relevant to disk storage systems in the computer industry. Here we summarize the information per-

---

Contributed by the Fluids Engineering Division for publication in the JOURNAL OF FLUIDS ENGINEERING. Manuscript received by the Fluids Engineering Division April 19, 1992; revised manuscript received February 2, 1993. Associate Technical Editor: Ho, Chih-Ming.

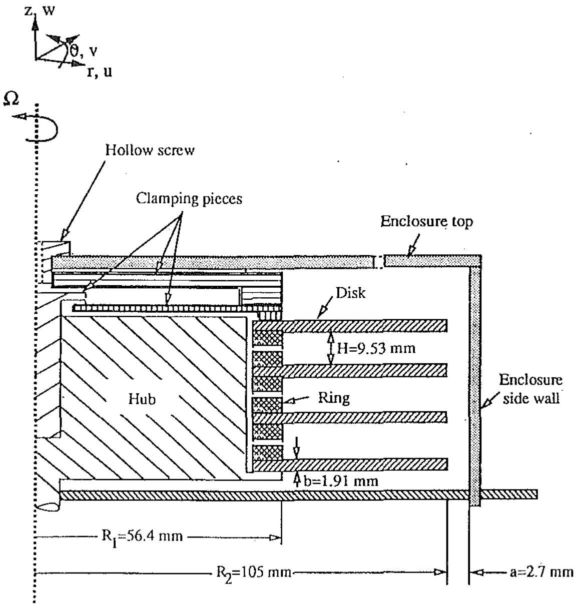

Fig. 1 Schematic of the experimental test section. In the absence of an imposed radial throughflow (ventilation) the disk spacer rings and the cylindrical enclosure were replaced with identical solid pieces and the hollow screw was absent.

tinent to centrally clamped, corotating disks surrounded by a stationary, axisymmetric enclosure, placing special emphasis on the effects of an imposed radial throughflow.

Early experimental works elucidating the basic characteristics of fluid motion in the space between pairs of corotating disks were qualitative and based primarily on flow visualization techniques. Table 1 in Schuler et al. (1990) summarizes the experimental studies most relevant to unobstructed magnetic disk storage devices which are of special interest to this investigation. We discuss them briefly here. The studies by Lennemann (1974), Kaneko et al. (1977) and, especially, Abrahamson et al. (1988) are noteworthy for visualizing a central core of fluid in solid-body rotation surrounded by a sheared layer of fluid containing circumferentially periodic foci of axial vorticity. It is now known that these spatially periodic structures rotate at approximately 80 percent of the disk speed of rotation and that their number (typically, between two and six) depends on the enclosure dimensions, the inter-disk spacing, and, most notably, the disk speed of rotation; see, for example, Usry et al. (1990).

Schuler et al. (1990) investigated the unobstructed, unventilated flow between corotating disks using the laser-Doppler velocimeter (LDV) technique. They also provided the first comprehensive theoretical scaling analysis identifying the nature and boundaries of the five overlapping regions composing this class of flows. From time records of the unsteady circumferential velocity component, these authors obtained the corresponding time-averaged mean and root mean square (rms) velocities along the axial (Z-coordinate) direction at four radial positions and along the radial (R-coordinate) direction on the midplane between the center pair of disks. The mean velocity profiles were found to agree reasonably well with the numerical calculations of Chang et al. (1990) even though the latter were based on a steady flow assumption. However, significant discrepancies between the measured and computed rms profiles were attributed to the periodic passage through the measurement volume of the large-scale, nonturbulent flow structures mentioned above. In this regard, Usry et al. (1990) discovered that the flow between a pair of disks corotating in a cylindrical enclosure was steady up to a critical value of the Reynolds number, $\mathrm{Re} = 4.73 \times 10^3$, corresponding to 64 rpm in their experiment. When present, the unsteadiness was found to be most pronounced near the radial location where the rms velocity was a maximum. Subsequent velocity measurements in the same flow configuration, made by Usry et al. (1990), showed that above $\mathrm{Re} = 4.73 \times 10^3$, the flow exhibited discrete dominant frequencies of values equal to integer multiples of the disk rotation frequency. The integer values were associated with the number of circumferentially distributed axially-aligned vortical structures present in the flow. Except for a hysteresis effect which was found to depend on whether the disk speed was increased or decreased during the course of experimentation, the transitions between integer values were very sharply defined. The values of the integers themselves were observed to decrease in increments of 1 (from 6 slightly above 64 rpm, to 2 past 3600 rpm) as the disk speed of rotation increased.

In addition to the above experimental studies, we note with special interest the numerical investigations of Chang et al. (1989, 1990), Schuler (1990), Tzeng and Humphrey (1991), Tzeng and Fromm (1990), and Humphrey et al. (1992) for unobstructed disk flow configurations, and the experimental and numerical investigations of Lennemann (1974), Abrahamson et al. (1988), Usry et al. (1990), Tzeng and Humphrey (1991), Humphrey et al. (1991), and Tzeng and Chang (1991) for obstructed configurations. Combined, these studies have been extremely useful for advancing a qualitative understanding of the physics of rotating disk flows, with and without obstructions, with and without radial ventilation, while serving to guide continuing experimental work. In this regard, the calculations of Chang et al. (1990) and Humphrey et al. (1992) in unobstructed configurations with imposed radial throughflows have been seminal to the present investigation. Thus, for example, the calculations of Humphrey et al. (1992) pro-

Nomenclature

a = disk-to-enclosure side wall spacing
b = disk thickness
Ek = $(=1/\mathrm{Re})$ Ekman number
f = frequency of mean flow oscillation in Hz
H = disk-to-disk spacing
N = $(=60f/\Omega)$ normalized value of f
N_h = number of holes in disk spacer ring
Q = total throughflow rate
r = radial coordinate
R = $(=r/R_2)$ normalized radial coordinate
R_h = radius of hole in disk spacer ring
R_1 = disk inner radius
R_2 = disk outer radius
Re = $(=\Omega R_2^2/\nu)$ Reynolds number
Ro = $(=V_0/V_t)$ Rossby number
T = fluid temperature
v = mean circumferential velocity component
v_{rms} = root mean square (rms) circumferential velocity component
V = $(=v/\Omega r)$ normalized mean circumferential velocity component
V_{rms} = $(=v_{\mathrm{rms}}/\Omega r)$ normalized rms circumferential velocity component
V_0 = $(=Q/3\pi N_h R_h^2)$ averaged throughflow velocity between center pair of disks at R_1
V_t = circumferential velocity of disk at $r = R_2$
z = axial coordinate, relative to midplane between center pair of disks
Z = $(=z/H)$ normalized axial coordinate
δ_E = Ekman layer thickness
ν = fluid kinematic viscosity
Ω = disk rotation rate in rpm

Table 1 Summary of major experimental and numerical studies of corotating disk configurations with imposed radial throughflow relevant to this investigation. In the table, $\nu = 1.56 \times 10^{-5}$ m^2/s for air and 9.03 $\times 10^{-7}$ m^2/s for water, both at T = 25°C.

Parameter	Chang et al. (1989)	Chang et al. (1990)	Abrahamson et al. (1991)	Humphrey et al. (1992)	Present study
Disk outer radius, R_2 (mm)	105	105	475	105	105
Disk inner radius, R_1 (mm)	56.4	56.4	210	56.4	56.4
Disk-to-disk spacing, H (mm)	9.53	9.53	28.7	9.53	9.53
Disk-to-enclosure side wall spacing, a (mm)	2.7	2.7	n/a	2.7	2.7
Disk thickness, b (mm)	1.91	1.91	9.5	1.91	1.91
Number of disks	2	2	2	2	4
Obstruction type when present	none	none	thin beam, rectangular cross section	none	none
Working fluid	air	air	water	air	air
Disk speed, Ω (rpm)	100, 300	2400, 4800	20	300	37, 300, 3600
$Re=\Omega R_2^2/\nu$ ($\times 10^5$)	0.073, 0.22	1.77, 3.55	1.91	0.22	0.027, 0.22, 2.66
$Ek=1/Re$ ($\times 10^{-6}$)	137.0, 45.05	5.64, 2.82	5.23	45.05	365.2, 45.05, 3.76
Throughflow direction	radial outflow	radial outflow	radial outflow	radial outflow, radial inflow	radial outflow, radial inflow
Throughflow path	evenly distributed through hub	evenly distributed through hub	openings in disk spacer (3 types: 24 evenly spaced, centered holes; semicircular holes; 24 evenly spaced holes of smaller diameter)	evenly distributed through hub	openings in disk spacer (2 types: 24 and 16 evenly spaced, centered holes)
$Ro=V_o/V_t$	0.009, 0.061	14.3, 28.5	0.045 to 0.48	0, ±0.02, ±0.05	-0.85 to 0.85
Type of data	laminar flow calculations of velocity and temperature	turbulent flow calculations of velocity and temperature	flow visualization (limited hot-film time-resolved measurements of circumferential velocity components)	laminar flow calculations of velocity and temperature	LDV measurements of mean and rms circumferential velocity component (limited time-resolved measurements)

vided detailed pictures of the structure of the cross-stream flow as a function of the Reynolds and Rossby numbers.

Prior experimental investigations concerning corotating disks with radial inter-disk throughflows imposed include the studies by Bakke et al. (1973), Szeri et al. (1983a,b), Owen et al. (1985), Mochizuki and Inoue (1990), and Abrahamson et al. (1991). In particular, Abrahamson et al. (1991) have visualized the effects of a radial outflow with and without obstructions present in the inter-disk space. The throughflow was introduced through discrete openings cut into the disk spacers. The resulting inter-disk flow field was found to be insensitive to the cross-section shape of these openings. For low throughflow values in the unobstructed flow case, the authors found that the central core of fluid in solid-body rotation was displaced radially outward. While the throughflow thickened the Ekman layers on the disks, it did not eliminate the circumferentially distributed vortical structures present in the flow. Increasing the throughflow was found to increase the number of these structures while decreasing their size. The obstruction was found to redirect part of the outward-directed throughflow radially inward, towards the hub, resulting in an elliptical shape for the fluid in solid-body rotation.

Table 1 summarizes the parameter ranges investigated in previous major studies of ventilated flows between corotating disks in fixed cylindrical enclosures. The conditions of the present study are included for comparison.

1.3 Objectives and Scope of the Present Study. The above review reveals an insufficient experimental data base to further the understanding of the fundamental aspects and practical consequences of imposing radial ventilation on the flow between corotating disks in enclosures. In this study, we present and discuss measurements of the mean and rms circumferential velocity components obtained in the unobstructed space between the center pair of four disks corotating in a fixed, axisymmetric cylindrical enclosure. Attention is focused on the effects of imposing a positive (outward-directed) or a negative (inward-directed) radial throughflow in the inter-disk space, with care taken to resolve the unsteady aspects of the motion. Although idealized, the unobstructed, axisymmetric configuration studied here allows the advancement of basic understanding while providing experimental data of practical value for design purposes. The latter also serves as a target for numerical calculation procedures purporting to predict this difficult class of flows.

The present experimental configuration allowing inter-disk ventilation is shown schematically in Fig. 1. This corresponds to four corotating disks with the possibility of zero, positive and negative radial throughflows. (Henceforth, positive radial outflow through the inter-disk space will be referred to as "blowing" and negative radial inflow as "sucking.") Except for the absence of the hollow screw and the replacement of the enclosure top and porous spacer rings by solid pieces, the geometrical arrangement with zero throughflow was identical to that shown in Fig. 1. For both the ventilated and unventilated configurations, the disks were clamped to a hub that rotates within the fixed cylindrical enclosure. Time-resolved measurements of the circumferential velocity component were obtained using the laser-Doppler velocimeter technique. From these data, time-averaged values of the mean and rms of this velocity component were obtained. Radial traverses were made along the midplane between the center pair of four disks for three speeds of rotation, three throughflow conditions, and two types of disk spacers. Axial traverses were made at two radial locations for the same conditions, but using only one of the two disk spacers. Experimental parameters were selectively varied to provide thorough (although not exhaustive) characterizations of the flows with and without ventilation. Flow unsteadiness was illustrated by visualizing time records and quantified by calculating their associated power spectra. Most of the power spectra revealed a distinct peak at a frequency equal to a multiple of the disk rotation frequency, supporting the presence of the periodic large-scale vortical structures discussed above. While Lennemann (1974) and Abrahamson et al. (1988) have shown that the number of these structures depends on the disk-enclosure geometry and the disk rotation rate, the effects of inter-disk ventilation, in particular, the sucking condition, have not been thoroughly quantified.

The rest of this communication is divided into three sections. Section 2 describes the experimental system and the measurement technique used for data acquisition and reduction. It also quantifies, where possible, the uncertainties in the data. Section 3 presents and discusses the measured results. This includes mean and rms circumferential velocity profiles as well as selected time records and their associated power spectra at various spatial locations. Section 4 summarizes the main findings of this study and provides recommendations for future work. A complete tabulation of all the data obtained in the course of this work is available upon request from the authors.

2 The Experiment

2.1 Test Section. The corotating components of the test section arranged for the ventilated flow experiments (blowing or sucking) consisted of four disks, three disk spacers (or rings), a hub, and three clamping pieces; see Fig. 1. Four aluminum disks taken from an IBM 8 in. drive were placed on the hexagonally shaped aluminum hub. The magnetic coatings on the disks were extremely smooth. Three aluminum rings, each with 24 equally spaced 3/16 in. diameter holes, were used to separate each pair of disks and allow the ventilation condition between them. Three additional aluminum rings, with 16 equally spaced 3/16 in. diameter holes, were also used in some limited experiments. The two ring types are referred to as ring #1 (24 holes) and ring #2 (16 holes), respectively. The hexagonal hub and the rings encircling it were machined to provide a tight fit. The rings were carefully mounted along with the disks to minimize vertical wobble and horizontal sliding motion. Three clamping pieces above the hub-rings-disks assembly were used to hold the rotating system components together.

All the above rotating pieces were attached to a Pope PS-13001 precision spindle which extended through the center of a 30 × 48 × 6 in. granite table supported by a steel cart. The granite table served as the stand for the test section and its large (750 lb) mass reduced any possible effects of external vibrations on the test section. The lower end of the spindle was fitted with a sprocket positive contact clutch driven by a DC servo motor. The maximum speed of the spindle was about 4100 rpm. The DC servo motor was equipped with a linear servo-amplifier, a DC tachometer, a magnetic rpm sensor, a digital stroboscope tachometer, and a frequency counter. The servo motor and its supplementary components were mounted on the base of the steel cart supporting the granite table. The cart was rolled in front of the LDV and immobilized by wooden blocks placed under it. With the test section fixed in place it was possible to accurately position the LDV optical probe volume.

The disks were surrounded by a stationary, cylindrically shaped, transparent Plexiglas piece with a snug-fitting top. Both the plastic cylinder and its top were 1/4 in. thick. The open end of the cylinder fit snugly into a circular groove cut into a Plexiglas base plate. This plate was attached to a second aluminum plate fixed to the granite slab. The three Plexiglas parts were machined to narrow tolerances in order to obtain the snug fits referred to and in this way isolate the flow within the enclosure from the surroundings. The use of Teflon tape between the interconnected Plexiglas pieces further guaranteed this condition. Four 3/16 in. diameter holes, each located at a 3 in. radius from the center of the top and spaced 90 deg apart, were drilled to allow an axisymmetric ventilation condition. The enclosure top also had a 5/8 in. diameter hole drilled through its center to allow for the insertion of a stationary hollow screw as part of the ventilation loop. Two O-ring seals, one between the hollow screw and the cylinder top, the other between the hollow screw and the rotating clamping pieces, prevented the leakage of air from the enclosure.

The test section was ventilated by means of an open loop flow system. This consisted of a pressurized air line feeding a DANTEC mineral oil droplet generator connected to the inlet point of the test section and a vacuum line connected to the exit point. For the blowing condition, the droplet-laden flow was transported through a 3/16 in. diameter Tygon tube to the hollow screw located on the top of the test section enclosure. The flow then followed a circuitous path: past the two pieces clamping all the disks together, down the spaces between the hexagonal hub and the spacer rings, through the holes in the rings to proceed radially outward through the inter-disk spaces, along the disk-to-enclosure side wall annular gap, and finally through the four equidistantly spaced holes in the enclosure top. These exit holes were connected to the vacuum line by means of three T-joints joined together by a 3/16 in. diameter Tygon tube. The length of the inlet and outlet Tygon tubes was minimized, and the relative orientations of these tubes with respect to the test section were fixed, in order to render constant and negligibly small their respectively induced pressure drops. To implement the sucking condition, the inlet and outlet connections for the blowing condition just described were simply interchanged.

The total radial throughflow imposed upon the three inter-disk spaces was measured using two Matheson 605 rotameters, one placed near the inlet and the other near the outlet of the test section. The droplet generator flow valves (there were two, one to regulate the air flow and the other to allow the introduction of particles) were adjusted to give the desired flow rate and the rotameters then removed. The removal of the rotameters from the flow path was necessary to avoid the accumulated deposition of mineral oil droplets within them and possible erratic behavior. Fortunately, this operation took no more than a few minutes, representing a small fraction of the total time spent on a run for a particular throughflow setting. It was ascertained that the rotameter impedances were sufficiently small that their removal from the path of the flow did not significantly alter the air flow rate.

The test section for the unventilated flow experiments was similar to that described above, except for the following. The enclosure top did not have the four holes required for ventilation and the hollow screw was absent for this arrangement. Solid, black-anodized aluminum rings, coated with fluorescent orange paint to reduce unwanted reflected light in both the blue and green frequencies, were used to separate each pair of disks. The enclosure side wall had a 3/8 in. diameter hole enabling the periodic introduction of mineral oil droplets for the LDV measurements. A small piece of tape placed over the hole on the inner side of the cylinder wall reduced its size by about 75%, thus minimizing any adverse effects of the hole on the flow within the enclosure. A minimum time of one minute was allowed for the droplet-air mixture to equilibrate with the air in the enclosure and for disturbances induced by this seeding procedure to be dampened.

2.2 Measurement Technique and Uncertainties. LDV measurements of the circumferential velocity component were made using the green light from a 2 W Lexel 95 argon ion laser. This was operated in back-scatter mode, but offset by a 25 deg angle. The DANTEC 55X modular optical system used and its associated electronic components have already been described in detail by Schuler et al. (1990). The pair of light beams emerging through the front lens of the LDV passed through the cylindrical wall of the enclosure and intersected at a small angle to form the optical probe volume in the inter-disk space. The beams passed through the cylinder wall symmetrically, with the beam angle bisector and the test section axis of rotation contained in the same plane. Because of the way the lens system projected the pair of light beams producing the optical probe volume, the plane containing these beams was not exactly perpendicular to the test section axis of rotation. The angle between the plane containing the two beams and the plane perpendicular to the axis of rotation was 4.75 deg. As a result, measurements near the disks were not possible due to beam cutoff by the top disk and extraneous reflections on the bottom disk. However, tilting the cart supporting the test section by this small angle eliminated the difficulty of taking data near the disks. The laser and its optical components were mounted on a traversing table connected to three stepping motors capable of moving the optical probe volume relative to the test section in three Cartesian coordinate directions to within ±0.1 mm over a range of 18 cm. The motors were controlled by an IBM PC/AT. For the current study, the table was moved in the radial and axial directions only.

The measurement and data reduction procedures for the ventilated and unventilated flow cases were identical. The LDV technique required the presence of light-scattering particles, here consisting of mineral oil droplets ranging in diameter from 0.5 to 2 microns. Droplet concentrations were typically high enough to yield signal rates ranging from 100 Hz at low speeds of rotation to 1000 Hz at high speeds. A series of 2500 Doppler bursts satisfying the counter's 5/8 validation criterion to within ±1.5% was stored in the buffer. To ensure a high-quality Doppler signal, the signal was constantly monitored and optical conditions optimized. This included readjusting the optics and counter settings as well as periodically wiping the inside surface of the cylinder to remove the inevitable film of oil resulting from centrifugally-driven droplet deposition. Measurements of the circumferential velocity component were taken along the radial direction at $Z = 0$, the symmetry plane between the center pair of disks, and along the axial direction at $R = 0.71$ near the hub, and $R = 0.86$ near the cylinder wall. Due to the scarcity of droplets in the solid-body rotation region, measurements for the unventilated condition could not be made at radial locations with $R < 0.6$, approximately 10 mm from the solid disk spacers. The combination of small particle concentrations and extraneous reflections in this region of the flow resulted in low signal-to-noise ratios and corresponding low data validation rates. Similarly, the poor quality of the signals obtained at radial locations with $R > 0.95$, approximately 5 mm from the cylinder wall, precluded making measurements in this region.

All the LDV data were collected and initially reduced by an IBM PC/AT software program. Initial data reduction involved a check-and-eliminate procedure to discard measurements falling beyond a range of five standard deviations from the mean value. From the remaining data, mean velocities, rms velocities, and time records were logged for each measurement location. Autocorrelations were obtained from the time records using the slotted correlation technique of Bell (1986). Applying the Fourier transform to the autocorrelations yielded the corresponding power spectra. The slotted autocorrelation technique accounted for the randomness in the arrival times of the velocity data by sorting them into equally-sized time bins. The size of the bins was optimized by a guess-and-correct procedure. Both the data collection and subsequent data processing programs were written in-house.

For the unventilated flow experiments, the periodic addition of mineral oil droplets mixed with air, introduced through a small hole in the side of the cylinder, was necessary. A minimum time of one minute was allowed for the mixture to equilibrate with the air in the enclosure and for disturbances induced by this seeding procedure to be dampened. Otherwise, the measurement and data reduction procedures were the same as for the ventilated flow experiments.

The uncertainties associated with LDV measurements in the present test section have already been discussed carefully in Schuler et al. (1990). For the mean and rms velocities, these arise from sources of error in the probe volume position, refraction effects, random effects due to the geometry of the test section, electronic noise, and the introduction of ventilation. Table 2 summarizes typical and maximum uncertainties affecting the main quantities of interest here.

The uncertainty in measuring the total radial throughflow, Q, passing through the three inter-disk spaces was typically ±1.6 percent and, at most, ±5 percent of the rotameter reading. However, due to the test section design, it was inevitable that the distribution of this throughflow should differ slightly among the three spaces. Unfortunately, it was not possible to avoid these differences or measure them accurately. For both the blowing and sucking conditions, relative to the center pair

Table 2 Summary of overall estimated percentage measurement uncertainties for the variables shown in the table

Dimensional variable	Type of uncertainty (%)			
	Systematic		Random	
	typical	maximum	typical	maximum
r	0.1	0.5	0.5	1
z	0.1	0.1	0.3	1
v	0.2	5	0.8	1.3
v_{rms}	5	50	0.8	3
Ω	—	—	2	3
Q	—	—	1.6	5

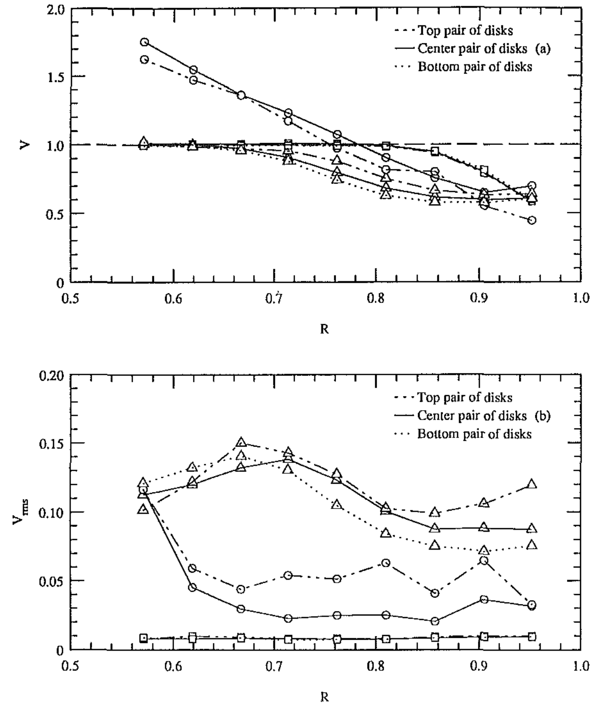

Fig. 2 Radial profiles of the (*a*) mean and (*b*) rms circumferential velocity at the midplanes of the three inter-disk regions for $\Omega \approx 37$ rpm ($Re = 2.73 \times 10^3$) using ring #1; △: Ro = 0.57, □: Ro = 0, ○: Ro = −0.57

Table 3 **Summary of experimental conditions investigated in this study. Data not shown are available upon request.**

Disk rotation rate Ω (rpm)	Re	V_t (m/s)	Traverse type (center pair of disks unless otherwise stated)	Disk spacer type	V_o (m/s)	Ro
37	2.73×10^3	0.41	Radial (Z = 0, and midplane of top and bottom disk pairs)	Solid ring, ring #1	0, ±0.23	0, ±0.57
37	2.73×10^3	0.41	Radial (Z = 0)	Solid ring, rings #1 and #2	0, ±0.23, ±0.35	0, ±0.57, ±0.85
300	2.22×10^4	3.30	Radial (Z = 0)	Solid ring, rings #1 and #2	0, ±0.23, ±0.35	0, ±0.070, ±0.11
3600	2.66×10^5	39.6	Radial (Z = 0)	Solid ring, rings #1 and #2	0, ±0.23, ±0.35	0, ±0.0058, ±0.0088
37	2.73×10^3	0.41	Axial (R = 0.71, 0.86)	Solid ring, ring #1	0, ±0.23	0, ±0.57
300	2.22×10^4	3.30	Axial (R = 0.71, 0.86)	Solid ring, ring #1	0, ±0.23	0, ±0.070
3600	2.66×10^5	39.6	Axial (R = 0.71, 0.86)	Solid ring, ring #1	0, ±0.23	0, ±0.0058

of disks, slightly more radial throughflow passed between the top pair of disks than between the bottom pair. Velocity measurements were taken in all three of the inter-disk spaces to ascertain the impact of this flow maldistribution upon the mean and the rms. Typical results, shown in Fig. 2, were identical qualitatively and close enough quantitatively to justify restricting the remainder of the detailed measurements to the center inter-disk space. Thus, in reporting the data, the Rossby number for the ventilated flow experiments is based on the total radial throughflow divided by 3, to obtain an average ventilation velocity per inter-disk space. To minimize the uncertainty associated with setting a radial throughflow condition, once fixed the throughflow remained unchanged while the disk speed of rotation was varied. While very convenient experimentally, Table 3 shows that this procedure led to relatively large values of Ro at low rpm and small values at high rpm. This is an important consideration when interpreting the experimental results.

3 Results and Discussion

The experimental results are presented and discussed in two parts. Section 3.1 deals with time-averaged results while Section 3.2 addresses flow unsteadiness. Table 3 summarizes all the conditions for which measurements were made. Radial and axial profiles of the circumferential velocity component were obtained for three rotation speeds (37, 300, and 3600 rpm), three ventilation conditions (unventilated, blowing and sucking), and three disk spacer types (solid ring #1 and ring #2). The radial profiles were taken along the midplane between the center pair of disks. The axial profiles were obtained at two radial locations ($R = 0.71$ and 0.86) covering the distance $Z = 0$ to $Z = 0.45$. In each experimental run, the total imposed radial throughflow was held constant while the LDV measurements were made. Time-averaged and rms values of velocity were derived from the time records obtained at each measurement location. All the quantities presented in the plots have been appropriately normalized as defined in the nomenclature.

3.1 Time-Averaged and RMS Results. Radial and axial profiles of the time-averaged (or mean) velocity and its rms are provided in Figs. 3-7, with the relevant measurement conditions listed in the figure captions. We summarize here the main observations derived from these results.

A comparison among Figs. 3-5 shows that ventilation significantly alters both the mean and rms velocity distributions in the inter-disk space at all three speeds of rotation. However, because it is the case with the largest absolute value of the Ro numbers (Ro = ±0.57 and ±0.85), the effect is strongest at 37 rpm. Compared to the unventilated flow, Fig. 3 shows that blowing substantially reduces the value of the mean velocity everywhere along the radial midplane relative to the value corresponding to solid-body rotation, while sucking increases it where $R < 0.78$ and reduces it where $R > 0.78$. (The dashed line along $V = 1$ corresponds to solid-body rotation.) The same trends are displayed by the mean velocity profiles for 300 rpm, but are barely distinguishable in the profiles for 3600 rpm.

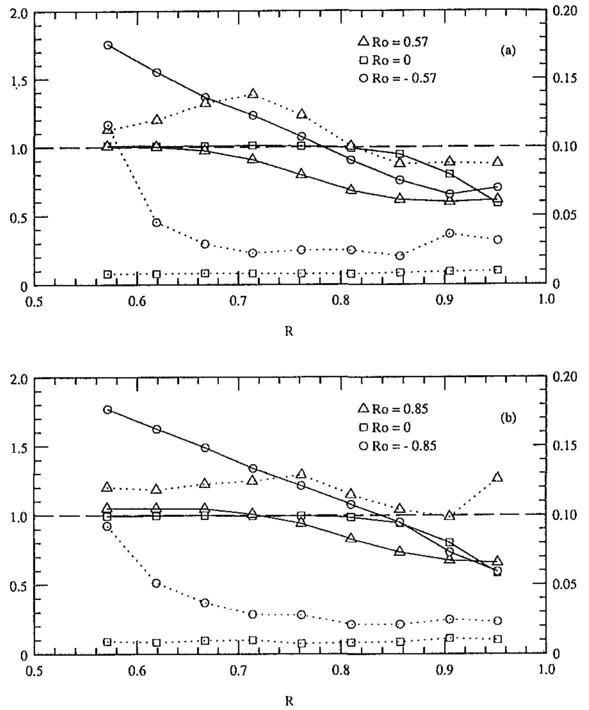

Fig. 3 Radial profiles of the mean (–) and rms (· · ·) circumferential velocity at $Z = 0$ for Ω = 37 rpm (Re = 2.73×10^3) using (*a*) ring #1 and (*b*) ring #2

The rms profiles for all three rpm display a marked dependence on the particular ventilation condition investigated. First, we note that in the absence of ventilation the rms (and mean) velocity profiles display the same variations with disk speed of rotation as measured by Schuler et al. (1990), namely: a uniform radial distribution of low rms for 37 rpm, denoting a steady flow; a nonuniform radial distribution of high rms for 300 rpm, denoting an unsteady flow; a mildly nonuniform radial distribution of rms intermediate between the previous two values for 3600 rpm, suggesting a flow that is more tur-

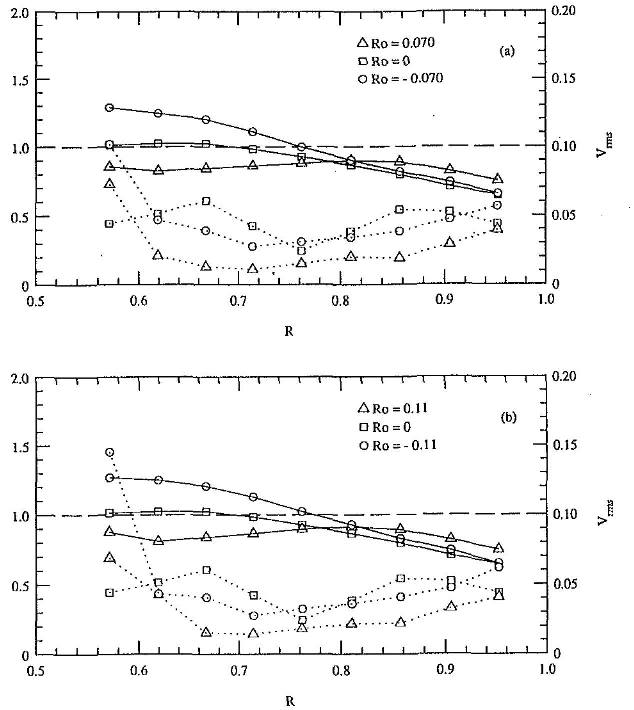

Fig. 4 Radial profiles of the mean (–) and rms (· · ·) circumferential velocity at $Z = 0$ for $\Omega = 300$ rpm ($Re = 2.22 \times 10^4$) using (*a*) ring #1 and (*b*) ring #2

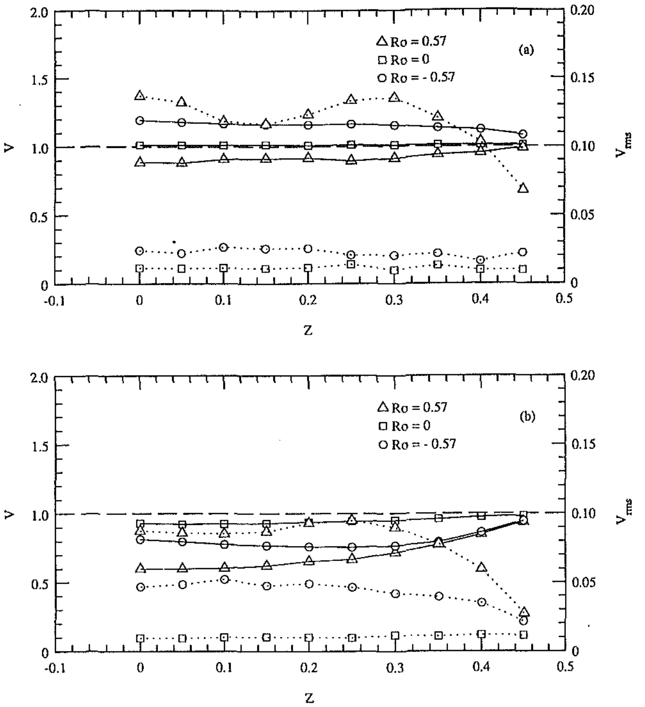

Fig. 6 Axial profiles of the mean (–) and rms (· · ·) circumferential velocity at (*a*) $R = 0.71$ and (*b*) $R = 0.86$ for $\Omega = 37$ rpm ($Re = 2.73 \times 10^3$) using ring #1

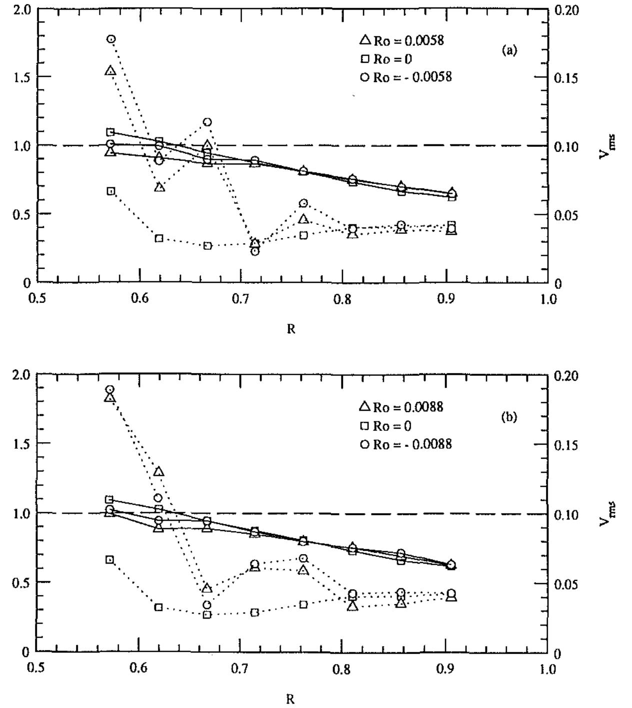

Fig. 5 Radial profiles of the mean (–) and rms (· · ·) circumferential velocity at $Z = 0$ for $\Omega = 3600$ rpm ($Re = 2.66 \times 10^5$) using (*a*) ring #1 and (*b*) ring #2

bulent than it is unsteady in its large-scale structures. In the work of Schuler et al. (1990) and Usry et al. (1990), it was argued that large nonuniform radial distributions of rms measured above a critical value of 64 rpm are associated with the large-scale, axially aligned, circumferentially periodic vortical structures present in the flow. From the present figures, it is clear that the imposition of a ventilation condition alters the rms completely and we expect the periodicity of the holes in the spacer rings to contribute to the complexity of the distributions. Thus, for example, at 37 rpm, both blowing and sucking increase the rms along the radial midplane, but by a much larger factor in the case of blowing. Because we know that the radial throughflows for both values of Ro (blowing and sucking) are laminar, then at least for the case of blowing we must attribute the rather large value of the rms to the periodic passage, through the fixed measurement probe volume, of the air jets emerging from the holes in the rotating disk spacer. That this is indeed the case is confirmed by the unsteady flow results presented further below.

Surprisingly, at 300 rpm, the relative roles of blowing and sucking are reversed, with the sucking condition yielding the higher rms and, hence, the more unsteady flow. However, at this rpm, both ventilation conditions lead to smaller values of the rms relative to the unventilated condition almost everywhere along the radial midplane. At 3600 rpm, for $R < 0.8$, the rms values with ventilation imposed (both blowing and sucking) exceed the corresponding unventilated flow values. That at 300 and 3600 rpm blowing should induce a smaller rms than sucking is attributed to two factors: (*a*) For the case of blowing, the more rapid entrainment of air emerging from the spacer holes into the disk Ekman layers, which reduces the direct impact of flow unsteadiness on the radial midplane. (*b*) For the case of sucking, the enhancement of flow instabilities at the location on the cylinder wall where the two Ekman layers turn to collide and jet back into the inner-disk space, along the radial midplane. At 3600 rpm, we believe it is the complicated, three-dimensional, unsteady (but nonturbulent) flow in the region near the spacer holes which accounts for the jaggedness observed in the rms distributions for ventilation of either sign.

Comparing the (*a*) and (*b*) profiles in Figs. 3–5 shows the effect on the inter-disk flow of varying the number of holes per disk spacer. The mean flow profiles show little dependence on the number of holes. At 3600 rpm, the rms profiles display a stronger sensitivity to this effect. Surprisingly, at 37 and 300

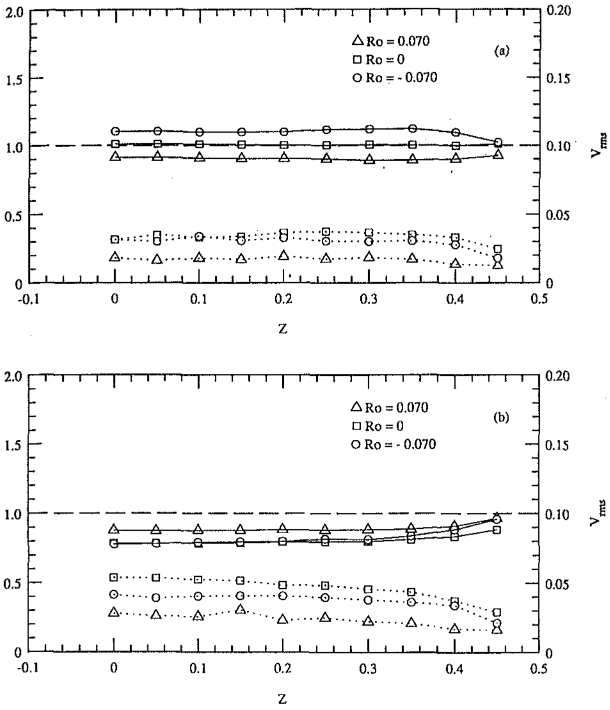

Fig. 7 Axial profiles of the mean (–) and rms (· · ·) circumferential velocity at (*a*) R = 0.71 and (*b*) R = 0.86 for Ω = 300 rpm (Re = 2.22×10^4) using ring #1

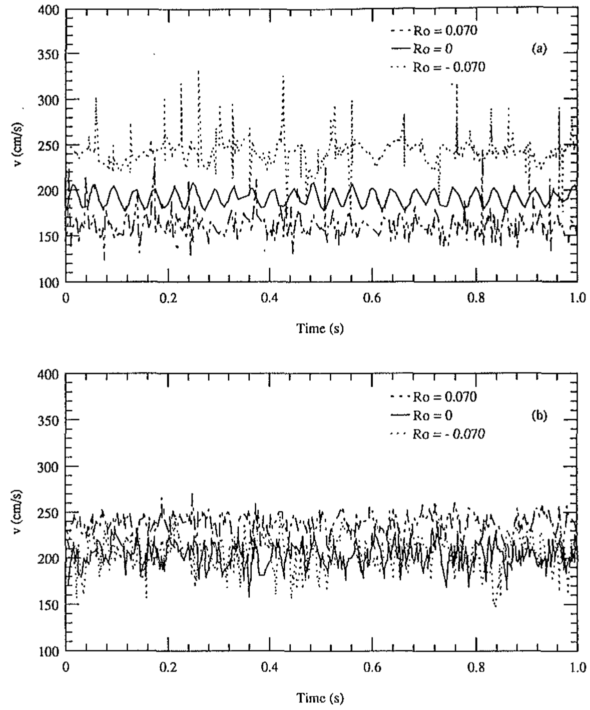

Fig. 8 Typical time records of the circumferential velocity at (*a*) R = 0.57 and (*b*) R = 0.95 for Z = 0 and Ω = 300 rpm (Re = 2.22×10^4) using ring #1

rpm, for which the values of the Rossby number are larger, the differences due to disk spacer type are even smaller.

Axial traverses of the mean and rms circumferential velocity component are shown in Figs. 6 and 7 for 37 and 300 rpm. In each figure, part (*a*) shows measurements near the disk spacers (R = 0.71) while part (*b*) shows measurements near the fixed cylinder wall (R = 0.86). At both speeds of rotation, the mean and rms velocity profiles display relatively little variation with Z. However, their overall values show a strong dependence on the particular ventilation condition imposed. Thus, for example, at R = 0.71 with Ω = 37 rpm, sucking raises the mean circumferential velocity in the bulk of the inter-disk space relative to the unventilated flow, while blowing lowers it. However, the blowing condition drastically increases the velocity rms, while there is little difference between the rms corresponding to the sucking condition and the unventilated flow. The large increase in the rms with the blowing condition imposed is attributed to the air jets emerging from the holes in the rotating spacers. Thus, much of this rms velocity is composed of nonturbulent, periodic pulsations. The same trends (in the rms dependence on ventilation) are observed for 37 rpm at R = 0.86 except that, at this radius nearer the cylinder wall, both blowing and sucking contribute significantly to increasing the rms. We note that the sucking condition at R = 0.86 leads to a reduction in velocity as opposed to the increase observed at R = 0.71. This is attributed to the ingestion of low speed fluid near the cylinder wall. Both the mean and rms velocity profiles obtained for 300 rpm display a much weaker dependence on the particular ventilation condition due to the lower values of the Rossby number imposed.

3.2 Velocity Time Records and Power Spectra. Typical velocity time records at two radial locations are plotted in Fig. 8 for Ω = 300 rpm and the three ventilation conditions. (The superficially apparent sparseness of the dotted and dashed profiles in the figure is not an indication of low data rates in the experiments. As explained above, the data rates were always sufficient to resolve the flow conditions investigated.) From data such as this we derived the corresponding power spectra, and from the spectra we chose those values of frequency, f, with energy significantly larger than the background threshold. Nondimensional values of these frequencies obtained at Z = 0 are plotted in Figs. 9(*a*)–(*c*) as a function of R for three ventilation conditions using ring #1 (24 holes). We take these non-dimensional values of f to be indicative of the presence of structures in the flow; either axially aligned as discussed in the Introduction, or in the cross-stream plane as calculated by Humphrey et al. (1992).

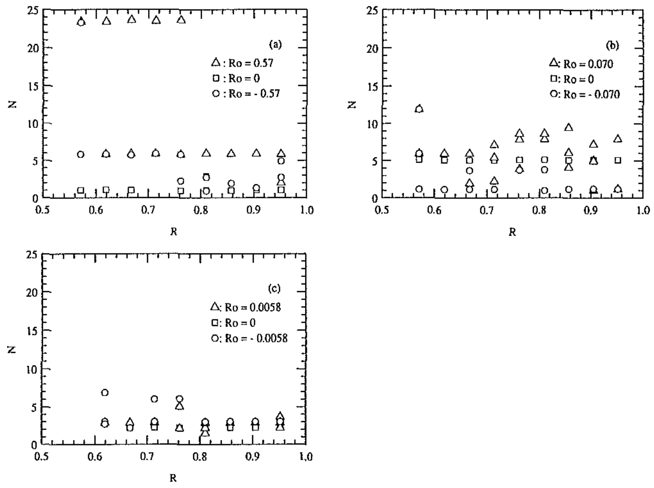

Fig. 9 Nondimensional dominant flow frequency, N, versus radial position, R, at Z = 0 using ring #1 for (*a*) Ω = 37 rpm (Re = 2.73×10^3); (*b*) Ω = 300 rpm (Re = 2.22×10^4); (*c*) Ω = 3600 rpm (Re = 2.66×10^5)

The results for 37 rpm are fairly straightforward to interpret. It is clear for the case of blowing that the periodicity of the jets (N = 24) emerging through the spacer holes is felt up to R = 0.76. Similarly, at R = 0.57, the presence of the holes is also registered for the case of sucking. In the absence of ventilation, the disk speed of rotation ($N = 1$) is sensed at almost all R. For both blowing and sucking the value of $N = 6$ suggests that both of these ventilation conditions are capable of triggering flow instabilities that evolve into axially-aligned vortical structures of the type and number visualized by Abrahamson et al. (1991), and measured by Usry et al. (1990) in the present test section for $\Omega > 64$ rpm.

The results for 300 and 3600 rpm are more difficult to interpret. The values of $N = 5$ for 300 rpm, and $N = 2$ for 3600 rpm, for the unventilated condition are in agreement with corresponding unventilated flow results obtained by Usry et al. (1990). Apparently, the number of disk spacer holes is not detected at $Z = 0$ for any value of R at these two speeds of rotation. For the blowing condition this suggests that, at these two speeds of rotation, the jets emerging from the spacer holes are rapidly entrained into the disk Ekman layers, away from the midplane ($Z = 0$) where the measurement probe was located. Notwithstanding, at most radial locations both blowing and sucking result in several, essentially integer, values of N suggesting various co-existing modes or structures of motion. At 300 rpm blowing tends to induce larger values of N (ranging from 2 to 9) than sucking, but only for sucking is the disk speed of rotation ($N = 1$) registered at essentially all R. Given the relatively low values of the Rossby numbers imposed at 3600 rpm, the marked sensitivity of the flow to the presence of large-scale structures for both the blowing and sucking conditions is quite remarkable and is an important consideration in the design of ventilated disk storage systems with high speeds of rotation.

4 Conclusions

Time-resolved and time-averaged measurements of the circumferential velocity component were obtained for the unobstructed flow of air between the center pair of four disks corotating in a fixed cylindrical enclosure. Both ventilated and unventilated radial throughflow conditions were explored, with the characteristics and structure of the flow displaying an equally complex dependence on both the blowing and sucking conditions. The data serve as a new target for numerical procedures aimed at predicting time-averaged quantities in unsteady, strongly-curved flows.

For values of the Rossby number such that $|Ro| < 0.01$, approximately, the mean velocity profiles show a relatively weak dependence on the ventilation condition. In contrast, the rms profiles are observed to depend significantly on the particular ventilation condition imposed over the entire range of Rossby numbers explored, $|Ro| < 0.85$. These conclusions are independent of the number of holes in the disk spacer rings investigated and are important for improving ventilated disk storage system designs.

A dimensionless frequency parameter, N, was defined that serves to quantify non-turbulent mean flow unsteadiness and is postulated to be related to the presence of large-scale structures in the flow. For the unventilated condition and at all speeds of rotation, the measured values of N agree with earlier findings. No general rules appear to emerge from the ventilated flow data that allow N to be predicted as a function of the Rossby number. However, for $|Ro| > 0.57$ the presence of holes in the disk spacer rings is sensed by the bulk of the inter-disk flow. The same cannot be said for smaller values of the Rossby number. For the blowing condition this suggests that there exists a critical value of the Rossby number, in the range 0.1–0.5, characterizing the immediate entrainment of the spacer jets into the disk Ekman boundary layers.

Earlier calculations of ventilated unsteady inter-disk flows, by Humphrey et al. (1992), revealed a marked sensitivity of the results obtained to the particular ventilation condition imposed. Thus, blowing was found to stabilize inter-disk flow at the expense of increased dissipation. In contrast, sucking significantly reduced dissipation, but at the expense of a strongly destabilized flow. The sensitivity of inter-disk flows to the boundary conditions imposed points to the importance of both the physical realism and accurate numerical representation of the boundary conditions. In this regard, present experimental results suggest that both blowing and sucking induce flow unsteadiness in rather complicated (not readily obvious) ways. Therefore, continuing experimental and numerical work, especially that aimed at improving disk storage system designs, must pay special attention to this problem, including analysis of the interactions between unsteady flow structures and inter-disk obstructions such as suspensions supporting magnetic heads.

Acknowledgments

The authors wish to express their sincere appreciation to the IBM Almaden Research Center in San Jose and the Computer Mechanics Laboratory of the University of California at Berkeley for its financial support of this work. The first author gratefully acknowledges a National Science Foundation Graduate Fellowship. Special thanks go to John Morton for his excellent work in manufacturing various parts of the complicated test section.

References

Abrahamson, S. D., Chiang, C., and Eaton, J. K., 1991, "Flow Structure in Head Disk Assemblies and Implications for Design," *Advances in Information Storage Systems*, Vol. 1, pp. 111–132.

Abrahamson, S. D., Koga, D., and Eaton, J. K., 1988, "An Experimental Investigation of the Flow between Shrouded Corotating Disks," Report MD-50, Thermosciences Division, Department of Mechanical Engineering, Stanford University.

Bakke, E., Kreider, J. F., and Kreith, F., 1973, "Turbulent Source Flow Between Parallel Stationary and Co-rotating Disks," *Journal of Fluid Mechanics*, Vol. 58, pp. 209–231.

Bell, W. A., 1986, "Spectral Analysis of Laser Velocimeter Data with the Slotted Correlation Method," *Proceedings of the AIAA/ASME Fourth Fluid Mechanics, Plasma Dynamics and Lasers Conference*.

Chang, C. J., Humphrey, J. A. C., and Greif, R., 1990, "Calculation of Turbulent Convection Between Corotating Disks in Axisymmetric Enclosures," *International Journal of Heat and Mass Transfer*, Vol. 33, No. 12, pp. 2701–2720.

Chang, C. J., and Li, H., 1989, "Three-Dimensional Numerical Simulation of Flows for Corotating Disks," IBM Research Report RJ 7167.

Chang, C. J., Schuler, C. A., Humphrey, J. A. C., and Greif, R., 1989, "Flow and Heat Transfer in the Space Between Two Corotating Disks in an Axisymmetric Enclosure," ASME *Journal of Heat Transfer*, Vol. 111, pp. 625–632.

Greenspan, H. P., 1968, *The Theory of Rotating Fluids*, Cambridge University Press.

Humphrey, J. A. C., Chang, C. J., Li, H., and Schuler, C., 1991, "Unobstructed and Obstructed Rotating Disk Flows: A Summary Review Relevant to Information Storage Systems," *Advances in Information Storage Systems*, Vol. 1, pp. 79–110.

Humphrey, J. A. C., Schuler, C. A., and Iglesias, I., 1992, "Analysis of Viscous Dissipation in Disk Storage Systems and Similar Flow Configurations," *Physics of Fluids A*, Vol. 4, pp. 1415–1427.

Kaneko, R., Oguchi, S., and Hoshiya, K., 1977, "Hydrodynamic Characteristics in Disk Packs for Magnetic Storage," *Review of the Electrical Communication Laboratory*, Vol. 25, pp. 1325–1336.

Kreith, F., 1968, "Convection Heat Transfer in Rotating Systems," *Advances in Heat Transfer*, Vol. 5, pp. 129–251.

Lennemann, E., 1974, "Aerodynamic Aspects of Disk Files," *IBM Journal of Research and Development*, pp. 480–488.

Mochizuki, S., and Inoue, T., 1990, "Self-Sustained Flow Oscillations and Heat Transfer in Radial Flow Through Co-rotating Parallel Disks," *Experimental Thermal and Fluid Science*, Vol. 3, pp. 242–248.

Owen, J. M., Pincombe, J. R., and Rogers, R. H., 1985, "Source-sink Flow Inside a Rotating Cylindrical Cavity," *Journal of Fluid Mechanics*, Vol. 155, pp. 233–265.

Schuler, C. A., 1990, "Investigation of the Flow between Rotating Disks in an Enclosure," Ph.D. thesis, University of California at Berkeley.

Schuler, C. A., Usry, W., Weber, B., Humphrey, J. A. C., and Greif, R., 1990, "On the Flow in the Unobstructed Space between Shrouded Corotating Disks," *Physics of Fluids A*, Vol. 2, No. 10, pp. 1760–1770.

Szeri, A. Z., Schneider, S. J., Labbe, F., and Kaufman, H. N., 1983a, "Flow Between Rotating Disks (Part 1, Basic Flow)," *Journal of Fluid Mechanics*, Vol. 134, pp. 103–131.

Szeri, A. Z., Schneider, S. J., Labbe, F., and Kaufman, H. N., 1983b, "Flow

Between Rotating Disks (Part 2, Stability)," *Journal of Fluid Mechanics*, Vol. 134, pp. 133–154.

Tzeng, H.-M., and Chang, C. J., 1991, "Obstructed Flow Between Shrouded Corotating Disks," *Physics of Fluids A*, Vol. 3, pp. 484–486.

Tzeng, H.-M., and Fromm, J. E., 1990, "Airflow Study in a Cylindrical Enclosure Containing Multiple Corotating Disks," IBM Research Report RJ 7334, San Jose, California.

Tzeng, H.-M., and Humphrey, J. A. C., 1991, "Corotating Disk Flow in an Axisymmetric Enclosure with and Without a Bluff Body," *International Journal of Heat and Fluid Flow*, Vol. 12, No. 3, pp. 194–201.

Usry, W. R., Schuler, C. A., Humphrey, J. A. C., and Greif, R., 1990, "Unsteady Flow Between Corotating Disks in an Enclosure with an Obstruction," *Proceedings of the Fifth International Symposium on Application of Laser Techniques in Fluid Mechanics*, Lisbon, Portugal.

On the Flow Structure Due to Corotating Disks With a Ventilated Hub

John Girard

Scott Abrahamson

Aerospace Engineering and Mechanics,
University of Minnesota,
Minneapolis, MN 55455

The effects of hub ventilation on the flow structure between corotating disks enclosed in a stationary cylindrical shroud have been studied using quantitative flow visualization. The ventilation flow resulted from the pumping of the rotating disks. The geometry of the ventilation holes and the total open area were varied and the flow structure was compared to the solid hub case. Many of the features present in the solid hub case remained in modified form. The radial extent of the region purged by the through-flow was independent of the hub open area, which ranged from 3.4 to 37.5 percent of the total hub area. Additionally, the radial extent of the purged region was found to be independent of the Reynolds number.

Introduction

The mechanics of the stationary flow field associated with corotating disks enclosed in a cylindrical shroud with a solid hub was investigated by Abrahamson et al. (1989), who divided the flow field into three distinct regions. The region adjacent to the hub was designated the Inner region, which rotates in solid body motion at disk speed. Little mixing occurs in this region and no boundary layers exist on the disks. Encircling the Inner region is the Outer region, which is distinguished by the presence of vortical structures which span the space between the disks and are evenly distributed in the circumferential direction. These vortices are responsible for the polygonal shaped boundary separating the two regions. Measurements and analysis of the Inner and Outer regions have been made by Schuler et al. (1990). The third identifiable region, designated the Shroud Boundary Layer region, is found adjacent to the shroud.

The current investigation considers the flow in a similar geometry with a significant difference. The hub was perforated to allow radially directed flow through the disk assembly. Previous investigations (Abrahamson et al., 1991; Chang et al., 1989; Humphrey et al., 1992; Kaneko et al., 1977; Owen and Pincombe, 1980; and Owen et al., 1985) have used an external pump to control the radial through-flow. In the current investigation, as in most disk drive applications, the rotating disks were the pump and controlled the through-flow. Hide (1968) studied source-sink flows associated with a rotating fluid. Using a rotating cylindrical cavity, Hide observed that fluid from a centrally positioned source moved radially until entrained into the disk boundary layers, which transported the fluid around the rotating core flow. A peripherally distributed sink provided an exit for this fluid. The present study differs from Hide's work in that the stationary shroud generates secondary flow structures in the core flow, but in the through-flow effected region, the flow is similar. The objectives of this study were to develop an understanding of both the effect of the through-flow on the above-described flow structure and the effects of different ventilation geometries. Two studies, each concerned with different aspects of the ventilation geometry, were performed. In the first study, the open area in the hub was held constant and two ventilation patterns were used. In the second study the ventilation hole pattern was fixed while the total open area (ventilation area) was varied. In both studies, the rotational rate was varied and the displacement of the Inner region away from the hub was used to indicate the effectiveness of the through-flow at purging the rotating cavity.

Experimental Facility

A large scale experimental facility, which uses water as the working fluid, was developed for these studies. The hub assembly consisted of four glass disks and three spacer rings as shown in Fig. 1. The upper and lower spacer rings were solid while the middle ring was perforated. Perforation of all spacers does not significantly effect the results. Using the hub radius (127 mm) as a length scale, the geometry is presented in dimensionless form. The disk radius was 2, the spacing between any two disks was 0.125, and the cylindrical shroud radius was 2.063. The centering device for the disks and spacers occupied 63 percent of the annulus between the spindle and disk inner radius.

In the first study, two spacer rings were used. One ring had 48 semicircular holes distributed evenly along the top and bottom of the spacer as shown in Fig. 1, while the second ring had 24 equivalent sized circular holes equally spaced around its midplane. Each spacer had an open area equaling 7.9 percent of the total area by using holes having a 3.63 mm radius. The second study used 4 spacer rings, each having the semicircular hole pattern. The open-area percentages of the total area were 3.4, 7.9, 18.3, and 37.5 when using hole radii of 2.37 mm,

---

Contributed by the Fluids Engineering Division for publication in the JOURNAL OF FLUIDS ENGINEERING. Manuscript received by the Fluids Engineering Division November 16, 1992; revised manuscript received January 5, 1993. Associate Technical Editor: J. Humphrey.

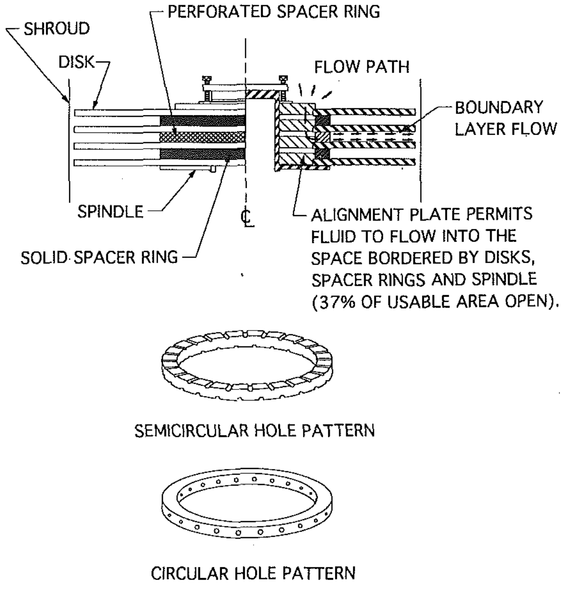

Fig. 1 Hub assembly

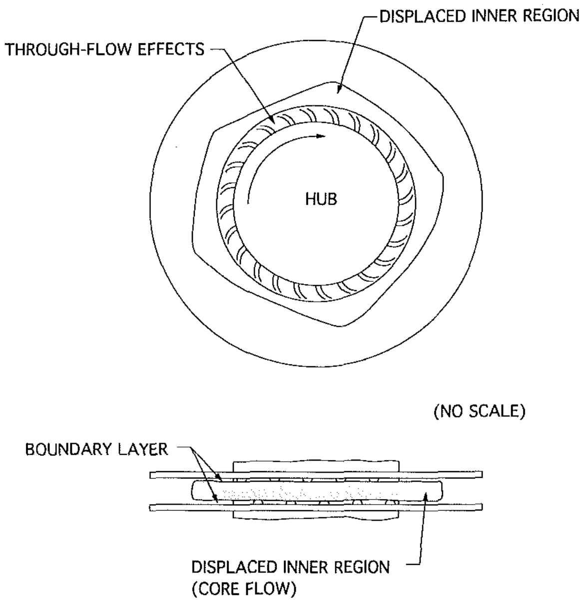

Fig. 2 Through-flow effects on flow structure

3.63 mm, 5.55 mm, and 7.94 mm, respectively. The design of the hub interior minimized the flow losses so as to isolate the effects of the spacer rings.

The Reynolds number, defined using the tip speed and radius of the disk, is Re = $\Omega R^2/\nu$, where Ω is the rotational speed, R is the disk radius, and ν is the kinematic viscosity. The Reynolds numbers ranged from 3.36×10^4 to 3.36×10^5.

To visualize flow structures, dye was introduced into the test volume. A detailed explanation of the dye technique can be found in Abrahamson et al. (1989). A video camcorder recorded the flow visualizations. Several trials were completed at each speed and hub configuration. From those trials, two were selected to study the region affected by the ventilation flow. The edge of this region was observed to be the transition from no dye to a high concentration of dye. A frame grabber captured individual video frames, which were analyzed on a computer. For each frame, eight measurements were made of the inner boundary of the displaced Inner region, which is described below. These measurements were averaged to obtain one value for each speed and hub configuration. The uncertainty in these measurements, estimated from the maximum and minimum values for each case, is approximately 8 percent. It should be noted that this uncertainty is not a measurement uncertainty per se, but the uncertainty in trying to assign a circular measurement to a shape that roughly resembles a polygon.

Discussion

A qualitative description of the flow field is presented first to give insight into the observed flow structures. The results were quantified to compare the effects of changing the hub configuration.

The flow field is nominally stationary, but the following discussion is cast from an unsteady perspective of the evolution of a visualization. Dye placed near the hub immediately showed the influence of the ventilation flow. From inside the hub, undyed fluid emerged from the hub as radial jets, which were turned in a tangential direction by the Coriolis force and merged as shown in Fig. 2. The merging jets formed a circular front, which was indifferent to the ventilated hub configuration. As the through-flow both neutralized and displaced dyed fluid radially outward, the dye front became distorted and began bulging outwards. When the visualization became stationary the former Inner region remained as a low mixing region displaced from the hub as shown in Fig. 2.

In its stationary state, the Inner region had a coarse polygonal shape as sketched in Fig. 2. For the 7.9 percent open-area ratio, the ventilation pattern (center holes or alternating semicircular holes) had no effect on the shape of the Inner region. As in the nonventilated case, the shape of the Inner region was influenced by the vortical structures present in the Outer region (see Abrahamson et al., 1989). However, unlike the solid hub case, the boundary separating the displaced-Inner and Outer regions was not smooth. The sides of the irregular polygonal-shaped displaced Inner region appeared to be formed by groups of structures rather than one large structure per side and except for the discussion below, no Re effects were observed.

For the two smallest open-area ratios, the low Re visualizations were slightly different in that small pockets of dye remained adjacent to the hub, between the ventilation holes, after the balance of dye in the region was neutralized. This indicates stagnant zones near the hub which were not observed in the high Re visualizations. Unique to the two large open-area ratios was a phenomonon where dyed fluid was drawn radially inward from the displaced Inner region toward the hub in inward-directed finger-like protrusions. These dye protrusions took a corkscrew path (with axes in the disk plane) toward the hub, but no rotational preference could be discerned.

Boundary layers along the disk surfaces were observed as layers of undyed fluid (ventilation flow) adjacent to the surfaces with a core of dyed fluid sandwiched between them. The region effected by the through-flow was observed (but not measured) to rotate slower than the disk speed, causing boundary layers to be generated. The boundary layers transported fluid from the through-flow affected region (see Fig. 2), around the displaced Inner region, out to the periphery of the disks. Spacer ring geometry had no observable effect on boundary layer development.

Quantitative measurements of the flow field were obtained from video and scaled by the hub radius. Figure 3 is a plot of the dimensionless radius of the ventilation-effected region as a function of Re. The two curves correspond to different ventilation patterns. As seen in the figure, the dimensionless radius of the displaced Inner region is approximately 1.4. The center hole configuration appears slightly more effective at displacing the Inner region away from the hub. However, the differences

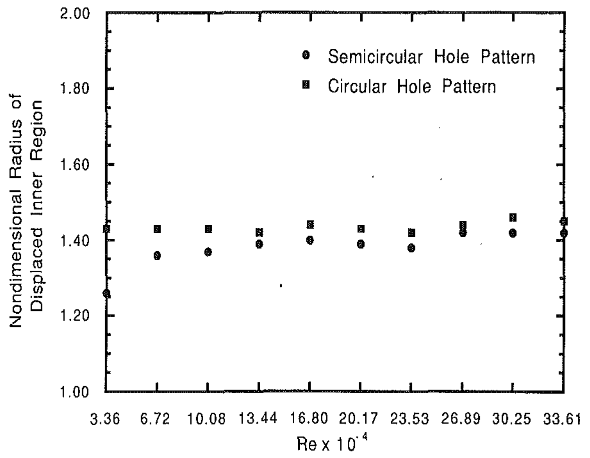

Fig. 3 Radius of displaced inner region versus Reynolds number for semicircular and circular hole patterns with 7.9 percent open area ratio

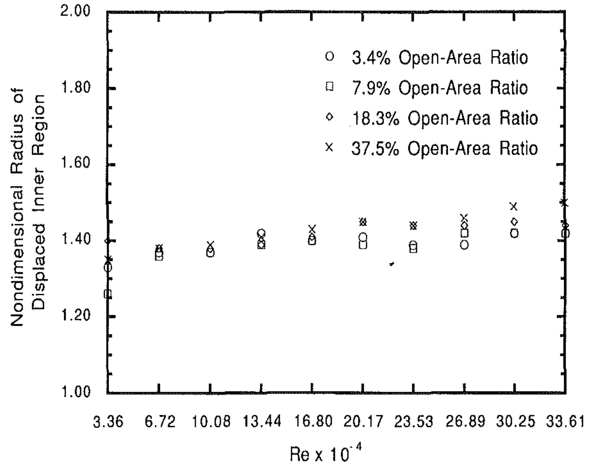

Fig. 4 Radius of displaced inner region versus Reynolds number, comparing open-area ratios for semicircular hole pattern

between the two curves are well within the experimental uncertainty of 8 percent, so the configurations yield essentially the same results. Figure 4 is a plot of the dimensionless radius of the effected region as a function of Re for the study varying the open-area ratio. The dimensionless radius appears to increase slightly with Re, but again this trend remains well within the experimental uncertainty. The visualizations indicate that the purging action of the flow adjusts to the disk rotational rate. The hub configuration does not effect the ventilation flow rate, since the Inner region was consistently displaced a constant distance.

The penetration radius did not vary over the range of Re used in this investigation. Owen (1988) showed that the entrainment rate into the disk boundary layer increased with increasing Re for a similar rotating cavity, but with a forced through-flow. This indicates that more fluid is pumped through the cavity as the rotational rate increases. Although the through-flow is not forced in this investigation, the expectancy is for the entrainment rate to increase with Re. However, the overall flow structure is unaltered by this increase in the entrainment rate. Fluid flowing in the disk layers passes around both the displaced Inner region and the Outer region. The shroud boundary layer accepts this excessive flow and redirects the flow leaving at the disk edge. Moveover, the structure of the flow field is not expected to be radically changed when varying disk separation distance. Calculations by Abrahamson and Lonnes (1992) indicate a strong exponential dependence between the through-flow and Reynolds number when the displacement of the Inner region is fixed at 1.4 hub radii. This is true for a wide range of disk separation distances. It is uncertain why the through-flow affected region is consistently 1.4 hub radii in extent. One parameter which might shed some light on Reynolds number dependence is the ratio of the hub to disk radii, which was held fixed at 1/2 in this investigation.

Conclusion

Although a rotating disk acts as a pump, attempts to use disk pumping to purge the cavity between a pair of corotating disks had limited success. Perforation of the hub allows flow to enter the space between the disks and rapid rotation spreads the flow uniformly between them. The purging capacity is limited by the boundary layers, which eventually entrain all of the inflow. Consequently, beyond the radial location of complete entrainment, there is no purging flow in the space between the disk boundary layers. As shown in Figs. 3 and 4, regardless of the Reynolds number and the size of the hub perforations, approximately 40 percent of the radial extent from the hub to disk radius is purged. The remaining 60 percent is similar to the nonventilated case. The displaced Inner region has low mixing when compared to the rest of the flow field and the Outer region is dominated by large-scale vortical structures.

Acknowledgment

This work was sponsored by International Business Machines Corporation.

References

Abrahamson, S. D., Koga, D. J., and Eaton, J. K., 1989, "The Flow Between Corotating Shrouded Disks," *Physics of Fluids A*, Vol. 1, No. 2.

Abrahamson, S. C., Chiang, C., and Eaton, J., 1991, "Flow Structure in HDAs and Implications for Design," *ASME Advances in Information Storage Systems*, Vol. 1.

Abrahamson, S., and Lonnes, S., 1992, "Radial Injection Between Corotating Disks," submitted for publication to ASME JOURNAL OF FLUIDS ENGINEERING.

Chang, C. J., Schuler, C. A., Humphrey, J. A. C., and Greif, R., 1989, "Flow and Heat Transfer in the Space Between Two Corotating Disks in an Axisymmetric Enclosure," *Journal of Heat Transfer*, Vol. 111, pp. 625–632.

Hide, R., 1968, "On Source-Sink Flows in a Rotating Fluid," *Journal of Fluid Mechanics*, Vol. 32, No. 4.

Kaneko, R. S., Oguchi, S., and Hoshiya, K., 1977, "Hydrodynamic Characteristics in Disk Packs for Magnetic Storage," *Review of the Electrical Communications Laboratory*, Vol. 25, Nos. 11, 12, pp. 1325–1336.

Owen, J. M., and Pincombe, J. R., 1980, "Velocity Measurements Inside a Rotating Cavity With Radial Outflow of Fluid," *Journal of Fluid Mechanics*, Vol. 99, No. 1.

Owen, J. M., Pincombe, J. R., and Rogers, R. H., 1985, "Source-Sink Flow Inside a Rotating Cylindrical Cavity," *Journal of Fluid Mechanics*, Vol. 155.

Owen, J., 1988, "Air-Cooled Gas-Turbine Discs: A Review of Recent Research," *International Journal of Heat and Fluid Flow*, Vol. 9, No. 4.

Schuler, C. A., Usry, W., Weber, B., Humphrey, J. A. C., and Greif, R., 1990, "On the Flow in the Unobstructed Space Between Shrouded Corotating Disks," *Physics of Fluids A*, Vol. 2, No. 10.

Influence of Vibration Amplitude on Laminar Flow Over a Plate Vibrating at Low Strouhal Number

N. K. Venkat
Spaulding Environmental Associates, Inc.,
Wakefield, RI 02879

M. Spaulding
Professor,
Department of Ocean Engineering,
The University of Rhode Island,
Kingston, RI 02881

The spectral and hydrodynamic response of laminar flow over a flat plate with a vibrating section forced in sinusoidal motion with a dimensionless amplitude ratio, H_0 *(vibration amplitude divided by plate length) varying in the range* $0.0 < H_0 < 0.1$ *is analyzed using numerical simulations. The Reynolds number, Re, based on the length of the vibrating plate, is fixed at 1000. The flow is simulated for Strouhal number, St, = 0.25 (low frequency). The spectral characteristics are obtained by performing Fast Fourier Transform (FFT) on the pressure coefficient time series data. The hydrodynamic analysis is performed by plotting stream function contour plot in the vicinity of the vibrating section for one vibration cycle. The model predicted results show that the friction and pressure coefficients over the vibrating body vary with vibration amplitude. For low amplitude ratios, the interaction of the external flow with the vibrating section is linear and there is little up or downstream influence. For high* H_0*, there is considerable downstream influence of the disturbance. Nonlinear energy transfer, as evidenced by the existence of a significant first harmonic in the pressure wave, takes place between the vibrating plate and the flow field. Energy transfer to the higher harmonics is less significant.*

Introduction

The interaction between a vibrating body and the overlying fluid is an important phenomenon in many engineering applications (Blevins, 1977 and Telionis, 1981). The unsteadiness may be caused by the change in shape of the flexible body or by disturbing the free-stream flow. Curle (1955) found that the time varying shear stresses act as dipole sources for noise generation from oscillating flows. Time varying normal and shear stresses, which act as sources for sound generation, can also be created when there is an external flow over an oscillating body or wall.

There is another class of important problems in fluid dynamics that involve unsteady forces. These are problems dealing with wave loads on offshore structures, wind loads on tall buildings, and airplane wings with flutter. The body shapes in offshore structures are generally bluff, so that separation accompanies the flow. These flow separations create unsteady forces on the structure which in turn oscillate and disturbs the external flow. These fluid-structure interactions create complicated flow patterns and induce nonlinearities in the flow field.

Before analyzing the coupled (solid/fluid interaction) problem, the hydrodynamic characteristics of external flow over a vibrating body have to be thoroughly investigated. Venkat and Spaulding (1991) developed a numerical model to predict the flow over a flat plate containing a section of length L vibrating in simple harmonic motion. The fluctuating flows investigated here are generated through imposed disturbances of known frequency and amplitude on the plate surface. The flow was simulated for Strouhal numbers varying in the range $0.0 < \mathrm{St} < 1.0$. The Reynolds number, Re, based on the vibrating plate length, L, was maintained at 1000 (or Reynolds number, Re = 9000, based on the length from the entry region of the domain to the leading edge of the vibrating section). The amplitude of vibration, H_0 was fixed at 0.1. For these flow conditions they showed the generation of higher harmonics in the pressure for medium and large Strouhal number cases due to nonlinear interaction between the vibrating region and the external flow. They observed that the nonlinear interaction between the vibrating fluid near the plate and the external flow is controlled not only by the Strouhal number but also by the Reynolds number and the vibration mode and amplitude of the plate. This paper investigates the impact of the vibration amplitude on the nonlinear interaction between the fluid and the vibrating plate.

Mathematical Formulation

A typical fluid-structure interaction problem is shown in Fig. 1. In the present work, the problem is decoupled and the hydrodynamic region is solved using the two-dimensional incompressible Navier–Stokes equations and conservation of

---

Contributed by the Fluids Engineering Division for publication in the JOURNAL OF FLUIDS ENGINEERING. Manuscript received by the Fluids Engineering Division September 12, 1991; revised manuscript received October 7, 1992. Associate Technical Editor: T. T. Huang.

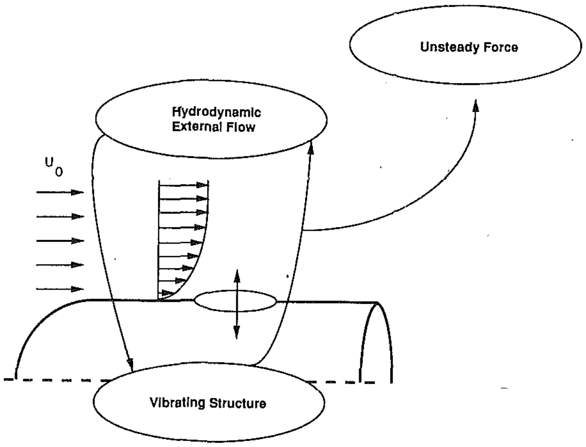

Fig. 1 **Schematic diagram for fluid-structure interaction problem**

mass equation in an $x-y$ coordinate system, formulated in terms of vorticity and stream function. The flexible structure influence comes through the known time dependent boundary condition at the wall. The physical domain is shown in Fig. 2(*a*). The flow equations and the associated boundary conditions are described in detail in Venkat and Spaulding (1991) and Venkat (1991), only a brief description of the formulation is given here. The governing equations, in dimensionless form, are given by

$$\frac{\partial \omega}{\partial t}+u\frac{\partial \omega}{\partial x}+v\frac{\partial \omega}{\partial y}=\frac{1}{\mathrm{Re}}\left[\frac{\partial^2 \omega}{\partial x^2}+\frac{\partial^2 \omega}{\partial y^2}\right] \quad (1)$$

$$\left[\frac{\partial^2 \psi}{\partial x^2}+\frac{\partial^2 \psi}{\partial y^2}\right]=-\omega \quad (2)$$

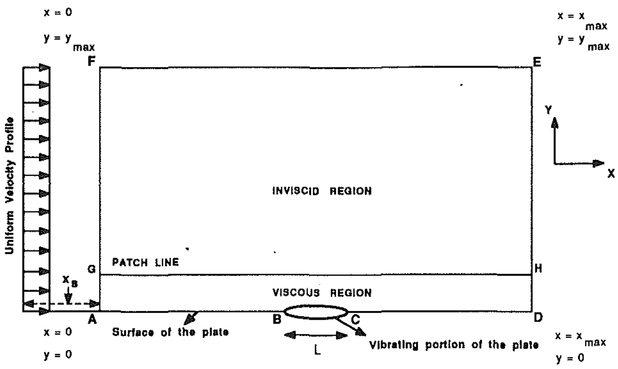

a) Physical Plane

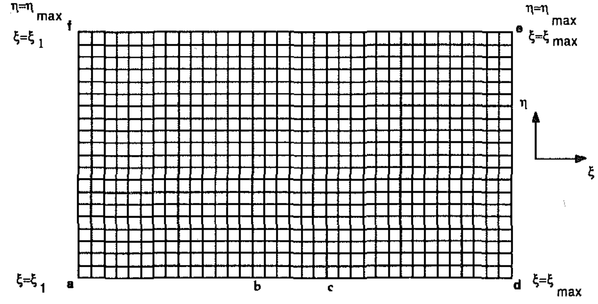

b) Computational Plane

Fig. 2 **Physical and computational planes for simulating viscous flow over a vibrating plate**

The velocity profile for a given Reynolds number at the upstream boundary is calculated using the Blasius equation (White, 1991) assuming that the leading edge of the plate (section FA) is located at a distance, x_s from the entry region of the model domain. In the present analysis, x_s is equal to 1. Top boundary (section FE) is kept sufficiently far away such that $u = 1$ and $\omega = 0$ (Fletcher, 1988). An alternate frictionless "wind tunnel" boundary condition is to specify $u = 1$ and $v = 0$ on FE. This effectively imposes a Dirichlet boundary condition $\psi_{\mathrm{FE}} = \psi_F$. As long as FE is sufficiently far from the vibrating section the global solution will be relatively insensitive to the particular boundary condition specification on FE. The normal second or higher order derivatives of stream function and vorticity are assumed zero at the downstream boundary (section DE; Fletcher, 1988).

On the plate surface, a section vibrates in simple harmonic motion (section BC). The equation for plate deflection is given by

Nomenclature

a = body vibration amplitude, m
C_f = friction coefficient on the plate surface
C_p = pressure coefficient on the plate surface
f = plate vibration frequency, Hz
H_0 = nondimensional body vibration amplitude ratio (a/L)
J = Jacobian of the transformation
L = characteristic length of the vibrating portion of the body, m
n = plate vibration mode
p = dimensionless pressure ($p = P/\rho U_\infty^2$)
P = fluids pressure, kg/m^2
Re = Reynolds number ($U_\infty L/\nu$)
Re_x = local Reynolds number ($U_\infty x/\nu$)
St = Strouhal number (fL/U_∞)
T = dimensional time (s)
t = dimensionless time ($t = TU/L$)
u, v = dimensionless horizontal and vertical velocities ($u = U/U_\infty$, $v = V/U_\infty$)
U, V = horizontal (along plate/cylinder) and vertical velocities (normal to plate/cylinder), m/s
U_∞ = free-stream velocity
x, y = nondimensional coordinates in the physical plane ($x = X/L$, $y = Y/L$)
x_{LE}, x_{TE} = leading and trailing edges of the vibrating section of the plate in the physical plane
$x_{\max}$ = length of the computational domain in the physical plane
x_s = nondimensional distance between the leading edge of the plate and the model entry domain
X, Y = dimensional coordinates in the physical plane
$y_{\max}$ = height of the computational domain in the physical plane
Φ = dimensional vorticity, 1/s
ρ = fluid density
Ψ = dimensional stream function, m^2/s
ξ, η = coordinates in the boundary fitted computational domain
$\xi_{\max}$ = length of the computational domain in the boundary fitted plane
$\eta_{\max}$ = height of the computational domain in the boundary fitted plane
ξ_{LE}, ξ_{TE} = leading and trailing edges of the vibrating section of the body in the boundary fitted computational plane
ψ, Φ = dimensionless stream function ($\psi = \Psi/LU$) and vorticity ($\omega = \Phi L/U$)
δ_{LE} = boundary layer thickness at the leading edge of the vibrating plate section
β,γ = metric coefficients in the boundary fitted plane

$$y_w(x,t) = H_0 \mathrm{Sin}\,(2\pi t \mathrm{St}) \mathrm{Sin}(n\pi x) \quad x_{\mathrm{LE}} < x < x_{\mathrm{TE}} \tag{3}$$

On the remainder of the plate (sections AB and CD)

$$y_w(x,t) = 0.0 \quad 0 < x < x_{\mathrm{LE}} \text{ and } x_{\mathrm{TE}} < x < x_{\max} \tag{4}$$

The stream function on the vibrating section of the plate is calculated by integrating the velocity of vibration along the plate surface. Simultaneously the derivative of the stream function in the y direction is set to zero to satisfy the no-slip boundary condition ($\partial\psi/\partial x = 0$). On the rest of the plate surface the stream function is constant and is zero. There is no direct boundary condition available for specifying the vorticity on the plate surface. It is therefore evaluated by applying the Poisson equation for stream function (Eq. (2)) on the plate surface.

The flow and associated boundary conditions are transformed to a boundary fitted computational plane (Venkat and Spaulding, 1991 and Venkat, 1991) where time dependent boundary motion is mapped to a constant, immovable coordinate line (Fig. (2), Thompson, 1982). This transformation allows the present problem, with time dependent boundaries, to be solved with relative ease.

Numerical Method

The Line Gauss Seidel numerical scheme of Napolitano and Walters (1986) is adopted for the present numerical simulations. The grid and the flow equations in the transformed plane are discretized using second order finite differences and the resulting algebraic equations form an $N \times N$ banded matrix. This matrix, along with the tranformed boundary conditions (Venkat and Spaulding, 1991), is solved using a Thomas Tri-Diagonal Matrix Algorithm (Bringen and McMillan, 1980 and Napolitano and Walters, 1986) from upstream to downstream for each time step. The time step is evaluated based on the stability analysis given in Roache (1972) and Peyret and Taylor (1983) for incompressible flows. The physical domain is divided into an inner viscous region and an outer inviscid region. In the outer inviscid region the Poisson equation for stream function with $\omega = 0$ (Eq. (2)) describes the flow while inside the boundary layer, solutions for both the stream function and vorticity must be obtained. The dividing line between these two regions depends upon the flow Reynolds number and the body geometry (Halim, 1986 and Venkat and Spaulding, 1991).

The unperturbed boundary layer solution is used as an initial guess for the stream function and the vorticity variables. Because of the nonlinearities in the flow equations the vorticity on the body and in the domain is under-relaxed to avoid instability for high frequency plate vibrations while the stream function in the domain is over-relaxed to speed the convergence. Absolute convergence criteria are used for both variables. The converged stream function and vorticity values for each time step are used to calculate the friction and pressure coefficients ($C_f(\xi, \eta = \eta_1, t)$, $C_p(\xi, \eta = \eta_1, t)$) on the plate surface. They are given by

$$C_f(\xi, \eta = \eta_1, t) = -\frac{2}{\mathrm{Re}} \left[\omega_w + \frac{2}{J} \left(\frac{\partial y}{\partial \xi} \frac{\partial v}{\partial \eta} - \frac{\partial y}{\partial \eta} \frac{\partial v}{\partial \xi} \right) \right] \tag{5}$$

$$C_p = (\psi,\ \eta = \eta_1,\ t) = p_\xi - p_{\xi_1} = \int_\xi^{\xi_1} \left[\frac{1}{J\mathrm{Re}} \left(\beta \frac{\partial \omega}{\partial \xi} - \gamma \frac{\partial \omega}{\partial \xi} \right) - \frac{\partial x}{\partial \xi} \frac{\partial u}{\partial t} - \frac{\partial y}{\partial \xi} \frac{\partial y}{\partial t} - \frac{1}{2} \frac{\partial (u^2 + v^2)}{\partial \xi} + v\omega \frac{\partial x}{\partial \xi} - u\omega \frac{\partial y}{\partial \xi} \right] d\xi' \tag{6}$$

where ω_w is the plate or wall vorticity, p_ξ is the reference pressure at $\xi' = \xi$, and p_{ξ_1} is the pressure at $\xi' = \xi_1$. The nonlinear characteristics of the flow field are analyzed by applying Fast Fourier Transform on the discrete numerical data (C_p) obtained from the numerical flow solutions. The data (2048 points) for the FFT analysis use the last cycle (steady state) of the time series, C_p data. In this approach, any subharmonics created during the transient stage are not included in the spectral analysis. The Fourier transform (Newland, 1975) is given by

$$\tilde{G} = \frac{1}{N} \sum_{r=0}^{r=N-1} g_r e^{-i\left(\frac{2\pi \mathrm{kr}}{\mathrm{N}}\right)},\ k = 0, 1, 2 \ldots.(N-1) \tag{7}$$

where g_r, $r = 0, 1, 2, \ldots.(N-1)$ is a series of discrete functional values of a function g equally spaced in time t such that $T = Ndt$ where T is the period, N is the number of equally spaced time intervals of the period and dt is the time interval. Thus modulus of $\tilde{G}$ (e.g., $|\tilde{G}|$) gives the spectral amplitude at various discrete frequencies.

Model Testing and Sensitivity Analysis

The numerical model has been tested against Blasius flow over a flat plate, cavity flow, and oscillatory flow in a channel with wavy walls. In each case the model predictions compared well with available analytic solutions, other numerical solutions or experimental observations. These applications are described in detail in Venkat (1991) and Venkat and Spaulding (1991). The problem of interest is to simulate the laminar flow over a flat plate, a section of which is subjected to vibratory motion. Before modeling the vibratory problem, the steady flow over a sinusoidal bump with an amplitude equal to the maximum amplitude of vibration under study was tested to characterize the impact of grid resolution and the size of the computational domain on the predicted results (Venkat, 1991).

The model was first tested for the influence of the location of up and downstream (sections FA and ED) and free-stream boundaries (section FE) on the numerical results. After some trial runs, the up and downstream boundaries were located 8 bump lengths away from the bump such that the deviation in C_f values between the Blasius solution and the model prediction at the downstream boundary was less than 2%. Similarly, the top boundary was located 6 bump lengths away from the body surface such that there was no influence of the boundary on the model predicted results.

Next the impact of the bump grid resolution in the x direction on the model predictions was analyzed. This was achieved by progressively increasing the number of grids on the bump. For each test run, the model predicted $C_f \sqrt{\mathrm{Re}}$ at the maximum bump amplitude position ($x = 8.25$) versus dy/dx ratio was plotted, where dx is the grid size in the x direction on the bump and dy is the grid size between the bump and the $\eta = 2$ line. This is shown in Fig. 4. As dy/dx increases (grid resolution in x increases) the skin friction coefficient at the bump decreases and reaches an asymptote around $dy/dx = 2.0$. This value of dy/dx was chosen for the subsequent grid spacing in the x-direction on the bump.

Finally, the number of grids on either side of the bump in the x-direction were decreased to determine the minimum number of grids while still maintaining an accurate solution. This ultimately decreases the computational time. The final grid domain (61×41) is shown in Fig. 3. Similar analysis is performed for unsteady flow over a vibrating plate. Uncertainties in the numerical results were estimated by comparing computations using different mesh sizes (81×51, 71×51, 61×51, 61×41). A detailed description of the sensitivity analysis is given in Venkat (1991).

Results and Discussions

The goal of the present work is to understand the influence of plate vibration amplitude on the flow while maintaining the Reynolds number at a fixed value. It was shown earlier (Venkat and Spaulding, 1991) that the nonlinear properties of the external flow are controlled by the term $v(\partial u/\partial y)$ at the plate surface. The velocity normal to the plate v is directly propor-

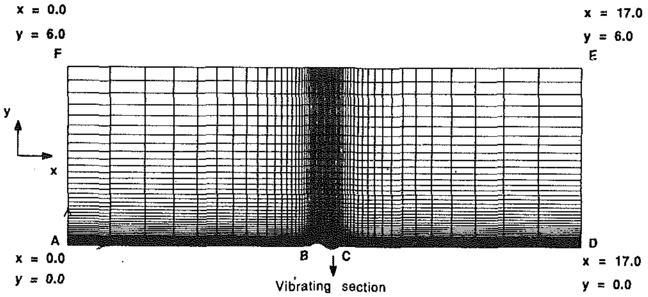

Fig. 3 61 × 41 grid domain for simulating viscous flow over the vibrating plate

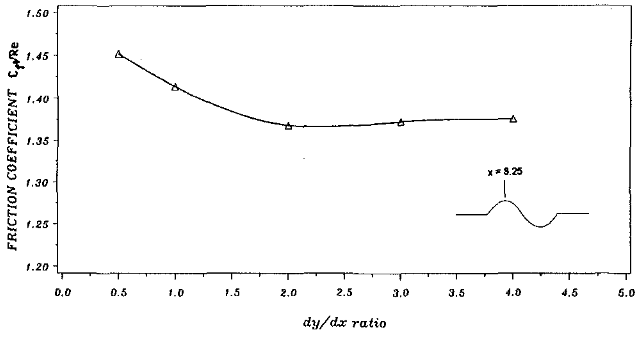

Re = 1000 Mode = 2 Ho = 0.15

Fig. 4 Variation of $C_f\sqrt{Re}$ with dy/dx ratio at x = 8.25

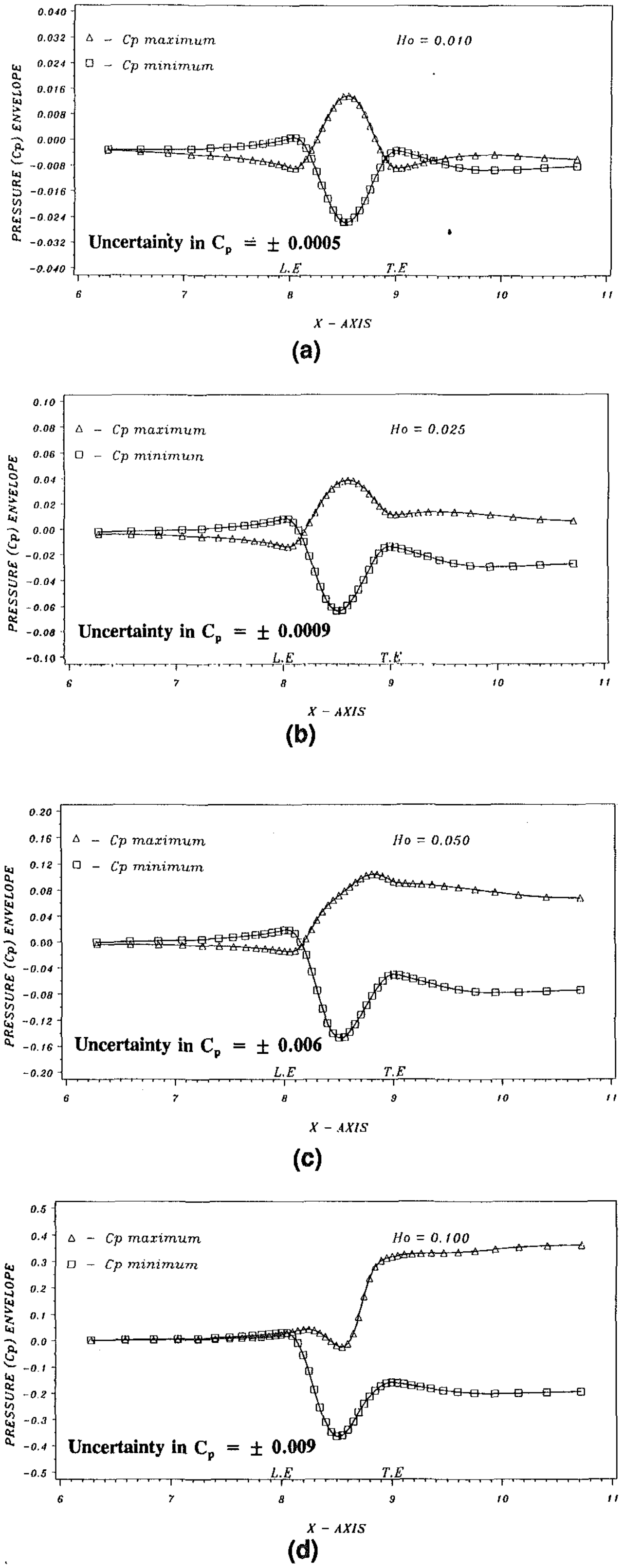

Fig. 5 Variation of pressure coefficient along the vibrating plate for different vibration amplitudes at Re = 1000, n = 2, and St = 0.25

tional to the frequency of oscillation of the body (Strouhal number) while the gradient of u in the y direction on the body surface ($\partial u/\partial y$) is controlled by the Reynolds number of the flow and the body vibration mode and amplitude. By varying the vibration amplitude both terms of the convective acceleration component of the flow momentum balance are affected. In the present study the nonlinear behavior of the external flow is analyzed in the range of $0.0<H_0<0.1$ while maintaining the Strouhal number, St at low (St = 0.25) value. The Reynolds number, Re, is fixed at 1000. The Reynolds number based on distance from the leading edge of the plate (point A in Fig. 2(a)) to the leading edge of the vibrating section (point B in Fig. 2(a), x_{LE} = 9.0), Re, is 9000. This gives a boundary layer thickness (δ_{LE}) to vibrating plate length ratio of 0.4743 at the leading edge of the vibrating section and hence the boundary layer is relatively thick compared to the plate length.

Low Frequency of Vibration (St = 0.25). The flexible section of the plate is forced to vibrate as shown in Fig. 2(a). The Strouhal number, St, is fixed at 0.25. The plate therefore vibrates slowly compared to the advective time scale of the free-stream flow. The value of H_0/δ_{LE} varies from 0 to 0.21 ($0<H_0<0.1$). The boundary layer is hence quite thick over the vibrating section and the shear rate relatively low. Simulations are run until the predicted flow field is in steady state, defined by comparing one plate vibration cycle to the next. The pressure envelope, defined as the maximum and minimum predicted pressure versus x for H_0 = 0.01 is shown in Fig. 5(a). The pressure coefficient, C_p, maximum decreases gradually until x = 8 and then increases significantly until x = 8.5. It then decreases until x = 9 and shows a gradual increase until x = 10 and becomes constant for the remaining portion of the plate. The opposite is observed for C_p minimum. Since the amplitude of vibration is small, the rate of change of shear stress along the vibrating section in the x direction is also small. The shear stress magnitude follows the deflection of the plate with little spatial shift. The uncertainty in C_p is +0.0005. When the amplitude is increased to 0.025 (Fig. 5(b)), the C_p maximum (minimum) curve increases (decreases) until x = 8.5, decreases (increases) until x = 9.0, and ultimately reaches a steady small value downstream. This happens because the C_t

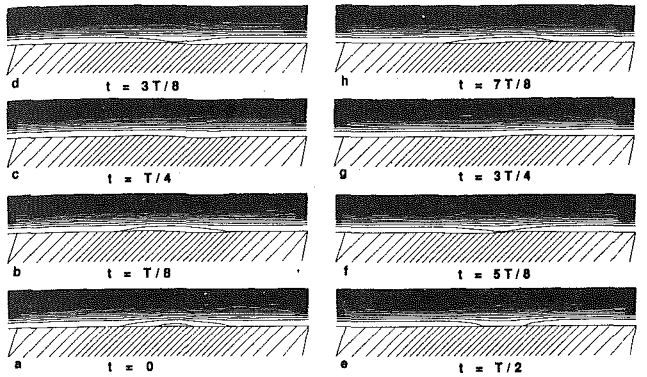

Fig. 6 Contour plot of stream function in the vicinity of the vibrating section of the plate for one complete cycle of vibration at T/8 time intervals for Re = 1000, n = 2, St = 0.25, and H_0 = 0.01

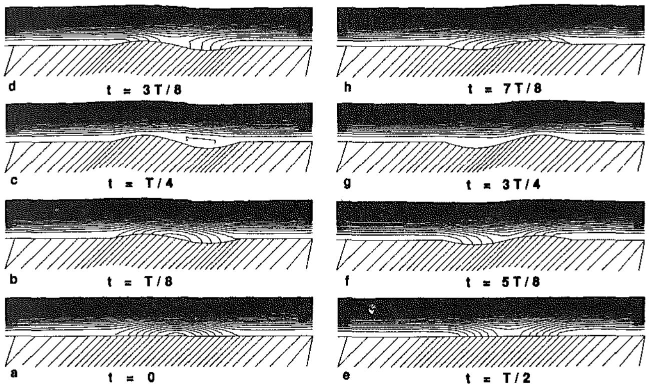

Fig. 7 Contour plot of stream function in the vicinity of the vibrating section of the plate for one complete cycle of vibration at T/8 time intervals for Re = 1000, n = 2, St = 0.25, and H_0 = 0.050

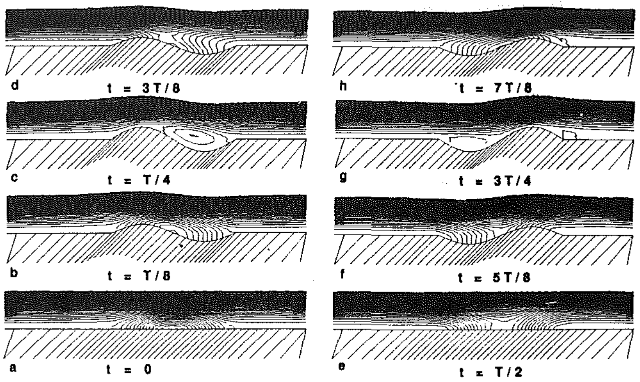

Fig. 8 Contour plot of stream function in the vicinity of the vibrating section of the plate for one complete cycle of vibration at T/8 time intervals for Re = 1000, n = 2, St = 0.25, and H_0, = 0.100

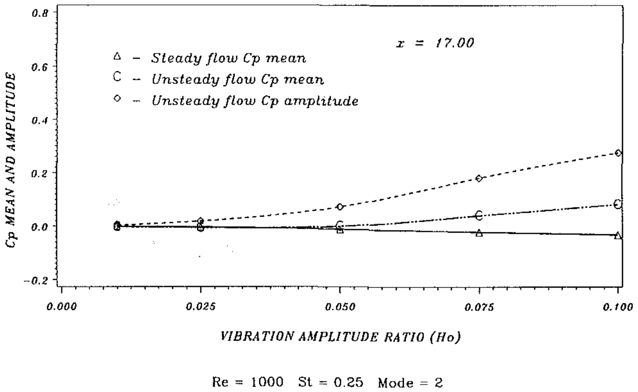

Fig. 9 Variation of mean and amplitude of downstream (x = 17.0) pressure wave with plate vibration amplitude for Re = 1000, n = 2, and St = 0.25

versus x curve deviates from the shape of the vibrating section as H_0 increases. The uncertainty in the predicted C_p for this amplitude is +0.0009. As the amplitude is increased further, the C_p envelope increases at the trailing edge of the vibrating section ($x > 0.9$) and reaches an increasingly larger constant value downstream. This is clearly shown in Figs. 5(c) and 5(d) for $H_0 = 0.05$ and 0.10, respectively. The corresponding C_p error estimates for $H_0 = 0.05$ and 0.10 are +0.006 and +0.009, respectively.

The increase in the pressure envelope range with vibration amplitude can be explained by analyzing the stream function plot for one complete plate oscillation at T/8 time intervals for various H_0. They are shown in Figs. 6, 7, and 8 for H_0 = 0.01, 0.05 and 0.10 cases, respectively. At $t = 0$ (Fig. 6(a)), the upward moving fluid on the first half of the vibrating section of the plate forms a small recirculation zone with the downward moving fluid on the second half of the vibrating section. As described in Venkat and Spaulding (1991), this recirculation zone creates a small pseudo-surface displacement in the vicinity of the vibrating section. The incoming flow is deflected very little because of the limited extent of this recirculation zone. The up and downstream influence due to the oscillating fluid is minimal. The small recirculation zone resembles a half sine wave ($n = 1$) with a very small amplitude (Fig. 6(a)). The fluid is also deflected in the same half sine shape and hence the increase (decrease) and the corresponding decrease (increase) in the C_p maximum (minimum) curve for $H_0 = 0.01$ (Fig. 5(a)). When the plate moves to the T/8 position, in addition to the plate velocity the plate deflection also disturbs the incoming fluid. Since the plate vibration amplitude is very small its influence is barely seen in Fig. 6(b). As the plate reaches the T/4 position (maximum displacement, zero vibration velocity), the flow remains attached to the plate (Fig. 6(c)). When the plate moves into the second quarter time period, very little incoming fluid moves into or out of the vibrating section (Figs. 6(d) and 6(e)). As the plate moves to the end of the third quarter time period, the flow again follows the plate geometry (Fig. 6(g)). In the fourth quarter, the fluid is pushed upward on the first half and pulled downward on the second half of the vibrating section. These movements create a recirculation cell similar to the $t = 0$ case. The flow pattern described above repeats for subsequent cycles. With increasing vibration amplitude the cell size at $t = 0$ increases (Fig. 7(a), $H_0 = 0.05$ and Fig. 8(a), $H_0 = 0.10$). The pressure coefficient increases correspondingly (Figs. 5(c) and 5(d)). At t = T/4, at high vibration amplitude ($H_0 > 0.05$), the flow separates from the plate and forms a separation bubble on the second half of the vibrating section (Fig. 7(c)). As expected, the size of the separation bubble increases with increasing vibration amplitude (compare $H_0 = 0.05$, Fig. 7(c) to $H_0 = 0.10$, Fig. 8(c)). As the plate moves to the second quarter time period (T/4 < t < T/2), unlike the low H_0 case, fluid near the vibrating section is disturbed (Figs. 7(d) and 8(d)). The incoming fluid is drawn into the low pressure region created by the downward motion of the first half of the plate whereas the upward motion of the later half of the plate displaces fluid normal to the plate which is eventually advected downstream (Figs. 7(e) to 7(f) and 8(e) to 8(f)). During the third quarter time period (t = 3T/4) the flow separates at the leading edge of the plate. The trough separation bubble size increases (Figs. 7(g) and 8(g)) with increasing H_0. In addition, a small separation bubble is created near the trailing edge of the vibrating plate for the highest amplitude case ($H_0 = 0.1$, Fig. 8(g)). These flow patterns show that the formation of

Table 1 Mean and amplitude of downstream pressure wave at x = 17.00 for various vibration amplitudes (x = 17, Re = 1000, n = 2, St = 0.25)

Strouhal Number	Vibration Amplitude	C_p Maximum	C_p Minimum	C_p Mean	C_p Amplitude
	0.010	-0.0055	-0.0115	-0.0085	0.0030
	0.025	0.0123	-0.0250	-0.0064	0.0187
0.250	0.050	0.0721	-0.0733	-0.0006	0.0727
	0.075	0.2020	-0.1412	0.0303	0.1716
	0.100	0.3555	-0.1937	0.0807	0.2744

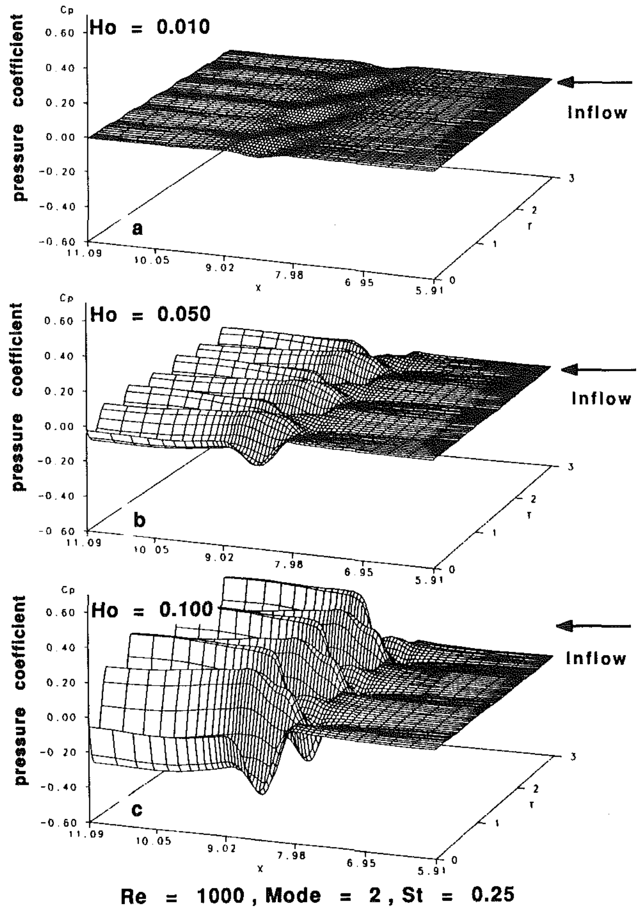

Fig. 10 Variation of pressure coefficient along the vibrating plate as a function of time for Re = 1000, n = 2, St = 0.25 and H_0 = 0.01, 0.050, and 0.100

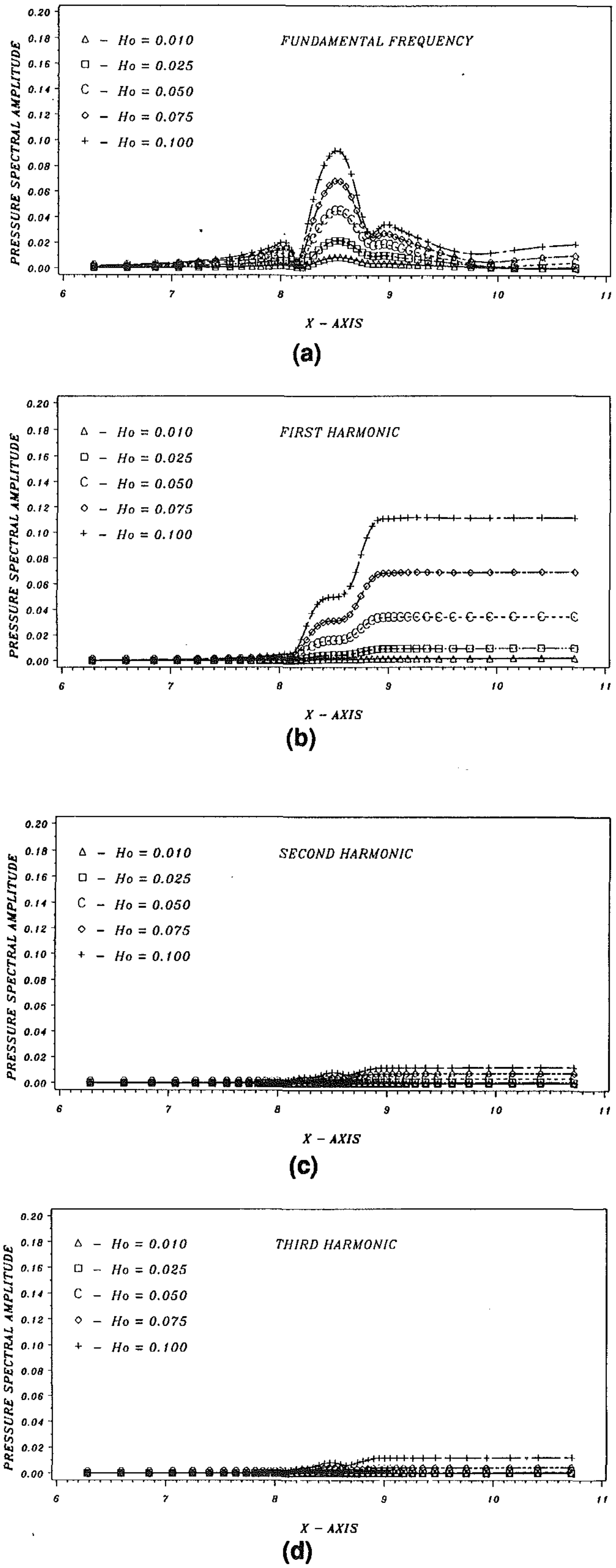

Fig. 11 Variation of pressure spectral amplitude of different frequencies along the vibrating plate for various vibration amplitudes at Re = 1000, n = 2, and St = 0.25

separation bubbles and the pseudo-surface displacement due to recirculation zones become significant with increasing vibration amplitude. This ulitmately increases the magnitude of the pressure and pressure envelope along the plate as shown in Fig. 5. The variation of the mean pressure and its amplitude with vibration amplitude at the downstream boundary is shown in Fig. 9 and Table 1. For low vibration amplitudes ($H_0 < 0.025$) the mean and the amplitude of the pressure wave varies linearly with vibration amplitude. This is due to the limited vertical advection of the fluid by the plate and the absence of flow separation at low and medium amplitudes. As the amplitude is increased further, the mean pressure and its vibration amplitude increase substantially due to the strong gradients in the C_f versus x curve (Venkat, 1991) on the vibrating plate.

The variation of pressure coefficient along the vibrating plate as a function of distance and time is shown in Figs. 10(a), 10(b), and 10(c) for H_0 = 0.01, 0.050 and 0.10, respectively. At a fixed time, the pressure behaves monotonically downstream of the vibrating section. The downstream behavior appears to be consistent with a line of dipoles distributed along the wall. The downstream pressure amplitude increases rapidly with increasing plate vibration amplitude. Upstream propagation of pressure perturbations are limited to approximately

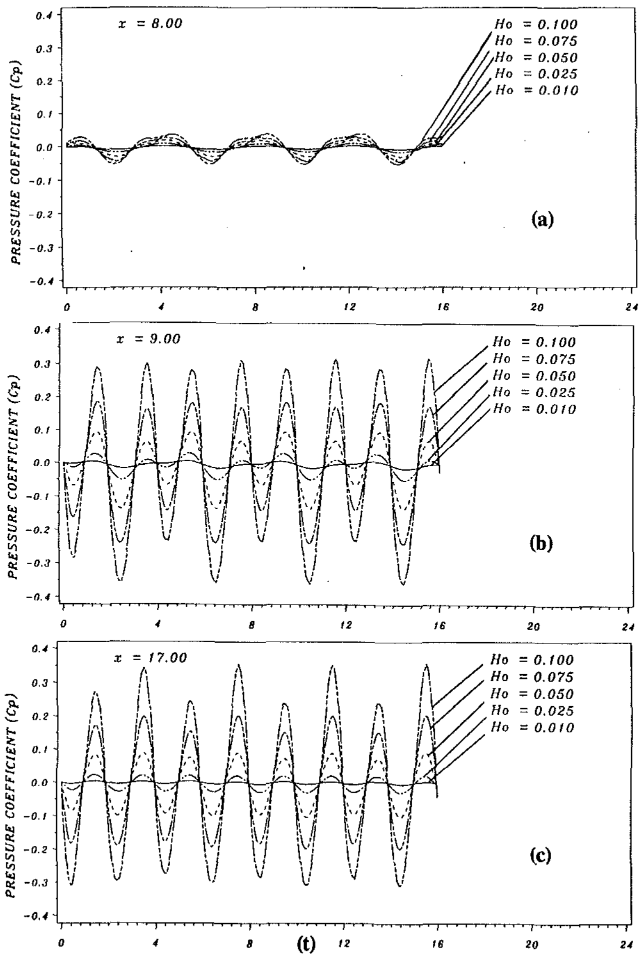

Fig. 12 Time series plot of pressure coefficient at the leading edge (x = 8.0), trailing edge (x = 9.0) and far downstream (x = 17.0) for various vibration amplitude at Re = 1000, n = 2 and St = 0.25

one vibrating plate length. A check was made to ensure that there were no Tollmein-Schlichting (T-S) waves generated by the vibrating section. The flow conditions for Re = 1000 and St = 0.25 are located well within the stable region of the stability diagram (based on linear stability theory) given in Fasel (1980), thus indicating no T-S waves are generated by the vibrating section.

The frequency characteristics of the propagating pressure wave were analyzed using Fast Fourier Transform techniques (Newland, 1975). The pressure spectral amplitude at zero, fundamental and higher harmonics are obtained from the FFT of C_p data at various plate locations. The pressure spectral amplitude at the fundamental frequency versus along plate distance, x, is shown in Fig. 11(a) for various H_0. The spectral amplitude generally increases until x = 8.5 (plate midpoint) and then decreases in the same way for the rest of the plate for H_0 = 0.01. The maximum spectral amplitude is slightly less than 0.01 for H_0 = 0.01. This shows that the response of the fluid to low amplitude vibrations is purely linear and controlled by the plate vibration amplitude. As H_0 is increased to 0.025, the trend of the fundamental frequency spectral amplitude versus x curve is similar to the H_0 = 0.01 result. However, its magnitude over the vibrating section and downstream increases due to the addition of significant energy from the vibrating plate. For high amplitudes (H_0 = 0.10) the fundamental spectral amplitude increases until x = 8.5 similar to previous cases and then decreases to a finite value downstream of the trailing edge. This occurs because the C_p envelope attains a steady value downstream for high amplitudes (Fig. 5) due to nonlinear interactions between the plate and the flow. The spectral amplitude of the first harmonic versus x is shown in Fig. 11(b). For low amplitude vibrations, is linearly related to the plate deflection. Nonlinear energy transfer due to the v $(\partial u/\partial y)$ term is very small and hence the first harmonic spectral amplitude is very small (almost zero) at low vibration amplitude. As the vibration amplitude increases, the nonlinear transfer of energy from the plate to the flow increases. Ultimately, this increases the first harmonic amplitude for medium and high H_0. The first harmonic amplitude increases with x starting near the leading edge of the plate. It remains approximately constant in the vicinity of the plate midpoint and then increases at the same rate as for the first half of the plate for the rest of the vibrating section. Downstream of the trailing edge of the plate the pressure amplitude remains constant. The amplitude increases with increasing H_0. Although there is some energy transfer to higher harmonics, the spectral amplitudes for the second and third harmonics are small for all amplitudes (Figs. 11(c) and 11(d)). The basic pattern is the same as for the first harmonic.

The time series plot of C_p and the corresponding pressure spectrum at x = 8.0, 9.0 and 17.0 are shown in Figs. 12 and 13, respectively. At the leading edge of the plate (x = 8.0), C_p oscillates with time and the oscillation amplitude increases with increasing H_0. The nonsinuous behavior and phase shift in the C_p versus t curve, are predominant for high H_0 (Fig. 12(a)). The corresponding pressure spectrum is shown in Fig. 13(a). It has a peak at the input frequency and its spectral magnitude at the input frequency increases with increasing H_0. Spectral peak at the first harmonic appears for $H_0 > 0.075$. C_p versus t at the trailing edge is shown in Fig. 12(b). C_p oscillations are larger than the corresponding leading edge results and its amplitude increases considerably with increasing H_0. Its pressure spectrum has large peaks at the fundamental, first and other higher harmonics compared to leading edge results. It is interesting to note that for $H_0 > 0.025$, the pressure spectral magnitude at the first harmonic is higher than that of the input frequency. At the downstream end (x = 17.0), all the energy is in the first harmonic for $H_0 < 0.05$. This is clearly seen in Fig. 13(c). For large H_0, energy is partitioned in both the fundamental and first harmonic, similar to Fig. 13(b). The spectral peak at the input frequency is smaller than the corresponding trailing edge results. The corresponding C_p versus t is shown in Fig. 12(c).

Conclusion

Based on the above simulations and discussion we conclude the following.

1) Low amplitude ratio ($H_0 < 0.025$):

The external flow senses the disturbance only at the vibrating section. Energy is added to the fluid at the input frequency on the first half and removed at the same frequency on the later half of the vibrating section. This behavior is similar to the potential flow analysis for small amplitude and frequency vibrations. There is little upstream and downstream influence of the disturbance observed in the external flow. The maximum pressure spectral amplitude at the input frequency is approximately equal to the body vibration amplitude. The external flow is controlled by the plate vibration amplitude. Energy transfer to higher harmonics is very small and the flow response is linearly related to the disturbance.

2) High amplitude ratio ($H_0 > 0.050$):

Nonlinear energy transfer takes place in the vicinity of the vibrating section and hence generates a first harmonic in the pressure wave at high amplitude ratios. Although there is evidence of nonlinearity in the external flow it is not strong enough to create higher harmonics. The upstream influence is minimal.

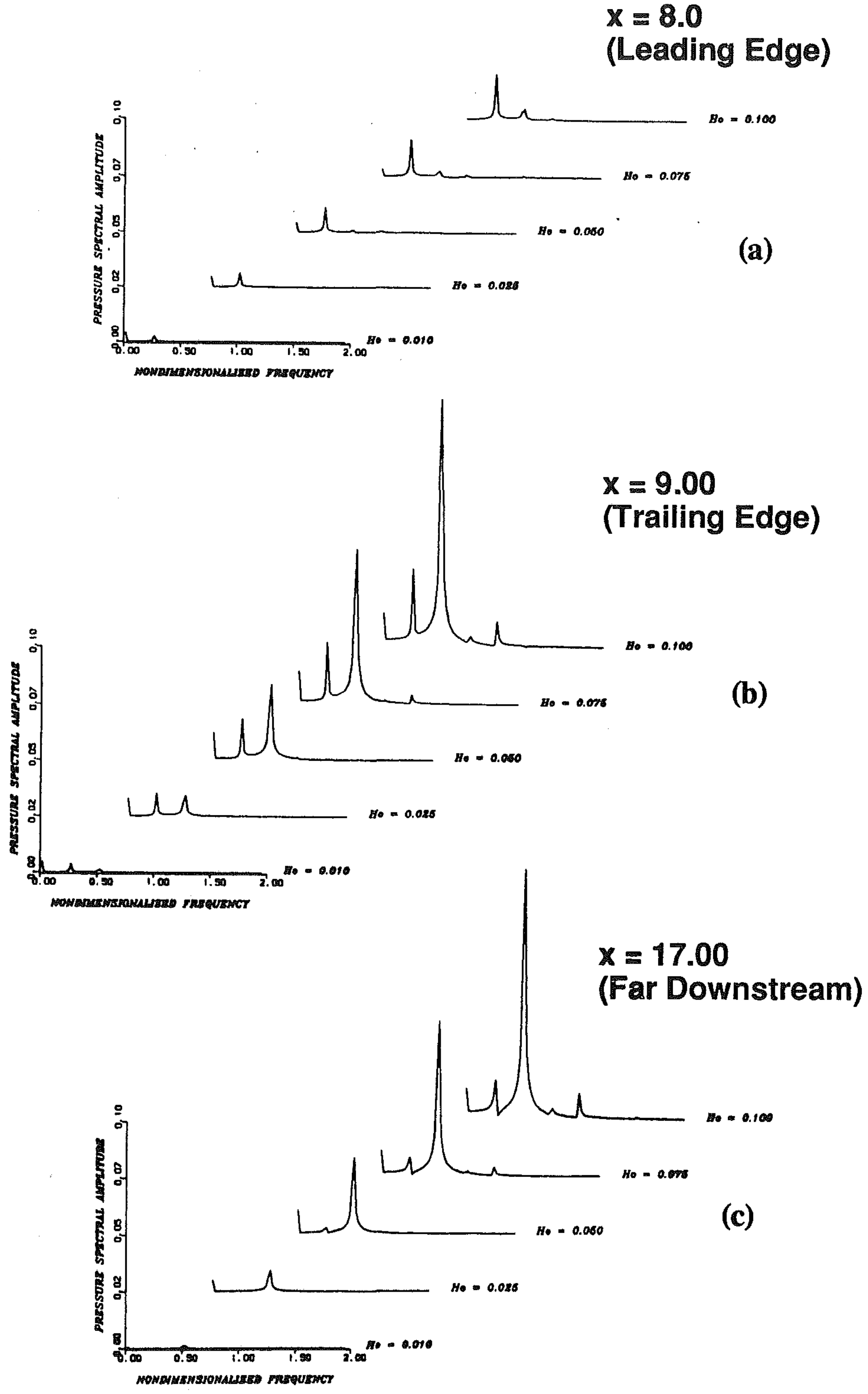

Fig. 13 Pressure spectrum at the leading edge (x = 8.0), trailing edge (x = 9.0) and far downstream (x = 17.0) for various vibration amplitudes at Re = 1000, n = 2 and St = 0.25

There is however considerable downstream influence in the external flow generated by the vibrating plate.

Acknowledgment

This research work was funded by the Office of Naval Research under contract no: 535413. The authors are thankful to the reviewers whose comments were useful in revising this manuscript. The first author would like to thank Prof. Frank White for his helpful comments.

References

Blevins, R. D., 1977, *Flow-Induced Vibrations*, Van Nostrand Reinhold, New York, NY.

Bringen, S. H., and McMillan, O. J., 1980, "Calculation of Two Dimensional

Inlet Flow Fields in a Supersonic Free Stream—Program Documentation and Test Cases," NASA CP-3221.

Curle, N., 1955, "The Influence of Solid Boundaries upon Aerodynamic Sound," *Proceedings of the Royal Society of London*, Series A, Vol. 231, pp. 505-514.

Fasel, H., 1980, "Recent Developments in the Numerical Solution of the Navier-Stokes Equations and Hydrodynamic Stability Problems," *Computational Fluid Dynamics*, McGraw-Hill, New York, NY, pp. 168-279.

Fletcher, C. A. J., 1988, *Computational Fluid Dynamics*, Vol. I and II, Springer-Verlag, New York, NY.

Goldstein, M. E., 1974, *Aeroacoustics*, NASA SP-346.

Halim, Ahmad, A. M., 1986, "Development of an Iterative Boundary Layer Type Solver for Axisymmetric Separated Flow," *AIAA Journal*, Vol. 24, No. 8, pp. 1298-1304.

Napolitano, M., and Walters, R. W., 1986, "An Incremental Block Line Gauss Seidal Method for the Navier-Stokes Equations," *AIAA Journal*, Vol. 24, No. 5, pp. 770-776.

Newland, D. E., *An Introduction to Random Vibrations and Spectra Analysis*, Longman Group Ltd., New York, 1975.

Peyret, P., and Taylor, T., 1983, *Computational Methods for Fluid Flow*, Springer-Verlag, New York, NY.

Roache, P. J., 1972, *Computational Fluid Dynamics*, Hermosa Publishing, Albuquerque, NM.

Telinois, D. P., 1981, *Unsteady Viscous Flows*, Springer Series in Computational Physics, Springer-Verlag, New York, NY.

Thompson, J. F., *Numerical Grid Generation*, North-Holland, 1982.

Venkat, N. K., 1991, "Numerical Simulation of Planar and Axisymmetric Unsteady Laminar Flow Over Vibrating Bodies," Ph.D. dissertation, Department of Ocean Engineering, The University of Rhode Island, Kingston, R.I., Jan.

Venkat, N. K., and Spaulding, M., 1991, "A Model to Predict the Nonlinear Response of Laminar Flow over Vibrating Bodies," ASME JOURNAL OF FLUIDS ENGINEERING, Vol. 113, No. 4, pp. 544-554, Dec.

White, F. M., 1991, *Viscous Fluid Flow*, McGraw-Hill, New York, NY.

G. A. Schohl
Senior Civil Engineer,
Engineering Laboratory,
Tennessee Valley Authority,
Norris, TN 37828

Improved Approximate Method for Simulating Frequency-Dependent Friction in Transient Laminar Flow

A new approximation to the weighting function in Zielke's (1967) equation is used in an improved implementation of Trikha's (1975) method for including frequency-dependent friction in transient laminar flow calculations. The new, five-term approximation was fitted to the weighting function using a nonlinear least squares approach. Transient results obtained using the new approximating function are nearly indistinguishable from results obtained using the exact expression for the weighting function.

Introduction

Wall shear stress in transient pipe flow varies both with instantaneous mean velocity and with rate-of-change of velocity, or frequency content of the velocity variation with time. For turbulent flow, the frequency dependence of shear stress is generally unpredictable with present methods. For laminar flow, however, solutions to the axisymmetric Navier-Stokes equations have provided methods for modeling the frequency dependence of shear stress. These solutions include Laplace transform techniques (e.g., Brown, 1962), which provide elegant solutions apparently restricted to relatively simple pipe systems, and the impulse-response technique (Suo and Wylie, 1989), which is, in principle, applicable to complex pipe networks. Compared with these approaches, the method introduced by Zielke (1967) for including frequency-dependent friction in finite difference calculations is undoubtedly the most straightforward to apply to complex networks with nonlinear boundary conditions. However, strict application of Zielke's method requires storage of all velocities computed at previous time steps at all computational points in order to evaluate an integral term involving weighted past velocity changes. Both the computer storage and the computational time required to evaluate this integral increase with simulation time which, for complex networks, discourages use of the method, or makes its use impracticable. Trikha (1975) and Suzuki et al. (1991) have devised approaches for reducing the computer resource requirements of Zielke's method. The approach of Suzuki et al. is the most accurate, but the approach of Trikha is the most efficient and simple.

In the present work, which was motivated by a desire to simulate pressure transients in pressure sensing lines (Schohl et al., 1987), Trikha's approach is improved. The improved approximate method provides results that are, for practical purposes, as accurate as the results obtained by Suzuki et al., and yet retains the same efficiency and simplicity as Trikha's original method.

One-Dimensional Equations for Transient Pipe Flow

The simplified continuity and momentum equations that are solved to compute one-dimensional unsteady flow in pipes (Wylie and Streeter, 1978) are

$$\frac{\partial H}{\partial t}+\frac{a^2}{g}\frac{\partial V}{\partial x}=0 \tag{1}$$

$$\frac{\partial V}{\partial t}+g\frac{\partial H}{\partial x}+\frac{4\tau_o}{\rho D}=0 \tag{2}$$

in which H = piezometric head, V = cross-sectional average velocity, t = time, x = longitudinal coordinate, a = acoustic wavespeed, g = acceleration of gravity, D = pipe diameter, τ_o = wall shear stress, and ρ = fluid density. Piezometric head, H, refers to the quantity $(p/\rho g + z)$ in which p = pressure and z = elevation.

Finite difference solutions of Eqs. (1) and (2), such as the method of characteristics (Wylie and Streeter, 1978) or the four-point, weighted implicit method, which is often referred to as Priessmann's scheme (Cunge et al., 1980), provide the ability to compute transient flow in networks of arbitrary complexity which have nonlinear boundary conditions. In these solutions, transient shear stress traditionally is represented by functions of the instantaneous mean velocity that are strictly valid only for steady flow. This approximation can be avoided for laminar flow by substituting Zielke's equation for frequency-dependent shear stress for τ_o in Eq. (2).

Zielke's (1967) Equation for Shear Stress

From the equation of motion for axisymmetric laminar flow of an incompressible fluid, Zielke derived the following equation relating wall shear stress in transient laminar pipe flow to instantaneous mean velocity and weighted past velocity changes:

$$\tau_o(x,t)=\frac{8\rho\nu}{D}\left[V(x,t)+\frac{1}{2}\int_o^t\frac{\partial V}{\partial u}W(t-u)du\right] \tag{3}$$

in which ν = fluid kinematic viscosity, W = a weighting function, and u = variable of integration. The weighting func-

---

Contributed by the Fluids Engineering Division for publication in the JOURNAL OF FLUIDS ENGINEERING. Manuscript received by the Fluids Engineering Division June 26, 1992; revised manuscript received November 2, 1992. Associate Technical Editor: R. L. Panton.

tion, $W(t)$, is expressed in terms of dimensionless time, τ, defined by

$$\tau = \frac{t}{T} \tag{4}$$

in which T, a time scale for cross-sectional mixing of laminar momentum, is defined as

$$T = \frac{D^2}{4\nu} \tag{5}$$

For $\tau \geq 0.02$, $W(t) \approx W_1(\tau)$ where

$$W_1(\tau) = e^{-26.3744\tau} + e^{-70.8493\tau} + e^{-135.0198\tau} + e^{-218.9216\tau} + e^{-322.5544\tau} \tag{6}$$

For $\tau > 0$ but ≤ 0.02, $W(t) \approx W_2(\tau)$ where

$$W_2(\tau) = 0.282095\tau^{-1/2} - 1.25 + 1.057855\tau^{1/2} + 0.9375\tau + 0.396696\tau^{3/2} - 0.351563\tau^2 \tag{7}$$

The weighting function W is expressed as approximately equal to W_1 and W_2 because insignificant terms in the infinite series that exactly represent W_1 and W_2 have been truncated in Eqs. (6) and (7). Using the method of characteristics with Eq. (3) representing shear stress, Zielke obtained results that agreed remarkably well with the experimental data of Holmboe and Rouleau (1967). The agreement was particularly good when compared with results obtained using the usual steady-state formulation for wall shear stress ($W = 0$ in Eq. (3)).

For numerical solution of Eq. (3), storage of all computed past velocities, or velocity changes, are required in order to evaluate the integral. At each time, t, values of $\partial V/\partial u$ at each past time are multiplied by corresponding values of $W(t-u)$ and time step size, Δt. The sum of these products for all past time steps approximates the integral. The sum cannot simply be accumulated with time because the values of $W(t-u)$ corresponding to each value of $\partial V/\partial u$ change with every change in time, t.

Method of Suzuki et al. (1991)

The method for numerical solution of Eq. (3) of Suzuki et al., which involves no additional approximations, is significantly more efficient than Zielke's original method. For $\tau > 0.02$, substitution of Eqs. (6) and (7) expand Eq. (3) as follows:

$$\tau_o(x,t) = \frac{8\rho\nu}{D}\left\{V(x,t) + \frac{1}{2}\int_0^{(t-0.02T)} \frac{\partial V}{\partial u} W_1[(t-u)/T]du + \frac{1}{2}\int_{(t-0.02T)}^{t} \frac{\partial V}{\partial u} W_2[(t-u)/T]du\right\} \tag{8}$$

The function W_1 is a sum of exponential terms, which may be expressed as

$$W_1(\tau) = \sum_{i=1}^{5} e^{-c_i\tau} \tag{9}$$

in which c_i = coefficients multiplying τ in Eq. (6). Substitution of Eq. (9) permits W_1 in Eq. (8) to be expressed as a function of time, t, times a function of the integration variable, u:

$$\tau_o(x,t) = \frac{8\rho\nu}{D}\left\{V(x,t) + \frac{1}{2}\sum_{i=1}^{5}\left[e^{-c_i t/T}\int_0^{(t-0.02T)} \frac{\partial V}{\partial u} e^{c_i u/T}du\right] + \frac{1}{2}\int_{(t-0.02T)}^{t} \frac{\partial V}{\partial u} W_2[(t-u)/T]du\right\} \tag{10}$$

In Eq. (10), the integrand in the first integral is a function of u only. Because its integrand no longer depends on t, the first integral may be evaluated numerically by accumulating a sum for each value of the sum index, i. The second integral still requires storage of computed past velocity changes and complete reevaluation at each time, t, but only for times greater than $(t - 0.02T)$, rather than for all past times. A disadvantage of this approach, compared with Trikha's method below, is that the number of past velocity changes that it is necessary to save, and the computer time required to evaluate the integral, varies with the parameters D (pipe diameter), ν (kinematic viscosity), and Δt (time step size) defining the time scale T. Under all conditions, the required computer storage and time exceed the requirements of Trikha's method.

Method of Trikha (1975)

Trikha eliminated the requirements of saving multiple past velocity changes and completely reevaluating the integral in Eq. (3) by approximating the weighting function, W, for all values of τ by the sum of three exponential terms as follows:

$$W(t) \approx W_{\text{app}}(\tau) = \sum_{i=1}^{3} m_i e^{-n_i\tau} \tag{11}$$

The coefficients m_i and n_i were determined by fitting Eq. (11) to the curve defined by Eqs. (6) and (7) according to the following criteria:

$$(a)\quad \int_0^\infty W_{\text{app}}(\tau)d\tau = \int_0^\infty W(t)dt$$

$$(b)\quad W_{\text{app}}(\tau) = W(t) \text{ at } \tau \approx 0.0001,\ 0.001, \text{ and } 0.01$$

$$(c)\quad |[W_{\text{app}}(\tau) - W(t)]/W(t)| < 0.02 \text{ for } \tau > 0.1 \tag{12}$$

The following solution was found for $W_{\text{app}}(\tau)$:

$$W_{\text{app}}(\tau) = 40.0e^{-8000\tau} + 8.1e^{-200\tau} + e^{-26.4\tau} \tag{13}$$

Using this approximation for $W(t)$, the integral in Eq. (3) takes the same form as the first integral term in Eq. (10). The

Nomenclature

a = acoustic wavespeed
c_i = ith coefficient multiplying τ in W_1
D = pipe diameter
g = acceleration of gravity
H = piezometric head ($p/\rho g + z$)
H_0 = fixed upstream piezometric head
L = pipe length
m_i = ith coefficient in exponential sum
n_i = ith coefficient multiplying τ in exponential sum
N = number of sample points for curve fit
p = pressure
t = time
Δt = time step size
T = time scale ($D^2/4\nu$)
u = variable of integration
V = cross-sectional average velocity
V_0 = initial, steady velocity
W = weighting function in Zielke's equation
W_{app} = Trikha's approximate weighting function
W_{new} = new approximate weighting function
W_1 = W for $\tau \geq 0.02$
W_2 = W for $\tau \leq 0.02$
x = longitudinal coordinate
y_{ij} = ith accumulated sum at point j
Δy_{ij} = ith incremental sum at point j
z = elevation
ν = fluid kinematic viscosity
ρ = fluid density
τ = dimensionless time
τ_0 = wall shear stress

integration in Eq. (3) is accomplished numerically by accumulating three sums, one for each exponential term, at each pipe computational section as the calculation moves forward in time. Details of the numerical implementation are provided in the following.

Improved Approximating Function

The following improved approximation to the weighting function, W, was determined by fitting the sum of five exponential functions to 143. sample values of W between $\tau = 0.00001$ and $\tau = 0.20$ using a nonlinear least squares approach:

$$W_{\text{new}}(\tau) = 1.051e^{-26.65\tau} + 2.358e^{-100\tau} + 9.021e^{-669.6\tau} + 29.47e^{-6497\tau} + 79.55e^{-57990\tau} \quad (14)$$

Equation (14) was obtained by minimizing a sum of squared relative errors expressed mathematically as follows:

$$\text{minimize} \sum_{i=1}^{N} \left(\frac{W_{\text{new}}(\tau_i) - W(t_i)}{W(t_i)} \right)^2 \quad (15)$$

in which $N = 143$. The ith error refers to the difference, for $\tau = \tau_i$, between the value of the weighting function predicted from Eq. (14) and the value predicted from Eqs. (6) and (7).

Figure 1 illustrates the agreement on a log-log scale of both Eqs. (13) and (14) with the sampled values from the weighting function defined by Eqs. (6) and (7). Equation (14) provides an excellent fit with the sampled points throughout the included range of τ values.

For values of τ greater than 0.2, which were not included in the least squares fitting and are not included in Fig. 1, Eqs. (13) and (14) both provide excellent fits to the weighting function. This agreement outside the fitted range of τ values is possible because the functions W_{app}, W_{new}, and W are all represented by sums of exponential terms for values of τ greater than 0.2.

For values of τ less than 0.00001, the fits to $W(t)$ provided by Eqs. (13) and (14) become progressively worse as τ is reduced. For small values of τ, $W(t)$ is represented by Eq. (6) which increases to infinity as τ is reduced to zero. The approximating functions, on the other hand, both asymptotically converge to maximum values equal to the sums (49.1 for W_{app} and 121.45 for W_{new}) of their m_i coefficients as τ is reduced to zero. For W_{app}, this behavior is evident for values of τ less than 0.0001 in Fig. 1.

Consequently, W_{new} should not be used to represent W for values of τ less than 0.00001, but this is of minor consequence in usual applications. Small values of τ correspond to small time intervals $(t - u)$ before the current computational time, t. Therefore, a lower limit on the value of τ imposes a lower limit on the size of the computational time step, Δt:

$$\Delta t_{\min} = \tau_{\min} T \quad (16)$$

in which $\tau_{\min}$ = minimum value of τ (0.00001) and $\Delta t_{\min}$ = minimum permissible time step. As an example, consider a 2-cm diameter pipe carrying oil with kinematic viscosity equal to 1×10^{-5} m^2/s. For $\tau_{\min} = 0.00001$, Eq. (16) specifies a minimum time step of 0.0001 seconds, a much smaller value than would normally be specified.

Two alternative approaches are proposed for cases in which time steps smaller than the minimum values imposed by Eq. (16) are required. The first approach is to determine an alternative approximating function, which would probably require more than five exponential terms, by extending the least squares fit to lower values of τ. The second approach is to use the method of Suzuki et al., except with W_{new} used for values of τ greater than 0.00001 and W_2 used for values of τ less than or equal to 0.00001.

Five is apparently the minimum number of summed exponential terms required to accurately fit the weighting function over a broad range of τ values. A three-term exponential sum fit to $W(t)$ using 76 sample points between $\tau = 0.00002$ and $\tau = 0.15$ represented the weighting function only marginally better than did Trikha's $W_{\text{app}}(\tau)$. The maximum difference between the least squares fit coefficients and Trikha's fit coefficients (Eq. (13)) was about 30 percent.

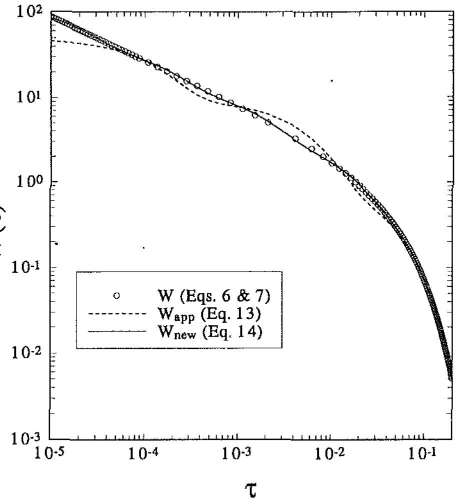

Fig. 1 Approximating functions compared with sample points from exact weighting function

Numerical Implementation

The numerical implementations of W_{new} and W_{app} are identical, except that W_{new} requires accumulation of five sums, rather than three, at each pipe computational section. In general, if $W(t)$ is approximated by a sum of k exponential terms in the form expressed by Eq. (11), the wall shear stress at computational point j at time t is

$$\tau_{oj}(t) = \frac{8\rho\nu}{D} \left[V_j(t) + \frac{1}{2} \sum_{i=1}^{k} m_i y_{ij}(t) \right] \quad (17)$$

In Eq. (17), $y_{ij}(t)$ is the ith accumulated sum at point j defined as

$$y_{ij}(t) = e^{-n_i t/T} \int_0^t \frac{\partial V_j}{\partial u} e^{n_i u/T} du \quad (18)$$

At time $t + \Delta t$, Eq. (18) becomes

$$y_{ij}(t+\Delta t) = e^{-n_i \Delta t/T} e^{-n_i t/T} \int_0^t \frac{\partial V_j}{\partial u} e^{n_i u/T} du + e^{-n_i (t+\Delta t)/T} \int_t^{(t+\Delta t)} \frac{\partial V_j}{\partial u} e^{n_i u/T} du \quad (19)$$

which, by comparison with Eq. (18) and definition of the incremental sum Δy_{ij}, can be rewritten as

$$y_{ij}(t+\Delta t) = e^{-n_i \Delta t/T} y_{ij}(t) + \Delta y_{ij}(t) \quad (20)$$

The incremental sum, equal to the second term on the right-hand side of Eq. (19), is evaluated by integration after assuming a linear variation of velocity, V, between time t and time $t + \Delta t$:

$$\Delta y_{ij}(t) \approx \frac{(1 - e^{-n_i \Delta t/T})}{n_i \Delta t/T} \left[V_j(t+\Delta t) - V_j(t) \right] \quad (21)$$

At the start of a numerical solution, the values of all sums, y_{ij}, are zero. At each subsequent time step, the values of the sums are updated as specified by Eq. (20) and the current values of frequency-dependent shear stress are evaluated using Eq. (17).

In Trikha's original presentation, an approximation for small Δt was made that is equivalent to approximating the quantity

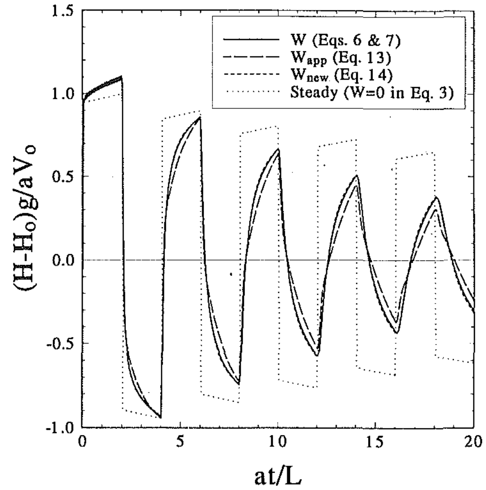

Fig. 2 Computed head fluctuation at downstream boundary of pipe

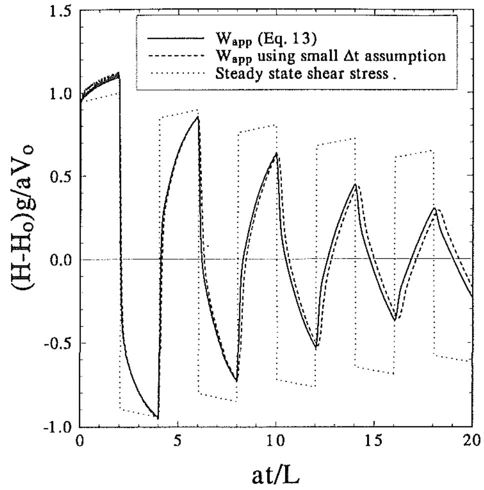

Fig. 4 Dispersive error resulting from small Δt assumption and use of W_{app}

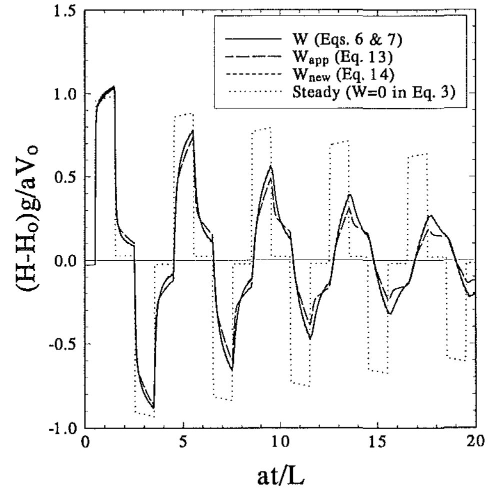

Fig. 3 Computed head fluctuation at midpoint of pipe

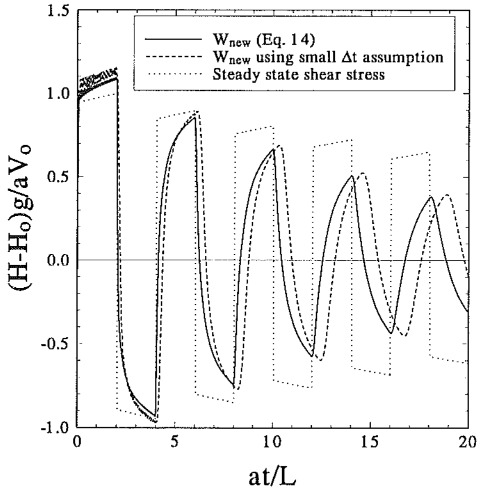

Fig. 5 Dispersive error resulting from small Δt assumption and use of W_{new}

$[1 - \exp(-n_i\Delta t/T)]/n_i(\Delta t/T)$ in Eq. (21) as equal to 1.0. However, as illustrated in the example below, this is a poor approximation that adds significant dispersive error to solutions. Furthermore, computational efficiency is only negligibly increased by this approximation because, unless the time step size is varied during a computation, for each value of i the quantity $[1 - \exp(-n_i\Delta t/T)]/n_i(\Delta t/T)$ is a constant that requires evaluation only at the beginning of the computation.

Comparisons

The experimental setup of Holmboe and Rouleau (1967) provides the standard example used for comparing frequency-dependent friction calculations. A reservoir with fixed piezometric head, H_o, supplies oil with kinematic viscosity of 3.97×10^5 m^2/s to a 36-m long, 2.54-cm diameter pipe bounded at its downstream end by a quick-closing valve. The acoustic wavespeed, a, through the oil within the pipe is about 1325 m/s. The initial velocity, V_o, of the oil is sufficiently small to ensure laminar flow. Following sudden closure of the downstream valve, the piezometric head is measured and recorded at the midpoint of the pipe and at the downstream boundary, just upstream from the valve.

Holmboe and Rouleau's experimental setup was simulated by solving Eqs. (1), (2), and (3) using the method of characteristics with distance step, Δx, and time step, Δt, selected to satisfy exactly the condition, $a\Delta t/\Delta x = 1$. Equation (3) was solved for four different representations of the weighting function: (1) W (Zielke's exact solution, Eqs. (6) and (7)), (2) W_{app} (Eq. (14)), (3) W_{new} (Eq. (13)), and (4) $W = 0$ (steady-state shear stress). Results are presented in terms of dimensionless head, $(H - H_o)g/aV_o$, as a function of dimensionless time, at/L, where L = pipe length. The dimensionless results were independent of the value of V_o as long as the initial flow was laminar. A time step corresponding to $at/L = 0.04167$ was used, but identical results were obtained for double this value.

Figures 2 and 3 compare piezometric heads computed using the four different representations of the weighting function. At both the downstream boundary (Fig. 2) and the pipe midpoint (Fig. 3), the results computed using the new approximating function, W_{new}, are nearly identical to the results computed using the exact weighting function, W.

Figures 4 and 5 illustrate the dispersive error resulting from Trikha's assumption for small Δt that was mentioned above. In Fig. 4, head fluctuations computed using W_{app} to represent the weighting function are compared. The fluctuations computed using Trikha's assumption for small Δt are out of phase with the fluctuations computed without this assumption and with fluctuations computed using steady state-shear stress. Figure 5 indicates that the dispersive error resulting from Trikha's assumption is even larger when W_{new} is used to represent the weighting function rather than W_{app}.

Conclusions

The new, five-term approximating function, W_{new}, accurately represents the weighting function in Zielke's equation for frequency-dependent shear stress for values of dimensionless time, τ, ranging from 0.00001 to 0.20. Transient results obtained using W_{new} in the improved implementation of Trikha's method are nearly identical to results obtained using the exact expression for the weighting function. The improved approximate method retains the same efficiency and simplicity as Trikha's original method.

References

Brown, F. T., 1962, "The Transient Response of Fluid Lines," ASME *Journal of Basic Engineering*, Vol. 84, pp. 547-553.

Cunge, J. A., Holly, F. M., Jr., and Verwey, A., 1980, *Practical Aspects of Computational River Hydraulics*, Pittman.

Holmboe, E. L., and Rouleau, W. T., 1967, "The Effect of Viscous Shear on Transients in Liquid Lines," ASME *Journal of Basic Engineering*, Vol. 89, pp. 174-180.

Schohl, G. A., Vigander, S., and Kuzniak, W. C., 1987, "Detection of Air in Sensing Lines from Standing Wave Frequencies," *Transactions of the American Nuclear Society*, Winter Meeting, Los Angeles, CA.

Suo, L., and Wylie, E. B., 1989, "Impulse Response Method for Frequency-Dependent Pipeline Transients," ASME JOURNAL OF FLUIDS ENGINEERING, Vol. 111, pp. 478-483.

Suzuki, K., Taketomi, T., and Sato, S., 1991, "Improving Zielke's Method of Simulating Frequency-Dependent Friction in Laminar Liquid Pipe Flow," ASME JOURNAL OF FLUIDS ENGINEERING, Vol. 113, pp. 569-573.

Trikha, A. K., 1975, "An Efficient Method for Simulating Frequency-Dependent Friction in Transient Liquid Flow," ASME JOURNAL OF FLUIDS ENGINEERING, Vol. 97, pp. 97-105.

Wylie, E. B., and Streeter, V. L., 1978, *Fluid Transients*, McGraw-Hill.

Zielke, W., 1968, "Frequency-Dependent Friction in Transient Pipe Flow," ASME *Journal of Basic Engineering*, Vol. 90, pp. 109-115.

S. K. Tang
Graduate Student.

N. W. M. Ko
Professor.
Mem. ASME

Department of Mechanical Engineering,
The University of Hong Kong,
Hong Kong

A Study on the Noise Generation Mechanism in a Circular Air Jet

An investigation of the noise generation mechanism of turbulent structures in a subsonic air jet has been done theoretically as well as experimentally. Based on the results obtained, it is proposed that the rate of change of velocities of the jet structures plays an important role in the generation of sound in an air jet.

Introduction

In the past few decades, both theoreticans and experimentalists have been engaged in researches into the production of noise from turbulent jets. The direction of investigation was mainly focused on the relationship between the far field jet noise and the activities of the large scale orderly structures within the turbulent shear layer of a jet.

The dynamics of the coherent structures in the shear layer have been studied extensively by numerous workers using the technique of conditional sampling and flow visualization (for instance, Crow and Champagne, 1971; Browand and Laufer, 1975; Yule, 1978 and Hussain and Zaman, 1980). It is now a well-known fact that the major activities in the jet are the pairings of vortex rings to form the coherent structures and their eventual breakdown. The results of Browand and Laufer (1975) and Hussain and Zaman (1980) demonstrates clearly that large rates of change of vortex ring velocities occur during the pairing process.

The above-mentioned processes have also been proposed to be the sound sources in an air jet (for instance, Ffowcs Williams and Kempton, 1978; Kibens, 1980; Laufer and Yen, 1983; and Bridge and Hussain, 1987). On the theoretical side, Ffowcs Williams and Kempton (1978), based on the concept of the instability waves, proposed a model for the pairing noise. However, their approach had not taken into account the physical vortex dynamics and did not suggest the actual mechanism for the generation of sound in the pairing process. Also, as discussed by Laufer and Yen (1983), the use of instability theory to study vortex interactions seems to be difficult and not obvious. On the other hand, Möhring (1978) worked out an expression for the far field pressure fluctuations produced by vortex ring pairing based on the dynamics of the interacting rings and thus provided a more realistic theoretical base for pairing noise. However, it had not discussed the factors that can affect pairing noise generation. Thus, the basic noise generation mechanism in the pairing process is still unknown.

On the experimental side, Kibens (1980) used acoustic excitation to establish the relationship of the jet noise and the vortex pairing process. However, it had not suggested the actual mechanism involved in the sound generation. Laufer and Yen (1983), with the instability wave approach, suggested that the rapid amplitude change of the convective instability waves within the first diameter of the jet is responsible for the jet noise emission. It seems that these instability waves correspond to the shear layer mode vortices in a laminar jet (Bridge and Hussain, 1987). However, the rapid amplitude change of the waves suggested by Laufer and Yen (1983) was not specifically related to the vortex dynamics within the shear layer. Thus, their results did not provide concrete evidence on the actual mechanism of the sound generation. Nor was the rapid change of amplitude be related to the earlier proposed acceleration–deceleration sequences of the vortex rings during the pairing process which might be closely associated with the sound generation (Laufer, 1974). Further, Laufer (1974) did not have direct evidence to substantiate his proposal at that time (Laufer and Yen, 1983). Thus, as there is difficulty in relating the dynamics of vortex pairing and the noise generated with the development of the instability waves, it is believed that the pairing noise generation mechanism, which is based on the dynamic parameters of the vortex filaments, is in need.

Bridges and Hussain (1987) showed how the initial condition of a jet affected the pairing noise while Hussain (1983), based on turbulent jet noise results, argued that it was the breakdown of vortex rings into substructures and the interaction of these azimuthally spaced structures that produced most of the noise. A cut-and-connect process has been proposed in Hussain (1986) as the noise generation mechanism. However, such a process could hardly be visualized because of the greatly diffused tracers in that region of the jet and their actual occurrence thus was questionable. Other researchers also studied the topic by means of the measurements of correlation between flow turbulence and far field pressure using laser doppler technique (Schaffer, 1979) and hot wire methods (Juve et al., 1980). Besides, Michalke and Fuchs (1975) rewrote Lighthill's equation in term of near field pressure fluctuations and demonstrated the importance of lower azimuthal mode structures in the noise production of an air jet. However, their results seem not to provide adequate answer to the question of how sound is produced by the jet structures.

Since Powell (1964) had shown that under low Mach number condition the source term in the wave equation could be rewritten as $-\rho_0 \nabla \cdot (\omega \times \mathbf{u})$, it is believed that motion of the vorticity bearing fluid is the chief source of noise in subsonic flows. At the same time, flow visualization illustrated clearly

---

Contributed by the Fluids Engineering Division for publication in the JOURNAL OF FLUIDS ENGINEERING. Manuscript received by the Fluids Engineering Division March 10, 1992; revised manuscript received December 4, 1992. Associate Technical Editor: Ho, Chih-Ming.

the process of vortex ring pairing and perturbed ring development (for instance, Browand and Laufer, 1975; Yule 1978; and Van Dyke, 1982). Thus, it is highly probable that these are the major noise sources in jet.

In the present paper, because of the lack of understanding of the basic noise generation mechanism as discussed above, models of noise production due to the activities of the vortex pairing and due to the interaction and decay of the coherent structures will be established. Based on the dynamics of the vortex filaments, the basic mechanism of noise generation and the dominant parameter that affects the generation of noise during the pairing and the breakdown process will also be discussed. It is hoped that this investigation can provide an answer to this aeroacoustic problem and to stimulate further studies in the topic.

The Noise Generation Models

Pairing Noise. Powell (1964) showed that in the calculation of sound generation by low Mach number flow an inhomogeneous wave equation of the form

$$\nabla^2 p - a_0^{-2}\frac{\partial^2 p}{\partial t^2} = -\rho_0 \nabla \cdot L \qquad (1)$$

can be derived from the basic compressible hydrodynamic equations. In Eq. (1), a_0 represents the ambient acoustic velocity, p a quantity equal to acoustic pressure in the far field, ρ_0 the density of ambient fluid and L the Lamb vector which in low Mach number and negligible entropy change takes the form

$$\mathbf{L} = (\nabla \times \mathbf{u}) \times \mathbf{u} = \omega \times \mathbf{u}. \qquad (2)$$

Möhring (1978) demonstrated the use of vector Green's function in solving Eq. (1) and obtained an expression for the far field pressure fluctuation produced by moving vortex ring as

$$p = \frac{\rho_0}{12\pi a_0^2 |\mathbf{z}|^3}\frac{\partial^3}{\partial t^3}\int [\mathbf{z}\cdot\mathbf{y}]\mathbf{y}\cdot[\omega(t - x/a_0) \times \mathbf{z}]d^3y, \qquad (3)$$

where **z** and **y** denote the position vectors of a point in the far and near fields respectively. For thin and planar vortex ring of circulation Γ and radius R propagating in the direction of its normal, Möhring (1978) showed that Eq. (3) could be reduced to

$$p \propto \frac{\partial^3}{\partial t^3}(\Gamma R^2 \xi) \qquad (4)$$

for constant **z**. ξ denotes the distance travelled by the vortex ring in the direction of its normal. Then, for two vortex rings with same circulation Γ and radius r_1 and r_2 at position ξ_1 and ξ_2 from a reference point in the flow field, respectively, it can be shown that

$$p \propto \frac{\partial^2}{\partial t^2}[\Gamma r_1 \dot{r}_1(\xi_1 - \xi_2)], \qquad (5)$$

where $\dot{r}_1$ represents differentiation with respect to time. Möhring (1978) had also shown that pairing noise was quadrupole in nature.

During pairing, the radii, axial positions and the velocities of the vortex rings can be obtained by Biot-Savart induction law as in the work of Kambe and Minota (1981). It is also observed in their paper that the maximum sound pressure results when the axial velocity of the trailing vortex ring is at its maximum value. This occurs when the trailing vortex ring slips through the leading vortex ring. The sound pressure as calculated using Eq. (5) takes the following form

$$p \propto \chi^2\left(\frac{2}{1+\chi^2}\right)^{1.5}\frac{(1-\chi^2)^2}{(1+\chi^2)E(\chi) - (1-\chi^2)K(\chi)}(\ddot{r}_1)^2, \qquad (6)$$

where χ denotes the radius ratio between the two vortex rings

Nomenclature

A = rate of change of velocity
a_0 = ambient acoustic velocity
D = diameter of the nozzle
E, K = complete elliptic functions of the first and second kind, respectively
$\hat{e}(\theta)$ = unit vector normal to $\hat{n}$ and inclines at an angle θ with the horizontal
f_e, L_e = frequency and amplitude of excitation
G_{xy} = cross spectral density functions between signal x and y
$\hat{n}$ = unit vector normal to the plane of the vortex ring
p = far field pressure fluctuation
r_i = radius of the ith vortex ring
R = radius of the vortex ring
R_i = initial radius of the vortex rings in the pairing case
R_o = mean radius of the unperturbed vortex ring
R_{xy} = cross correlation between signals x and y
S = mean shear rate
St_D, St_θ = Strouhal numbers, fD/U_e, $f\theta/U_e$
U = local mean velocity
U_e = exit velocity of jet
u = fluctuating velocity in the radiation direction
V = mean flow velocity
V_i = induced velocity
V_s = velocity due to shear rate
x, r = coordinates along the axial and radial direction of the jet, the origin being at the center of the nozzle exit unless in the far field sound equation
y, **z** = near and far field distances, respectively
α = amplification rate of perturbation wave amplitude
Γ, ω = circulation and vorticity, respectively
Ω = recovered fluctuating vorticity
γ_{xy}^2 = coherence function between signals x and y, respectively
ϵ = initial core radius to vortex ring radius ratio
θ = momentum thickness of the initial boundary layer unless in the far field equation
ξ_i = axial position of the ith vortex ring
ρ_0 = density of ambient fluid
σ, δ = amplitudes of perturbation wave in the axial and radial direction, respectively
σ_t = turbulence intensity
τ = time
χ = radius ratio of vortex rings
æ = acceleration
ζ = axial position of an element on the perturbed vortex ring relative to the centre of the ring

Superscripts

$\cdot$ = differentiation with respect to time
$\cdot\cdot$ = second differentiation with respect to time

Subscripts

p = signal associated with the prongs of hot wire probe
j = signal associated with the jet structures
t = combined signal from prongs and jet structures
x, r = axial and radial components

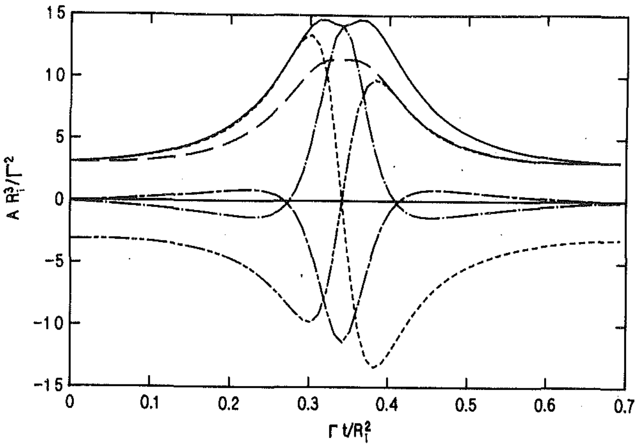

Fig. 1(*a*) Acceleration time signals for $S = 10$

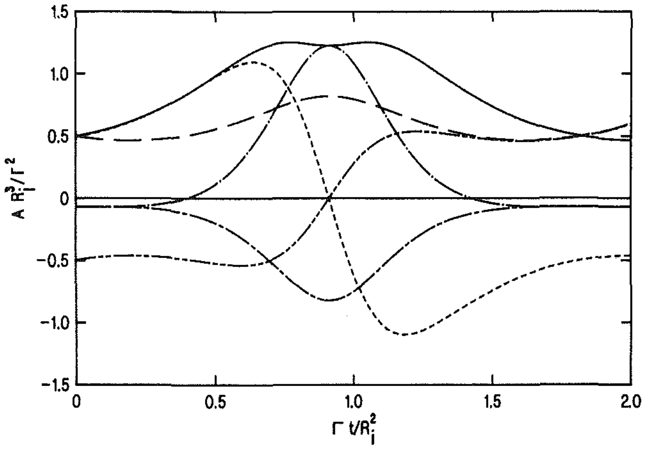

Fig. 1(*b*) Acceleration time signals for $S = 0$
Trailing vortex ring:
— · —, radial acceleration;
·····, axial acceleration;
——, acceleration magnitude;
Leading vortex ring:
— · —, radial acceleration;
— · · —, axial acceleration;
— —, acceleration magnitude;

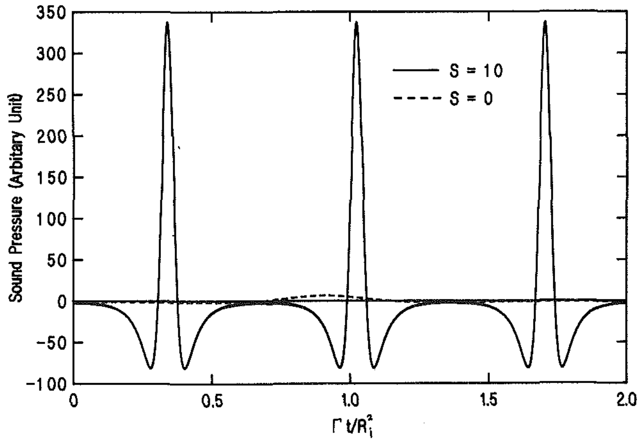

Fig. 1*c*) Far field pressure time variations
——: $S = 10$;
— — —: $S = 0$.

Fig. 1 Time variations of acceleration and far field pressure

at the instant of slip through and $\chi \leq 1$. K and E represent, respectively, the complete elliptic functions of the first and second kind. $\ddot{r}_1$ can also be expressed analytically as

$$\ddot{r}_1 \propto \frac{(1+\chi^2)^{1.5}}{\chi(1-\chi^2)}\left(\frac{(1+\chi^2)}{(1-\chi^2)}E(\chi)-K(\chi)\right)$$
$$\left(\frac{2}{1-\chi^2}E(\chi)-K(\chi)+\frac{3\log\chi}{8\chi}\right.$$
$$\left.+\frac{(1-\chi)}{4\chi}\log\left(\frac{8}{\epsilon}\left(\frac{2}{(1+\chi^2)}\right)^{0.75}e^{-0.25}\right)\right). \qquad (7)$$

where ϵ represents the initial core radius to vortex ring radius ratio. It can be observed that the dominant term in the pressure expression is the radial acceleration unless for very small χ but this condition can never exist in real pairing interaction.

In the presence of a background shear flow, the velocities of the elements on the vortex rings are given by the sum of the induced velocity, V_i, and the local mean velocity within the flow field, V_s. Let S denote the strength of the averaged mean shear rate and is normalized by the factor R_i^2/Γ. One obtains

$$V_s = \frac{S\Gamma}{R_i}\left(1-\frac{R}{R_i}\right)+V, \qquad (8)$$

where V is the mean flow velocity at $r = R_i$. Figures 1(*a*) and 1(*b*) show, respectively, the time variation of the acceleration of the vortical elements for $S = 10$ and $S = 0$. It can be observed that the maximum acceleration values for $S = 10$ are approximately 10 times those of $S = 0$. It is also noted that the shear flow decreases the duration of the occurrence of high acceleration. Figure 1(*c*) shows the time variations of the pressure signals for $S = 0$ and 10. It is observed that the pressure amplitude peaks at the instant when the radial acceleration magnitude of the vortical elements is maximum showing that the pairing process radiates maximum noise at the slip through instance of the vortex rings. The acceleration plots also illustrate that the axial acceleration peaks only at a short time earlier than the radial acceleration. This may suggest that the absolute acceleration or deceleration of vortical structures can act as an indicator for sound generation in the pairing process. For $S \neq 0$, Eq. (5) still holds but an additional term due to the increase in the relative velocity between the rings under the presence of the mean shear has to be included in Eq. (6). Thus, obtains

$$p \propto \chi^2\left(\frac{2}{1+\chi^2}\right)^{1.5}\frac{(1-\chi^2)^2}{(1+\chi^2)E(\chi)-(1-\chi^2)K(\chi)}(\ddot{r}_1)^2$$
$$+\frac{2\chi(1-\chi)}{(1+\chi^2)}S\ddot{r}_1. \qquad (9)$$

If S increases, the relative velocity between the vortex rings increases and results in faster slip through but larger χ. It is found from Eq. (7) that the first term on the right hand side of Eq. (9) is more singular when χ tends to unity than the second term showing that the former is more significant in the production of sound. Figure 1(*c*) confirms this point. However, the importance of the acceleration term remains unchanged. Also observed in Fig. 1(*c*) is that the frequency of noise production is higher for $S = 10$, suggesting that mean shear rate has the effect of increasing the sound power radiated.

In jet flow, the shear rate decreases with the distance from the nozzle exit. However, since the results of Hussain and Zaman (1980) show that the axial span of the slip through process is less than a diameter of the nozzle, the pairing noise producing region of the jet is confined at a small volume within the flow field before the end of the potential core. Thus, S can be approximated by the averaged mean velocity gradient at the slip through position.

Breakdown Noise

After the pairing activities of the vortex rings finish, perturbation waves grow along the peripheral of the ring structures

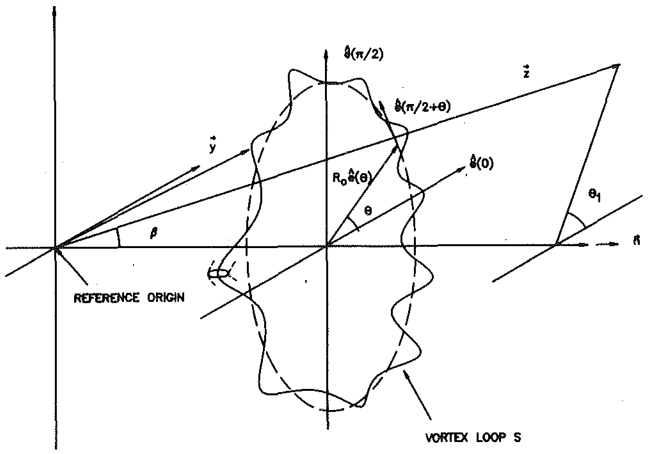

Fig. 2 Sketch of breakdown model and notations

under a kind of instability proposed by Widnall and Sullivan (1973) until the perturbed ring structures break down into substructures.

Since there is no external force applied to a free shear layer and it had been shown by Lighthill (1952, 1954) that the sound energy produced by turbulence is infinitesimal when compared to total hydrodynamic energy of flow in low Mach number condition, from Eqs. (1) and (2) one obtains $\int L\,dv = 0$ and $\partial/\partial t \int \mathbf{y}\cdot L\,dv = 0$ (see Möhring, (1978). Thus, the integral in Eq. (3) can be applied to the perturbed ring as,

$$p=\frac{\rho_0}{12\pi a_0^2|\mathbf{z}|^3}\frac{\partial^3}{\partial t^3}\int(\mathbf{z}\cdot\mathbf{y})(\mathbf{y}\times\omega)\cdot\mathbf{z}dv, \tag{10}$$

where the retarded time $t-|\mathbf{z}|/a_0$ is to be used in ω.

To solve Eq. (10) in this case, a line integral along the peripheral of the perturbed ring structure has to be obtained. From visualization pictures of Van Dyke (1982) and the theoretical model of perturbed ring of Widnall and Sullivan (1973), it is reasonable to assume in simple case that the perturbation waves on the ring are sinusoidal in azimuthal angle (Fig. 2). Thus, one can observe that the position of a point on the ring loop with reference to the centre of the ring can be expressed in the form $\mathbf{y} = \mathbf{y}(\zeta, r, \theta)$ such that

$$\zeta=\sigma(t)\cos(m\theta) \text{ and } r=R_0+\delta(t)\cos(m\theta), \tag{11}$$

where m denotes the number of perturbation waves on the ring, R_0 the mean radius of the perturbed ring, and σ and δ determine, respectively, the perturbation wave amplitudes in axial and radial directions (Fig. 2). The azimuthal constituents found by Fuch (1974) are believed to be closely related to m. One obtains for any $\mathbf{y}$ that

$$\mathbf{y}=\xi\hat{n}+r\hat{e}(\theta),$$

giving

$$\mathbf{y}=(Ut+\sigma(t)\cos(m\theta))\hat{n}+(R_0+\delta(t)\cos(m\theta))\hat{e}(\theta),$$

$$\hat{\mathbf{z}}=\cos(\beta)\hat{n}+\sin(\beta)\hat{e}(\theta_1),$$

and

$$\hat{\omega}(\mathbf{y})=\frac{d\xi}{ds}\hat{n}+\frac{dr}{ds}\hat{e}(\theta)+r\frac{d\theta}{ds}\hat{e}\left(\theta+\frac{\pi}{2}\right). \tag{12}$$

Expanding the integral in Eq. (9) and since m is usually greater than 2 (Hussain and Zaman, 1980 and Van Dyke, 1982), the integrals that take the form in Eq. (13) vanish, that is,

$$\int\cdots d\xi=\int\cdots dr=0. \tag{13}$$

Thus, one obtains for the ring core under the assumption of negligible change in Γ as

$$\int_{\text{core}}(\hat{\mathbf{z}}\cdot\mathbf{y})(\mathbf{y}\times\hat{\omega})\cdot\hat{\mathbf{z}}dv=\Gamma\int_0^{2\pi}r^2\xi(\sin^2(\beta)\cos^2(\theta-\theta_1)-\cos^2(\beta))d\theta. \tag{14}$$

Here, in order to simplify Eq. (14), one further assumption has to be made. It is shown from water jet visualization of Van Dyke (1982) that the exterior of the perturbed ring structure distorts in a way opposite to that of the ring core, it is assumed that the exterior and the core of the structure moves in opposite directions. Equation (10) becomes for $R_0 \gg \delta$

$$p_{\text{core}}\propto\frac{\partial^2}{\partial t^2}\int_0^{2\pi}(r\xi)\dot{r}[\cos^2(\beta)-\sin^2(\beta)\cos^2(\theta-\theta_1)]d\theta, \tag{15}$$

where $\dot{r}$ represents differentiation with respect to time. Thus, the overall sound emission from the perturbed vortex ring system becomes

$$p_{ov}\propto\frac{\partial^2}{\partial t^2}\int_0^{2\pi}[(r\xi\dot{r})_{\text{core}}+(r\xi\dot{r})_{\text{ext}}](\cos^2\beta-\sin^2\beta)\cos^2(\theta-\theta_1)d\theta$$

and thus $p_{ov}\propto\frac{\partial^2}{\partial t^2}\int_0^{2\pi}\sigma\dot{\delta}\cos^2(m\theta)[\cos^2(\beta)-\sin^2(\beta)\cos^2(\theta-\theta_1)]d\theta$,

giving

$$p_{ov}\propto\left(\cos^2(\beta)-\frac{1}{2}\sin^2(\beta)\right)\frac{\partial}{\partial t^2}(\sigma\dot{\delta}), \tag{16}$$

as σ and δ are independent of azimuthal position. Since both σ, δ, and their time derivatives are still abstract quantities, it is worthwhile to relate them to variables concerning with fluid motions such as acceleration or velocity. If one takes the velocity of propagation of the vortical filaments on the ring as the sum of the local mean velocity, U, in the flow field and its self induced velocity, a change in the radial position of the filaments is accompanied by a change of their propagation velocities. Consideration of the mean velocity profile of the jet gives for x and r as the axial and radial position, respectively,

$$U=f(x,r).$$

Therefore

$$\Delta U=\frac{\partial f}{\partial x}\Delta x+\frac{\partial f}{\partial r}\Delta r$$

and

$$\Delta U\simeq\frac{\partial f}{\partial r}\delta r,$$

as $\partial f/\partial x \simeq 0$ and can be neglected for Δx and Δr being of the same order. For the self-induced velocity, Arms and Hama (1965) proposed that it could be approximated by a function of the local curvature. Thus, for small Δr, that is, small perturbation amplitude in the radial direction, the rate of change of the longitudinal velocity and vortical filaments is proportional to the rate of change of their radial positions for small magnitude of perturbation wave, therefore

$$\ddot{\sigma}\propto\dot{\delta}. \tag{17}$$

Based on the experimental results of Widnall and Sullivan (1973), for a core of definite size, an exponential unstable growth of perturbation wave amplitude is suggested. Integration of Eq. (17) gives for positive real constants A and B that

$$\sigma=A(\exp(\alpha t)-1)$$

and

$$\delta=B(exp(\alpha t)-1), \tag{18}$$

where α is the amplification rate of the perturbation wave amplitude. Longitudinal propagation acceleration of vortical filament equals to $A\alpha^2 \exp(\alpha t)$. Then, by considering the time derivative term in Eq. (16), it can be observed that

$$\frac{\partial^2}{\partial t^2}(\sigma\dot{\delta}) = AB\alpha^3 \exp(\alpha t)[4\exp(\alpha t) - 1], \qquad (19)$$

showing that the larger the value of $\exp(\alpha t)$ the greater the amplitude of sound radiated out from the system as $1 \leq \exp(\alpha t)$ for $t \geq 0$. Denoting æ as the axial acceleration of vortical element, then $æ_x = A\alpha^2 \exp(\alpha t)$. The radial acceleration $æ_r$ and the absolute acceleration æ of the vortical elements can be expressed as

$$æ_r = B\alpha^2 \exp(\alpha t) \text{ and } æ = \alpha^2\sqrt{A^2+B^2}\exp(\alpha t) \qquad (20)$$

respectively. Therefore, the vortical element accelerates in both x and r direction once perturbation waves start to grow on the peripheral of the ring structure. Although the acceleration term diverges exponentially as time goes to infinity, however, by restricting the consideration to the time before the breakdown process, Eq. (19) becomes

$$\frac{\partial^2}{\partial t^2}(\sigma\dot{\delta}) = AB\alpha^2 æ_x(4æ_x - A\alpha^2) = S(æ_x). \qquad (21)$$

This shows that the sound produced under the perturbation wave development is of second order with respect to $æ_x$ and thus $æ_r$ and æ. However, since $æ_x \geq A\alpha^2$ as $\exp(\alpha t) \geq 1$ and $|S(æ_x)|$ is an increasing function of $æ_x$ for $æ_x \geq A\alpha^2/4$, the larger the acceleration or deceleration of the vortical filaments on the ring the greater the far field pressure level.

The above simple models for the far field pressure fluctuations produced by the vortex ring pairing and by the perturbed ring structure breakdown have shown that in both cases the aerodynamic noise generated is related to the rate of change of velocity of the vortical elements of the jet structures. However, the assumption of negligible change of circulation of the vortical elements in both cases may render difficulty in the interpretation of the experimental results. For the breakdown noise model, because the ring structure is no longer thin, the assumption of uniform properties across the core of the ring may introduce uncertainty. Also, the amplitude of the perturbation waves on the ring structure will eventually become so large that the assumption of small wave amplitude becomes invalid and thus Eq. (7) no longer holds. However, it is believed that the structure breaks down once the wave amplitude becomes large. Small perturbation wave amplitude in jets before the breakdown of the ring structure has been confirmed by the visualization pictures of Laufer (1983). Nevertheless, these will be discussed later.

Apparatus and Experimental Technique

The experiments were carried out inside an anechoic chamber of usable size 6.25 × 5 × 3.5 m^3. The jet exit velocity, U_e, was 47.7 m/s and the turbulence intensity at the nozzle exit was 0.5 percent of the mean flow in the unexcited condition (Ko and Tang, 1990). Diameter of the jet, D, was 20.22 mm. The exit boundary layer of the jet had a shape factor of 2.58 and a mean velocity profile collapsed with the Blasius profile.

The experiment in this investigation consisted of two sections. As the theoretical models suggest a close relationship between the far field pressure fluctuations and the rate of change of velocity of the structures in the jet, the first part of the experimental investigation involved the measurements of these quantities within the first twelve diameters of the jet. An array of three hot wires was employed for this purpose. The rate of change of the vorticity bearing fluid was calculated using a method similar to that in rigid body motion after valid structure signatures on the three hot wire time traces were identified under a pre-set threshold level (Appendix A). In the pairing region, the paths of measurements and the orientation of the array were designed to be parallel to that of vortical elements. Within the breakdown region, that is, for $3 \leq x/D \leq 12$, assuming small perturbation wave amplitudes, paths of measurement were chosen to be the lines of constant y/D for simplicity. All these paths were determined from the vorticity isocontours of Hussain and Zaman (1980) and the educed results in the present excited jets. In order to avoid the high frequency signals in the flow field from contaminating the results, all the time signals used in this part of the investigation were narrow band filtered at the frequency of interest.

The second part of the investigation involved the measurements of correlation between the flow signal and the far field pressure fluctuations of the jet. An 1 in. Brüel and Kjær condenser microphone located at $x/D = 50$, $y/D = 29$ on the horizontal plane of symmetry of the jet (about 30 deg to the jet axis) was used to record the latter signals. In the breakdown experiment because of some technical constraints, the microphone was located at $y/D = -29$ instead. Juve et al. (1980) and Schaffer (1979) had also measured far field noise signals at these positions. Single hot wire probe with long prongs ($\simeq 1.5\ D$) was inserted vertically into the jet for flow measurements in order to minimize the probe interference effect (Richarz, 1980 and Juve et al., 1980). In the present study, it was found that the introduction of such an intrusive device raised the far field pressure fluctuations at the frequency of interest by 1–2 db in the pairing region and accounted for as much as 3–4 db in the downstream flow region. In order to reduce such contamination effect, a coherence correction method was established (Appendices B and C). The validity of such method will be discussed later. The paths of measurements simply followed those adopted above. The hot wire was also yawed at the appropriate angle so that the flow component along the radiation direction could be recorded. The hot wire anemometer used in the present investigation was of the constant temperature type. Inaccuracy of measurement was approximately 5 percent.

Acoustic excitation was applied to the jet because it has been shown to be capable of amplifying the jet flow structures and thus offers better structure recovery. Error in the acceleration-deceleration calculation can be minimized (for instance, Crow and Champagne, 1970 and Hussain and Zaman, 1980). Due to different requirements, different excitation conditions were adopted in the pairing and breakdown experiments. In both cases the excitation sound pressure level was measured by an 1/8 in. Brüel & Kjær condenser microphone at the exit edge of the exciter. The axisymmetric modes of the jet were excited. Also, it had been checked that the loudspeaker did not produce distorted signals within the range of sound pressure level tried in the experiments.

A computer controlled x-y table was used for traversing hot wire within the jet flow field.

Results and Discussion

Acoustic Response of the Jet. It had been shown that acoustic excitation amplified the far field pressure fluctuations of the jet. Thus, the selection of the excitation frequency f_e and its pressure level L_e in the pairing experiment was based on the far field noise spectra of the jet under excitation. The range of pure tone excitation was 2.75 kHz $\leq f_e \leq$ 12 kHz and L_e = 105 dB for all frequency of excitation in the frequency determination trial. f_e could not be too low in this case in order to avoid the imposed sound field from contaminating the jet noise measurements. The far field noise spectra obtained are shown in Fig. 3(a). Broadband amplification in the noise spectrum is observed with an excitation frequency f_e of 3.6 kHz. However, for f_e = 3.8 kHz ($St_D \simeq 1.61$, $St_\theta \simeq 0.006$), a much narrower band amplification is obtained and it is highly probable that the subharmonic of the preferred shear layer

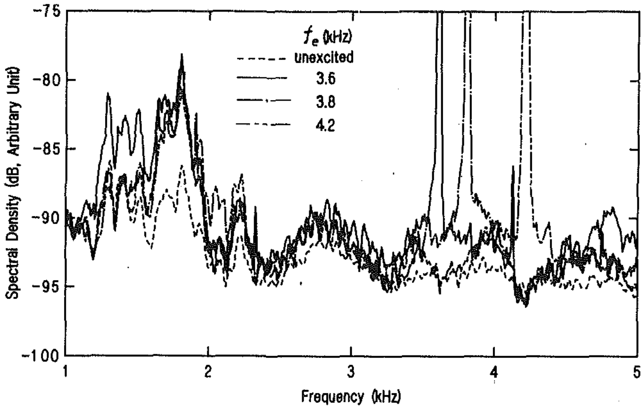

Fig. 3(*a*) Pure tone frequencies. L_e = 105 db.
- - -, Unexcited; —, 3600 Hz; — · —, 3800 Hz; — · · —, 4200 Hz.

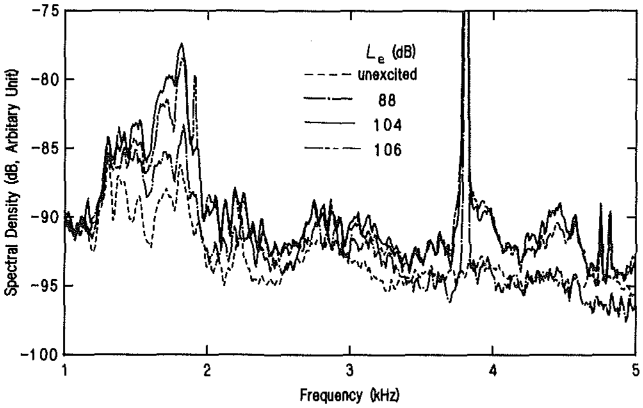

Fig. 3(*b*) Excitation levels. f_e = 3.8 kHz.
· · ·, Unexcited; — · —, 88 dB; —, 104 dB; — · · —, 106 dB.

Fig. 3 Far field spectra of jet under acoustic excitation at x/D = 50, y/D = 29

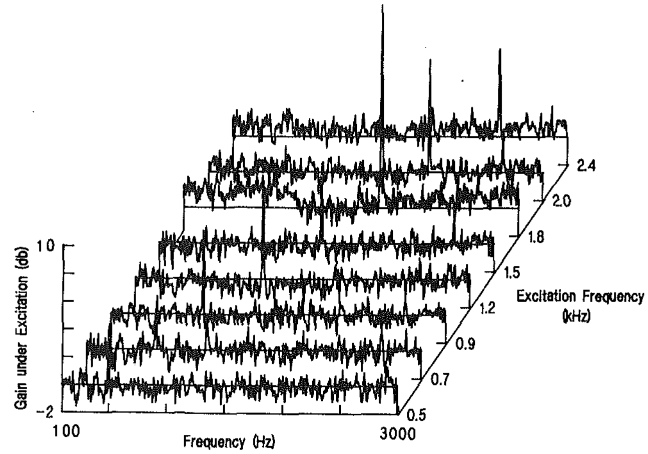

Fig. 4(*a*) Spectral gain of axial velocity of fluctuations under different excitation frequency. At x/D = 4.0, y/D = 0.3; L_e = 120 dB.

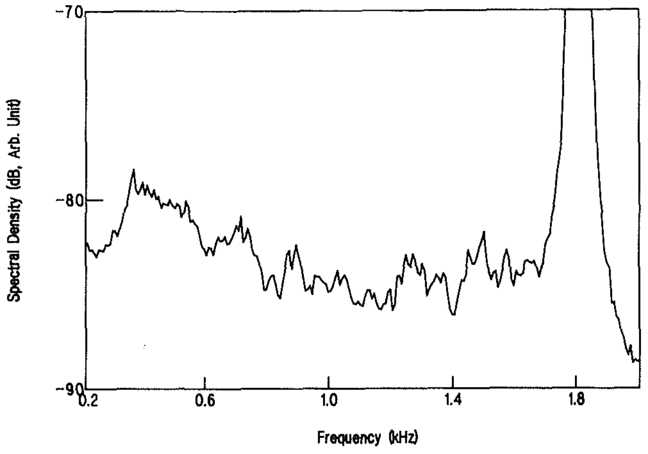

Fig. 4(*b*) Far field spectrum at x/D = 50, y/D = −29. L_e = 120 dB, f_e = 1.8 kHz.

mode structure is excited. As will be shown later, the educed vorticity isocontours had confirmed the occurrence of pairing of vortex rings in this flow region. Because of the narrower band amplification, suggesting repetitive occurrence of pairing, f_e is adopted as the excitation frequency in the pairing experiments.

Figure 3(*b*) shows the effect of L_e on the noise spectra under f_e of 3.8 kHz excitation. The spectral level at 1.8 kHz increases with L_e and its peak appears to be more distinct. However, a sharp spectral peak at 1.9 kHz also grows in amplitude and becomes comparable in magnitude with that at 1.8 kHz for $L_e \geq 105$ dB. Thus, $L_e \geq 105$ dB is not desirable for excitation because this frequency component is not a significant contributor to the far field noise. Therefore, the jet was excited at $St_D = 1.61$ ($\mathrm{St}_\theta \simeq 0.006$) with $L_e = 104$ dB ($\simeq 0.23$ percent of the jet dynamic head, $0.5\ \rho U_e^2$).

For the vortex breakdown experiment, excitation of the jet at lower frequency and the applied sound source being closer to the breakdown region were adopted so as to make the ring structures more coherent. Amplification of the low frequency components of turbulence at $x/D = 4.0$ and $y/D = 0.3$ is found under f_e of 1.8 kHz and at 120 dB forcing (Fig. 4(*a*)) and thus was adopted. Figure 4(*b*) shows the far field noise spectrum of the excited jet and the broadband components between 370 Hz and 500 Hz ($\mathrm{St}_D \simeq 0.2$) are generated from the pairing of vortices or structures and the eventual breakdown of the paired structures. Similar broadband peak has been observed on the far field noise spectrum of air jets (for instance, Schaffer, 1979 and Juve et al., 1980).

Pairing Experiments. Figure 5(*a*) shows the axial fluctuating velocity spectra obtained by single hot wire at the location $x/D = 1.75$, $y/D = 0.2$ (within the potential core) and $x/D = 1.5$, $y/D = 0.8$ (outside the jet boundary). The presence of a distinct spectral peak around 1.8 kHz suggests the occurrence of pairing of structures in that region (Hussain and Zaman 1980). Figure 5(*b*), which shows the educed fluctuating vorticity isocontours, further confirms the presence of vortex pairing within the first two diameters of the excited jet. Thus, the signals from the hot wire array was 1/3 octave band filtered at 1.8 kHz. Threshold level for valid structure signature identification on each time trace was taken to be 1.0 σ_t, where σ_t is the rms value of the corresponding time signal.

The axial distributions of the acceleration or deceleration of the vortical elements on vortex rings during pairing along the selected paths are shown in Fig. 6(*a*). However, before going into any discussion, it has to be pointed out that the data on the figure contain no time information as vortex rings do not necessarily arrive at the same axial position at the same time. It is the trends that are interested in this investigation.

The two acceleration peaks observed on the inner path within the potential core in Fig. 6(*a*) have been confirmed by repeated experiments and are also found in unexcited jet (not shown here). This suggests that there may exist two mutual slip-through processes of the vortex rings within this region $0.8 \leq x/D \leq 2.5$. The first acceleration peak at $x/D \simeq 1.3$ suggests the occurrence of the first slip through process. The second ac-

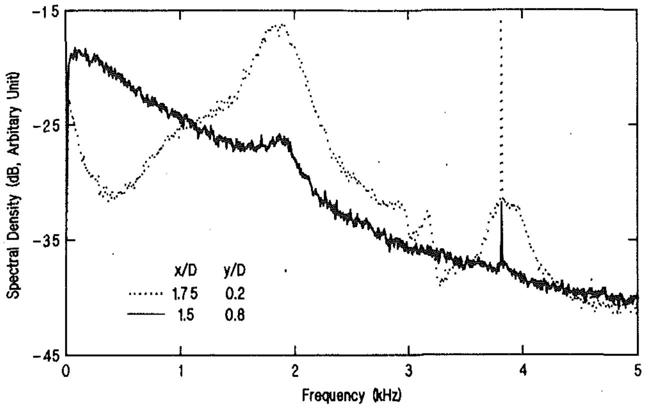

Fig. 5(*a*) Spectra of axial velocity fluctuations
. . . , $x/D = 1.75$, $y/D = 0.2$;
—, $x/D = 1.5$, $y/D = 0.8$.

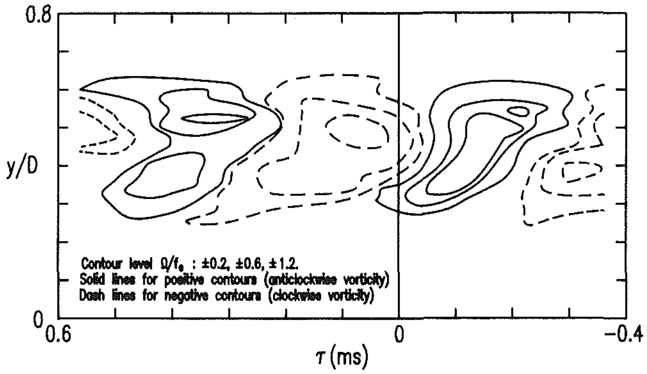

Fig. 5(*b*) Coherent vorticity isocontour map at $x/D = 1.4$. Triggering wire at $x/D = 0.8$, $y/D = +0.1$.

celeration peaks at $x/D \simeq 1.85$ may be the result of the second slip through process in which the former leading vortex ring slips through the expanded trailing vortex. The deceleration trough at $x/D \simeq 2.4$ may come from the remnant leading vortex ring which generally decelerates as it moves away from the jet axis at that stage. It is probably not due to the paired structures because their time signals had been removed by filtering.

Data from the outer path, despite small in magnitude, show a trend that supports the model suggested above (Fig. 6(*a*)). The initial large deceleration of the vortical elements of the leading vortex ring is a typical event in pairing. The deceleration troughs at $x/D \simeq 1.4$ and 1.9 show the corresponding existence of vortex ring slip-through process. However, the positive peak at $x/D \simeq 1.1$ remains unexplained. This may be the effect of the accelerating trailing vortex ring which comes close to the leading vortex ring. The low magnitude of the deceleration should not be surprising as the deceleration of the expanding vortex ring is much less than the acceleration of the smaller ring (Fig. 1).

The coherences between the flow signal u and the far field pressure fluctuations p at the frequency at 1.8 kHz, are shown in Fig. 6(*b*). The coherences have been corrected by the correction method shown in Appendices B and C. It can be observed that the peaks for the γ_{uj}^2 at the inner path within the potential core, except that at $x/D = 2.25$, are at the same axial positions as the corresponding ones in Fig. 6(*a*). Same phenomenon is also observed for those at the outer path of Fig. 6(*a*) and 6(*b*). This implies that the generation of noise due to vortex ring pairing is highly correlated with the acceleration or deceleration of the pairing vortex rings. This point agrees with the theoretical predicted results in the previous section

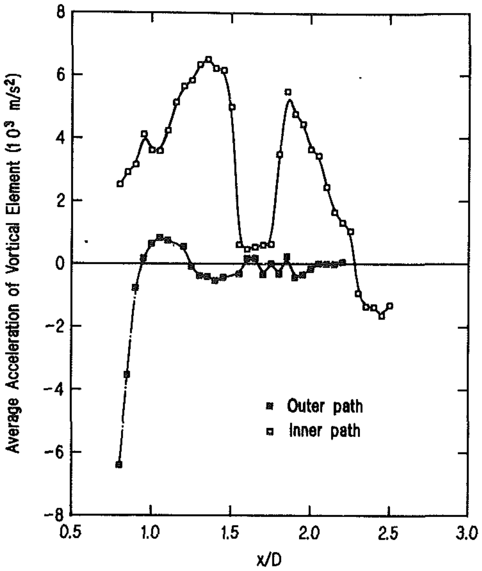

Fig. 6(*a*) Average acceleration of vortices within pairing region

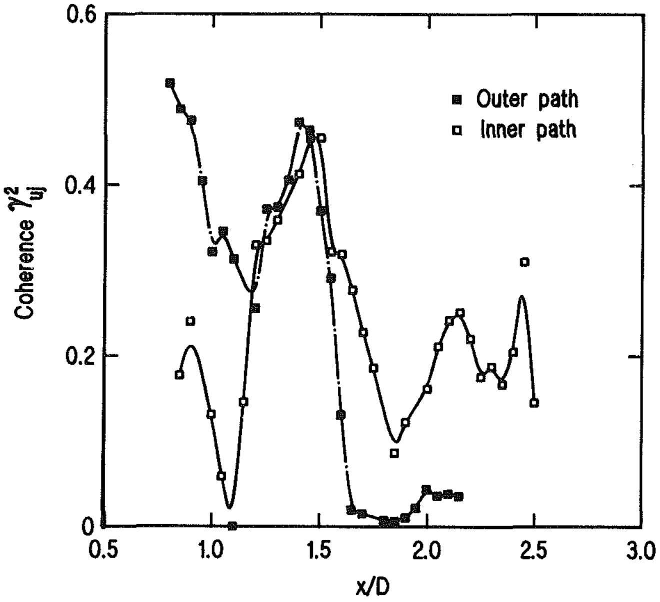

Fig. 6(*b*) Coherence between axial velocity fluctuations and far field pressure fluctuations.
□, Inner path; ■, outer path.

that acceleration of vortical elements on the vortex rings are important in the generation of pairing noise. The only unknown sound source at $x/D \simeq 2.25$ may be the result of the nonzero first and second time derivatives of Γ during the rapid slip-through process or more diffused coherent structures or both. The effect of a decrease in Γ of the vortex rings can be observed by expanding Eq. (5) at the slip through instant. It can be shown that

$$p \propto 2r_1\dot{r}_1(\dot{\xi}_1-\dot{\xi}_2)\frac{\partial\Gamma}{\partial t}+\Gamma\frac{\partial^2}{\partial t^2}[r_1\dot{r}_1(\xi_1-\xi_2)]. \qquad (22)$$

If $\partial\Gamma/\partial t$ is negative, the two terms on the right-hand side of the above equation are of opposite sign thus results in a drop in the magnitude of the radiated sound. The lower coherence data around the proposed second slip through location may be the outcome of such changes in the structures. Thus, it is reasonable to believe that substantial noise is generated under

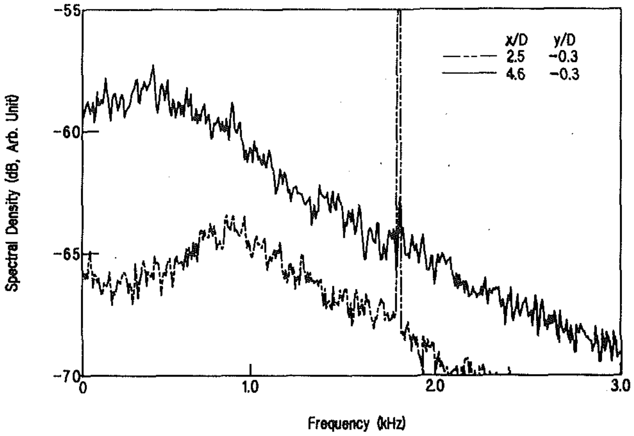

Fig. 7 Spectra of axial velocity fluctuations. L_e = 120 dB, f_e = 1.8 kHz. — · · —, x/D = 2.5, y/D = −0.3; —, x/D = 4.6, y/D = −0.3.

high acceleration or deceleration of the vortical elements. The better matching of the outer path data may also suggest that the effect of Γ is the main cause of the above mentioned discrepancy as the change in circulation of the outwardly going vortices during pairing is smaller (Hussain and Zaman, 1980).

Ring Structure Breakdown. It can be observed from Fig. 7 that an excitation of frequency f_e of 1.8 kHz and L_e = 120 dB stabilizes pairing of the jet structures at about 850 Hz. Besides, the spectrum obtained at $x/D = 4.6$, $y/D = -0.3$ shows the presence of the frequency peak at about 420 Hz and 850 Hz. This implies that pairing of the 850 Hz structures into 420 Hz structures occurs in the region $x/D \geq 3.5$. Since the dominant frequency components in the far field pressure fluctuations under excitation are between 370 to 500 Hz, the 420 Hz structures observed are the azimuthally correlated structures in the jet flow field (Michalke and Fuchs, 1975). The breakdown of the perturbed ring structures brings about disorder and loss of circumferential coherence, resulting in lower noise production efficiency. Typical examples for such kind of drop in the noise production efficiency are the quin-axial jet noise suppressor of Scharton and White (1972) and the screen perturbed jets of Arndt et al. (1974). Thus, the time signals obtained from the hot wire array were 1/3 octave band filtered at the frequency of 420 Hz. Further, coherence data in later discussions are also obtained at this frequency. Threshold level for the structure identification was chosen to be 0.8 σ_t, where σ_t represents the rms value of each individual time signal.

The acceleration or deceleration distributions obtained in the breakdown region are shown in Fig. 8(*a*). Similarity in the distributions to those of the pairing case for $x/D < 5.5$ (Fig. 6(*a*)) supports again the occurrence of pairing of the 850 Hz structures into the 420 Hz structures in this region. For $x/D \geq 6$, the rapid development of the perturbation wave amplitude on the ring structures may be responsible for the increase in the axial or radial acceleration of the inwardly-going vortical elements of the structures. Data of Widnall and Sullivan (1973) also showed a drop in the value of the spatial amplification rate. This suggests that there is an eventual drop in the acceleration or deceleration of the vortical elements on the perturbed ring, thus explaining the trough at $x/D = 7$ on the curve for the inner path in Fig. 8(*a*). Large rate of change of the velocity of the vortical elements means high strain on the vortex rings. As such stretching of the vortex filaments requires energy, such trough may be the result of a restoring process similar to that in loaded spring systems. The rise in the acceleration that follows indicates further increase in the rate of growth of perturbation wave amplitude. Figure 9 illustrates the spectral development of the axial fluctuating velocity signals for $6 \leq x/D \leq 12$. The gradual decrease in the peak frequency for $x/D > 7$ suggests the breakdown of the highly perturbed ring structures. Thus, the large scale axial acceleration measured at $x/D \simeq 7.5$ signals the breakdown of the 420 Hz vortex rings. Data obtained after that are very scattered and become irrelevant in the present study. For $x/D \leq 7$, deceleration of the vortical elements on the perturbed rings is observed. Those elements that move away from the jet axis convect in a lower mean velocity environment and decelerate. The sharp change at $x/D \simeq 7.2$ may be the consequence of the ring breakdown.

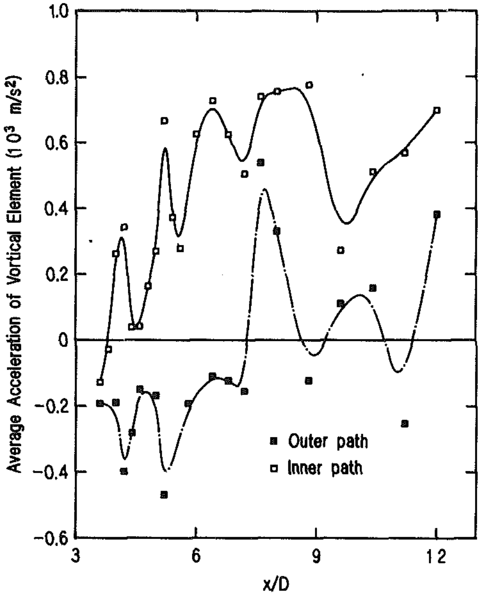

Fig. 8(*a*) Average acceleration of vortical elements within breakdown region

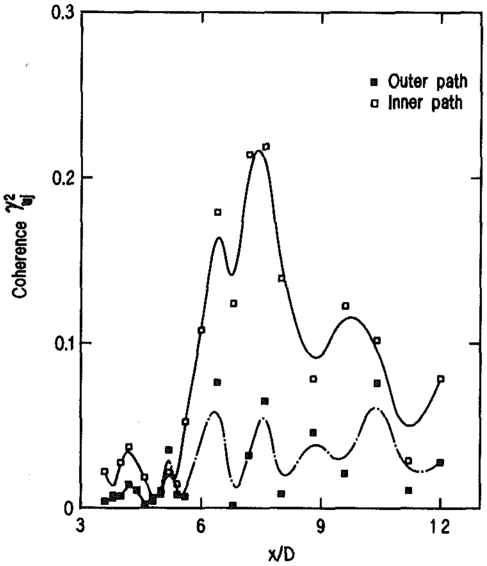

Fig. 8(*b*) Coherence between axial velocity fluctuations and far field pressure fluctuations within breakdown region. □, Inner path; ■, outer path.

Coherence distributions near 420 Hz in the breakdown region are shown in Fig. 8(*b*). The small coherence values for $x/D < 6$ are expected since pairing of the organized structures to 420 Hz structures involves low acceleration and deceleration

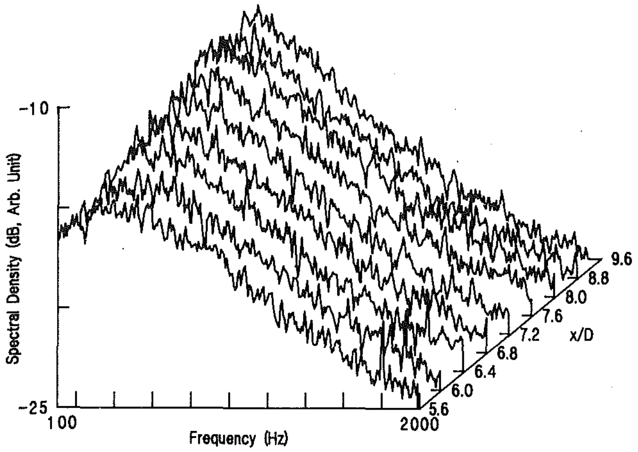

Fig. 9 Spectra of axial velocity fluctuations within breakdown region. Along $y/D = -0.3$.

and does not produce much noise (as can be seen in Fig. 4(*b*)). Though the coherence values are only about 0.2, the coherence spectra obtained at this region (which is not shown here) indicate the dominant coherence peak at this frequency while those at the other frequency, except that at the excitation frequency, are less than 0.05. As will be discussed in the next section, the distributions agree with that of the noise-flow turbulence correlation of Juve et al. (1980). Thus, the noise within the mentioned frequency band is believed to come from the breakdown of rings. Also from Fig. 8(*b*), there are coherence peaks at the locations where maximum acceleration or deceleration of the vortical elements are found (Fig. 8(*a*)). The agreement in the peak positions further supports the above findings that the rate of change of velocity is the basic mechanism in noise generation. The drop in the coherence after the breakdown of rings at $x/D \simeq 7.5$ is consistent with the findings of other workers as mentioned before (for instance, Schaffer, 1979 and Arndt et al., 1974).

Other Discussions

It can be observed in Figs. 6(*a*) and 8(*a*) that the magnitude of the rate of change of the velocity of the vortical elements obtained in the pairing region is generally one order of magnitude higher than that in the breakdown region. Comparison between the vortex pairing results in the two regions shows that the pairing activity in the region $3.6 \leq x/D \leq 6$ is much less noisy than that in the early pairing region ($0.8 \leq x/D \leq 2.5$). These results again strongly manifest that the rate of change of speed of the vortical elements on the vortex rings plays a key role in the noise emission in circular jet.

In the coherence measurement results shown in Figs. 6(*b*) and 8(*b*) the lower value of coherence obtained along the outer paths may be due to the more diffused state of the rings and the high local random turbulence (Browand and Laufer, 1975). The scattered data and lack of definite trend along the outer path in Fig. 8(*b*) make interpretation of the results difficult. Since the ring structures at their breakdown stages are usually very diffused and unstable, a gradual decrease in the circumferential correlation of structure signals is highly expected. This may result in the scattering of the data obtained.

Also observed in Fig. 8(*b*) is that the coherence distribution agrees with the distribution of the noise-flow turbulence correlation of Juve et al. (1980). The positions of the maximum correlation for $St_D = 0.15$ and 0.3 are located at $x/D \simeq 6.5$ and 8, respectively, giving an interpolated position of $x/D = 7.5$ for $St_D = 0.18$. This agrees with the present result at $x/D = 7.2$. Besides, with laser doppler anenometry, Schaffer (1979) found that the source term of noise at $St_D = 0.2$ is greatest at $x/D \simeq 8$. The small discrepancy in the spatial location of the maximum correlation or coherence is due to the shortening of the potential core length under controlled acoustic excitation (Lepicovsky et al., 1985). This shows further that the adopted correction method for probe interference gives the correct distribution of the coherence between the far field pressure fluctuations and flow turbulence.

Conclusions

In the present study, a mathematical method is introduced to correct the effect of probe noise contamination of the far field jet noise signal. The obtained coherence distributions show good agreement with those of other researchers.

Simple theoretical models for the noise emission from vortex ring evolution in the free shear layer have been established with reference to the flow visualization pictures and to the experiments carried out within the noise production region of the jet proposed by various researchers.

In the pairing model, the motions of the vortex rings are obtained by Biot-Savart induction law. The far field noise is calculated using Möhring's formula. The model suggests that maximum sound power is radiated at the instant of the occurrence of the slip through process. This is also the instant at which the vortex rings are highly accelerating or decelerating. Change of the vortex ring circulation is neglected in the present study but it can be deduced that a negative rate lowers the magnitude of the radiated sound. This implies that the second slip through of vortex rings occurs in jet is less noisy than the first one. This point and the dependence of sound radiation on the acceleration or deceleration of the vortex rings are confirmed by the experimental results obtained from the jet excited at the first subharmonic of the shear layer mode frequency.

The development of the perturbation waves on the ring structures in a free shear layer has been shown to be noise producing for small wave amplitude. The proposed model also suggests that the sound magnitude increases with it and thus the rate of change of speed of the vortical elements on the ring structures until the structures breakdown. Experimental results obtained after the end of the potential core of the excited jet ($St_D \simeq 0.8$) show that the breakdown noise is less correlated with the flow signals than the pairing noise. However, similar to the pairing case, the sound radiated depends on the rate of change of speed of the vortical elements on the ring structures.

The present investigation into the noise production mechanism of the coherent structures in a subsonic jet under controlled acoustic excitation has shown that the sound generated by vortices is correlated with the acceleration or deceleration of the vortical elements of both the thin vortex rings in the pairing stage and the relatively thicker vortex rings during the breakdown process. This finding suggests that the noise produced through the pairing of vortices and through the ring breakdown comes from the same mechanism of a rate of change of the propagation velocity of the vortical elements. Thus, of such a change in speed, be they of acceleration or deceleration, within the jet flow field is the basic mechanism for the emission of sound in jet. The present results clarify the role of the rate of change of velocities of the vortical elements on the generation of jet noise.

Acknowledgment

This study was partly supported by research grants from the Committee on Research and Conference Grants, University of Hong Kong, and the University and Polytechnic Grants Committee, Hong Kong.

References

Arms, R. J., and Hama, F. R., 1965, "Localized-induction Concept on a Curved Vortex and Motion of Elliptic Ring," *Physics of Fluids*, Vol. 8, pp. 533-569.

Arndt, R. E. A., Tran, N. C., and Barefoot, G., 1974, "Turbulence and Acoustics Characteristics of Screen Perturbed Jets," *AIAA Journal*, Vol. 12, pp. 261-262.

Bridges, J. E., and Hussain, A. K. M. F., 1987, "Roles of Initial Conditions and Vortex Pairing in Jet Noise," *Journal of Sound and Vibration*, Vol. 117, pp. 289-311.

Browand, F. K., and Laufer, J., 1975, "The Role of the Large Scale Structures in the Initial Development of Circular Jets," *Proc. 4th Biennial Symposium on Turbulence in Liquids*, University of Missouri-Rolla, Science Press, pp. 333-344.

Crow, S. C., and Champagne, F. H., 1971, "Orderly Structures in Jet Turbulence," *Journal of Fluid Mechanics*, Vol. 48, pp. 547-591.

Curle, N., 1955, "The Influence of Solid Boundary Upon Aerodynamic Noise," *Proceedings Royal Society*, (London), Series A, Vol. 231, pp. 505-514.

Ffowcs Williams, J. E., and Kempton, A. J., 1978, "The Noise From Large Scale Structure of a Jet," *Journal of Fluid Mechanics*, Vol. 84, pp. 673-694.

Fuchs, H. V., 1976, "Resolution of Turbulent Jet Pressure Into Azimuthal Components," AGARD-CP-131, Paper 27.

Hussain, A. K. M. F., and Zaman, K. B. M. Q., 1980, "Vortex Pairing in a Circular Jet Under Controlled Excitation. Part 2. Coherent Structure Dynamics," *Journal of Fluid Mechanics*, Vol. 101, pp. 493-544.

Hussain, A. K. M. F., 1983, "Coherent Structures—Reality and Myth," *Physics of Fluids*, Vol. 26, pp. 2816-2850.

Hussain, A. K. M. F., 1986, "Coherent Structures and Turbulence," *Journal of Fluid Mechanics*, Vol. 173, pp. 303-356.

Juve, D., Sunyach, M., and Comte-Bellot, G., 1980, "Intermittancy of Noise Emission in Subsonic Cold Jet," *Journal of Sound and Vibration*, Vol. 71, pp. 319-332.

Kambe, T., and Minota, T., 1981, "Sound Radiation from Vortex Systems," *Journal of Sound and Vibration*, Vol. 74, pp. 61-72.

Kibens, V., 1980, "Discrete Noise Spectrum Generated by an Acoustically Exicted Jet," *AIAA Journal*, Vol. 18, pp. 434-441.

Ko, N. W. M., and Tang, S. K., 1990, "Effect of External Exciter on the Far Field Noise of an Air Jet," *Journal of Sound and Vibration*, Vol. 137, pp. 154-158.

Lau, J. C., and Fisher, M. J., 1975, "The Vortex-street Structure of 'Turbulent' Jets. Part 1," *Journal of Fluid Mechanics*, Vol. 67, pp. 299-337.

Laufer, J., 1974, "On the Mechanism of Noise Generation by Turbulence," Omaggio a Carlo Ferrari, pp. 451-464. Libreria Editrice Universitaria Levrotto & Bella, Torino.

Laufer, J., and Yen, T., 1983, "Noise Generation by a Low-Mach-Number Jet," *Journal of Fluid Mechanics*, Vol. 134, pp. 1-31.

Lepicovsky, J., Ahuja, K. K., and Burrin, R. H., 1985, "Tone Excited Jets, Part III: Flow Measurements," *Journal of Sound and Vibration*, Vol. 102, pp. 71-91.

Lighthill, M. J., 1952, "On Sound Generated Aerodynamically I. General Theory," *Proceedings Royal Society*, (London), Series A, Vol. 211, pp. 564-587.

Lighthill, M. J., 1954, "On Sound Generated Aerodynamically II. Turbulence as a Source of Sound," *Proceedings Royal Society*, (London), Series A, Vol. 222, pp. 1-32.

Michalke, A., and Fuchs, H. V., 1975, "On Turbulence and Noise of an Axisymmetric Shear Flow," *Journal of Fluid Mechanics*, Vol. 70, pp. 179-205.

Möhring, W., 1978, "On the Vortex Sound at Low Mach Number," *Journal of Fluid Mechanics*, Vol. 85, pp. 685-691.

Powell, A., 1964, "Theory of Vortex Sound," *Journal of the Acoustical Society of America*, Vol. 36, pp. 177-195.

Ribner, H. S., 1969, "Quadrupole Correlations Governing the Pattern of Jet Noise," *Journal of Fluid Mechanics*, Vol. 38, pp. 1-24.

Richarz, W. G., 1980, "Jet Noise Diagnostics: Spurious Sound Generated by Hot-wire Turbulence Interaction," *Journal of the Acoustical Society of America*, Vol. 67, pp. 73-77.

Schaffer, M., 1979, "Direct Measurements of the Correlation Between Axial In-Jet Velocity Fluctuations and Far Field Noise Near the Axis of a Cold Jet," *Journal of Sound and Vibration*, Vol. 64, pp. 73-83.

Scharton, T. D., and White, P. H., 1972, "Simple Pressure Source Model of Jet Noise," *Journal of the Acoustical Society of America*, Vol. 52, pp. 399-412.

Van Dyke, 1982, *An Album of Fluid Motion*, Parabolic Press.

Widnall, S. E., and Sullivan, J. P., 1973, "On the Stability of Vortex Rings," *Proceedings Royal Society*, (London), Series A, Vol. 332, pp. 335-353.

Yamada, H., and Matsui, T., 1978, "Preliminary Study of Mutal Slip-Through of a Pair of Vortices," *Physics of Fluids*, Vol. 21, pp. 292-294.

Yule, A. J., 1978, "Large Scale Structures in the Mixing Layer of a Round Jet," *Journal of Fluid Mechanics*, Vol. 89, pp. 413-432.

Zaman, K. B. M. Q., and Hussain, A. K. M. F., 1980, "Vortex Pairing in a Circular Jet under Controlled Excitation. Part 1. General Jet Response," *Journal of Fluid Mechanics*, Vol. 101, pp. 449-492.

Zaman, K. B. M. Q., and Hussain, A. K. M. F., 1984, "Natural Large-Scale Structures in the Axisymmetric Mixing Layer," *Journal of Fluid Mechanics*, Vol. 138, pp. 325-351.

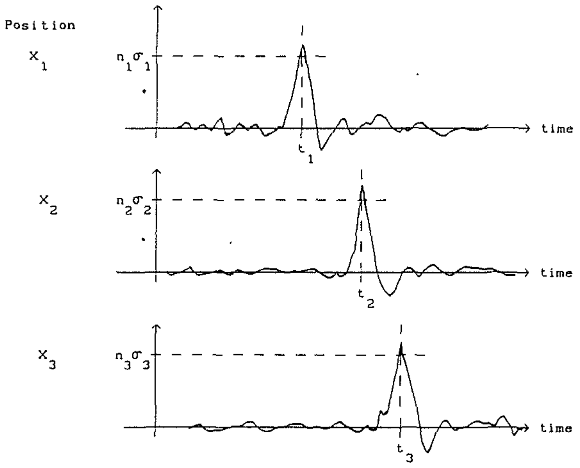

Fig. A1 Calculation scheme

APPENDIX A

Calculation of the Rate of Change of Velocity of Coherent Structures. It has been shown by Lau and Fisher (1975) and Zaman and Hussain (1984) that the large positive and negative spikes on the time signals obtained within the jet flow field are signatures of the large-scale structures. Their identification on the time trace and their passage time across a point in the flow field can be obtained under a chosen threshold level. Figure A 1 shows the scheme.

Acceleration or deceleration of the structure in the direction parallel to the measuring device is

$$\frac{2}{t_3-t_2}\left[\frac{x_3-x_1}{t_3-t_1}-\frac{x_2-x_1}{t_2-t_1}\right]. \tag{a1}$$

Accuracy of the acceleration measurement depends on the sampling rate and the error in the measurement of separation between the hot wires. The error in the present measurement is about 15 percent.

APPENDIX B

The Correction Method for Coherence Measurements With Prongs. In turbulent free shear layer, $\partial^2 u^2/\partial t^2$, where u denotes the flow velocity at a particular point in the radiation direction, contributes partly to the far field noise. This means that both the coherent and random signals (this refers to the flow signals that bear poor coherence with those at other points within the flow field) inside the layer have their contributions if one considers only one point inside the flow. However, because of the lack of coherence and short life span of the latter kind of signal, its contribution to the far field noise integral tends to be zero. Thus, it can be assumed that the noise from an air jet comes only from the coherent structures.

When a small solid body is inserted into the flow, the additional noise produced, which had been formulated by Curle (1955), has been shown to be proportional to $\partial u^2/\partial t$ (Richarz, 1980).

The derivation of the method starts with the expression that far field noise $p_t(t)$ equals the sum of prong noise $p_p(t)$ and jet turbulence noise $p_j(t)$, that is

$$p_t(t)=p_p(t)+p_j(t). \tag{b1}$$

By definition, the coherence between p and u is

$$\gamma^2(f)=\frac{|G_{ut}(f)|^2}{G_{uu}(f)G_{tt}(f)}. \tag{b2}$$

For a convective type of flow instability, the fluctuating part of u varies sinusoidally with time and thus it can be observed from the expressions of the jet and prong noise that p_p and p_j are 90 deg out of phase with each other. Let R_{xy} denote the cross correlation between signals x and y,

$$R_{tt} = R_{pp} + R_{jj} + R_{pj} + R_{jp}. \qquad \text{(b3)}$$

It can be shown under the stated condition that $R_{pj} + R_{jp} = 0$. Thus, $G_{tt}(f)$ can be written in the following form:

$$G_{tt}(f)\Delta f \fallingdotseq \mathbf{p}_p^2(f) + \mathbf{p}_j^2(f) \qquad \text{(b4)}$$

and $G_{uu}(f)\Delta f$ is $\mathbf{u}^2(f)$. $\mathbf{p}$ denotes the rms value of the pressure fluctuation at the frequency f. Also, Eq. (b2) can be expanded into the form

$$\gamma^2(f) = \frac{|G_{up}(f)|^2 + |G_{uj}(f)|^2}{\mathbf{u}^2(f)\ (\mathbf{p}_p^2 + \mathbf{p}_j^2)}\,(\Delta f)^2. \qquad \text{(b5)}$$

Therefore, denoting $\mathbf{f}$ as the ratio of p_p to p_j, then

$$\gamma_{uj}^2(f) = (1+\mathbf{f}^2)\gamma^2(f) - \mathbf{f}^2\gamma_{up}^2(f). \qquad \text{(b6)}$$

Thus, the only unknown in Eq. (b6) is $\gamma_{up}^2(f)$.

APPENDIX C

Method to Estimate Coherence Between Prong Noise and Flow Signals. Noise produced from prong-flow interaction is of the form

$$p = C\int_0^1 \bar{U}\,\frac{\partial u}{\partial t}\,dx = C\sum \bar{U}\,\frac{\partial u}{\partial t}\,\Delta x, \qquad \text{(c1)}$$

where the integral is to be taken along the length of the prongs. From Navier-Stoke equation and for a convective type of instability, u varies sinusoidally with time so that the modulus of cross spectrum between flow signal at the prong u_0 and $\partial u/\partial t$ can be related to that between u_0 and u simply by the equation

$$\left|G\left(u_0, \frac{\partial u}{\partial t}\right)\right| = \omega_f |G(u_0, u)|, \qquad \text{(c2)}$$

where ω_f represents the frequency of the signal u. Also, for prong inserted vertically into the flow, it can be assumed as the scale of structure impinging on the obstacle surface is large such that the u signals along the length of the prong are in phase and thus $G(u_0, u)$ are real. Beside, the velocity correlation between signals at points i and j along the length of the prong can be expressed, as used by Ribner (1969) and Richarz (1980) in the study of jet noise, in the form

$$R_{ij}(r, \tau) = \overline{u'^2}\exp(-ar^2)g(\tau), \qquad \text{(c3)}$$

where r represents the distance between points i and j along the length of prong, $\overline{u'^2}$ the mean variance of velocity fluctuations in the flow field and g an exponential function of τ^2 and is independent of r when the direction of structure propagation is perpendicular to the prong stem.

Coherence between u_o and prong noise p is defined as

$$\gamma_{u_0p}^2 = \frac{|G(u_0, p)|^2}{G(u_0, u_0)G(p, p)}$$

$$\simeq \frac{\left[\sum_{j=0}^{n} \lim_{T\to\infty} \frac{1}{T}\int_{-T}^{T} R_{0j}(j\Delta x, \tau)\cos(\omega\tau)d\tau\right]^2}{\overline{u'^2}\left[\sum_{i,j}^{n} \lim_{T\to\infty}\frac{1}{T}\int_{-T}^{T} R_{ij}(r, \tau)\cos(\omega\tau)d\tau\right]}, \qquad \text{(c4)}$$

where $n = 1/\Delta x$ and $\gamma = |i - j|\Delta x$. Denoting $\exp(-a\Delta x^2)$ by λ, Eq. (c4) can be simplified to

$$\gamma_{u_0p}^2 \simeq \frac{\left[\sum_{j=0}^{n} \bar{U}_j \lambda^{j^2}\right]^2}{\sum_{i,j}^{n} \bar{U}_i \bar{U}_j \lambda^{(i-j)^2}}. \qquad \text{(c5)}$$

A rough approximation for $\bar{U}_i$ is that $\bar{U}_i(r) = \bar{U}_0\exp(-br^2)$ and if η denotes $\exp(-b\Delta x^2)$, Eq. (c5) becomes

$$\gamma_{u_0p}^2 = \frac{\left[\sum_{j=0}^{n} (\eta\lambda)^{j^2}\right]^2}{\sum_{i,j}^{n} \eta^{(i^2+j^2)}\lambda^{(i-j)^2}}. \qquad \text{(c6)}$$

The value of λ can be obtained by coherence measurements within the jet flow field while η can be found from the mean velocity profile.

It can be observed that for moderate value of λ, the greater the mean velocity gradient the larger the coherence value as the expression becomes more and more dependent on flow signals surrounding the point 0. Also, if the prong is placed inside the potential core so that $\eta = 1$ and $\lambda \simeq 1$, unity coherence between the flow signal at the measuring point and the far field noise is resulted. Thus, in the initial pairing region, where the cross sectional area of the potential core is large and the surrounding mean shear rate is high, the coherence is taken as unity. Outside the jet flow field, η is again close to 1, and the estimated γ_{up}^2 equals 0.2.

Experimental Observations of Flow Instability in a Helical Coil

(Data Bank Contribution*)

D. R. Webster

J. A. C. Humphrey

Department of Mechanical Engineering,
University of California at Berkeley,
Berkeley, CA 94720

Experimental observations were made for the nominally fully developed flow through a helically coiled pipe of circular cross-section with a curvature radius to pipe radius ratio $R_c/a = 18.2$. Laser-Doppler measurements of the instantaneous streamwise velocity, u_θ, and the cross-stream circumferential velocity, u_ϕ, components were obtained along the midplane of the pipe cross-section. The Reynolds number range explored was $3800 < Re < 10500$ ($890 < De < 2460$) and spans the laminar and turbulent flow regimes. Time integration of the velocity records has yielded previously unavailable mean and rms velocity profiles. In the range $5060 < Re < 6330$, the time records of the velocity components reveal periodic flow oscillations with $St \approx 0.25$ in the inner half of the pipe cross-section while the flow near the outer wall remains steady. A frequency doubling ($St \approx 0.5$) is also observed at some midplane locations. This low frequency unsteadiness is distinct from the shear-induced turbulent fluctuations produced with increasing Re first at the outer wall and later at the inner wall of the coiled pipe. Simple considerations suggest that the midplane jet in the recirculating cross-stream flow is the source of instability.

Introduction

The flow through coiled pipes is of considerable engineering interest and of fundamental scientific importance. Turbulent flows through helical coils occur in numerous industrial processes and laminar flows arise in, for example, various bioengineering applications. Consequently, the respective characteristics of fully developed laminar and turbulent flows through helical coils have been studied extensively and, at least for the laminar case, are fairly well explained. In contrast, the transitional regime lying between laminar and fully turbulent flow has received sparse attention and remains poorly understood. As discussed below, pipe curvature tends to dampen high frequency turbulent fluctuations, hence the manner of "transition to turbulence" in a helical coil is ambiguous. This experimental investigation addresses the transitional flow regime in a helical coil by providing quantitative time-dependent point measurements of velocity obtained with a non-intrusive laser-Doppler velocimeter (LDV).

The flow through a helical coil is uniquely different from that through a straight pipe due to the secondary flow pattern induced by the imbalance in the radial direction ($\phi = 0, \pi$) between the outwards-directed centrifugal force and the inwards-directed pressure force acting on the fluid. Shown in Fig. 1 is a cartoon of the secondary streamlines. The two counter-rotating vortices, called Dean vortices, are present at all flow rates. Also shown in Fig. 1 is the toroidal coordinate system which, neglecting the helix angle, is perfectly suited for describing the helical coil geometry. The three orthogonal coordinate directions are r, the radial distance from the pipe center; ϕ, the poloidal angle; and θ, the toroidal angle.

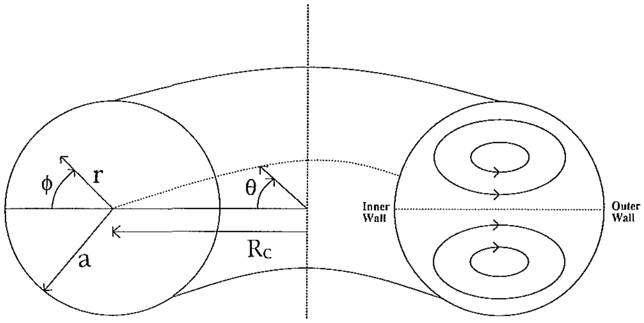

Fig. 1 Toroidal coordinate system and a cartoon of the secondary flow streamlines

It is known from experiments that the effect of coil curvature is to suppress high frequency turbulent fluctuations. This results in a higher value of Re for establishing fully turbulent flow in a curved pipe compared to a straight pipe (White, 1929; Taylor, 1929; and Sreenivasan and Strykowski, 1983). Figure 2 illustrates the turbulence suppression. By providing a comparison between the friction factor for the helical coil measured in this work and that in a straight pipe. The sharp discontinuity observed at Re = 2300 in the friction factor curve for the straight pipe marks the sudden transition to turbulence. In contrast, the friction factor curve for the helical coil is fairly smooth, indicating that the emergence of turbulence in this flow is gradual. A slight discontinuity in the slope of this curve

---

*Data have been deposited with the JFE Data Bank. To access the file for this paper, see intructions on p. 542 of this issue.

Contributed by the Fluids Engineering Division for publication in the JOURNAL OF FLUIDS ENGINEERING. Manuscript received by the Fluids Engineering Division March 16, 1992; revised manuscript received December 16, 1992. Associate Technical Editor: F. M. White.

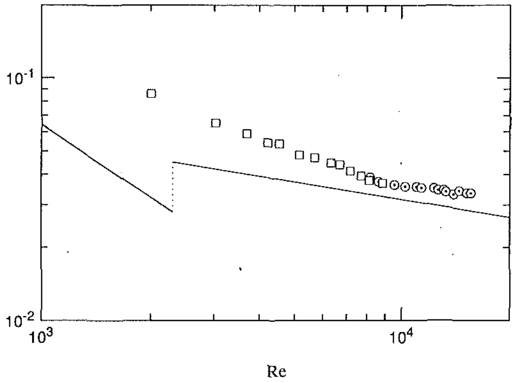

Fig. 2 Comparison between the friction factor measured in the present helical coil with R_c/a = 18.2 (□ data from manometer, ⊙ data from transducer) and the established correlation for straight pipe flow (——). The present measurements have an uncertainty of ±5 percent and are consistent with the results of White (1929) and Ito (1959).

is noticeable near Re = 8000. Beyond this point the flow is considered to be fully turbulent. This value of Re agrees with that predicted by Ito's (1959) correlation for the Re required to establish fully turbulent flow in a coil with the present dimensions.

As will be shown, in the range $2300 < \text{Re} < 8000$ in our coil, the effect of pipe curvature is to suppress high frequency turbulent fluctuations present in the inlet flow or generated by shearing of the fluid at the curved pipe walls. For Re > 8000, the rate of production of the fluctuations exceeds their rate of damping. Hence, the expression "transition to turbulence" as it applies to straight pipes is inappropriate when applied to the flow through a helical coil. Nevertheless, for ease of discussion the regime spanning steady laminar flow and fully turbulent flow in a coil will be referred to here as the "transitional" regime. The important points to note about the transitional regime are its gradual (noncatastrophic) nature and the relatively high value of Re required to maintain a turbulent state.

It is not yet known exactly how curvature works to suppress turbulence in helical coils. Certainly, the streamwise acceleration of the inlet flow near the inner wall of the coil works to laminarize the motion there. But the uniform laminarization of the flow throughout the pipe cross-section and the persistence of the laminar flow regime further downstream in the coil are not understood. To our knowledge, only two studies have addressed the problem, qualitatively. Taylor (1929) and Sreenivasan and Strykowski (1983) documented values of the transitional Reynolds numbers marking the onset and completion of the gradual transition process. In his celebrated flow visualization experiments, Taylor (1929) observed an oscillatory state of motion in the transitional flow regime. Sreenivasan and Strykowski (1983) also noted a sinusoidal unsteadiness of the motion near the inner wall of the pipe at a lower value of Re than that for which the flow became turbulent at the outer wall (first) and the inner wall (second). The latter authors detected the unsteadiness by means of hot wire anemometers placed along the midplane of the pipe cross-section, at distances one quarter of the radius from the inner and outer walls, respectively. They noticed that the characteristics of the transitional regime were dependent on the location in the pipe cross-section. Near the inner wall, oscillations with fairly well defined frequencies characterizing the flow unsteadiness grew in amplitude before higher harmonics started to appear. Turbulence near the inner wall emerged by the gradual superposition of higher order frequencies on the fundamental frequency. In contrast, near the outer wall turbulence emerged by high frequency "bursts." The sinusoidal oscillations at the inner wall always preceded the turbulent bursts at the outer wall. Neither Taylor (1929) nor Sreenivasan and Strykowski (1983) provide quantitative values of velocity or of the oscillation frequencies in the transitional flow regime.

The objective of the present study has been to quantify the features of the unsteady periodic flow in a coiled pipe as a function of Re in the transitional flow regime. Numerical simulations of curved flows indicate where in the pipe cross-section velocity measurements should be performed. Marcus (1984), in the Taylor-Couette concentric cylinder flow configuration, and Finlay et al. (1988), in a curved duct of rectangular cross-section, show a transition from steady counter-rotating vortices to a wavy-vortex flow structure. If it exists, a flow structure in the helical coil approximating a wavy-vortex flow will be detected by measuring the velocity along the midplane of the pipe cross-section. Hence, this communication is specifically devoted to a discussion of velocity component measurements made on the midplane of the cross-section of a helical coil, at a streamwise location where the flow is nominally fully developed. For clarity, the sinusoidal unsteadiness observed in the transitional regime will be referred to as the "low frequency unsteadiness" because it is distinct from high frequency turbulence.

Experimental Apparatus and Measurement Procedure

The experiments were performed in a closed-loop water flow system of which a schematic is shown in Fig. 3. The straight plastic pipe segment connected to the inlet of the helical coil

Nomenclature

a = pipe cross-section radius
d = ($=2a$) pipe cross-section diameter
De = ($=\text{Re}(a/R_c)^{1/2}$) Dean number
f = ($=2\Delta Pd/\rho LU^2$) nondimensional friction factor
f_d = dominant frequency
L = length
N = number of data points in a set
r = radial coordinate in the pipe cross-section
R_c = coiled pipe radius of curvature
Re = ($=Ud/\nu$) Reynolds number
S = power spectral density
St = ($=f_d d/U$) dominant Strouhal number
u_ϕ = instantaneous cross-stream circumferential velocity component
u_θ = instantaneous streamwise velocity component
$\bar{u}_\phi$ = mean (time-integrated) value of u_ϕ
$\bar{u}_\theta$ = mean (time-integrated) value of u_θ
$\tilde{u}_\phi$ = rms (time-integrated) value of u_ϕ
$\tilde{u}_\theta$ = rms (time-integrated) value of u_θ
U = bulk streamwise velocity
ΔP = pressure drop
ϕ = poloidal angle in the pipe cross-section
ν = fluid kinematic viscosity
θ = toroidal angle
ρ = fluid density
σ = standard deviation of any member of the data set
σ_{gb} = standard deviation due to velocity gradient broadening
σ_m = standard deviation of the mean of a data set

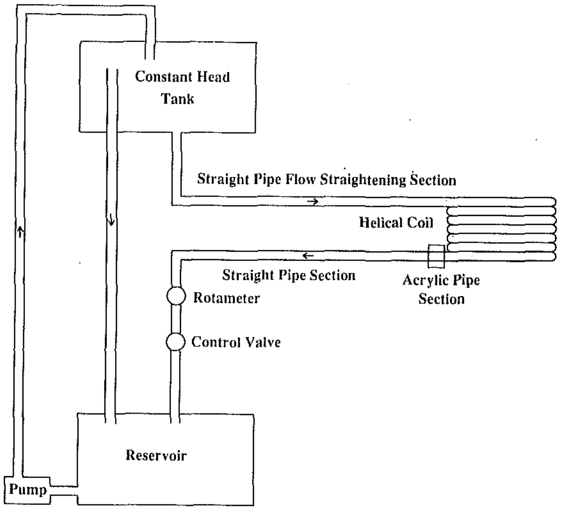

Fig. 3 Schematic of the constant head water flow system and the helical coil

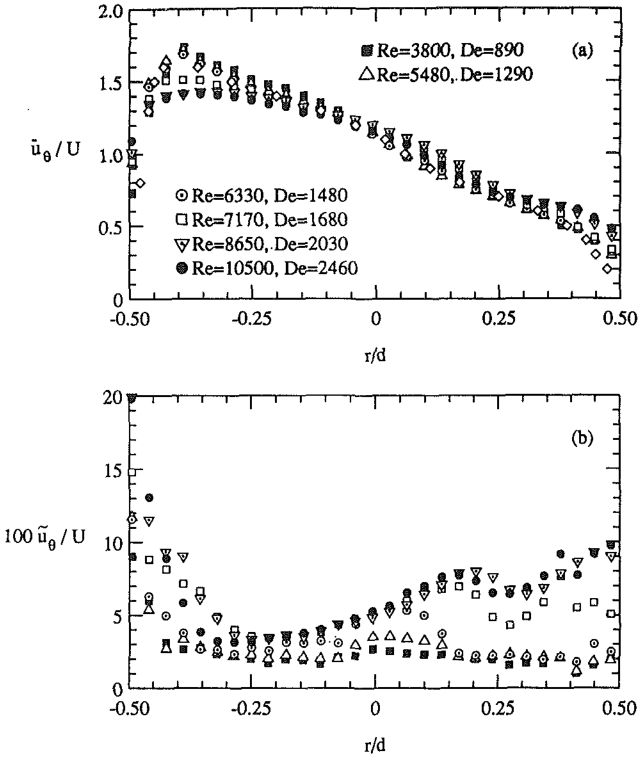

Fig. 4 Mean (*a*) and rms (*b*) of u_θ along the coiled pipe midplane as a function of Re. Also shown is the mean midplane profile (◇) of u_θ calculated by Goering (1989) for Re = 3580 and R_c/a = 20 (De = 800)

test section is 40 pipe diameters in length and of inner diameter 3.81 ± 0.05 cm. The first 14 pipe diameters in this segment contain soda straws packed into the pipe to straighten the flow. The helical coil consists of a 3.81 ± 0.05 cm inner diameter Tygon tube coiled to a diameter of 69.3 ± 0.2 cm, measured from the center of the tube ($R_c/a = 18.2$). The coil turns 5¼ revolutions and the helix angle is 3.40 ± 0.02 deg. To support the Tygon coil, eight Unistrut columns are arranged equidistantly along the perimeter of a circle and linked with plywood slats oriented at the correct pitch to form a continuous helical ramp. Coiling the Tygon tube leads to a slightly elliptic tube cross-section, which was measured with a micrometer to be at worst 3 percent out of round (3 percent is comparable to that of other studies of helical coils). Sreenivasan and Strykowski (1983) have noted that a small departure from circularity produces a comparably small lowering of the transitional Re. No further attempt was made to quantify the effect of ellipticity in this work.

A short transparent straight acrylic Plexiglass pipe section was constructed to allow optical access for the LDV measurements of the flow. The outside of the acrylic section is flat, while the inside was bored to 3.81 ± 0.05 cm to match the inner diameter of the Tygon tube. Great care was taken while gluing the acrylic section in place to insure that the transition from the Tygon tube to the acrylic section was smooth to the touch along the inside surface. The acrylic section is two pipe diameters long and is located at the outlet of the coil (i.e., 5¼ revolutions from the coil inlet). The acrylic section is followed by a straight piece of Tygon tube 30 pipe diameters in length.

Observations of neutrally-buoyant dye injected into the fluid near the tube wall upstream of the acrylic section revealed a smooth transition of the flow going from the Tygon tube into the acrylic section. All of the LDV measurements were performed at a location one pipe diameter into the acrylic section, after confirming that fully developed helical coil flow characteristics were being observed at this measurement location. That this was indeed the case is supported by two pieces of evidence. First, measurements of the velocity components at a single flow rate (Re = 5900) upstream of this location, 2/3 of a pipe diameter into the acrylic section (the optical access position furthest upstream), yielded mean and rms profiles as well as unsteady characteristics identical to those obtained at one pipe diameter. Second, as shown in Fig. 4(*a*), there is excellent agreement between present measurements of the mean streamwise velocity component at Re = 3800 and the profiles calculated by Goering (1989) for very similar flow parameters. Goering's (1989) profile is the result of solving the finite difference approximation to the Navier-Stokes equations for two-dimensional steady flow. The abscissa in Fig. 4(*a*) corresponds to the midplane illustrated by the continuous line on the left hand side of Fig. 1. In this and all the other velocity profile plots $r/d = 0.5$ indicates the inner wall location and $r/d = -0.5$ indicates the outer wall location.

The majority of the velocity component measurements were made through the side wall of the acrylic section using a DANTEC 55X modular optics LDV system in off-axis backscatter mode. For measurements of the streamwise velocity component at the three locations closest to the inner and outer pipe walls, respectively, the collection optics were relocated directly below the probe volume, at 90 deg relative to the entering beams, in order to improve the signal to noise ratio. The elliptical probe volume of the LDV system was estimated to be 1.0 mm long and 0.1 mm in diameter, based on the $1/e^2$ intensity boundary. It was moved with a precision of ±1/240 mm in any of three orthogonal directions by means of computer (IBM AT) controlled step motors. Corrections to the intersecting beams angle and the probe volume location, based on the index of refraction of the acrylic and water, were made using the formulae in Azzola and Humphrey (1984). (We note a typographical error in that paper: to be correct, the right-hand sides of Eqs. (4), (14), and (21) in Appendix I should be divided by the index of refraction of the fluid inside the pipe.)

Essentially neutrally-buoyant cornstarch particles, ranging in size between 1 to 10 μm, were used for seeding the flow. Reasonable signal to noise ratios were obtained by mixing one tablespoon of cornstarch into the 270 liters of water required by the flow system.

The two components of velocity were measured separately. The green-light wavelength of the LDV system was used to measure both components. For each measurement location, 2500 (4000 at some locations and Re) validated Doppler bursts and their time increments were recorded. The data rate was controlled to be low enough to insure that an accurate long-term mean could be obtained, but also high enough, as de-

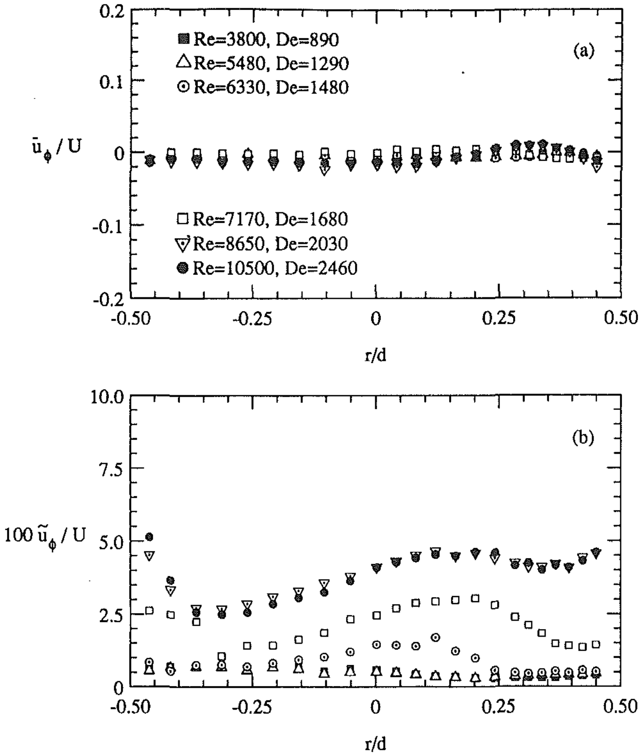

Fig. 5 Mean (*a*) and rms (*b*) of u_ϕ along the coiled pipe midplane as a function of Re

termined by the Nyquist criterion, to resolve nonturbulent flow oscillations. For all the results shown here the data rates varied between 40 and 50 Hz, approximately.

Power spectra were calculated from the velocity component time records using the slotted auto-correlation technique described by Bell (1986), which allows for the random variation in particle arrival times. Mean and rms values of velocity were computed by time-integrated averaging. This yielded values for these quantities in excellent agreement with the ensemble averaging approach.

Uncertainty Considerations

The uncertainty in the Reynolds number of the flow was estimated to be ±4 percent based on the uncertainty of the bulk velocity and that of the viscosity through variation in temperature. The sources of error affecting the mean and rms velocity measurements were: (1) systematic (and correctable) errors in the beam angle and optical probe volume location due to refraction of the beams by the curved acrylic wall (mentioned above); (2) additional (random) refraction effects; (3) filter bias; (4) finite-sample size; (5) velocity bias; (6) particle settling considerations and; (7) velocity gradient broadening.

The random uncertainty in the position of the optical probe volume was largely a function of the uncertainty incurred in determining its initial reference position and was shown to be negligible for the present measurements. Filter bias was also shown to be negligible by comparing data at various filter settings. The uncertainty due to finite-sample size was minimal because of the relatively large number of Doppler bursts collected. Velocity bias was reduced by time-integrating the LDV data numerically to determine the mean and rms. The settling velocity of the cornstarch particles was estimated to be 10^{-4} to 10^{-5} m/s which is negligible relative to the speed of the flow. The effect of gradient broadening at measurement locations away from the pipe walls was small since the velocity gradients across the probe volume were small.

The magnitude of the gradient broadening effect was not small for the streamwise velocity component measurements made near the outer wall, where the velocity gradient is relatively steep. Expressions from which the magnitude of the effect may be estimated for $\bar{u}_\theta$ and $\tilde{u}_\theta$, respectively, are given by Humphrey (1977). Unfortunately, these formulae cannot be used here because the values of $\partial\bar{u}_\theta/\partial r$ and $\partial^2\bar{u}_\theta/\partial r^2$ cannot be estimated with sufficient accuracy. However, we do note in these formulae that the rms due to gradient broadening is proportional to the velocity gradient (i.e., $\sigma_{gb} \sim (\partial\bar{u}_\theta/\partial r)$).

An estimate of the gradient broadening uncertainty in $\tilde{u}_\theta$ can be obtained from the data in Fig. 4(*b*). We know that at Re = 3800, the flow is laminar and steady everywhere in the pipe. This is supported by the values of $\tilde{u}_\theta$ (and of $\tilde{u}_\phi$ in Fig. 5(*b*)) which, at this Re, range between 0.5 percent and 3 percent. These levels of the rms for u_θ and u_ϕ are commensurate with that expected from the background noise associated with the measurement technique. However, the values of $\tilde{u}_\theta$ at Re = 3800 for the two data points nearest the outer wall (r/d = −0.49 and −0.46) are significantly larger than 3 percent. This is attributed to the gradient broadening effect.

The correction for gradient broadening is implemented as follows. From the formula in Humphrey (1977) an estimate of the rms due to gradient broadening relative to the gradient broadening at Re = 3800 is:

$$\frac{\sigma_{gb}}{(\sigma_{gb})_{\mathrm{Re}=3800}} = \frac{\dfrac{\partial\bar{u}_\theta}{\partial r}}{\left(\dfrac{\partial\bar{u}_\theta}{\partial r}\right)_{\mathrm{Re}=3800}} \tag{1}$$

The velocity gradient near the wall is expected to vary with Re. We can estimate the dependence of $\partial\bar{u}_\theta/\partial r$ on Re from the $\bar{u}_\theta$ profiles in Fig. 4(*a*). The central finite difference approximation is used to determine the ratio of velocity gradients at r/d = −0.46. The corrections to σ_m is determined by noting that:

$$\sigma_c^2 = \sigma_m^2 - \sigma_{gb}^2 \tag{2}$$

where the "m" and "c" subscripts denote measured and corrected values, respectively. The outer wall values of $\tilde{u}_\theta$ plotted in Fig. 6 have been corrected for the gradient broadening effect. The magnitude of σ_{gb} at Re = 3800 is determined by requiring that 100 $\tilde{u}_\theta/U$ equal 2.5 percent, which is a value consistent with the rest of the profile. None of the other plots for $\tilde{u}_\theta$ presented here have been corrected for gradient broadening. The gradient broadening effect on $\bar{u}_\theta$ is to slightly increase the values of the profile near the outer wall. The effects of gradient broadening on $\bar{u}_\phi$ and $\tilde{u}_\phi$ were found to be negligible.

After accounting for all major sources of uncertainty in the LDV measurements, the total random uncertainties in the mean and rms of the velocity components in the bulk of the flow are both estimated to be ± 3 percent. Experimental reproducibility was ascertained by repeating measurements of selected results to within the stated uncertainties for essentially identical test conditions.

The value of the dominant frequency used to calculate the Strouhal number was determined from power spectra obtained from the velocity time records. Ten independent time records, each consisting of 2000 validated Doppler bursts, were collected at each measurement location. The Strouhal number reported at each measurement location is the average of those appearing in the ten power spectra. Its standard deviation is $\sigma_m = \sigma/\sqrt{N-1}$ (Young, 1962). The standard deviation, σ, was estimated to be ± 10 percent, from which it follows that σ_m = ±3 percent, approximately, for N = 10.

Results and Discussion

All the data provided in the plots discussed in this section have been filed with the *Journal of Fluids Engineering* (see JFE Data Bank Contribution, below). The measurements in-

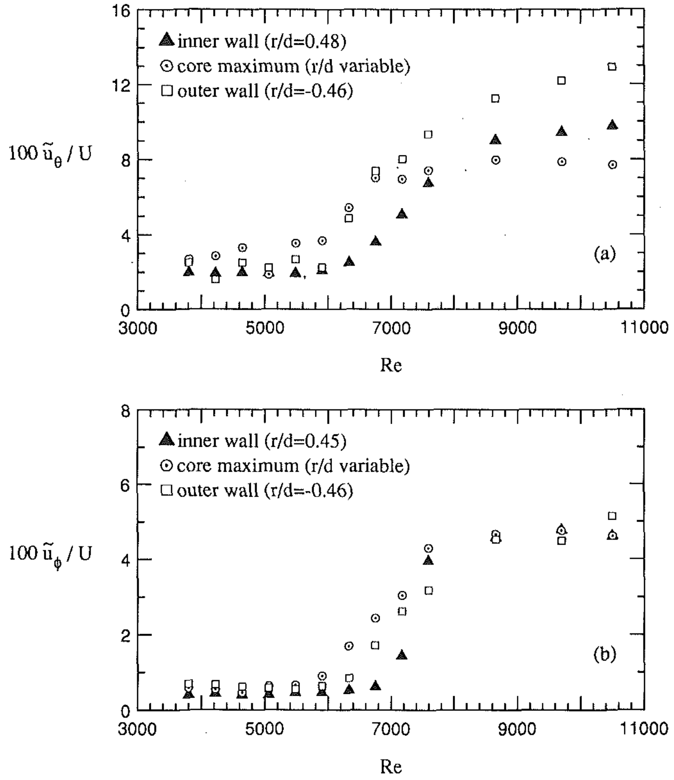

Fig. 6 Near wall and core variation of $\tilde{u}_\theta$(*a*) and $\tilde{u}_\phi$ (*b*) as a function of Re. The value of $\tilde{u}_\theta$ at the outer wall location has been corrected for gradient broadening in this figure only.

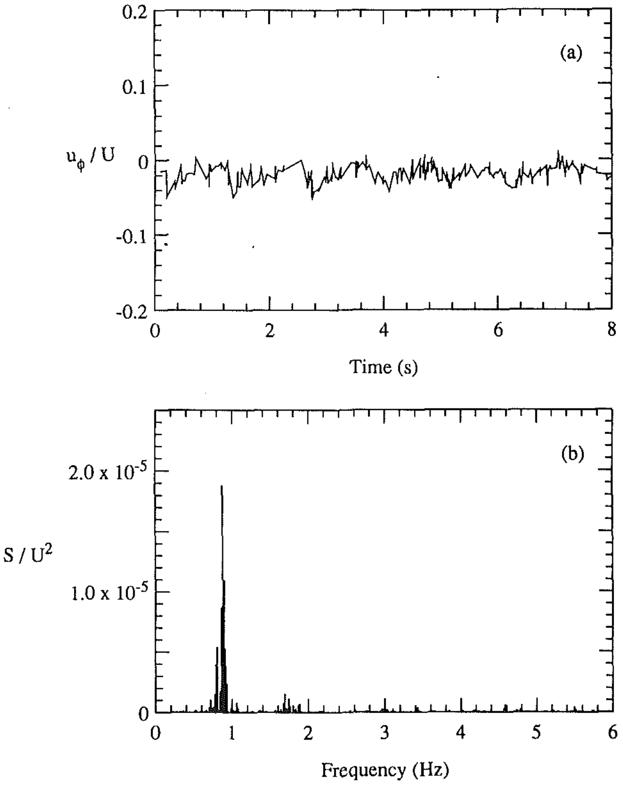

Fig. 7 Time record (*a*) and power spectrum (*b*) of u_ϕ on the midplane of the coiled pipe, 2.3-mm from the inner wall for Re = 5060, De = 1190

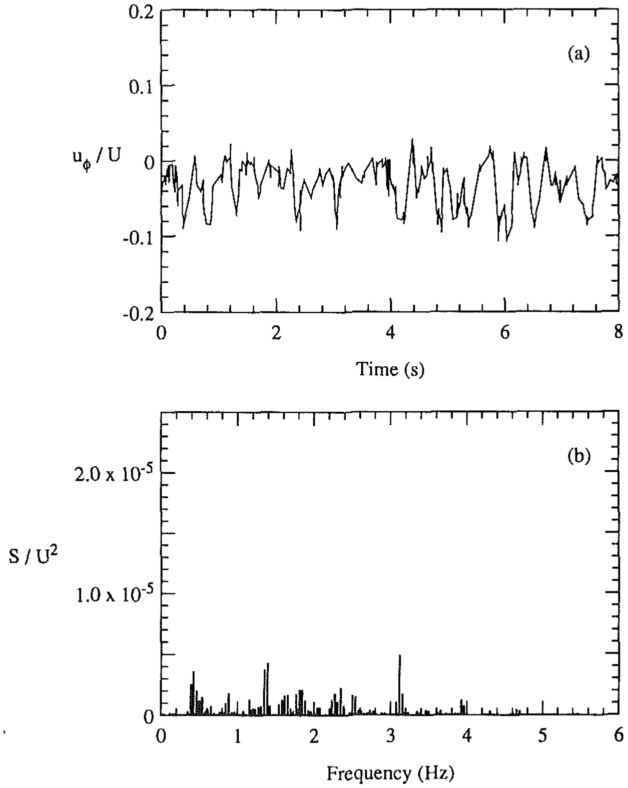

Fig. 8 Time record (*a*) and power spectrum (*b*) of u_θ on the midplane of the coiled pipe, 2.3-mm from the inner wall for Re = 6750, De = 1580

clude values of the mean and rms of u_θ and u_ϕ obtained for thirteen values of Re in the range $3800<\mathrm{Re}<10500$ $(890<\mathrm{De}<2460)$. Figures 4 and 5 show profiles of the dimensionless mean and rms of u_θ and u_ϕ measured along the pipe midplane for six values of Re. Figure 6 shows the two rms velocity components as a function of Re at three pipe midplane locations. Figures 7 and 8 show typical velocity component time records and their associated power spectra. Finally, Figs. 9 and 10 show plots of St versus position on the pipe midplane for different values of Re.

A superposition of the profiles for $\bar{u}_\theta$ in Fig. 4(*a*) will show that this quantity increases with increasing Re near the pipe inner wall, while it decreases at the outer wall. This tendency of the flow toward a more uniform distribution of the streamwise velocity along the pipe midplane is expected as turbulent diffusion aids in the redistribution of momentum with increasing Re. We note from these profiles that, except for a relatively thin layer of fluid near the outer wall, the mean streamwise velocity component increases with increasing distance from the pipe inner wall. According to Rayleigh's circulation criterion (see Drazin and Reid, 1981) for two-dimensional flow in, for example, a curved channel, this is a condition for stable flow. The criterion is proposed by Sreenivasan and Strykowski (1983) to explain the "global stabilization" experienced by a turbulent flow as it laminarizes in a curved pipe in spite of the fact that shearing of the fluid at the pipe wall, especially at the outer wall, tends to promote turbulence.

The profiles for $\tilde{u}_\theta$ in Fig. 4(*b*) show that this quantity increases with increasing Re near the pipe inner and outer walls, and in the core of the flow. The maximum in $\tilde{u}_\theta$ in the core is located near the pipe center at low Re and is gradually displaced towards the pipe inner wall as Re increases. As discussed below, increases of $\tilde{u}_\theta$ in the core is primarily associated with a non-turbulent low-frequency sinusoidal oscillation of the type previously observed by Sreenivasan and Strykowski (1983). Near the outer wall we find no evidence of low frequency oscillations, the increase in rms with Re there being attributed to shear-induced production of turbulence. At sufficiently large Re (Re > 6750) shear-induced turbulence also contributes to the rms near the inner wall.

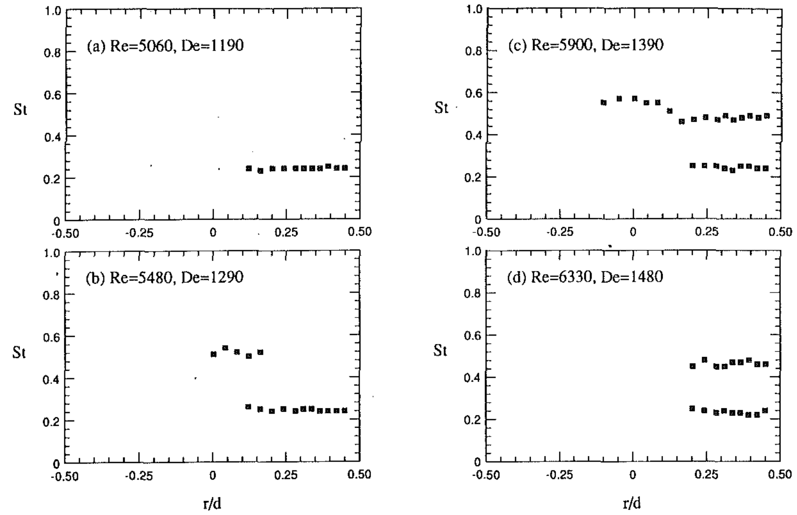

Fig. 9 Nondimensional dominant frequency for u_ϕ at four Re. ■ indicates the dominant Strouhal number at the measurement location on the midplane of the coiled pipe.

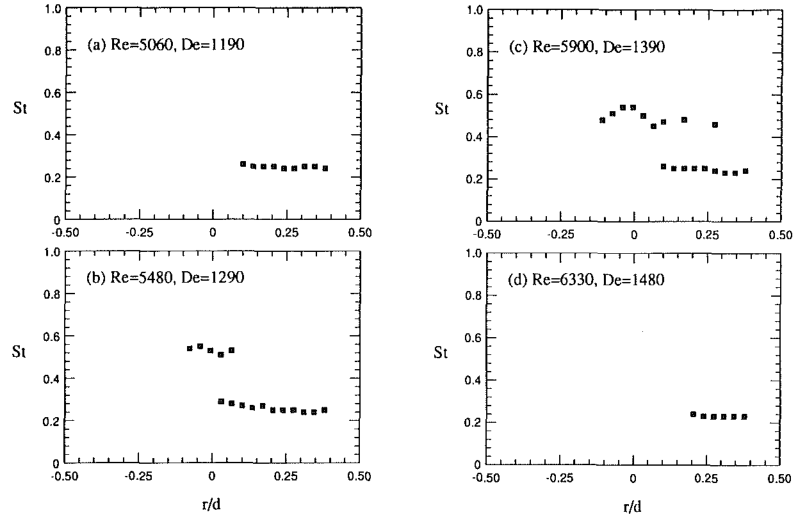

Fig. 10 Nondimensional dominant frequency for u_θ at four Re. ■ indicates the dominant Strouhal number at the measurement location on the midplane of the coiled pipe

The profiles for $\overline{u}_\phi$ shown in Fig. 5(a) reveal that this velocity component was not significantly different from zero. A very minor, but measurable, asymmetry in the profiles is attributed to both the effect of the helix angle on the flow and the small uncertainty in the probe volume location relative to the pipe midplane. The profiles for $\tilde{u}_\phi$ in Fig. 5(b) display the same qualitative trends with Re already discussed for $\tilde{u}_\theta$.

Figure 6 provides plots of $\tilde{u}_\theta$ and $\tilde{u}_\phi$ as a function of Re for three different positions on the pipe midplane; near the inner and outer walls of the pipe, and the (variable) midplane location where the maximum arises in the core of the flow. Because of the negligible contribution of gradient broadening to the measurements of $\tilde{u}_\phi$ near the outer wall, the low values of this quantity at that location confirm the steady laminar nature of the flow there for Re < 6330. Both sets of data for $\tilde{u}_\theta$ and $\tilde{u}_\phi$ show these quantities increasing significantly at all three locations for the range 6330 < Re < 7590. At high Re (Re > 8650) the profiles for $\tilde{u}_\theta$ and $\tilde{u}_\phi$ differ significantly in their respective magnitudes near the pipe walls, the values for $\tilde{u}_\theta$ being larger. This is expected since shear-induced turbulence contributes directly to $\tilde{u}_\theta$ which, in turn, contributes to $\tilde{u}_\phi$ through pressure redistribution effects (see, for example, Tennekes and Lumley, 1972).

Time records and power spectra for u_ϕ at two Re are plotted in Figs. 7 and 8. Each record was obtained at the same location on the midplane of the pipe cross-section, 2.3 mm (0.12a) from the inner wall. This is the measurement location closest to the inner wall in Fig. 5. The characteristics of the flow at this location are considered to be representative of its behavior near the inner wall. It should be noted that the abscissa of the power spectra in these two figures stops at 6 Hz because nothing significant was detected beyond this value for Re < 6750. This observation is in agreement with previous observations that pipe curvature suppresses high frequency turbulent fluctuations at values of Re larger than the critical value for the flow through a straight pipe. (Although not shown here, velocity time records and power spectra for u_ϕ and u_θ at Re = 4850 at this measurement location revealed a steady laminar flow.)

The power spectrum for Re = 5060 (Fig. 7) shows a distinct nonturbulent flow oscillation with a single dominant frequency of approximately 0.85 Hz (St ≈ 0.25). As Re increases further, the oscillation frequency (St ≈ 0.25) persists at this measure-

Table 1 Reynolds numbers bounding the transition flow regime in helical coils of similar R_c/a

	Taylor (1929)	Sreenivasan and Strykowski (1983)	Current Investigation
R_c/a	18.6	17.2	18.2
Unsteadiness	Re ≈ 5830	Re ≈ 5000	Re ≈ 5060
Complete turbulence	Re ≈ 7100	Re ≈ 7100	Re ≈ 7590

ment location until approximately Re = 6750 (Fig. 8) when no distinctly dominant frequency emerges in the power spectrum.

A comparison between the Reynolds numbers bounding the transitional flow regime determined by previous investigators and those found in this work is provided in Table 1. For the current investigation, the first appearance of unsteadiness as determined from the power spectra occurs at Re = 5060. The determination of Re for fully turbulent flow is based on the significant increase in rms seen in Fig. 6 between Re = 6330 and Re = 7590. Thus, we take Re = 7590 to characterize fully turbulent flow; a value slightly below the Re = 8000 determined from the friction factor plot in Fig. 2. Although the curvature ratios are slightly different for the cases considered in the table, the results are consistent throughout.

Plots of the dominant St, obtained from the power spectra for the time records of u_ϕ, are given in Fig. 9 as a function of Re and position along the midplane of the pipe-cross section. For example, the peak at about 0.85 Hz (St ≈ 0.25) appearing in the power spectrum in Fig. 7 was averaged with the values obtained from nine additional independent spectra and the result appears as the datum closest to the inner wall in Fig. 9(*a*). At the measurement locations with more than one dominant frequency, each St is represented by an individual datum. Measurements locations with no dominant frequency are devoid of a symbol.

For Re = 5060 in Fig. 9, a flow oscillation with St ≈ 0.25 spans the distance from the inner wall to nearly the center of the pipe. At Re = 5480, the region of oscillation with St ≈ 0.25 remains. In addition, a frequency doubling phenomenon near the pipe center with St ≈ 0.5 is observed. This agrees with the "second harmonic" observations made by Sreenivasan and Strykowski (1983). The power spectra for Re = 5900 reveal that the physical domain with St ≈ 0.25 is reduced to a slightly smaller region near the inner wall, while the domain with St ≈ 0.5 has grown appreciably, extending towards both the inner and outer walls. At Re = 6330, oscillations with St ≈ 0.25 and St ≈ 0.5 are respectively present in the region close to the inner wall. As Re is increased further, the power spectra fail to reveal distinct frequencies with large energy. It should be noted that, although the region of flow unsteadiness was found to extend past the midplane center for some Re, no distinct low frequency unsteadiness was observed near the outer wall for the present experimental conditions. This is consistent with the qualitative observations of Sreenivasan and Strykowski (1983).

The corresponding data for St based on the time records for u_θ are shown in Fig. 10. The data rate at the three measurement locations closest to the inner wall was not high enough to resolve the flow unsteadiness there. For this reason these locations are devoid of symbols irrespective of the flow characteristics. The results in Fig. 10 based on u_θ are very similar to those shown in Fig. 9 based on u_ϕ. However, a noteworthy difference between the two figures is the appearance of an oscillation with St ≈ 0.5 close to the inner wall at Re = 5900 and 6330 when St is based on u_ϕ. This is not shown in the plots of St based on u_θ.

From the St plots it is concluded that the flow is similar to, but distinct from, the wavy-vortex flow mentioned in the Introduction. In a wavy-vortex flow the interface location between vortex pairs undulates and a corresponding oscillation in the time-resolved secondary velocity can be measured at a fixed point corresponding to the time averaged interface location. In the helical coil, u_ϕ near the pipe inner wall oscillates in this way but no corresponding oscillations are observed near the outer wall. Thus, the unsteadiness observed near the inner wall of the coiled pipe is similar to a wavy-vortex flow, however the frequency doubling at some locations and for some values of Re, and the lack of low-frequency unsteadiness near the outer wall, distinguish this flow from a wavy-vortex flow. There is currently no explanation for the frequency doubling appearing in Figs. 9 and 10.

Concluding Discussion

Profiles of the mean and rms for two velocity components, and the associated unsteadiness of the flow as characterized by its Strouhal number, have been measured along the midplane of a helically coiled pipe for conditions spanning the laminar and turbulent flow regimes. The spatial dependence of the rms measurements is intriguing. The flow unsteadiness shown in Figs. 9 and 10 first appears at Re = 5060, while the maximum for $\tilde{u}_\theta$ in the core of the flow first appears at Re = 5480. (The Re was increased incrementally but no measurements were taken between Re = 5060 and 5480.) It seems reasonable to attribute the rms maximum in the core of the flow to the low-frequency non-turbulent flow oscillations described in relation to Figs. 9 and 10. For Re < 6330, the rms is small near the walls. This indicates that coil curvature is suppressing turbulent fluctuations that would be produced by steep velocity gradients at the walls. For Re > 6330, the increase in rms near the walls is attributed to high frequency shear-induced turbulent fluctuations indicating that the turbulence suppression ability of the coil diminishes with increasing Re. The rms maximum in the core persists at high Re and seems to level out at approximately 8 percent for $\tilde{u}_\theta$ and 4.5 percent for $\tilde{u}_\phi$. We suggest that low frequency unsteadiness of the type distinctly observed for 5060 < Re < 6330 continues to influence the flow once in the fully turbulent regime, even though it is not distinctly observable in the power spectra. (This has been the observation of Belaidi et al. (1993) for the turbulent flow developing in a 90 deg curved duct of rectangular cross-section.)

The questions remain: What is the origin of the instability producing the low frequency unsteadiness observed in a helical coil, and what is the mechanism for maintaining it? It is evident from Figs. 9 and 10 that the unsteadiness originates in the inner half of the pipe cross-section at low Re (Re ≈ 5060), and extends beyond the pipe center at higher Re. Figure 1 shows that the flows returning along the top and bottom of the pipe cross-section collide at the midplane of the pipe near the inner wall. The merged cross-stream flow jets away from the inner wall along the pipe midplane.

An examination of the velocity profile of this cross-stream jet, generated numerically by Goering (1989) in a coil with Re = 3580 (De = 800) shows that the jet satisfies Rayleigh's inflection point theorem and Fjørtoft's theorem for possible instability (Drazin and Reid, 1981). Clearly, the cross-stream jet in a helical coil is not a strictly inviscid parallel flow since it entrains fluid while undergoing accelerated and decelerated motions sequentially in moving from the inner to the outer wall. However, in the core of the flow where we observe the maximum in the rms it is reasonable to suggest that the midplane jet is unstable, in the sense of a Bickley jet, to a sinuous (even) mode (Drazin and Reid, 1981). Coughlin and Marcus (1992) also point to the radial jet as the source of instability in the Taylor-Couette concentric cylinder geometry for the emergence of the wavy-vortex and modulated wavy-vortex flows.

We conclude by noting that other evidence of low frequency oscillations in laminar and turbulent flows through curved conduits is to be found in the studies of Chang et al. (1983), Arnal et al. (1993), and Belaidi et al. (1993). The geometrical configurations investigated by these authors all correspond to relatively short bends (90 deg $< \theta <$ 180 deg) of square or rectangular cross-section and the range of the parameters explored are similar. Notwithstanding the dissimilarities in the bend angle and cross-section shape with respect to our coil, the midplane profile for $\tilde{u}_\theta$ measured by Chang et al. (1983) at the $\theta = 90$ deg location for Re = 56,700 in a duct of square cross-section with $R_c/a = 6.7$ displays the same qualitative features as the profiles for $\tilde{u}_\theta$ measured here at the highest Re. That flow was also calculated by solving finite difference approximations to the three dimensional steady Navier-Stokes equations with a two-equation (k-ϵ) model of turbulence. The profile predicted for $\tilde{u}_\theta$ did not display the maximum observed experimentally in the core of the flow. To capture this effect a calculation must account for the low frequency unsteady nature of the flow in addition to the high frequency turbulence.

JFE Data Bank Contribution

The data shown in Figs. 4 through 10 have been filed with the *Journal of Fluids Engineering* under the title HELICOIL. The order of appearance of the data in the file is as shown in the plots. The file is self-explanatory and the notation employed is consistent with the paper for ease of use. To access this file, see instructions on p. 542 of this issue.

Acknowledgments

The authors gratefully acknowledge the financial support of this investigation by the Institute for Scientific Computing Research at Lawrence Livermore National Laboratory through grant award numbers ISCR 89-04, ISCR 89-05, and ISCR 90-04.

References

Arnal, M., Goering, D. J., and Humphrey, J. A. C., 1992, "Unsteady Laminar Flow Developing in a Curved Duct," *Int. J. Heat and Fluid Flow*, Vol. 13, pp. 347–357.

Azzola, J., and Humphrey, J. A. C., 1984, "Developing Turbulent Flow in a 180 deg Curved Pipe and its Downstream Tangent," Lawrence Berkeley Laboratory Report #LBL-17681.

Belaidi, A., Johnson, M., and Humphrey, J. A. C., 1992, "Flow Instability in a Curved Duct of Rectangular Cross-Section," ASME JOURNAL OF FLUIDS ENGINEERING, Vol. 114, pp. 585–592.

Bell, W. A., 1986, "Spectral Analysis of Laser Velocimeter Data with the Slotted Correlation Method," *Proceedings of the AIAA/ASME Fourth Fluid Mechanics, Plasma Dynamics and Lasers Conference*.

Chang, S. M., Humphrey, J. A. C., and Modavi, A., 1983, "Turbulent Flow in a Strongly Curved U-Bend and Downstream Tangent of Square Cross-Section," *PhysicoChemical Hydrodynamics*, Vol. 4, No. 3, pp. 243–269.

Coughlin, K. T., and Marcus, P. S., 1992, "Modulated Waves in Taylor-Couette Flow. Part 2. Numerical Simulation," *Journal of Fluid Mechanics*, Vol. 234, pp. 19–46.

Drazin, P. G., and Reid, W. H., 1981, *Hydrodynamic Stability*, Cambridge University Press, New York, N.Y.

Finlay, W. H., Keller, J. B., and Ferziger, J. H., 1988, "Instability and Transition in Curved Channel Flow," *Journal of Fluid Mechanics*, Vol. 194, pp. 417–456.

Goering, D. J., 1989, "The Influence of Curvature and Buoyancy in Three-Dimensional Pipe Flows," Ph.D. thesis, Dept. of Mechanical Engineering, University of California at Berkeley.

Humphrey, J. A. C., 1977, "Flow in Ducts with Curvature and Roughness," Ph.D. thesis, Imperial College, London.

Ito, H, 1959, "Friction Factors for Turbulent Flow in Curved Pipes," ASME *Journal of Basic Engineering*, Vol. 81, pp. 123–134.

Marcus, P. S., 1984, "Simulation of Taylor-Couette Flow. Part 2. Numerical Results for Wavy-Vortex Flow with One Travelling Wave," *Journal of Fluid Mechanics*, Vol. 146, pp. 65–113.

Sreenivasan, K. R., and Strykowski, P. J., 1983, "Stabilization Effects in Flow Through Helically Coiled Pipes," *Exp. in Fluids*, Vol. 1, pp. 31–36.

Taylor, G. I., 1929, "The Criterion for Turbulence in Curved Pipes," *Proceedings of the Royal Society*, Series A, Vol. 124, pp. 243–249.

Tennekes, H., and Lumley, J. L., 1972, *A First Course in Turbulence*, The MIT Press, Cambridge, MA.

White, C. M., 1929, "Streamline Flow Through Curved Pipes," *Proceedings of the Royal Society*, Series A, Vol. 123, pp. 645–663.

Young, H. D., 1962, *Statistical Treatment of Experimental Data*, McGraw-Hill, New York, N.Y.

Turbulent Swirling Flow in Short Cylindrical Chambers

A. Riahi[1]

P. G. Hill

The University of British Columbia,
Vancouver, B.C., Canada V6T 1W5

Turbulent swirling flow in a short closed cylindrical chamber has been measured with laser Doppler anemometry. The swirl was generated by a rotating roughened disk and measured during steady and transient conditions with a smooth disk. The velocity and turbulence fields were found to be strongly dependent on swirl Reynolds numbers (in the range $0.3 \times 10^6 < \Omega R^2/\nu < 0.6 \times 10^6$*) and on chamber length-to-diameter ratio (in the range* $0.1 \le L/D \le 0.5$*). With a roughened disk the flow was nearly independent of Reynolds number though still strongly dependent on chamber length-to-diameter ratio.*

1 Introduction

Swirl in the cylinders of spark ignition engines has been shown to have important effects on the rate of combustion and on engine efficiency. Nagao and Tanaka (1983), for example, have shown by tests on three spark-ignition engine combustion chambers that swirling the fuel-air mixture around the piston axis (at up to 5 times engine rpm) can cut burning duration in half, allow the engine to operate with leaner mixtures and significantly improve engine efficiency. As Young (1981) has shown, shorter burning periods are generally associated with reduced cycle-to-cycle variations so that increased swirl could in principle have a beneficial effect on engine emissions. Another effect of swirl, however, is enhanced heat transfer to the chamber walls and this could reduce engine efficiency. Swirl may also adversely affect the volumetric efficiency. Thus it is not surprising that in practice there appears to be an optimum swirl intensity in spark-ignition engines.

A full understanding of the effect of swirl on flame propagation and heat transfer in spark-ignition engines would require considerable knowledge of the effect of transient swirl on the mean velocity and turbulence distributions. Measurement of such quantities in engines is difficult because of rapid transients and cycle-to-cycle variations in the presence of combustion. A number of workers have therefore studied swirl in closed chambers. Dyer (1979), Inoue et al. (1980), and Wahiduzzaman (1985) generated transient swirl in closed cylindrical chambers by sudden injection of combustible mixture. Inoue et al., for example, compared the results of injections at either 0 or 30 deg to the radial direction. Comparing the second case to the first at a given time after injection, the turbulence intensity almost doubled and the combustion duration was halved. Similar results were observed by Dyer who measured the transient velocity, turbulence and temperature fields after nearly tangential injection, and also determined combustion duration.

Wahiduzzaman (1985) studied the effect of swirl on the rate of heat transfer to the wall of constant-volume cylindrical chambers with different length-to-diameter (L/D) ratios. His method of swirl generation was similar to that of Dyer. He deduced from his measurements that the Nusselt number pertaining to the average surface heat rate is proportional to the 0.8 power of the swirl Reynolds number based on the half-radius velocity. He also found that at a given swirl Reynolds number the Nusselt number increases as aspect ratio L/D is decreased.

Studies of steady-state swirl in short cylinders are nevertheless of interest because of what they may reveal about flow patterns and the relationship between swirl and turbulence generation. This insight is a necessary precursor to full understanding of the transient case. As an example of prior work on steady swirl in short cylinders, Daily and Nece (1960) have observed the flow between stationary and rotating disks in a cylindrical space of L/D between 0.0063 to 0.109. They observed three regimes of flow within the chamber depending on the disk rotational Reynolds number ($\Omega R^2/\nu$) and the L/D ratios:

(*a*) Laminar flow with the boundary layers on the rotor and stator merged together; hence core velocity changes continuously across the chamber from rotor to stator
(*b*) Laminar flow with distinct boundary layers on the rotor and stator. Between the boundary layers is a core region in which the velocity remains axially invariant.
(*c*) Turbulent counterpart of regime (*b*)

With L/D equal to 0.1, Daily and Nece observed the transition from regime (*a*) to (*b*) at a Reynolds number of about 200. With further increase in Reynolds number the boundary layers became thinner until a critical Reynolds number of about 4×10^5 at which transition was observed, beginning at the top radius and moving inward in such a way that the boundary layers again merged. With further increase in Reynolds number (above 10^6) the turbulent boundary layers again became distinct and an identifiable core region of nearly uniform tangential velocity was observed between the stationary and rotating disks. For the case $L/D = 0.1$ the ratio of this core

---

[1] Now at Pratt & Whitney Canada, Longueuil, Quebec.

Contributed by the Fluids Engineering Division for publication in the JOURNAL OF FLUIDS ENGINEERING. Manuscript received by the Fluids Engineering Division February 16, 1992; revised manuscript received February 8, 1993. Associate Technical Editor: J. Humphrey.

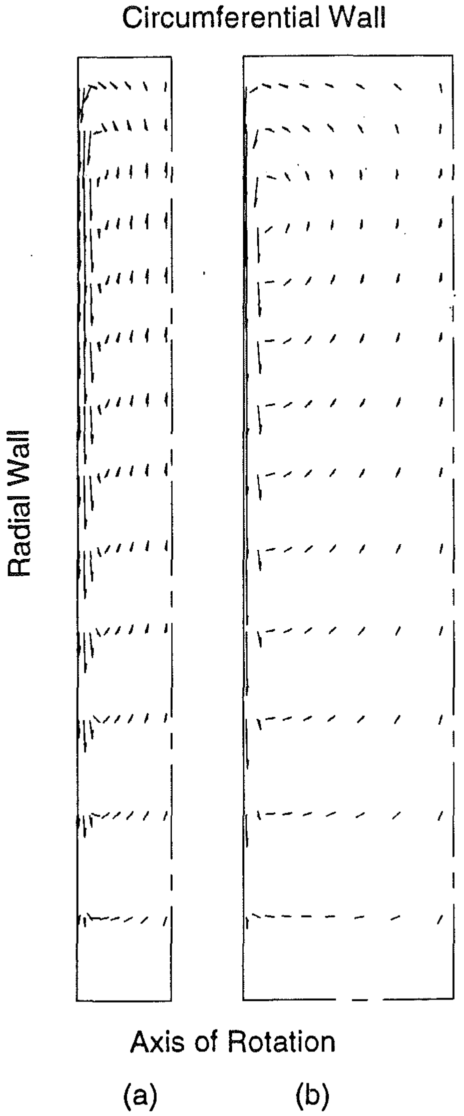

(a) (b)

Fig. 1 Secondary flow pattern in closed chambers with two aspect ratios. (*a*) L/D = 1/10, (*b*) L/D = 1/5

velocity to the disk tip velocity was 0.412. Daily and Nece were able to calculate the frictional torque coefficients for each of these flow regimes but their observations did not include turbulence quantities or secondary flow.

During the burning period in an internal combustion engine the combustion chamber L/D is of order 0.1. This means that secondary flow in such a chamber plays a very important role in turbulence generation and in swirl decay. The secondary flow in short cylinders arises because of the imbalance (in the boundary layer on the end walls which may be flat) between the radial pressure gradient and the radial gradient of the centrifugal force $\rho w^2/r$ in which w is the tangential velocity in the boundary layer and ρ is the local density. Between the end boundary layers the radial pressure gradient is essentially equal to $\rho W^2/r$ where W is the tangential velocity of the bulk of the flow between the boundary layers. Because radial and axial velocity components are much smaller than W, the radial pressure gradient $\partial P/\partial r$ is essentially independent of z, the axial coordinate, and thus in the boundary layer $\partial P/\partial r > \rho w^2/r$ and there arises a radially inward acceleration $w\ (\partial w/\partial r)$. The result of this is shown typically in Fig. 1 which represents calculated velocity vectors in the meridian planes of cylinders with L/D equal to 0.1 and 0.2. Here the walls on the top and left side of each section are stationary in each case, and only one-quarter of the meridian plane is shown. In each case the meridian velocity components are much less than W. Nevertheless, they have a large effect (particularly for the case $L/D = 0.1$) upon wall friction, swirl decay, and turbulence generation because this secondary flow convects the highly turbulent fluid from the outer cylindrical wall across the large end wall area. In a previous paper (Riahi, et al., 1990), we have shown that the large effect of curvature on turbulent shear stress at the circumferential wall and on the nonisotropy of the turbulent velocity components are well accounted for, in various experimental results, by the Wilcox and Chambers (1977) method. The implication of that work for the understanding of swirling flows in short cylinders is that not only secondary flow but also streamline curvature must be included in any adequate account of the flow field development.

In summary it appears that while studies of swirling combustion in short cylinders reveal strong effects of swirl on both combustion rate and heat transfer, there is insufficient published information on the link between swirl, turbulence and these combustion and heat transfer effects. There is first of all a need for further data on the effect of swirl on the velocity and turbulence fields with no combustion and with steady-state swirl at those "high" Reynolds numbers in the range of practical interest.

The purpose of this paper is to present the results of an experimental study of the swirling velocity and turbulence fields in short cylinders under steady-state and transient conditions. The steady-state swirl was generated by steady rotation of a disk covering one end wall of the chamber.

2 Experimental Aparatus

2.1 Swirl Chamber. Figure 2 shows the swirl chamber with the thin shaft-driven disk at the left-hand side. The walls of the chamber are thick and the shaft is provided with a labyrinth seal designed by Pierik (1987) to permit combustion of swirling mixtures though only cold flow experiments are described in this paper. The chamber diameter is 10.16 cm and, as shown, has L/D equal to 0.5. Spacer blocks were provided to reduce the length-diameter ratio to 0.3 or 0.1. The driving disk is a 0.076 cm thick disk 9.825 cm in diameter and driven by a 0.635 cm diameter steel shaft. The disk was driven by a DC motor at speeds in the range 200–3000 rpm.

Shown in Fig. 2 are the two quartz windows mounted on the curved side-walls of the chamber to allow entrance and exit of laser beams used in velocity measurement. The chamber and motor were mounted on a 3-dimensional traversing table used to control the focusing point of the laser beams.

Early experiments showed that a smooth-surface disk provided considerable swirl but relative turbulence intensities (w'/W) less than 0.01. To increase the turbulence intensities a thin perforated grating with roughness elements of about 1.5 mm in average height and average spacing of 0.55 cm was fastened to the smooth disk. This raised peak relative turbulence intensities to approximately 0.025. It is chiefly the roughened disk data that we present in this paper.

2.2 Diagnostic Instrumentation. The mean velocity and turbulence intensity measurements were made with laser Doppler anemometry (LDA) in forward scattering, as described by Drain (1972). The system components were manufactured by Thermal Systems Incorporated (TSI). A 15 mW He-Ne laser (Model No. 9124) was used as the source supplying light at 632.8 nm wavelength.

Leaving the source the laser beam passed through a collimator (Model No. 9108) and beam splitter (Model No. 9115-2) which produced two beams of equal intensity 50 mm apart. The Bragg cell (Model No. 9180) was used to shift the frequency of one of the beams by 40 MHz. The two beams were focused to a single point with a lens of 250 mm focal length (Model

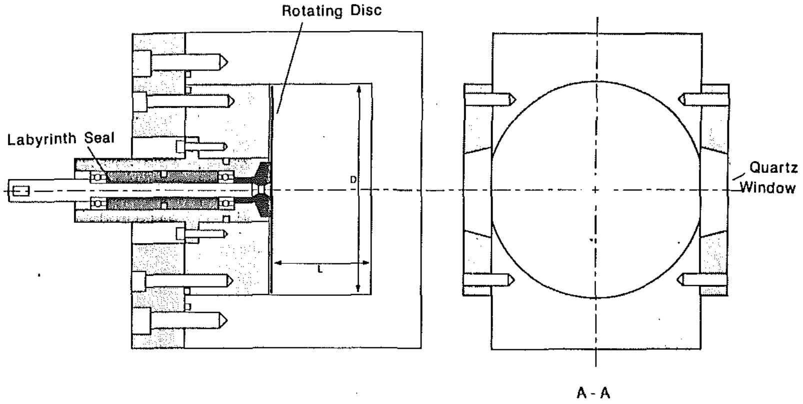

Fig. 2 Schematic of the cylindrical chamber with rotating disk

Table 1 Skewness and flatness factors for LDA signal distributions Re = 0.47 × 10^6 $L/D = 1/2$

r/R	skewness	flatness
0.069	0.03	2.86
0.1379	0.05	3.08
0.207	0.013	2.87
0.2759	0.0213	2.9
0.3448	0.0465	2.85
0.4138	0.034	3.07
0.4828	0.01	3.06
0.5517	0.0076	3.0
0.6207	0.034	3.0
0.6897	0.0248	3.15
0.7586	−0.002	3.0
0.8276	−0.04	3.1
0.8966	0.007	3.15

No. 9118). The angle between the two beams was 11.4 deg. The ellipsoidal measuring volume was 1.9 mm in the axial direction and 0.18 mm in the transverse direction. The fringe spacing was 3.19 μm so that the typical number of stationary fringes was $0.18/3.9 \times 10^{-3} = 57$.

The light scattered by particles traversing the measuring volume was collected by two lenses of 250 mm focal length (Model No. 9140) which focused the collected light on the 0.2 mm aperture of the light detector. The collected light was converted into an electrical analog signal by a photomultiplier (Model No. 9160). The output signal from the photomultiplier was processed by a counter-type signal processor (Model No. 1980B) as described by Adrian and Fingerson (1981).

To minimize the possibility of centrifugal separation of seeded particles, water was used instead of air as the working fluid. With water, particle seeding was found to be unnecessary.

2.3 Data Collection and Processing. Passing from the photomultiplier to the counter-type signal processor, the signal was filtered by a series of low- and high-pass filters. After rejection of erroneous signals, the frequency of a preset number of cycles was measured and recorded. The recorded frequency was subsequently processed by the FIND software (provided by TSI) to extract velocity and other statistical information.

(*a*) *Steady-State Data Processing.* Due to the random nature of LDA signals, large collections of data points are expected to have normal distributions, i.e., skewness and flatness factors of zero and three, respectively. For steady-state measurements, 5000 data points at 13 radial locations were collected. If the agreement were close, the data points were stored for post processing; otherwise the measurement was repeated until satisfactory conditions were attained. A margin of ±5 percent from normal distribution for skewness and flatness factors was considered acceptable. Table 1 shows typical skewness and flatness factors calculated for flow with a disk Reynolds number of 0.47 × 10^6.

For this case McLaughlin and Tiederman (1973) have proposed the following averaging procedure was to reduce the biasing error. With w_i being the ith velocity in a set of N determinations the average velocity is given by

$$\overline{w} = \frac{\sum_{i=1}^{N} \left(\frac{1}{w_i}\right) w_i}{\sum_{i=1}^{N} \frac{1}{w_i}} = N / \sum_{i=1}^{N} \frac{1}{w_i} \tag{1}$$

With the average velocity determined, the rms fluctuation w' was determined from

$$w' = \sqrt{\frac{1}{N} \sum_{i=1}^{N} (w_i - \overline{w})^2} \tag{2}$$

For the steady-state measurements, mean velocity determination by the continuous and total burst methods typically differed by two percent. Using the continuous method on data sets satisfying the skewness and flatness criteria mentioned above, the mean velocity determination with and without the biasing correction differed by only 0.5 percent. The corresponding difference in the rms fluctuations was one percent. Though the total burst method is the most accurate method of measurement (after biasing correction), it reduces the data rate. In steady-state measurement, this is of no concern. However in transient measurements reduced data rate can be detrimental. For this reason the total burst mode of analysis was not adopted, and an inherent error of two percent was attributed to the velocity measurements. Appendix A gives the method and result of the uncertainty analysis.

(*b*) *Transient Data Processing.* For the measurements of transient swirl, data were collected at seven radial locations. At each location, ten batches of 5000 data points were collected. The mean velocity and turbulence intensity decay were then obtained by the following procedure.

The transient data collection was initiated by switching off the motor. Post processing of the data revealed a slow decay of bulk velocity during the first 100 ms followed by a much faster decay in the case of $L/D = 1/2$. This observation indicated that the disk does not come to rest instantaneously due to the inertia of the DC motor shaft. Hence, it was decided to ignore the data in the first 100 ms after the motor was switched off.

The best mean velocity curve for each of the ten data files, at each of the seven locations, was determined over a time span of 100 to 600 ms after the motor had been switched off.

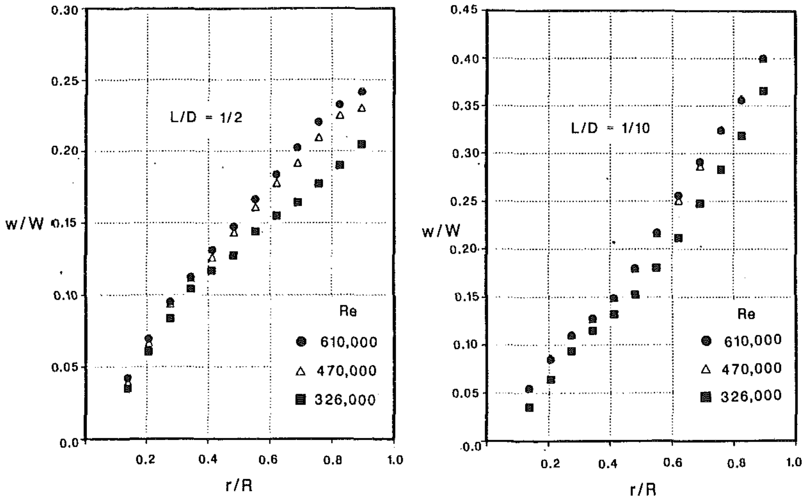

Fig. 3 Dimensionless tangential velocity profile generated by a smooth disk at mid-plane of chamber

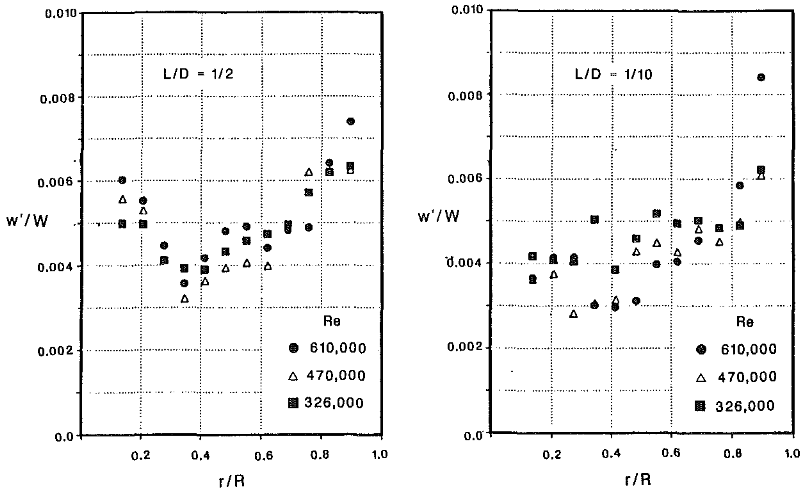

Fig. 4 Dimensionless rms velocity profile generated by the smooth disk at mid-plane of chamber

The exponential curve of the form $w_e(t) = \exp(a + bt + ct^2 + dt^3)$ was found to provide a good fit to the raw data.

The total time span was then divided into 20 equal 25 ms time windows and the mean velocity at the mid-point of each window was obtained (w_{ei}). The rms velocity (w_{rms}) at these mid-points (for each of the 10 data files) were then calculated by the following equation:

$$(w_{rms})_k = \sqrt{\frac{1}{N}\sum_{i=1}^{N}(w_i - w_{ei})^2}$$

where N corresponds to the total number of data points in the kth time window interval.

The mid-point mean and rms velocities for each window were then ensemble-averaged over the m data files, using the following equations:

$$(w)_{ens\ k} = \frac{1}{m}\sum_{j=1}^{m} w_{kj}$$

$$(w_{rms})_{ens\ k} = \frac{1}{m}\sum_{j=1}^{m}(w_{rms})_{kj}$$

These are the ensemble-averaged mean and rms velocities at the mid-point of the kth window; m is the total number of data files per location (10 in the present case).

3 Experimental Results and Analyses

3.1 Steady-State Results. Riahi (1990) has reported in tabular form the experimental measurements of relative tangential velocity and relative turbulence intensity for the swirling flow generated by the smooth disk. For 2 of these cases (L/D = 1/2, 1/10) the data are plotted in Figs. 3 and 4 to show the typical effects of L/D and Reynolds number defined as

$$\mathrm{Re} = \frac{\Omega R^2}{\nu}$$

in which R is the radius of the rotating disk (very nearly equal to the cylinder radius) Ω is the rotational speed, and ν is the kinematic viscosity (1.48×10^{-7} m^2/s for water). The disk rotation speeds were 1180, 1700, and 2090 rpm and all of these measurements were made at the mid-plane of the chamber. Figure 3 indicates that the velocity field approaches Reynolds-number independence only at the highest Reynolds number. In contrast the relative turbulence intensity appears, within experimental uncertainty, to be approximately independent of Reynolds number.

From Figures 3 and 4 we can see that—

(a) The maximum mid-plane mean tangential velocity for a given aspect ratio L/D occurred at the highest disk rotational speed. However, from Fig. 3 we see that the maximum velocity

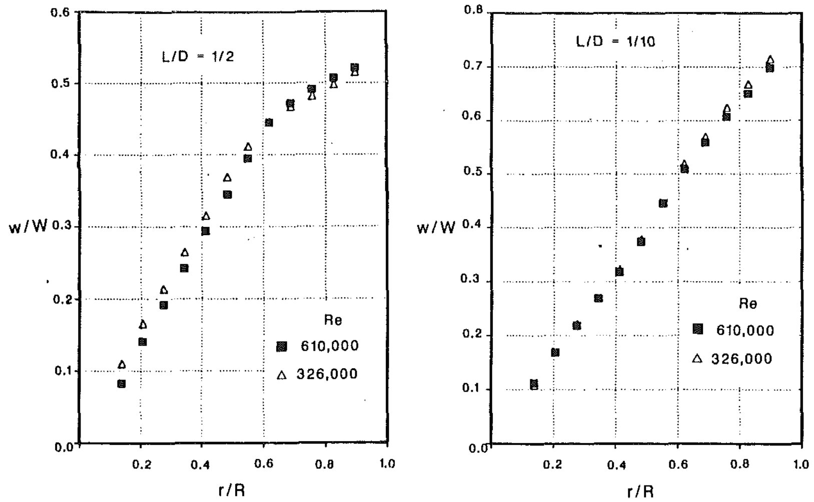

Fig. 5 Dimensionless tangential velocity profile generated by the roughened disk at mid-plane of chamber

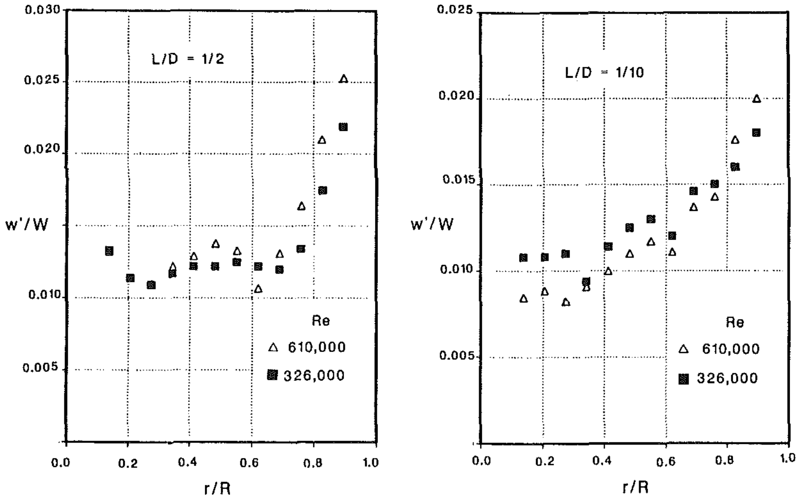

Fig. 6 Dimensionless rms velocity profile generated by roughened disk at mid-plane of chamber

is substantially greater with the lowest L/D. The maximum mid-plane tangential velocity at $r/R = 0.9$ varies with L/D at the same Reynolds number. This effect was also observed by Daily and Nece; at low L/D the slowing down effect of the chamber walls is low. For the case $L/D = 1/10$ and approximating the inner part of the swirl as solid body rotation, Daily and Nece (1960) reported that the ratio of core angular velocity β to rotor angular velocity Ω in the chamber with $L/D = 0.1$ at $\mathrm{Re} = 4.4 \times 10^6$ was 0.412. The corresponding ratio in the chamber with $L/D = 0.1$ at $\mathrm{Re} = 0.61 \times 10^6$ in the present investigation is 0.4. Though the Daily and Nece result pertains to a higher Reynolds number flow, direct comparison is applicable since our velocity profiles tend to be Reynolds-number independent. The Daily and Nece results (which also pertain to a smooth disk) suggest that the flow in the chamber with $L/D = 0.1$ becomes fully turbulent at $\mathrm{Re} = 0.5 \times 10^6$.

(*b*) The turbulence intensity is apparently fairly uniform near the center of the chamber and much larger near the outer wall where turbulence is generated in a region of high shear and enhanced by the effect of streamline curvature. In the central region of the flow where the rotation is close to solid body and thus nearly strain-free, one would expect little turbulence generation. In contrast near the outer wall the radial gradient of angular momentum is negative so the flow is unstable and high turbulence generation can be expected.

(*c*) The turbulence intensity level was small; the maximum intensity was 0.85 percent of the disk tip speed. To increase the turbulence intensity the impeller disk surface was uniformly roughened by fastening to it a thin grating with sharp roughness elements of height approximately 1.5 mm. These elements were arranged in a square grid with spacing 0.55 cm. As shown in Part II of this paper the roughness height can be quantified in terms of equivalent sound grain roughness (as defined by Schlichting) of 1.5 mm.

Figure 5 shows a close approach to Reynolds-number independence of the mean velocity field and a close approach to solid body rotation for the case $L/D = 1/10$.

Figure 6 shows that the roughened disk produces much higher turbulence intensity than the smooth disk. There is still the tendency for the turbulence intensity to be uniform in the central part of the chamber and considerably larger toward the outer curved boundary.

As explained in the introduction, an interesting feature of the swirling flow in closed chambers is that little or no axial variation of mean velocity is to be expected except in thin regions near the boundaries. Figure 7 shows the axial profile of mean tangential velocity for the cases of $L/D = 1/2$ and $L/D = 1/10$. Clearly the axial variation is negligible in both cases. (This is consistent with the measurements of Dyer, of Wahiduzzaman, and of Daily and Nece.)

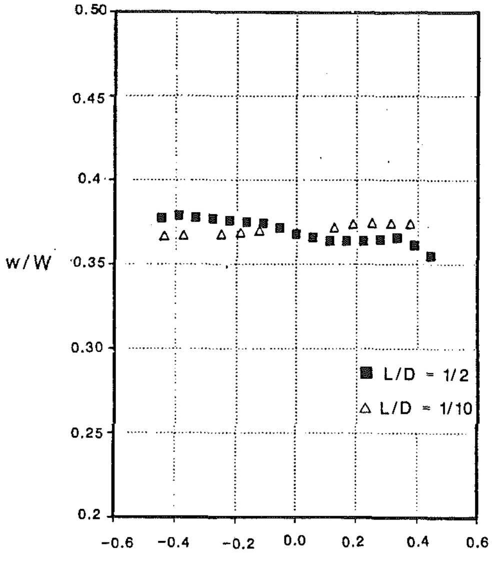

Fig. 7 Variation of mid-radius dimensionless tangential velocity profile across the chamber with roughened disk (Re = 0.326 × 10^6)

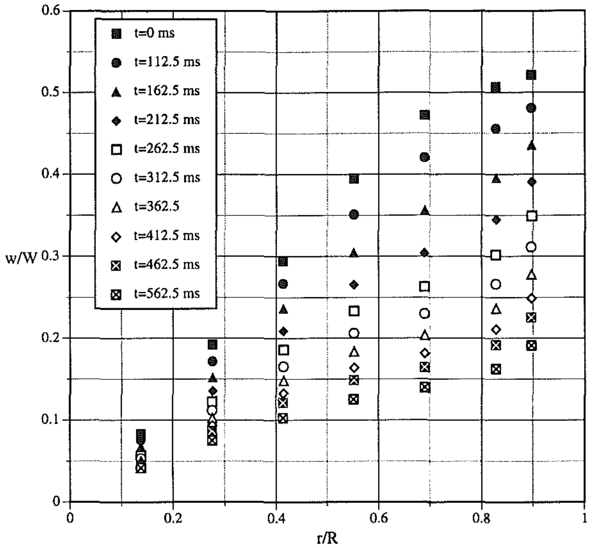

Fig. 8 The decay of tangential velocity in a chamber with aspect ratio equal to 1/2 initial Re = 0.61 × 10^6

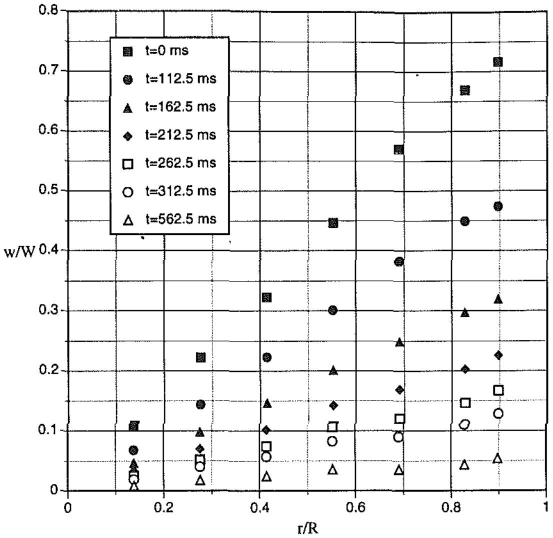

Fig. 9 The decay of tangential velocity in a chamber with aspect ratio equal to 1/10; initial Re = 0.61 × 10^6

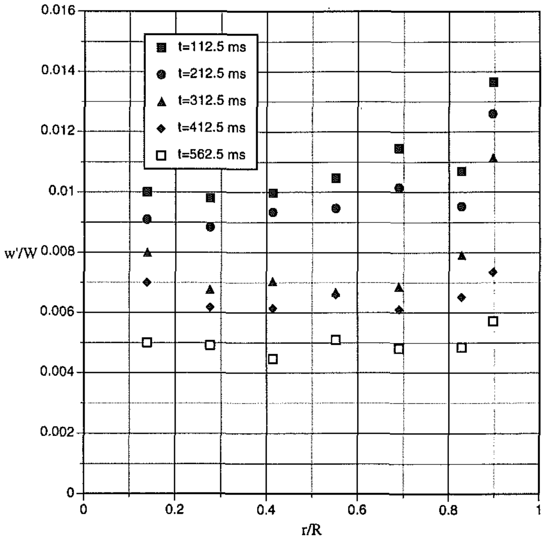

Fig. 10 The decay of turbulence intensity in a chamber with aspect ratio equal to 1/2; initial Re = 0.61 × 10^6

3.2 Transient Measurements. In this section the velocity and turbulence intensity measurements pertaining to the decaying flow field in chambers with aspect ratio equal to 1/2 and 1/10 are presented. In each case, the steady-state flow field was first generated by a roughened impeller disk while the mean tangential velocity at each measuring point was being monitored in real time. Once the previously measured steady-state velocity was attained, the disk rotation was stopped and the decay was observed. By short-circuiting the motor, the disk could be stopped in considerably less than 100 ms. The data were collected over a time span of 600 ms after the motor was switched off. However, the averaging process (explained in section 3.3) was only applied to the collected data in the time span of 100 to 600 ms i.e., the data in the first 100 ms were neglected. This insured that the actual decay rate was only measured after the disk had completely come to rest.

Figures 8 and 9 show the variation of mean velocity with radius for $L/D = 1/2$ and $L/D = 1/10$ at different times using the averaging procedure outlined above. It can be seen that in the case of $L/D = 1/10$, the decay takes place much more quickly than with $L/D = 1/2$. It should be noted however that in the interval 0–100 ms the disk inertia effects in the case of $L/D = 1/2$ are significant. In each case W signifies the disk tip velocity at $t = 0$.

Figures 10 and 11 show the decay of turbulence intensity in chambers of $L/D = 1/2$ and 1/10, respectively. The turbulence appears to decay appreciably faster in the short chamber; this is associated with faster reduction of mean velocity and reduced rates of turbulence generation near the wall. As L/D is reduced there is an increase in wall surface area per unit volume, and secondary flow is increasingly important. Both of these factors will affect the friction torque per unit mass of fluid and the rate of turbulence generation.

4 Conclusions

The mean velocity and turbulence intensity characteristics pertinent to swirling flow generated by a rotating disk inside a closed cylindrical chamber with different length-to-diameter ratios ($0.1 < L/D < 0.5$) were investigated in the present

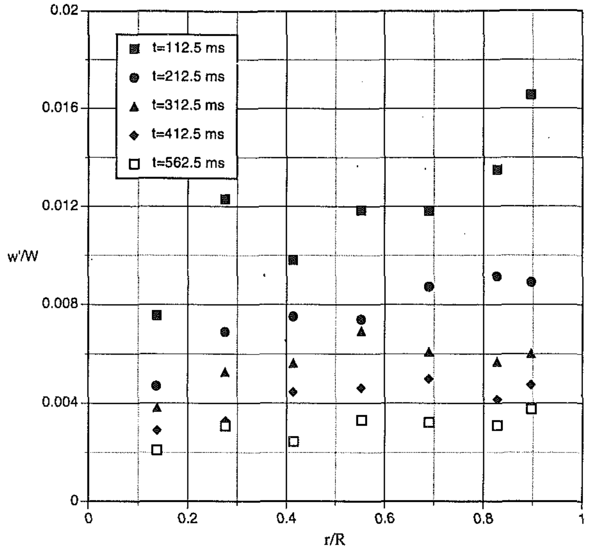

Fig. 11 The decay of turbulence intensity in a chamber with aspect ratio equal to 1/10; initial Re = 0.61 × 10^6

study. The steady-state mean velocities in swirling flow were measured by the Laser Doppler Anemometer with an estimated error of about 4 percent. Steady-state and transient mean velocities and turbulence intensities were shown to be repeatable within this range. The following conclusions were drawn:

(*i*) A steady-state nearly solid-body type of rotation was generated by both smooth and roughened impeller disks in chambers of $0.1 < L/D < 0.5$.

(*ii*) The steady-state mean swirl velocity and turbulence intensity distributions are a strong function of chamber length-to-diameter (L/D) ratios. The mean bulk velocity increases with decreasing L/D ratio.

(*iii*) The mean tangential velocity distribution is Reynolds-number independent at high Reynolds numbers. The lower limit at which flow conditions appear to be independent of Reynolds number is a function of chamber L/D ratio and turbulence intensity distribution. At low levels of turbulence intensity, Reynolds-number independency appears to have been attained in the chamber of $L/D = 1/10$ at Re = 0.61×10^6. At high levels of turbulence intensity (with the roughened disk), Reynolds number independency was apparent at all chamber L/D ratios ($0.1 < L/D < 0.5$).

(*iv*) The present study appears consistent with the Daily and Nece (1960) observation of the existence of two types of flow regimes generated by a rotating disk inside a closed chamber (transitional and fully turbulent flow). However, the present study suggests that by roughening the disk, only one flow regime will prevail in the Reynolds number and L/D ranges investigated. This regime is fully turbulent flow with separate boundary layers on rotor and stator.

(*v*) With flows generated by a roughened disk, the boundary layers on both rotor and stator are thin. Hence, the bulk flow is uniform across the chamber (no axial variation) except near the boundaries.

(*vi*) The rate of decay of mean tangential velocity and turbulence intensity is a strong function of chamber L/D ratio. The peak velocity decayed by as much as 33 percent in the first 50 ms in the chamber with $L/D = 1/10$, whereas with $L/D = 1/2$ 33 percent velocity decay required 200 ms. Turbulence intensity decayed rapidly in the first 100 ms after which it reached a quasi-steady condition in the chamber with $L/D = 1/10$, whereas the maximum decay with $L/D = 1/2$ occurred between 300 and 400 ms.

(*vii*) The faster decay rate of mean velocity and turbulence intensity in the shortest chamber ($L/D = 1/10$) can be attributed to the presence of strong secondary flows as well as to the increase in chamber surface-area-to-volume ratio. The secondary flows give rise to a thin boundary layer on the curved wall of the chamber, which results in higher shear stress and wall heat fluxes.

APPENDIX A

Error Estimation

In assessing the absolute uncertainty of the average velocity determinations, we note first of all that absolute rpm of the disk, driven by a small variable speed motor, tended to drift by a maximum of 140 rpm (or 6 percent of the maximum speed). These fluctuations were of low frequency and were caused by small changes in loading on the motor due to the frictional torque between the shaft and water seal. The mean velocity data are reported in dimensionless form w/W_{tip} where W_{tip} is the disk tip speed measured at the time the swirl velocity measurements were made. We assume the small variation in Reynolds number due to tip speed fluctuation in the above range did not significantly affect the measured velocities.

The errors arising in the LDA signal processing can be considered by writing the velocity determination as

$$w = |f_d - f_s| d_f \tag{3}$$

in which f_d is the Doppler frequency, f_s is the shift frequency, and d_f is the fringe spacing. We estimate the error in the shift frequency to be 0.2 percent. This was measured by focusing the measurement volume on a stationary surface and measuring the signal frequency. This frequency should be equal to the pre-set shift frequency. Wahiduzzaman (1985) estimated the error in the Doppler frequency to be 0.25 percent. We estimate the error in the calculated fringe spacing to be two percent.

Using the method of Kline and McClintock (1953) we can write that the relative error in the velocity determination from these (assumed independent) error sources can be written

$$\sigma_w = \sqrt{\sum \left| \frac{\partial w}{\partial \xi_i} \sigma_{\xi_i} \right|^2}$$

in which ξ_i is the ith independent variable and σ_{ξ_i} is its relative error. Applying this to Eq. (3) we have

$$\sigma_w = \sqrt{\left(\frac{\Delta f_d + \Delta f_s}{f_d - f_s}\right)^2 + \left(\frac{\Delta d_f}{d_f}\right)^2} \tag{4}$$

For a typical velocity of 5 m/s the Doppler frequency is 1.56 MHz, the shift frequency is 1 MHz and fringe spacing is 3.19 μm and we can calculate

$$\sigma_w = \sqrt{\left[\frac{1.56(.0025) + 0.002}{1.56 - 1}\right]^2 + (0.02)^2} = 2.2 \text{ percent}$$

Based on the foregoing error analyses, a maximum error of 4.2 percent can be estimated for the dimensionless velocity data reported in the present paper.

References

Adrian, R. J., and Earley, W. L., 1975, "Evaluation of LDV Performance Using Mie Scattering Theory," *Proc. of the Minnesota Symp. on Laser Anemometry*, pp. 426–454.

Daily, J. W., and Nece, R. E., 1960, "Chamber Dimension Effects on Induced Flow and Frictional Resistance of Closed Rotating Disc," ASME *Journal of Basic Engineering*, pp. 217–229.

Drain, L. E., 1972, *The Laser Doppler Technique*, Wiley.

Dyer, T. M., 1979, "Characterization of One and Two-Dimensional Homogeneous Combustion Phenomena in a Constant-Volume Bomb," SAE Paper No. 790353, Vol. 88, pp. 1196–1216.

Inoue, T., Nakanishi, K., Noguchi, H., and Iguchi, S., 1980, "The Role of Swirl and Squish in Combustion of SI Engine," *VDI Berichte No. 370*, pp. 181–188.

Kline, S. J., and McClintock, F. A., 1953, "Describing Uncertainties in Single Sample Experiments," *Mechanical Engineering*, Vol. 75, pp. 3–8.

McLaughlin, D. K., and Tiederman, W. K., 1973, "Biasing Correction for Individual Realization of Laser Anemometer Measurements in Turbulent Flows," *Physics of Fluids*, Vol. 16, pp. 2082–2088.

Nagao, A., and Tanaka, K., 1983, "The Effect of Swirl Control on Combustion Improvement of Spark Ignition Engines," *Proceedings I. MechE Conference on Combustion in Engineering*, Oxford.

Pierik, R. J., 1987, "Swirling Combustion of Premixed Gaseous Reactants in a Short Cylindrical Chamber," M.A.Sc. thesis, University of British Columbia.

Rilahi, A., 1990, "Turbulent Swirling Flow in Short Cylindrical Chambers," Ph.D. thesis, University of British Columbia.

Riahi, A., Salcudean, M., and Hill, P. G., 1990, "Computer Simulation of Turbulent Swirling Flows," *International Journal for Numerical Methods in Engineering*, Vol. 29, pp. 533–557.

Riahi, A., and Hill, P. G., 1992, "Turbulent Swirling Flow in Short Cylinders," Report 92-01 Alternative Fuels Laboratory, Department of Mechanical Engineering, University of British Columbia, Vancouver, B.C., Canada, May 1.

Young, Michael B., 1981, "Cyclic Dispersion in the Homogeneous-Charge Spark-Ignition Engine—A Literature Survey," SAE Paper No. 810020.

Wahiduzzaman, S., 1985, "A Study of Heat Transfer Due to a Decaying Swirling Flow in a Cylinder with Closed Ends," Ph.D. thesis, Purdue University.

Wilcox, D. C., and Chambers, T. L., 1977, "Streamline Curvature Effects on Turbulent Boundary Layers," *American Institute of Aeronautics and Astronautics Journal*, Vol. 15, No. 4, pp. 574–580.

I. Sahin
Western Michigan University,
Mechanical and Aeronautical
Engineering Department,
Kalamazoo, MI

J. Crane

K. Watson

Naval Surface Warfare Center,
Dahlgren Division,
Coastal Systems Station,
Panama City, FL

Added Mass Coefficients for Submerged Bodies by a Low-Order Panel Method

The added mass coefficients for two and three-dimensional submerged bodies were calculated using a low-order panel code. The source and dipole strengths, and the panel surface area for each panel, were used to compute the integrals needed for added mass in all six degrees of motions. Several applications of this method were used in comparing the results with the theoretical, when available, experimental or other numerical results. The method was found to be successful in predicting the added mass coefficients using relatively low numbers of panels.

Introduction

Low-order panel methods where the singularity strengths are constant on each panel have been used successfully (Sahin et al., 1990) in predicting hydrodynamic force and moment coefficients of underwater vehicles. In addition to these coefficients, another important set of parameters in formulating the equation of motion of a body in a fluid is the added mass and the added moment of inertia of the body undergoing maneuvers. While the effects of the added mass and the added moment of inertia are routinely neglected in predicting the motion of aircraft, they are extremely important to the motion of underwater vehicles. The added mass and the added moment of inertia are viewed as the mass and the moment of inertia of the fluid moving with the body while the body is in motion. The details for the derivation of the added mass and the added moment of inertia can be found in Newman (1977) or Kochin et al. (1964). The added mass tensor is defined as:

$$m_{ji}=\rho\int\int_S \phi_i \frac{\partial \phi_j}{\partial n}\, dS \quad i, j=1, 2, \ldots, 6 \qquad (1)$$

where ρ is the fluid density, ϕ is the velocity potential, n is the outward normal direction, S is the area and m_{ji} is the added mass (or moment of inertia) in the j-direction corresponding to a motion in i-direction. The indices 1 through 3 correspond to linear motions in x, y, and z directions (surge, sway, and heave), and the indices 4 through 6 correspond to rotations about the x, y, and z-axes (roll, pitch, and yaw). It can be easily shown that the added mass coefficients are symmetric, i.e., $m_{ji} = m_{ij}$. Therefore, for a general body there are twenty-one independent, nonzero added mass coefficients. If the body is symmetrical with respect to one or more axes of symmetry, this number is reduced substantially.

In low-order formulations the velocity potentials are the doublet values, μ, on each surface panel, and in the absence of surface blowing or suction, the normal derivatives of the potential are the source strengths, σ. Therefore, the added mass contribution of each panel is simply the product of dipole strength, ϕ (or μ), the normal velocity $\partial\phi/\partial n$ (or σ), and the panel area. The summation of this product on all panels of the geometry gives the added mass or the added moment of inertia as in Eq. (1) for the specified motion of the body. PMARC (Ashby et al., 1988), a publicly available code, was modified accordingly to accommodate the added mass calculations for the total configuration as well as specific components.

PMARC was then applied to predicting the added masses and the moments of inertia of several two and three-dimensional shapes. Two-dimensional applications include the circular cylinder and the elliptical cylinder, the circular cylinder with vertical fins, and a Lewis form cylinder. Three-dimensional applications include spheroids with different length/diameter (l/d) ratios and a Lewis-form submersible. All two-dimensional applications and the spheroid have exact (analytical) solutions. The versatility of this method is that it can easily be applied for arbitrary bodies with very small effort.

Two-Dimensional Bodies

In order to simulate the flow around a two-dimensional body with PMARC, the geometry of a high-aspect ratio body was modeled. The coordinate system used in PMARC has the x-axis aligned with the free-stream, y-axis is in the lateral direction and the z is the vertical axis, positive upwards. In all two-dimensional applications the cross-sections were located at the xz-plane. Therefore, when modeling two-dimensional modes, the forward motion (surge) represented the lateral 2-D mode, the heave (in z-direction) represented the vertical mode, and the pitch in PMARC (3-D) represented the only possible 2-D rotation. As expected, the results were sensitive to the aspect ratio, defined by the ratio of a characteristic length in the xz-plane to a characteristic length in the y-direction.

Contributed by the Fluids Engineering Division for publication in the JOURNAL OF FLUIDS ENGINEERING. Manuscript received by the Fluids Engineering Division September 30, 1991; revised manuscript received September 28, 1992. Associate Technical Editor: R. L. Panton.

Circular Cylinder. A unit-radius circular cylinder was modeled for different l/R ratios. The analytical solution for the added mass was available through conformal mapping. Because of the symmetry with respect to centroidal axes, the rotational added mass was zero and the linear added masses (per unit length) in surge and heave were equal, i.e., $m_{22} = m_{33} = \pi\rho R^2$, where R was the radius of the cylinder. The cylinder was represented by N_{ch} panels around the circumference and N_{sp} panels in spanwise direction. Based on our previous experience with the cylinders (Sahin et al., 1990), distribution of circumferential panels were adjusted such that the leading edge was a corner instead of a vertical panel. It was also determined that the use of an end patch had negligible effect on the results, therefore, the end patches were omitted from the paneled geometry. In order to represent a two-dimensional phenomenon with a three-dimensional geometry, a very high aspect ratio (in this case, l/R) was necessary. This was found to be true since results were strongly dependent on the l/R rather than the panel densities in the chordwise and spanwise directions (N_{ch} and N_{sp}). Several panel sensitivity studies using quadrisection series (where the number of circumferential and spanwise panels are doubled) indicated that the results did not change considerably with the number of panels beyond a reasonable number of panels in both directions. The results shown in Table 1 were computed by using sixteen chordwise (circumferential) and four spanwise panels, per unit spanwise length. Another representation of the results, in order to emphasize three-dimensionality, was to calculate added mass contributions from the center panels. In Table 1, results from the total panels and from the half cylinder were illustrated. As expected, the center panel results converged to the exact solution faster than using all panels.

Elliptical Cylinder. In a manner similar to that of a circular cylinder, an elliptical cylinder with a large aspect ratio was modeled. The analytical results for the linear added masses are: $m_{22} = \pi\rho b^2$ for the horizontal motion, and $m_{33} = \pi\rho a^2$ for the vertical motion. The only rotational added moment of inertia is for the pitch, and it is given by $m_{55} = \pi\rho(a^2-b^2)^2/8$. In these expressions the added mass coefficients are per unit length of the elliptical cylinder, and a and b are the semi-major and the semi-minor axes in the x-and z-directions, respectively.

The geometry modeling for the elliptical cylinder was done for a 2:1 ellipse of major and minor axes $2a = 4$, $2b = 2$. The free-stream was in the direction of the major axis, x. As in the circular cylinder case, results for the added mass were found to be fairly insensitive to the number of circumferential (in the xz-plane) and spanwise (in the y-direction) panels. Convergence was influenced substantially by the length of the cylinder as higher values yield better approximation to the two-dimensional theory.

The added mass computations for the horizontal, vertical, and rotational motions were shown in Table 2. In general, results converged to the theoretical value in a consistent fashion. The behavior of the convergence was somewhat different from the circular cylinder case. This was due to the fact for each motion there is a favorable distribution of panels in that direction. For example, in horizontal motion the full-cosine distribution in paneling (where a higher number of panels were used near the ends) would yield better results. However, in order to facilitate a uniform comparison, the panel spacings in all directions were kept equal. The correlation for the rotational added mass appears to be the worst among the three modes. This can be attributed to the paneling scheme and results could be improved by using more favorable panel distributions, such as cosine spacing in appropriate directions, for each mode.

Lewis-Form Cylinder. In this study the two-dimensional added mass coefficients for a Lewis-form body are investigated using a cylinder with a Lewis-form cross-section. Lewis-forms are parametrically generated bodies, first suggested by Lewis (1928). The details of the geometry for the Lewis forms also appear in Landweber and Macagno (1967) and von Kerczek (1969). The three-dimensional added mass results for a submarine with Lewis-form cross-sections will be presented later.

Lewis forms are generated by rounding the corners for a rectangular shape with circular arcs. The linear added masses per unit length for the horizontal motion (in y-direction), and the vertical motion (in z-direction) are: $m_y = C_y\rho\pi H^2/4$, and $m_z = C_z\rho\pi B^2/4$, respectively, where B is the width, and H is the height. The coefficients C_y and C_z can be calculated by using conformal mapping as in previous cases. One such calculation can be found in Wald (1969) showing the variation of these coefficients as a function of B/H ratio and the area coefficient $C_s = S/BH$ where S is the cross-sectional area. In Table 3, the results for C_y and C_z calculations are compared with the exact values from Wald (1969). As in the previous two-dimensional cases, the relevant parameter appears to be the length (l) of the cylinder, higher values of l giving better correlation with the exact solution. In these computations, the number of circumferential panels was 28, and the length of spanwise panels was kept uniform by increasing the number

Table 1 **Nondimensional added mass for a unit radius cylinder**

l/R	Using all panels	Using center panels
2.5	2.375	2.984
5	2.968	3.096
10	3.049	3.127
20	3.093	3.135
40	3.118	3.140

Exact solution: $\pi = 3.14159$.

Table 3 **Added mass coefficients for a Lewis-form cylinder ($B=50$, $H=15$, $C_s=0.95$)**

l/B	C_y	C_z
1	1.279	0.880
2	1.376	1.000
4	1.432	1.070
8	1.460	1.104
Exact solution	1.462	1.110

Table 2 **Nondimensional added masses for an elliptical cylinder ($2a=4$, $2b=2$)**

	Heave added mass $m_{22}/\rho a^2$		Surge added mass $m_{33}/\rho b^2$		Rotational added mass $m_{55}/\rho(a^2-b^2)^2/8$	
l/b	Center panels	All panels	Center panels	All panels	Center panels	All panels
10	3.020	2.809	3.118	2.950	3.026	2.933
20	3.106	2.969	3.170	3.065	3.099	3.050
40	3.118	3.103	3.148	3.131	3.104	3.027

Exact solutions: $\pi = 3.14159$ for all cases.

Table 4 Nondimensional added mass for a flat plate ($t/B = 0.01$, $a = B/2$)

l/B	Using all panels	Using center panels
5	2.970	3.070
10	3.040	3.100
20	3.093	3.127

Exact solution: $\pi = 3.14159$.

Table 5 Nondimensional added masses for a cylinder with vertical fins

l/a	m_{22}'	m_{33}'	m_{55}'
5	4.959	2.762	1.058
10	5.279	2.920	1.076
20	5.453	3.003	1.077
40	5.543	3.046	1.080
Exact solution	5.323	3.142	1.066

Table 6 Nondimensional added mass for a unit-radius sphere

Number of panels	$m_{33}' = m_{33}/\rho a^3$
126	1.909
264	2.048
864	2.088

Exact solution: $2\pi/3 = 2.094$.

of spanwise panels proportionately with increasing l. As in other two-dimensional applications, the predictions of added mass coefficients by PMARC are considered good.

Flat Plate. The analytical result of the only nonzero added mass for a thin flat plate is given as $m_{33} = \rho\pi a^2$ where a is the half-width of the plate (Newman, 1977). In studying this case some modifications were necessary. Flat (Neumann-type) panels in PMARC could not be used since they would yield zero source strengths. Therefore, instead of a flat plate with zero thickness, a thin plate with a small thickness/chord ratio (1 percent) was modeled. The corners were rounded by using a Lewis form of $C_s = 0.9995$, $B = 2a = 10$, and $H = 0.1$ units; for these values the radius of curvature for the corners was calculated to be 0.015 units.

Added mass calculations are shown in Table 4 as a function of aspect ratio (width/length). As can be seen from this table, the correlation between the exact solution and the computed results improved with increasing aspect ratios. As in previous two-dimensional applications, the added mass calculated by using the center panels instead of total panels improved the convergence of the results.

Cylinder With Vertical Fins. As the last two-dimensional application, a circular cylinder with two vertical fins was studied. This was of significance because of the existence of similar fins in underwater vehicles. The exact solutions for the linear added masses in horizontal and vertical motions are $m_{22} = \pi\rho[a^2 + (b^2 - a^2)^2/b^2]$, and $m_{33} = \pi\rho a^2$, respectively, where a is the radius of the circle and b is the distance from the center of the circle to the tip of the fin. The rotational added mass coefficient could be found in Nielsen (1988) as

$$m_{55} = (\pi\rho b^4/8)\{[(1+R^2)^2\tan^{-1}(1/R)]^2 + 2R(1-R^2)(R^4 - 6R^2 + 1)\tan^{-1}(1/R) - \pi^2R^4 + R^2(1-R^2)^2\} \quad (2)$$

where $R = a/b$ was the ratio indicating the relative size of the fins with respect to the radius of the cylinder. PMARC modeling for this geometry included vertical extension with a small thickness. It was determined that the reducing the thicknesses of the fins improved the correlation with the theoretical results. The results were computed by using fin thickness of 1 percent of the cylinder radius.

Consistent with the other two-dimensional applications, the results depended strongly on the length of the cylinder formed. The values chosen for the comparisons were for a cylinder of unit radius ($a = 1$), and the fins with the span of 0.5 units ($b = 1.5$). The number of circumferential panels was kept at 28 and the width of the spanwise panels was kept at unit length. Comparisons of the linear and rotational added mass coefficients from PMARC with the exact solutions were presented in Table 5 in terms of $m_{22}' = m_{22}/\rho[a^2 + (b^2 - a^2)^2/b^2]$, $m_{33}' = m_{33}/\rho a^2$, and m_{55}' similarly defined from the Eq. (2). Because of the sharp corners in this configuration, some care was required in paneling for different types of motions. For example, the rotational motion results are influenced by the number of panels at the fin tip, while the horizontal motion results are improved by increasing the number of panels at the vertical portion of the fins. The results for the vertical motion improved by increased values of l. It appeared that correlations with the exact solutions could be improved by adjusting the panel distributions in the preferred directions for a mode of interest. As expected, the correlations improved with b/a values approaching 1. Overall, the correlation of the results with the exact solutions is satisfactory.

Three-Dimensional Bodies. Theoretical calculations of the added masses for three-dimensional bodies are understandably more difficult than the two-dimensional case. The exact solutions were confined to bodies expressed in closed form. These are sphere, ellipsoid, and the special case of the ellipsoid with circular cross section: the spheroid. In the following sections, the added mass results for a sphere, spheroids with different length/diameter ratios, and a submerged body with Lewis-form cross-sections are presented.

Sphere. One of the simplest three-dimensional bodies for the added mass analysis is the sphere. Because of the symmetry with respect to all three centroidal axes, all rotational added masses are zero, and the analytical solution for the added mass in linear motion (in any direction) becomes: $m_{11} = m_{22} = m_{33} = 2\pi\rho a^3/3$, where a is the radius of the sphere. In other words, the added mass of the sphere is half the displaced mass. The details of this derivation could be found in Lamb (1945).

The added mass for a sphere by using several numbers of panels are shown in Table 6 with the exact solution. Results show that convergence to the exact solution can be improved by increasing the number of panels. As in previous cases, the panel distribution in the free-stream direction was adjusted such that the leading edge was a corner. A full-cosine panel distribution in the free-stream direction was used, and the circumferential panels were equally spaced. Prediction of the added mass coefficient for a sphere by using PMARC is good.

Spheroid. PMARC was applied to a spheroid with maximum cross-section of a circle with the radius b. The streamline profile of the spheroid was of an ellipse of semi-axes a and b, and the slenderness ratio a/b was also the length/diameter ratio l/D. The symmetry with respect to the centroidal axis of a cross-section (yz-plane) dictated that the non-zero added mass coefficients are the longitudinal added mass m_{11}, the lateral added mass $m_{22} = m_{33}$, and the rotational added mass $m_{55} = m_{66}$. The exact solutions for the added masses are:

$$m_{11} = \frac{4}{3}\pi\rho ab^2\frac{A_o}{2-A_o} \quad (3)$$

$$m_{22} = m_{33} = \frac{4}{3}\pi\rho ab^2\frac{B_o}{2-B_o} \quad (4)$$

$$m_{55} = m_{66} = -\frac{4}{15}\frac{\pi\rho ab^2(b^2-a^2)^2(C_o-A_o)}{2(b^2-a^2)+(C_o-A_o)(a^2+b^2)} \quad (5)$$

where quantities A_o, B_o, C_o were given by the following equations:

$$A_o = p \int_0^\infty \frac{dt}{p^2+1)(1+t)\sqrt{(p^2+t)}} \tag{6}$$

$$B_o = C_o = p \int_0^\infty \frac{dt}{(1+t)^2\sqrt{p^2+t}} \tag{7}$$

and p is the l/d (or a/b) ratio. The nondimensionalized added masses become:

$$\mu_x = \frac{m_{11}}{\frac{4}{3}\pi\rho ab^2}, \quad \mu_y = \mu_z = \frac{m_{22}}{\frac{4}{3}\pi\rho ab^2},$$

$$\mu_{yy} = \mu_{zz} = \frac{m_{55}}{\frac{4}{15}\pi\rho ab^2(a^2+b^2)} \tag{8}$$

For spheroids of l/D = 5, 10, and 15 PMARC predictions and the analytical results for the nondimensional added masses were shown in Tables 7, 8, and 9. For the forward motion, the effects of spanwise and chordwise number of panels are included separately while the lateral and rotational motions the quadrisection results are presented by doubling the number of panels in both directions. In general, the increase in the total number of panels improved the agreement between the theory and the computation. As can be seen from these results, the prediction of added mass coefficients is satisfactory.

Table 7 Nondimensional added mass for a spheroid in forward motion

			$l/D=5$	$l/D=10$	$l/D=15$
N_{ch}	N_{sp}	N_{total}	$\mu_x \cdot 10^2$	$\mu_x \cdot 10^2$	$\mu_x \cdot 10^2$
4	10	40	5.2235	1.8311	0.9409
4	20	80	5.0530	1.7767	0.9204
4	40	160	4.9810	1.7446	0.9093
8	10	80	5.9745	2.1048	1.0836
8	20	160	5.7760	2.0411	1.0598
8	40	320	5.6940	2.0044	1.0472
16	10	160	6.1719	2.1772	1.1215
16	20	320	5.9665	2.1109	1.0967
16	40	640	5.8819	2.0732	1.0839
Exact solution			5.9121	2.0706	1.0865

Table 8 Nondimensional added mass for a spheroid in lateral motion

			$l/D=5$	$l/D=10$	$l/D=15$
N_{ch}	N_{sp}	N_{total}	μ_y	μ_y	μ_y
4	10	40	0.8678	0.9259	0.9419
8	20	160	0.8870	0.9506	0.9688
16	40	640	0.8922	0.9564	0.9743
Exact solution			0.8943	0.9602	0.9787

Table 9 Nondimensional added mass for a spheroid in rotation

			$l/D=5$	$l/D=10$	$l/D=15$
N_{ch}	N_{sp}	N_{total}	μ_{yy}	μ_{yy}	μ_{yy}
4	10	40	0.6768	0.8067	0.8423
8	20	160	0.6954	0.8600	0.9074
16	40	640	0.6972	0.8764	0.9278
Exact solution			0.7099	0.8835	0.9371

Lewis-Form Submerged Body. The last case for PMARC prediction of added mass was for a submerged body of Lewis-form cross sections. The characteristics of a Lewis-form shape were discussed earlier. The submerged body has the length to width ratio (l/B) of 2.74, width to height ratio (B/H) of 2.37, and a parallel mid-body of about 62 percent of the body length. Comparison of the added mass prediction with PMARC, the strip-theory results, and the theoretical results for two equivalent ellipsoids (based on the moment of inertias and the equivalent l, B, H values) are shown in Table 10. The axial added mass for the strip theory was zero. Total number of panels used in PMARC was 1080, using full cosine spacing along in the axial direction and equal spacing along the circumferential direction. The sign difference between the different values was the result of different conventions. The linear motion added masses are nondimensionalized by $\rho\ l^3$, and the rotational added masses are nondimensionalized by $\rho\ l^5$.

The results shown in Table 10 did not appear to correlate well among each other. This was because comparisons were based on very different methods. In strip theory the two-dimensional coefficients are used with empirical correlations. In equivalent ellipsoids comparisons, the fullness of the body does not match to that of the ellipsoid. Based on our success in predicting added mass coefficients in two and three-dimensional bodies reported in previous sections, we expect that the PMARC results to be the most reliable among the four methods shown in Table 10. The PMARC results were also checked by varying the panel numbers and distributions.

Conclusions

The low-order panel code PMARC was modified and the new code was applied to the prediction of added mass coefficients for several two and three-dimensional bodies. The method was found to be successful in calculating the added masses in all applications, except the Lewis-form body since the added masses results compared to PMARC were not under identical conditions. Further studies can be made when additional experimental and theoretical results become available for different bodies.

The added mass is an important hydrodynamic quantity for all bodies undergoing a motion in a fluid. It is an especially important design consideration for bodies moving in or under a liquid, although a similar emphasis on added mass can be found in analyses of missiles, and parachutes in single and cluster configurations.

The method introduced in this study provides a designer, or an analyst, a new approach in predicting the added mass of an underwater vehicle. The versatility and the ease of use of this method makes it an attractive tool for prediction.

Table 10 Nondimensional acceleration added masses for a Lewis-form submersible

Motion	PMARC	Strip theory	Equiv. ellipsoid1	Equiv. ellipsoid2
Surge	4.78 E-3	--*	−7.58 E-3	1.68 E-2
Sway	2.02 E-2	−5.11 E-2	−3.29 E-2	8.65 E-2
Heave	9.25 E-2	−2.38 E-2	−1.85 E-1	4.68 E-1
Roll	3.43 E-3	−9.41 E-4	−7.61 E-4	4.75 E-3
Pitch	4.46 E-3	−1.46 E-2	−9.03 E-3	7.40 E-2
Yaw	8.03 E-4	−2.82 E-2	−1.24 E-3	1.12 E-2

Note: Equivalent Ellipsoid 1 is generated by the ratios of moment of inertias, e.g., $R_1 = I_{xx}/I_{yy}$, and $R_2 = I_{zz}/I_{yy}$.
Equivalent Ellipoid 2 is generated by $l = 2a$, $B = 2b$, and $H = 2c$.
* Strip Theory does not calculate a surge added mass.

Acknowledgement

The first author was supported by a ONT/ASEE-Navy Senior Summer Faculty Fellowship, and a Western Michigan University Faculty Research Grant.

References

Ashby, D. L., Dudley, M. R., and Iguchi, S. K., 1988, "Development and Validation of an Advanced Low-Order Panel Method," NASA TM-101024.

Kochin, N. E., Kibel, I. A., and Roze, N. V., 1964, *Theoretical Hydromechanics*, Interscience Publishers, Wiley.

Lamb, H., 1945, *Hydrodynamics*, Dover Publications.

Landweber, L.,and Macagno, M., 1967, "Added Masses of Two-Dimensional Forms by Conformal Mapping," *Journal of Ship Research*, Vol. 11, No. 2, June.

Lewis, F. M., 1928, "The Inertia of Water Surrounding a Vibrating Ship," *Transactions, The Society of Naval Architects and Marine Engineers*, Vol. 37.

Newman, J. N., 1977, *Marine Hydrodynamics*, MIT Press.

Nielsen, J. N., 1988, *Missile Aerodynamics*, Nielsen Engineering and Research Inc., Mountain View, CA.

Sahin, I., Watson, K. P., and Crane, J. W., 1990, "Application of PMARC to Some Classical Inviscid Flow Problems," NCSC Technical Note TN 970–90, May.

von Kerczek, C., and Tuck, E. O., 1969, "The Representation of Ship Hulls by Conformal Mapping Functions," *Journal of Ship Research*, Vol. 13, No. 4, Dec.

Wald, Q., 1969, "Estimation of the Stability Derivatives of a Deeply Submerged Submarine," *General Dynamics*, Electric Boat Division Report No. U411-69-023, Mar.

Prediction of Three-Dimensional Steady Incompressible Flows Using Body-Fitted Coordinates

P. Tamamidis

D. N. Assanis

Department of Mechanical and
Industrial Engineering,
University of Illinois at Urbana-Champaign,
Urbana, IL 61801

A finite-volume method for three-dimensional, steady, incompressible flows in complex geometries is presented. The method uses generalized Body-Fitted Coordinates to accurately take into account the shape of the boundary. A collocated scheme is employed, which uses the three covariant velocities and the pressure as main variables. Continuity is coupled with the momentum equations using the SIMPLEC algorithm. It is found that the SIMPLEC algorithm can provide savings in computational time of up to 40 percent compared to calculations with SIMPLE. Sensitivity studies are also performed to find optimum values of the underrelaxation parameters. The method is validated against experimental results for the case of the flow in a 90 deg curved duct of square cross-section and comparatively strong curvature. The application of the method to the prediction of flows in complex geometries is then illustrated.

1 Introduction

Three-dimensional viscous flows are found in a wide range of practical engineering problems, such as curved ducts, intake and exhaust manifolds, gas turbine blade passages, and internal combustion engines. A characteristic of these configurations is the irregular shape of the boundary, which makes the prediction of the flow field a difficult task. A promising approach for solving the Navier-Stokes equations in such complex domains is through the use of Body-Fitted Coordinate systems (BFC). However, several alternative BFC formulations have been reported in the literature so far.

Important differences among the proposed formulations lie in the form of grid arrangement and choice of dependent variables in the momentum equations. For instance, Hirt et al. (1974) used a nonstaggered grid with cartesian velocities as the main variables in the momentum equations. Due to the nonstaggered grid arrangement, a special procedure was employed to prevent the decoupling of the velocity and pressure fields. Rhie (1983) employed a two-dimensional collocated grid arrangement where all variables were located at the common grid positions. The velocity and pressure were coupled by a special interpolation scheme, whose convergence behavior was later improved by Majumdar (1988). Reggio and Camarero (1987) have also used a collocated grid arrangement in their three-dimensional studies. To avoid unrealistic fields which could appear with such a discretization, an opposed difference scheme was used for pressure and fluxes in the main flow direction.

On the other hand, Vanka et al. (1980) presented a semi-implicit, three-dimensional calculation procedure for partially elliptic flows using a staggered grid with cartesian velocities as the main variables. Nakayama (1984) applied a staggered grid with one cartesian velocity component stored at each cell face to the study of three-dimensional elliptic flows. Demirdzic et al. (1980) presented an alternative procedure using a staggered grid; in their two-dimensional arrangement, one contravariant velocity component was stored at each cell face. However, the use of staggered grids necessitates additional storage allocations, requires more interpolations, and makes code development more cumbersome compared to collocated or nonstaggered grids. Also, using Cartesian or contravariant velocity components yields a pressure equation of complicated form, especially in three-dimensional problems. However, this difficulty can be eliminated through the use of covariant velocities, as reported in the two-dimensional procedures of Karki (1986), Talpallikar et al. (1990), and Tamamidis (1990).

The objective of this work is to develop an improved method for solving three-dimensional, steady, incompressible flows using Body-Fitted Coordinates (BFC). Our scheme employs a collocated grid following the approach of Rhie (1983). However, rather than using cartesian variables, the proposed scheme uses the three covariant velocities and the pressure as main variables. This way, the advantages of using the covariant velocity components as dependent variables are coupled with the other advantages of collocated grids. Continuity is coupled with the momentum equations using the SIMPLEC algorithm.

Following a brief presentation of the method, this paper reports on its validation and application to the study of flows in curved ducts. The characteristic phenomenon in such flows is the secondary motion arising from the channel curvature. This secondary flow causes high pressure losses and results in a spatial redistribution of streamwise velocity. The results demonstrate the potential of the present method for providing realistic answers to problems of practical interest.

Contributed by the Fluids Engineering Division for publication in the Journal of Fluids Engineering. Manuscript received by the Fluids Engineering Division January 17, 1992; revised manuscript received February 19, 1992. Associate Technical Editor: R. K. Agarwal.

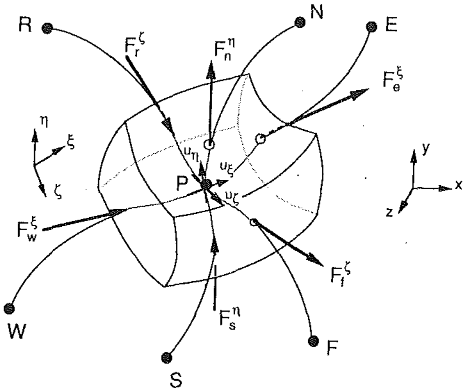

Fig. 1 Perspective view of a hexahedronal control volume

2 Theoretical Formulation

The equations governing fluid flow can be written in the following general form (Patankar, 1980)

$$\nabla \cdot \mathbf{J}_\phi = S_\phi \qquad (1)$$

where ϕ is a variable, S_ϕ is the source term associated with this variable, and $\mathbf{J}_\phi$ represents the transport of ϕ due to advection and diffusion and is given by

$$\mathbf{J}_\phi = \rho \mathbf{V} \phi - \Gamma_\phi \nabla \phi \qquad (2)$$

where $\mathbf{V}$ is the velocity vector and Γ_ϕ is the diffusion coefficient of ϕ. The governing transport equations for mass and momentum fit in the general structure of Eq. (1) with different meaning of ϕ only. Hereafter the index ϕ is omitted to simplify notation.

Equation (1) is solved using a finite volume formulation. The first step of this formulation is performed by integrating Eq. (1) over an arbitrary hexahedronal control volume in the physical space, such as the one shown in Fig. 1. Using Gauss' theorem we obtain

$$\int_{cs} \mathbf{J} \cdot \mathbf{n} ds = \int_{c\forall} S d\forall \qquad (3)$$

where the subscripts cs and $c\forall$ stand for control surface and control volume, respectively; $\forall$ can be any volume, s is the surface which encloses $\forall$, and $\mathbf{n}$ is the unit normal on s.

The surface integral at the LHS of Eq. (3) can be broken into six integrals

$$\int_{cs} \mathbf{J} \cdot \mathbf{n} ds = \int_{e} \mathbf{J} \cdot \mathbf{n} ds + \int_{w} \mathbf{J} \cdot \mathbf{n} ds + \int_{n} \mathbf{J} \cdot \mathbf{n} ds + \int_{s} \mathbf{J} \cdot \mathbf{n} ds + \int_{f} \mathbf{J} \cdot \mathbf{n} ds + \int_{r} \mathbf{J} \cdot \mathbf{n} ds \qquad (4)$$

where the subscripts e, w, n, s, f, and r stand for the east, west, north, south, front, and rear control surfaces, respectively.

Extending the 2-D procedure of Tamamidis (1990) in three-dimensions, the flux through a surface where ξ_i = const can be decomposed into a main flux term J_m and a flux J_{no} arising due to the nonorthogonality of the grid, i.e.,

$$J^{\xi_i} = \int_{\xi_i} \mathbf{J} \cdot \mathbf{n} ds = J_{m,i} - J_{no,i} \qquad (5)$$

with

$$J_m^{\xi_i} = [Ja(\rho u^{\xi_i} \sqrt{g^{ii}} \phi - \Gamma \phi_{\xi_i} g^{ii}) \Delta\xi_j \Delta\xi_k]_i \qquad (6a)$$

$$J_{no}^{\xi_i} = [Ja\Gamma(\phi_{\xi_j} g^{ij} + \phi_{\xi_k} g^{ik}) \Delta\xi_j \Delta\xi_k]_i \qquad (6b)$$

where $i = 1, 2, 3$, $j = 1, 2, 3$, $k = 1, 2, 3$, ϕ_{ξ_i} is the partial derivative of ϕ with respect to ξ_i, and (i, j, k) change cyclically. Also, u^{ξ_i} denotes the ξ_i contravariant velocity component defined by

$$u^{\xi_i} = \frac{u(\xi_i)_x + v(\xi_i)_y + w(\xi_i)_z}{\sqrt{g^{ii}}} \qquad (7)$$

where $\xi_1 \equiv \xi$, $\xi_2 \equiv \eta$, $\xi_3 \equiv \zeta$. The symbol Ja denotes the Jacobian of the transformation, given by

$$\mathrm{Ja} = x_\xi y_\eta z_\zeta + x_\zeta y_\xi z_\eta + x_\eta y_\zeta z_\xi - x_\zeta y_\zeta z_\eta - x_\eta y_\xi z_\zeta - x_\zeta y_\eta z_\xi \qquad (8)$$

The terms g^{ij} are the contravariant metric components, given by

$$g^{ij} = (\xi_i)_x(\xi_j)_x + (\xi_i)_y(\xi_j)_y + (\xi_i)_z(\xi_j)_z \qquad (9)$$

The fluxes involving the metric g^{ij}, $i \neq j$, become zero when the grid is orthogonal.

The source term S can be considered constant over the control volume. Therefore, the volume integral at the RHS of Eq. (3) can be written:

$$\int_{c\forall} S d\forall = S\mathrm{Ja}\Delta\xi\Delta\eta \qquad (10)$$

Now, substituting Eqs. (5) through (7) into Eq. (4), we obtain the flux equation in the computational space:

$$J_{m,e}^\xi - J_{m,w}^\xi + J_{m,n}^\eta - J_{m,s}^\eta + J_{m,f}^\zeta - J_{m,r}^\zeta = S_{\text{cart}} + S_{no} \qquad (11)$$

where S_{cart} is the cartesian source term

$$S_{\text{cart}} = S\mathrm{Ja}\Delta\xi\Delta\eta \qquad (12a)$$

and S_{no} is the source term due to nonorthogonality

$$S_{no} = J_{no,e}^\xi - J_{no,w}^\xi + J_{no,n}^\eta - J_{no,s}^\eta + J_{no,f}^\zeta - J_{no,r}^\zeta \qquad (12b)$$

The term S_{no}, which is diffusive in nature, becomes less important for high Reynolds number flows since the convective terms in the LHS of Eq. (11) prevail; also, it goes to zero as

Nomenclature

a = coefficient in discretization equation
De = Dean number
D_h = hydraulic diameter
g^{ij} = metric factor
h_{ξ_i} = scale factor
J^{ξ_i} = flux through a surface where ξ_i = const
Ja = Jacobian of the transformation
p = pressure
Re = Reynolds number
S = source term in Navier-Stokes equations
u, v, w = x-, y-, z-components of the velocity vector
u^{ξ_i} = contravariant velocity component
u_{ξ_i} = covariant velocity component
w = underrelaxation factor
Γ = diffusion coefficient (e.g., dynamic viscosity)
ξ_i = coordinate in the transformed space
ϕ = a variable (e.g., velocity)

Subscripts

no = nonorthogonality
x, y, z = partial derivative in the physical space
ξ_i = partial derivative in the computational space

the grid becomes orthogonal. For highly nonorthogonal grids this term becomes important.

3 The Numerical Solution Procedure

3.1 Choice of Velocity Components as Dependent Variables. The choice of velocity components as dependent variables is one of the discriminating differences among existing BFC formulations. In the present formulation, a collocated grid arrangement with the covariant velocities as the main variables for momentum is used. A three-dimensional sketch of this arrangement, is shown in Fig. 1. The advantage of using the covariant velocities as the main variables in the momentum equations is that the cross-derivative pressure terms are eliminated. In this scheme, the mass fluxes (which have the same direction as the contravariant velocities) are also stored at the centers of the cell faces.

3.2 Discretization of Momentum Equations. The flux equation, Eq. (11) can be discretized in the computational space using finite differences. A suitable procedure for the case of cartesian coordinates has been presented in (Patankar, 1980). This procedure can be extended for BFC since the flux equation applied to the computational space which is cartesian-like. Since this extension is straightforward, it will not be reproduced here. The resulting algebraic equation can be written as

$$a_P\phi_P = a_E\phi_E + a_W\phi_W + a_N\phi_N + a_S\phi_S + a_F\phi_F + a_R\phi_R + b_\phi^* \qquad (13)$$

where b is the sum of S_{cart} and S_{no}. Equation (13) is the discretization equation for ϕ. The coefficients appearing in this equation involve convective and diffusive fluxes through the cell faces.

The discretization equations for the covariant velocities u_ξ, u_η, and u_ζ can be derived from the discretization equation for ϕ. Since all cartesian velocities are stored at the same grid location, their discretization equations will have identical coefficients except for the external source terms. Using Eq. (13), we have

$$a_Pu_P = a_Eu_E + a_Wu_W + a_Nu_N + a_Su_S + a_Fu_F + a_Ru_R + b_u^* \qquad (14a)$$

$$a_Pv_P = a_Ev_E + a_Wv_W + a_Nv_N + a_Sv_S + a_Fv_F + a_Rv_R + b_v^* \qquad (14b)$$

$$a_Pw_P = a_Ew_E + a_Ww_W + a_Nw_N + a_Sw_S + a_Fw_F + a_Rw_R + b_w^* \qquad (14c)$$

The covariant velocity u_{ξ_i} is defined by

$$u_{\xi_i} = \frac{ux_{\xi_i} + vy_{\xi_i} + wz_{\xi_i}}{(x_{\xi_i}^2 + y_{\xi_i}^2 + z_{\xi_i}^2)^{1/2}} \qquad (15)$$

The denominator of Eq. (15) is usually referred to as scale factor h_{ξ_i}. Combining Eq. (15) with Eqs. (14*a*)–(14*c*) we obtain the discretization equation for u_{ξ_i}

$$a_Pu_{\xi_i,P} = a_Eu_{\xi_i,E} + a_Wu_{\xi_i,W} + a_Nu_{\xi_i,N} + a_Su_{\xi_i,S} + a_Fu_{\xi_i,F} + a_Ru_{\xi_i,R} + b_{\xi_i,\text{curv}} + b_{\xi_i} \qquad (16)$$

The source term $b_{\xi_i,\text{curv}}$ arises due to the curvature of the grid lines and could also be derived using tensor algebra. We should note here that the pressure gradient term, which consists only of main derivatives (i.e., the cross derivatives are zero) is included in the source term b_{ξ_i}. More details on the formulation of the curvature and pressure source terms can be found in Tamamidis (1990).

3.3 Calculation of Pressure. In this work, the SIMPLEC algorithm of Raithby (1984) is used to couple the momentum and continuity equations. This algorithm is a modification of the well-known SIMPLE algorithm (Patankar, 1980). Though the SIMPLEC algorithm has been originally applied for a staggered grid in a cartesian coordinate system using cartesian velocities as the main variables, this work extends it to collocated grids in nonorthogonal BFC. In our case, covariant velocities are used instead of cartesian as the main variables. To avoid checker-board pressure fields, which are commonly associated with collocated grids for incompressible flows, we adopt Rhie's (1983) interpolation approach, including the modifications suggested by Majumdar (1988). After some manipulation, the pressure correction equation can be written in the following form

$$a_Pp'_P = a_Ep'_E + a_Wp'_W + a_Np'_N + a_Sp'_S + a_Fp'_F + a_Rp'_R + b \qquad (17)$$

where the source term b is the mass imbalance in the control volume. Following the solution of Eq. (17), the covariant velocities at cell centers and the pressures are corrected as follows

$$u_{\xi_i} = u_{\xi_i}^* + u'_{\xi_i} \qquad (18a)$$

$$p = p^* + p' \qquad (18b)$$

The corrections of the mass flow rates are performed by correcting the respective component of the covariant velocity in the following equation

$$F^{\xi_i} = \text{Ja}\ \rho[u_{\xi_i}h_{\xi_i}g^{ii} + u_{\xi_j}h_{\xi_j}g^{ij} + u_{\xi_k}h_{\xi_k}g^{ik}]\Delta\xi_j\Delta\xi_k \qquad (19)$$

where the indices change cyclically, i.e., no index summation is implied.

3.4 Boundary Conditions. Boundary conditions need to be specified for the covariant velocity components and the pressure corrections. Three types of boundary conditions are used in this work: inlet and exit boundary conditions, and boundary conditions at the walls. At the inlet, covariant velocities are specified. At the exit, covariant velocities assume their values at the upstream grid location (i.e., the flow at an exit boundary is treated as fully developed). At the walls, no-slip is assumed. For the pressure correction equation, the same boundary conditions are used, i.e., the respective coefficient in the pressure correction equation is set to zero (Patankar, 1980). The pressures on solid walls are calculated by setting the normal derivative of p equal to zero; at inflow and outflow boundaries, the values of pressure are found by linear extrapolation from interior points.

4 Method Validation

4.1 Comparison of SIMPLE with SIMPLEC. Extensions of the SIMPLE and SIMPLEC pressure-velocity coupling algorithms in BFC using a collocated grid arrangement, with the covariant velocities as the main variables, have not been reported in the literature. Therefore, it is important to compare the performance of these two algorithms before using the present method.

As a test case, the two algorithms are compared for a 90 deg curved duct flow using a 38 × 11 × 11 grid. The linear solver used for the solution of the algebraic systems of equations is the tridiagonal matrix algorithm, coupled with the ADI (Alternating Direction Implicit) procedure. Convergence is assumed when the maximum normalized residual is less than 10^{-2}. Figure 2 compares the convergence behavior of SIMPLE and SIMPLEC as a function of the pressure underrelaxation factor w_p; the velocity underrelaxation factor w_u was used as a parameter. Figure 2 shows that for relatively low values of w_u, there exists a range of w_p values that can be used without considerably affecting the convergence rate. As w_u is increased, the required number of iterations is considerably reduced, but convergence becomes more sensitive to values of w_p used. To minimize the number of iterations for convergence, there is an optimum value of w_p for each w_u. Figure 2 also suggests that SIMPLEC can work for a wider range of w_u and w_p than SIMPLE. It was found that, at least for this test case, the following relationships give the optimum value of w_p as a

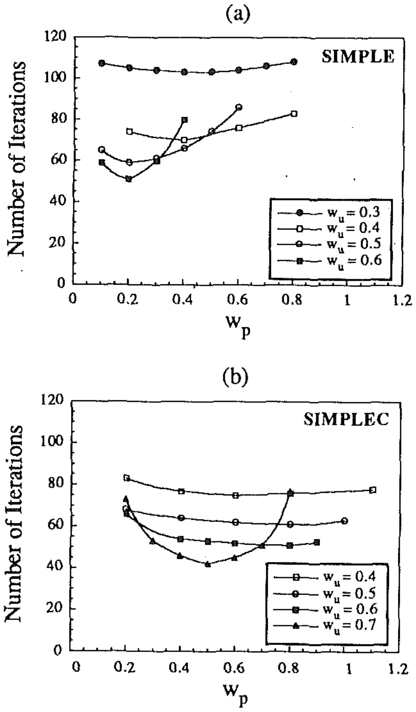

Fig. 2 Comparison of SIMPLE with SIMPLEC algorithm

function of w_u, when using the SIMPLE and SIMPLEC algorithms:

$$w_p = 0.8 - w_u \text{ (SIMPLE)}; \quad w_p = 1.2 - w_u \text{ (SIMPLEC)}$$

We should note here that when solving the momentum equations, one sweep of the domain is sufficient for both algorithms. However, for the pressure correction equation, one sweep of the domain is sufficient only for the SIMPLEC algorithm, but two sweeps are required for the SIMPLE procedure; the latter was found to be stable only for a narrow range of underrelaxation factors when one sweep of the domain was used. Thus, although for each algorithm's best case the minimum number of iterations was relatively close (42 for the SIMPLEC versus 51 for the SIMPLE), the savings of computer time were 40 percent when using SIMPLEC. Note that the corresponding times on a Cray-Y/MP were 6.51 CPU seconds for SIMPLEC and 9.12 seconds for SIMPLE. Therefore, SIMPLEC leads to considerable savings in computer time.

4.2 Comparison With Experiments. The method is validated by comparing predictions with experiments (Taylor et al., 1982) for flow in a 90 degree curved duct of square cross-section. The grid used consists of 61 × 21 × 21 nodes, as shown in Fig. 3(*a*). The Re number based on the hydraulic diameter of the duct is 792, which corresponds to the flow of water with velocity equal to 0.0198 m/s. The dimensions of the duct at each cross-section are 40 × 40 mm, and the radius of curvature of the suction side is 72 mm.

Figure 3(*b*) shows the flow development at the vertical midplane. The "core" fluid, defined as fluid of velocity greater than about 0.9 of the maximum at each streamwise station (Taylor et al., 1982), is found progressively closer to the outer wall, with a correspondingly low velocity region adjacent to the suction side. This redistribution of streamwise velocity is caused by the secondary flow in the duct, as illustrated in Figs. 3(*c*)–3(*d*). Due to this secondary flow, core fluid is convected from the pressure surface along the sidewalls, and low momentum boundary-layer fluid from the sidewalls is accumulated at the inner wall. It is important to note that the extent of the core flow determines the relative magnitude of the secondary flow, i.e., the narrower the distribution of core flow, the larger the secondary velocities. Further downstream from the bend (see Fig. 3(*d*)) the secondary flow gradually diminishes. Our predicted character of the flow is in good qualitative agreement with the experimental observations of Taylor et al. (1982).

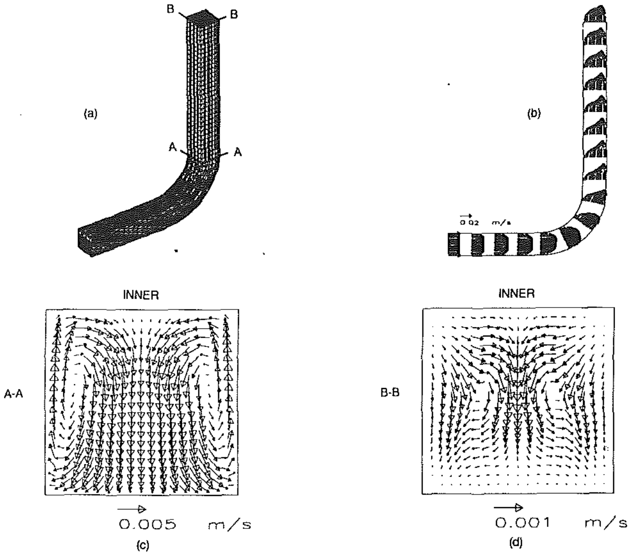

Fig. 3 Flow in a 90 degree curved duct of square cross-section. (*a*) The grid (61 × 21 × 21), (*b*) the flow field in middle plane $z = z_{max/2}$, (*c*) and (*d*) secondary flow development in planes normal to streamwise direction.

To explore the ability of the present method to predict correct magnitudes of flow velocities, a quantitative comparison of our results with the measurements of Taylor et al. (1982) has been performed at a distance equal to 2.5 hydraulic diameters downstream from the bend. The distribution of the calculated streamwise velocity is plotted against the measured one at various radial locations. As in (Taylor et al., 1982), the velocities have been normalized with respect to inlet velocity. Further, the gapwise distance z, and the radial distance r have been made nondimensional according to the following relations

$$z^* = 1 - \frac{z}{z_{1/2}}$$

$$r^* = \frac{r - r_0}{r_i - r_0}$$

where r_0 and r_i are the outer and inner radii, respectively. The calculated velocities are in good agreement with the experimental results, as shown in Fig. 4. Some discrepancies are attributed to the limitations of the hybrid scheme used in this work. Overall, however, this method can correctly predict flows, both in terms of general character and magnitudes.

5 Application to Duct Flows

Having validated the method, its application to a range of duct flows is illustrated in this section. Flows in ducts with curved surfaces are characterized by the formation of counter rotating vortices. The tests to be reported in this section will investigate the capability of the method to predict physically correct trends in such complex flows. The grids used in the subsequent studies have been generated using the transfinite interpolation method, presented in detail by Thompson et al. (1985). All grids are orthogonal except otherwise noted.

5.1 Laminar Flow in a 180 Degree Curved Duct. The first application of this method is the flow in a 180 degree curved duct of square cross-section. This flow is characterized by the

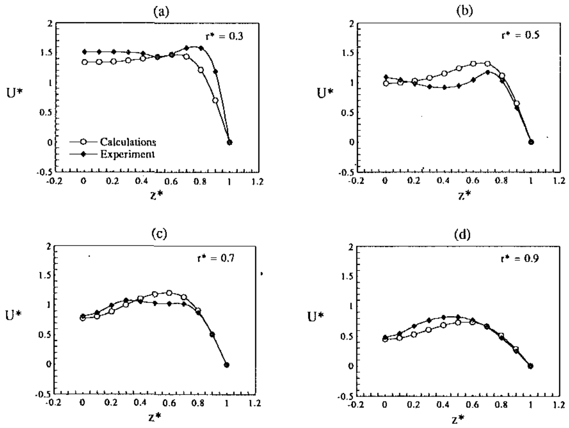

Fig. 4 Comparison of calculated axial velocity versus measured at 2.5 hydraulic diameters downstream of the bend

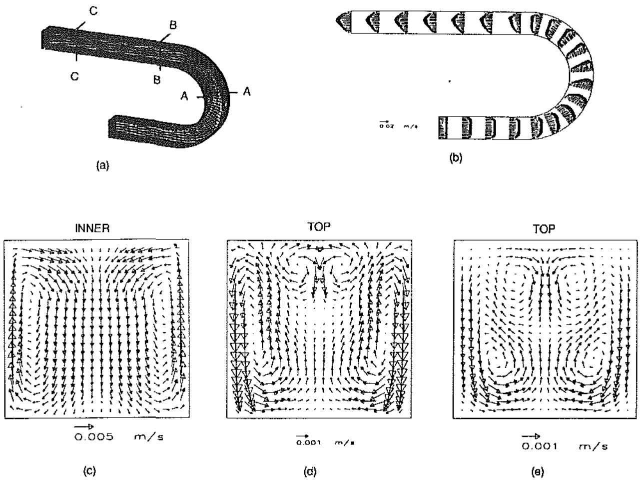

Fig. 5 Flow in a 180 degree curved duct of square cross-section. (*a*) The grid (81 × 22 × 22), (*b*) the flow field in middle plane $z = z_{max/2}$, (*c*) through (*e*) secondary flow development in planes normal to streamwise direction.

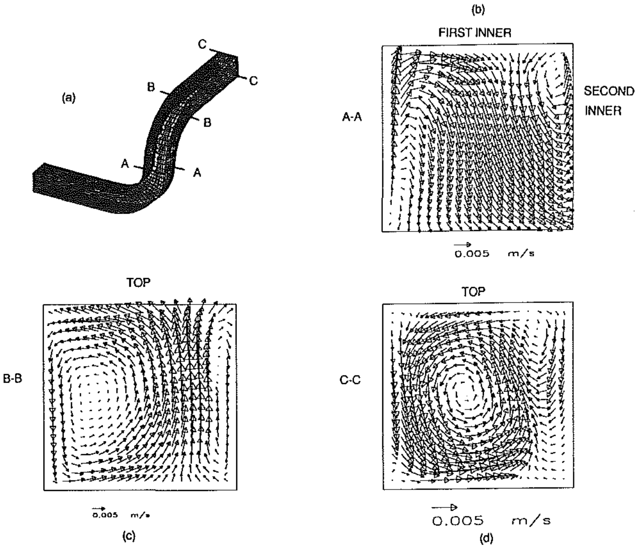

Fig. 6 Flow in a two right-angle curved duct of square cross-section. (*a*) The grid (71 × 21 × 21), (*b*) the flow field in middle plane $z = z_{max/2}$, (*c*) through (*e*) secondary flow development in planes normal to streamwise direction.

formation of two pairs of counter-rotating vortices. This phenomenon, known as Dean's instability, occurs beyond a Dean number of about 150, as discussed by Cheng et al. (1976), Ghia and Sokhey (1977), and Duh and Shih (1989). The Dean number (De) is defined as

$$\mathrm{De} = \left(\frac{\frac{1}{2} D_h}{R_c} \right)^{1/2} \mathrm{Re}$$

where D_h the hydraulic diameter and R_c the mean radius of curvature.

The cross-sectional dimensions of the duct are 40 × 40 mm, and the radius of curvature of the suction side is 72 mm. The grid used for our study consists of 81 × 22 × 22 nodes, as shown in Fig. 5(*a*). The Re number based on duct's hydraulic diameter is 792, which corresponds to the flow of water with velocity equal to 0.0198 m/s. The Dean number for this flow is 369.

Figure 5(*b*) shows the flow development at the vertical middle plane. As was in the case of the 90 deg curved duct, the core fluid is found progressively nearer to the outer wall, with a correspondingly low velocity region adjacent to the suction side. However, after about 150 degrees, the core fluid starts shifting backwards, toward the centerline. This redistribution of streamwise velocity is caused by the secondary flow in the duct, as illustrated in Figs. 5(*c*)-5(*e*). At the 90 deg location, one pair of vortices is only present. However, at about 170 deg a second pair of vortices appears, which becomes stronger at some distance after the bend. The resultant loss in streamwise momentum near the outer wall is absorbed near the central core of the duct. The results for this case show good qualitative agreement with the numerical calculations of Cheng et al. (1976), and Ghia and Sokhey (1977).

The appearance of the second pair of vortices near the outer wall is caused by the centrifugal instability, as first explained by Stuart (1963). In the region near the central outer wall, an instability is caused by the imbalance between the pressure gradient and the centrifugal force. The former is positive in the radial direction, while the latter decreases from a maximum value to zero at the outer wall. However, the flow near the inner wall is stable. In industrial applications, this instability phenomenon in curved ducts may increase friction resistance, and thus, influence the efficiency of the operation. These issues need to be investigated further.

5.2 Flow in a Two Right-Angle Curved Duct. The next application of the method is the laminar flow in a two right-angle curved duct of square cross-section. To the best of our knowledge, studies on this duct shape have not been reported in the literature. The grid used consists of 71 × 21 × 21 nodes, as shown in Fig. 6. The fluid, which is water, enters with a velocity of 0.03 m/s; the cross-sectional area of the duct is 40 × 40 mm, and each of the two inner radii is 72 mm. The Re number for this case is equal to 1200.

Figures 6(*b*)-6(*d*) illustrate the secondary flow development at three locations, denoted by AA, BB, and CC in Fig. 6(*a*). In section AA (Fig. 6(*b*)), two counter-rotating vortices are starting to form. These two initial vortices are of unequal strength due to subsequent curvature effects. As the fluid enters the cross section connecting the two bends, the initial vortex pattern is modified and strong convection of the fluid towards the second inner surface is observed. Downstream of the second bend, the centrifugal forces generated from the first bend squeeze the flow close to the sidewall. This forcing of the flow eventually produces a pair of vortices of considerably different magnitude, as evidenced in Fig. 6(*c*). Further downstream, the size of the larger vortex grows, and its center shifts toward the centerline of the duct (see Fig. 6(*d*)). This way, a swirling motion is formed in the downstream section of the duct.

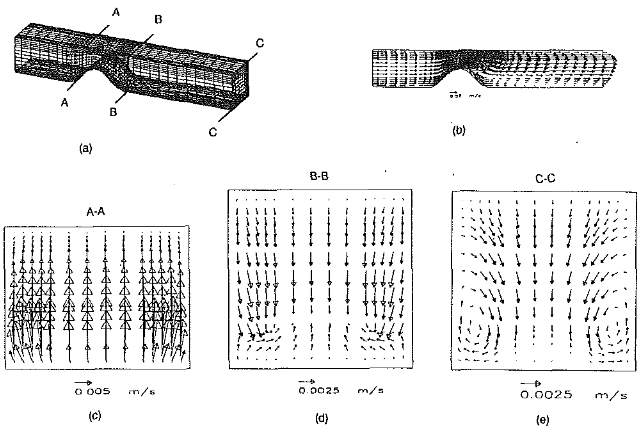

Fig. 7 Flow in a straight duct with a constriction. (*a*) The grid (47 × 16 × 16), (*b*) the flow field in middle plane $z = z_{max/2}$, (*c*) and (*d*) secondary flow development in planes normal to streamwise direction.

5.3 Straight Duct With a Constriction. Last, the method is applied to the prediction of the flow in a straight duct with a constriction. A similar test case has been numerically investigated by Reggio and Camarero (1987). The nonorthogonal mesh used for this case consists of 47 × 16 × 16 nodes as shown in Fig. 7(*a*). At the inlet, the Re number is 800 which corresponds to flow of water with a velocity equal to 0.02 m/s. The duct is of square cross-section (40 × 40 mm) everywhere except at the constriction.

Figure 7(*b*) shows the velocity field at the vertical mid-plane. The flow at this plane is characterized by a recirculation zone caused by the existence of the constriction in the duct. An interesting phenomenon is the development of a secondary flow in planes normal to the streamwise direction, as shown in Figs. 7(*c*)-7(*e*). As explained by Reggio and Camarero (1987), when the flow reaches the constriction, the bottom surface layer is squeezed towards the upper wall. Then, as it trails the rear of the obstruction, this layer is forced towards the vertical mid-plane. This results in the development of two symmetric vortices in the cross-sectional planes. Further downstream, towards the exit plane, the size of these counter-rotating vortices is growing.

6 Conclusions

In this paper, a calculation procedure for predicting three-dimensional, steady, incompressible flows has been presented. The method uses Body-Fitted Coordinates (BFC) in collocated grid arrangements with the covariant velocities as main variables. The SIMPLE and SIMPLEC velocity-pressure coupling algorithms were compared, showing that SIMPLEC can lead up to 40 percent computational savings over SIMPLE.

Application of the method has been illustrated for several duct flows in complex geometries. The characteristic phenomenon in such flows is the secondary motion arising from the channel curvature. Good qualitative and quantitative results were obtained using this procedure. The results demonstrate the potential of the present method for providing realistic answers to problems of practical interest.

Acknowledgment

This material is based upon work supported by the National Science Foundation under grants No. CTS-8858310. The National Center for Supercomputing Applications at the University of Illinois at Urbana-Champaign provided computer time on the CRAY-Y/MP system for this study.

References

Cheng, K. C., Lin, R. C., and Ou, J. W., 1976, "Fully Developed Laminar Flow in Curved Rectangular Channels," ASME JOURNAL OF FLUIDS ENGINEERING, Vol. 98, pp. 41-47.

Demirdzic, I., Gosman, A. D., and Issa, R. I., 1980, "A Finite-Volume Method for the Prediction of Turbulent Flow in Arbitrary Geometries," *Lect. Notes Phys.*, Vol. 144, pp. 144-150.

Duh, T. Y., and Shih, Y. D., 1989, "Fully Developed Flow in Curved Channels of Square Cross Sections Inclined," ASME JOURNAL OF FLUIDS ENGINEERING, Vol. 111, pp. 172-177.

Ghia, K. N., and Sokhey, J. S., 1977, "Laminar-Incompressible Viscous Flow in Curved Ducts of Rectangular Cross-Sections," ASME JOURNAL OF FLUIDS ENGINEERING, Vol. 99, pp. 640-648.

Hirt, C. W., Amsden, A. A., and Cook, J. L., 1974, "An Arbitrary Lagrangian-Eulerian Computing Method for All Flow Speeds," *J. Comput. Phys.*, Vol. 14, pp. 227-253.

Karki, K. C., and Patankar, S. V., 1986, "Calculation Procedure for Viscous Incompressible Flows in Complex Geometries," *Numerical Heat Transfer*, Vol. 14, pp. 295-307.

Majumdar, S., 1988, "Role of Underrelaxation in Momentum Interpolation for Calculation of Flow with Nonstaggered Grids," *Numerical Heat Transfer*, Vol. 13, pp. 125-132.

Nakayama, A., 1984, "A Finite Difference Calculation Procedure for Three-Dimensional Turbulent Separated Flows," *Int. J. Numer. Meth. Eng.*, Vol. 12, pp. 1247-1260.

Patankar, S. V., 1980, *Numerical Heat Transfer and Fluid Flow*, Hemisphere, Washington, D.C.

Reggio, M., and Camarero, R., 1987, "A Calculation Scheme for Three-Dimensional Viscous Incompressible Flows," ASME JOURNAL OF FLUIDS ENGINEERING, Vol. 109, pp. 345-352.

Rhie, C. M., and Chow, W. L., 1983, "Numerical Study of the Turbulent Flow Past an Airfoil with Trailing Edge Separation," *AIAA J.*, Vol. 11, pp. 1525-1532.

Stuart, J. T., "Hydrodynamic Stability, 1963," *Laminar Boundary Layers*, L. Rosenhead, ed., Oxford University Press, p. 505.

Talpallikar, M. V., Yang, H. Q., and Przekwas, A. J., 1990, "Numerical Analysis of Turbulent Flow in I.C. Engine Port/Valve Assembly," ASME Paper No. 90-ICE-10.

Tamamidis, P., 1990, "Numerical Prediction of Subsonic Turbulent Recirculating Flows Using Boundary-Fitted Coordinates," M.S. thesis, University of Illinois at Urbana-Champaign, Urbana, IL.

Taylor, A. M. K.P., Whitelaw, J. H., and Yianneskis, M., 1982, "Curved Ducts With Strong Secondary Motion: Velocity Measurements of Developing Laminar and Turbulent Flow," ASME JOURNAL OF FLUIDS ENGINEERING, Vol. 104, pp. 350-359.

J. F. Thompson, Z. V. A. Warsi, and C. W. Mastin, 1985, *Numerical Grid Generation, Foundations and Applications*, North-Holland, New York, N.Y.

VanDoormal, J. P., and Raithby, G. D., 1984, "Enhancements of the SIMPLE Method for Predicting Incompressible Fluid Flows," *Numerical Heat Transfer*, Vol. 7, pp. 147-163.

Vanka, S. P., Chen, B. C. J., and Sha, W. T., 1980, "A Semi-Implicit Calculation Procedure For Flows Described in Boundary-Fitted Coordinate Systems," *Numerical Heat Transfer*, Vol. 3, pp. 1-19.

Interpretation of Impeller Flow Calculations

J. Tuzson
Gas Research Institute,
Chicago, IL 60631

Most available computer programs are analysis and not design programs. Therefore the intervention of the designer is indispensable. Guidelines are needed to evaluate the degree of fluid mechanic perfection of a design which is compromised for practical reasons. A new way of plotting the computer output is proposed here which illustrates the energy distribution throughout the flow. The consequences of deviating from optimal flow pattern is discussed and specific cases are reviewed. A criterion is derived for the existence of a jet/wake flow pattern and for the minimum wake mixing loss.

Introduction

Most available computer programs for turbomachinery fluid mechanics calculations are for analysis and not for design (McNally, 1985). The impeller geometry is an input and the flow pattern is the output. But the objective of the designer is to determine the optimal blade angle distribution and the best meridional geometry. Therefore he has to proceed by trial and error.

While some promising design programs have been developed recently (Zangeneh, 1991), a fully automated computer procedure is hindered by two main factors: cost of computer time and practical design considerations. Detailed, three-dimensional calculations of impellers require large computers and are time consuming. Therefore industrial machines are still mostly designed by empirical rules. These empirical rules and the intuition of the designer must not be underestimated since they contributed significantly to the present state of the technology. They will continue to play an important role in the future but must be founded on a solid understanding of the underlying phenomena.

Practical considerations require that the ideal impeller design be compromised for off-design performance, cavitation, etc., and for manufacturing and cost reasons. The most severe manufacturing constraints is that the blade-wrap should almost be the same on hub and shroud, otherwise excessive blade lean results, which is difficult to manufacture. Blade-wrap is the circumferential angle subtended by the blade. Blade-lean is the angle of the trailing edge with the meridional plane. Minimal axial length, dictated by shaft dynamics, influences the choice of the meridional contour. Examples of performance constraints are when the head at shut-off or the maximum power demand is prescribed, the same impeller is to be machined to different diameters, or different impellers need to fit in the same housing to provide a full line of pumps at least cost. The economically "best" impeller is not necessarily perfect from a fluid mechanics point of view.

Convergence of successive computer runs can be helped by the designer. Iteration toward the best design is greatly accelerated by a good initial guess and by enlightened corrections. Intervention by the designer is, therefore, absolutely essential. This, however, raises the question: What is the theoretically optimal design and how to recognize the degree of perfection of the design from the computer print-out.

The objective of this paper is to inquire into this interpretation of the impeller flow calculations and to propose approaches for approximating the best design.

Design Principles

Turbomachinery serves to increase the energy (total pressure or enthalpy) of the fluid stream. Since the rotary motion of the impeller can only produce torque, only the angular momentum of the fluid can be increased in the impeller. This is expressed by Euler's equation.

Fluid particles will follow a certain path, a streamline through the impeller. The first rule of a good impeller is that the same energy, and therefore the same angular momentum, should be imparted to the fluid on each of the streamlines. Diffusion can transform kinetic energy into pressure but cannot change the total energy of the fluid. Nonuniform, spanwise energy distribution in the streamlines will result in streamwise vortex shedding in the wake as evidenced in several, well-known studies (Batchelor, 1979; and Betz, 1932). Mixing of a nonuniform shear-flow always causes a loss.

Since the angular momentum gradually rises throughout the impeller on each of the streamlines from inlet to exit, the question arises at what location should the energy of adjacent streamlines be compared.

A flow of uniform energy in the absolute frame of reference would require that the angular momentum remain the same on each surface orthogonal to the relative streamlines. This is shown in the Appendix. In the usual coordinate system (see Fig. 1) (Vavra, 1960), when the flow is described in the meridional and on the circumferential surface, the gradient of the angular momentum would have to be zero in the direction of the orthogonal to the projection of the streamline in the hub-

---

Contributed by the Fluids Engineering Division for publication in the JOURNAL OF FLUIDS ENGINEERING. Manuscript received by the Fluids Engineering Division January 9, 1990; revised manuscript received December 11, 1992. Associate Technical Editor: U. S. Rohatgi.

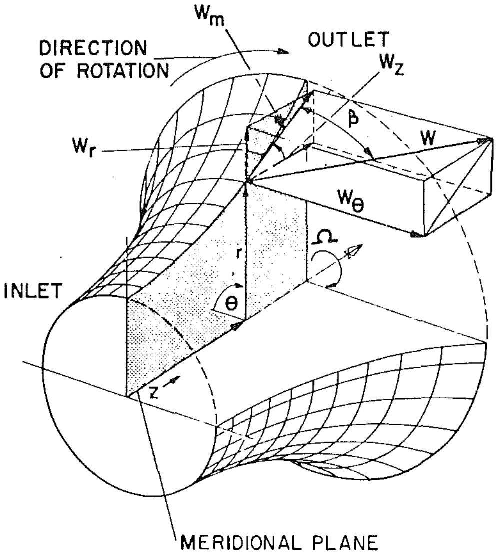

Fig. 1 Coordinate system and definition of variables

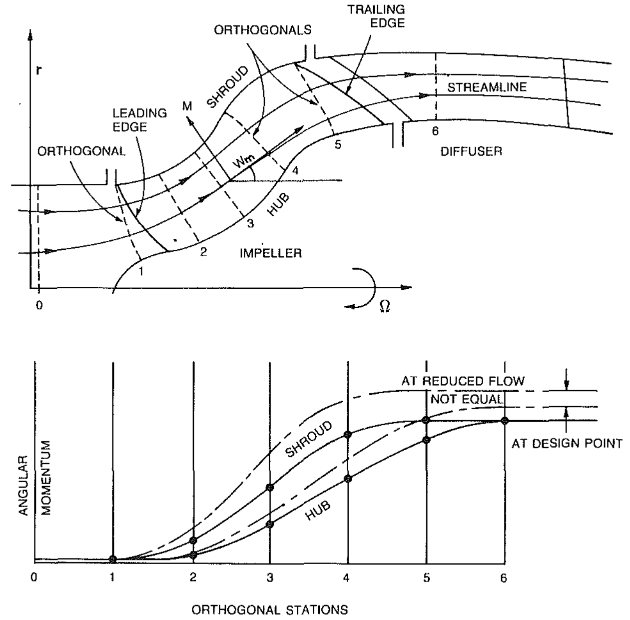

Fig. 2 Meridional plane projection of flow pattern in a mixed flow pump and corresponding angular momentum diagram at design point and at reduced flow

to-shroud and also in the blade-to-blade planes (see Figs. 2 and 4). This requirement is quite general and applies equally to centrifugal, mixed flow, or axial compressors, pumps, or turbines.

If these requirements are satisfied then the flow in the meridional plane would be identical to a potential, axisymmetric, steady flow. Such a potential flow assumption has often been used to calculate meridional streamlines in impellers. These, relatively simple, calculations have been found useful by practicing engineers. However, certain conditions must be fulfilled. A potential flow solution only establishes the kinematic possibility of the flow pattern but does not assure dynamic stability. For example, the potential flow solution is unstable for bluff bodies (d'Alambert's Paradox) but happens to be stable for airfoils (Birkhoff, 1983). A steady separated region of low momentum fluid can only exist if it is in a stable position.

Uniform angular momentum distribution requires that leading and trailing edges of the blades must be orthogonal to the streamlines. This is the case in compressors and some pumps. But on most pumps the leading edge is cut back, presumably to obtain an acceptable blade lean. Also a slanted leading edge, like swept wings, may reduced incidence losses at part load. In mixed flow pumps, leading and trailing edges are definitely not orthogonal and suggest difficulties. In these, less energy will be imparted along the hub than the shroud at reduced flow (Pfleiderer, 1961). Therefore a shear flow results downstream, which can give rise to unusual, recirculating flow pattern (Munson, 1980). It is the cause of exit recirculation. A similar condition accounts for the swirl in the draft tube of hydroturbines. In axial flow machinery, use of other than "free vortex" distribution is a deliberate, nonideal trade-off against more favorable flow conditions at the blade tips (Wilson, 1984).

It is apparent from the above that knowledge of the angular momentum distribution is essential for evaluating impeller flow and for understanding the consequences of a nonoptimal design.

Angular Momentum Plot

The customary method for presentation of the results of a computer flow analysis is to plot the relative flow velocity in the impeller against the fraction of the streamline length from leading to trailing edge. A comparison between pressure side and suction side streamlines can give a qualitative indication of the "blade loading" or "energy input" since the relative velocity difference is related to the pressure difference across the blade, albeit not linearly. More meaningful are the maximum Mach number or velocity at the inlet, and the relative velocity decrease or diffusion on the blade suction side. High Mach numbers and rapid diffusion can signal losses (Dallenbach, 1961). High inlet velocities in pumps often signal cavitation. However, these plots do not inform about the energy and angular momentum distribution.

A new kind of plot is proposed here (Figs. 2 and 4), which consists of the angular momentum on several, parallel streamlines in the meridional and blade-to-blade surfaces plotted against a reference scale with stations corresponding to orthogonals to the relative streamlines. Numerical derivations can be found in standard references (Vavra, 1960).

In the ideal flow case, when the angular momentum increase is identical on all streamlines, all plots corresponding to individual streamlines would coincide and only one line would be present. It is desirable that the curve on the plot rise gradually first and taper off toward the trailing edge. This will

Nomenclature

I = rothalpy, ft^2/s^2
p = pressure, lb/ft^2
r = radial coordinate, ft
s = coordinate along streamline, ft
V = flow velocity vector in the absolute, stationary frame of reference, ft/s
V_θ = circumferential component of V, ft/s
W = flow velocity vector in the relative, rotating frame of reference, ft/s
W_1 = relative velocity in wake, ft/s
W_2 = relative velocity in jet, ft/s
z = axial coordinate, ft
β = angle of W from meridional in direction of rotation
θ = circumferential coordinate
Ω = angular velocity of impeller, 1/s
ω = vorticity vector in relative frame of reference, 1/s
ρ = fluid density, lb s^2/ft^4

unload the leading and trailing edges of the blade at design flow.

In practice, the angular momentum curves will not coincide (see Fig. 2). For example, when the blade leading edge is cut back the angular momentum curve of the shroud in the meridional plane will rise sooner and may join the curve of the hub toward the exit. These plots will show the degree of uniformity of the angular momentum distribution, which is a measure of the fluid mechanic perfection of the impeller design. The designer must also have an understanding of the consequences of deviating from the ideal flow pattern, which will be discussed in the next section.

Consequences of Nonuniform Energy Distribution

Past work on shear flows, stability, and secondary flows, which would apply to turbomachinery impellers, was concentrated on turbulence modeling, transition to turbulence, and boundary layers in advanced aerospace calculations (Bayly, 1988; Moser, 1987; Georgescu, 1985; Shivamoggi, 1986; Bradshaw, 1974; Wisler, 1987; and Cain, 1986). Several studies of Bradshaw have been published on the effect of streamline curvature on shear layers, the most recent being a review article with 77 references (Bradshaw, 1987).

The issue of concern here is not the losses in the impeller but the nonuniform absolute flow, which might arise, for example, from spanwise variation of lift and not from viscous losses. Boundary layers in impellers have two important manifestations: skin friction losses and blockage, which distorts the flow pattern. Typically, impeller skin friction losses account for less than five percent efficiency reduction. At the high Reynold's numbers encountered in practice dissipation processes are slow and are completed far downstream but their origin is in the impeller. The blockage resulting from boundary layers or from leading edge, inviscid separation strongly affects the energy increase in the impeller. Some of these cases will be enumerated here.

Shear flows in general are unstable. For example, the shear layer between two parallel streams of different velocities develops waves and finally rolls up in vortices, as has been shown in the classical study of Helmholtz (Helmholtz, 1868 and Lamb, 1945). This instability is inviscid and does not depend on viscosity.

The instability or stability of shear flows is strongly affected by transverse pressure gradients. Pressure gradients arise from accelerations such as centrifugal or Coriolis accelerations. They can arise from the curvature of streamlines or from the rotation of the frame of reference.

When the transverse inertia force, and therefore the pressure gradient, is directed from the lower energy fluid toward the higher energy fluid the shear layer separating the two flows tends to be stabilized. This has been proven by analysis (Bayly, 1988 and Tuzson, 1977) and by experiment (Johnston, 1972 and 1976). A well-known example is the stagnant, low energy core of a vortex which remains stable and unmixed in spite of the high velocities and the high shear at the core boundary. It is precisely the fast rotation and high centrifugal pressure gradient that stabilizes the flow. It was shown (Hogg, 1989) that the $k-\epsilon$ turbulence model does not capture these effects and that a Reynolds stress closure model is needed. When, on the other hand, the angular momentum of the fluid decreases with the radius in the vortex and therefore the energy of the fluid also decreases with the radius, instability is enhanced and more rapid mixing occurs (Leibovich, 1984). Examples of such conditions in impellers will be described below.

Flow in the Meridional Plane. At correct incidence and in the absence of preswirl, the flow at the inlet has no absolute tangential velocity and therefore any transverse pressure gradient is due to streamline curvature in the meridional plane. It will be directed from shroud to hub. If an unstable shear flow is to be avoided the streamwise increase of angular momentum on the shroud should not exceed that on the hub and the shroud curvature should be minimized. This often conflicts with the requirement to minimize the axial length of the impeller. In impellers with radial exits, curvature in the meridional plane should be avoided at the exit to obtain a well-behaved, uniform, parallel flow entering the radial diffuser.

In mixed flow impellers the trailing edge of the blade is slanted and therefore the velocity profile does not give a good indication of the perfection of the flow. Uniform exit velocity distribution does not correspond to uniform angular momentum. Especially at reduced flow, less energy will be imparted to the flow at the hub than at the shroud (Pfleiderer, 1961). At the impeller exit a swirling flow will be produced in which the angular momentum will increase with the radius. The centrifugal pressure gradient will predominate and will be directed from the low energy core toward the high energy flow at greater radius. This is a stable, axisymmetric shear-flow configuration. Therefore a low momentum, reversing core flow can persist and will not mix. This is the basic mechanism of the exit reverse flow observed in mixed flow pumps at reduced flow rate (Keller, 1985 and 1988).

In axial flow machinery the ideal, irrotational, constant angular momentum distribution is a "free vortex" distribution. In high performance, multistage machines other distributions are used (Wilson, 1984) in which the angular momentum increases with the radius and which, therefore, are stable. An axial shear flow results and is tolerated as a trade-off against more favorable flow conditions at the blade tips.

Flow on the Blade-to-Blade Stream Surface. A particular manifestation on nonuniform flow is when a jet/wake flow pattern is present (Dean, 1960; Johnston, 1966; Japikse, 1987; and Rohne, 1991). This flow pattern consists of two regions in the blade-to-blade direction divided by the separation streamline. The low velocity, W_1 region is near the suction side of the blade and the high velocity, W_2 region near the pressure side. Assume that the loss in rothalpy (see Appendix) of the wake region is $(W_1^2 - W_2^2)/2$. This is the energy lost by friction by the relative flow in the separated wake region. At a particular location the static pressure is the same and the radius is the same on either side of the separation streamline.

The absolute energy increase in the impeller above the inlet energy on each streamline is given by the relation:

$$\Omega r V_\theta = \Omega^2 r^2 + \Omega r W \sin\beta$$

where β is the angle of the separated streamline from the meridional in direction of the sense of rotation. It will be noted that if $\beta < 0$ (backwards curved blades) then the energy increase in the wake region is greater than in the jet and can make up for the losses. The two regions have equal energy when

$$(W_2^2 - W_1^2)/2 = -\Omega r (W_2 - W_1)\sin\beta$$
$$(W_2 + W_1)/2\Omega r = -\sin\beta$$

(see Fig. 3).

In this particular case no energy loss occurs when the jet and wake mix at the impeller exit. Therefore this equation expresses the condition for optimal flow pattern. It is not surprising then that some compressors having substantial flow separation and a pronounced jet/wake flow nonetheless operate at high efficiency. More generally it can be stated that boundary layers in a rotating impeller do not necessarily have lower energy than the main stream.

In radial bladed impellers the flow angle will be approximately zero ($\beta = 0$) and, therefore, the energy of the jet will be greater than that of the wake. Depending on the "loading," $W/\Omega r$, the energy of the two streams will tend to equalize with increasing backsweep $\beta < 0$. In most pumps, where typically

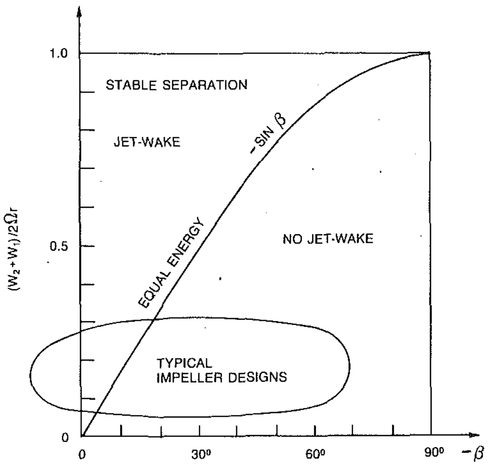

Fig. 3 Criterion for the presence of jet/wake flow patterns $(W_2 + W_2)/2\Omega r = -\sin\beta$

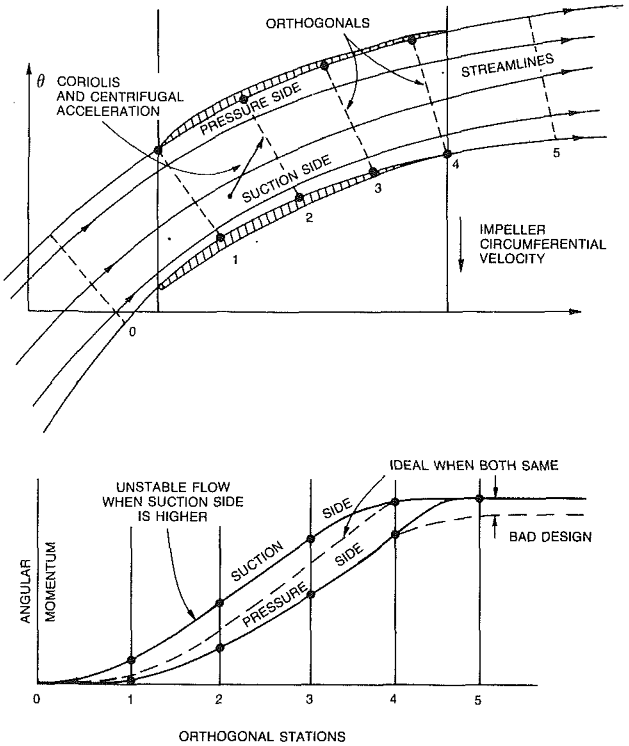

Fig. 4 Projection of flow pattern on the circumferential, blade-to-blade stream surface and corresponding angular momentum diagram

$\beta = -70$, and the wake would have more energy, the jet/wake flow pattern is not observed.

The dominant pressure gradient in an impeller is directed from the wake toward the jet. This tends to stabilize the separation streamline if the jet has higher energy. Mixing is avoided and separation persists throughout the impeller. For strongly backwards curved blades the wake has higher energy while the pressure gradient retains its direction. This destabilizes the separation and typically no jet/wake flow pattern is observed.

A similar effect can be observed in the case of leading edge separation. Separation on the suction side, encountered at reduced flow, is stabilized and persists into or throughout the impeller. Separation on the pressure side, at increased flow rate, is unstable, mixes, and the flow is reattached further on. It is desirable therefore to avoid "loading," that means, an increase of angular momentum on the suction side at the blade tips up to the location where the orthogonal originating at the leading edge of the pressure side intercepts the suction side profile (see Fig. 4). A similar situation exists at the impeller exit. Ideal flow would require that the blades be unloaded toward the trailing edge.

It is apparent from these examples that the angular momentum distribution is an important indicator of the fluid mechanic perfection of an impeller.

Summary and Conclusions

Currently available computer programs for calculating fluid flow in impellers are mostly analysis programs. The impeller geometry must be input and corrected by the designer. The compromises encountered in practical designs require that the designer interpret the computer print out and exercise a well informed judgment when selecting modifications. The objective of this paper is to provide guidelines and examples for interpreting calculated flow pattern and for estimating their effect on performance. A new way of plotting the data and rules of interpretation are offered here.

Specifically the following points are made:

1 The ideal impeller imparts uniform energy (total pressure or enthalpy), to the fluid on all streamlines. This requires that the angular momentum be the same on surfaces which are orthogonal to all the relative streamlines.

2 The above conditions imply that the leading and trailing edges of the blades would have to be orthogonals to the streamlines.

3 To evaluate the degree of fluid mechanic perfection of an impeller design, it is proposed that the angular momentum increase on several streamlines in the meridional and the blade-to-blade projections be plotted against a reference scale with stations corresponding to common orthogonals to all streamlines.

4 The consequence of a nonuniform angular momentum distribution is that a shear flow results. While generally unstable, shear flows are stabilized or destabilized by transverse accelerations (centrifugal or Coriolis) and resulting pressure gradients, especially in rotating flows. When the positive, transverse (not streamwise) pressure gradient in a shear flow is in the direction of increasing total energy, the shear flow is stabilized. Examples are given.

5 On the blade-to-blade stream surface, in the presence of a jet/wake flow pattern, it is shown that when

$$(W_2 + W_1)/2\Omega r = -\sin\beta$$

the total energy of the jet and the wake regions are the same and therefore no mixing loss occurs at the impeller exit. Therefore this represents the ideal case. It is also shown that jet/wake flow pattern is only stable when the absolute energy of the jet is higher than that of the wake, which is most likely to occur in highly loaded, radial impellers.

The above rules should help designers to interpret computer calculations, to anticipate the consequences of nonideal flow, and to decide on further modifications for arriving at the best compromise between practical requirements and flow mechanic perfection.

References

Batchelor, G. K., 1967, *An Introduction to Fluid Dynamics*, Cambridge University Press, pp. 583–588.

Batchelor, G. K., 1979, *An Introduction to Fluid Dynamics*, Cambridge Unviersity Press, pp. 591.

Bayly, B. J., Orszag, S. A., "Instability Mechanisms in Shear-Flow Transition," *Annual Review of Fluid Mechanics*, Vol. 20, pp. 359–391.

Betz, A., 1932, "Verhalten von Wirbelsystemen," *ZAMM Bd. XII*, No. 3, pp. 164–174.

Bradshaw, P., 1974, "Prediction of Turbulent Shear Layers in Turbomachines," *Symposium on Fluid Mechanics, Acoustics, and Design of Turbomachinery*, Pennsylvania State Univ.

Bradshaw, P., 1987, "Turbulent Secondary Flows," *Annual Review of Fluid Mechanics*, Vol. 19, pp. 53–74.

Cain, A. B., and Thompson, M. W., 1986, "Linear and Weakly Nonlinear Aspects of Free Shear-Layer Instability, Roll-up, Subharmonic Interaction and Wall Influence," *AIAA Journal*, pp. 1047.

Dallenbach, F., 1961, "Aerodynamic Design and Performance of Centrifugal and Mixed Flow Compressors," SAE 268 A, Jan. 9–13.

Dean, R. C., Jr., and Senoo, Y., 1960, "Rotating Wakes in Vaneless Diffusers," ASME *Journal of Basic Engineering*, Sept., pp. 563–570.

Georgescu, A., 1985, *Hydrodynamic Stability Theory*, Martinus Nijhoff Publ.

Helmholtz, H., 1868, "Über discontinuirliche Flüssigkeitbewegungen," *Berliner Monatsbericht*, Apr. 1868; *Philosofisches Magazin*, Nov. 1868, Wissenschaftliche Abhandlungen, Leipzig 1882, 3. pp. 146.

Hogg, S., and Leschziner, M. A., 1989, "Computation of Highly Swirling Confined Flow with a Reynolds Stress Turbulence Model," *AIAA Journal*, Vol. 27, pp. 57–63.

Japikse, D., 1987, "Critical Evaluation of Three Centrifugal Compressors with Pedigree Data Sets," ASME *Journal of Turbomachinery*, pp. 1–9.

Johnston, J. P., 1966, "Losses in Vaneless Diffusers of Centrifugal Compressors and Pumps," ASME *Journal of Engineering for Power*, Jan., pp. 49–62.

Johnston, J. P., and Rothe, P. H., 1967, "Effects of System Rotation on the Performance of Two-Dimensional Diffusers," ASME JOURNAL OF FLUIDS ENGINEERING, Sept., pp. 422–430.

Johnston, J. P., Halleen, R. M., and Lezius, D. K., 1972, "Effects of Spanwise Rotation on the Structure of Two-Dimensional Fully Developed Channel Flow," *Journal of Fluids Mechanics*, Vol. 56, No. 3, pp. 533–557.

Keller, J. J., and Egli, W., 1985, "Force- and Loss-Free Transition Between Flow States," *Journal Applied Mathematics and Physics* (ZAMP), Vol. 36, pp. 854–889.

Keller, J. J., Egli, W., and Althaus, R., 1988, "Vortex Breakdown as a Fundamental Element of Vortex Dynamics," *Fluid Dynamics Research*, Vol. 3, pp. 31–42.

Lamb, H., 1945, *Hydrodynamics*, 6th ed., Dover, pp. 370–375.

Leibovich, S., 1984, "Vortex Stability and Breakdown: Survey and Extension," *AIAA Journal*, pp. 1192–1206.

McNally, W. D., and Sockol, P. M., 1985, "Review-Computational Methods for Internal Flows with Emphasis on Turbomachinery," ASME JOURNAL OF FLUIDS ENGINEERING, Vol. 107, pp. 6–22.

Moser, R. D., and Moin, P., 1987, "The Effects of Curvature in Wall-Bounded Turbulent Flows," *Journal of Fluid Mechanics*, Vol. 175, pp. 479–510.

Munson, B. R., 1980, "Rotational Inviscid Flow in a Variable Area Annulus, Pipe, or Channel," ASME JOURNAL OF FLUIDS ENGINEERING, Vol. 102, pp. 437.

Pfleiderer, C., 1961, *Die Kreiselpumpe*, Springer-Verlag, pp. 269–271, 408–416.

Rohne, K. H., and Banzhaf, M., 1991, "Investigation of the flow at the Exit of an Unshrouded Centrifugal Impeller and Comparison With the 'Classical' Jet-Wake Theory," ASME *Journal of Turbomachinery*, Oct., pp. 654–659.

Serrin, J. 1959, "Mathematical Principles of Classical Fluid Mechanics," *Encyclopedia of Physics*, Vol. VIII/1, Fluid Dynamics I, Springer-Verlag, pp. 187.

Shivamoggi, B. K., 1986, *Stability of Parallel Gas Flows*, Ellis Horwood.

Tuzson, J., 1977, "Stability of a Curved Free Streamline," ASME JOURNAL OF FLUIDS ENGINEERING, Sept., pp. 603–605.

Vavra, 1960, *Aero-Thermodynamics of Turbomachinery*, Wiley, pp. 201–228.

Wilson, D. G., 1984, *The Design of High-Efficiency Turbomachinery and Gas Turbines*, The MIT Press, Chapter 6.

Zangeneh, M., 1991, "A Compressible Three-Dimensional Design Method for Radial and Mixed Flow Turbomachinery Blades," *International Journal of Numerical Methods in Fluids*, Vol. 13, pp. 599–624.

APPENDIX

In a steadily rotating frame of reference (Ω), Bernoulli's equation is replaced by the rothalpy I. It remains constant on a relative streamline when no viscous losses occur:

$$I=\frac{W^2}{2}-\frac{\Omega^2 r^2}{2}+\frac{p}{\rho}=\frac{V^2}{2}-V_\theta \Omega r+\frac{p}{\rho}=\text{constant}$$

since from the velocity triangle

$$W^2-\Omega^2 r^2=V^2-2V_\theta \Omega r$$

Here V_θ is the tangential component of the absolute velocity and $V_\theta r$ the angular momentum.

The gradient of the rothalpy is

$$\nabla I=\nabla\left(\frac{V^2}{2}+\frac{p}{\rho}\right)-\nabla V_\theta \Omega r=Wx(\omega+2\Omega) \tag{1}$$

here ω is the relative vorticity vector.

The vector $(\omega+2\Omega)$ stands for the absolute vorticity of the flow. It is zero if the inlet flow is irrotational and if there are no losses in the impeller. Then the rothalpy is constant throughout the impeller (Batchelor, 1967, 1979, p. 162).

In the usual coordinate system (Vavra, 1960), projections in the hub-to-shroud and blade-to-blade directions are used as shown in Figs. 1, 2, and 4. The three components of the gradient of the rothalpy, Eq. (1), are then taken in the streamwise direction, in the direction of the normal to the projection of the velocity W in the meridional plane, and in direction of the normal to the velocity W on the blade-to-blade surface.

1 Assuming streamline coordinates, the right-hand side of Eq. (1) cannot have a component in the streamwise direction parallel to W and therefore the gradient of the rothalpy in the streamwise direction must be zero:

$$\frac{\partial}{\partial s}\left(\frac{V^2}{2}+\frac{p}{\rho}\right)-\frac{\partial}{\partial s}\,(V_\theta r\Omega)=0$$

The fluid energy increase in the streamwise direction is equal to the increase of the angular momentum multiplied by the constant angular velocity Ω, even if the flow is rotational and $(\omega+2\Omega)$ is not zero.

This is Euler's equation.

2 The two other components of the gradient of the rothalpy are normal to projections of the relative velocity on the hub-to-shroud plane and the blade-to-blade surface. When the absolute flow is irrotational $(\omega+2\Omega)=0$ the gradients of the rothalpy must be zero. Then the gradient of the absolute energy can only be zero if the gradient of the angular momentum normal to the relative velocity is also zero.

Turbulent Flows in a Model SDR Combustor

T.-M. Liou
Professor,
Power Mechanical Engineering Department.

Y.-Y. Wu
Graduate Student,
Power Mechanical Engineering Department.

Department of Power Mechanical Engineering,
National Tsing Hua University,
Hsinchu, Taiwan 30043

An experimental study is reported on the isothermal flow fields in a model solid-propellant ducted rocket combustor with two opposing side inlets. The measurements were made by using a four-beam two-color laser-Doppler velocimeter (LDV). Three values of momentum ratio (M_a/M_s) *of the axial- to side-inlet jet—0.025, 0.11, and 1.28—were selected to investigate their effects on the flow characteristics. The Reynolds number, based on the air density, combustor height, and bulk velocity, was* 4.56×10^4. *The flow field was characterized in terms of the mean-velocity vectors and contours, joint probability functions, mean reattachment lengths, spreading rate of the axial-jet width, and Reynolds stress and turbulence kinetic energy contours. The LDV measured mean reattachment lengths were found to well agree with the corresponding flow-visualization photograph. In addition, the three* M_a/M_s *values provided three characteristic flows which are useful in testing the computational models. Further, correlations between the present cold-flow and previous reacting-flow studies were documented in detail. It was found that from the fluid dynamic point of view* $M_a/M_s = 0.11$ *was preferable to the other two values of* M_a/M_s.

Introduction

When a solid-propellant ducted rocket (SDR) (Kinroth and Anderson, 1980; Besser, 1984) operates as a ramjet sustainer, the fuel-rich gas plume exhausted from a solid-propellant gas generator mixes and reacts with the ram air supplied from the side-inlet ducts attached to the combustor periphery (Figs. 1 and 2). The flow field resulting from such a noncoaxial mixing involves very complex phenomena, including sudden-expansion, noncoaxial jet impingement, recirculation, and redevelopment. In particular, the penetration depth of the axial jet, the recirculating-flow pattern in the dome region, and the separation bubbles immediately behind the side air streams are closely related to the fuel-air mixing, flame holding, and combustion performance. Consequently, for the development of SDR combustors it is desirable to investigate the detailed fluid dynamics process computationally or experimentally.

Experimentally, Schadow (1972, 1975, 1981a) and Mitsuno et al. (1987) studied the combustion characteristics of SDR combustors, such as combustion efficiency and ignition, by using nonmetallized and metallized propellants. Schadow and Chieze (1981b) also conducted water tunnel and windowed combustion tests, and proposed the importance of ignition location and penetration ability of fuel-rich gas plume on the efficiency of combustion in a SDR combustor. Zetterström et al. (1983, 1985) investigated the combustion performance of a SDR combustor through phases of water-tunnel flow studies, propane-fuel combustion tests and solid-propellant tests with a gas generator. Choudhury (1982) investigated the characteristics of a SDR motor by using thermocouple measurements and gas chromatography analysis, and showed that the vortices in the dome region was crucial to the stable operation of the burner, and anything tending to weaken these vortices should be avoided. Chuang et al. (1989) investigated the flow field in a two-dimensional SDR motor with two fuel-rich gas injection slits by using Schlieren, laser light-sheet, and surface flow

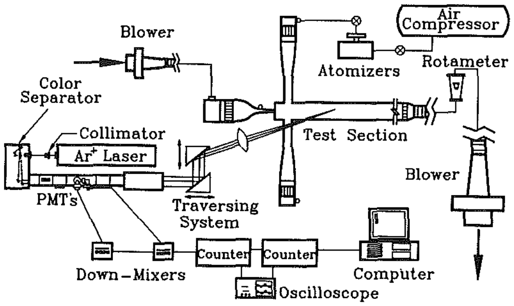

Fig. 1 Sketch of overall experimental system

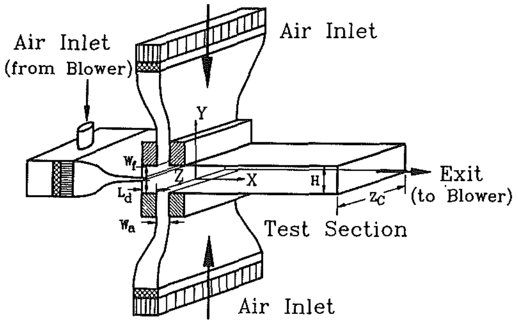

Fig. 2 Sketch of configuration and coordinate system of the test chamber

---

Contributed by the Fluids Engineering Division for publication in the JOURNAL OF FLUIDS ENGINEERING. Manuscript received by the Fluids Engineering Division June 3, 1991; revised manuscript received January 8, 1993. Associate Technical Editor: C. J. Freitas.

visualization techniques. Subsequently, Hsieh et al. (1989) conducted detailed laser doppler velocimetry (LDV) measurements of flow velocities, turbulence intensities, and Reynolds shear stresses for the same model.

Chen and Tao (1984) computationally studied the reacting flows in an axisymmetric SDR combustor with annular side inlet and concluded the importance of general geometric and aerodynamic parameters for the specific impulse of the combustor investigated. Vanka et al. (1985) performed three-dimensional calculations of the reacting flows in a typical SDR motor. The impact of the geometrical parameters on the residual fuel fraction and the combustion efficiency were investigated. Recently, Cherng et al. (1987, 1988) also conducted two- and three-dimensional calculations of the reacting flows in various SDR combustion combustors.

Although the aforementioned works have provided valuable information relevant to the SDR combustors, more quantitative measurements of various mean-flow parameters and fluctuating velocity covariances are still required for a better understanding of the relations among fluid dynamics, mixing, and combustion processes. Accordingly, the purposes of this work are (1) to characterize the flow field in a SDR combustor in terms of mean-flow parameters and fluctuating velocity covariances using LDV techniques, and (2) to find some parallel relations between this cold-flow study and previous reacting-flow investigations. In addition, the measured mean reattachment lengths will be verified with a companion flow-visualization study. It is hoped that the obtained data are also useful for evaluating computational models.

Experimental System and Conditions

Experimental System. Figure 1 shows a schematic drawing of the overall experimental system. Air was drawn into the test chamber through settling chambers, honeycombs and screens, 10:1 contractions, and side-inlets by a DC motor driven turbo blower (3500 rpm/3 phase/10 hp) at the downstream end. The axial jet was provided through a 152:1 contraction by another blower (3480 rpm/3 phase/5 hp) located upstream of the axial inlet. The air in the chamber then flowed through the rectangular duct, a flow straightener, a rotameter, and a bellows, and was exhausted by the DC motor driven turbo blower.

A two-color, four-beam, two-component LDV system was set up in a backscatter configuration. A 5-W argon-ion laser provided the coherent light source. The 514.5 nm (green) and 488 nm (blue) lines were first separated into four beams. Each of the two pairs of beams had one beam Bragg-shifted by 40 MHz to eliminate the ambiguity of flow direction and fringe bias. The two pairs of beams were finally focused into the test model to form a probe volume consisted of two nominally orthogonal sets of fringes. The approximate probe volume dimensions, based on $1/e^2$ extent of light intensity, were 0.06 mm in diameter and 0.65 mm long (480 mm focal-length lens) or 0.13 mm in diameter and 3.65 mm long (1200 mm focal-length lens). The optical system was aligned so that the two sets of fringes in the probe volume were inclined at 46.1 deg and −43.9 deg to the chamber centerline for measurements of $U + V$ and $U - V$ components of velocity. The probe volume can be positioned with 0.01-mm resolution by mounting the focusing lens on a three axis traversing table. The seeding particles were introduced into the air stream by twelve atomizers symmetrically located on the walls of the three settling chambers. The atomizers were operated by filtered compressed air and salt water, and produced particles in the size range of 0.5–5 μm. The salt solution was mixed to give a nominal 0.8-μm particle after the droplet dried. The detected signals were electrically downmixed to the appropriate frequency shift of 2 to 10 MHz in the present work. Then two counter processors with 1 ns resolution were used to process the Doppler signal. The Doppler signals were monitored on an oscilloscope, and the digital outputs of the counter processors were fed directly to a micro-computer for storage and analysis. Depending on the location of the probe volume in the flow, typical coincidence rates were between 500 to 3000 per second with a 50 μs coincidence window which is much smaller than the estimated integral time scale (order of 1 ms based on chamber height and U_{REF}) and, yet, large enough to avoid the bias resulting from a low data rate of small coincidence window (Petrie et al., 1988).

The test model consisted of two short rectangular side-inlet ducts, an axial injection slit, and a rectangular chamber, as sketched in Fig. 2. The two 20-mm long rectangular side-inlet ducts intersected the chamber walls at an angle of 90 deg, and were separated azimuthally by 180 deg, whereas the injection slit was located at the center of the head plate, and directed along the chamber axis. The internal dimensions of the side-inlet ducts and axial injection slit were 15 × 120 mm^2 and 1.58 × 120 mm^2, respectively. The chamber model was made of 5-mm thick Plexiglas, and the chamber duct had a cross sectional area of 30 × 120 mm^2, and was 2000-mm long from the axial zero-reference point to the exit.

Nomenclature

B_j = axial-jet half-width (mm)
H = combustor height (30 mm)
k = turbulence kinetic energy, $k \equiv 3/4\ (\overline{u^2} + \overline{v^2})$
L_d = dome height (15 mm)
$\dot{m}$ = mass flow rate (kg/s)
$\dot{m}_{in}$ = total inlet mass flow rate (kg/s)
M_a = momentum of axial inlet (kg.m/s^2)
M_s = momentum of side inlets (kg.m/s^2)
Re = combustor Reynolds number, $\equiv \rho U_{\mathrm{REF}} H/\mu_t$
U = axial mean velocity (m/s)
u = axial velocity fluctuation (m/s)
U_{MAX} = maximum velocity at each X^* station
U_{REF} = combustor bulk mean velocity (m/s), $U_{\mathrm{REF}} = 23.86$ (m/s)
$-\overline{uv}$ = turbulent shear stress (m^2/s^2)
V = transverse mean velocity (m/s)
v = transverse velocity fluctuation (m/s)
W_a = width of side inlet (15 mm)
W_f = width of axial inlet (1.6 mm)
X = combustor axial coordinate (mm)
X^* = normalized combustor axial coordinate, $X \geq 0$: $X^* \equiv X/H$; $X \leq 0$: $X^* \equiv X/L_d$
X' = normalized combustor axial coordinate, $X' \equiv (X + L_d)/H$
Y = combustor transverse coordinate (mm)
Y^* = normalized combustor transverse coordinate, $\equiv Y/(H/2)$
Z = combustor spanwise coordinate (mm)
Z_c = combustor spanwise width (120 mm)
Z^* = normalized combustor spanwise coordinate, $\equiv Z/(Z_c/2)$
ρ = air density (Kg/m^3)
μ_t = molecular dynamic viscosity (Kg/m-s)

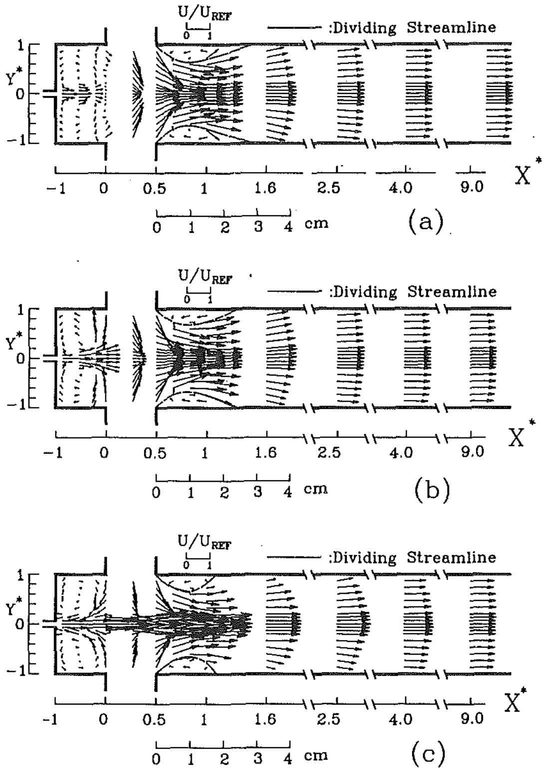

Fig. 3 Mean flow-patterns in terms of velocity vectors for (*a*) M_a/M_s = 0.025, (*b*) M_a/M_s = 0.11, and (*c*) M_a/M_s = 1.28

Experimental Conditions. The velocity measurements were made at 4 stations, i.e., $Y^* = \pm 1$ and $Y^* = \pm 2$, and 13 axial stations for the side-inlet ducts and the test chamber, respectively, and at 17 locations per station along the central plane ($Z^* = 0.0$). Three values of momentum ratio of axial- to side-inlet jet—M_a/M_s = 1.28, 0.11, and 0.025—were selected to study their effects on the characteristics of the flow field. A chamber bulk mean velocity of 23.9 m/s was maintained for all three aforementioned M_a/M_s for comparison purpose, and used as a reference to nondimensionalize the experimental results. The Reynolds number, based on the chamber height (0.03 m) and bulk mean velocity, was 4.56×10^4. A single Reynolds number was adopted in the present work since the mean flow field was approximately invariant for $2.9 \times 10^3 < \mathrm{Re} < 2.0 \times 10^5$, as found for the case without axial inlet jet (Liou et al., 1988). Moreover, the head plate was fixed at one-half chamber height upstream of $X^* = 0$ according to the fact that at this position the fraction of the inlet mass flow rate bifurcated into the region between the head plate and $X^* = 0$ is maximum for the case without axial inlet jet (Liou et al., 1988).

The mean velocity, turbulence kinetic energy (k), and Reynolds shear stress ($\overline{uv}$) profiles at the side-inlet reference planes $Y^* = \pm 2$ and coaxial-inlet reference plane $X^* = -1$ for the tested momentum ratios are rather uniform, except near the walls, due to the acceleration of the bell-mouth 10:1 and 152:1 contractions. The maximum deviations from the uniform and symmetric mean-velocity profiles at these reference planes are within 1.8 and 1.2 percent, respectively. The levels of k and $\overline{uv}$ are $2 \times 10^{-4}\ U^2_{\mathrm{REF}}$ and $3.3 \times 10^{-5}\ U^2_{\mathrm{REF}}$, respectively, at $Y^* = \pm 2$, and approximately zero at $X^* = -1$.

The present experimental investigation was undertaken in a rectangular chamber with a cross-section aspect ratio of 4:1. The two-dimensionality checks of the spanwise axial and transverse mean-velocity profiles have been conducted, and the profiles for various X^* stations are rather symmetric about $Z^* = 0$, and the two-dimensionality is within 2.7 percent of U_{REF}.

Uncertainty Estimates. The mean velocity and turbulence intensity components were calculated from the probability density function of the measurements (Liou et al., 1988). There were typically 4096 realizations at each measuring location. The corresponding statistical error was between 0.1 and 2.4 percent in the mean-velocity component and between 2.2 and 3.1 percent in the turbulence intensity component for the 95 percent confidence level. The error in U_{REF} was ± 1.4 percent.

In this study, the LDV velocity bias error was first corrected by using the well-known weighting method of McLaughlin and Tiedermen (1973) for regions where local turbulence intensity was below about 25 percent (Drain, 1980). The difference between weighted and unweighted data sets was found to be below 2 percent. For regions in the shear layers of the axial jet, in the impinging zone of side-inlet jets, and in the separation bubbles, the turbulence level was typically very high, and near-zero velocities frequently appear due to flow reversal resulting in very large weighting vectors and, in turn, in an overcorrection. For these regions, therefore, measurements were repeated using the equal time interval sampling, and the error due to velocity basis was found to be within 4.6 percent.

The check of mass continuities for the measured mean axial velocity profiles after being corrected for velocity bias error was made. The continuity error was within 3.7 percent and was larger for the stations cutting across the separation bubbles located immediately downstream of the side-inlet ports. These separation bubbles will be shown shortly. The sources of the continuity error may be partly reduced by using a rotatmeter (Fig. 1) with a finer scale to monitor the blower output more accurately.

Results and Discussion

Mean Flow Pattern. The measured mean flow patterns for M_a/M_s = 0.025, 0.11, and 1.28 are presented in terms of velocity vectors in Fig. 3, and are found to be rather symmetric with respect to the combustor axis. The plot reveals significant influence of the value of M_a/M_s on the mean flow pattern, especially the recirculating flow in the dome region ($-1 < X^* < 0$). For M_a/M_s = 0.025, Fig. 3(*a*), the axial jet is too weak to penetrate through the two side jets, and thus deflected by the side jets to form a pair of weak counterrotating vortices in the dome region. In contrast, the axial jet for the case of M_a/M_s = 1.28, Fig. 3(*c*), is so strong that it is able to penetrate directly through the impinging zone of the two side jets. The axial jet in the dome region has an almost constant width and, hence, acts as a flat plate deflecting the side jets toward the dome plate ($X^* = -1.0$) to form two counterrotating vortices whose rotational directions are opposite to those shown in Fig. 3(*a*). Two more observations can be made from the M_a/M_s = 0.025 case. First, Fig. 3(*a*) shows that near the upstream corners ($X^* = 0$, $Y^* = \pm 1$) of the side-inlet ports there is a small and narrow pair of recirculating vortices, which is absent for the case of M_a/M_s = 1.28, generated by the entrainment of the side jets. Second, the motion of the nearly stagnant fluids in the region of ($X^* = 0$, $-0.2 \le Y^* \le 0.2$) is characterized by the bimodal probability density function (PDF) as shown by Fig. 4, which is a plot of iso-contours of joint PDFs of u- and v- fluctuations. Similar bimodal PDF has also been found around the stagnation point in the side-dump combustors without the axial jet (Liou et al., 1990). These bimodal PDFs indicate large scale oscillations resulting from the out-of-phase modulation in the velocity profiles of two side-inlet jets (Nosseir and Behar, 1986). In contrast, there is no bimodal PDF in the corresponding region for the M_a/M_s = 1.28 case, as indicated by Fig. 4, due to the disappearance of the stagnant

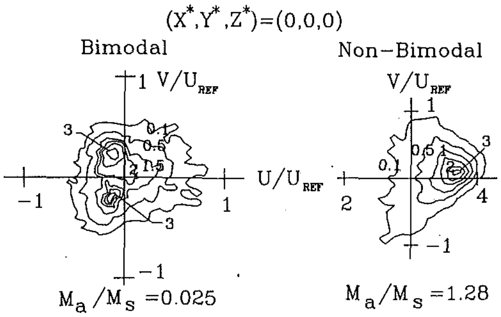

Fig. 4 Iso-contours of joint PDFs of axial and transverse mean velocities at (X^*, Y^*, Z^*) = (0, 0, 0). (Uncertainty in U/U_{REF} and V/U_{REF}: less than ±3.6 percent.)

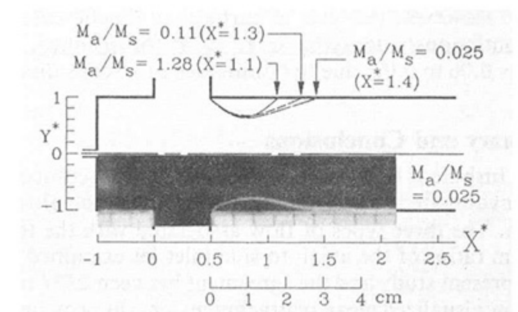

Fig. 5 Reattachment lengths for different M_a/M_s. (Uncertainty less than ±5 percent.)

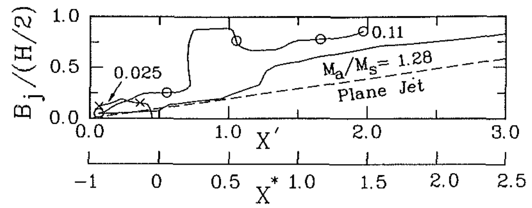

Fig. 6 Streamwise variation of the axial-jet width for M_a/M_s = 0.025, 0.11, and 1.28 (dashed line: plan jet). (Uncertainty in $2B_j/H$: ±3.8 percent.)

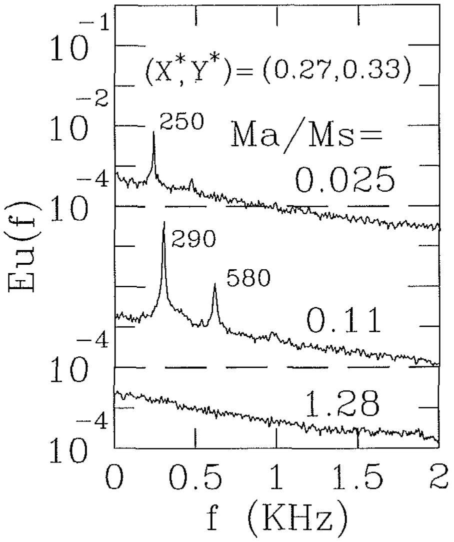

Fig. 7 Velocity power spectrum profiles at (X^* = 0.27, Y^* = 0.33) for M_a/M_s = 0.025, 0.11, and 1.28. (Uncertainty in $Eu(f)$ less than ±7.2 percent.)

fluids caused by the penetration of the strong axial jet. For the same reason, the bimodal PDF is not observed in the corresponding region of M_a/M_s = 0.11 case, either. For M_a/M_s = 0.11, a value between 0.025 and 1.28, Fig. 3(*b*) indicates that the central part of the axial jet penetrates through the side jets, and the edge part is deflected by the side jets to form a pair of counterrotating vortices, similar to those shown in Fig. 3(*a*) but stronger in strength, in the dome region.

Around the downstream corners (X^* = 0.5 and Y^* = ±1 in Fig. 3) of the side-inlet ports, the sharp turning of the side jets leads to a pair of separating bubbles immediately downstream of the side inlets. In between the two separation bubbles lies a nozzle-like flow passage where the core flow undergoes contraction and expansion. Further downstream, the mean flow redevelops and becomes unidirectional as $X^* > 4$, and approaches nearly fully developed as $X^* > 9$.

The reattachment length of the separating bubble has historically been used to assess the overall predictive capability of turbulence models. Its variation with M_a/M_s is thus shown in Fig. 5, where a typical flow-visualization result using light thread attached to the wall for M_a/M_s = 0.11 is also included for comparison. It is obvious that in Figs. 3 and 5 the reattachment length decreases with increasing M_a/M_s because the push strength produced by the axial jet and then forcing the separated stream to flow toward the side walls ($X^* > 0.8$, Y^* = ±1, Fig. 5) is proportional to the penetration depth of the axial jet and in turn to the M_a/M_s.

Noncoaxial Mixing. Information on the local strength of mixing between the axial jet and the side jets can be provided by plotting the axial-jet half-width B_j (defined as the transverse distance between Y_m where $U = U_{\max}$ and $Y_{0.5}$ where U = 1/2 $U_{\max}$) versus streamwise distance X^*, as shown in Fig. 6, which is obtained from mean-velocity ($U/U_{\max}$) contours. It can be seen that the spread of the axial jet for M_a/M_s = 1.28 first remains approximately constant and then increases up to nearly two times the width of a two-dimensional plane jet ($0.5 \le X^* \le 0.8$). As the flow proceeds further downstream, the spread rate of the axial jet parallels that of the two-dimensional plane jet. On the other hand, the spread of the axial jet for M_a/M_s = 0.025 is inhibited by the side jets near X^* = 0 and, therefore, confined in the dome region. The most interesting case is M_a/M_s = 0.11. For this case, Fig. 6 shows that the width of the axial jet in general increases at a rate faster than that of the two-dimensional plane jet and that of M_a/M_s = 1.28 case. In particular, it grows abruptly between X^* = 0 and X^* = 0.5, indicating that very strong mixing between the axial jet and the side jets occurs in this region.

The connection between the enhanced mixing of M_a/M_s = 0.11 and flow oscillation can be drawn from the velocity power spectral analysis (Liou and Wu, 1992). Typical power spectra of the axial-velocity fluctuations at (X^*, Y^*) = (0.27, 0.33) in the impingement region ($0 < X^* < 0.5$) are shown in Fig. 7 for the three investigated cases. The fundamental frequencies at f = 250 Hz and 290 Hz can be clearly identified for M_a/M_s = 0.025 and 0.11, respectively, and the harmonic frequency at f = 580 Hz is also observed for M_a/M_s = 0.11. In these two cases, the distinct peak frequencies in the velocity power spectra represent the well organized flow structures (Schadow et al., 1987). Moreover, the peak value in M_a/M_s = 0.11 case is higher than that in M_a/M_s = 0.025 case, indicating a more coherent flow structure in M_a/M_s = 0.11 case. Consequently, a stronger mixing process induced by the more organized structure is found for M_a/M_s = 0.11 in the region between X^* = 0 and 0.5. As for the M_a/M_s = 1.28 case, there is no distinct peaks and therefore lacking of coherent structures in the region between X^* = 0 and 0.5, a rationale for the low spread rate of the axial-jet half-width and thus poor noncoaxial mixing in this region.

To achieve highest combustion efficiency in the combustor investigated it was reported that two processes were critical

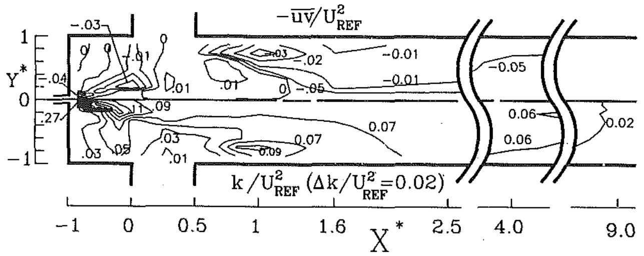

Fig. 8 Contours of Reynolds shear stresses and turbulence kinetic energy for M_a/M_s = 0.11. (Uncertainty in $\overline{uv}/U^2_{REF}$ and k/U^2_{REF}: less than ±4.2 percent.)

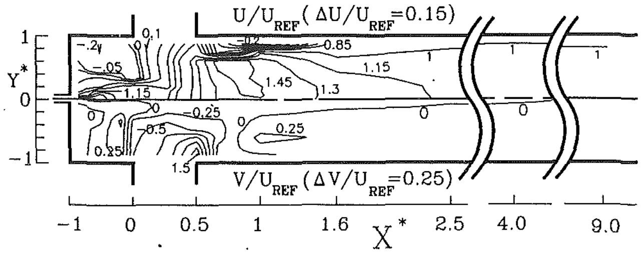

Fig. 9 Contours of U/U_{REF} and V/U_{REF} for M_a/M_s = 0.11. (Uncertainty: see Fig. 4 caption.)

(Schadow and Chieze, 1981a): (1) axial-plume ignition in the extreme fore-end of fuel (axial jet)/air (side jets) mixing region near the axial-jet port to achieve highest, near stoichiometric local combustion temperatures before excessive air mixing occurred, and (2) good penetration of the ignited, reaction plume into the air stream to achieve good mixing and combustion. Among the three cases studied, only the M_a/M_s = 0.11 case (Figs. 6 and 3(*b*)) meets the above-mentioned two critical processes. In the other two cases, M_a/M_s = 1.28 (Figs. 6 and 3(*c*)) and 0.025 (Figs. 6 and 3(*a*)), either little axial/side jet mixing has taken place in the dome region for the former or the axial jet does not penetrate into the side jets for the latter. The close correlation between this study and the work of Schadow and Chieze (1981b) can be further illustrated by the following comparison. Based on combustion efficiency measurement and flame characteristics photography, Schadow and Chieze (1981b) found that (1) axial plume ignition occurred downstream of the side inlets for M_a/M_s = 0.86 (or M_s/M_a = 1.16 in Schadow and Chieze, 1981), (2) that plume ignition near the axial-inlet port and good reacting plume penetration through the side-inlet air were obtained for M_a/M_s = 0.2 (or M_s/M_a = 5.02), resulting in highest combustion efficiency, and (3) that the flame was confined in the dome region upstream of the side inlets for M_a/M_s = 0.065 (or M_s/M_a = 15.4). These results parallel those observed in the present work for M_a/M_s = 1.28, 0.11, and 0.025, respectively.

Fluctuation Velocity Correlations Nondimensionalized Reynolds shear stresses for M_a/M_s = 0.11 are plotted as contours in Fig. 8. Large values of $-\overline{uv}$ are distributed along the shear layers where steep mean-velocity gradients prevail, as shown by the mean-velocity (U/U_{REF} and V/U_{REF}) contours in Fig. 9. Peak values of $-0.04U^2_{REF}$ and $-0.03U^2_{REF}$ (Fig. 8) are, respectively, found to occur around $X^* = -0.8$, a narrow one early in the axial-jet shear layer (Fig. 9, U/U_{REF}), and X^* = 0.0, a broader peak where the axial-jet shear layer (Fig. 9, U/U_{REF}) and the side-jet shear layer (Fig. 9, V/U_{REF} intersect. Around X^* = 1.0, a short distance upstream of reattachment (X^* = 1.3), another broader peak of $-\overline{uv} = -0.03U^2_{REF}$ (Fig. 8) appears in the separation-bubble shear layer (Fig. 9, U/U_{REF}). Figure 8 also shows that peaks of turbulence kinetic energy, k, follow those of Reynolds shear stress since turbulence extracts energy from the mean flow by working Reynolds stresses against mean-velocity gradients. The peak values of k are 0.27, 0.11, and $0.09U^2_{REF}$ at X^* = −0.8, 0.0, and 1.0, respectively. The highest peak, k = 0.27, occurring around X^* = −0.8, will enhance fuel/air mixing in this region, and as a result, tend to facilitate axial-plume ignition near the axial-plume port. In addition, the dome recirculating flows shown in Fig. 3(*b*) ensure flame anchorage. The peak values of k around X^* = 0.0 and 1.0, and the jet-width growth shown in Fig. 6 all suggest good mixing and combustion. These observations again tend to support the fulfillment of two critical processes by the M_a/M_s = 0.11 case.

As $X^* > 4$, the lack of mean-velocity gradients, as shown by Fig. 3, results in the lack of energy extraction from the mean flow. This fact illustrates the approximately invariant mean velocity profiles (Fig. 3(*b*)) in the region far downstream. However, the level of turbulence kinetic energy (Fig. 8) is continuously decaying as $X^* > 4$, for instance, from k/U^2_{REF} = 0.06 to 0.02, due to dominance of viscous dissipation.

Summary and Conclusions

The turbulent flow field in a simulated SDR combustor has been investigated experimentally using LDV and flow visualization. The three types of flow associated with the three momentum ratios of the axial- to side-inlet jet examined in detail in the present study and the agreement between LDV measured and flow visualized mean reattachment lengths provided a good test of computational models. As M_a/M_s increased from 0.025 to 1.28, the rotational direction of vortices in the dome region reversed, the penetration depth of the axial-jet increased, and the size of separation bubbles decreased. It was found that M_a/M_s = 0.11 was preferable to M_a/M_s = 0.25 and 1.28 for the reason of more appropriate axial-jet penetration, axial/side jet mixing, dome recirculating flow pattern, and turbulent kinetic energy distribution. Furthermore, the results and discussion presented in this cold-flow study were found to provide physical illustrations, from the fluid dynamical point of view, for the ignition, flame characteristics, and combustion efficiency occurring in the corresponding reacting flows investigated by previous researchers.

Acknowledgment

Support for this work was partially provided by the National Science Council of the Republic of China under contract NSC-80-0401-E007-02.

References

Besser, H. L., 1984, "Solid Propellant Ramrockets," *Ramjet and Ramrocket Propulsion Systems for Missiles*, Chapter 7, AGARD Lecture Series No. 136, Monterey, CA, Sept. 5-6.

Chen, L., and Tao, C. C., 1984, "Study of the Side-Inlet Dump Combustor of Solid-Ducted Rocket with Reacting Flow," AIAA-84-1378, AIAA/SAE/ASME 20th Joint Propulsion Conference.

Cherng, D. L., Yang, V., and Kuo, K. K., 1987, "Theoretical Study of Turbulent Reacting Flows in a Solid-Propellant Ducted Rocket Combustor," AIAA-87-1723, AIAA/SAE/ASME/ASEE 23rd Joint Propulsion Conference.

Cherng, D. L., Yang, V., and Kuo, K. K., 1988, "Simulations of Three-dimensional Turbulent Reacting Flows in Solid-Propellant Ducted Rocket Combustors," AIAA-88-3042, AIAA/SAE/ASME/ASEE 24th Joint Propulsion Conference.

Choudhury, P.R., 1982, "Characteristics of a Side Dump Gas Generator Ramjet," AIAA-82-1258, AIAA/SAE/ASME 18th Joint Propulsion Conference.

Chuang, C. L., Cherng, D. L., Hsieh, W. H., Settles, G. S., and Kuo, K. K., 1989, "Study of Flowfield Structure in a Simulated Solid-Propellant Ducted Rocket Motor," AIAA-89-0011, AIAA 27th Aerospace Sciences Meeting.

Drain, L. E., 1980, *The Laser Doppler Technique*, Wiley, New York, NY, pp. 136-145.

Hseih, W. H., Chuang, C. L., Yang, A. S., Cherng, D. L., Yang, V., and Kuo, K. K., 1989, "Measurement of Flowfield in a Simulated Solid-Propellant Ducted Rocket Combustor Using Laser Doppler Velocimetry," AIAA-89-2789, AIAA/ASME/SAE/ASEE 25th Joint Propulsion Conference.

Kinroth, G. D., and Anderson, W. R., 1980, *Ramjet Design Handbook*, McDonnel Douglas Co.

Liou, T. M., and Wu, S. M., 1988, "Flowfield in a Dual-Inlet Side-Dump Combustor," *Journal of Propulsion and Power*, Vol. 4, No. 1, pp. 53–60.

Liou, T. M., Wu, S. M., and Hwang, Y. H., 1990, "Experimental and Theoretical Investigations of Turbulent Flow in a Side-Inlet Rectangular Combustor," *Journal of Propulsion and Power*, Vol. 6, No. 2, pp. 131–138.

Liou, T. M., and Wu, Y. Y., 1992, "Spectral Characteristics of Velocity and Wall Pressure in a Ducted Flow with Dual Side and One Axial Inlets," *Sixth International Symposium on Application of Laser Technology to Fluid Mechanics*, 20–23, July, Lisbon, Portugal.

Mitsuno, M., Kuwahara, T., and Kosaka, K., 1987, "Combustion of Metallized Propellants for Ducted Rockets," AIAA/SAE/ASME/ASEE 23rd Joint Propulsion Conference.

McLaughlin, D. K., and Tiederman, W. G., 1973, "Biasing Correlation for Individual Realization of Laser Anemometer Measurement in Turbulent Flows," *The Physics of Fluids*, Vol. 16, No. 12, pp. 2082–2088.

Nossier, N. S., and Behar, S., 1986, "Characteristics of Jet Impingement in a Side-Dump Combustor," *AIAA Journal*, Vol. 24, No. 11, pp. 1752–1757.

Petrie, H. L., Samimy, M., and Addy, A. L., 1988, "Laser Doppler Velocity Bias in Separated Turbulent Flow," *Experiments in Fluids*, Vol. 6, pp. 80–88.

Schadow, K. C., 1972, "Boron Combustion Characteristics in Ducted Rockets," *Combustion Science and Technology*, Vol. 5, pp. 107–117.

Schadow, K. C., 1975, "Fuel-Rich, Particle-Laden Plume Combustion," *AIAA Journal*, Vol. 13, No. 12, pp. 1553–1554.

Schadow, K. C., 1981a, "Boron Combustion in Ducted Rockets," *Ramjets and Ramrockets for Military Applications*, Chapter 22, AGARD-CP-307.

Schadow, K. C., and Chieze, D. J., 1981b, "Water Tunnel and Windowed Combustion as Tools for Ducted Rocket Development," 1981 JANNAF Propulsion Meeting, *CPIA-PUB-340*, Vol. 2, pp. 101–115.

Schadow, K. C., Wilson, K. J., and Gutmark, E., 1987, "Characterization of Large-Scale Structures in a Forced Ducted Flow with Dump," *AIAA Journal*, Vol. 25, No. 9, pp. 1164–1170.

Vanka, S. P., Craig, R. R., and Stull, F. D., 1985, "Mixing, Chemical Reaction and Flow Field Development in Ducted Rockets," AIAA-85-1271, AIAA/SAE/ASME/ASEE 21st Joint Propulsion Conference.

Zetterström, K. A., Sjöblom, B., and Jammo, A., 1983, "Solid Ducted Rocket Engine Combustors," *Proceedings of Sixth International Symposium of Air Breathing Engines*, ISABE paper No. 83-7001.

Zetterström, K. A., and Sjöblom, B., 1985, "An Experimental Study of Side Dump Ramjet Combustors," *Proceedings of Seventh International Symposium of Air Breathing Engines*, ISABE paper No. 85-7024.

Simulation of the Nonreacting Flow in a Bluff-Body Burner; Effect of the Diameter Ratio

Luis-Filipe Martins

Ahmed F. Ghoniem

Massachusetts Institute of Technology,
Cambridge, MA 02139

Axisymmetric vortex simulation is used to study the unsteady dynamics of the flowfield generated by the interaction between two concentric jets initially separated by a thick bluff-body. The computational scheme treats convective transport in a Lagrangian sense by discretizing the vorticity into a number of finite-area vortex ring elements which move along particle trajectories during each convective substep, thus reducing the numerical diffusion and allowing simulations at high Reynolds number. In this paper, investigation is focused on the time-dependent dynamics and the effect of the diameter ratio across the bluff-body on the wake flow. In both cases simulated, the dynamics is governed by the shedding of large vortex eddies from the inner and outer sides of the bluff-body. Mixing between the two streams is enhanced by the merging of these eddies downstream the bluff-body and the formation of composite structures. We find that the frequency of shedding, the level of fluctuations and the degree of organization are strongly dependent on the diameter ratio. The fluctuation associated with this shedding increases as the diameter ratio becomes larger. The origin and mechanism of shedding in each case are determined from the results.

I Introduction

A large class of turbulent diffusion flames utilized in industrial and propulsion applications can be modeled by two concentric jets of fuel and oxidizer separated by a thick annular interface known as a bluff-body. The latter is used to create a recirculation zone in which the two streams thoroughly mix and react. Experimental studies of the nonreacting and reacting flows in this geometry have been conducted to investigate the stability of the combustion process (Roquemore et al., 1982, and 1984) and to determine the turbulent flame structure under these circumstances (Namazian et al., 1988 and 1989). In most cases, and for a range of inner jet/annular flow velocity ratio, which depends on the diameter ratio across the interface, large-scale oscillations and vortex shedding downstream the bluff-body were observed in both the nonreacting and reacting flows. In this work, we apply an axisymmetric vortex method to simulate the unsteady flow in this configuration. Numerical results are used to investigate the dynamic processes leading to vortex shedding, mixing and strong oscillations in this system.

Strong oscillations were observed in the nonreacting flow experiment of Kenworthy (1971) who found that as the velocity ratio approached unity, the fluctuation level increased substantially. The possible role of acoustics in these oscillations was ruled out by varying the velocity of the streams and the interface diameter, and by widely differentiating between the acoustic frequencies of the system and those associated with convective time scales. It was concluded that the oscillations were primarily axisymmetric and were generated in the wake of the bluff-body. The presence of strong fluctuations, associated with the downstream motion of large eddies, was supported by the flow visualization studies of Li and Tankin (1986) under nonreacting and reacting flow conditions in a well controlled experiment. Similar observations were made by Kelly et al. (1989 and 1990). The origin and mechanism leading to flow fluctuation in the bluff-body wake are the subject of this paper.

In most experimental studies, the time-dependent dynamic behavior of the recirculation zone is photographically documented. Point measurements are used to describe the mean flow in terms of streamline plots. These plots show that the flow pattern is substantially altered as the velocity ratio across the bluff-body changes. Figure 1 depicts three different average streamline patterns for bluff-body flows. Figure 1(*a*), reproduced from Kenworthy (1971), exhibits experimental results for the effect of the velocity ratio on the structure of the wake behind a bluff-body with a diameter ratio $D_a/D_j = 4$. The velocity was measured on a uniform grid using a hotwire in nonreacting air streams, and the streamlines were obtained by integrating the values of the velocity. Figure 1(*b*), taken from Roquemore et al. (1983), depicts a schematic representation of the streamlines in a reacting flow downstream a bluff-body with $D_a/D_j = 29$. The instantaneous streamline pattern was inferred from flow visualization studies of the reaction zone. Figure 1(*c*), obtained from the computations of Martins (1990), shows the average streamline pattern for a configuration with

---

Contributed by the Fluids Engineering Division for publication in the JOURNAL OF FLUIDS ENGINEERING. Manuscript received by the Fluids Engineering Division February 26, 1991; revised manuscript received July 10, 1992. Associate Technical Editor: S. A. Ragab.

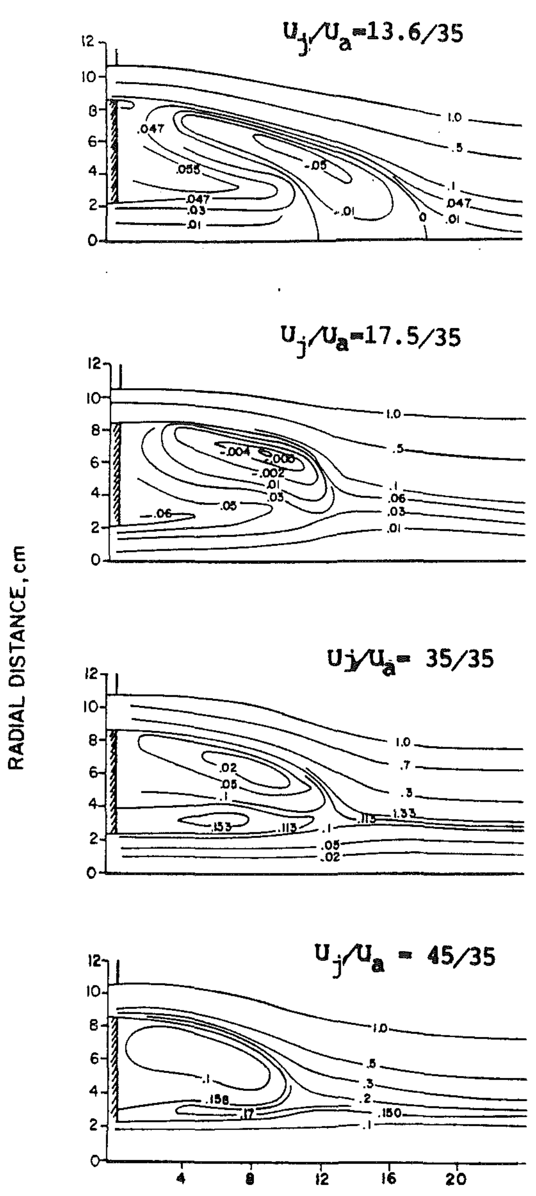

Fig. 1(*a*)

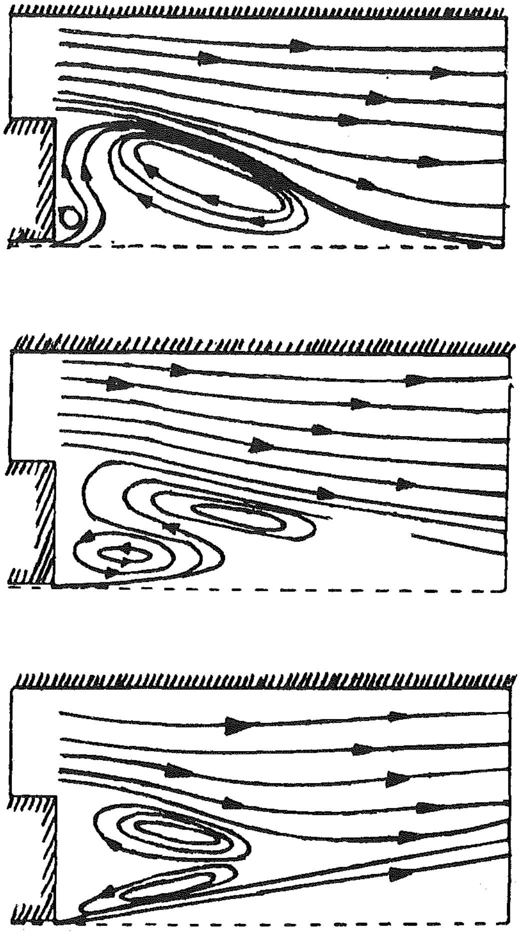

Fig. 1(*b*)

D_a/D_j = 10, at four different velocity ratios. The streamlines were obtained from instantaneous velocity values averaged over a sample of more than a 1000 time steps. The detail of the numerical simulation, the averaging procedure, and the reason for choosing the sample size will be discussed in the Results section of this paper.

These results indicate that the flow in the wake of the bluff-body gradually changes from a recirculating flow downstream a sudden expansion at low jet velocity to a jet flow with weak outside recirculation at high jet velocities. This transition from annular flow dominated wake to a jet dominated wake is accompanied with the shortening of the overall recirculation zone length, the displacement of the stagnation point(s) off the axis of symmetry and the reversal of the entrainment pattern from that of jet fluid into the annular flow, into annular fluid into the jet flow. As we will show in this paper, the strong dependence of the average streamline pattern on the velocity ratio starts at the time-dependent level, i.e., the instantaneous flow exhibits substantial changes as the velocity ratio is varied. Another parameter, which affects the flow dynamics, is the diameter ratio of the inner jet to the annular flow.

In this paper, we use vortex simulation to study the origin of the oscillation in a nonreacting bluff-body flow with equal velocities for the jet and annular flows. The formulation of the scheme is described in some detail in Section II. One novel feature of the implementation of the vortex method is the utilization of the finite-element method to obtain solutions for the Laplace equation which is used to model the velocity component necessary to satisfy the potential boundary condition. This implementation endows the computer code with a degree of flexibility not available before. In Section III, the effect of the diameter ratio on the dynamics is investigated by comparing results for two different configurations. In both cases, the computed mean velocity profiles and peak frequencies are compared with experimental results. In Section IV, we summarize and review some preliminary conclusions.

II Formulation and Numerical Scheme

The two-dimensional continuity and momentum equations for an incompressible, axisymmetric, nonswirling flow are:

$$\nabla \cdot \mathbf{u} = 0, \text{ or } \frac{\partial}{\partial r}(ru) + \frac{\partial}{\partial z}(rv) = 0, \tag{1}$$

$$\frac{\partial u}{\partial t} + \mathbf{u} \cdot \nabla u = -\frac{1}{\rho_f}\frac{\partial \mathrm{p}}{\partial \mathrm{r}} + \nu\left(\frac{\partial^2 u}{\partial r^2} + \frac{1}{r}\frac{\partial u}{\partial r} - \frac{u}{r^2} + \frac{\partial^2 u}{\partial z^2}\right),$$

$$\frac{\partial v}{\partial r} + \mathbf{u} \cdot \nabla v = -\frac{1}{\rho_f}\frac{\partial p}{\partial z} + \nu\left(\frac{\partial v}{\partial r^2} + \frac{1}{r}\frac{\partial v}{\partial r} + \frac{\partial^2 v}{\partial z^2}\right) \tag{2}$$

where ρ_f is the fluid density, $\nabla = \partial/\partial r\, \mathbf{e}_r + \partial/\partial z\, \mathbf{e}_z$, $\mathbf{u}$ is the velocity vector, u and v are the velocity components in the

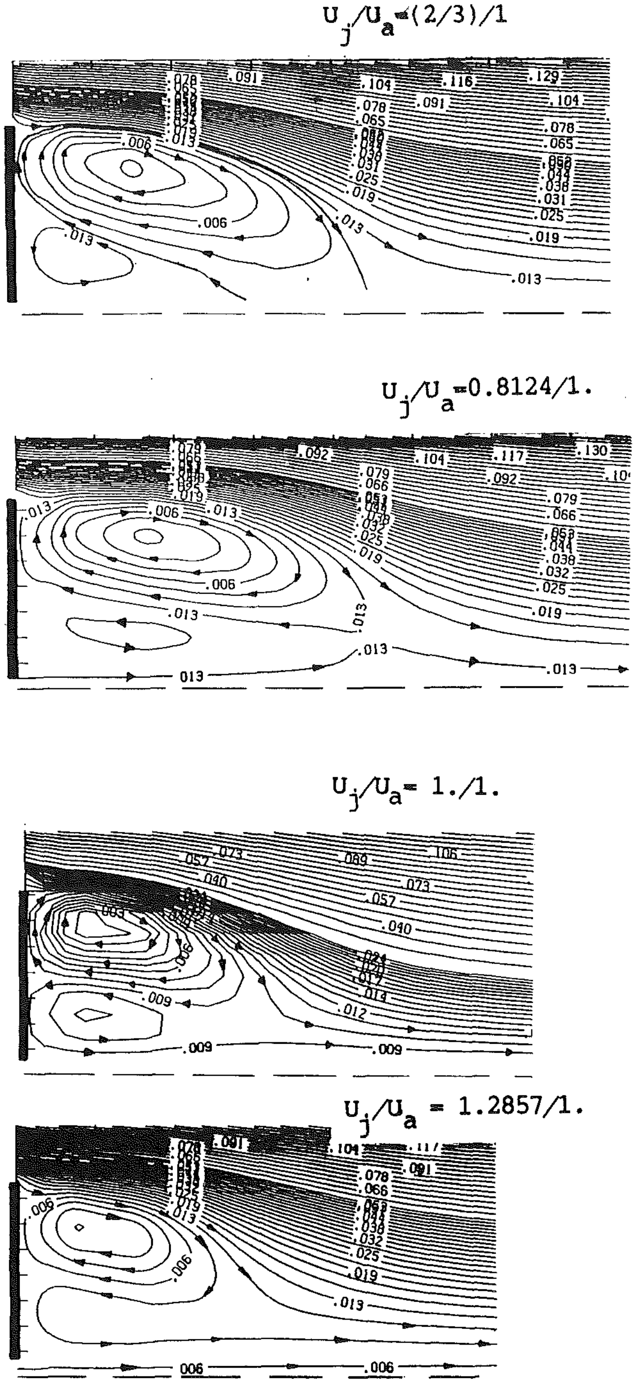

Fig. 1(*c*)

Fig. 1 The average streamline pattern for bluff-body flows at different jet/annular flow velocity ratios: (*a*) experimental results of Kenworthy obtained for D_a/D_j = 4; (*b*) a schematic representation based on the reacting flow experiment of Roquemore et al. showing an annular flow dominated regime (top), a transitional regime (middle) and a jet flow dominated regime (bottom); (*c*) numerical results obtained for D_a/D_j = 10

radial, r-direction and axial, z-direction, respectively, t is time, p is pressure, and ν is the kinematic viscosity. The flow is restricted to the meridian plane and the origin of the coordinate system is set at the beginning of the computational domain, see Fig. 2. The solution of Eqs. (1) and (2) is subject to:

(*a*) the no-slip condition, $\mathbf{u}_t(\mathbf{x}_s, t) = 0$, where $\mathbf{u}_t$ is the velocity component tangential to the solid surfaces and $\mathbf{x}_s$ is the boundary coordinate, and,

(*b*) the no-flow (potential) condition, $\mathbf{u}_n(\mathbf{x}_s, t) = 0$, where $\mathbf{u}_n$ is the velocity component normal to the boundary along the solid walls of the domain. At the inlet and exit sections, the normal velocity must also be specified.

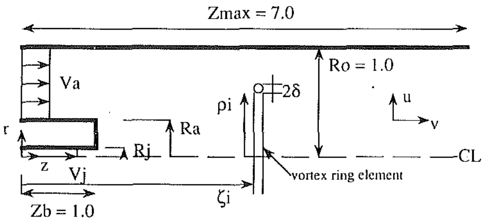

Fig. 2 The geometry of the computational domain and the definition of variables

In vortex methods, the momentum equation is replaced by the vorticity transport equation which is obtained by taking the curl of Eq. (2),

$$\frac{\partial\omega}{\partial t}+\mathbf{u}\cdot\nabla\omega-u\frac{\omega}{r}=\frac{1}{R}\left(\frac{\partial^2\omega}{\partial r^2}+\frac{1}{r}\frac{\partial\omega}{\partial r}-\frac{\omega}{r^2}+\frac{\partial^2\omega}{\partial z^2}\right) \qquad (3)$$

where $\omega = \partial u/\partial z - \partial v/\partial r$ is the vorticity in the aximuthal direction. Note that the pressure term disappears since $\nabla \times \nabla p = 0$, and that $u\omega/r$ is the vorticity stretch term associated with the radial expansion or contraction of vortex lines. In Eq. (3), variables are normalized with respect to the appropriate combination of the channel radius, R_0, and the annular flow velocity, U_a. The Reynolds number is defined as $R = U_aR_0/\nu$.

The continuity equation is satisfied using Stokes' stream function, ψ, defined such that:

$$u=-\frac{1}{r}\frac{\partial\psi}{\partial z} \text{ and } v=\frac{1}{r}\frac{\partial\psi}{\partial r}. \qquad (4)$$

Substituting in the definition of vorticity, we get the following relationship between vorticity and the stream function,

$$\nabla_r^2\psi=\frac{\partial}{\partial r}\left(\frac{1}{r}\frac{\partial\psi}{\partial r}\right)+\frac{\partial^2}{\partial z^2}\left(\frac{\psi}{r}\right)=-\psi(\mathbf{x}, t). \qquad (5)$$

The axisymmetric vortex method is based on the discretization of the vorticity field into a number of finite-area, vortex-ring elements, and the transport of these elements along particle trajectories during the convective substeps. Vorticity diffusion is simulated using a combination of random walk and a deterministic component. In the following, the derivation of the scheme is summarized.

First, the vorticity field is discretized into a number, N, of infinitely thin vortex rings;

$$\omega(\mathbf{x}, t)=\sum_{i=1}^{N}\Gamma_i\delta(\mathbf{x}-\mathbf{X}_i). \qquad (6)$$

where Γ_i is the circulation of the vortex element initially located at $\mathbf{X}_i$. The velocity induced by a collection of thin vortex rings is obtained by substituting Eq. (6) into Eq. (5). The resulting expression for the stream function is:

$$\psi(\mathbf{x}, t)=\sum_{i=1}^{N}\frac{\Gamma_i}{2\pi}(s_{1i}+s_{2i})[K(\lambda_i)+E(\lambda_i)]; \qquad (7)$$

where

$$s_{2i/1i}=\sqrt{(z-\zeta_i)^2+(r+/-\rho_i)^2},$$

and,

$$\lambda_i=(s_{2i}-s_{1i})/(s_{2i}+s_{1i}), \qquad (8)$$

while,

$$K(\lambda)=\int_0^1 1/\sqrt{((1-\lambda^2t^2)(1-t^2))}\,dt,$$

and

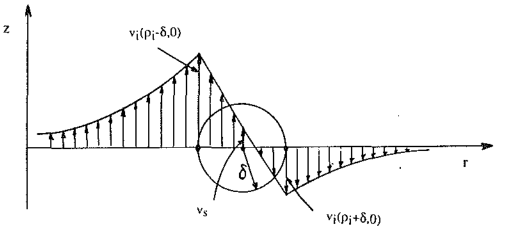

Fig. 3 The velocity distribution induced by a finite-area vortex ring element

$$E(\lambda)=\int_0^1 1/\sqrt{((1-\lambda^2t^2)/(1-t^2)}dt, \tag{9}$$

In the above, the coordinates of the center of the vortex-ring element, whose circulation Γ_i, is $\chi_i(\mathbf{X}_i, t) = (\rho_i, \zeta_i)$ where $\chi_i(\mathbf{X}_i, 0) = \mathbf{X}_i$; $K(\lambda)$ and $E(\lambda)$ are the complete elliptic integrals of the first and second kind, respectively, and $0 < \lambda < 1$.

The trajectories of a collection of vortex rings, due to the combined action of convection and diffusion, are obtained using an algorithm that satisfies Eq. (3). The velocity components are obtained from Eq. (4);

$$u_\omega(\mathbf{x}, t)=\sum_{i=1}^{N} u_i(\mathbf{x}, t), \text{ and } v_\omega(\mathbf{x}, t)=\sum_{i=1}^{N} v_i(\mathbf{x}, t); \tag{10}$$

where

$$u_i(\mathbf{x}, t)=-\frac{\Gamma_i}{2\pi r_i}\frac{(z-\zeta_i)(s_{1i}+s_{2i})}{s_{1i}s_{2i}} \times\left[K(\lambda_i)-\left(\frac{s_{2i}}{s_{1i}}+\frac{s_{1i}}{s_{2i}}\right)\frac{E(\lambda_i)}{2}\right]; \tag{11}$$

and

$$v_i(\mathbf{x}, t)=\frac{\Gamma_i}{2\pi r_i}\left[\left(\frac{r-\rho_i}{s_{1i}}+\frac{r+\rho_i}{s_{2i}}\right)\{K(\lambda_i)-E(\lambda_i)\} +\frac{s_{2i}-s_{1i}}{2}\left\{\frac{r+\rho_i}{s_{2i}^2}-\frac{r+\rho_i}{s_{1i}^2}\right\}E(\lambda_1)\right]. \tag{12}$$

where $r_i = |\mathbf{x} - \chi_i|$ and $\mathbf{u}_\omega$ is the vorticity induced velocity. The velocity induced by an infinitely thin vortex ring approaches infinity as $|\mathbf{x} - \chi_i| \rightarrow 0$. To avoid this nonphysical behavior, elementary vortex rings with finite cores are used to discretize the vorticity field in Eq. (6). We assume that each vortex-ring element has a finite, circular core, with radius δ within which the vorticity is finite, $\omega_0 = \Gamma_i/\delta^2$ (the equivalent of a Rankine vortex element in the two-dimensional method). Instead of evaluating the field produced by such element, it is assumed that the induced velocity field within the core varies linearly between a finite value, to be determined next, at the center of the ring core and a value calculated using Eqs. (11), (12) at the outer edge. This approximation is similar to the one used by Chorin (1973) in the two-dimensional method. This choice of the core function has been shown to work well in two-dimensional simulations, see Chorin (1973), Sod (1979), Choniem and Sherman (1985), Chorin (1978), and Ghoniem and Martins (1991). The velocity at the center of the ring, $r = \delta$, is the self-induced velocity, v_s, given approximately by the classical expression:

$$u_s=0, \text{ and } v_s=\frac{\Gamma}{2\pi\rho}\left(\ln\frac{8\rho}{\delta}-0.25\right) \tag{13}$$

which holds for $\delta/\rho < 1$. Nonetheless, this expression will be used for all values of δ/ρ. The velocity at the outer edge of the core is computed from Eqs. (11, 12), at point $\mathbf{x} = \chi + (\delta, 0)$ where $\chi = (\rho, \zeta)$ is the coordinate of the vortex-ring center. A schematic diagram showing the velocity distribution induced by a finite-area vortex ring element is shown in Fig. 3. For a point $\mathbf{x}$, the rotational velocity induced by a ring element at $\chi = (\rho, \zeta)$ is as follows:

If $|\mathbf{x} - \chi| > \delta$, u_ω and v_ω are given by Eqs. (11) and (12). If $|\mathbf{x} - \chi| < \delta$, u_ω is obtained by interpolation between 0 at χ and $u(\chi + \delta\mathbf{e})$, where $\mathbf{e}$ is the unit vector in the direction of $(\mathbf{x} - \chi)$. v_ω is obtained at $\mathbf{x}$ by interpolation between v_s at χ and $v(\chi + \delta\mathbf{e})$.) (14)

Another velocity component must be added to $\mathbf{u}_\omega$ to satisfy the potential boundary condition. This component is $\mathbf{u}_p = \nabla\phi$ and ϕ satisfies the following conditions:

$$\nabla^2\phi=0; \text{ with } \frac{\partial\phi}{\partial n}(s)=(\mathbf{V}_p-\mathbf{u}_\omega(s))\cdot\mathbf{n} \tag{15}$$

In the above, s is an arc length defined on the boundary of the domain, ∂D, and measured from an arbitrary point, i.e., on ∂D: $\mathbf{x} = \mathbf{x}(s)$, and all variables are expressed as functions of s. $\mathbf{V}_p$ is the velocity of the boundary (zero on stationary boundaries), or is the fluid velocity as it crosses the domain. The solution of Eq. (15) is obtained using a finite-element discretization of the domain, assuming linear basis functions for ϕ, and a Galerkin weighted residual minimization to approximate the differential equation by a set of linear algebraic equations. The total velocity is $\mathbf{u} = \mathbf{u}_\omega + \mathbf{u}_p$.

The motion of the vortex-ring elements is determined so that the vorticity field they are used to approximate satisfies Eq. (3), up to a numerical approximation error. This motion is split into two components: convection and diffusion. In the first component, the vorticity field satisfies $d\omega/dt - u(\omega)/r = 0$ (Helmholtz theorem). This is equivalent to $d(\omega/r)/dt = d\Gamma/dt = 0$ (Kelvin theorem), i.e., vortex-ring elements move along particle trajectories with fixed circulation, although the vorticity changes due to stretch. Note that the vorticity stretch term is implicity included in our analysis since the velocity field induced by a vortex ring depends on its radius. This should be expected since for a ring with radius ρ and core radius δ, $\pi\rho^2\delta$ = constant (continuity) and $\Gamma = 2\pi\rho\delta\omega = 2\omega/r$ constant. This convective substep is implemented by integrating the equivalent system of differential equations:

$$\frac{d\chi_i}{dt}=\mathbf{u}(\chi_i, t) \tag{16}$$

In the computations, a second-order time integration scheme was used to update the location of the vortex elements, requiring two evaluations of the velocity of the vortex-ring elements in each computational time step. The evaluation of the elliptic integrals was performed using an efficient method described in Hofsommer et al. (1963) and Byrd et al. (1954). Moreover, dense tables of these integrals were constructed at the beginning of the run, and second-order interpolation polynomials were used to find their values at the desired points. The second component of motion, diffusion, is implemented by moving the elements each time step according to the following algorithm proposed by Sod (1979). The diffusion operator in Eq. (3) is incorporated in two fraction steps. In the first step, random walk is used to obtain a stochastic solution of the first part of the diffusion operator:

$$\frac{\partial\omega}{\partial t}=-\frac{1}{R}\left(\frac{\partial^2\omega}{\partial r^2}+\frac{\partial^2\omega}{\partial z^2}\right) \tag{17}$$

by adding two independent, zero-mean Gaussian random numbers (η_1, η_2) to the trajectory of each vortex element (Ghoniem and Sherman, 1985). The standard deviation of the random numbers is $\sqrt{2\Delta t/R}$ where Δt is the time step. In the second part of the diffusion substep, the solution of the second part of the diffusion operator,

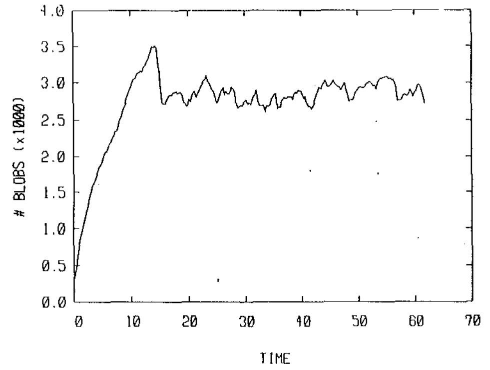

Fig. 4 The number of the vortex-ring elements (blobs) in the domain for D_a/D_j = 4 and same velocity for the jet and annular flow

$$\frac{\partial\left(\frac{\omega}{r}\right)}{\partial t} = -\frac{1}{R}\frac{1}{r}\frac{\partial\left(\frac{\omega}{r}\right)}{\partial r} \tag{18}$$

is obtained using the method of characteristics. By simple transformation of variables in Eq. (18), it can be shown that (ω/r) is constant along the characteristic line defined by $t + Rr^2/2$ = constant. Thus, the elements are displaced in the radial direction to satisfy

$$\rho_i^2(t+\Delta t) = \rho_i^2(t) - \frac{2\Delta t}{R} \tag{19}$$

Note that as before ω/r = constant is equivalent to Γ = constant. The last term, which represents the adjustment of the element vorticity as its radius changes to maintain the constancy of the total circulation is identically zero in the two-dimensional planar case.

The no-slip condition is implemented by computing the slip velocity, u_s, at a number of selected points, separated by a distance h, along the solid boundary of the bluff-body, and generating vortex elements with strength $\Gamma = -u_s h$ at these points (Chorin, 1978). These elements are treated as vortex sheets that diffuse into the interior of the flow and are then transformed into vortex-ring elements when they move outside a small distance normal to the wall. The thickness of this diffusion sublayer, which resembles a numerical laminar sublayer, is of the order of magnitude of the standard derivation of the random walk.

The numerical parameters used to obtain the results presented below were as follows: the time step, Δt = 0.05, the length of the vortex sheets used to satisfy the no-slip boundary condition along the bluff-body walls, h = 0.05 (the walls of the channel were treated as potential walls, i.e., no vorticity was created along the channel walls), the absolute value of the circulation assigned to each wall, Γ_i = .05/12 (i.e., when the slip velocity is equal to the annular flow velocity, 12 vortex sheets are generated to satisfy the no-slip boundary condition at this point), the vortex sheet sublayer thickness normal to each solid wall is 1.5 times the standard deviation of the random walk. All results were obtained at R = 7000, which is expected to be within the transition-to-turbulence regime. The geometry of the computational domain is shown in Fig. 2. The origin of the coordinate system coincides with the left-hand side of the domain. The incoming flow velocities at the inlet section in the jet and the annular flow sides have top-hat profiles and are imposed at a distance equal to one channel radius upstream of the bluff-body face. At the exit plane, imposed a distance equal to six channel radii downstream the bluff-body face, vortex elements are deleted and potential flow component of the velocity is assumed constant across the channel.

III Results

Computations were performed for two cases: D_a/D_j = 4 (0.4 R_0/0.1 R_0) and 10 (0.5 R_0/0.05 R_0). For each configuration, simulations were obtained at several velocity ratios. In this paper, we will discuss the results for a single velocity ratio, U_a/U_j = 1, for the two configurations described above. Results of different velocity ratios for the second configuration are presented and analyzed by Ghoniem and Martins (1991) in other articles. We focus on the unsteady flow dynamics and the processes leading to the mixing between the two streams when their velocities are equal. The Reynolds number of all the simulations is kept at 7000. Although this is lower than the value used in most experimental studies, previous work has shown that the large-scale structures of shear flows are weakly affected by the value of the Reynolds number, as long as the later is beyond its critical value for transition. Moreover, increasing the Reynolds number leads to the creation of more vortex elements, generated to capture the small scales of the flow, and this increases the cost of the computations. Thus, for the purpose of understanding the physics of the large-scale structure of bluff-body flow, we confine our simulations to R = 7000.

III.1 Thin Bluff Body. We start by analyzing the results of the thin bluff-body, D_a/D_j = 4. To obtain these results, the computation started with a potential flow throughout the domain and vortex elements were introduced on the walls of the bluff-body to satisfy the no-slip boundary condition. As the flow reached a stationary state, in which a fixed pattern repeated itself periodically, or almost periodically, the number of vortex elements in the domain fluctuated between two limits, as seen in Fig. 4. The sharp drop in the number of vortex elements after the initial rise is due to the passage of a strong eddy that forms during the initial transient from a potential flow to a stationary shear flow. This drop occurs only in the cases of thin bluff-bodies. The weak fluctuations in the number of vortex elements following this transient is associated with the formation and shedding of large vortical structures near the bluff-body, and their departure from the computational domain. The fact that the flow has reached stationary state is evident from Fig. 4. Note that perfect periodicity is not expected since the flow is not forced at any particular frequency. Moreover, the random walk algorithm used to simulate diffusion introduces random perturbations which manifest themselves as nonperiodic fluctuations throughout the flow.

Figure 5 shows the vortex-ring elements and their instantaneous velocities at different time steps during a typical cycle. Each frame in Fig. 5 shows the computational results in a single time step inside the area between the outer wall of the channel and the centerline of the bluff-body. Only a part of the computational domain is shown in the streamwise direction. The cyclic events that take place in this flow consist of the following five events which are shown in the five frames in Fig. 5:

1 The formation of a large toroidal eddy, which rotates in the clockwise direction, on the outer edge of the bluff-body due to the roll-up of the annular flow boundary layer. During this part of the cycle, some of the inner-jet fluid escapes along the centerline.

2 The formation of a smaller toroidal eddy, which rotates in the counter-clockwise direction, on the inner edge of the bluff-body due to the roll-up of the inner jet boundary layer. This eddy remains confined by the annular-flow eddy.

3 The separation of the annular-flow eddy from the bluff-body as the jet-eddy fills the gap between it and the bluff-body face.

4 The separation of the jet eddy from the bluff-body face

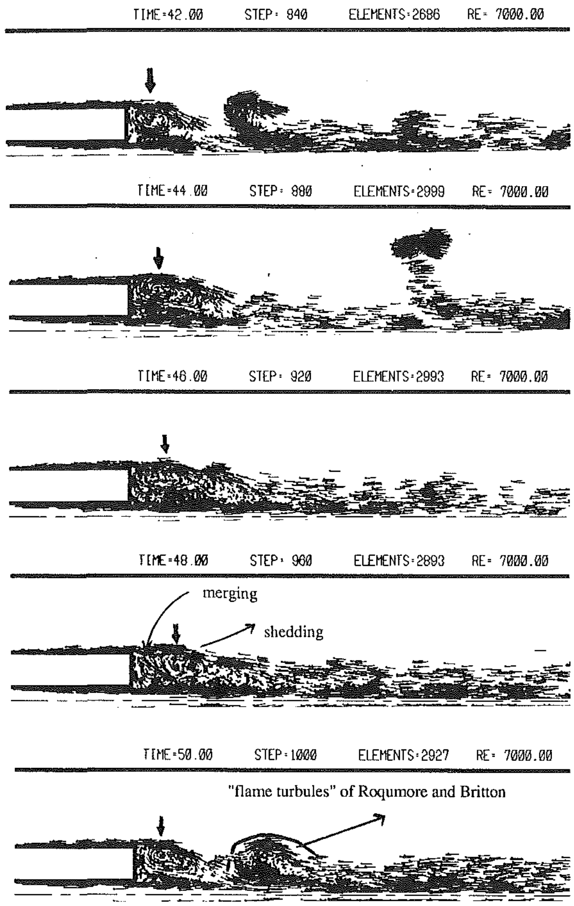

Fig. 5 The vortex ring elements and their velocity vectors at different time steps during a typical cycle for $D_a/D_j = 4$. Arrows identify the large eddies.

as it is entrained by the annular-flow eddy while the latter is flowing downstream.

5 The pairing of these two eddies as they flow downstream and the formation of a single composite structure within which the two fluids mix.

The entire series of events, (1) to (5), repeats themselves again during each cycle. The same events can be inferred from the streamline plots of the flow in the near-wake region of the bluff-body, shown in Fig. 6 at four different time steps within the same cycle as in Fig. 5. To obtain the streamlines, the velocity, computed on a uniform grid, is integrated and then contours of constant ψ are plotted. This process involves some inevitable averaging and smoothing. The streamlines are shown between the bluff-body face and a point located halfway between the bluff-body face and the exit of the computational domain, and between the centerline and a point in the free stream. The series of events described above is evident from these plots. Vorticity generated on the inner and outer sides of the bluff-body have opposite signs, consistent with the slip velocity over the corresponding walls, and hence form eddies that rotate in opposite directions as shown by the arrows on the streamline. The jet fluid that escapes the roll-up process is also indicated by the streamlines moving along the centerline of the channel. As the two toroidal eddies merge, the vorticity within the new structure is reduced by cancellation and the overall rotation of the new structure becomes less pronounced than the individual eddies before merging.

It is interesting to note here, without discussing the detail of the evidence, that large-scale vortex shedding from the wake of the bluff-body occurs due to the destabilization of the recirculation zone induced by the action of the inner jet. At much lower jet velocities, it is found that the recirculation zone behind the bluff-body remains almost steady, i.e., no large-scale shedding is observed, with weak oscillation on the shear layer between the recirculation zone and the incoming flow. As the inner-jet velocity is increased, its penetration into the recirculation zone becomes deeper. At a critical velocity ratio, the jet breaks through the recirculation zone and vortex shedding from the wake becomes significant. The fundamental mechanism of this destabilization is not yet clear. Evidently the roll-up of the boundary layer of the inner jet forms an eddy which competes for the space between the eddy formed from the annular flow and the bluff-body surface, causing the annular-flow eddy to separate from the latter.

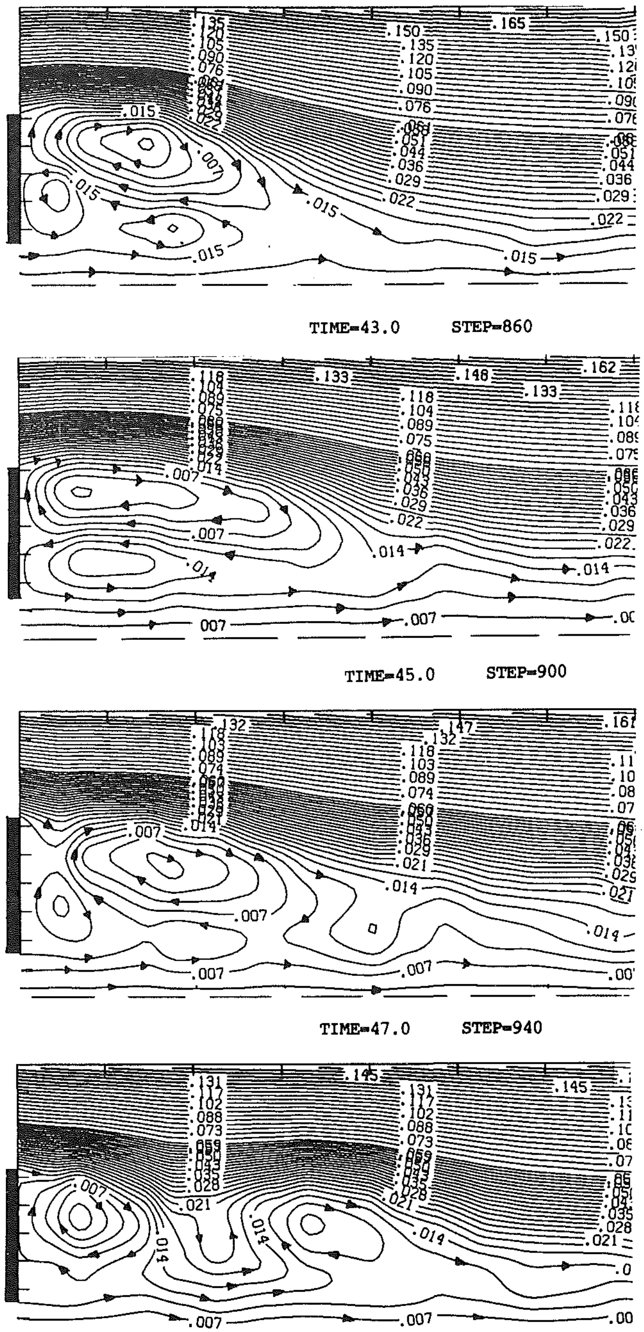

Fig. 6 The streamlines in the near wake region for the case shown in Fig. 5

The unsteady dynamics is characterized by the frequency of

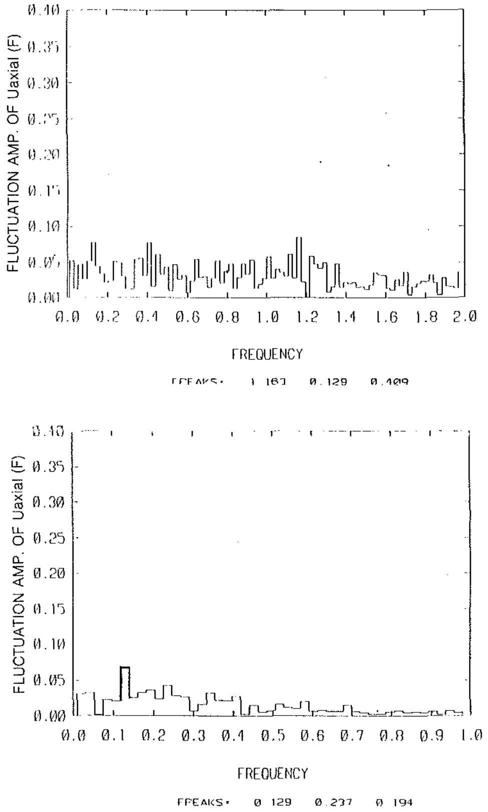

Fig. 7 Streamwise velocity spectra at x = (0.0, 1.47), shown on top, and x = (0.4, 1.37), shown in bottom, depicting the frequencies normalized as Strouhal numbers

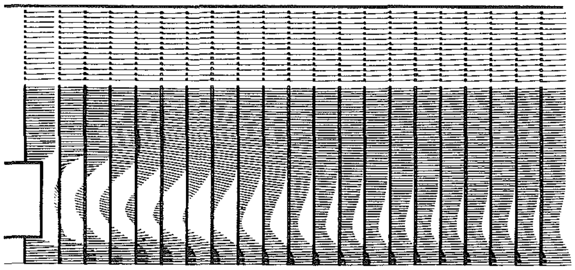

Fig. 8 The computed mean velocity on a grid

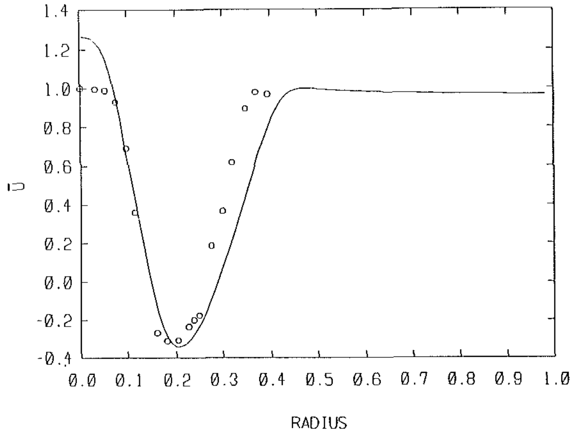

Fig. 9 A comparison between the measure, -o-o-, and computed, · · · ·, streamwise velocity at a distance, 0.4 downstream the bluff-body face

eddy shedding which is obtained by determining the frequency of velocity fluctuations. It is expected that the dominant frequency will depend on the location of the velocity measurement point since several shedding and pairing events co-exist in the domain. Moreover, other frequencies are expected to appear in the velocity fluctuation due to the nonlinear interaction between the different modes of oscillation. The frequency was measured by collecting a sample of streamwise velocity at several points close to the bluff-body, and performing a Fourier transform to identify the frequency at which higher peaks occur.

Two spectra, which correspond to a point located along the centerline slightly downstream the average length of the recirculation zone, and a point located along the outer radius of the bluff-body and almost the same axial distance as the first point, i.e., at **x** = (0.00, 1.47) and (0.40, 1.37), are shown in the upper and lower sides of Fig. 7, respectively. The two spectra show two peaks at 1.163 and 0.129, respectively associated, as will be shown next, with shedding along the jet axis and the outer edge of the bluff-body. Note that the frequency in this figure is normalized by the radius of the channel and the annular flow velocity. The first spectrum, measured along the jet axis, shows a peak at a frequency very close to the peak frequency in the second spectrum. The presence of this peak in both spectra indicates that the structure responsible for its formation, which is shed at this frequency, covers the entire region between the two points. The formation and shedding mechanism of this structure will be discussed next.

The origin of the peak in the spectrum shown at the upper side of Fig. 7 can be identified by computing a Strouhal number based on the jet diameter and velocity, $\mathrm{St}_j = fD_j/U_j = 0.23$. This is close to the most preferred frequency of a free jet (Ho and Huerre, 1984) and is close to the frequency measured by Kenworthy (1971) in the same configuration, St = 0.25. Kenworthy (1971) measured this same frequency also when the annular flow was turned off, confirming that its origin is the jet instability. Thus, in this case, shedding from the inner edge of the bluff-body is due to the inner jet instability. On the other hand, the peak in the spectrum on the lower part of the figure is associated with the shedding from the outer edge of the bluff-body. This can be established if we define a Strouhal number on the basis of the annular-flow velocity and the bluff-body outer diameter, $\mathrm{St}_a = fD_a/U_a = 0.1$. This is the characteristic frequency of shedding from a bluff-body without an inner jet (a center-body). The latter has been found, both numerically and experimentally, and for a variety of bluff-body configurations, to be O(0.1–0.2) (Najm and Ghoniem, 1991).

The mean flow is obtained by averaging the velocity field, computed on a fixed grid, over a sample of almost 1000 time steps. This sample is long enough to cover several large-scale sheddings at the lowest observed frequency. The average velocity on the grid is depicted in Fig. 8 and the corresponding streamlines are shown in Fig. 1(*c*). In the experimental and numerical results, the recirculation zone consists of two counter-rotating bubbles, the average stagnation point is away from the centerline of the flow, and the average reattachment length is almost 1.5 the outer bluff-body diameter. Note that in this axisymmetric simulation, a stagnation point in a meridian plane corresponds to a circle in the azimuthal plane. While there is a good overall agreement between the two results, some of the detail of the computed flow in the recirculation zone are different from the experimental measurements. This is, in part, due to the lack of three-dimensional mechanisms in the simulation. However, these mechanisms do not seem to influence the large-scale features of the flow. Note that these "direct" simulations do not involve any adjustable parameters.

More comparisons between the computed results and Kenworthy's measurements are shown in Fig. 9, where the average axial velocity is plotted across a section located one bluff-body radius downstream the bluff-body face. The disagreement be-

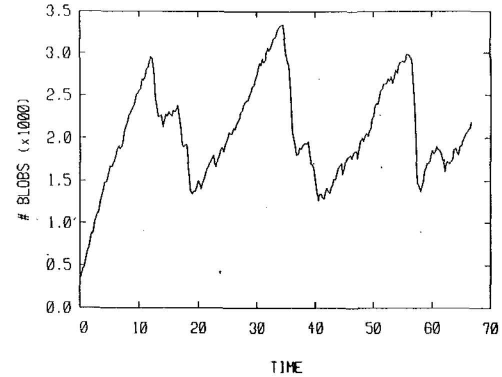

Fig. 10 The total number of vortex ring elements in the domain for D_a/D_j = 10, and the same velocity for the jet and annular flow. The figure shows three cycles starting at t = 7.5 and ending at 67.

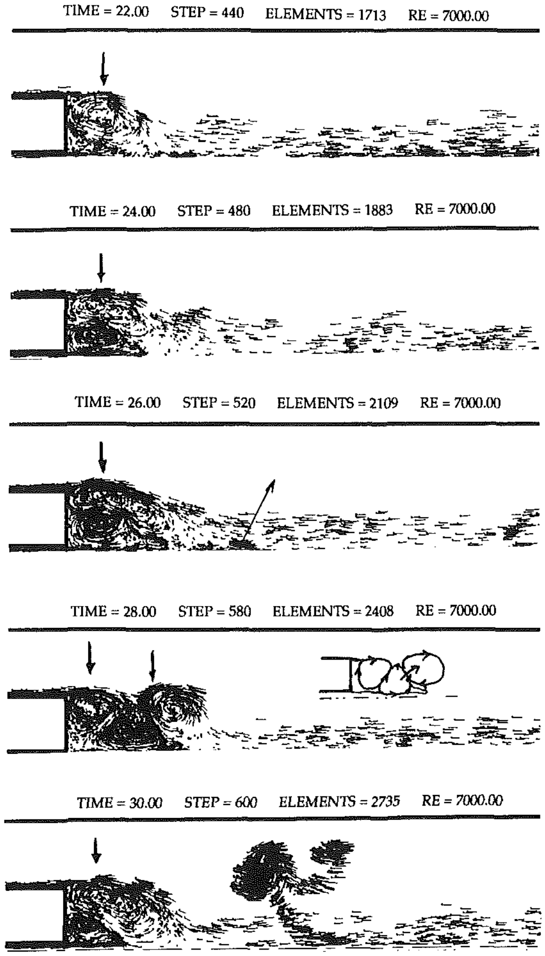

Fig. 11 The vortex ring elements and their velocity vector at different time steps during a complete cycle

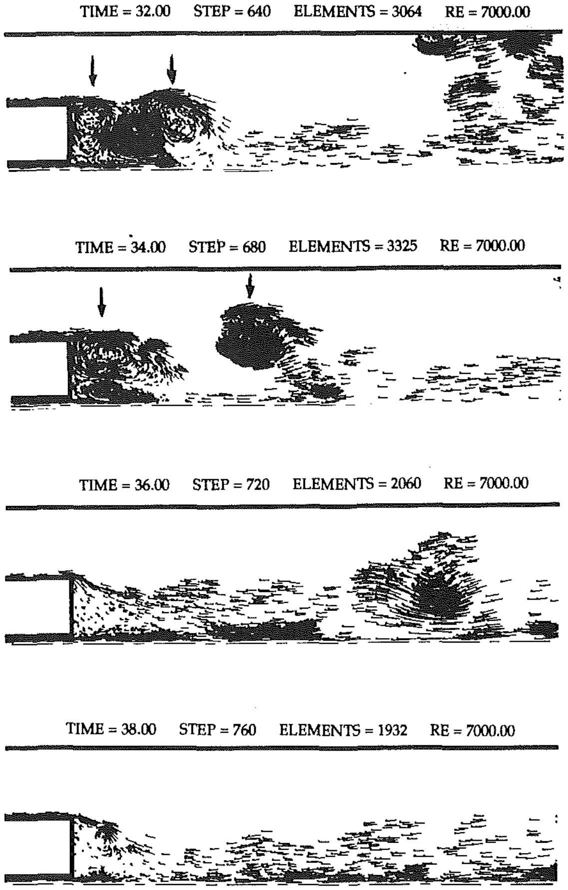

Fig. 11 (cont)

tween the results within the jet is due to the mismatch between the velocity profile at the bluff-body within the jet, being parabolic in the computation and somewhat more flat in the experiment.

There is a strong qualitative similarity between the numerical results of the unsteady flow and the flow visualization pictures of Kenworthy (1971). In the latter, two recirculation bubbles, near the inner jet and the outer diameter of the bluff-body, are identified. Another interesting qualitative similarity is seen between the unsteady dynamics of the incompressible flow here and the results of the reacting flow experiment of Roquemore et al. (1984). In that study, it was found that the combustion process is highly intermittent and is associated with the shedding of "fireballs" or flame "turbules," an expression coined by those authors to describe the flame structure in their experiment. Our numerical simulation indicates that since the pairing between the two eddies shed on the jet and annular flow sides is the mechanism governing the mixing between the fuel and air streams, combustion must occur within these composite eddies in an intermittent fashion. Clearly, the form of the combustion zone within these composite eddies will exhibit the characteristics of a vortex-ring structure, thus the name turbule.

An extensive account of the formation and shedding of large-scale vortical eddies in the nonreacting and reacting flows was also given by Li and Tankin (1986). These experiments and extensive numerical simulations done using the code described in this paper have shown that the dominant flow structure depends on the velocity ratio and the diameter ratio of the bluff-body (see Martins, 1990 and Ghoniem and Martins, 1991). In the reacting flow case, it is expected that heat release would also affect the unsteady flow structure, and that system acoustics may play a role in determining the peak frequencies. Simulations and analysis of bluff-body stabilized reacting flow will be performed in the future.

III.2 Thick Bluff Body. We now describe the results obtained for the case D_a/D_j = 10, selected to model the experiment of Kelly et al. (1989) and (1990). This experiment was performed using methane as a jet fluid and air for the annular flow, i.e., two steams with two different densities, in a nonreacting and a reacting mode. The results of this experiment, as well as previous work on jet mixing, indicate that the similarity parameter governing the overall behavior of this flow, such as jet penetration and entrainment, is the momentum ratio of the two streams, i.e., $\rho_a U_a^2/\rho_j U_j^2$. Thus, we compare

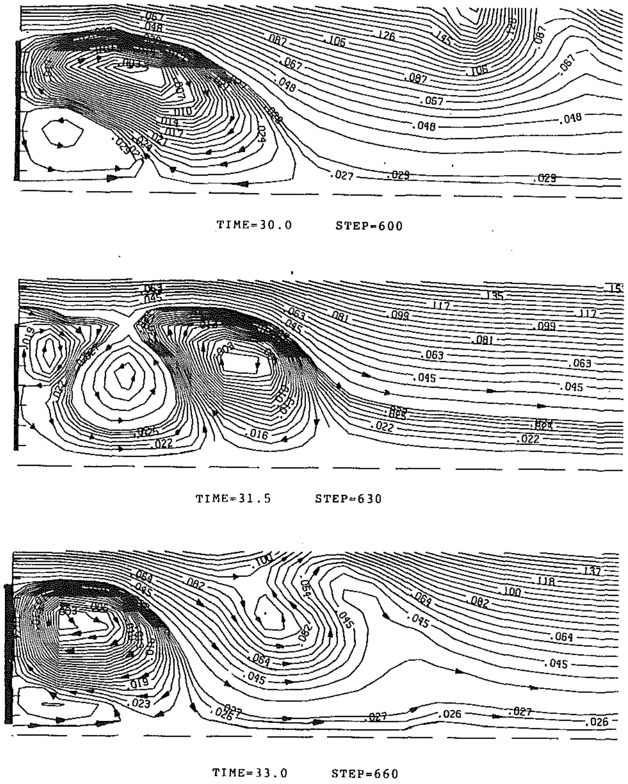

Fig. 12 Instantaneous streamline plots for the case shown in Fig. 11

our simulation results with the experimental data at the same momentum ratio.

The fluctuation of the total number of vortex elements in the computational domain, shown in Fig. 10, is much higher, and occurs at a lower frequency than in the previous case, indicating stronger, slower shedding. The transient from $t = 0$ to a stationary flow takes less time and produces a smaller peak in the number of elements than in the previous case. The fluctuations in the number of elements indicate that within each cycle, there are three subcycles identifiable by the presence of two small peaks followed by a continuous rise in the number of elements. The reason for the two peaks, and the dynamics of the flow within the wake during each major cycle is examined using the vortex elements and streamline plots next.

According to Fig. 10, a full cycle starts around $t = 20$ and lasts until $t = 40$. Figure 11 shows the vortex elements and their instantaneous velocity vectors during the formation and shedding of two eddies on the inner and outer sides of the bluff-body, their pairing into a composite eddy, and re-initiation of the shedding process during this time span. Before $t = 21$, most elements in the domain move towards the exit with very few rings rolling up into eddies at the bluff-body. During the growth of the annular flow and the jet eddies on the inner and outer edges of the bluff-body, respectively, corresponding to $21 < t < 28$, some of the jet fluid escapes the roll-up process and moves along the centerline in clumps of almost unmixed fluid. For $25 < t < 28$, the two eddies separate from the bluff-body. The reason for the separation of the annular-flow eddy from the bluff-body face appears to be the growth of the jet eddy to a size which covers the entire face of the bluff-body and competes with the annular-flow eddy. Meanwhile, the separation of the annular-flow eddy, which entrains with it the jet-flow eddy, leaves room for the formation of another eddy on the annular flow side. The two separated eddies leapfrog and/or pair into a composite structure while two new eddies form at the bluff-body during the period $28 < t < 33$.

The shedding-pairing process repeats itself for $30 < t < 33$. The formation of new eddies at the bluff-body continues during the pairing of the previous pair of eddies. However, the process of formation of new eddies, due to reasons which are not clearly understood, breaks down leading to the dissipation of these eddies and the establishment of a laminar-like flow or a "lull" period during which eddies are not formed in the wake of the bluff-body, as shown in Fig. 11, during the period of $34 < t < 36$. This disorganized state, during which the fluid from both sides of the bluff-body moves downstream without rolling up into well defined large eddies, continues until $t = 39$ when the entire cycle repeats itself again.

The formation/shedding of a large composite structure from the wake occupies a period of $\Delta t = 7.5$ (150 computational time steps). During a complete cycle, which lasts for a total of $t = 20$, two composite eddies are shed, followed by a lull period of $t = 5$. Thus, a complete cycle corresponds to two subcycles of composite eddy sheddings followed by a lull period. The pairing of two eddies, or the formation of a composite structure from the jet and annular flow fluids, is the process by which mixing in this flow is greatly enhanced. The lull period, or the period of "confused" flow, as suggested by Sturgess and Seyd (1983) has been observed experimentally in similar flows. In the case of a larger diameter ratio, it has been observed that flame turbules are shed from the downstream edge of the recirculation zone of the bluff-body, followed by a period of "confused flow" during which no shedding was observed. This lull period ends when two toroidal eddies form at the bluff-body and the shedding resumes. We found from computations at higher velocity ratios, $1 < U_j/U_a < 2$, that the higher the velocity ratio, the longer is the lull period. At velocity ratios of two and higher, the annular flow recirculation zone becomes weaker and smaller and the inner jet acts almost like a free jet. This trend is evident from the average streamline plots in Fig. 1.

The streamline plots of selected time steps during a complete cycle are shown in Fig. 12. In these plots, we emphasize the processes leading to the shedding of the annular-flow eddy and the jet eddy, their pairing into a composite eddy, and the onset of the second part of the cycle. The first process occurs as the jet eddy grows to a size where it separates the annular-flow eddy from the face of the bluff-body. As the annular flow eddy moves downstream, it entrains the jet eddy and a composite eddy forms. The separation of this composite structure is followed by the roll-up of the boundary layer on the outer diameter of the bluff-body and the formation of a new eddy.

To further quantify the most important frequencies in the dynamics of this flow, we look at the spectra of the axial velocity at two stations, $\mathbf{x} = (1.47, 0.00)$ and $(1.27, 0.5)$, shown on the upper and lower parts of Fig. 13. The first is at a distance 0.47 from the bluff-body and along the centerline. The highest peaks there are found at St = 0.135 and 0.22. Kelly et al. (1989) found that the highest peaks around this station are at St = 0.08 and 0.25. In the second spectrum, which is measured at a station along the outer edge of the bluff-body and at a distance 0.27 downstream of the bluff-body, the largest peaks are at St = 0.135 and 0.05. It is interesting to notice that the first frequency corresponds to a subcycle during which a composite structure is formed and shed from the wake, and the second corresponds to the complete cycle which includes two subcycles and a lull period. The shedding frequency of the composite structure from the wake of the bluff-body, described in terms of a Strouhal number based on the bluff-body diameter and the annular flow velocity is 0.135. This is different from the previous case in which the Strouhal number was 0.1. However, as indicated before, the wake shedding frequency ranges between 0.1 and 0.2. Thus, this frequency still corresponds to vortex shedding at the wake of the bluff-body.

Since vortex shedding is observed in many wake flows, it is desirable to define a universal Strouhal number which ap-

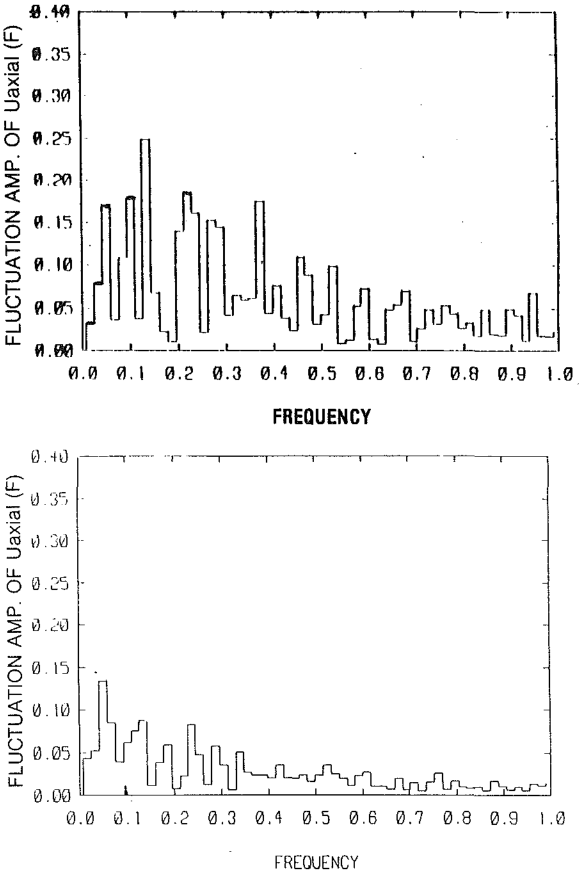

Fig. 13 Frequency normalized as a Strouhal number, spectral at two locations: (*a*) along the centerline at a point 0.77 downstream the bluff-body face; and (*b*) along the edge of the bluff-body at a distance 0.27 downstream the bluff-body face

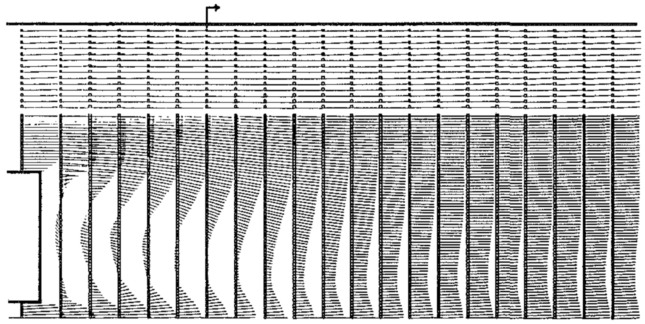

Fig. 14 The computed average velocity vectors

proaches the same value for all cases. This has been attempted before by Calvert (1967) and Griffin (1979). A Strouhal number $St^* = fD^*/U^*$, where D^* is the diameter of the wake at which vortex shedding is observed and U^* is the mean flow velocity at the same point, has been suggested for this purpose. In our computations, $D^* = D_a$, as shown in Figs. 1 and 11. The average velocity in the channel is 0.7525. Thus, $St^* = 0.18$. The values reported for a planar and an axisymmetric wake are 0.17 and 0.19, respectively.

The average velocity vector in the domain is shown in Fig. 14. In Fig. 15, we present a comparison between the numerical results and the experimental measurements of Kelly et al. (1989). Some of the difference between the two profiles is due to: (1) the Reynolds number effect, being 7000 in the numerical simulations and 48000 in the experiment; (2) the velocity profile at the exit of the jet being fully developed in the numerical simulation and flat in the experiment; and (3) the lack of three-dimensional mechanisms in the numerical simulation. We mention, in particular, that the exit profile of the jet is expected to have an effect on the detail of the recirculation zone, as observed by Ghoniem and Gagnon (1987).

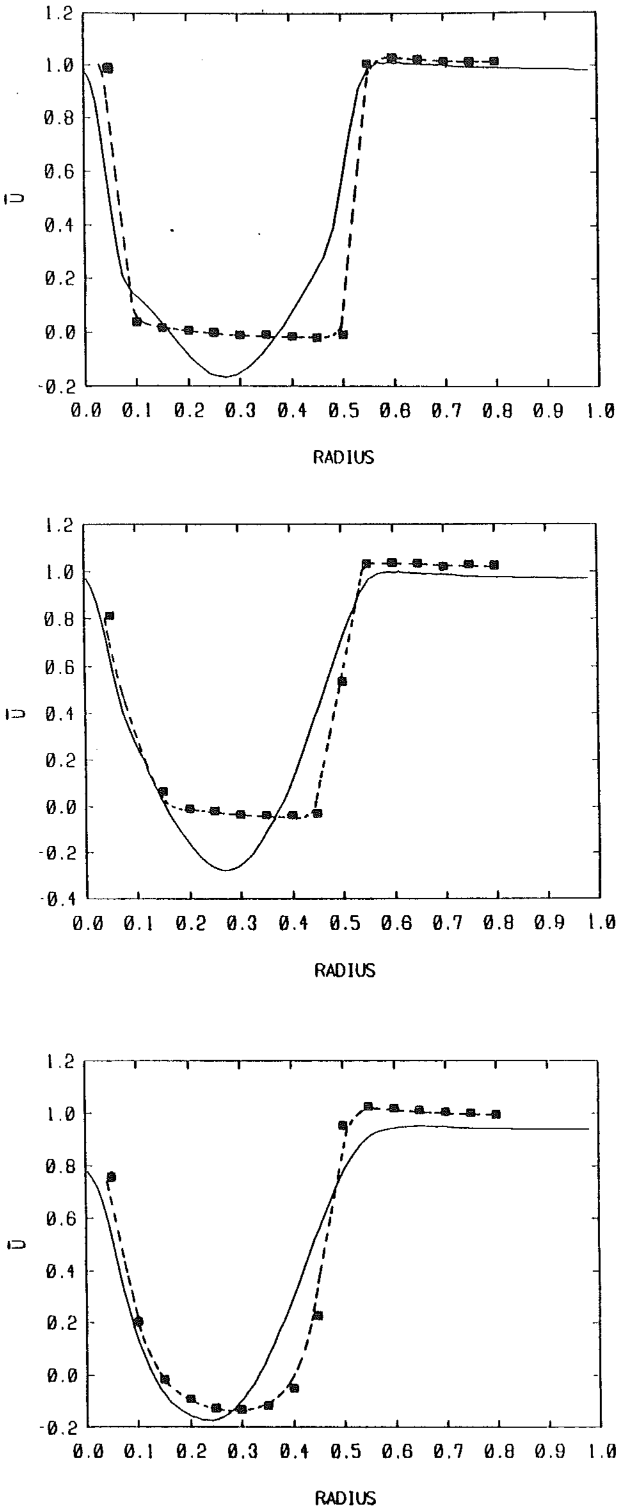

Fig. 15 Comparison between the computed and measured average streamwise velocity at three axial stations a distance 0.1, 0.2, and 0.4 downstream the bluff-body face, shown from top to bottom. Continuous lines depict numerical simulation results and broken lines show experimental data.

IV Conclusions

Vortex simulation has been used to study the dynamics of the flow generated by the interaction between two concentric jets separated by a bluff-body. The Lagrangian form of the scheme minimizes numerical diffusion and allows simulation at high-Reynolds number. The time-dependent computation reveals very strong dynamics which govern the mixing between the two streams. Comparison with experimental data show that the a priori prediction of the mean velocity distribution and the dominant frequencies are accurate.

In this incompressible model, the origin of the fluctuations is a fluid dynamics instability related to the evolution of the separating vorticity layers which leads to vortex shedding on both sides of the bluff-body. Shedding is inhibited if the inner jet velocity is much smaller than the annular flow velocity. The destabilization of the recirculation zone due to the presence of the inner jet is associated with the formation of large eddies as the vorticity carried by the jet fluid rolls up downstream the bluff-body. Shedding results from the competition between the annular flow eddy and the jet eddy as they compete trying to attach to the bluff-body face. The mixing between the two flows is governed by the merging of eddies forming on the inner and outer edges of the bluff-body and the formation of structures at the downstream end of the wake. Within these structures, combustion is expected to occur leading to an overall intermittent appearance of the reaction zone, as observed experimentally.

In both geometries, the flow is jet dominated, i.e., the jet penetrates the recirculation zone and entrains the annular fluid as it leaves the wake region while the average stagnation point is off-axis. The entrainment mechanism is the merging of the two eddies. The level of fluctuations increases and the frequency of shedding decreases as the diameter ratio increases. In both cases, the average length of the overall recirculation bubble is almost 1.5 the diameter of the bluff-body. The organization of the flow is less pronounced as the diameter ratio increases and as the jet velocity increases. As the diameter ratio increases, periods of no shedding, or lull, are observed between shedding. The lull period extends further as the diameter ratio or the velocity ratio increases. In both cases, with proper normalization, the Strouhal number of shedding is O(0.1-0.2), in general accord with wake flows.

Acknowledgment

This work is supported by the Air Force Office of Scientific Research Grant 84-0356, the National Science Foundation Grant CBT-8709465 and the Department of Energy, Energy Conservation and Utilization Technology program, grant DE-FG04-87AL44875. Computer support was provided by the John von Neumann National Supercomputer Center.

References

Byrd, P. F., and Friedman, M. D., 1954, *Handbook of Elliptic Integrals for Engineers and Physicists*; Springer-Verlag, p. 323.

Calvert, J. R., 1967, "Experiments on the Low-speed Flow Past Cones," *Journal of Fluid Mechanics*, pp. 273-289.

Chorin, A. J., 1973, "Numerical Study of Slightly Viscous Flow," *Journal of Fluid Mechanics*, Vol. 57, pp. 785-796.

Chorin, A. J., 1978, "Vortex Sheet Approximation of Boundary Layers," *Journal of Computational Physics*, Vol. 27, pp. 428-442.

Ghoniem, A. F., and Sherman, F. S., 1985, "Grid-free Simulation of Diffusion using Random Walk Methods," *Journal of Computational Physics*, Vol. 61, pp. 1-37.

Ghoniem, A. F., and Martins, L.-F., 1991, "Simulation of the Non-reacting Flow in a Bluff-body Burner; Effect of the Velocity Ratio," 29th AIAA Aerospace Sciences Meeting, Reno, Nevada, Jan.

Ghoniem, A. F., and Gagnon, Y., 1987, "Vortex Simulation of Laminar Recirculating Flows," *Journal of Computational Physics*, Vol. 68, pp. 346-377.

Griffin, O. M., 1979, "Universal Similarity in the Wakes of Stationary and Vibrating Bluff Structures," ASME Paper No. 80-WA.Fe-4, Oct.

Ho, C.-M., and Huerre, P., 1984, "Perturbed Free Shear Layers," *Annual Review of Fluid Mechanics*, Vol. 16, pp. 365-424.

Hofsommer, D. J., and van de Riet, R. P., 1963, "On the Numerical Calculation of Elliptic Integrals of the First and Second Kind and the Elliptic Functions of Jacobi," *Numerische Mathematik*, Vol. 5, pp. 291-302.

Kenworthy, J. S., 1971, "The Flow and Mixing in Double Concentric Jets," Ph.D. thesis, University of Sheffield, Sept.

Kelly, J. T., Namazian, M., Schefer, R. W., and Perrin, M., 1989, "Characterization of Non-premixed Bluff-body Burner Flame," 1989 GRI Annual Report, GRI 89/0150.

Kelly, J. T., Namazian, M., Schefer, R. W., and Perrin, M., 1990, "Characterization of Non-premixed Bluff-body Burner Flames," 1990 GRI Annual Report, GRI 90/0153.

Li, X., and Tankin, R. S., 1986, "A Study of Cold and Combusting Flow Around Bluff-body Combustor," Spring Meeting of the Western States Section, The Combustion Institute, NASA Lewis Research Center, Cleveland, OH, May 5-6.

Martins, L. F., 1990, "Vortex Computations of Axisymmetric High Reynolds Number Flows in Complex Domains," Ph.D. thesis, M.I.T., June.

Najm, H. N., and Ghoniem, A. F., 1991, "Numerical Simulation of the Convective Instability in a Dump," *AIAA Journal*, Vol. 29, pp. 911-919.

Namazian, M., Kelly, J., and Schefer, R. W., 1988, "Near Field Instantaneous Flame and Fuel Concentration Structures," *Twenty-Second (International) Symposium on Combustion*, The Combustion Institute, Pittsburgh, PA, pp. 627-634.

Namazian, M., Schefer, R. W., and Kelly, J., 1989, "Concentration Imaging Measurements in Turbulent Concentric Jet Flows," 27th AIAA Meeting, Reno, Nevada, Jan. 9-12.

Roquemore, W. M., Britton, R. L., and Sandhu, S. S., 1982, "Investigation of the Dynamic Behavior of a Bluff-body Diffusion Flame Using Flame Emission," AIAA-82-0178, AIAA 20th Aerospace Sciences Meeting, Jan. 11-14, Orlando, FL.

Roquemore, W. M., Tankin, R. S., Chiu, H. H., and Lottes, S. A., 1984, "The Role of Vortex Shedding in A Bluff-body Combustor," *Symposium on Experiments and Techniques in Turbulent Reactive and Non-Reactive Flows*, ASME 105th Winter Annual Meeting.

Roquemore, W. M., Bradley, R. P., Stutrud, J. S., Reeves, C. M., Obringer, C. A., and Britton, R. L., 1983, "Utilization of Laser Diagnostics to Evaluate Combustor Models," AGARD Conference Proceedings No. 353, *AGARD Propulsion and Energetics Panel Symposium on Combustion Problems in Turbine Engines*, Cosme, Turkey, October 3-6.

Sod, G. A., 1979, "Automotive Engine Modeling with a Hybrid Random Choice Method II," SAE paper 790242, Detroit, MI, 1979.

Sturgess, G. J., and Syed, S. A., 1983, "Dynamic Behavior of Turbulent Flow in a Widely-Spaced Co-Axial Jet Diffusion Flame Combustor," AIAA-83-0575, AIAA 21st Aerospace Sciences Meeting, Jan. 10-13, Reno, Nevada.

Jure Marn
Reactor Engineering Division,
Jožef Stefan Institute,
61111 Ljubljana, Slovenia

Ivan Catton
Mechanical, Aerospace and Nuclear
Engineering Department,
University of California, Los Angeles,
Los Angeles, CA 90024

Analysis of Flow Induced Vibration Using the Vorticity Transport Equation

Crossflow induced vibrations are the subject of this work. The analysis is two dimensional. The governing equations for fluid motion are solved using linearized perturbation theory and coupled with the equations of motion for cylinders to yield the threshold of dynamic instability for an array of cylinders. Parametric analysis is performed to determine the lowest instability threshold for a rotated square array and correlations are developed relating the dominant parameters. The results are compared with theoretical and experimental data for similar arrays and the discrepancies are discussed.

Introduction

Flow-induced vibrations have been found to be detrimental to fluid machinery. It is important, however, to distinguish between oscillations of single and multiple adjacent objects in a flow. This work deals with a theoretical investigation of the latter. The former have been thoroughly addressed in the past. A good review of a single body subject to different forms of instabilities is presented in a recent book by Blevins (1990).

In the late 1960's Connors (1970) discovered a peculiar connection between the structural mass damping parameter and Strouhal number at the onset of instability which hinted at the relative unimportance of vortex shedding that was then thought to be the major contributor to instability of both single and multiple objects or structures. It was not until the early 1980's that the scientific community began to address the issues set forth in this early work. The bulk of the past research has been experimental. Lever and Weaver (1984) were the first to formulate a one-dimensional analytical model based on mass and momentum conservation equations. Their model was more recently revisited by Yetisir and Weaver (1988) and Marn and Catton (1991).

Discrepancies between experiment and prediction and the need for empirical adjustment (in terms of a pressure loss term) of the one dimensional model called for a two dimensional approach. The Fourier analysis, normal modes approach developed by Marn and Catton (1991) has improved the prediction of the reduced velocity threshold for streamwise instabilities but does not adequately address the type of cross stream motion needed to look for instabilities in a multiple body domain.

A drawback of the models described above is that they are limited in their applicability. The Lever and Weaver (1984) model is appropriate if the motion of one cylinder does not affect the others (or if all cylinders but one are fixed) while the Marn and Catton (1991) analysis into normal modes is only appropriate for a row of flexible cylinders. This paper concentrates on semi-infinite (finite depth, infinite width) and finite (44 cylinders) arrays.

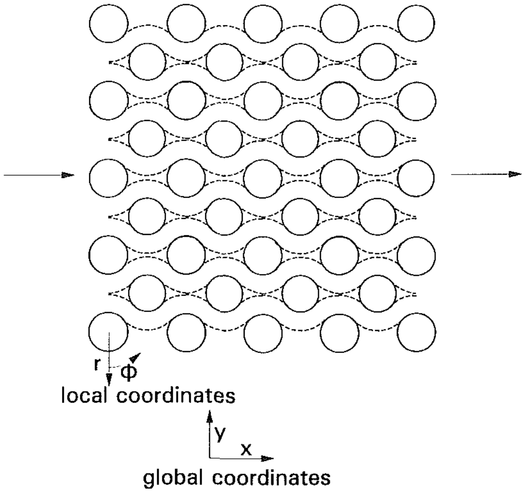

Fig. 1 The geometrical setup

Geometrical Description and General Assumptions

Figure 1 depicts the geometrical array that will be addressed. The depth of both the semi-infinite (finite depth, infinite width) and the finite (44 cylinders) arrays was arbitrarily chosen to be 11 cylinders. The array shown is usually referred to as a rotated square array. By varying the angle between the cylinders several other array configurations used in heat exchanger design can be realized (e.g., normal triangular or parallel triangular arrays). The flow is from the left and exits at the right with constant velocity. A constant inlet velocity is chosen. Two sets of coordinates are used in the computation (see Fig. 1). The global coordinate system is Cartesian and is used to de-

---

Contributed by the Fluids Engineering Division for publication in the JOURNAL OF FLUIDS ENGINEERING. Manuscript received by the Fluids Engineering Division February 10, 1992; revised manuscript received February 3, 1993. Associate Technical Editor: F. T. Dodge.

scribe the solid movement. The local coordinate system is cylindrical and is used for fluid motion analysis.

The problem described is complex and will require several assumptions. To evaluate the onset of instability phenomena, one must establish the proper criteria for such an occurrence. The instability of structures manifests itself by rapidly growing amplitudes. A formal depiction of the instability will be given in the section on governing equations.

The first assumption used is that the tubes oscillate about the nominal no-load position with a given frequency used later as a basis for a form of general temporal solution. The validity of this assumption is de facto used by most experimentalists while determining the onset of instability, see Pettigrew et al. (1988). If one evaluates the data reported, one discovers that the threshold of instability is reported as a function of reduced velocity and not as a function of apparent position of the tube at the time of instability occurrence. The latter would probably be impossible to determine as the researcher would need to detect the instability by measuring the acceleration or actual displacement of the tube.

The flowfield is assumed to be incompressible. Next, the unperturbed flowfield (i.e., an average/bulk stream) velocity is constant and unchanging with respect to the cylinders. Experiments by Simonin and Barcouda (1986) and Halim and Turner (1986) for a rotated square array as well as work performed by Leicher et al. (1991) for normal square array are used to justify this assumption. These experiments were used as a basis for the design of the basic computational flowfield cell shown in Fig. 2. The streamtube attaches to and separates from the tube at some angle of attachment. By using this idea one effectively takes into account the wake (and standing vortices) between the cylinders and treats them as a separate region with a slip surface between the two.

Numerical Considerations

The geometry best suited to describe the basic cell in Fig. 2 is a cylindrical one. By coupling a sufficient number of cells together one describes a streamtube meandering between a row of cylinders. This geometry is nearly orthogonal (if the cylinders are perturbed, i.e., slightly displaced from the neutral position) which helps simplify the governing equations. One can assign properties to each cell separately thus achieving a finite depth of the row. By coupling several rows together the array's width becomes finite. If one uses only two rows and mirrors them over a global x-axis, the array effectively becomes infinitely wide.

An algorithm for the stability analysis is composed of the following steps:

- Assume cylinder perturbations in the x, y directions.

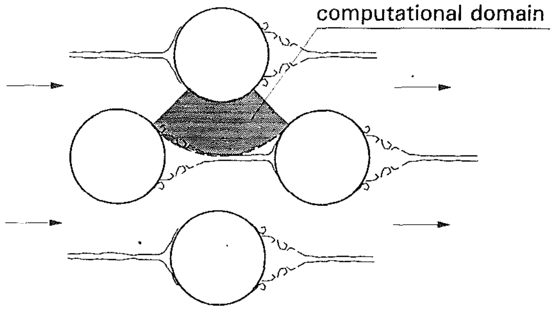

Fig. 2 The computational cell

- Calculate the vorticity generation caused by such perturbations (invoking appropriate assumptions).
- Calculate the components of the disturbed velocity field using the vorticity and mass conservation equations.
- Calculate the pressure distributions on the cylinder surfaces using the momentum equation.
- Integrate the pressure along the cylinder surfaces to calculate the components of force acting on the cylinders.
- Perform an optimization procedure to determine the distribution of cylinder perturbations and frequency ratios that yield the lowest possible threshold of fluidelastic instability.

Model Equations

This section discusses the equations governing fluid and solid motion. For the sake of brevity some of the steps used in the standard perturbation analysis are omitted. The equations are divided into fluid and solid parts.

Fluid Part. In accordance with the assumptions noted above, the velocity field is decomposed into a mean and perturbed part. The vorticity transport equation, see Panton (1984), is found by noting that the terms of higher order in perturbation can be neglected. The result is

$$\frac{\partial \eta}{\partial t}+\frac{V_\theta}{r}\frac{\partial \eta}{\partial \theta}=\nu\frac{1}{r}\frac{\partial}{\partial r}\left(r\frac{\partial \eta}{\partial r}\right)+\nu\frac{1}{r^2}\frac{\partial^2 \eta}{\partial \theta^2} \tag{1}$$

where η is the vorticity, r and θ are the local flow coordinates, and V_θ is the angular component of the mean velocity. The vorticity is defined as

$$\eta=\nabla\times\mathbf{u} \tag{2}$$

where $\mathbf{u}$ stands for velocity vector.

The following scaling is used, see Fig. 3,

Nomenclature

F = force, subscripts x and y denote respective Cartesian coordinate components
Re, Re_s = ordinary and streaming Reynolds numbers
X = tube displacement in x direction
Y = tube displacement in y direction
c = damping parameter
d = diameter of the tube
i = imaginary unit
k = tube stiffness
m = tube mass (per unit length)
p = pressure
r = radial coordinate
$r_{\mathrm{inn,out}}$ = inner and outer radii of computational domain
$\mathbf{v}$ = velocity vector
V = mean velocity vector with components V_θ and V_r
$\mathbf{u}$ = perturbed velocity vector with components v_θ and v_r
t = time
x, y = Cartesian coordinates

Greek letters

Σ = sum
δ = logarithmic decrement
η = z component of vorticity
θ = angular coordinate
θ_0 = side borders of computational domain
ν = kinematic viscosity
ω = frequency, subscript n denotes natural frequency
ρ = density

Other symbols

* = dimensionless quantities
x = cross product
$\Im$ = imaginary part of complex number
$\Re$ = real part of complex number

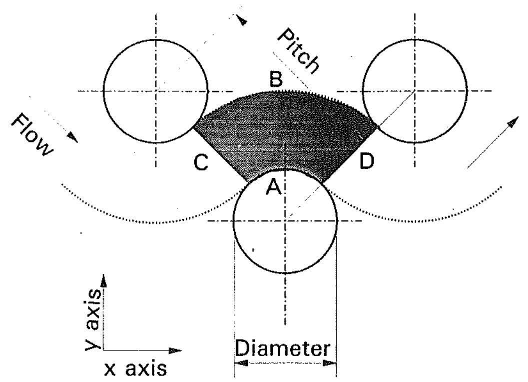

Fig. 3 The streamtube and cylinder

$$t=\frac{t^*}{\mu};\ r=r^*d;\ x=x^*d;\ y=y^*d;\ \tilde{V}_{\theta,r}=V^*_{\theta,r}V_\theta$$

$$p=p^*\rho V_\theta \omega_n;\ F=F^*\rho V_\theta d^2\omega_n;\ \tilde{\eta}=\eta^*\frac{V_\theta}{d} \tag{3}$$

$$\tilde{X}=X^*d;\ \tilde{Y}=Y^*d$$

where x and y represent global Cartesian coordinates used in evaluation of cylinder movements and X and Y are the amplitudes in the respective directions. r is used for the local cylindrical coordinate system. Note that the 2-D approximation yields units of pressure as Pa/m and force as in N/m.

If one uses the assumption of a stationary character of the problem, one can use the following form of general temporal solution for vorticity, velocity, and cylinder motion amplitudes.

$$\tilde{X}=X(x,y)e^{i\omega t};\ \tilde{Y}=Y(x,y)e^{i\omega t}$$

$$\tilde{\eta}=\eta(r,\theta)e^{i\omega t};\ \tilde{V}_\theta=V_\theta(r,\theta)e^{i\omega t};\ \tilde{V}_r=V_r(r,\theta)e^{i\omega t} \tag{4}$$

Scaling the governing equations and dropping the asterisks for convenience yields the following dimensionless equation for the disturbance vorticity

$$\frac{\omega}{\omega_n}i\eta+\frac{\mathrm{Re}_s}{r\mathrm{Re}}\frac{\partial\eta}{\partial\theta}=\frac{\mathrm{Re}_s}{\mathrm{Re}^2}\left[\frac{1}{r}\frac{\partial}{\partial r}\left(r\frac{\partial\eta}{\partial r}\right)+\frac{1}{r^2}\frac{\partial^2\eta}{\partial\theta^2}\right] \tag{5}$$

Three dimensionless parameters appear in the Eq. (5),

$$\text{Reynolds number}\quad \mathrm{Re}=\frac{V_\theta d}{\nu}$$

$$\text{Streaming Reynolds number}\quad \mathrm{Re}_s=\frac{V_\theta^2}{\omega_n\nu}$$

$$\text{Ratio of frequencies}\quad \frac{\omega}{\omega_n} \tag{6}$$

The ratio of streaming Reynolds to ordinary Reynolds number is usually referred to as reduced velocity and is used as a fluid structure interaction parameter. This ratio is believed to be one of the most important parameters for determining the threshold of instability.

Next, the boundary conditions are presented. On the cylinder surface, the velocity of the fluid matches that of the cylinder (no slip condition). The cylinder motion becomes a source of vorticity. The outer boundary of the fluid cell borders on the wake region of an adjacent cylinder. The location of the boundary is assumed to be fixed and a slip or zero vorticity flux surface is assumed. A rigorous treatment of this boundary condition would require calculation of the adjacent cylinder vortex motion and matching the pressure across the interface. This would amount to a complete cylinder motion simulation and would only be done if the approximations used here did not yield satisfactory results. Entrance and exit of the fluid cell will be matched with upstream and downstream fluid cells. This requires that the inlet velocity be matched at the interface. In algebraic terms,

$$\text{at } r=r_{\mathrm{inn}},\quad \eta=i\frac{\omega}{\omega_n}\frac{\mathrm{Re}}{\mathrm{Re}_s}\left\{\frac{\partial}{\partial y}\left[X(r,\theta)\right]-\frac{\partial}{\partial x}\left[Y(r,\theta)\right]\right\}\pm\frac{1}{2}$$

$$\text{at } r=r_{\mathrm{out}},\quad \frac{\partial\eta}{\partial r}=0$$

$$\text{at } \theta=-\theta_0,\quad \eta=\eta^-$$

$$\text{at } \theta=+\theta_0,\quad \eta=\eta^+ \tag{7}$$

where ±1/2 represents the vorticity due to constant mean velocity assumption.

The next step is to evaluate the angular component of the velocity. Using the mass conservation equation in cylindrical coordinates,

$$\frac{\partial}{\partial r}(rv_r)+\frac{\partial v_\theta}{\partial\theta}=0 \tag{8}$$

the definition of vorticity,

$$(\nabla\times\mathbf{u})_z=\frac{1}{r}\left[\frac{\partial}{\partial r}(rv_\theta)-\frac{\partial v_r}{\partial\theta}\right] \tag{9}$$

and some algebraic manipulation yields the following equation for evaluation of the angular velocity component:

$$2\eta+r\frac{\partial\eta}{\partial r}=3\frac{\partial v_\theta}{\partial r}+r\frac{\partial^2 v_\theta}{\partial r^2}+\frac{v_\theta}{r}+\frac{1}{r}\frac{\partial^2 v_\theta}{\partial\theta^2} \tag{10}$$

with boundary conditions

$$\text{at } r=r_{\mathrm{inn}},\quad v_\theta=i\frac{\omega}{\omega_n}\frac{\mathrm{Re}}{\mathrm{Re}_s}\left[-Y\sin\theta+X\cos\theta\right]$$

$$\text{at } r=r_{\mathrm{out}},\quad \frac{\partial v_\theta}{\partial r}=0$$

$$\text{at } \theta=\pm\theta_0,\quad \frac{\partial v_\theta}{\partial\theta}=0 \tag{11}$$

The pressure is evaluated using the real part of the momentum equation,

$$\frac{1}{r}\frac{\partial p}{\partial\theta}=\frac{\mathrm{Re}_s}{\mathrm{Re}^2}\left[\frac{\partial^2 v_\theta}{\partial r^2}+\frac{1}{r}\frac{\partial v_\theta}{\partial r}+\frac{1}{r^2}\frac{\partial^2 v_\theta}{\partial\theta^2}+\frac{2}{r^2}\frac{\partial v_r}{\partial\theta}\right]-\frac{\mathrm{Re}_s}{\mathrm{Re}}\left[\frac{1}{r}\frac{\partial v_\theta}{\partial\theta}+\frac{v_r}{r}\right] \tag{12}$$

An integral equation for evaluation of pressure on the cylinder's surface is derived with the help of Eq. (8),

$$p=\int_{-\theta_0}^{\theta_0}\left[\frac{\mathrm{Re}_s}{\mathrm{Re}^2}\left(r_0\frac{\partial^2 v_\theta}{\partial r^2}+\frac{\partial v_\theta}{\partial r}\right)\right]d\theta \tag{13}$$

When solving for the pressure distribution around a cylinder in an array of cylinders one needs to consider the differences in the flow relative to that of a single cylinder. Irrotational flow over a single cylinder produces a pressure distribution resembling part of a cosine curve.

A cylinder in an array will experience a different pressure distribution when compared to a single cylinder in a flowfield, especially if displaced from its neutral position. If one assumes all four neighbors of a flexible cylinder remain rigid, then the thickest density of streamlines occurs on the side of maximum cylinder displacement and the lowest on the opposite side. The streamlines of the wake sheet resemble an annulus thus the anticipated pressure distribution will not be the same as that for flow over a single cylinder. The streamlines sketched in Fig. 4 would lead one to expect an almost linear variation around the cylinder. This is for a cylinder positioned deep in

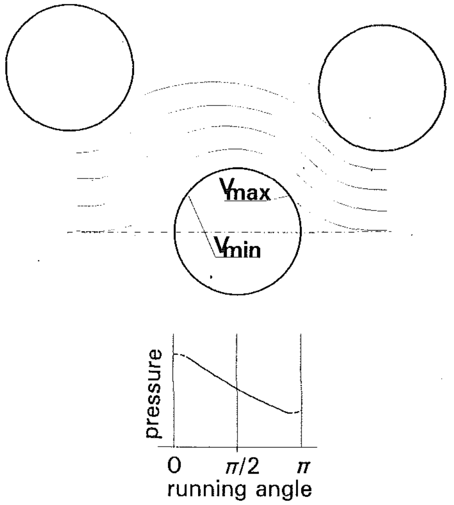

Fig. 4 Flow around cylinder in array

the bundle, at least three rows behind the first cylinder. Experiments measuring the oscillating pressure on the time scale of a single oscillation have not yet been performed thus one is led to verify the assumption of the streamline form with velocity measurements.

An experiment performed to check the intuitive conclusion described above consisted of measuring the mean velocity in a cylinder array using Laser Doppler Anemometry. The setup and theoretical assumptions are described in Leicher et al. (1991). The main conclusions were that the streamlines resemble those shown in Fig. 4 not only in the rotated square array (as shown earlier by Simonin and Barcouda, 1986 and Halim and Turner, 1986) but also in square arrays.

To simplify the calculations, the additional assumption is made that there is no radial pressure gradient on the fore and aft borders of the computational cell. Since the pitch to diameter rates are rather small and the working fluid is incompressible, this assumption is not too restrictive.

Lastly, the forces in the x and y directions are evaluated by integrating over the pressure where the limits of integration are the assumed points of attachment and detachment which coincide with symmetric upstream and downstream boundaries of the computational cell.

Solid Part. To describe the solid motion, one needs a different set of equations. The equations of cylinder motion are usually given in the following form:

$$\begin{aligned} m\ddot{X}+c\dot{X}+kX&=\Sigma F_x(x,y,t)\\ m\ddot{Y}+c\dot{Y}+kY&=\Sigma F_y(x,y,t) \end{aligned} \tag{14}$$

where c denotes damping parameter and k denotes structure stiffness. Both parameters are scaled

$$c=Am\delta\omega_n;\quad k=m\omega_n^2 \tag{15}$$

where A is a constant, usually equal to 2π.

Using the notation, scaling and assumptions introduced above, one arrives at

$$\begin{aligned} \left(\frac{\omega}{\omega_n}\right)^2\frac{m}{\rho d^2}X+iA\frac{\omega}{\omega_n}\frac{m\delta}{\rho d^2}X+\frac{m}{\rho d^2}X&=\frac{\mathrm{Re}_s}{\mathrm{Re}}\Sigma F_x(x,y)\\ \left(\frac{\omega}{\omega_n}\right)^2\frac{m}{\rho d^2}Y+iA\frac{\omega}{\omega_n}\frac{m\delta}{\rho d^2}Y+\frac{m}{\rho d^2}Y&=\frac{\mathrm{Re}_s}{\mathrm{Re}}\Sigma F_y(x,y) \end{aligned} \tag{16}$$

The amplitude value has meaning only if it is real. It can be shown by analysis of a simpler problem (analysis into normal modes, Marn and Catton, 1991) that Eq. (16) is homogeneous. The Eq. (16) can also be rearranged as

$$\left\{\left(\frac{\omega}{\omega_n}\right)^2\left[\frac{m}{\rho d^2}-\Re\left(\frac{\Sigma F_x}{\mathbb{R}}\bigg|_{\bigcirc\left(\left(\frac{\omega}{\omega_n}\right)^2\right)}\right)\right]+\left[\frac{m}{\rho d^2}-\Re\left(\frac{\Sigma F_x}{\mathbb{R}}\bigg|_{\bigcirc(1)}\right)\right]\right\}$$
$$+\left\{i\frac{\omega}{\omega_n}\left[\frac{A\delta m}{\delta d^2}-\Im\left(\frac{\Sigma F_x}{\mathbb{R}}\bigg|_{\bigcirc\left(\frac{\omega}{\omega_n}\right)}\right)\right]\right\}=0 \tag{17}$$

for stream wise direction (cross stream similar) where $\Re$ denotes real part of the force, $\Im$ an imaginary part, and $\mathbb{R}$ the ratio X Re/Re$_s$. Note that the eigenvalues of expressions in square brackets represent the solutions for static and dynamic instabilities, and $\bigcirc$ ( ) stands for the function of particular order specified in parenthesis.

It should be noted that the Eq. (16) is only homogeneous for a two dimensional approximation. In the case of three dimensions the equation of cylinder motion acquires an additional term associated with bending of the tube in direction perpendicular to the plane defined by the set of coordinates used in this work.

This work is concerned only with dynamic instability, i.e., one associated with the ratio ω/ω_n to the first power and this is a reason why only the corresponding terms are kept throughout the pressure integration. The ω/ω_n dependency stems from the applications of the boundary conditions which is evident if one attempts to solve the problem analytically as shown in Marn and Catton (1991).

Results for Semi-Infinite Array

The set of equations developed above cannot be solved analytically because the geometrical domain changes as the cylinders move, thereby making the boundary conditions very complex. A simple accurate scheme for the solution of the problem is found by using a finite difference discretization with alternate direction implicit (ADI—see Minkowycz et al., 1988) splitting. Second order accuracy is preserved with central differences. The normal derivatives at the boundaries were evaluated using first-order accurate discretization, although second order upwind discretization for the normal derivatives was utilized without much difference in the results.

Results are presented in the form of graphs depicting the onset of instability for various sets of parameters. The basic case investigated is a rotated square array with pitch to diameter ratio of 1.5 and Reynolds number of 10^4. The differences arising from using various disturbance patterns, changing Reynolds numbers and pitch to diameter ratio are evaluated. Cross stream and streamwise instabilities are compared as well.

The parameters chosen to be varied were those imposed on the heat exchanger designer by structural or other constraints. The parameters a designer is given to operate with are usually:

- pitch to diameter ratio, P/d
- Reynolds and streaming Reynolds numbers, Re and Re$_s$
- mass damping parameter,
- array orientation relative to the flow,

The results presented were calculated with the designer's needs in mind.

Instability as a Function of Disturbance Patterns. The onset of instability changes with the initial positions of the cylinders relative to each other. Figure 5 was obtained by assuming certain initial disturbance patterns (i.e., initial phase lags of the cylinders) and plotting the threshold of instability for different values of mass damping parameter. It was found that the pattern selected had a considerable impact on the threshold of instability. Our task was to find the pattern yielding the lowest onset of instability. Figure 5 presents cases with the cylinders arranged in 1) a sine pattern in x and cosine in y direction, and 2) a sine pattern in both directions. More patterns were chosen (i.e., all the cylinders initially on the same side, arranged symmetrically about the centerline, etc.) but the

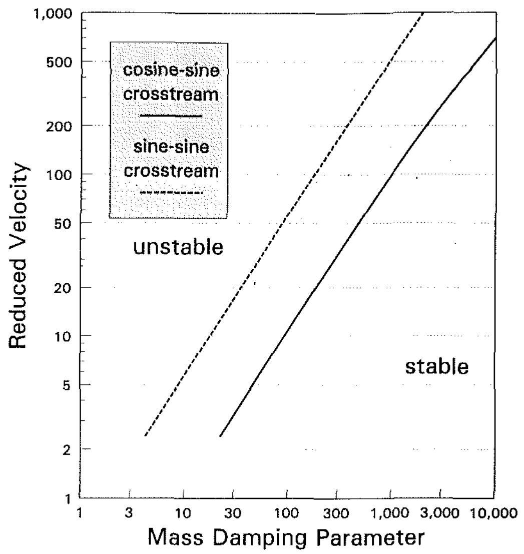

Fig. 5 Instability as a function of disturbance patterns

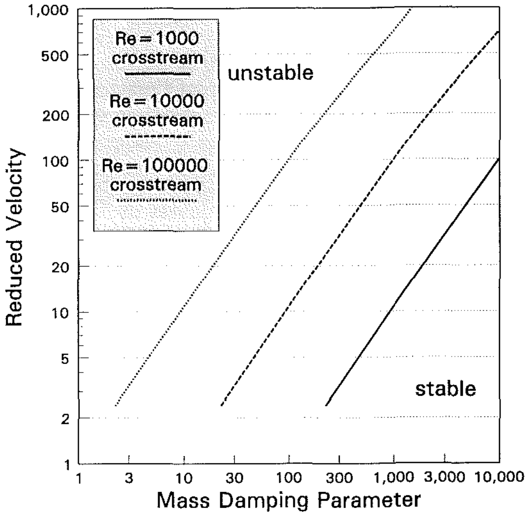

Fig. 6 Instability as a function of different Reynolds numbers

presented ones were yielding the most dangerous combination causing dynamic instabilities. To find the most dangerous of all possible patterns, an algorithm for numerical optimization would be required. Of all of the instabilities investigated the cross stream direction was most important as the results consistently showed a lower (and thus more dangerous) threshold of instability than in the streamwise direction.

Influence of Different Reynolds Numbers. Figure 6 shows the effect of gap Reynolds number (Re number based on mean velocity through the gap) on the onset of instability. The calculations were made using $\mathrm{Re} = 10^3$, 10^4 and 10^5. The results show that if smaller diameter tubes are chosen (lower Re number), the stiffness (and subsequently ω_n) of the tubes needs to be substantially increased in order to preserve the same critical mass damping parameter. This is (from a heat transfer point of view) not a desirable property of the system. The relationship between increased velocity (and subsequently the corresponding mass flux) and diameter is linear, i.e., if one increases velocity by, say, 50 percent, one has to increase the diameter of the tubes by the same amount to keep the same reduced velocity and thus position on Fig. 6.

Effect of Pitch to Diameter Ratio. Figure 7 presents thresh-

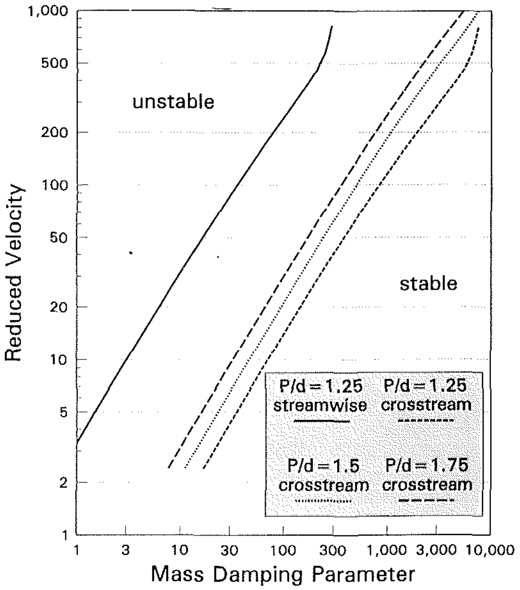

Fig. 7 Instability as a function of pitch to diameter ratio

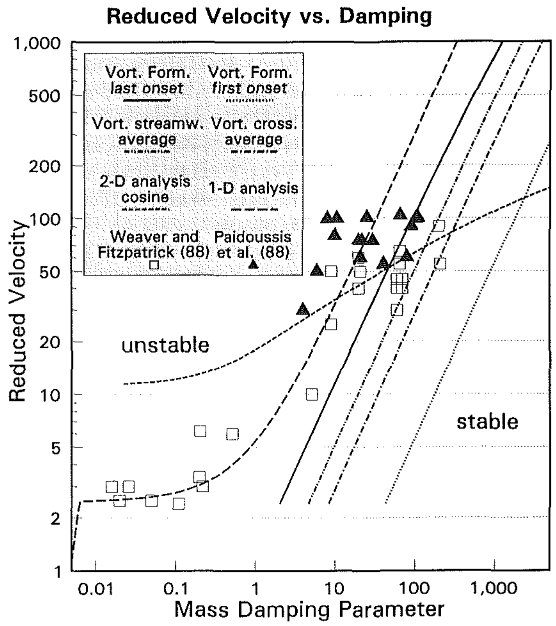

Fig. 8 Comparison of threshold of instability predictions

olds of instability for different pitch to diameter ratios, P/d. Decreasing the P/d ratio causes the structure to become less and less stable. In addition to the reported experimental results which predict the same behavior, this is also intuitively reasonable: decreased tube spacing leads to more pronounced effects between adjacent tubes.

Comparison of Various Methods. Figure 8 shows a comparison of theoretical predictions and experimental results. All the data were taken for a rotated square array with a pitch to diameter ratio of 1.5. These data are utilized in theoretical predictions as well. The present work is compared with the 1-D model reported by Marn and Catton (1990) and based on the Yetisir and Weaver work (1988) and the 2-D analysis into normal modes, reported by Marn and Catton (1991).

The figure presents four predictions by the current model: the onset of the first unstable cylinder (the conditions under which the least stable of all cylinders starts to oscillate); the

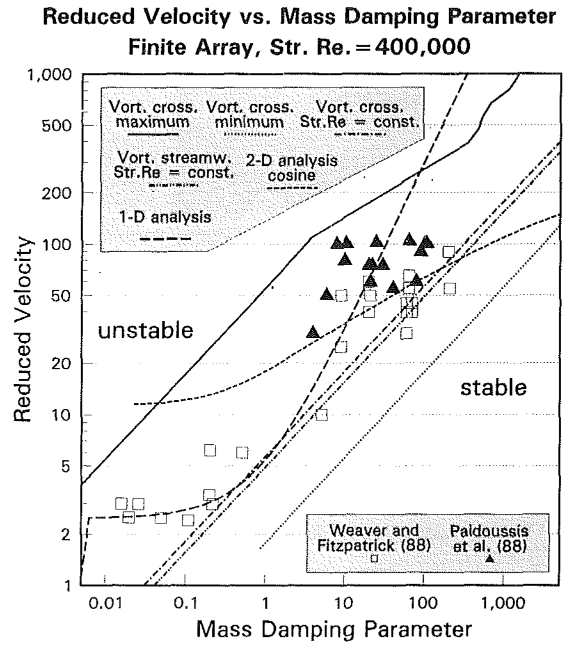

Fig. 9 Comparison between theoretical predictions and experiments

onset of last unstable cylinder (the conditions under which the most stable cylinder experiences instability); and averaged values for the cross stream and for the streamwise directions. The averaged results are the ones which have to be taken into consideration for designing heat exchangers. A single tube vibrating in an otherwise stable array will be quickly damped. When the last tube becomes unstable, all of the tubes are vibrating, a condition which is to be avoided at all cost. The average result is obtained as a geometrical average over the results of all tubes. It should be noted, however, that there are no experimental results to corroborate our statement other than the fact that the geometrical averaging results in the onset of fluidelastic instability close to the one reported in experiments, and that could be interpreted as a cyclical argument. Thus the method is arbitrary and based on engineering judgement.

Using the average result yields a conservative prediction of the onset of instability when compared to the recorded data. This is attributable to several factors: 1) it has been shown in the past that 2-D predictions of the instability threshold produce more conservative results than 3-D models (Squire's theorem) and 2) the calculated results in the lower reduced velocity range are not only due to multiple tube dynamic instability (where tubes actively influence each other), but also due to divergence and single mode fluidelastic instability (highly damped fluids) as reported earlier by Marn and Catton (1991).

Results for Finite Array of Cylinders

Figure 9 is similar to Fig. 8 with the exception that it features the analysis valid for a finite array of cylinders. It is not the difference in the array which is the most significant in this figure it is rather a change of slope that reveals another aspect of both sets of calculation: the importance of Reynolds versus. streaming Reynolds numbers. Only one, Re or streaming Re number, can be kept constant while the reduced velocity value determines the other one. Keeping Re number constant, invariably results in the slope of 1.0 whereas the constant streaming Re number causes the slope to attain the well known and documented slope of 0.5. The grounds for this variation are not offered yet but will have to be addressed in the future. Figure 9 portrays a comparison between experimental results (Weaver and Fitzpatrick, 1988 and Paidoussis et al., 1988) and their corresponding theoretical predictions for a 1-D model (Marn and Catton, 1990), a 2-D analysis into normal modes (Marn and Catton, 1991) and the vorticity formulation presented in this paper. It is worth noting that in both the streamwise and cross stream directions, the predictions almost coincide and are roughly proportional to the mass damping parameter to the power 0.5. The results presented are for an assumed constant streaming Reynolds number of 400,000. The actual streaming Reynolds number would be determined for a design using the design criteria. The figure includes the lower threshold of instability (labeled minimum), i.e., when the first tube becomes unstable, and the upper threshold (denoted maximum), where all the tubes will be unstable for a given mass damping parameter.

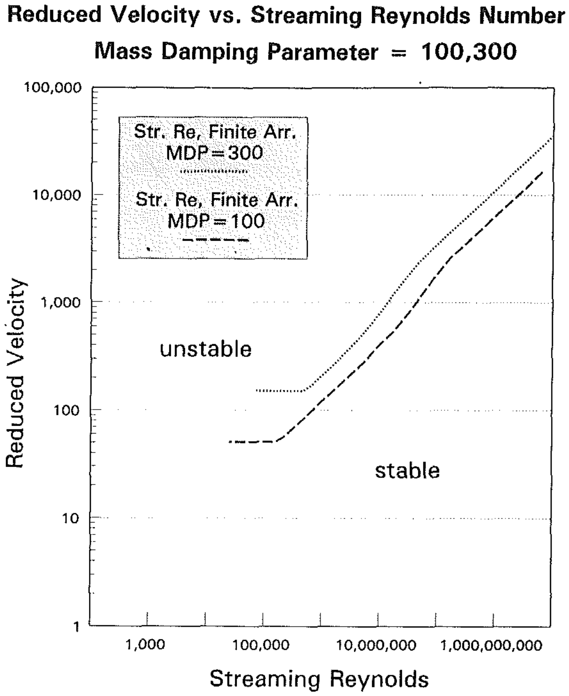

Fig. 10 Instability as a function of different streaming Reynolds numbers

Why there is a cluster of data in the lower left corner of Fig. 9 remains unanswered by this model. Much larger data compilations found in Blevins (1990) suggest that instability detection is difficult, resulting in a very wide band of data for low values of the mass damping parameter.

Figure 10 shows the dependence of the reduced velocity on the streaming Reynolds number using two values for the mass damping parameter, 300 (roughly air) and 100. The paragraph at the end of this section provides appropriate dependency on both, Reynolds and streaming Reynolds numbers, although the comparison with experimental data suggest that use of latter seems to be more appropriate.

Figure 11 compares the results obtained by keeping the Reynolds number constant with those obtained by keeping the streaming Reynolds constant. The results are somewhat puzzling to the authors. It seems that those performing experiments deliberately (or inherently) kept the streaming Reynolds constant while increasing the reduced velocity. Blevins (1990) noted in his book that none of the current models were capable of predicting the instability of an untested heat exchanger tube array any closer than the band of data presented in Mulcahy et al. (1986). He performed a data fit of several experiments and the results obtained through this work follow his fit rather nicely.

Figure 12 shows the weak dependence of fluidelastic instability on pitch to diameter ratio. This suggests reducing it in

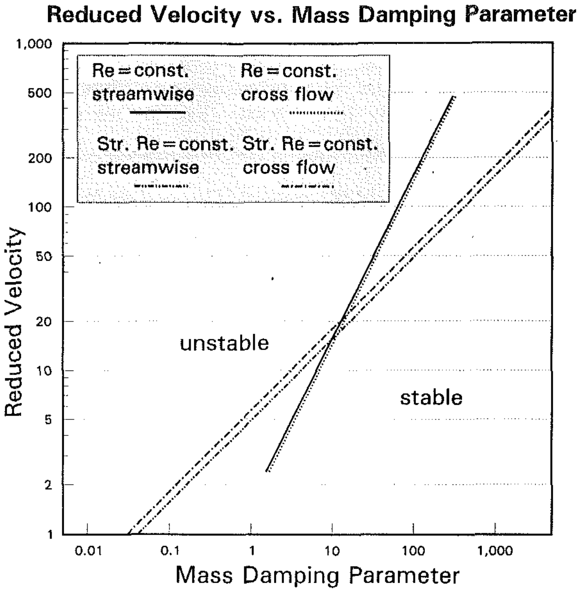

Fig. 11 Comparison based on Reynolds and streaming Reynolds numbers

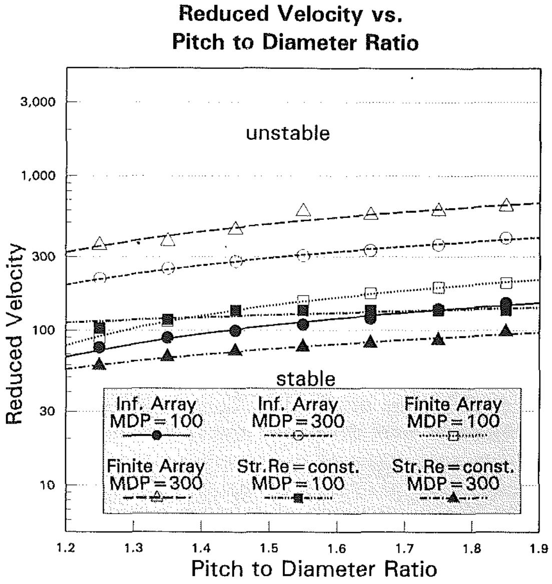

Fig. 12 Instability as a function of pitch to diameter ratio

heat exchanger design as a greater tube (number) density enhances heat transfer and consequently increases the overall efficiency of the exchanger.

Finally, the results presented here are used to develop a correlation to predict the threshold for dynamic instability in an arbitrary staggered array. The critical velocity is correlated as a function of streaming Reynolds number by:

$$\frac{U}{\omega_n d} = 0.0174 \left[\frac{m\delta}{\rho d^2 \pi}\right]^{1/2} (\text{Re}_s)^{2/5} \ln\left(70\,\frac{P}{d}\right) \tag{18}$$

It is correlated as function of Reynolds number for $500 < \text{Re} < 40{,}000$ by:

$$\frac{U}{\omega_n d} = 0.06 \left[\frac{m\delta}{\rho d^2 \pi}\right]^{1.01} e^{(1.05(P/d) + 0.01\alpha + 1.2\times 10^{-4}\text{Re})} \tag{19}$$

where both correlations have been developed using simplified regression analysis utilizing several sample calculations.

Uncertainty. The uncertainty in this analysis is introduced through the second-order central-difference discretization and the linear perturbation assumptions. To further determine the uncertainty the case of $P/d = 1.50$ arranged within rotated square array for set of mass damping parameters was run on a finer grid (22869 grid points as compared to regular 4851 grid points). The value for reduced velocity was then compared to normal, coarser, grid value. The difference was found to be between 0.7 and 2.5 percent depending on the reduced velocity.

Discussion

In addition to numerical confirmation of experimentally determined relationships between the mass damping parameter and the reduced velocity (or ratio of Reynolds to streaming Reynolds numbers), there are at least two aspects of our work that deserve some discussion.

The ratio of true to natural frequency does not have any bearing on the onset of instability. In the case of vortex shedding, the structural Strouhal number determines the most likely frequency of instabilities. In the case of fluidelastic instability, the reduced velocity depends on mass damping parameter, angle of attachment (or the geometry of the array) and viscosity of the flowfield, but the true frequency is absent from the list of parameters which follows from Eq. 16. There are three parameters on the left hand side. The first and the last represent the mass and spring model in the description of the problem while the second describes the damping. The right-hand side of the equation accounts for the forces acting on the model. Equation (16) is a complex equation with the real part accounting for static instability (divergence) and the imaginary part for dynamic instability, which is further shown in Eq. (17). If the forces vary linearly with the frequency ratio, then the frequency ratio cancels from the dynamic description of the problem thus showing that the frequency ratio is not germane to the issue of dynamic instability. It was shown by Marn and Catton (1991) that if the frequencies in the x and y directions don't vary considerably, the forces are indeed linearly dependent on the ratio of frequencies. The dependence is introduced through the application of boundary conditions on the cylinder surface. There have been numerous studies published (see Table 1 by Marn, 1991), supporting the idea that the frequencies in the x and y directions are virtually identical. There is no apparent relationship between frequency and other important parameters reported which would indicate that the nonlinear effects determine the ratio of frequencies for dynamic instabilities. The good agreement between experimental and numerical data indicate that the linearized perturbation modeling suffices.

The second intriguing question is the influence of Reynolds and streaming Reynolds number on the onset of dynamic instability. There has not been much experimental work performed where both parameters change while keeping the geometrical setup constant, probably as the kind of experiment would require different kinds of fluids. Our numerical results indicate that if one keeps the structure's (recall our definition of structure being solid and fluid part simultaneously) Reynolds number constant, while changing the mass damping parameter during evaluation of the corresponding reduced velocity for the onset of dynamic instability, the slope on log-log graph equals 1. It is widely accepted that the slope should equal 0.5, and indeed this results is obtained if one keeps the structure streaming Reynolds constant. This implies a distinct, critical, value of streaming Reynolds number at which the fluidelastic instability becomes important. Admittedly, this assertion seems to be in contradiction with the expression given by Eq. (19), however, this expression is only a correlation and is of limited applicability. In particular, Fig. 10 indicates the point (for the finite array of cylinders) beyond which the critical streaming

Reynolds number starts to rise. The point is slightly dependent on mass damping parameter but is always close to 2×10^5.

Both points discussed are somewhat contrary to what intuitive reasoning would lead us to believe, yet are worth exploring further. The answer to the first one lies in nonlinear perturbation analysis of the problem and comparison of the frequency ratio calculation with experimentally determined values. The answer to the second is an experimental study focused on both Reynolds and streaming Reynolds numbers.

Conclusions

A vorticity formulation of the instability problem has been used to establish the onset of fluidelastic instability. Perturbation equations were developed and solved numerically. The fluid forces were obtained by integrating the pressure along the surface of the cylinders and then incorporated as the right hand side of the equations of cylinder motion to predict a threshold of dynamic instability. Criteria for the occurrence of instability were explained and a simple optimization and parametric study was implemented by varying the disturbance patterns, the Reynolds number, the geometry, and the pitch to diameter ratios.

The structure is shown to require a higher mass damping parameter for the same reduced velocity when the pitch to diameter ratio decreases. Reynolds number variations influence the results in predictable manner, assuming the flow regime remains stable. A comparison of calculated results with those predicted or measured earlier shows a conservative prediction of instability of a semi-infinite array and a satisfactory prediction for a finite array. There is no "data fitting" implemented in the model; the independent parameters used in the analysis to obtain the reduced (gap) velocity are the initial disturbance pattern, the pitch to diameter ratio, the angle of attachment, the Reynolds and streaming Reynolds numbers and the diameter of the tubes in the array.

A parametric analysis of the effect of independent variation of the Reynolds number and streaming Reynolds numbers is given. The effects of parameters has never been independently explored experimentally but the results obtained while keeping streaming Reynolds number constant show agreement with available experimental data.

The equations of fluid and solid motion are coupled at the interface and used to predict the threshold of instability. The results are summarized in formulas linking reduced velocity to mass damping parameter, Reynolds or streaming Reynolds number, angle of attachment and pitch to diameter ratio.

Acknowledgment

Authors would like to thank U.S. Department of Energy for sponsoring this work through grant No. DE-FG07-89ER12902 and Slovene Ministry of Science and Technology for sponsoring the revision of the work under grant No. Z2-0363-106-93. The authors are indebted to the reviewers and editors for many helpful suggestions and improvements of this paper.

References

Andjelic, M., Austermann, R., and Popp, K., 1990, "Multiple Stability Boundaries of Tubes in a Normal Triangular Cylinder Array," *Flow Induced Vibrations 1990*, Vol. PVP-189, Nashville, Tennessee, pp. 87–98.

Blevins, R. D., 1990, *Flow Induced Vibrations*, Van Nostrand Reinhold, New York, NY.

Chandrasekhar, S., 1981, *Hydrodynamic and Hydromagnetic Stability*, Dover, New York, NY.

Chen, S. S., 1987, *Flow Induced Vibration of Circular Cylindrical Structures*, Verlag, Berlin.

Connors, H. J., 1970, "Fluidelastic Vibration of Tube Arrays Excited by Cross Flow," Paper presented at the *Symposium on Flow Induced Vibration in Heat Exchangers*, ASME Winter Annual Meeting.

Dhaubhadel, M. N., Reddy, J. N., and Telionis, D. P., 1987, "Finite-Element Analysis of Fluid Flow and Heat Transfer for Staggered Bundles of Cylinders in Cross Flow," *International Journal for Numerical Methods in Fluids*, No. 12, Vol. 7, Dec., pp. 1325–1342.

Gibert, R. J., Chabrerie, J., and Sagner, M., 1978, "Vibrations of Tube Arrays in Transversal Flows," *BNES-Vibration in Nuclear Plant, Int. Conf. Keswick*, UK, pp. 205–213.

Halim, M. S., and Turner, J. T., 1986, "Measurements of Cross Flow Development in a Staggered Tube Bundle," *3rd Int. Symp. on Applications of Laser Anemometry to Fluid Mechanics*, Paper 21.7, Lisboa Portugal.

Leicher, M., Marn, J., and Catton, I., 1991, "Flow Visualization of a Square Array of Cylindrical Tubes: an Experimental Study Using Laser Doppler Anemometry," *1991 Winter Annual Meeting*, Vol. FED-128, pp. 217–224, Atlanta, GA.

Lever, J. H., and Weaver, D. S., 1984, "On the Stability Behaviour of Heat Exchanger Tube Bundles," Parts I and II, *1984 Symp. on Flow Induced Vibrations*, Vol. 2, ASME.

Marn, J., and Catton, I., 1991, "Flow Induced Vibrations in Cylindrical Bundles: Two Dimensional Analysis into Normal Modes," *Proc. 1991 National Heat Transfer Conference*, Vol. HTD-165, Minneapolis, MN, pp. 9–14.

Marn, J., and Catton, I., 1991, "Flow Induced Vibrations of Cylindrical Structures Using Vorticity Transport Equation," *1991 Winter Annual Meeting*, Vol. FED-129, Atlanta, GA, pp. 75–82.

Marn, J., and Catton, I., 1991, "Stability of Finite Cylinder Array Subjected to Single Phase Cross Flow," *1991 Winter Annual Meeting*, Vol. PVP-224/FED-126, Atlanta, GA, pp. 1–4.

Marn, J., 1991, "Cross Flow Induced Vibrations in Staggered Arrays of Cylindrical Structures," Ph.D. dissertation, UCLA.

Minkowycz, W. J., Sparrow, E. M., Schneider, G. E., and Pletcher, R. H., 1988, *Handbook of Numerical Heat Transfer*, Wiley Interscience, New York, NY.

Mulcahy, T. M., Halle, H., and Wambsganss, M. W., 1986, "Prediction of Tube Bundle Instabilities; Case Studies," *Argonne National Laboratory Report ANL-86-49*.

Paidoussis, M. P., Price, S. J., Nakamura, T., Mark, B., and Njuki, W., 1988, "Flow-Induced Vibrations and Instabilities in a Rotated-Square Cylinder Array in Cross Flow," *1988 Int. Symp. on Flow Induced Vibrations and Noise*, Vol. 3, ASME.

Panton, R. L., 1984, *Incompressible Flows*, Wiley, New York, NY.

Pettigrew, M. J., Tromp, J. H., Taylor, C. E., and Kim, B. S., 1988, "Vibration of Tube Bundles in Two-Phase Cross-Flow: Part 2—Fluidelastic Instability," *1988 Int. Symposium on Flow-Induced Vibration and Noise*, 1988 ASME Winter Annual Meeting, Chicago, IL, Vol. 3.

Price, S. J., Paidoussis, M. P., Macdonald, R., and Mark, B., 1987, "The Flow Induced Vibration of a Single Flexible Cylinder in a Rotated Square Array of Rigid Cylinders with Pitch to Diameter Ratio of 2.12," *Journal of Fluids and Structures*, Vol. 1, pp. 359–378.

Simonin, O., and Barcouda, M., 1986, "Measurement of Fully Developed Turbulent Flow across Tube Bundle," *3rd Int. Symp. on Applications of Laser Anemometry to Fluid Mechanics*, Paper 21.5, Lisboa, Portugal.

Sparrow, E. M., and Molki, M., 1982, "Effect of a Missing Cylinder on Heat Transfer and Fluid Flow in an Array of Cylinders in Cross-Flow," *International Journal of Heat Mass Transfer*, No. 4, Vol. 25, Apr., pp. 449–456.

Toyama, S., Mori, H., and Suzuki, M., 1987, "Flow Patterns Through Tube Bundles and Particulate Fouling onto Cylinders," *Particulate Science and Technology*, pp. 397–408, No. 4, Vol. 5, pp. 397–408.

Weaver, D. S., and Fitzpatrick, J. A., 1988, "A Review of Cross-Flow Induced Vibrations in Heat Exchanger Tube Arrays," *Journal of Fluids and Structures*, Vol. 2, 1988, pp. 73–93.

Yetisir, M., and Weaver, D. S., 1988, "On an Unsteady Theory for Fluidelastic Instability of Heat Exchanger Tube Arrays," *1988 Int. Symp. on Flow Induced Vibrations and Noise*, Vol. 3, ASME.

A Note on Laminar Flow in Uniformly Porous Tubes

K. Schnitzlein
Institut für Technische Chemie,
Technische Universität Braunschweig,
W-3300 Braunschweig, Germany

A numerical analysis of the steady, laminar, incompressible flow in a constant diameter tube with uniform mass suction at the wall is made to study the development of the flow for the entire range of wall Reynolds numbers. It is shown that for small suction rates the state of flow can reach the similarity condition at least at distinct positions at the tube axis. For higher suction rates similarity profiles are found to occur only if the flow exhibits an asymmetric behavior with respect to the point of complete mass extraction.

Introduction and Objective

The subject of fluid flow in cylindrical tubes with wall suction has recently received increasing attention due to the development of high performance diesel particulate traps (Schnitzlein and Löwe, 1990). There were numerous theoretical investigations in the past, almost all dealing with incompressible, laminar flow and uniform suction. In the investigations it was attempted to determine the axial pressure variations, the wall shear stress, and the shapes of the velocity profile in a porous tube.

Besides solutions of the complete Navier-Stokes equations (e.g., Friedman and Gillis, 1967), solutions based on the similarity of flow profiles were proposed (e.g., Weissberg, 1959; White, 1962; Terrill and Thomas, 1969). In this case only those solutions to the equations of motion are considered in which the shapes of the nondimensional velocity profiles do not vary with distance along the tube axis. This constitutes a considerable mathematical simplification of the problem. But, the results which are generally presented in terms of a wall Reynolds number Re_w, show multiplicity and instability effects for uniform suction: Similarity solutions were found to exist for $0 \leq \mathrm{Re}_w \leq 2.3$ and for $\mathrm{Re}_w \geq 9.1$. No similarity solutions were found for $2.3 < \mathrm{Re}_w < 9.1$. Each of these solutions is characterized by the existence of two different velocity profiles corresponding to the same wall Reynolds number.

For the application of these similarity solutions to the description of laminar flow in porous tubes it is important to know whether the thus obtained profiles agree well with the profiles encountered in real porous tube flow. As experimental (Quaile and Levy, 1975) and simulation results (Friedman and Gillis, 1967) indicate, only for weak suction ($\mathrm{Re}_w \leq 1$) can the condition of similarity be achieved over a substantial portion of the tube. The validity range of the similarity solutions shrinks to a point as $\mathrm{Re}_e \rightarrow 2.3$ (Quaile and Levy, 1975). In each case only the first of the double solutions could be obtained in this way.

Up to now, to the author's best knowledge, nobody has ever attempted to show whether the similarity profiles for $\mathrm{Re}_w > 9.1$, with their quite unusual shapes, can appear in real porous tube flow, at least locally. It is the objective of this paper to investigate this topic by a detailed analysis of laminar flow in porous tubes with suction at the wall.

Formulation of the Problem

The numerical analysis is based on the following assumptions:

- The flow through the tube is two-dimensional, symmetric, steady, laminar and has no significant property value variations.
- The usual configuration, open tube with one end closed (e.g., Quaile and Levy, 1975), is replaced by a tube with both ends open. Consequently, now the flow enters the tube at both sides, of course with reversed signs. Furthermore, the suction length is doubled in order to absorb all the incoming mass. For uniform suction at the wall the problem can be regarded to be symmetrical with respect to the midpoint of the porous section. In the following this point is referred to as *point of complete mass extraction*.

  This configuration has been chosen because it offers the possibility of easily achieving an asymmetrical behavior of the flow, as is shown in the following. For the symmetric case this configuration is essentially analogous to the usual configuration. This was verified by comparing numerical solutions obtained for both configurations for some representative values of the wall Reynolds number.
- Absorption takes place at a uniform rate over a finite section of the tube ($x_1 \leq x \leq x_2$). To allow any upstream influence caused by the abrupt change of the boundary conditions at the wall of the tube especially for high suction rates, the absorbing region was shifted away from the immediate vicinity of the tube inlets.
- At the inlets a fully developed laminar velocity profile is assumed. These profiles might correspond to the physical situation in which the nonporous sections of the pipe are joined smoothly to the porous section and the non-porous sections are of sufficient length to allow the attainment of Poisseuille flow.

Contributed by the Fluids Engineering Division for publication in the JOURNAL OF FLUIDS ENGINEERING. Manuscript received by the Fluids Engineering Division July 10, 1992; revised manuscript received November 12, 1992. Associate Technical Editor: F. T. Dodge.

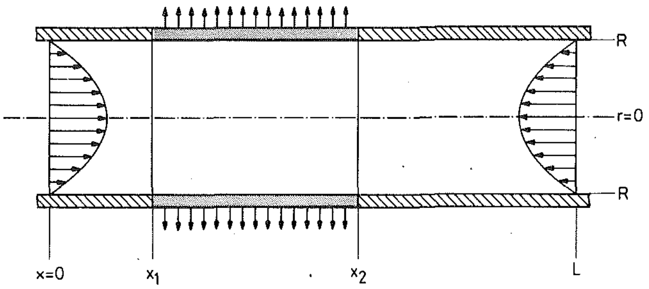

Fig. 1 Porous tube configuration

The configuration of the porous tube is shown in Fig. 1. Then the equations of continuity and momentum become

$$\nabla \mathbf{v} = 0$$
$$-\rho \nabla \mathbf{v}\mathbf{v} + \mu \nabla \mathbf{v}^2 - \nabla p = 0 \qquad (1)$$

with the boundary conditions:

$$\begin{array}{llccc} x=0 & 0 \le r \le R & u = 2\bar{u}_0(1-(r/R)^2) & v=0 & \\ x=L & 0 \le r \le R & u = -2\bar{u}_0(1-(r/R)^2) & v=0 & \\ r=0 & 0 \le x \le L & \partial u/\partial r = 0 & v=0 & \\ r=R & x_1 \le x \le x_2 & u=0 & v=v_w & (2) \\ r=R & 0 \le x < x_1 & u=0 & v=0 & \\ r=R & x_2 \le x \le L & u=0 & v=0 & \end{array}$$

Solution Procedure

The calculation of the flow field and the pressure proceeds along the lines of the SIMPLER algorithm (Semi-Implicit Method for Pressure Linked Equations Revised) developed by Patankar (1980). The method is based on a series of predictor and corrector steps. Starting with a guessed flow field, the algorithm continues by making pressure corrections from iteration to iteration until the velocities calculated in conjunction with the corrected pressure field satisfy the momentum and continuity equations simultaneously. To ensure the required accuracy (residual of the continuity equation $<10^{-8}$) up to 8000 mesh points have been used which are axially distributed over the solution domain by an Eulerian adaptive grid selection strategy (Oran and Boris, 1987).

Results and Discussion

It is well known that for tube flow with suction at the wall the lower limit of the region of turbulent flow is much lower than for a tube with impermeable walls (Quaile and Levy, 1975). Therefore, to avoid any falsification of our results due to a possible transition from laminar to turbulent flow, the simulations were performed for a sufficiently low value of the axial Reynolds number ($\mathrm{Re}_r = 100$). For higher values of Re_r numerical instabilities were observed to occur especially in the vicinity of the point of complete mass extraction indicating a possible transition of the flow regime there.

To facilitate the comparison with the similarity solutions the results are presented in terms of a dimensionless axial velocity

$$\tilde{u}(x, r) = \frac{u(x, r)}{\bar{u}(x)} \qquad (3)$$

which equals the first derivative of the similarity function $f(r)$ (White, 1962). The average axial velocity $\bar{u}(x)$ at any cross section, which was used to normalize all velocity profiles, was found by numerical integration.

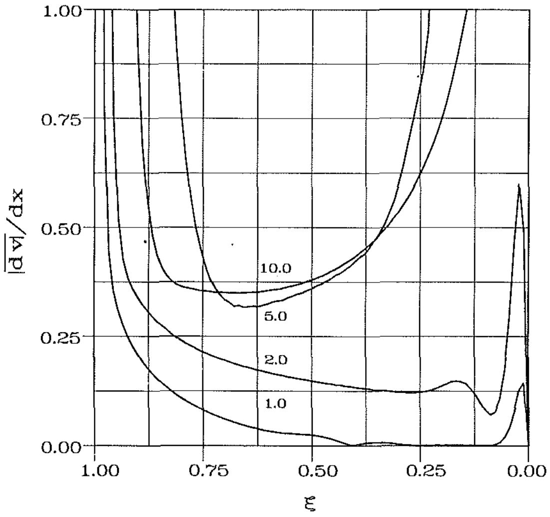

Fig. 2 $\overline{|\partial v|}/\partial x$ **versus suction length for different** Re_w **(symmetric problem)**

In order to obtain a general scaling for all values of Re_w a new dimensionless axial coordinate is defined, as suggested by Weissberg (1959):

$$\xi = 1 - \frac{2\,\mathrm{Re}_w}{\mathrm{Re}_r}\frac{(x-x_1)}{R} \quad \text{valid in the range } x_1 \le x \le x_2$$

The transformed axial coordinate ξ, which represents the actual suction length, varies between 1 at $x = x_1$, and -1 at $x = x_2$.

If any of the similarity solutions occur either over a substantial portion of the tube or at distinct positions along the tube axis, these positions should be characterized by the fact that the assumption of fully developed laminar flow

$$\frac{\partial v(x, r)}{\partial x} = 0$$

is locally fulfilled over the entire radius. Therefore, in order to locate such positions the course of $\partial v/\partial x$ should be considered. Instead of plotting $\partial v/\partial x$ over the solution domain, the course of the radially averaged absolute axial gradient of the radial velocity $\overline{|\partial v|}/\partial x$ is plotted versus the suction length for different values of Re_w (see Fig. 2). Then, if $\overline{|\partial v|}/\partial x = 0$ it follows that $\partial v/\partial x = 0$ on all points on the radius, and vice versa. Due to symmetry of the problem with respect to the point of complete mass extraction the consideration can be restricted to the range $0 \le \xi \le 1$.

As can be seen in this figure, for $\mathrm{Re}_w = 1$ the condition of similarity is achieved within the range $0.07 \le \xi^* \le 0.42$. This is in good agreement with the results obtained by Weissberg (1959). The corresponding velocity profile is almost identical

Nomenclature

f = similarity function
L = tube length
r = radial coordinate
p = pressure
R = tube radius
Re_w = wall Reynolds number: $\rho v_w R/\mu$
Re_r = axial Reynolds number: $\rho \bar{u}_0 R/\mu$
u = axial velocity
$\bar{u}_0$ = average axial velocity at the inlets
$\mathbf{v}$ = velocity vector
v = radial velocity
v_w = radial velocity at the wall
x = axial coordinate
ξ = dimensionless axial coordinate
ρ = density
μ = dynamic viscosity

Superscripts

$*$ = locus where the condition of similarity is achieved

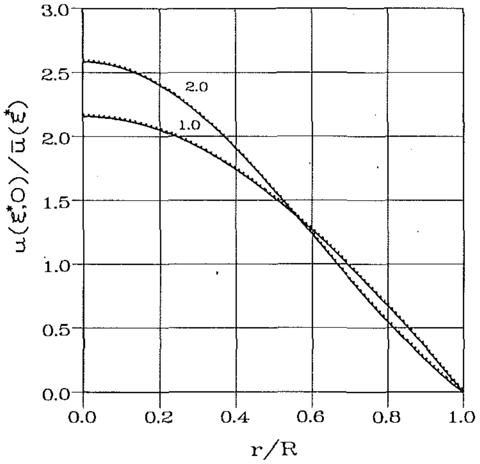

Fig. 3 Comparison between similarity solutions (dotted lines) and calculated velocity profiles (continuous lines) for small suction rates ($Re_w = 1.0$: $0.07 \le \xi^* \le 0.42$, $Re_w = 2.0$: $\xi^* = 0.09$)

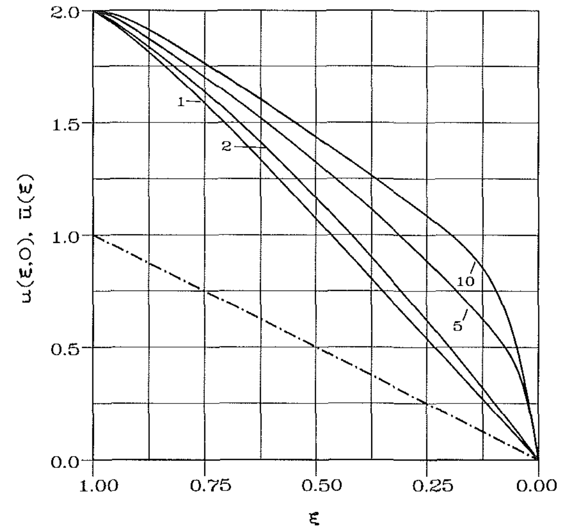

Fig. 4 Axial centerline velocity (continuous line) and average axial velocity (dashed-dotted line) versus suction length

Table 1

Re_w	$(L-x_2)/(x_2-x_1)$
10.0	0.27
15.0	0.46
20.0	0.73

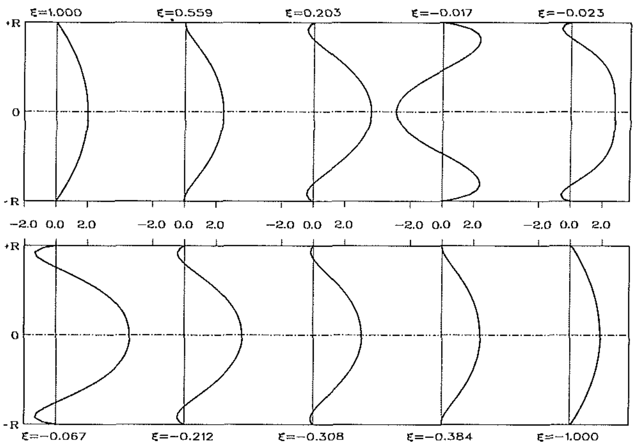

Fig. 5 Development of axial velocity profiles for $Re_w = 10$

to the first similarity solution (see Fig. 3). For $Re_w = 2$ the entrance region extends all the way from the inlet to the point of complete mass extraction (i.e., $\xi = 0$). But, at $\xi^* = 0.09$ the function $|\partial v|/\partial x$ shows a pronounced local minimum indicating that the condition of similarity may approximately be achieved there. The corresponding velocity profile confirm this supposition (see Fig. 3). Again, differences between the two profiles can hardly be seen.

In the immediate vicinity of the point of complete mass extraction $|\partial v|/\partial x$ approaches zero, too. Therefore, it cannot be excluded that the second similarity solution can in principle occur there. But, even with a much higher resolution than that used in the present work, the calculation of these profiles is a difficult task, especially as Re_w approaches zero.

As Re_w increases the validity range of the similarity solution ξ^* shrinks to a point while moving toward $\xi = 0$. For $Re_w = 2.305$, where similarity theory predicts only one solution, ξ^* coincides with the point of complete mass extraction.

For higher suction rates the curves shown in Fig. 2 do have a local minimum but the velocity profiles at their point of minimum are rather different from their correspondent similar solutions: As Re_w increases the center line velocity increases and backflow at the wall becomes more and more pronounced.

Then, the question arises whether any corresponding similarity profiles can be obtained if some of the assumptions are modified and of what kind these modifications must be. To evaluate these conditions the similarity profiles are considered in detail: All similarity profiles for $Re_w > 9.1$ are characterized either by an inflection point or by two turning points with a minimum between the axis and the tube wall (Terrill and Thomas, 1969), e.g., for $Re_w > 10$ backflow is predicted to occur at the tube axis. According to Eq. (3), to obtain such negative values for $\tilde{u}(\xi, 0)$ either the axial center line velocity $u(\xi, 0)$ or the average axial velocity $\bar{u}(\xi)$ must be negative. As Fig. 4 shows neither becomes negative along the entire suction length for all values of Re_w.

As long as the suction rate at the wall is uniform the functional form of the average axial velocity $\bar{u}(\xi)$ is represented by the straight line, as shown in Fig. 4. Therefore, backflow at the tube axis can only be achieved if $u(\xi, 0)$ becomes zero downstream of the point of complete mass extraction, i.e., $u(\xi, 0) = 0$ for $\xi < 0$. Then $\tilde{u}(\xi, 0)$ becomes zero in the range of $-1 \le \xi \le 0$, i.e., the flow is asymmetrical with respect to the point of complete mass extraction. Now, it may be possible to obtain the similarity profiles corresponding to $Re_w > 9.1$.

Such an asymmetry can be achieved by assuming different lengths for the nonporous sections at the inlets of the tube. Retaining the parabolic inlet velocity profile at the left-handed inlet by regarding the respective nonporous section as sufficiently long, the modified boundary condition at $x = L$ are given by

$$0 \le r \le R \quad p = p_0 \quad \frac{\partial v}{\partial x} = 0 \qquad (5)$$

By decreasing the length of the right-handed nonporous section, i.e., $x_2 \le x \le L$, the asymmetry of the profiles can be increased. The ratios of the nonporous lengths used in the calculations are shown in Table 1. For this arrangement the development of the flow for $Re_w = 10$ is shown in Fig. 5, indicating the asymmetric state of flow with respect to the point of complete mass extraction:

As can be seen in this figure, the velocity gradient at the wall becomes zero at $\xi = 0.559$ causing backflow to develop at the wall. At $\xi = 0$ the velocity profile abruptly changes its shape, because $\bar{u}(\xi)$ reverses its sign. Backflow is observed to occur

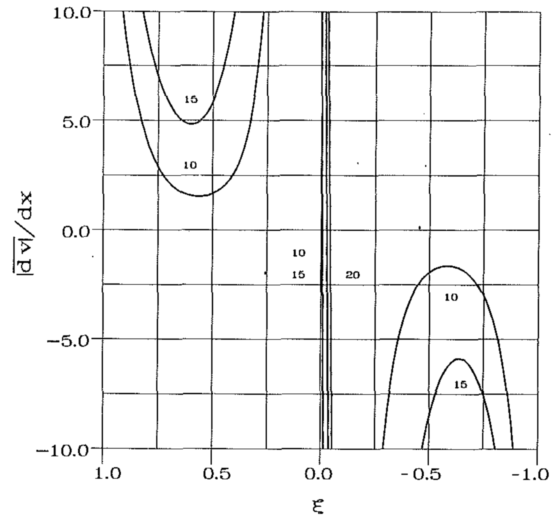

Fig. 6 $\overline{|\partial v|}/\partial x$ versus suction length for different Re_w (asymmetric problem)

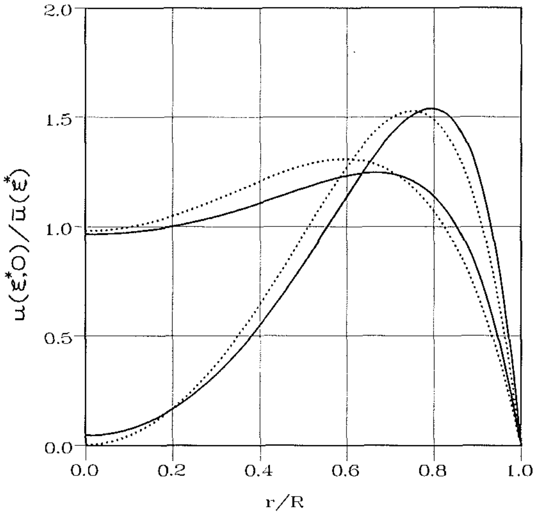

Fig. 7 Comparison between similarity solutions (dotted lines) and calculated velocity profiles (continuous lines) for $Re_w = 10$, $\xi^* = 0.01$

at the center of the tube as long as $u(\xi, 0)$ remains positive. From that point on, the dimensionless center line velocity increases until it reaches its maximum value at $\xi = -0.067$. The further development of the velocity profile shows a similar but reversed behavior in comparison to the first section of the tube ($0 < \xi < 0.75$) nearly reestablishing the parabolic velocity profile at $\xi = -1$.

To obtain positions on the tube axis where the dimensionless axial velocity profiles are in close agreement with the similarity profiles, the course of $\overline{|\partial v|}/\partial x$ is again plotted vs. the suction length (see Fig. 6).

As expected, now both solutions can be found downstream beyond the point of complete mass extraction in the immediate vicinity of the point where $\overline{|\partial v|}/\partial x$ becomes zero. As Fig. 7 shows for $Re_w = 10$, the profiles for the dimensionless axial velocity are in good, at least qualitative, agreement with the similarity profiles corresponding to the same wall Reynolds number.

It should be noted that for $Re_w = 9.105$, where similarity theory predicts only one solution, ξ^* again coincides with the point of complete mass extraction.

Conclusions

Based on a numerical analysis of laminar tube flow with uniform suction at the wall, it was shown that only for small suction rates ($Re_w < 2.3$) the state of flow at least locally achieves the similarity condition. For high suction rates ($Re_w \geq 9.1$) with symmetric entry conditions none of the published similarity solutions can be obtained. These can be observed to occur only in the asymmetric case, i.e., when the point where the axial center line velocity becomes zero, does not coincide with the point of complete mass extraction. This condition corresponds to the real situation where the tube is open at both ends and the nonporous sections at the inlets are of different lengths. Then all the similarity solutions can be obtained at distinct positions at the tube axis irrespective of the ratio of the nonporous lengths.

References

Friedman, M., and Gillis, J., 1967, "Viscous Flow in a Pipe With Absorbing Walls," ASME *Journal of Applied Mechanics*, Vol. 34, pp. 819–822.

Oran, E. S., and Boris, J. P., 1987, *Numerical Simulation of Reactive Flow*, Elsevier Science Publishing Co., New York, pp. 210–216.

Quaile, J. P., and Levy, E. K., 1975, "Laminar Flow in a Porous Tube With Suction," ASME *Journal of Heat Transfer*, Vol. 97, pp. 66–71.

Patankar, S. V., 1980, *Numerical Heat Transfer and Fluid Flow*, Hemisphere Publishing, pp. 133–134.

Schnitzlein, K., and Löwe, A., 1990, "Numerical Simulation of the Performance of Ceramic Fiber Coil Diesel Particulate Traps," *Chemical Engineering Science*, Vol. 45, pp. 2671–2678.

Terrill, R. M., and Thomas, P. W., 1969, "On Laminar Flow Through a Uniformly Porous Pipe," *Applied Science and Research*, Vol. 21, p. 3767.

Weissberg, H. L., 1959, "Laminar Flow in the Entrance Region of a Porous Pipe," *Physics of Fluids*, Vol. 2, pp. 510–516.

White, F. M., Jr., 1962, "Laminar Flow in a Uniformly Porous Tube," ASME *Journal of Applied Mechanics*, Vol. 29, pp. 201–204.

G. L. Chahine[1]

G. F. Frederick

R. D. Bateman

Dynaflow, Inc.,
Fulton, MD 20759

Propeller Tip Vortex Cavitation Suppression Using Selective Polymer Injection

This paper presents results of experiments where selective injection of a drag-reducing polymer solution into the tip vortex region of the blades of an 11.5 in. diameter propeller was effective in significantly delaying tip vortex cavitation. The most critical phase of the investigation was the selection of the position of the injection ports. For well-positioned injection ports, at a fixed water channel speed the propeller cavitation number had to be decreased by as much as 35 percent in order to reestablish cavitation inception. Injections of water and a viscous mixture of water and glycerin for the same conditions did not affect the inception characteristics of the modified blades. Preliminary analysis of the results indicates that the viscoelastic properties of the Polyox solution injected in the vortex core played a significant role in thickening the viscous core of the tip vortex and thus reducing the pressure drop at the vortex center without affecting circulation or lift.

1 Introduction

Over the past years intensive efforts have been devoted to the reduction of tip vortex cavitation. The first attempts involved the modification of the blade shape in order to unload the blade tip. Despite the success of these attempts, demand for increased speeds and performance lead to the research of other means to further decrease cavitation inception (Platzer and Sounders, 1979). These efforts paralleled similar efforts in aeronautical engineering where the tip vortices of large aircraft wings can cause a serious safety hazard to smaller following airplanes. Various schemes have been devised and tested on lifting surfaces or three-dimensional single blades. These include: installing an end plate, sail, or bulb at the foil tip; roughening the foil surface or edge; and injecting a mass of fluid from the tip. For marine propeller applications, however, attaching an additional structure to the propeller may cause additional cavitation problems as well as a penalty in efficiency.

Mass injection schemes appear to be the most attractive (Platzer and Sounders, 1979). The study of (Sounders and Platzer, 1981) showed that pure water injection at a significantly high rate was effective in delaying tip vortex cavitation inception. Less positive results were, however, obtained recently with pure water injection at lower rates whereas more encouraging results are seen with dilute polymer solutions (Fruman and Aflalo, 1990; Inge and Bark, 1983; Chahine et al., 1991). These results confirm earlier studies by Hoyt (1978) who showed significant effects of polymer solutions on vortex cavitation inception in a vortex chamber, and by Chahine and Fruman (1979), and Chahine (1981) who showed significant effects of dilute polymer solutions on the dynamics of *non-spherical* bubbles.

2 Experimental Setup and Facilities

The tests were carried out in the cavitation tunnel located on site. The test section is 12 ft long and 2 ft wide. Water depth in the test section may be varied from about 6 in. to 24 in. using a sluice gate which controls the position of the water free surface. Large windows on the two sides and bottom of the test section provide excellent accessibility for observation and flow visualization studies.

Test section velocities up to 30 fps can be achieved, and the ambient pressure can be reduced to about 2 ft of water absolute. The facility is equipped with a removable lid on which the strut pod and propeller were mounted to a shaft dynamometer to allow measurement of thrust and torque. A magnetic pick up tachometer measured the rotation speed of the propeller. Pressure taps and pitot tubes allowed measurement of pressures and velocities in the test section. A data acquisition system enabled timely recording of the various test parameters.

A stroboscopic system was used for the visualization study. The strobe element was fed signals through the external triggering input line from the magnetic pick up on the propeller shaft. This was extremely useful since it allowed a quick matching of the propeller rotational speed (rpm) with the strobe flashing. This effectively "froze" the propeller blade motion for observation and considerably simplified cavitation inception detection since the eye would in fact average over a large number of rotations the appearance (or not) of cavities along the propeller blades. In addition a delay box enabled control of the phasing of the flashes. A manual control in the form of a knob allowed the experimenter to select at will the par-

---

[1] Also Research Professor, Department of Mechanical Engineering, The Johns Hopkins University, Baltimore, MD.

Contributed by the Fluids Engineering Division for publication in the JOURNAL OF FLUIDS ENGINEERING. Manuscript received by the Fluids Engineering Division April 20, 1992; revised manuscript received September 28, 1992. Associate Technical Editor: T. T. Huang.

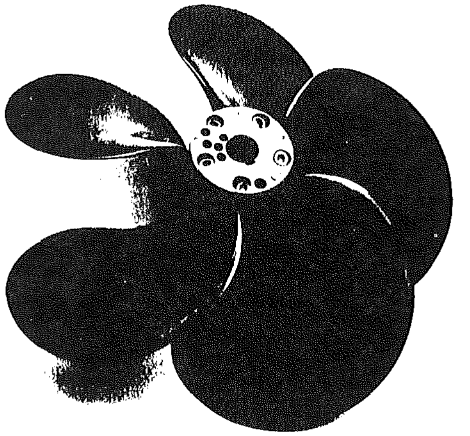

Fig. 1 Picture of propeller used in the injection tests

ticular blade of the five in the propeller to be observed and to place it (i.e., the location of its freezing) where it needed to be in the view field for easy observation. Thus, by simply modifying the phasing one was able to switch between blades being observed by bringing the desired one within the field of view. Photographic recording of the visual observation was done using the stroboscopic system described above and both still and video photography.

2.1 Polymer Solution Evaluation Setup. In order to control and test the polymer solutions needed for the injection tests a procedure for systematic testing of the polymer solution effectiveness was implemented. This procedure was based on the measurement of the viscous drag of a dilute polymer solution in a pipe flow, and allowed us to determine during the propeller tests if the polymer solution had degraded or not due to mechanical tearing of the molecules, aging, or to microbiological action, etc. This setup also allowed us to check periodically if the injected polymers were accumulating in the bulk water of the cavitation tunnel to a degree which would modify the basic properties of the water and alter the results. The test procedure was relatively simple. The polymer solution was force-fed using compressed air through a test pipe and the pressure difference across the test pipe (viscous drag) was measured using a differential pressure manometer, and the flow rate was measured using a simple volume measurement and a stop watch.

3 Propeller and Shaft Modifications

An old navy surface ship propeller model was selected for the tests (Fig. 1). This five-bladed propeller has an approximate diameter of 11.5 in. and was selected because it was designed to have low tip vortex cavitation inception characteristics and had been previously extensively tested (Barr et al., 1966). Important practical reasons also guided its choice; mainly it shape, size, and configuration type enable one with reasonable efforts to fit it with drilled injection ports without modifying the smoothness of its surface.

After photographic and visual observations of this propeller preliminary positions of injection ports were selected. Only two of the five blades were modified as described in the following. In order to assess two injection location possibilities, the two blades were modified differently, and were both fed simultaneously through the propeller shaft. This had the advantage of allowing simultaneous observation of the behavior of the flow about the unchanged propeller blades and about the two blades fitted with injection ports in exactly the same water flow conditions.

3.1 Injection System. The shaft was then modified, by partial hollowing and adaptation, to receive the modified propeller. Appropriate seals were positioned in the hub to create a feed chamber to receive the injection fluid and prevent its leakage. This chamber was directly fed using adequate piping from a feed tank located outside the channel and through the cover of the channel. The feed tank was a sealed chamber whose pressure could be controlled by the channel vacuum pump or a compressed air source and by a bleed valve. A metering device was located in the injection line and allowed monitoring of the flow injection rate.

The propeller was also fitted with a plenum that received the fluid arriving through the hollow shaft and then distributed it to the two blades fitted with injection ports. Leaks through the two end faces of the propeller hub were prevented by using face seals. A "fairwater" was adapted to attach the propeller and the shaft and streamline the incoming flow.

In order to avoid air entrainment into the channel only very limited cavitation inception tests were conducted above 15 ft/s. This had the disadvantage of preventing the study of the high J value range (see Eq. (1)).

An intensive series of tests were then conducted to:

(*a*) Determine baselines for tip vortex cavitation inception on the propeller.

(*b*) Observe dye injection from the injection ports into the flow.

(*c*) Observe effects of polymer injection on the tip vortex cavitation inception characteristics.

(*d*) Observe effects of water and water plus glycerin solution injection on the tip vortex cavitation inception characteristics.

Inception tests were conducted on the propeller by fixing the water speed in the test section and the ambient pressure in the channel and then changing the propeller rotation speed (rpm) until cavitation occurred. The rpm was then reduced very carefully until cavitation disappeared and the characteristics of the desinence point (rpm, P_{ambient}, V_{channel}) were recorded. The ambient pressure in the channel was then changed and the tests repeated until the full curve was obtained. Propeller thrust and torque were also simultaneously measured using the channel dynamometer.

4 Importance of the Injection Port Location

This study included the investigation of a series of injection port positions on the blade tip. The initial design of the injection lines was such that the tubes were cut off at about 1/8 in. before the blade tip. The tube tips were cut at an angle selected to match the blade shape then filled with epoxy and drilled at the desired locations (see Fig. 2(*a*)). Four injection port locations were selected in this manner—two on each of the blades numbered No. 1 and No. 3 (see sketches in Figs. 3(*a*) and 3(*b*)). Polymer solution injection from these locations showed no significant effect on cavitation inception or appearance.

Visualization studies using dye with the injection fluid showed that the injected polymer solution was not getting into the core of the tip vortex. Instead it was swept by the water flow along the surface of the blade and, as a result, took a path parallel to the tip vortex line near it. This indicated that the injection ports needed to be moved closer to the propeller tip. Therefore, an additional thin groove was machined on each blade and fitted with a 1/32 in. diameter tube in order to extend the location of the ports closer to the blade edge. One of the new injection ports was located on the pressure side of Blade No. 1 in order to force the injected fluid to sweep around the blade edge and swirl into the tip vortex core (Fig. 3(c)). The other injection port on Blade No. 3 was selected very close to the location of the root of the observed tip vortex cavity (Fig. 3(*d*)).

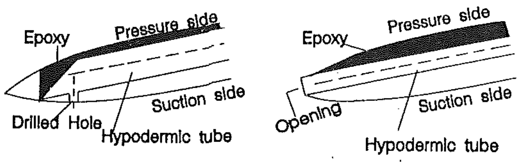

a. Initial Configuration b. Final Configuration

Fig. 2 Sketch of tube embedded in the propeller blade

Visualization tests of the entrainment of the injected polymer solutions from these new locations started showing some positive but marginal effects. After several other corrections described in Chahine et al. (1991) we decided to risk slightly modifying the blade surface smoothness and used larger injection tubes, but took the precaution of insuring that any resulting protrusion be on the blade pressure side so as to minimize any secondary cavitation. This also had the advantage of helping the injected fluid get into the tip vortex by placing it where the roll-up of the boundary layer occurred. We then fitted three 1/16 in. tubes into grooves, again with two on Blade No. 1 and one on Blade No. 3 (Figs. 3(*g*) and 3(*h*). On both blades the ports were as close as possible to the blade edge and were a little more in from the edge on the pressure side of each blade. The relative position of the single port (Blade No. 3) was in between the two ports on Blade No. 1. Significant effects of the polymer injection were immediately observed with this configuration on both blades. Since positive results were seen, a decision was made to postpone the search for better injection positions until the future, and to proceed with a detailed investigation of the effect of polymer concentration, injection flow rate, and nature of the injected fluid on the cavitation inception characteristics with this configuration of blade injection ports. Figure 2(*b*) shows a sketch of the injection tubes layout.

5 Summary of the Results of Injection Tests

A series of injection tests was then conducted using both modified blades. The importance of polymer solution concentration and polymer solution injection rate was investigated. The importance of the precise injection location was inferred from a comparison of the results of blades No. 1 and No. 3 modified as described above. In the figures presented below Blade No. 5 is one of the three unmodified blades and serves as a baseline to evaluate the two modified blades.

Figure 4 shows a summary of tests for three different Polyox WSR301 concentrations (3000, 5000, and 7000 ppm). As seen on the figure, the unmodified Blade No. 5 at a given cavitation number, σ, repeatability gave higher advance coefficients, J, than those obtained with Blades No. 1 and No. 3. The cavitation inception number, σ, and the advance coefficient J are defined as follows:

$$\sigma=\frac{P_{\mathrm{amb}}-P_v}{1/2\rho V^2},\quad J=\frac{V}{nD},\tag{1}$$

where P_{amb} is the far field pressure in the channel, P_v is the vapor pressure, ρ is the liquid density and V is the inflow velocity. D is the propeller diameter and n its rotation speed.

Similarly, Blade No. 3 equipped with a single injector almost always gave better results than Blade No. 1 equipped with two injectors, even though Blade No. 3 ejected half the amount of polymer solution as Blade No. 1. This highlights the fact that Blade No. 3 has a better injector location. It is apparent from the figure that significant effects due to the polymer injection are observed, especially at the higher values of σ. We presently do not have enough elements to conclude about any real dependence on σ, since the experimental conditions at the lower values of σ became polluted with air bubbles entrained in the test section of the channel. Note in addition that increasing rpm (reducing J) in fact amounts to a reduction of the actual cavitation number. This is not apparent only because of the particular definition of σ which does not reflect the local conditions within the tip vortex of the propeller. In order to minimize the effects of gaseous bubble entrainment on the tip vortex dynamics, most tests were conducted at a low channel test section velocity, V = 10 ft/s.

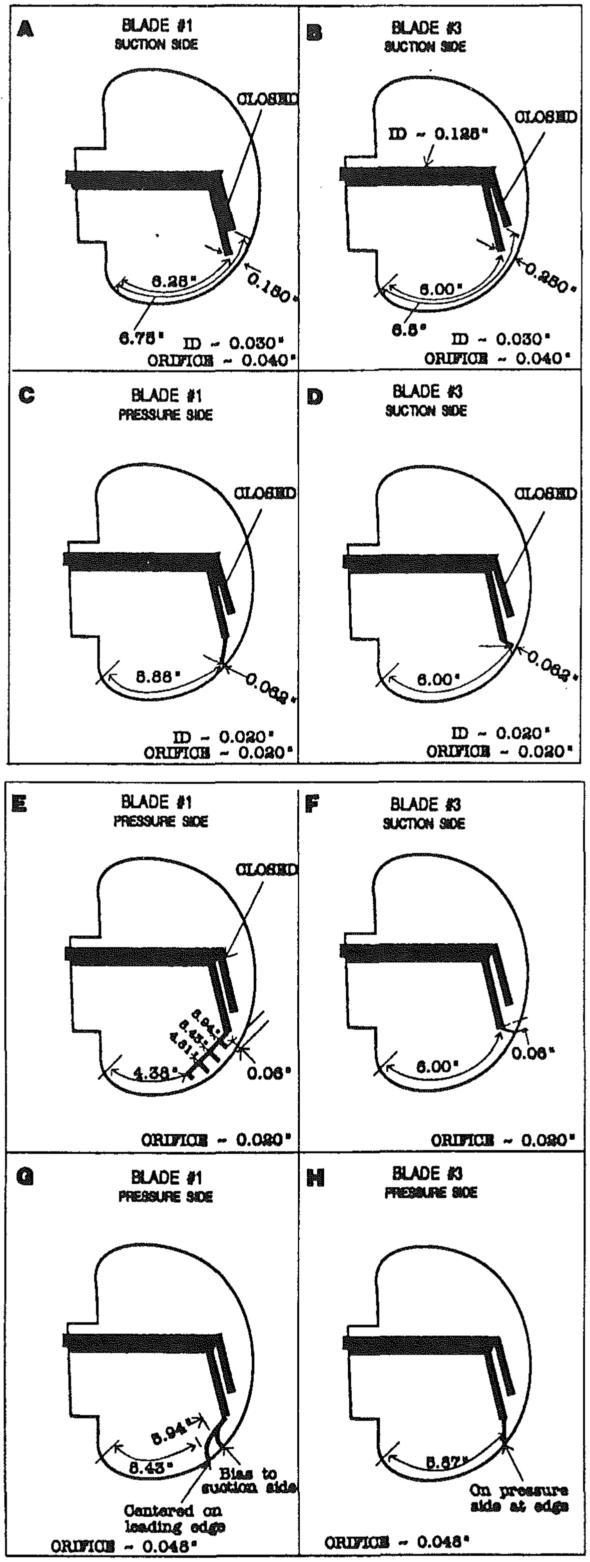

Fig. 3 Sketch of successive positions of injection ports on the two blades

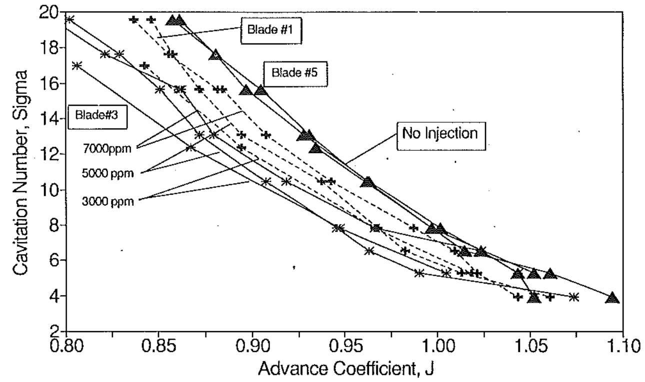

Fig. 4 Influence of various polyox solution injection on tip cavitation inception. V = 10 ft/s. (Uncertainty in advanced coefficient J = ±1.0 percent and in cavitation number = ±2.0 percent at 95 percent confidence level)

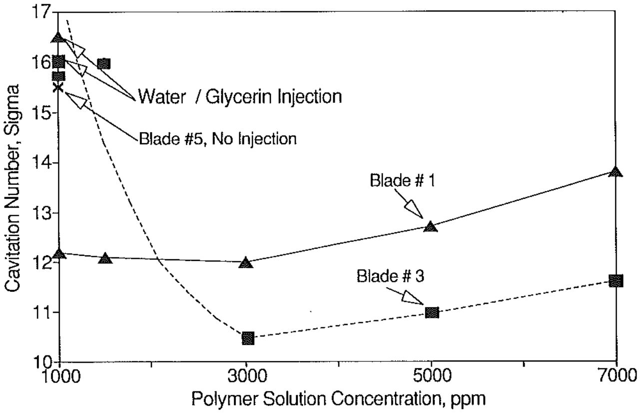

Fig. 5 Influence of the concentration of injected polyox solutions on tip vortex cavitation inception. V = 10 ft/s. J = 0.9 Composite picture of all runs—Comparison with water and water/glycerin solution injection. (Uncertainty in polymer solution concentration = ±1.0 percent and in cavitation number = ±2.0 percent at 95 percent confidence level)

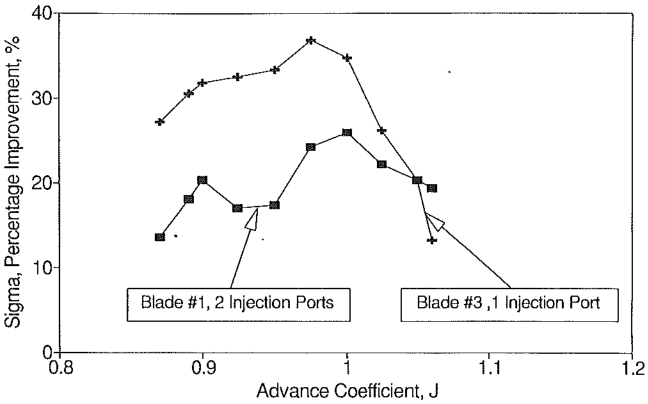

Fig. 6 Improvement in the cavitation number at inception—corresponds to Fig. 8. V = 10 ft/s, injection rate = 70 cc/min/injector. (Uncertainty in advanced coefficient J = ±1.0 percent and in percentage improvement of cavitation number = ±2.0 percent at 95 percent confidence level)

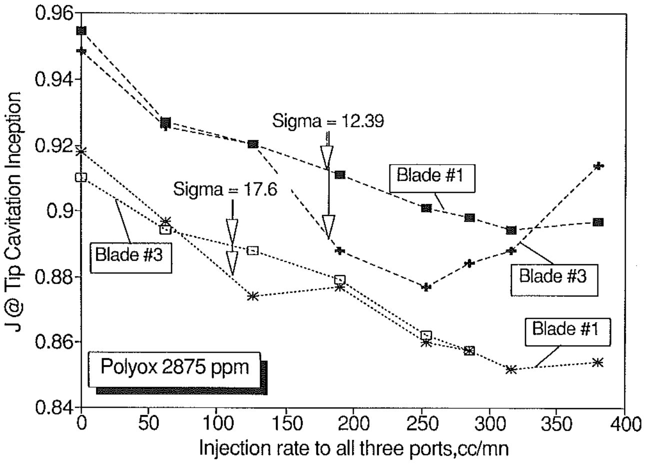

Fig. 7 Influence of the rate of injection of polyox WSR 301 on the advance coefficient J at tip vortex cavitation inception. V = 10 ft/s. (Uncertainty in injection rate ±3.0 percent and in advanced coefficient J = ±1.0 percent at 95 percent confidence level)

Figure 5 shows the influence of the concentrations of Polyox WSR301 injected on the cavitation number at inception. A range of concentration between 1000 and 7000 ppm is covered. This figure is a "cut" through the curves (cavitation number, σ, versus advance coefficient, J) at a constant value of J, here selected to be 0.9. Also shown on the same figure are the results obtained with water injection from the same blades. It appears from the curves that 3000 ppm is close to an optimum injection rate for the injection positions and the injection port sizes studied. At this point we do not have enough elements to explain the reasons for this behavior. We can only speculate that at the low flow rates tested, below some minimum polymer concentration (say 2000 ppm in this case) *selective* injection directly in the core is not effective and is comparable to water or glycerine solution injection. Injection of larger quantities of polymer solution on the periphery of the core (twice in this case) seems to be efficient at the lower polymer concentrations.

Figure 6 presents percentages of improvement—i.e., decrease—in the values of σ needed to obtain cavitation for the 3000 ppm Polyox solution case. This figure shows that improvement of the order of 35 percent in the conditions that cause cavitation inception to occur can be obtained, i.e. at the same depth the propeller rpm and the ship advance velocity can be increased by more than 17 percent before cavitation occurs.

It is very apparent from the above figures that the location of the injection port is very important for the elimination of steady tip vortex cavitation. Indeed even with twice the injection flow rate of Blade No. 3, Blade No. 1 achieves only about two thirds of the improvement observed with Blade No. 3. However, this conclusion seems to depend on the cavitation number. At the lower values of the cavitation number, σ, this limited test series (especially in terms of the flow speed) appear to indicate that the injection configuration of Blade No. 3 becomes much less good than Blade No. 1 which continues to be effective at delaying cavitation inception. Combined with our earlier comment about the presence of a large number of relatively large bubbles at the low cavitation numbers and the inefficiency of polymer injection in preventing the growth of these bubbles, it may be that the scheme on Blade No. 1, by injecting the polymers not exactly in the core region but on its periphery, may be efficient in delaying the capture of the large bubbles by the vortex. These comments are, however, only of a speculative nature at this point and need to be confirmed in future work. In any case the results of the tests presented here at the lower ambient pressures and at the higher channel velocities (higher J) are to be reconfirmed in future studies due to tunnel limitations as explained earlier.

5.1 Influence of the Injection Rate. The influence of the injection rate on the effectiveness of polymer injection in delaying tip vortex cavitation is illustrated in Fig. 7. In order to reduce testing time, a channel speed and an ambient pressure were first selected. Then for each injection flow rate, the rpm

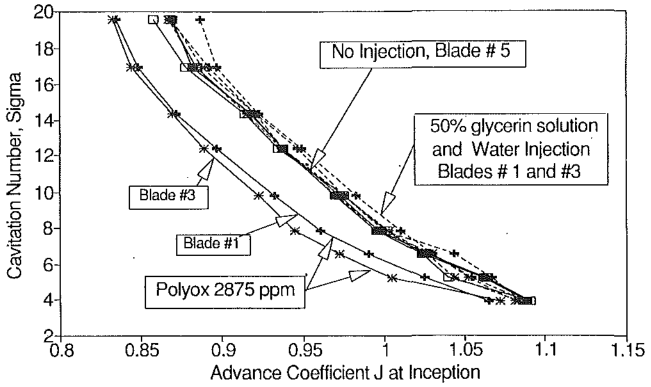

Fig. 8 Comparison of cavitation inception curves at blade #5 with no injection and blades #3 (1 injection port) and #1 (2 injection ports) with pure water, polyox and glycerine solutions. Injection rate = 100 cc/min/port. (Uncertainty in advanced coefficient $J = \pm 1.0$ percent and in cavitation number = ±2.0 percent at 95 percent confidence level)

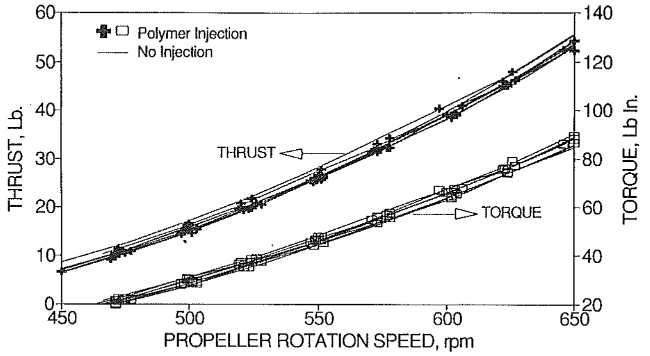

Fig. 9 Comparison of thrust and torque on propeller with and without polymer injection at several ambient pressure (0.18 atm $< P_{amb} < 0.79$ atm). Polyox WSR 301-2875 ppm. Injection rate 250 cc/min, 3 injectors, $V = 10$ ft/s, (Uncertainty in propeller rotation speed = ±0.5 percent and in thrust = ±2.0 percent at 95 percent confidence level)

of the propeller—and therefore the advance coefficient, J—at which cavitation inception would occur was noted. When the injection rate is zero the J value is that of the unmodified propeller. For nonzero values of the injection rate a reduction in the value of J (an increase in rpm) is needed for cavitation inception to occur. Figure 7 shows the results obtained for two values of the cavitation number, σ. Both values of σ—12.4 and 17.6—were selected in a range where gaseous bubble influence was minimal. The observed differences between the values of J at zero injection rate indicate the amount of data uncertainty (e.g. 0.95 and 0.955 for $\sigma = 12.4$, indicate an uncertainty of the order of 1 percent). A significant amount of drop in the value of J can already be observed at an injection rate for all ports of 60 cm^3/min (about 20 cm^3/min/port). (We would like to note here that we were not able to measure directly the rate in each port during the tests. However, preliminary tests conducted on the modified propeller outside of the channel showed practically no difference between the three ports. During the tests the flow rates depend obviously on the local pressure at the exit of each port. Since all three ports used for tests reported on in the paper were generally in the same vicinity, the variation of the pressure drop between the injection port and the three ports was negligible so that we can assume for an order of magnitude estimate that the flow rates were about the same in all three injectors.) At that injection rate J decreased by 3 percent. This performance improvement continues to increase with the injection rate. At the relatively low cavitation number, $\sigma = 12.4$, Blade No. 3 appears to exhibit a minimum value of the advance coefficient at inception for the total flow rate in the range of 230–240 cm^3/min (75–80 cm^3/min per port). At this minimum, the improvement in J is about 8 percent. On Blade No. 1 and for both modified blades at $\sigma = 17.6$ there is no distinct maximum cavitation reduction point. However, the amount of cavitation retardation appears to attain a saturation range when the injection rate exceed about 310 cm^3/min for all ports. These results indicate the existence of an optimal injection rate.

5.2 Injection of Water and Glycerin. In order to check if the positive results observed earlier were due to mass injection only, or because the injected mass was very viscous, or if directly related to the viscoelastic character of the drag reducing polymers, we tested the influence on the propeller tip vortex cavitation of the injection of pure water and of a 50 percent mixture of water and glycerin.

Figure 8 shows the results of two series of tests. In the first series a solution of 3000 ppm of Polyox WSR301 is injected from Blade No. 1 equipped with two injection ports, and from Blade No. 3 equipped with a single injection port. In the second series of tests shown in the figure pure water is injected from Blade No. 1 and Blade No. 3 at the same injection rate (about 70 cm^3/min/injector) and the new characteristics of these blades (cavitation number, σ, versus advance coefficient, J) are compared with those of Blade No. 5. The injection of the same flow rate of pure water is seen to have little effect on the cavitation inception of the blades. In fact a small effect in the opposite direction (enhanced or earlier cavitation) can be observed on blade No. 1. This is probably due to the injection with the water of some bubble nuclei. This could also be interpreted as due to cavitation of the injected water jet. During injection of polymer solutions this secondary effect is overshadowed by the opposing cavitation inception retardation effect (pressure rise in the vortex viscous core) due to the presence of the viscoelastic fluid.

Also shown on the figure is the injection of a highly viscous mixture of 50 percent water and 50 percent glycerine—viscosity of the order of 10 centipoises, close to that of a 3000 ppm concentration Polyox solution. Here again little effect of the viscous solution injection is seen. If any, the effect seems again to be negative on Blade No. 1 showing for a given advance coefficient, J, an increase in the cavitation number at tip vortex cavitation inception.

The results presented above strongly indicate that the viscoelastic properties of the polymer solutions are responsible for the observed significant delay in the cavitation inception of the tip vortex cavitation on the tested propeller.

5.3 Influence on Thrust and Torque. The positive results observed in these tests would not be of interest if they were accompanied by any detrimental effects such as loss of performance, due to increased drag or reduced thrust or torque. This is the case for a *homogeneous*, *uniform* solution of polymers which induces improvement in cavitation inception characteristics but is also accompanied by an undesirable loss of thrust. To investigate this, thrust and torque of the propeller were measured simultaneously during the tests in the presence and absence of injection. The results of these measurements are shown in Figs. 9.

The solid lines were obtained in absence of any fluid injection, while the *unconnected* symbols indicate measurements made when a solution of 2875 ppm of Polyox WSR301 was injected from both Blade No. 1 equipped with two injection ports and Blade No. 3 equipped with a single injection port. The injection rate from the three ports totaled 250 cm^3/min. Figure 9 indicates that no measurable influence of the polymer injection is obtained on either thrust or torque. Details of the observations (Chahine et al., 1991) clearly indicate that variations in thrust and torque on the curves in Fig. 9 are due to changes in the ambient pressure. Variations due to mass injection of the polymer solution could not be detected. This is

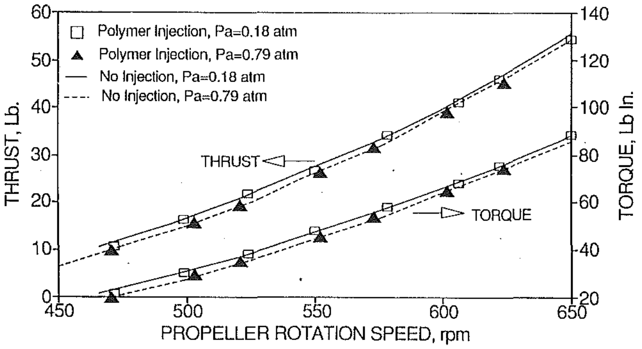

Fig. 10 Comparison of thrust and torque on propeller with and without polymer injection at high ambient pressure in the channel. Polyox WSR 3012875 ppm. Injection rate = 250 cc/min, 3 injectors, V = 10 ft/s. (Uncertainty in propeller rotation speed = ±0.5 percent and in thrust = ±2.0 percent at 95 percent confidence level)

illustrated in Fig. 10 for one particular value of the ambient pressure.

These results allow us to conclude that the tip vortex cavitation inception improvements observed with the injection of polymer solutions are not accompanied by any measurable decrease in propeller performance.

6 Preliminary Analysis

6.1 Importance of the Injection Location. The results obtained in this study corroborate results obtained by Fruman et al. (1990) on two elliptical planform three-dimensional foils. These observations, as well as LDV measurements of the velocity profile across the tip vortex strongly indicated that operating the foil in a homogeneous polymer solution reduces the value of tip vortex cavitation inception by decreasing the intensity of the circulation, Γ. When the polymer solution is injected exclusively in the tip vortex core area, the circulation is not modified. Instead, laser velocimetry indicated that the viscous core is thickened and the maximum tangential velocity is reduced. This results in an increase in the pressure at the axis of the tip vortex and a decrease in the cavitation inception number, σ, without any decrease in the foil lift.

This could be intuitively interpreted as follows. The "inviscid" portion of the vortex flow remains unmodified by the *selective* polymer injection (therefore, Γ remains the same), while the flow in the viscous core is modified and its angular velocity reduced due to the viscoelastic effects of the solution (therefore, the pressure at the axis is raised). From the viewpoint of potential flow theory, the lift and thrust due to the blade arises from the vortex sheet formed at the trailing edge of the blade. The effect of causing the entire liquid to contain polymer may then be thought to cause a 'smearing' of this sheet, thus weakening it and reducing lift. Similarly, locating the injection ports inappropriately might cause some undesirable effects. Thus it is critical that the injection be performed in a manner such that the polymer solution is directly injected into the vortex core.

This reasoning is supported by a simple two-dimensional Rankine vortex model. In this model the tangential velocity, V_θ, is related to the vortex circulation, Γ, by the relations:

$$V_\theta = \frac{\Gamma}{2\pi r}; \quad r \geq a_c; \quad V_\theta = \omega r = \frac{\Gamma r}{2\pi a_c^2}; \quad r \leq a_c. \tag{2}$$

The pressure field is then known analytically and given in a non-dimensional form by the equations:

$$\bar{P}(r) = 1 - \frac{\Omega}{2}\left(\frac{a_c}{r}\right)^2; \quad r \geq a_c,$$

$$\bar{P}(r) = 1 - \Omega\left[1 - \frac{1}{2}\left(\frac{r}{a_c}\right)^2\right]; \quad r \leq a_c, \tag{3}$$

where pressures are normalized with the local pressure, P_{amb}, and Ω is given by the expression:

$$\Omega = \frac{\rho}{P_{\text{amb}}}\left\{\frac{\Gamma}{2\pi a_c}\right\}^2. \tag{4}$$

This equation shows that the pressure on the axis can be raised by either increasing a_c or decreasing Γ. The injection of Polyox solution has apparently increased the viscous core size, a_c, since the thrust and torque of the propeller, thus Γ were not significantly modified.

6.2 Explanation of Observed Results. Different mechanisms may contribute to increasing the pressure on the vortex axis depending on how mass injection takes place and on the substance used. Three distinct mechanisms can be cited here:

1. The rotational flow about the vortex core is decelerated by transfer of momentum from the existing mass of fluid to the newly added mass.
2. In the case of an injected fluid that is more viscous than water (e.g., polymer or water/glycerin solutions), the viscosity of the fluid in the core is increased by addition of the injected substance. This increased viscosity modifies the vortical flow in such a way as to reduce rotational speed, and thus circulation.
3. In the case of polymer solution injection, the rheology of the fluid is modified from Newtonian to viscoelastic. Additional strain and stress forces come into play and absorb a portion of the rotational energy of the vortex. These added stresses also modify the pressure field, raising the pressure in the core center away from vapor pressure.

6.3 Mass Injection Effect. Mechanism 1 should in principle apply to both water and polymer additives. This mass addition can be modeled by placing a point source at the injection port on the hydrofoil or propeller blade. Then the equations of continuity, momentum and vorticity in the inviscid approximation are given by:

$$\nabla \cdot \underline{V} = \dot{m}$$

$$\frac{\partial \underline{V}}{\partial t} + \underline{V} \cdot \nabla \underline{V} = -\frac{1}{\rho}\nabla p - \dot{m}(\underline{V} - \underline{V}_s) - \frac{\underline{F}}{\rho} + \underline{g},$$

$$\frac{D\underline{\omega}}{Dt} = \underline{\omega} \cdot \nabla \underline{V} - \dot{m}\underline{\omega}, \tag{5}$$

where $\underline{V}$ is the fluid velocity, $\underline{\omega}$ the vorticity vector, ρ the fluid density, and p the pressure. $\dot{m}$ corresponds to the relative rate of mass increase due to the source. The momentum equation includes the reaction force $\underline{F}$ on the point source.

This force may work to help increase the thrust of the propeller. The vorticity equation also has an additional term due to the point source. Since the injection of mass into the flow corresponds to a positive value of the source strength, the implication is that the last term in the vorticity equation will help reduce the vorticity of the total flow. This equation suggests that it is important to locate the injection port in the high vorticity region of the tip vortex. Based on the results presented here this effect appears to be minimal at the considered flow rates of injection of water or a purely viscous fluid. It is speculated from previous observations that polymer injection is more effective since it is accompanied with a "swelling" of the injected jet in the surrounding fluid. This swelling does not occur with a purely Newtonian fluid.

6.4 Importance of Using a Viscoelastic Fluid. A universally accepted model for polymer solutions behavior does not exist. However, some aspects of the behavior can be highlighted by using the following Oldroyd 3-parameter viscoelastic behavior

$$\sigma_{ij}^D + \tau_g \frac{d\sigma_{ij}^D}{dt} = 2\mu\left(\epsilon_{ij}^D + \theta_g \frac{d\epsilon_{ij}^D}{dt}\right), \tag{6}$$

where σ_{ij}^D represents the deviatoric components of the stress and ϵ_{ij}^D the deviatoric components of the strain. θ_g and τ_g are characteristic relaxation times of the polymer. To account for this behavior of the viscoelastic fluid, the following generalized Navier Stokes equation can be used:

$$\rho\left[\frac{\partial \underline{V}}{\partial t} + \underline{V}\cdot\nabla\underline{V}\right] = \rho\underline{g} + \nabla\cdot(-p\underline{\underline{I}} + \underline{\underline{\sigma}}^D). \tag{7}$$

The last term in Eq. (7) is related to the velocity gradients and the flow history through the constitutive Eq. (6). In the case of a line vortex-flow and a simple Rankine vortex, the radial component of Eq. (7) simplifies to:

$$\frac{\partial(p-\sigma_{rr}^D)}{\partial r} = \frac{\partial p^*}{\partial r} = \rho\,\frac{V_\theta^2}{r} + \frac{(\sigma_{rr}^D - \sigma_{\theta\theta}^D)}{r}, \tag{8}$$

p^* or $(p-\sigma_{rr}^D)$ is the normal stress in the fluid which has to decrease below p_v for cavitation to occur. For a Newtonian fluid $\sigma_{rr}^D = \sigma_{\theta\theta}^D = 2\mu\epsilon_{rr}^D = 2\mu\epsilon_{\theta\theta}^D = 0$. For a viscoelastic fluid described by Eq. (6), σ_{rr}^D and $\sigma_{\theta\theta}^D$ can be finite and are determined by the equations:

$$\sigma_{rr}^D = \sigma_{ro}e^{-t/\tau_g}; \quad \sigma_{\theta\theta}^D = \sigma_{\theta o}e^{-t/\tau_g}. \tag{9}$$

σ_{ro} and $\sigma_{\theta o}$ are initial condition values of pressure-like normal stresses along the radial and tangential directions. They could be introduced, for instance, through initial non-zero values of the radial velocity V_r due to the polymer mass injection.

Considering the case where the flow due to the mass injection has a behavior intermediate between that due to a spherical source and a line source (to account for "swelling"); say

$$V_r = q/r^\alpha; \quad 1 \le \alpha \le 2, \tag{10}$$

and integrating the momentum equation between a point M in the vortex core and "infinity" one obtains:

$$p^*(M) = p_{\text{Newt}}(M) + \frac{2\mu q}{r_M^{\alpha+1}}\, e^{-t/\tau_g}, \tag{11}$$

where $p_{\text{Newt}}(M)$ is the value of the pressure at M if the fluid were Newtonian, μ is the dynamic viscosity, and τ is the polymer relaxation time to deformation. Equation (7) shows that a pressure increase relative to the Newtonian case is observed if a "swelling" viscoelastic core is present. With the simplified model used this increase decays exponentially with time with a time constant equal to the polymer relaxation time for deformation, τ_g. This pressure increase is probably maintained by a feedback mechanism between injection and flow field behavior. When the pressure rises the injection rate goes down, then goes back up as soon as the pressure drops.

7 Conclusions

Following an extensive but rather empirical effort to find a good location for polymer solution injection in the tip region of a propeller, this study demonstrated the feasibility of the concept of tip vortex cavitation suppression by selective polymer injections. The following conclusions were drawn from the study:

1. Injection of solutions of a drag reducing polymer into the tip vortex area of the blade was effective in delaying tip vortex cavitation inception.
2. Some combinations of polymer concentration injection rate (in the range 3000 ppm and 80 cm^3/min/part) showed a decrease in the cavitation number at inception as large as 35 percent.
3. Injections of pure water and a 50 percent water-glycerin viscous mixture did not show any improvement in the tip vortex cavitation characteristics of the propeller.
4. The location of the injection port was seen to be extremely important. Optimum injection port location appears to be on the suction side tip of the blade at the tip vortex attachment point, with injection directly into the core. Out of two configurations studied, the better one achieved improvements in the cavitation inception characteristics that were at least 50 percent better than the second one, even though the less performing configuration had injection rates twice as large.
5. The selective local injection of the polymer solutions did not adversely affect either propeller torque or thrust.
6. Selective injection makes the concept practical by reducing the weight of the polymers needed for injection and by not effecting the propeller performance.

These conclusions are obviously to be confirmed for other ranges of the variables that were not tested in this study, more precisely for higher values of J, and the Reynolds number.

8 Experimental Uncertainty

The pressure in the water tunnel is measured with an error of ±100 Pascals. The water channel speed is measured with a pitot tube allowing an error of 0.5 percent. This results in a maximum possible error on the cavitation number of less than 2 percent in the worst experimental conditions (lowest ambient pressures, highest velocities). Since cavitation inception was detected visually one should add an error of about 1 percent due to the observer's sensitivity to the appearance of cavitation events. Errors due to variations in the channel nuclei contents which could be large are minimized by the fact that we conducted comparative tests (with and without polymer injection) in the same water conditions. Repeatability accuracies of the data presented is within 1 percent. The propeller rotation speed is measured with an accuracy of 0.5 percent. The polymer solution concentration rate is obtained with an accuracy of 1 percent. The error in the measurement of the polymer injection rate can be as high as 3 percent, while the thrust and torque of the propeller are measured with an accuracy of 2 percent.

Acknowledgment

The work described in this paper was conducted in execution of an SBIR contract sponsored by the Naval Sea Systems Command, Washington D.C. We would like to acknowledge the contributions of several colleagues at DYNAFLOW, Inc.

References

Barr, R. A., Walker, K. W., and Lindenmuth, W. T., 1966, "The Design and Testing of a Series of Six Propellers...," Hydronautics, Inc. Technical report 455-2, Apr. (confidential).

Chahine, G. L., 1981, "Experimental and Asymptotic Study of Nonspherical Bubble Collapse," *Proceedings IUTAM Symposium on Mechanics and Physics of Bubbles in Liquids*, Pasadena, CA, June also in *Applied Scientific Research*, Vol. 38, pp. 187-197, 1982.

Chahine, G. L., Frederick, G. S., and Bateman, R. D., 1991, "Propeller Tip Vortex Cavitation Suppression Using Selective Polymer Injections," DYNAFLOW, Inc. Technical Report 91001-1, Aug.

Chahine, G. L., and Fruman, D. F., 1979, "Dilute Polymer Solution Effects on Bubble Growth and Collapse," *Physics of Fluids*, Vol. 22, No. 7, pp. 1406-1407.

Fruman, D. H., and Aflalo, S. S., 1990, "Tip Cavitation Inhibition by Drag-Reducing Polymer Solutions," ASME JOURNAL OF FLUIDS ENGINEERING, Vol. 112.

Hoyt, J., 1970, "Vortex Cavitation in Dilute Polymer Solutions," *Cavitation and Multiphase Flow Forum*, Fort Collins, CO, June.

Inge, C., and Bark, G., 1983, "Tip Vortex Cavitation in Water and in Dilute Polymer Solutions," Royal Institute of Technology Technical Report TRITA-Mek 83-12.

Platzer, G. P., and Souders, W. G., 1979, "Tip Vortex Cavitation Delay with Application to Marine Lifting Surfaces: A Literature Survey," DTNSRDC-79/051.

Souders, W. G., and Platzer, G. P., 1981, "Tip Vortex Cavitation Characteristics and Delay of Inception on a Three-Dimensional Hydrofoil," DTNSRDC-81/007.

P. Ligneul
Research Head,
Schlurnberger Industries,
92542 Montrouge, France;
Formerly, Research Scientist,
Bassin D'Essais des Carenes,
Paris, France

R. Latorre
Professor,
School of Naval Architecture and
Marine Engineering,
University of New Orleans,
New Orleans, LA 70148

Study of Nuclei Distribution and Vortex Diffusion Influence on Nuclei Capture by a Tip Vortex and Nuclei Capture Noise

Earlier studies of cavitation nuclei behavior in the presence of a Rankine tip vortex have shown that the nuclei is attracted or captured by the vortex pressure field and during this process noise is produced by the rapid nuclei growth. The present paper extends the study of Ligneul and Latorre (1989). The capture of nuclei by the tip vortex was characterized by an index M which depends on the nuclei radius, initial location, and the vortex circulation. To clarify the nuclei distribution effected by this capture process, the frequency of nuclei capture is derived in terms of the nuclei distribution N(R). The influence of the tip vortex axial diffusion on the nuclei capture process is formulated and number results presented to show how vortex diffusion delays the nuclei capture. The paper closes with a discussion of the numerical simulation of the nuclei capture and noise generation by the tip vortex.

Introduction

At certain conditions encountered during the operation of marine propeller and other lifting surfaces, the radiated noise increases due to the growth and collapse of cavitation nuclei in the low pressure regions of the tip vortex shed from the blade tips, (Ross, 1976; Hsu, 1991). Theoretical and numerical studies by Bovis (1980), Latorre (1980), Levkovskii (1978), Ligneul and Latorre (1989) have shown that the nuclei in the presence of a tip vortex is attracted to the tip vortex core. The rapid growth of the nuclei results in the characteristic bursts of the noise signal before visible tip vortex cavitation appears (Latorre, 1980). At higher propeller revolutions, the tip vortex cavity forms with a relatively smaller increase in the inception noise level.

In the analysis of Latorre and Ligneul (1989) the capture of spherical nuclei in the presence of a tip vortex was modeled and the analytical calculations compared with available numerical results.

In the present work, the capture model developed by Ligneul and Latorre (1989) is extended to include:

1 Influence of tip vortex diffusion on the nuclei capture process.

2 Influence of variation of nuclei size in the incoming fluid.

3 Clarification of the noise generation process as consisting of a monopole acoustic pressure q_m and a dipole acoustic pressure q_d.

Modeling the Nuclei Capture by the Tip Vortex. In the nuclei capture model the tip vortex is idealized as a Rankine vortex. The experimental measurements of the tip vortex structure by Steinbring et al. (1991) show that the tip vortex flow resembles a Rankine vortex. These measurements show the velocity distribution is linear across its diameter while the outer tangential velocity distribution decreases approximately as $1/r$.

Ligneul and Latorre (1989) modeled the capture of a spherical nucleus of radius R_0 located a distance L_i from the center of a Rankine vortex with circulation Γ and radius R_1 (Fig. 1).

The relative magnitude of the initial acceleration in the e_r and e_θ (Fig. 1) directions was found to be characterized by a parameter M, defined as follows

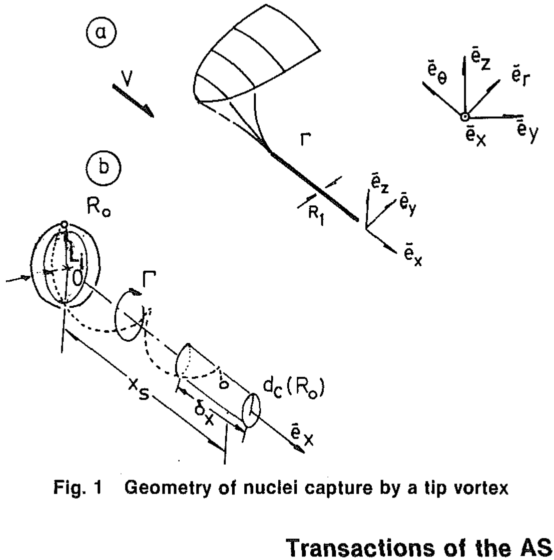

Fig. 1 Geometry of nuclei capture by a tip vortex

Contributed by the Fluids Engineering Division for publication in the JOURNAL OF FLUIDS ENGINEERING. Manuscript received by the Fluids Engineering Division March 4, 1992; revised manuscript received January 7, 1993. Associate Technical Editor: D. P. Telionis.

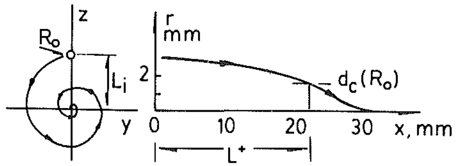

Fig. 2 Comparison of nuclei capture length L^* with numerical results of Latorre (1980)

$$L_i \geq R_1 \quad R_a \frac{L_i}{R_0} = M$$

$$L_i \leq R_1 \quad R_a \frac{R_1}{R_0} = M \tag{1}$$

where

$$R_a = \left(\frac{6\pi\nu}{\Gamma}\right)^{1/2} \tag{2}$$

This leads to three cases based on the order of M.

(i) Case I $M \gg 1$: The rotation acceleration is not larger than the attraction acceleration. The spherical nuclei undergo rotation around the vortex before the attraction occurs.

(ii) Case II $M = 1$: The rotation acceleration and attraction acceleration have the same order of magnitude. The spherical nuclei undergo both rotation and attraction.

(iii) Case III $M \ll 1$: The attraction acceleration is larger than the rotation. The spherical nuclei is captured with minimum rotation around the vortex center.

Illustration of Nuclei Capture by the Tip Vortex. The nuclei trajectory in the presence of a tip vortex was obtained by numerical integration of the governing equation of nuclei growth and motion by Latorre (1980). The solid line in Fig. 2 shows the numerical obtained trajectory for $M = 1.72$. Following the classification scheme, for $M > 1$ the nucleus initially rotates around the tip vortex before being captured. In order to isolate the capture phase of the trajectory, Ligneul and Latorre (1989) introduced the critical radial distance from the tip vortex axis denoted by $d_c(R_0)$ and a corresponding critical axial length L^*.

$$d_c(R_0) = \frac{R_0}{R_a} \tag{3}$$

and

$$L^* = VT_\upsilon \left(\frac{L_i}{d_c(R_0)}\right)^4 \tag{4}$$

where

$$T_\upsilon = \frac{R_0^2}{3\upsilon} \tag{5}$$

Figure 2 illustrates how $d_c(R_0)$ and L^* define the point on the nucleus trajectory when the nucleus rotation around the vortex is completed and the nucleus enters the tip vortex and is captured. This comparison shows that by determining $d_c(R_0)$ and L^* it is possible to isolate the nucleus capture. It is possible to model the influence of vortex diffusion as well as the influence of nuclei distribution $N(R)$ on the tip vortex capture process for $M \leq 1$.

Modeling of Nuclei Distribution *N(R)* Capture. As discussed earlier, the initial nucleus position L_i and radius R_0 at the time corresponding to $x = 0$ influence the frequency of the nuclei capture occurring at a given axial position $x > 0$.

The frequency (number per unit time) f of nuclei passing through a ring element at radius $r = L_i$ and width δr is given by:

$$f\delta r = 2Vrdr \int_{R_{\min}}^{R_{\max}} n(R)dR \tag{6}$$

where $R_{\min}$ and $R_{\max}$ are the minimum and maximum radii of the nuclei.

Each nucleus transverses a distance $x_s(R_0)$ before entering the critical radius $R = d_c(R_0)$ (Fig. 1(*b*)). The distance x_s which corresponds to L^* and can be approximated as:

$$x_s = \frac{12\pi^2 V}{\Gamma^2} \frac{r^4}{R_0^2} \tag{7}$$

Therefore the ring thickness δ corresponds to a cylinder at x_s with length increment δ_x:

$$\delta_x = \frac{48\pi^2 \upsilon V}{\Gamma^2} \frac{r^3 \delta r}{R_0^2} \tag{8}$$

The cylinder $(x_s, \delta x_s)$ is determined by the range of nucleus size $R - (\delta R/2)$ to $R + (\delta R/2)$:

$$N[R, \delta R] = \int_{R-(\delta R/2)}^{R+(\delta R/2)} N(R)dR \tag{9}$$

where $N(R, \delta R)$ or $N(R)$ is simply the number of nuclei per unit volume. Thus the frequency of nuclei passing

$$f = F[R, \delta R, \delta r, r] \tag{10}$$

is transformed into a density of nuclei growing events given as a function per unit length

$$\frac{\partial f}{\partial x} = \frac{R^2 N(R, \delta R)}{r^2} \cdot \frac{\Gamma^2}{24\pi\upsilon} \tag{11}$$

or in terms of radius r:

$$\frac{\partial f}{\partial r} = \frac{RN(R)}{\sqrt{x}} \frac{\Gamma}{4} \sqrt{\frac{V}{3\upsilon}} \tag{12}$$

The frequency of events is:

Nomenclature

$D(\mathrm{Re})$ = nuclei drag coefficient
$d_c(R_0)$ = critical radial distance
f = frequency of nuclei per unit time
f_0 = initial nuclei frequency
L_i = initial nuclei position
L_0 = location at which nuclei enters capture phase
$N(r)$ = nuclei size distribution
M = nuclei capture index
m = distance from nuclei to observer

P = pressure
Pac = acoustical pressure
P_v = vapor pressure
q_d = dipole acoustical source
q_m = monopole acoustical source
r = nuclei radius
R_a = tip vortex parameter
R_e = nuclei Reynolds number
R_0 = initial nuclei radius
R_1 = vortex radius
r = nuclei trajectory radius
T = time

T_υ = viscous time scale
V = velocity
V_θ = tangential nuclei velocity
x = axial distance
upper bars = nondimensional values
Γ = vortex circulation
χ = distance
α = nuclei parameter
δ_r = vortex-nuclei parameter
γ = diffusion
ρ = fluid density
ν = fluid viscosity

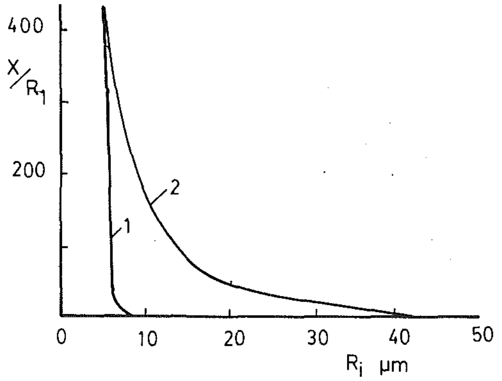

Fig. 3 Study I. Results of nuclei capture simulation by tip vortex. Nuclei radius R_0 and capture location X/R_1 (details in Table 1). 1) Calculation without viscous diffusion; 2) calculation with viscous diffusion.

$$f=\frac{\Gamma}{2}\sqrt{\frac{XV}{3\upsilon}}\,RN(R)+f_0 \tag{13}$$

The initial value of f_0 is determined by the nuclei directly influenced so that

$$r_0 \leq d_c(R_0) \tag{14}$$

Thus the frequency f_0 is described by the initial number of nuclei passing through the disk of radius $d_c(R_0)$ shown in Fig. 2.

$$f_0=\int_{r=0}^{d_c(R_0)} VN(R,\delta R)rdr \tag{15}$$

The frequency of nuclei capture can be written as:

$$f=\frac{\Gamma}{2}\sqrt{\frac{xV}{3\upsilon}}\,N(R_0)R+\int_{r=0}^{d_c(R_0)} VN(R)rdr \tag{16}$$

Influence of Tip Vortex Diffusion. The solution of Bovis (1980) is taken as the first approximation for the tip vortex with viscous diffusion:

$$V_\theta=\frac{\Gamma}{2\pi r}\,(1-e^{\frac{-r^2}{4\upsilon t}}) \tag{17}$$

This translates into the radial pressure gradient:

$$\frac{\partial P}{\partial r}=\frac{V_\theta^2}{r}=\frac{\Gamma^2}{4\pi^2 r^3}\,(1-e^{\frac{-r^2}{4\upsilon t}}) \tag{18}$$

The radial pressure gradient in Eq. (18) results in a new nondimensional equation for nuclei trajectory radius r which is based on the governing equation obtained by Ligneul and Latorre (1989):

$$\ddot{\bar{r}}=-3\dot{\bar{r}}\left(\frac{\dot{R}}{R}+\frac{D(R_e)}{R}\right)-\left(\frac{2\epsilon^2\alpha^4\gamma^2}{r^3}\right) \tag{19}$$

where the bubble drag coefficient is given as a function of Reynolds number Re:

$$D(\mathrm{R_e})=1+0.197\mathrm{R_e^{0.63}}+2.6\times10^{-4}\mathrm{R_e^{1.38}} \tag{20}$$

and

$$\alpha=\frac{R_i}{L_i} \tag{21}$$

$$\epsilon=\frac{R_0^3}{6\pi\upsilon R_1^2} \tag{22}$$

$$\gamma=[1-\exp[-3r^2L_1^2/4\bar{t}R_0^2]] \tag{23}$$

With the inclusion of the vortex diffusion, it is possible to examine the influence of the tip vortex diffusion on the distance x/R_1 transversed by a given nucleus of radius R_0 before it reaches the critical capture radius given by $r=d_c(R_0)$ in Eq. (3).

Table 1 Parameters used in the simulation of nuclei capture by a tip vortex (Fig. 3)

Item	Symbol	Units	Value
Vortex circulation	Γ	m^2	1.0×10^{-1}
Vortex radius	R_1	m	1.06×10^{-3}
Velocity	V	m/s	1.2×10^{-1}
Nuclei position	L_i	m	4.14×10^{-3}
Initial nuclei radius	R_i	m	1×10^{-6}
Maximum nuclei radius	R	m	6×10^{-5}
Pressure	$P-P_v$	Pa	1.32×10^{-1}

Table 2 Parameters used in example calculation of nuclei capture and noise (Fig. 4)

Item	Symbol	Units	Value
Vortex circulation	Γ	m^2/s	0.101
Vortex radius	R_1	m/s	1.06×10^{-3}
Velocity	V_1	m/s	12.0
Nuclei position	L_i	m	1.5×10^{-3}
Nuclei radius	R_0	m	$5.\times10^{5}$
Pressure	$P-P_v$	Pa	1.5×10^{5}
$d_c(R_0)$	$d_c(R_0)$	m	3.66×10^{-3}
R_A	—	—	1.366×10^{-2}
L_0	—	—	9.0

When diffusion is present there is a reduction of the tip vortex circulation Γ_0 to 0.8 Γ_0. Figure 3 compares the distance x/R_1 for nucleus having an initial radius in the range of $5<R_i<40$ μm for a tip vortex with and without diffusion. The values used in the calculation are summarized in Table 1.

The comparison in Fig. 3 shows that without diffusion the nuclei of $R_i<8$ μm are captured while with diffusion there is a larger range of nuclei which are not captured. Consequently, there is a delay in the capture of a nucleus caused by vortex diffusion.

Nuclei Capture and Noise Generation Calculation Example. To illustrate the results for the nuclei capture and noise, calculations were made for the case summarized in Table 2. The calculations were begun when the nucleus location r from the vortex axis reaches the capture value $L_0=9.0$ given in Table 2.

$$r=d_c(R_0)\bullet L_0$$

The corresponding values of r, $\dot{r}$, $\dot{R}$, R, at this point were then used in the governing equations (Ligneul and Latorre, 1989):

$$\ddot{\bar{r}}=-3\dot{\bar{r}}\,\frac{\dot{\bar{R}}}{\bar{R}}+k_1(\dot{\bar{r}},\dot{\bar{\theta}},\alpha)+0(M)^2 \tag{24}$$

$$\bar{r}\ddot{\bar{\theta}}+2\dot{\bar{r}}\dot{\bar{\theta}}=3k_2(\bar{r},\dot{\bar{\theta}},\alpha)\,\frac{\dot{\bar{R}}}{\bar{\bar{R}}}+0(M)^2 \tag{25}$$

$$\ddot{\bar{x}}=-3\dot{\bar{x}}\,\frac{\dot{\bar{R}}}{\bar{\bar{R}}}+0(M)^2 \tag{26}$$

$$r\geq\alpha \qquad k_1=\alpha^4\left(\bar{r}\bar{\theta}^2-\frac{3}{\bar{r}^3}\right) \qquad k_2=\frac{1}{\bar{r}}-\bar{r}\,\dot{\bar{\theta}} \tag{27}$$

$$r\geq\alpha \qquad k_1=\bar{r}\,\dot{\bar{\theta}}^2-3r \qquad k_2=\bar{r}(1-\dot{\bar{\theta}}) \tag{28}$$

The results were nondimensional using the following expressions:

Trajectory	$\bar{r}=r/L_i$
Nuclei Radius	$\bar{R}=R/R_0$
Time	$\bar{T}=T/T_v$ where $T_v=\frac{R_0^2}{3\upsilon}$

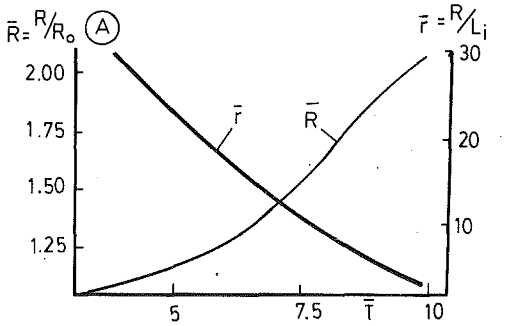

Fig. 4(*a*) Nuclei trajectory radius $\bar{r}(\bar{t})$ and Nuclei radius $\bar{R}$

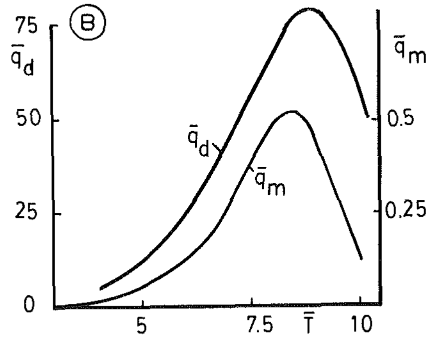

Fig. 4(*b*) Monopole acoustic pressure $\bar{q}_m$ and Dipole acoustic pressure $\bar{q}_d$

Fig. 4 Study II. Simulation of nuclei capture and corresponding noise generation (details in Table 2)

Monopole Acoustic Pressure $\bar{q}_m = \frac{q_m^T v^2}{R_0^3}$

Dipole Acoustic Pressure $\bar{q}_d = \frac{q_d T_v}{R_0^3}$

The acoustic pressure for a single nucleus, denoted by P_{ac} is a combination of Monopole and Dipole acoustic pressure:

$$P_{ac} = \frac{-\rho}{4\pi}\left[\frac{q_m}{m} + q_d \frac{\partial}{\partial t}\left(\frac{1}{m}\right)\right] \tag{29}$$

where

$$q_m = \frac{d}{dt}\,(R^2\dot{R}(t)) \tag{30}$$

$$q_d = (R^2\dot{R}(t)) \tag{31}$$

$$m = \text{distance from source to observer} \tag{32}$$

The calculation results for the parameters in Table 2 are shown in Fig. 4. This figure corresponds to the case where the nucleus has reached the critical capture radius *r*. The nondimensionalized trajectory $\bar{r}$ versus time $\bar{t}$ is shown in Fig. 4(*a*). This shows that the nuclei are effectively captured by $t = 10$. The corresponding nucleus radius $\bar{R}$ is shown in Fig. 4(*a*). At the point of capture, the nucleus has doubled its initial radius, $R = 2.05$.

In Fig. 4(*b*) q_m and q_d are plotted as functions of $\bar{t}$. It is clear by comparing the figures that the maximum value of the monopole source q_m occurs at $t = 8.75$. These curves correspond to the earlier calculations of P_{ac} (Latorre (1980)). The benefit of writing the noise from nuclei capture in terms of q_m and q_d, is that Eq. (29) allows the present results to be used to model the noise generated by a nuclei captured by a helical tip vortex from a marine propeller.

Discussion and Conclusion

The formulation and numerical results presented in this paper provide the basis for treating the tip vortex diffusion caused by fluid viscosity as well as the statistical nuclei size population when modeling the capture of nuclei by tip vortex.

Based on these nuclei capture results, it is possible to treat the problem in two parts. I) the capture of the nuclei beginning at the critical trajectory radius $d_c(R_0)$ and II) the rapid growth and the corresponding noise generation in the final state of nucleus capture. Regarding I:

1 A formulation which models a nucleus undergoing the tip vortex capture process and the frequency of nucleus capture is introduced.

2 The formulation to model the influence of tip vortex diffusion is obtained. Comparison of numerical simulations with and without vortex diffusion shows that the vortex diffusion delays the nucleus capture.

3 The numerical simulation with and without tip vortex diffusion indicated that the vortex diffusion will not influence nuclei with radii smaller than 8 μm. This indicates that the cavitation nucleus capture by a tip vortex has a high pass effect of consolidating the larger cavitation nucleus in the vortex.

Regarding II:

4 The rapid growth and corresponding noise generation simulation can now be considered as necessary in the situation when the characteristic index $M \leq 1$.

5 In addition to simulating the measured noise spikes measured in the tests (Latorre, 1980), the numerical results show that this spike is generated by both Monopole and Dipole acoustic noise source terms.

The present study allows for the extension to the model of tip vortex capture by helical vortices representative of an operating propeller.

Acknowledgments

This paper is part of an on-going study began while the second author was a research scientist at the Bassin d'Essais des Carenes, Paris 5/83-1/84. The research is sponsored by the French Ministry of Defense (DRET).

The authors are grateful to Mrs. Mercedes Latapie for typing this manuscript.

References

Bovis, A., 1980, "Asymptotic Study of Tip Vortex Cavitation," *Proceedings ASME Cavitation and Multi Phase Flow Forum*, New Orleans, Mar., pp. 85-92.

Hsu, C. C., 1991, "Studies of Scaling of Tip Vortex Cavitation Inception on Marine Lifting Surfaces," ASME JOURNAL OF FLUIDS ENGINEERING, Vol. 113, pp. 504-508.

Latorre, R., 1980, "Study of Tip Vortex Cavitation Noise from Foils," *International Shipbuilding Progress*, Vol. 27, pp. 676-685.

Levkovskii, Yu. L., 1978, *Structure of Cavitating Flow*, Sudostroyeniye Publishing House, Leningrad, pp. 147-159 (in Russian).

Ligneul, P., and Latorre, R., 1989, "Study on the Capture and Noise of Spherical Nuclei in the Presence of the Tip Vortex of Hydrofoils and Propellers," *Acoustica*, Vol. 68, No. 1, pp. 1-13.

Ross, D., 1976, *Mechanics of Underwater Noise*, Pergamon Press, New York, NY, pp. 253-280.

Stinebring, D. R., Farrell, K. J., and Billet, M. L., 1991, "The Structure of a Three-Dimensional Tip Vortex at High Reynolds Number," ASME JOURNAL OF FLUIDS ENGINEERING, Vol. 113, pp. 496-503.

R. D. Gould
Assistant Professor.
Assoc. Mem. ASME

K. W. Loseke
Graduate Research Assistant.

Mechanical and Aerospace Engineering,
North Carolina State University,
Raleigh, NC 27695

A Comparison of Four Velocity Bias Correction Techniques in Laser Doppler Velocimetry

Data from a two-component dual-beam laser-Doppler Velocimeter were used to evaluate four different velocity bias correction methods. The data were collected over a range of valid data rates from 100 Hz to 20 kHz at four flow locations in a shear layer. Turbulence intensities ranged from 15 to 100 percent. Flow statistics were calculated using these proposed velocity bias correction techniques. The results were compared to the unbiased values, which were obtained using an approximated equal-time sampling technique. Some of the correction schemes performed well at low turbulence levels, but became ineffective at high turbulence levels. One ad hoc empirical correction scheme showed relatively good results throughout.

Introduction

Velocity bias is an error inherent in the statistical analysis of burst measurements from the laser Doppler velocimeter (LDV). McLaughlin and Tiederman (1973) were the first to document this bias error, which was shown to be a result of the particle arrival probability in the probe volume of the LDV. More specifically, the probability of a seed particle entering the probe volume, and thus the probability of a measurement being made, is higher when the velocity is greater than the average velocity. Similarly, the probability of making a measurement (realization) is lower when the velocity is less than the average velocity. The result of recording more velocity measurements at higher than average velocities causes the calculated statistical mean to be biased toward higher velocities. The magnitude of the velocity bias error has been shown by Gould et al. (1989) and others (Nejad and Davis, 1986 and Petrie et al., 1988) to be relatively insignificant at low turbulence levels but as large as 40 percent or more at high turbulence levels, where the LDV is more useful than hot wire anemometry. Other biases, which are mainly hardware dependent, have been summarized by Edwards (1987). When analyzing velocity bias, three conditions are usually assumed: 1) uniform seed density, 2) a spherical probe volume, and 3) isotropic conditions existing inside the probe volume. The first condition eliminates the need to consider nonuniform seeding effects from the analysis while the latter two conditions eliminate the need to consider directional dependence.

The first of the correction methods considered here is the two-dimensional weighting function proposed by McLaughlin and Tiederman (1973), which is subsequently referred to as the MT2-D method. They hypothesized that the bias error is proportional to the magnitude of the instantaneous velocity, and introduced a weighting function that is the inverse of this magnitude. The next technique proposed was the time between data (TBD) method of Barnett and Bentley (1974), who utilize the time between each realization, or the interarrival time, as the weighting function to correct for velocity bias. Hoesel and Rodi (1979) devised the next method utilizing the time that a seed particle remains in the probe volume, or the residence time, as the weighting function. The residence time (RT) correction of Hoesel and Rodi was not tested in this study due to the lack of particle residence time data. Chen and Lightman (1985) adapted a method, first introduced by Edwards and Baratuci (1984) using simulated data, to actual LDV data which is referred to as the conditional measurement rate (CMR) method. The most recent correction scheme was introduced by Nakao et al. (1987) and uses an empirical function, which attempts to transform the skewed (i.e., biased) probability density function (pdf) into a symmetrical Gaussian (normal) distribution shape. Therefore, it is referred to here as the velocity pdf shape (VPS) correction technique. Table 1 is a summary of the weighting functions and the data that are required for each method.

Each of the aforementioned correction methods, except for the RT technique, was applied to each LDV data set. The procedure required to employ each method is discussed along with any difficulties which were encountered. Corrected axial mean velocities were calculated and compared to the unbiased values and will be presented in this paper.

The goal of this study is to expand the knowledge base of velocity bias corrections by demonstrating the worthiness of each correction technique for various seed densities in differing regions of turbulence. Because velocity bias is such a difficult phenomenon to describe, it is difficult to generalize findings. However, it can be said that the same data were used for each correction scheme and that the results presented here are self-consistent.

Contributed by the Fluids Engineering Division for publication in the JOURNAL OF FLUID ENGINEERING. Manuscript received by the Fluids Engineering Division January 28, 1992; revised manuscript received November 16, 1992. Associate Technical Editor: E. E. Michaelides.

Table 1 Proposed weighting functions

Name	Authors	Weighting function, w_i	Data
MT2-D	McLaughlin and Tiederman (1973)	$1/\lvert V_i\rvert$	u, v
TBD	Barnett and Bentley (1974)	τ_{i+1}	u, τ
RT	Hoesel and Rodi (1979)	t_i	u, t
CMR	Edwards and Baratuci (1984)	$\langle r(V)\rangle/r(V)$	u, v, τ
VPS	Nakao et al. (1987)	$[1+(\bar{u}-u_i)/\bar{u}]^{1.5}$	u

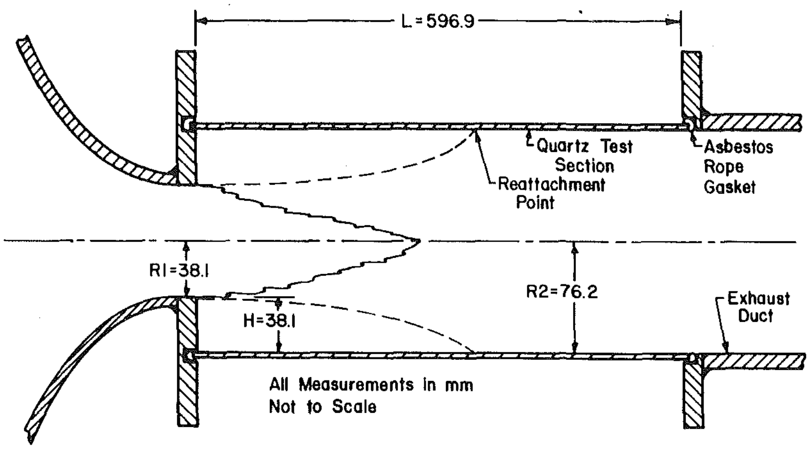

Fig. 1 Test section geometry

Correction Procedure

The LDV data used in this comparison is from a previous study performed by Gould et al. (1989). Simultaneous 2-D velocity measurements were taken in the shear layer of an axisymmetric sudden expansion flow at an axial location two step heights downstream of the nozzle. Dimensions for the sudden expansion geometry are given in Fig. 1 and also in the nomenclature table. The inlet centerline velocity was maintained at 22.0 ± 0.1 m/s throughout the testing giving a Reynolds number based on step height of 5.57×10^4. Frequency shifting (5 MHz) was employed in both components to eliminate incomplete signal bias. Probe volume diameters were 250 μm and 150 μm, respectively, for the axial (green) and radial (blue) components. Two TSI (model 1990) counter processors with coincidence timing logic (10 μs window) were used in the fixed fringe count (N cycle = 16) mode. An atomizer followed by an evaporation-condensation unit was used to produce monodisperse dioctyl phthalate (DOP) seed particles approximately 1 μm in diameter. For further details about the system see Gould et al. (1990 and 1988). Sample populations included 6400 individual velocity realizations for each velocity component and time between realization data. Four radial positions in the shear layer were used to give nominal turbulence intensities of 15, 35, 65, and 100 percent. Statistical uncertainties in the mean velocity estimate, for a Gaussian distributed population having 6400 samples and for a 95 percent confidence level, are 0.4, 0.9, 1.6, and 2.5 percent at the four radial positions, respectively (Yanta and Smith, 1973). Seeding densities were controlled to give nominal coincident valid data rates of 100, 500, 1k, 5k, 10, and 20k Hz at each location. It is important to note that multiple realizations per burst were allowed to occur with this LDV system and did occur at high valid data rates as will be shown later. This effect would reduce the velocity bias error when compared to data where only a single realization per burst was allowed (Meyers and Clemmons, 1979).

The unbiased result was determined using the now well accepted technique of approximate equal-time sampling first introduced by Stevenson et al. (1982), and referred to as the saturable detector (Edwards, 1987), which eliminates the foun-

Nomenclature

CMR = conditional measurement rate correction method
DVR = data validation rate (processor valid data rate)
E_i = defined as $(\bar{u}-u_i)/\bar{u}$
H = step height of sudden expansion (38.1 mm)
Hz = frequency unit (1/s)
LDV = laser Doppler velocimeter
MRD = multiple realization data
MT2-D = McLaughlin-Tiederman 2-D correction method
$P(y)$ = probability of event y (unitless)
$P(x|y)$ = conditional probability of event x (unitless)
pdf = probability density function
$r(V)$ = conditional measurement rate (unitless)
R_1 = inlet radius of sudden expansion (38.1 mm)
R_2 = outlet radius of sudden expansion (76.2 mm)
Re_H = Reynolds number ($U_oH/\nu=5.57\times10^4$)
RT = residence time correction method
SRD = single realization data
STD = standard uncorrected analysis
t = probe volume residence time (s)
TBD = time between data correction method
TI = local turbulence intensity ($\mathrm{TI}\equiv\sqrt{\overline{u'^2}}/\bar{u}$) (unitless)
u = axial velocity (m/s)
U_o = inlet centerline velocity (22.0 ± 0.1 m/s)
v = radial velocity (m/s)
V = magnitude of velocity vector (m/s)
VPS = velocity PDF shape correction method
w = weighting function (varies)
σ = standard deviation (m/s)
τ = interarrival time (s)

Super/Subscripts

$\bar{\ }$ = mean value
c = corrected value
i = summing variable
ub = unbiased value

Table 2 Summary of unbiased data ($H = 38.1$ mm)

x/H	2.0			
r/H	0.833	1.000	1.129	1.207
$\bar{u}_{ub}$ (m/s)	20.4	13.2	6.96	3.86
σ_{ub} (m/s)	2.97	4.43	4.36	3.74
TI(%)	14.6	33.6	62.6	97.0

dation for velocity bias. This technique requires a relatively high seeding rate, which may not be achievable in some flows, and control electronics so that the signal processor can be inhibited from recording data for a user selected fixed time interval. If the seed density is high enough a measurement is recorded almost immediately after the processor is released thus giving nearly equal time sampling. Gould et al. (1986 and 1989) have determined that the seed density must be such that the valid coincident data rate is greater than approximately three times the characteristic frequency of the microscale (i.e., reciprocal of the micro time scale) for this technique to produce unbiased results. Edwards (1987) suggested a more conservative criteria; that the product of valid data rate and micro time scale (DVR$\cdot\tau_\lambda$) should be greater than five. Recently, Winter et al. (1991) have suggested that the integral time scale is the proper flow scale to use. They concluded this by using both the integral and micro time scales in their particle arrival probability model and found that the integral time scale gave the unbiased result for their sample and hold processor when using the TDB correction scheme. Use of the micro time scale in their model resulted in overcorrection. Table 2 summarizes the unbiased results for each radial location.

The correction techniques used in this study employ one of two methods for incorporating the weighting functions and subsequently calculating the mean and standard deviations for a stationary process. The first method uses ensemble analysis as its basis and applies a weighting function to each data point. The ensemble "corrected" mean and standard deviation values can be obtained with the following relations:

$$\bar{u} = \frac{\sum^{N} u_i \cdot w_i}{\sum^{N} w_i} \tag{1}$$

$$\sigma = \sqrt{\frac{\sum^{N} (u_i - \bar{u})^2 \cdot w_i}{\sum^{N} w_i}} \tag{2}$$

where N is the number of data points and w_i is the weighting function. The second method of analysis uses discrete random variable analysis as its basis. In this case a continuous variable is transformed to a discrete variable by creating a histogram from the randomly sampled data. The range of the variable is divided into equal segments (bins). The population of each bin is increased by one each time a velocity value falls within the range of that bin. The pdf is created by dividing the population of each bin by the total population. The weighting function for this case is applied with the following relations:

$$\langle V \rangle = \sum^{K} V_i \cdot P(V_i) \cdot w_i \tag{3}$$

$$\sigma = \sqrt{\sum^{K} (V_i - \langle V \rangle)^2 \cdot P(V_i) \cdot w_i} \tag{4}$$

where K is the number of discrete values or bins, V_i is the discrete velocity value for the ith bin, $P(V_i)$ is the probability of the ith bin given by the velocity pdf and $\langle\ \rangle$ denotes the expected value. Again, w_i is the weighting function.

Before any corrections were applied, the sample populations were first modified by discarding data outside the range of $\pm 3\ \sigma$ from the mean value as is standard practice in LDV work. This filtering should remove only spurious data and not valid turbulent data. Care was used to preserve the time history of the sample population during this process.

The MT2-D and TBD correction methods are the simplest and most straightforward to implement, assuming one has the necessary equipment. A 2-D LDV system is required in order to use the MT2-D correction method while interarrival time data is necessary in order to use the TBD correction method. To employ the MT2-D correction, the magnitude of the particle's instantaneous velocity vector was calculated from the instantaneous axial and radial velocity components and the weighting function was the inverse of this magnitude. The TBD weighting function was simply the following realization's interarrival time. Both of these correction methods used the ensemble analysis technique given by Eq. (1).

The CMR method was the most complex of the correction techniques tested here and is based on the premise that interarrival times for velocity intervals of a turbulent flow are Poisson distributed, as is the case for laminar flow with uniform seeding. Three variations of this technique were explored in this study. CMR1 and CMR2 were both presented in the original paper by Chen and Lightman (1985), while CMR3 is a slight variation of CMR1. The weighting function, as shown in Table 1, is $\langle r(V)\rangle / r(V)$ where $r(V)$ is the conditional measurement rate of velocity V and $\langle r(V)\rangle$ is calculated as shown in Eq. (3) with a weighting function of unity. Although $r(V)$ is termed a "rate," it is derived from a probability density function and is actually unitless. Edwards and Baratuci (1984) defined $r(V)$ as the probability that the conditional interarrival time, τ, is zero for the discretized velocity interval, $(V, V+dV)$ of the velocity pdf. Note that V must be interpreted as the magnitude of the velocity vector in this analysis. The conditional interarrival time, τ, is defined as the time to the *next* data point on the condition that a sample having a velocity V has just been measured. A conditional probability, denoted as $P(x|y)$, is the probability that event x will occur given that event y has occurred. Therefore, the probability of the conditional interarrival time can be denoted as $P(\tau|V)$, where V is the magnitude of the velocity vector and the conditional measurement rate, $r(V)$, is defined as $P(0|V)$.

In order to use any of the CMR methods the velocity range must first be divided into bins creating a discrete velocity histogram. Since 2-D measurements were made here a histogram of the magnitude of the velocity vector was constructed. The number of discrete bins or intervals chosen in this study was 10. The proper number of bins should be able to balance the effects of: 1) small sample size per bin and, 2) limited information potential from too few bins, and thus relies on the total sample population of each trial. This method showed erratic performance initially, which was found to be due, in part, to small sample sizes in some of the discrete velocity bins. In an effort to improve performance, a minimum bin sample size requirement equal to 1 percent of the total population was imposed, such that those velocity bins having fewer than 1 percent of the total population were not allowed to affect the correction on the remaining velocity bins. Furthermore, the weighting factors, w_i, for the velocity bins having populations below this minimum threshold were assumed to be unity. The highest magnitude velocity bins were typically the only ones affected. Once the corresponding bin was found for the ith velocity measurement, τ_{i+1}, the interarrival time of the next realization was also stored. The velocity pdf is created once all the data has been stored in the corresponding bins by normalizing the bin populations with the total population. From this point, CMR1 and CMR3 required the creation of the pdf for the interarrival time data, τ, for each velocity bin. The proper choice of the discrete interarrival time bin intervals is dependent upon knowledge of the flow time scales. Edwards (1987) suggested using a time interval that is small compared to the flow integral time scale. The corrected velocity was found to be very strongly influenced by the choice of this time interval. The CMR2 method eliminates user-selected time intervals and does not require the creation of pdf's for τ data. Instead, the conditional measurement rate is approximated by taking the inverse of the ensemble average of the interarrival time data for each bin, which is described as:

$$\overline{r(V)} = \frac{1}{\frac{1}{M}\sum^{M}\tau_i} \tag{5}$$

where M is the population of interarrival times in each discrete velocity bin. The weighting function for CMR2, w_i, is then equal to $\langle \overline{r(V)} \rangle / r(V)$.

The determination of interarrival time bin intervals, when using the CMR1 and CMR3 methods, was automated as follows. Similar to the velocity pdf procedure, the entire range of interarrival time values, from $\tau = 0$ to $\tau = \tau_{\mathrm{MAX}}$, was divided into an equal number of intervals (6 were used here). Next the pdf's for the conditional interarrival time data of each discrete velocity bin were created. It was found in initial runs that τ_{MAX} sometimes lay far outside the distribution of a majority of the points. To rectify this, a $+3\sigma$ was imposed as the upper boundary of the interarrival time data before the interarrival time pdf was created.

The CMR1 method estimates the probability of $\tau = 0$ (i.e., $P(0 \mid V)$) and thus the conditional measurement rate, $r(V)$, as the probability of the first bin in the newly created interarrival time pdf. The CMR3 method goes one step further by calculating a least squares fit of a Poisson distribution curve to the interarrival time pdf and solves explicitly for $P(0 \mid V)$. The weighting functions were calculated using the expression shown in Table 1.

The VPS method differs from the other correction schemes in that it uses an empirical relation as the weighting function and has no fundamental basis. The authors also state that uniform seed density is unnecessary when using this correction and thus the method, in principle, is applicable in highly turbulent regions with poor seeding conditions. The method is based on the premise that the velocity pdf's should be Gaussian in shape. This premise certainly can not be true in anisotropic flows where turbulent triple products (skewness) are nonzero. However, the method is very simple to employ since one needs only the original 1-D velocity realizations. As was discovered here, however, a modification to the VPS method is required in order to apply it to LDV data obtained from regions exceeding ≈ 33 percent turbulence intensity. This limitation was not mentioned in the original paper but can be demonstrated readily by rewriting the weighting function listed in Table 1 for the maximum and minimum velocity values as:

$$w_{i,\max-\min} = (1 \pm 3 \cdot TI)^{1.5} \tag{6}$$

This expression results when one notes that the range of measurements, $u_{i,\max-\min}$, is bounded by $\bar{u} \pm 3\sigma$, and that $TI = \sigma/\bar{u}$. Equation (6) now defines the maximum and minimum weighting factors for a given turbulence level. It can be seen that when $TI > 1/3$, the weighting factors are complex for some values (i.e., the large positive ones if $\bar{u}$ is positive) of the instantaneous axial velocity.

To avoid eliminating the affected data points (which are the ones responsible for velocity bias), two variations were employed in this study. VPS1 uses the absolute value of the expression in the square brackets before applying the exponent, while VPS2 takes the absolute value of the second argument in the square brackets (i.e., $(\bar{u} - u_i)/\bar{u}$) if the value of that argument is less than -1. Thus, the two variations can be described as:

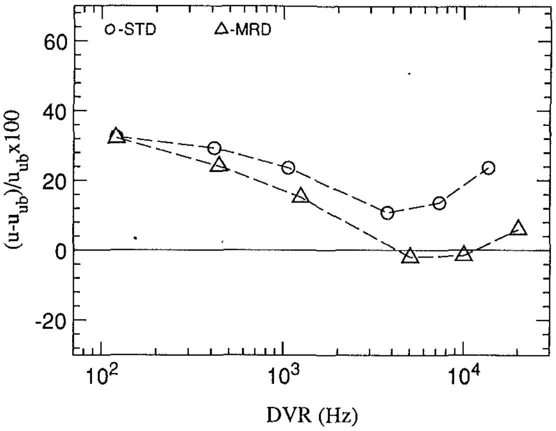

Fig. 2 Uncorrected mean axial velocities for single and multiple realization data

$$\text{VPS1:}\quad w_i = |1 + E_i|^{1.5} \tag{7}$$

$$\text{VPS2:}\quad w_i = \begin{cases} (1 + E_i)^{1.5} & \text{IF } E_i \geq -1 \\ (1 + |E_i|)^{1.5} & \text{IF } E_i < -1 \end{cases} \tag{8}$$

$$E_i = (\bar{u} - u_i)/\bar{u} \tag{9}$$

This method uses the ensemble analysis technique and can be applied only after $\bar{u}$ is calculated.

Elimination of Multiple Realizations

Multiple realization data (MRD) occurs when more than one measurement is taken from the same seed particle before it leaves the probe volume. This effect can be nullified with proper LDV set-up, but the data presented here were not taken using such a set-up since multiple realizations were unavoidable for the elevated coincident valid data rates used in this study.

The most influential factor in the occurrence of multiple realizations is the use of frequency shifting, which is precisely why Meyers and Clemmons (1979) referred to it as Bragg cell bias in their study. Use of frequency shifting allows a fixed number of fringes to pass the particle before it moves an appreciable distance. Assuming minimal processor dead time, the system quickly resets and is ready to accept another measurement before the seed particle leaves the probe volume. Obtaining more measurements from slower than average seed particles offsets the effect of velocity bias. It should also be noted that the high local turbulence level cases were measured at locations in the shear layer where the local mean velocities were small, thus increasing the probability of multiple realizations. Figure 2 shows the trend of the uncorrected mean axial values compared to the data validation rate (DVR) at the 65 percentage turbulence level for two data sets. One set contains multiple realization data (MRD) while the other contains only single realization data (SRD). The SRD set was created from the MRD set by removing multiple realizations as described below. This figure confirms that the multiple realization data reduces the effect of velocity bias and that the effect of Bragg cell bias increases with increasing DVR.

Multiple realization were determined by calculating a probe volume residence time, t, for each realization by assuming that the velocity remains constant as the particle passes through the probe volume. Then, using an effective probe volume diameter (axial direction only) to account for the Gaussian distribution of the beam, an estimate of the residence time was determined. This time was then compared to the interarrival time of the following realization and if it was greater than the next interarrival time, this next data point was considered a multiple realization and discarded. The interarrival time of the discarded point was added to the following data point in order to preserve the time history of the data set. Figure 3 shows the

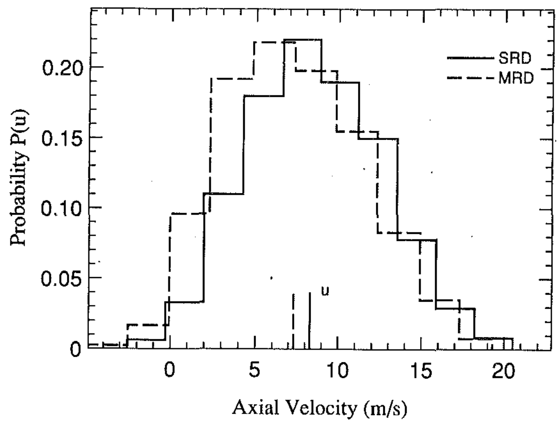

Fig. 3 Comparison of pfd's for single realization data and multiple realization data

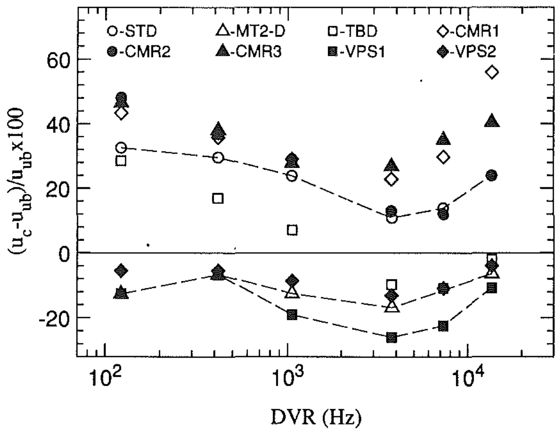

Fig. 6 Corrected axial mean velocities at 65 percent TI

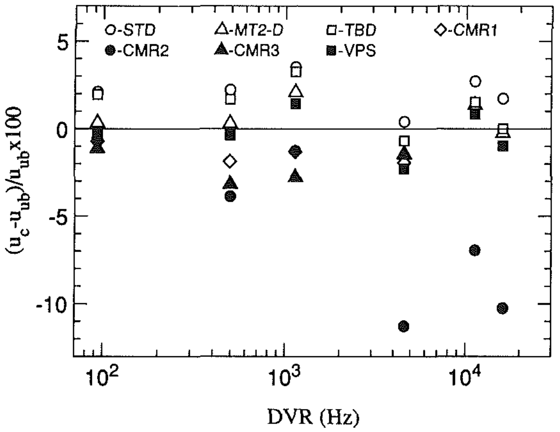

Fig. 4 Corrected axial mean velocities at 15 percent TI

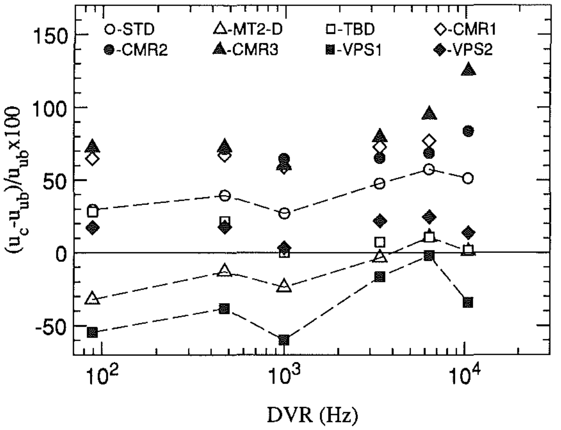

Fig. 7 Corrected axial mean velocities at 100 percent TI

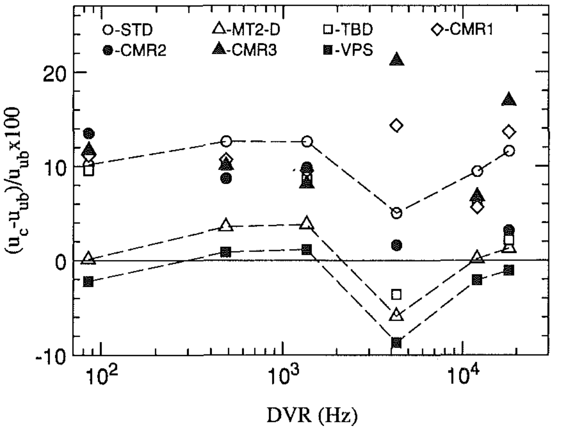

Fig. 5 Corrected axial mean velocities as 35 percent TI

probability density functions of the single realization data and the multiple realization data for a high DVR trial at the 65 percent turbulence level. The single realization data shows obvious biasing towards a higher velocity when compared to the multiple realization data. This indicates that a majority of the discarded data had velocity values below the mean velocity value, proving the existence of Bragg cell bias.

Since Bragg cell bias is detrimental to evaluating the effects of velocity bias correction techniques, all the data except for a few trials were modified as described above to remove the multiple realizations. The exceptions to this were all the 15 percent turbulence level trials, due to its minimal effect in this case, and the trials of 100 Hz DVR for all the other turbulence levels, due to the poor clock resolution necessary to record the longer interarrival times.

Results and Discussion

Figures 4 through 7 show the resulting "corrected" mean axial flow velocities compared with the unbiased velocities and with each other. Values greater than zero on the y-axis represent mean measured flow velocities greater than the unbiased velocity. Lines connecting the data are included on these figures to show trends only and should not be interpreted otherwise. It should also be noted that the uncorrected velocity (standard ensemble average) is not always the largest one in every case, which indicates that some correction schemes actually increase the velocity bias error.

At the 15 percent TI location, the uncorrected result was within 4 percent of the unbiased result for all DVRs. The LDV research community is in reasonable agreement that low turbulence intensity data need not be corrected for velocity bias because the error is typically small, as shown here. This study indicates that the MT2-D and VPS methods work well at low turbulence levels.

The results for the 35 percent TI location showed an increase in the magnitude of the velocity bias error as expected (Fig. 5). The biased velocities were approximately 10 percent higher than the unbiased ones at all the DVRs. However, a warning is in order for all high DVR cases. When using a constant sample population, as is usually done, increasing the DVR decreases the sample duration time and may result in an undesirable and possibly misleading condition where less information about low frequency turbulence phenomena is collected.

Figure 6 shows that the uncorrected bias errors vary over the range of DVRs. A maximum bias error of 33 percent occurs at 100 Hz DVR while a minimum bias error occurs when DVR = 5 kHz. A decreasing trend is still present in these uncorrected velocities even though multiple realizations have been removed. It is not clear at this time whether multiple realization data still exists in the remaining sample or another unknown effect is taken place to offset velocity bias. The uncorrected values for the highest turbulence location (Fig. 7), show a different trend in comparison to the 65 percent turbulence level and velocity bias errors between 30 to 50 percent result for this case. The 100Hz DVR value has the lowest error while the 10kHz DVR value has the highest error.

At the 35 percent TI location, the MT2-D correction showed good agreement with the unbiased values over the range of DVRs, with the largest overcorrection at 5kHz DVR. At higher turbulence levels, the MT2-D resulted in overcorrections at all DVRs by 10 to 30 percent. Interestingly, the MT2-D method resulted in a nearly constant correction factor which produced a trend similar to the uncorrected values over the range of DVRs.

The time between data (TBD) method provided marginal improvement over the standard ensemble average method at low DVRs as shown in Figs. 4 through 7. However, at higher DVRs, the TBD results lie approximately half-way between the uncorrected and the MT2-D values. Interestingly, when the TBD correction was applied to the multiple realization data, its performance was marginal when compared to the uncorrected data. Its increased effectiveness in the high DVR trials is thus linked to the elimination of multiple realizations and, in fact, the process used to discard the unwanted multiple realizations accomplishes a similar task as the TBD correction attempts to. Thus, the results presented here indicate that the TBD method is a viable correction when multiple realizations are non-existent.

The conditional measurement rate (CMR) methods, as mentioned previously, were the most difficult to implement. Additionally, they also showed the most widely varying results. These methods were also the only ones tested here that actually showed an increase in velocity bias errors in many of the trials. It should be pointed out that some of the points for the CMR1 and CMR3 methods at the two highest DVRs are not plotted since they far exceeded the other values. The three methods gave corrected results which differed greatly between each other at the high DVRs for all turbulence levels, while giving similar results for the lower DVRs. It is believed that the longer interarrival time bin widths associated with the lower DVRs produce a more stable situation. The CMR methods increased mean velocity bias errors over the uncorrected value by as much as 70 percent, and were also found to be sporadic and generally unpredictable throughout the trials and thus cannot be recommended without further examination.

The two empirical shape corrections (VPS) closely followed the trend of the uncorrected results and, in fact, tracked the MT2-D correction to a very high degree. This correction does not require 2-D data or interarrival time information, and thus is much simpler to implement than the other methods. Since the argument in the weighting function does not become negative at the two lower turbulence levels, there was no difference in the results between the two variations of this method in these regions. The differences between these corrected velocities and the uncorrected values were fairly constant for all DVRs, but varied depending on turbulence levels. The shape correction method proved to be a reliable one at the two low turbulence levels as shown in Figs. 4 and 5. At the 65 percent TI level, VPS1 showed a trend towards overcorrection and produced the most overcorrected results of all the correction methods tested here. This was also true for the 100 percent TI level, where the error averaged 50 percent. As expected, VPS1 results remained close to the MT2-D corrected results as was demonstrated in the original study of Nakao et al. (1987), where the MT2-D corrected velocity was assumed to be the unbiased velocity.

The second variation (VPS2), introduced here to eliminate negative arguments in the weighting factor, proved to be much more effective. At the 65 percent TI level, the corrected results were better than those produced by the MT2-D correction, but were still overcorrected by up to 12 percent. The results actually improved at the highest turbulence level (TI = 100 percent) where the variation in the weighting function would have its greatest effect. VPS2 gave corrected values that agreed to within 20 percent of the unbiased values at this highest turbulence level. Overall, this correction method gave the best performance by agreeing to within 15 percent, or better, of the unbiased values for most DVRs and turbulence levels.

Summary and Conclusions

Several velocity bias correction methods were applied to the same two-component LDV data sets. The complexity of implementing these methods varied widely. The least effective were the conditional measurement rate schemes. Not only did they often increase the mean velocity bias error when compared with the uncorrected value (not to mention the unbiased value), but they also displayed the most erratic behavior between data rate extremes. This fact and the added complexity of their implementation appear to make them undesirable for eliminating velocity bias. Further research is needed to discover the source of their erratic behavior. The TBD method was found to give minimal correction at low DVRs, while giving better agreement with the unbiased values at higher DVRs. However, these results occurred only after eliminating multiple realization data. The issue of multiple realizations per seed particle should always be addressed prior to applying any correction since correcting "unbiased" data can lead to substantial error. The MT2-D correction appears to work well at low turbulence levels, and also shows promise at higher turbulence levels when the data rate is high.

The most surprising results came from the pdf shape correction schemes. This correction method not only proved to be better in most trials than any of the others, but consistently gave improved values over the uncorrected data. However, the problem with complex weighting factors at high turbulence levels (>33 percent TI) must be addressed.

The results indicate that the second pdf shape correction method (VPS2), first introduced here, gives the best bias correction for the wide range of turbulence levels and data rates used in this study.

References

Barnett, D. O., and Bentley, H. T., 1974, "Statistical Bias of Individual Realization Laser Velocimeters," *Proc. of the Second International Workshop on Laser Velocimetry*, Engineering Extension Series, Purdue University, #144, pp. 428-444.

Chen, T. H., and Lightman, A. J., 1985, "Effects of Particle Arrival Statistics on Laser Anemometer Measurements," ASME Winter Annual Meeting, Miami Beach, FL, Nov. 17-22.

Edwards, R. V., ed., 1987, "Report of the Special Panel on Statistical Particle Bias Problems in Laser Anemometry," ASME JOURNAL OF FLUIDS ENGINEERING, Vol. 109, pp. 89-93.

Edwards, R. V., and Baratuci, W., 1984, "Simulation of Particle Measurement Statistics for Laser Anemometers," Preprints for the Ninth Symposium on Turbulence, Univ. of Missouri-Rolla, Rolla, MO, Oct 1-3, Paper #35.

Gould, R. D., Stevenson, W. H., and Thompson, H. D., 1986, "A Parametric Study of Statistical Velocity Bias," Laser Institute of America: *Proceedings of the Flow & Particles Diagnostics*, Vol. 58, Arlington, VA, No. 10-13, pp. 89-96.

Gould, R. D., Stevenson, W. H., and Thompson, H. D., 1988, "Turbulence Characteristics of an Axisymmetric Reacting Flow," NASA Contractor Report 4110.

Gould, R. D., Stevenson, W. H., and Thompson, H. D., 1989, "Parametric Study of Statistical Bias in Laser Doppler Velocimetry," *AIAA Journal*, Vol. 27, No. 8, pp. 1140-1142.

Gould, R. D., Stevenson, W. H., and Thompson, H. D., 1990, "Investigation of Turbulent Transport in an Axisymmetric Sudden Expansion," *AIAA Journal*, Vol. 28, No. 2, pp. 276–283.

Hoesel, W., and Rodi, W., 1977, "New Biasing Elimination Method for Laser-Doppler Velocimeter Counter Processing," *Review of Scientific Instrument*, Vol. 48, No. 7, pp. 910–919.

McLaughlin, D. K., and Tiederman, W. G., 1973, "Bias Correction for Individual Realization of Laser Anemometer Measurements in Turbulent Flows," *Physics of Fluids*, Vol. 16, No. 12, pp. 2082–2088.

Meyers, J. F., and Clemmons, J. I., 1979, "Processing Laser Velocimeter High-speed Burst Counter Data," *Laser Velocimetry and Particle Sizing*, Hemisphere Publishing Corp., pp. 300–312.

Nakao, S., Terao, Y., and Hirata, K., 1987, "New Method for Eliminating the Statistical Bias in Highly Turbulent Flow Measurements," *AIAA Journal*, Vol. 25, No. 3, pp. 443–447.

Nejad, A. S., and Davis, D. L., 1986, "Velocity Bias in Two Component Individual Realization Laser Doppler Velocimetry," Laser Institute of America: *Proceedings of the Flow & Particles Diagnostics*, Vol. 58, Arlington, VA, Nov. 10–13, pp. 78–88.

Petrie, H. L., Samimy, M., and Addy, A. L., 1988, "Laser Doppler Velocity Bias in Separated Turbulent Flows," *Experiments in Fluids*, Vol. 6, pp. 80–88.

Stevenson, W. H., Thompson, H. D., and Roesler, T. C., 1982, "Direct Measurement of Laser Velocimeter Bias Errors in a Turbulent Flow," *AIAA Journal*, Vol. 20, No. 12, pp. 1720–1723.

Winter, A. R., Graham, L. J. W., and Bremhorst, K., 1991, "Effects of Time Scales on Velocity Bias in LDA Measurements using Sample and Hold Processing," *Experiments in Fluids*, Vol. 11, pp. 147–152.

Yanta, W. J., and Smith, R. A., 1973, "Measurements of Turbulence Transport Properties with a Laser Doppler Velocimeter," AIAA paper 73-169.

S. M. Tieng
Associate Professor.

Y. C. Wang
Graduate Student.

Institute of Aeronautics and Astronautics,
National Cheng Kung University,
Tainan, Taiwan 70101

Holographic Visualization of Convective Flow Around a Heated Rotating Cone of Finite Length

The convective flow around a heated rotating cone of finite length is investigated experimentally by means of 3-D and real-time holographic interferometry at rotational speeds of up to 4600 rpm and rotational angles from 0 to 90 deg. This advanced optical technique allows visualization of the thermal boundary layer, it's unstable transition region and the turbulent zones, as well as providing a detailed visual analysis of the holographic fringe patterns, information about the thickness of the thermal boundary layer, and a new method for detecting and determining the critical points and critical Reynolds numbers of the transition region. The results are compared with previously obtained experimental data.

1 Introduction

The problems associated with flow phenomena and convective heat transfer that arise from the rotation of a heated cone of finite length are not only of considerable fundamental research interest but also of great practical importance in the field of engineering. Wu (1959), was the first to analytically study flow phenomena in the laminar, incompressible flow regime while Tien (1960), was the first to investigate the characteristics of convective heat transfer under boundary layer approximations. Since then, many authors (Hartnett and Deland, 1961; Kreith et al., 1962; Tien and Campbell, 1963; Hering and Grosh, 1963; Kappesser et al., 1973; Kobayashi and Izumi, 1983; and Wang and Kleinstrener, 1990) have concentrated both theoretically and experimentally on these subjects.

In general, agreement between experimental and theoretical results under laminar boundary layer conditions are satisfactory; however, rotating systems involve not only laminar but also transitional and turbulent boundary layer which develop as the rotational speed is increased. Since it is impossible to analyze these transitional and turbulent regimes by exact solutions on the motion and energy equations, semi-empirical methods are usually used.

Many experimental investigations were employed in an attempt to acquire detailed and accurate empirical information about the flow structure and heat transfer rate, as they play important roles in the analysis of these turbulent systems. For example, the smoke visualization method was used to observe complex flow structure (Kegelman et al., 1983; Kobayashi and Izumi, 1983; Kobayashi et al., 1987), while hot-wire, stethoscope and mass transfer techniques were employed to detect and measure transition behavior and turbulent convective transfer rates (Tien and Campbell, 1963; Kreith et al., 1962, Kappesser et al., 1973; Kobayashi and Izumi, 1983; Kohama and Kobayashi, 1983; and Kobayashi et al., 1987). Unfortunately, however, the agreement between experimental and theoretical results for both partially turbulent and turbulent flow over rotating cones is not very satisfactory (Kreith, 1968) due in part to experimental limitations and also to the simplifying assumptions employed in the theoretical analysis. Thus, new and advanced techniques are continuously needed to explore new or unexpected physical phenomena which could considerably affect the heat transfer during convective flow.

Holographic interferometry, an advanced optical technique, has a number of advantages over previously reported techniques for thermal flow field diagnostics, not the least of which includes simultaneous nonintrusive measurements of 2 or 3-D temperature distribution and real time 3-D holographic observation of the flow. In addition, it has a higher sensitivity to slight changes in fluid density than either smoke or schlieren, shadowgraph visualization and possesses such a high degree of spatial resolution as to allow visualization of very small test flow fields (Tieng and Chen, 1990; Tieng and Lai, 1990; Tieng and Yan, 1992; Tieng and Lai, 1992; Tieng et al., 1992; and Chang et al., 1992).

In this paper, laser holographic interferometry is employed in order to visualize the thermal flowfield generated by a heated cone of finite length rotating in still air. Subsequent analysis of the holograms provided quantitative measurements of the asymmetric 3-D thermal boundary layer thickness at different angles of rotation (with respect to the vertical axis), as well as information concerning transition behavior, including the location of critical points and Reynolds number values and their quantitative interrelationship. Analysis of novel turbulent phenomena that occurred over the cone is also included.

2 Test Apparatus

The experiment employed three test cones having base diameters of 40, 64, and 110 mm and vertex angles ϕ = 30, 45,

---

Contributed by the Fluids Engineering Division for publication in the JOURNAL OF FLUIDS ENGINEERING. Manuscript received by the Fluids Engineering Division March 25, 1992; revised manuscript received January 7, 1993; Associate Technical Editor: Ho, Chih-Ming.

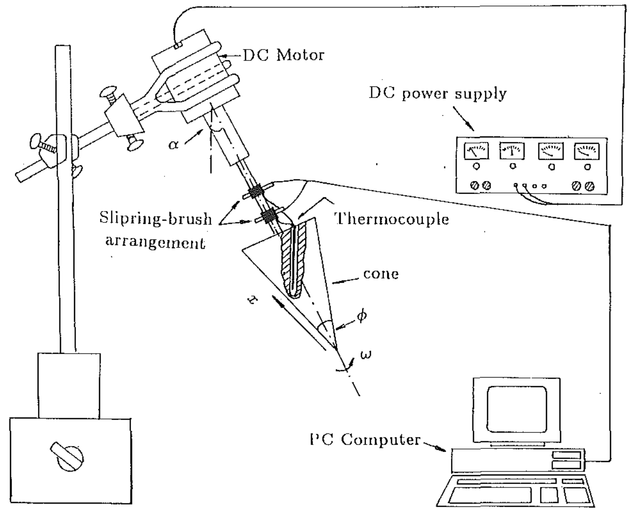

Fig. 1 Schematic diagram of the test apparatus

and 90 deg, respectively. As shown in a schematic diagram of the test apparatus (Fig. 1), the aluminum cones were attached to a rotating shaft driven by a variable speed DC motor capable of maintaining rotational rates of up to 4600 rpm. The shaft was designed to be as small as possible in order to minimize heat conduction along it. The surface temperature of the cone was measured by a micro-thermocouple probe inserted into a hole (dia of 1 mm) in the cone base which was drilled at an inclined angle to the cone axis. A slipring-brush arrangement allowed the thermocouple to be directly attached to the measuring device. Care was taken to minimize the frictional effect within each slipring and brush unit as well as the eccentricity, even though preliminary experimentation showed that an increase in the eccentricity from 0.05 to 0.2 mm had no detectable influence on the flow pattern.

The Biot numbers of each cone can be calculated in the following manner:

$$\mathrm{Bi} = (L_s/K_s)/1/h = (hL_s)/K_s$$

where, L_s = volume/surface area

$$h = 25\mathrm{W/(m^2.{}^\circ C)}\ (\text{at } T_f = 143^\circ\mathrm{C})\ (\text{Tien, 1960})$$

$$K_s = 221\mathrm{W/(m.{}^\circ C)}\ (\text{aluminum, at } T_s = 260^\circ\mathrm{C})\ (\text{Bayazitoglu and Otisik, 1988})$$

Thus,

$$\mathrm{Bi} = \begin{array}{l} 5.9\times10^{-4}\ (\phi = 30\ \text{deg}) \\ 8.6\times10^{-4}\ (\phi = 45\ \text{deg}) \\ 10.4\times10^{-4}\ (\phi = 90\ \text{deg}) \end{array}$$

These results indicate that the test cones can be taken as an isothermal or lumped system at any given instant (Incropera and Dewitt, 1990).

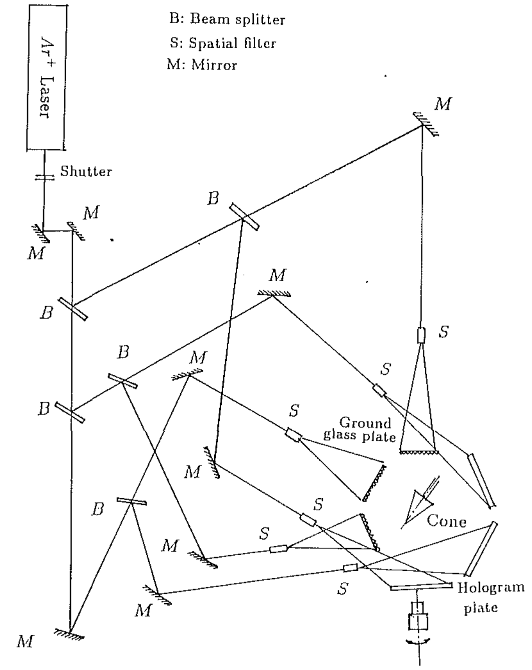

Fig. 2 Schematic diagram of the optical system: laser diffuse-illumination holographic interferometry

3 Optical System

A schematic diagram of the diffuse-illumination holographic interferometry testing system is shown in Fig. 2. The introduction of a diffuser (ground glass plate) in the optical path of the object beam makes it possible to record the optical pathlengths of light rays that pass through the flow field in many different directions. A single frequency Ar^+ laser, having a wavelength of 5145 Å and an output of 1.2 W (Innovar 306, Coherent Inc. with etalon), was used as the light source. The laser beam was split into three object and three reference beams by five circular variable beam splitters. Three conventional hologram plates (Agfa 10E56 4 in. × 5 in.) each providing a viewing range of about 20 deg, were arranged with a mutual intersection angle of 60 deg for simultaneous holographic recording. Holograms were formed by making two exposures; one of the stationary and the other of the rotating cone. The developed hologram was illuminated with the original reference beam in order to reconstruct the fringe pattern of the flow field which was then photographed.

Real-time holographic interferometry was employed in order to visually analyze flow evolution as the rotating speed of the cone was increased. The advantage of this technique lies in its in situ capability of continuously monitoring the evolution process, whereas the double exposure technique is only able to capture transient phenomena. Except for replacing the conventional holographic plate with a HC-300 controlled ther-

Nomenclature

Bi = Biot number
h = heat transfer coefficient
K_s = thermal conductivity
L = cone slant height
L_s = characteristic length of the cone. L_s = volume/surface area
$\overline{\mathrm{Re}}$ = overall rotational Reynolds number. $\overline{\mathrm{Re}} = (\omega L^2 \sin \phi/2)/\nu$
Re_c = critical Reynolds number. $\mathrm{Re}_c = (\omega X_c^2 \sin \phi/2)/\nu$
T_f = film temperature. $T_f = (Ts + T_\infty)/2$
T_s = cone surface temperature
T_∞ = ambient temperature
X = coordinate direction along the lateral surface of the cone
X_c = critical point coordinate
α = rotational angle
μ = fluid viscosity
ν = fluid kinematic viscosity ($\nu = \mu/\rho$)
ρ = density of air
ω = cone angular velocity
ϕ = cone vertex angle

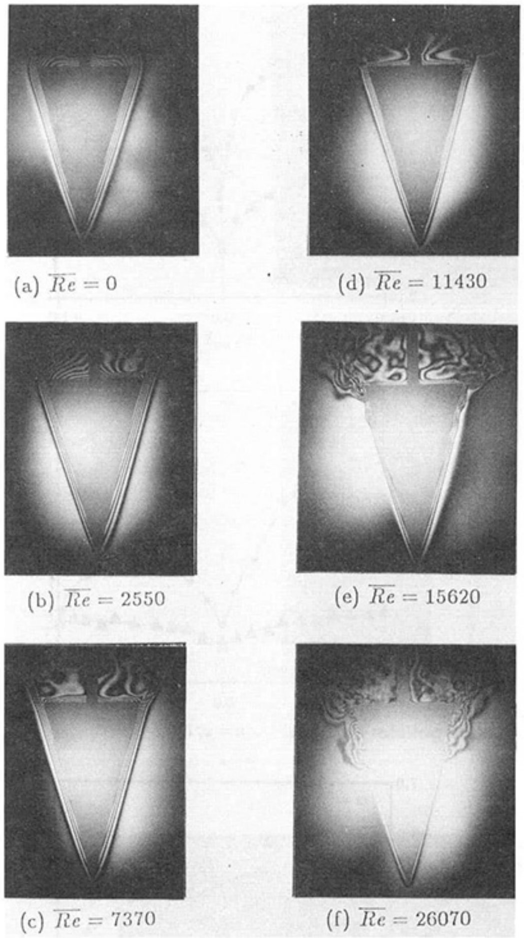
(a) $\overline{Re}=0$ (d) $\overline{Re}=11430$

(b) $\overline{Re}=2550$ (e) $\overline{Re}=15620$

(c) $\overline{Re}=7370$ (f) $\overline{Re}=26070$

Fig. 3

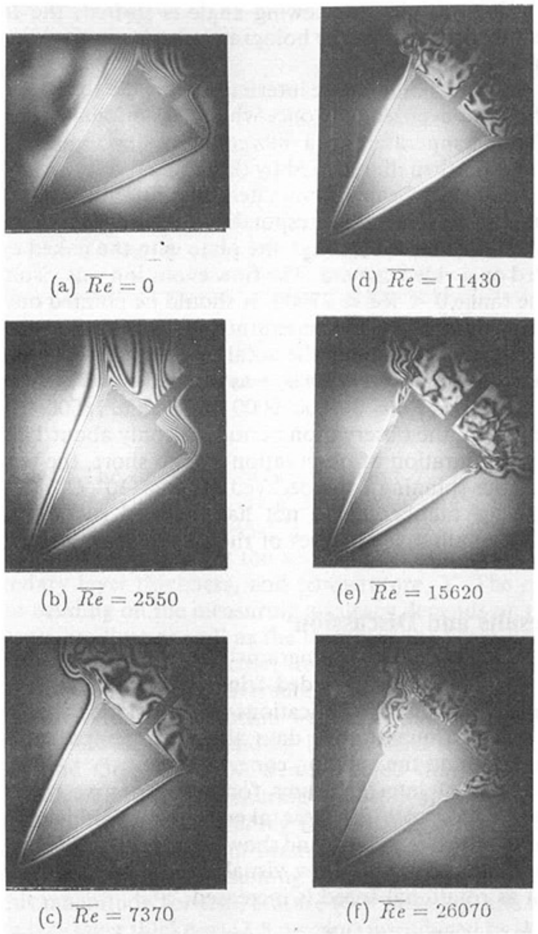
(a) $\overline{Re}=0$ (d) $\overline{Re}=11430$

(b) $\overline{Re}=2550$ (e) $\overline{Re}=15620$

(c) $\overline{Re}=7370$ (f) $\overline{Re}=26070$

Fig. 4

moplastic plate, the system was set up in the same manner for diffuse-illumination holographic interferometry as described above (see Fig. 2).

4 Experiment

The experiment was carried out using heated cones with the rotational speeds ranging from zero to 4600 rpm. The rotational axis of the heated cone with respect to the direction of gravitational force, was sequentially inclined at each of the following angles: 0, 45, and 90 deg for all test cases.

The holographic experiments consisted of two parts. One was double exposure diffuse-illumination holographic interferometry, while another the real time holographic interferometry.

For detailed analysis of the convective flow around the cone, double exposure holographic interferograms were taken at a series of discrete rotational Reynolds numbers of Re = 0, 2550, 7370, 11430, 15620, and 26070.

The cone was first heated by a Bunsen burner to a temperature 30° C higher than that desired, the flame taken away, and the cone then rotated at the required speed. Approximately one to two minutes later, when the desired temperature was reached (260° C) and a steady convection established, the holograms were photographed. Holograms were formed by making two exposures (1/500 s); one of the stationary cones at ambient temperature (25° C), and the other at the desired temperature and rotational rate.

Once the exposed holograms are developed and reconstructed by the reference beam, the fringe patterns can be observed with the naked eye or photographed with a camera. Note that the viewing angle is dependent on the aperture size

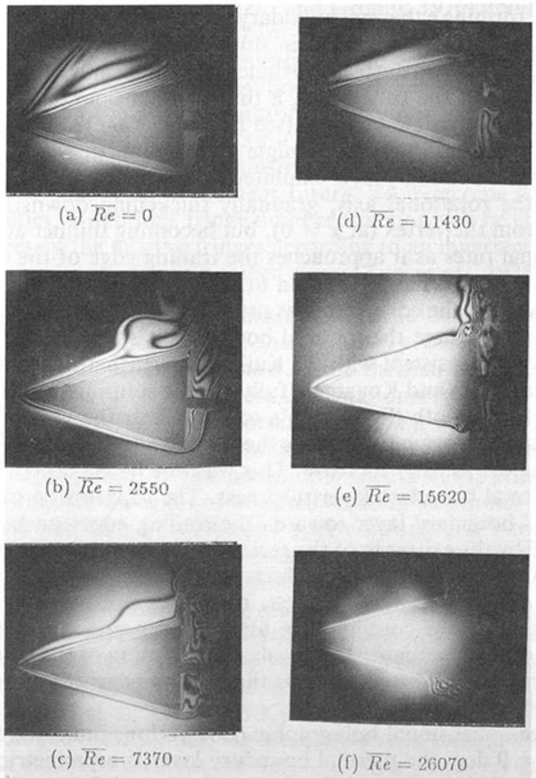
(a) $\overline{Re}=0$ (d) $\overline{Re}=11430$

(b) $\overline{Re}=2550$ (e) $\overline{Re}=15620$

(c) $\overline{Re}=7370$ (f) $\overline{Re}=26070$

Fig. 5

Figs. 3-5 Holographic visualization pictures of the convective flow around a heated rotating cone (ϕ = 30 deg) at different values of $\overline{Re}$ and α: 3(a-f) for α = 0 deg; 4(a-f) for α = 45 deg; 5(a-f) for α = 90 deg

and the diffuser. As the viewing angle is shifted, the fringe pattern (as seen through the hologram) changes, providing the 3-D flow information.

For real-time holographic interferometry, the thermoplastic hologram was exposed only once while the stationary cone was at ambient temperature and subsequently developed in situ. The plate was then illuminated by the original reference beam, while the object beam illuminated the rotating cone. The changing fringe pattern corresponding to the evolution of the flow, can be observed through the plate with the naked eye or recorded on a video camera. The flow evolution was visualized over the range $0 < \mathrm{Re} < 27000$. It should be pointed out that in order to minimize the temperature decrease during the real time observation process, the total evolutionary process (in our case, Re from 0 to 27000) was divided into three observation steps (i.e., Re = 0-9000, 9000-18000, and 18000-27000). For each step, the observation period was only about 1.5 minute. As the duration of observation was so short, the temperature of the spinning cone decayed only 20-30° C, and thus the Grashof number could not have altered sufficiently to affect the qualitative analyses of the flow visualization.

5 Results and Discussion

The holographic interferograms photographed under different test conditions provided fringe patterns that gave not only reliable qualitative indications of the detailed flow structures, but also quantitative data about the temperature distribution around the rotating cone.

Three sets of interferograms for the respective rotational angles of 0, 45, and 90 deg were taken by using double exposure holographic interferometry and shown in Figs. 3-5. They clearly illustrate the convective flow visualization, as well as its evolution as rotational speed is increased.

(a) Thermal Boundary Layer. Fringe patterns extend only over a narrow zone in the immediate vicinity of the entire cone surface forming a thermal boundary layer and directly indicates the temperature distribution in this region. Even at high rotational rates when unsteady turbulent flow appears (i.e., above the surface of the cone base), a thin thermal boundary layer is still clearly visible below it (see Figs. 3-5 (*e-f*)).

For the case in which the angle of rotation, α, was 0 deg, the thermal boundary layer exhibited axisymmetric distribution about the rotational axis, gradually thickening downstream away from the vertex (at $x = 0$), but becoming thinner at low rotational rates as it approaches the trailing edge of the cone near $x = L$ (see Figs. 3(*a*) and 6(*a*)). A higher transfer rate is expected at the cone vertex as usual, and at the trailing edge of the cone where the thermal boundary is suppressed. This behavior is consistent with the Kuiken's perturbation solution (Kuiken, 1968) and Koyama's fully elliptic solution (Koyama, et al., 1985). Both the Kuiken's solution near the vertex at $x = 0$ and the Koyama's towards the trailing edge at $x = L$ gave a steep heat transfer increase. This was due to the decrease in the thermal boundary layer thickness. The suppression of the thermal boundary layer towards the trailing edge can be explained by the existence of the recirculation zone over the cone base surface, which will be discussed later in 5-C in futher detail. Due to the recirculation, the fluids passing over the trailing edge are continuously attracted towards the center region of the cone case. As a result, the diffusion of the boundary layer is suppressed towards the trailing edge at low rotational rates.

Three-dimensional holographic observations indicated that for $\alpha \neq 0$ deg, the thermal boundary layer is asymmetrically distributed about the cone's rotational axis (see Figs. 4, 5, (*a*, *b*)). Note, however, that this asymmetry disappears at high rotational rates ($\overline{\mathrm{Re}} > 10{,}000$) (see Figs. 4, 5 *d-f*)). For the case of $\alpha = 45$ deg, the quantitative relationship between $\eta = (X/L)$ and thickness is shown in Fig. 6(*b*), where $-1 < \eta < 0$ stands for the left and $0 < \eta < 1$ for the right lateral surface on the hologram picture.

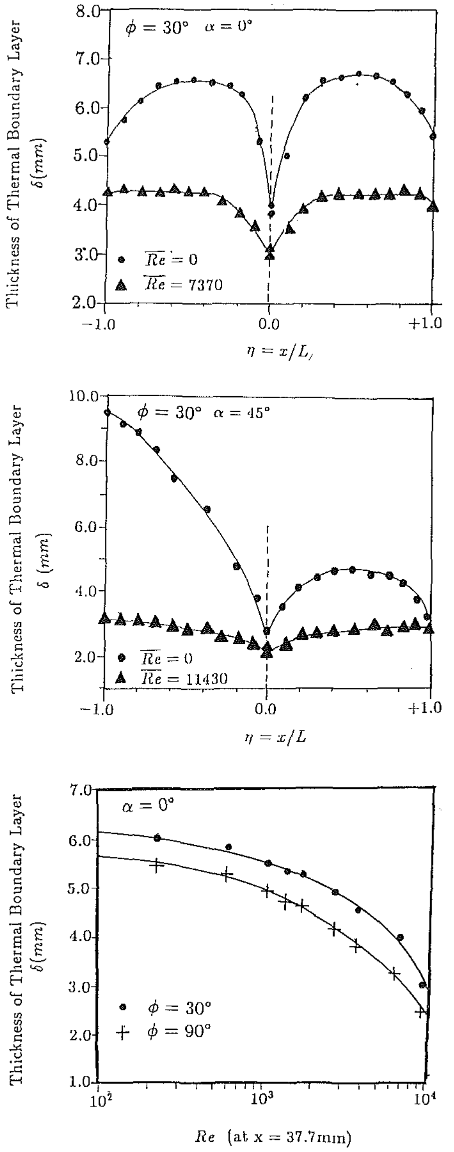

Fig. 6 Thickness of thermal boundary layer versus: (*a*) $\eta = X/L$ at $\alpha = 0$ deg (● for $\overline{Re} = 0$; ▲ for $\overline{Re} = 7370$); (*b*) $\eta = X/L$ at. $\alpha = 45$ deg (● $\overline{Re} = 0$, ▲ for $\overline{Re} = 11430$); and (c) Re at $x = 37.7$ mm (+ for $\phi = 90$ deg, ● for $\phi = 30$ deg)

The flow current in the boundary layer is driven by rotation to approach the surface of the cone, resulting in a general decrease of the thermal boundary layer thickness as rotational speed increases. Figure 6(*c*) plots variance in thermal boundary layer thickness versus rotational Reynolds number at $x = 37.7$ mm. Note that the thickness decreases as the cone vertex angle increases which suggests that the average convective conductance increases with both increasing rotational speed and the cone vertex angle.

The thickness of the thermal boundary layer was determined from the hologram by measuring the distance from the cone surface to the outermost detectable fringe rather than by complicated holographic tomography (Tieng and Chen, 1990). The results from this simple method were found to be consistent with those values calculated from the formal definition of the thermal boundary layer thickness for which the ratio was $[(T_s - T)/(T_s - T_\infty) = 0.99$. Here, T is the temperature at the leading edge of the boundary layer, T_s the temperature at the

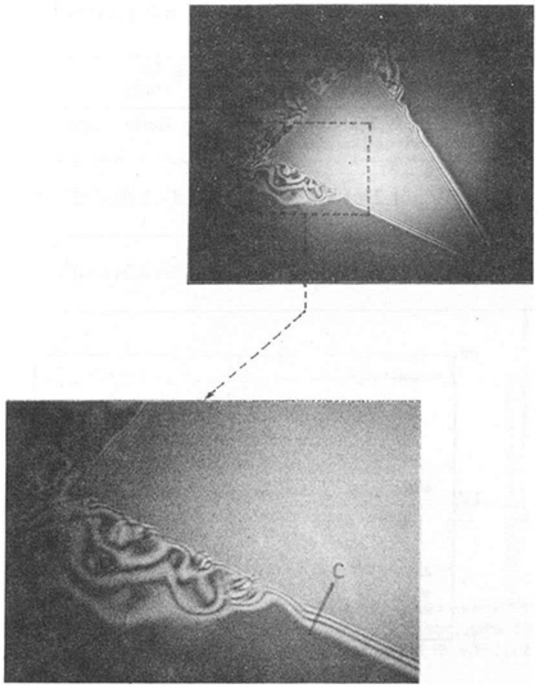

Fig. 7(*a*) Holographic visualization picture of thermal boundary layer transition and the spiral vortices of a heated rotating cone. C denotes the onset of the transition region

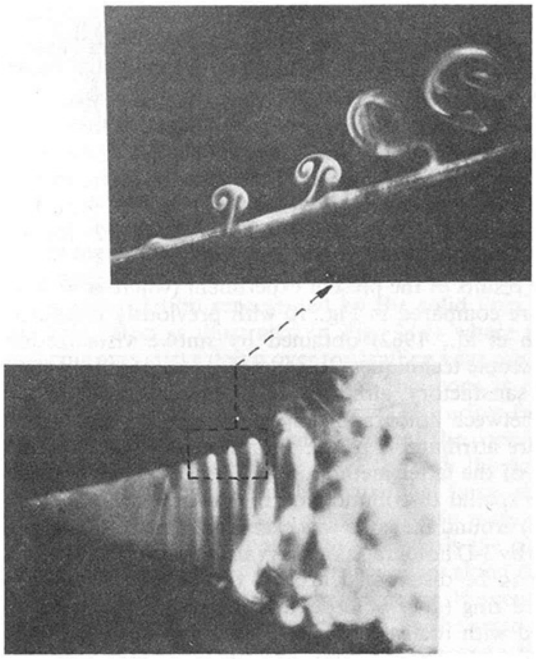

Fig. 7(*b*) Smoke visualization picture of an unheated rotating cone (after Kobayashi and Izumi, 1983)

cone surface, and T_∞ the ambient temperature. The error introduced by this simple measuring method was evaluated to be in the range of 4 percent. For example, given conditions $\phi = 30$ deg, $\alpha = 0$ deg, $T_s = 260°$ C, and a measured boundary thickness value of 6.3 mm ($x = 37.7$ mm), then according to the definition of the thermal boundary layer thickness $((T_s - T)/(T_s - T_\infty) = 0.99]$, the temperature T at the leading edge of the boundary layer should be 27.3° C. If, however, the temperature at the outermost fringe is reconstructed by Abel inversion (Tieng et al., 1992), a T' value of 40° C is obtained. The deviation between T and T' is 12.7° C and corresponds to a relative error of approximately 4 percent.

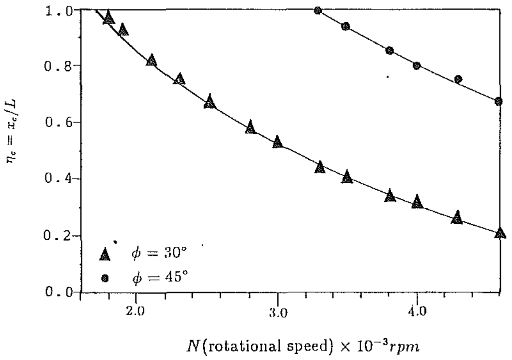

Fig. 8 Location of critical point versus rotational speed (▲ for ϕ = 30 deg, ● for ϕ = 45 deg)

The beam bending effect is a major source of uncertainty in this method, affecting the accurate determination of both boundary layer thickness, and temperature, T. The effect of beam bending on the measuring accuracy depends on the temperature gradient as well as the length of the beam path traversing the flow. In our case, however, the temperature was moderate (260° C), the traversing path very short (only 20 cm), so the deflection of the beam was very small. An evaluation of the extent of light bending by the lens imaging method (Hauf and Grigull, 1970), demonstrated that there was no visible deflection to a measuring accuracy of 0.1 mm. Therefore, the errors in determining the location of the outermost fringe edge (resulting from beam bending) can be expected to be less than 2 percent (assuming a thickness of 5 mm). Errors of this magnitude for temperature (6–8 percent), and thermal boundary layer thickness (2.5 percent) introduced by the beam bending effect were also reported for a rotating cylinder (dia. 60 mm, length 0.45 m) (Hauf and Grigull, 1970) and a sphere (dia. 35 mm) (Tieng and Yan, 1992).

In order to acquire more detailed and accurate information concerning the 3-D thermal boundary layer, it is necessary to reconstruct the 3-D temperature distribution. Since a portion of the overall fringe structure is missing due to blockage by the opaque cone, data reconstruction may prove difficult and will be conducted in the near future. To overcome these difficulties, a fictitious fringe number function will be chosen to represent the missing fringes according to an invariance of the area under the fringe number curve (Zien et al., 1975).

(b) Boundary Layer Transition. It can be observed from the real time holographic interferometry that as rotational speed increases, the thickness of the thermal boundary layer steadily decreases. At high enough rotational rates, the thermal boundary deviates from normal developing behavior and detaches from points near the lateral surface of the cone (see Fig. 7(*a*) point C). This behavior is similar to the phenomena reported for the cases of a heated rotating horizontal cylinder (Hauf and Grigull, 1970) and sphere (Tieng and Yan, 1992). Note the wavy unstable vortices which occur after the separation (C) point (enlarged portion of Fig. 7(*a*)).

This phenomenon can be reasonably related to the existence of laminar-turbulent transitions in the lateral surface boundary layer of an unheated cone rotating in still fluid (Tien and Campbell, 1963; Kappesser et al., 1973; Kreith et al., 1962; Kobayashi et al. 1987; and Kobayashi and Izumi, 1983). According to these studies, the actual flow field around a rotating cone generally involves not only a laminar boundary layer but also a transition region in which the boundary layer changes from laminar to fully turbulent. The transition region begins at a critical point, X_c, where the flow first becomes unstable and progresses through an area of regular spiral vortices, until

Table 1 Critical Reynolds number values for a heated cone rotating in still air by using holographic visualization

Cone Vertex angle θ	Rotational angle ϕ	Present measured Re_c		Previous measured Re_c (after Kreith et al., 1962)	
		$N_1 = 2{,}000$ rpm	$N_2 = 4{,}600$ rpm	By Smoke visualization	By stethoscope
30°	0°	10255	10952	1.2×10^4	$(1.5 \sim 2.0) \times 10^4$
	45°	10098	11137		
	90°	9937	10784		
45°	0°	29000	29800	3.2×10^4	$(3.5 \sim 4.2) \times 10^4$
	45°	28980	30010		
	90°	30027	30237		

regions of irregular, random turbulence are reached. This transition region is clearly illustrated by Fig 7(*b*), in which an unheated cone rotating in air is visualized by the smoke visualization method (Kobayashi and Izumi, 1983). Even though at a first approximation it would seem that the flow structure around a rotating heated cone (Fig. 7(*a*)) should be much more complicated than that of an unheated rotating one (Fig. 7(*b*)), there are remarkable similarities between the two systems. Most notable are the existence of critical points and the presence of regular spiral vortices downstream from them. The beginning point on the transition region for the unheated rotating cone, reasonably corresponds to the separation point of the isothermal fringes for the heated rotating cone. Furthermore, the regular spiral vortices existing downstream of the critical points in Fig. 7(*b*) generally approximate the isothermal fringe spiral curls in Fig. 7(*a*). These similarities provide the basis for a new experimental method which can readily measure critical points, critical Reynolds numbers of the transitional boundary layer, and the direction of regular spiral vortices.

Using holographic interferometry, the shift in the critical position along the lateral surface (x direction) was determined directly by measuring the separation position of the isothermal fringes, and subsequently plotted in Fig. 8 for cone vertex angles of 30 and 45 deg as rotational rate increases. From real time holographic observation, it is clear that Xc shifts toward the cone vertex with increasing rotational speed due to the increase in centrifugal force resulting in an increase in instability. Also note from Fig. 8, that for cones having smaller vertex angles, the critical points shift much closer to the cone vertex as rotational speed is increased. This fact is attributable to a larger centrifugal component acting normal to the lateral surface of the cone. For the case of laminar boundary layer, this shift behavior indicates that even though the average heat transfer rate decreases with decreasing cone vertex angle due to a thickening of the thermal boundary layer (see Fig. 6(*c*)), the average conductance can be expected to increase when $\overline{Re} > Re_c$. This is due in part to the movement of the critical point closer to the vertex of the cone, as well as to the larger convective conductance in the turbulent flow.

It was also observed from the holograms that the rotational angle did not appreciably affect the general shape of the flow patterns, (see Fig. 3(*f*) for $\alpha = 0$ deg and Fig. 4(*f*) for $\alpha = 45$ deg) the critical position and the critical Reynolds number under conditions where the overall rotational Reynolds numbers, $\overline{Re}$, were greater than 15,000. In these cases, it appears that the effect of the gravitational field, if it exists at all, is negligible.

The critical Reynolds number [$Re_c = (\omega x_c^2 \sin \phi/2)/\nu$] can be directly determined from measured data of the location of critical points in the holograms. The critical Reynolds number values for cones having vertex angles of 30 and 45 deg, at different rotational angles of 0, 45 and 90 deg, are presented in Table 1 and compared with previously measured data.

At a rotational speed of 4600 rpm, the measured Re_c values for cones with vertex angles of 30 and 45 deg were 10,952 and 29,800, respectively. Obviously, then, Re_c increases with increasing cone vertex angle due to a lessening of the centrifugal effect of the force balance in the boundary layer. These results are consistent with previous research (Kreith et al., 1962) and Kobayashi and Izumi, 1983). As before, the critical Reynolds number remains relatively unchanged over different rotational angles suggesting that the gravitational field also does not severely affect transition behavior. Note that Re_c remains nearly constant as rotational speed changes (see Fig. 9); a fact that was reported previously by Kreith et al., (1962) for an ϕ of 53.5 deg.

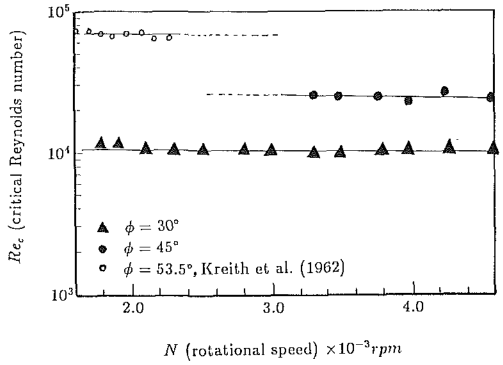

Fig. 9 Critical Reynolds number versus rotational speed (▲ for ϕ = 30 deg, ● for ϕ = 45 deg), ○ for ϕ = 53.5 deg (after Kreith et al., 1962)

The results of the present experiment (where ϕ = 30 and 45 deg) are compared in Fig. 10 with previously measured data (Kreith et al., 1962) obtained by smoke visualization and stethoscopic techniques. In general, agreement between methods is satisfactory, although deviations do exist. Large deviations between holographically and stethoscopically measured data are attributable to the poor sensitivity and spatial resolution of the latter method.

The spatial distribution of the separation points (critical points) around the cone was examined from different viewing angles by 3-D holographic observation. The critical points were found to be distributed around the cone so as to form an inclined ring (at $\alpha \neq 0$ deg), whose angle of inclination increased with increasing α. The ring-like distribution is very similar to the spiral vortex ring observed by smoke visualization; moving with the rotating cone through the boundary layer transition region (see Fig. 7(*b*)). Note that the inclined angle of the spiral vortex ring has been used to determine the direction of the spiral vortex angle (Kobayashi and Izumi, 1983 and Kobayashi et al. 1987); however, whether or not the present observed separation ring can be used to duplicate this function has not yet been verified.

(c) Turbulent Zone. An examination of Figs. 3-5 reveals that the isothermal fringes over the base of a heated cone of finite length undergo very complicated changes at rotational speeds from 1300 to 4600 rpm and illustrate the presence of irregular and unsteady turbulent flow, even though neither the turbulent boundary layer nor boundary layer transition have

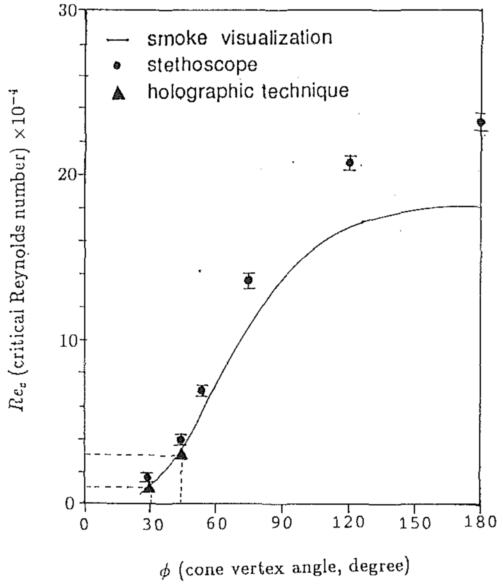

Fig. 10 Critical Reynolds number versus cone vertex angle. : measured by smoke visualization (Kreith et al., 1962); ●: measured by stethoscope·[Ɨdenotes mean deviation for measurement (Kreith et al., 1962); ▲ : measured by present holographic technique

yet occurred on the cone lateral surfaces, as shown in Figs. 3(*c*), 3(*d*), 4(*c*), and 4(*d*) at Re = 7370, 11,430. To our knowledge, this interesting phenomenon has never been reported, either in theory or in experimentation but it can be explained in terms of interactions between buoyancy and centrifugal effects. For instance, consider the case at $\alpha = 0$. For a stationary heated cone of finite length, both the theoretical and experimental velocity vector distributions, and flow visualization diagrams (obtained from the particle tracking method) (Koyama et al., 1985) clearly show that fluid passing over the trailing edge of the cone is continuously drawn into the center region of the base, while in the vicinity of the cone base surface, fluid flows outward from the center forming a region of recirculation represented by the solid lines in Fig. 11(*b*). This effect is illustrated in Fig. 3(*a*) where the isothermal contours curve down over the trailing edge toward the center region of the cone base. When this cone is rotated, another current as dotted lines in Fig. 11(*b*) arises from the centrifugal effect. The rotational motion of the cone induces a circumferential velocity in the fluid through the action of viscosity. Due to the action of the centrifugal force, the fluid is impelled along the cone surface. To satisfy mass conservation, fluid far from the cone moves towards the cone, replacing the fluid which has been thrown away along the cone surface. Therefore, over the cone base surface, the centrifugal current is moving in the same direction as the recirculation current near the cone base surface, but in an opposite direction further far from the base. Therefore, a thin thermal boundary layer can be found in the vicinity of the base surface, while complicated fringe patterns exist in the region out from the base surface. At low rotational rates, an upward plume with deformed (curved) isothermal contours is formed (see Fig. 3(*b*)) due to an outward flowing current (centrifugal current) that is weaker than the inward flowing one (buoyancy current). As the rotational speed is increased, the outward flowing curring becomes stronger, gradually opposing the buoyancy current force and generating turbulent flow in the process (see Fig. 3 (*e*, *f*). Since irregular eddying or crosswise mixing in the turbulent zone improves heat dissipation between the fluid and the cone surface, a steep increase in the rate of both average and local heat transfer at the cone base surface can be expected.

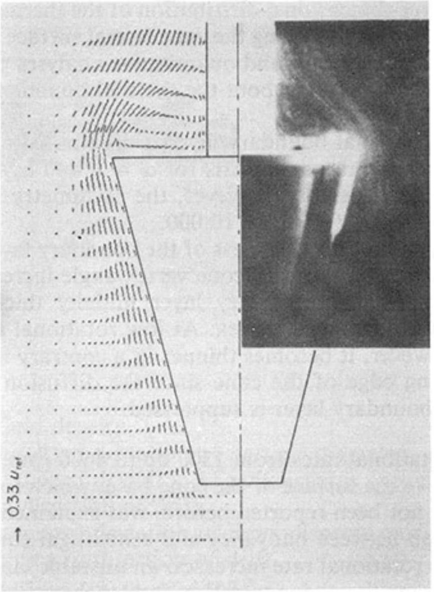

Fig. 11(*a*) Velocity field (left) and powder flow visualization (right) around a stationary unheated frustum (after Koyama et al., 1985)

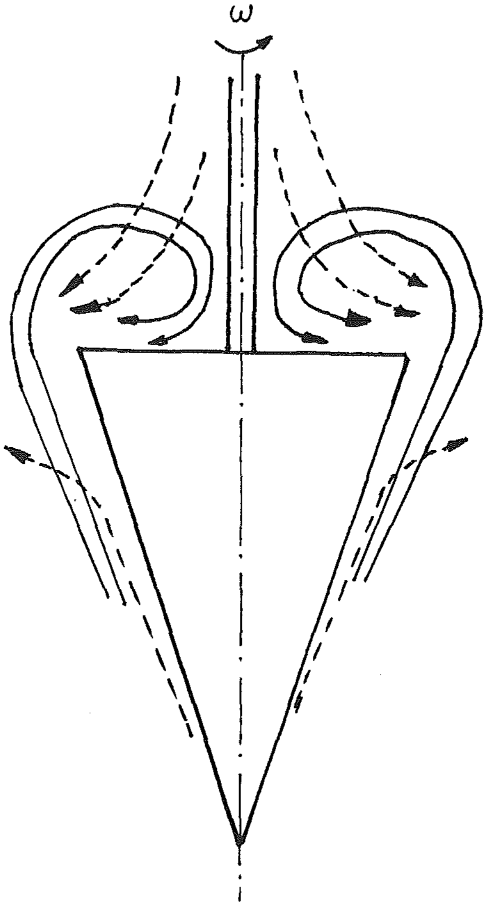

Fig. 11(*b*) Schematic diagram of the interaction between recirculation and centrifugal currents above the upper end surface. Solid line: recirculation current; dotted: centrifugal current

Conclusions

Three-dimensional diffuse-illumination and real-time holographic interferometry were successfully applied in order to visualize and analyze the 3-D convective flow around a heated rotating cone of finite length.

The three-dimensional distribution of the thermal boundary and its development along the cone lateral surface were clearly visualized. Qualitative and quantitative analyses provided the following conclusions about the thermal boundary layer:

1. The thermal boundary layer is distributed axisymmetrically about the rotational axis for $\alpha = 0$ and asymmetrically for $\alpha \neq 0$. In general, however, the asymmetry in the latter cases disappears for $\overline{\text{Re}} > 10{,}000$.
2. In general, the thickness of the boundary layer decreases as the rotational speed or cone vertex angle increases.
3. The thermal boundary layer initially thickens downstream away from the vertex. At low rotational rates ($\overline{\text{Re}} <$ 5000) however, it becomes thinner in a contrary manner near the trailing edge of the cone since the diffusion rate of the thermal boundary layer is suppressed.

For rotational rates from 1300 up to 4600 rpm, a turbulent zone above the surface of the cone base, which to our knowledge has not been reported before, was explained in terms of interaction between buoyancy and centrifugal currents.

As the rotational rate increases, an unstable laminar to turbulent region (involving spiral vortices), becomes clearly visible on the cone's lateral surface.

In the transitional regions, the following conclusions hold:

1. The critical point shifts toward the cone vertex, as the rotational speed is increased. For those cones with small vertex angles, this shift is more pronounced.
2. The effect of gravity on critical point location and Reynolds number is not appreciable and can thus be neglected for high rotational speed.
3. Re_c remains unchanged over different rotational angles and speeds, but increases with increasing cone vertex angle.
4. For those cones where $\alpha \neq 0$, critical points are distributed around the lateral surface on the cone forming an inclined ring, whose angle of inclination increases with increasing rotational angle.
5. Re_c results, measured by holographic interferometry, generally agree with those obtained from other techniques, although some deviations do exist.

In previous research, the problems of boundary layer transition were mainly studied experimentally using stethoscope or hot wire techniques to detect the frequency spectra or velocity fluctuations but at the price of the flowfield intrusion, relatively large probes and low resolution and sensitivity. On the other hand, holographic interferometry, with its high sensitivity, spatial resolution and nonintrusive flowfield, is an impressive diagnostic tool for measuring the thickness of the thermal boundary layer, the location of critical points and the Reynolds numbers of boundary layer transitions.

Acknowledgment

The authors gratefully acknowledge the financial support of the National Science Council of the Republic of China under contract No. NSC80-0401-E-006-47.

References

Bayazitoglu, Y., and Otisik, M. N., 1988, *Elements of Heat Transfer*, McGraw-Hill, New York, N.Y.

Chang, K. C., Tieng, S. M., and Chen, C. C., 1992, "Effect of Composition Change on Temperature Measurement in Premixed Flame by Holographic Interferometry," *Optical Engineering*, SPIE, Vol. 31, pp. 353–362.

Hartnett, J. P., and Deland, E. C., 1961, "The Influence of Prandtl Number on the Heat Transfer from Rotating Nonisothermal Disks and Cones," ASME *Journal of Heat Transfer*, Vol. 83, pp. 95–96.

Hauf, W., and Grigull, U., 1970, "Optical Methods in Heat Transfer," *Advances in Heat Transfer*, Vol. 6, pp. 133–366.

Hering, R. G., and Grosh, R. J., 1963, "Laminar Combined Convection from a Rotating Cone," ASME *Journal of Heat Transfer*, Vol. 85, pp. 29–34.

Incropera, F. P., and Dewitt, D. P., 1990, *Fundamentals of Heat and Mass Transfer*, 3rd Edition, Wiley, New York, N.Y.

Jogata, R. C., and Collins, D. J., 1972, "Finite Fringe Holographic Interferometry Applied to a Right Circular Cone at Angle of Attack," ASME *Journal of Applied Mechanics*, Vol. 39, pp. 897–903.

Kappesser, R., Greif, R., and Cornet, I., 1973, "Mass Transfer to Rotating Cone," *Applied Scientific Research*, Vol. 28, pp. 442–452.

Kegelman, J., Nelson, R. C., and Mueller, T. J., 1983, "The Boundary Layer on an Axisymmetric Body With and Without Spin," *AIAA Journal*, Vol. 21, pp. 1485–1491.

Kobayashi, R., and Izumi, H., 1983, "Boundary-Layer Transition on a Rotating Cone in a Still Fluid," *Journal of Fluid Mechanics*, Vol. 127, pp. 353–364.

Kobayashi, R., Kohama, Y., Arai, T., and Ukaku, M., 1987, "The Boundary-Layer Transition on Rotating Cones in Axial Flow with Free-Stream Turbulence," *JSME International Journal*, Vol. 30, pp. 423–429.

Kohama, Y., and Kobayashi, R., 1983, "Boundary-Layer Transition and the Behavior of Spiral Vortices on Rotating Sphere," *Journal of Fluid Mechanics*, Vol. 137, pp. 153–164.

Koyama, H., Nakayama, A., Ohsawa, S., and Yamada, H., 1985, "Theoretical and Experimental Study of Free Convection from a Vertical Frustum of a Cone of a Finite Length," *International Journal of Heat and Mass Transfer*, Vol. 28, pp. 969–976.

Kreith, F., Ellis, D., and Giesing, J., 1962, "An Experimental Investigation of the Flow Engendered by a Rotating Cone," *Applied Scientific Research*, Sec. A, Vol. 11, pp. 430–440.

Kreith, K., 1968, "Convective Heat Transfer in Rotating Systems," *Advances in Heat Transfer*, Vol. 5, pp. 129–251.

Kuiken, H. K., 1968, "Axisymmetric Free Convection Boundary Layer Flow Past Slender Bodies," *International Journal of Heat and Mass Transfer*, Vol. 11, pp. 1141–1153.

Tien, C. L., 1960, "Heat Transfer by Laminar Flow from a Rotating Cone," ASME *Journal of Heat Transfer*, Vol. 82, pp. 252–253.

Tien, C. L., and Campbell, D. T., 1963, "Heat and Mass Transfer From Rotating Cones," *Journal of Fluid Mechanics*, Vol. 17, pp. 105–112.

Tieng, S. M., and Chen, H. T., 1990, "Holographic Tomography by SART and its Application to Reconstruction of 3D Temperature Distribution," *Wärme- und Stoffübertragung*, Vol. 26, pp. 49–56.

Tieng, S. M., and Lai, W. Z., 1991, "Digital Phase Shift Holographic Interferometry and Its Application in the Experimental Flow Study," *Optical and Quantum Electronics*, Vol. 23, pp. 593–601.

Tieng, S. M., and Yan, A. C., 1992, "Investigation of Mixed Convection by Holographic Interferometry," AIAA, *Journal of Thermophysics and Heat Transfer*, Vol. 6, pp. 727–732.

Tieng, S. M., and Lai, W. Z., 1992, "Temperature Measurement of Reacting Flowfield by Phase Shift Holographic Interferometry," AIAA, *Journal of Thermophysics and Heat Transfer*, Vol. 6, pp. 445–451.

Tieng, S. M., Chang, K. C., and Huang, J. M., 1992, "Application of Laser Holographic Interferometry to Temperature Measurements in Buoyant Air Jets," AIAA, *Journal of Thermophysics and Heat Transfer*, Vol. 6, pp. 377–379.

Wang, T. Y., and Kleinstrener, C., 1990, "Similarity Solution on Combined Convection Heat Transfer from a Rotating Cone or Disk to Non-Newtonian Fluids," ASME *Journal of Heat Transfer*, Vol. 112, pp. 939–944.

Wu, C. S., 1959, "The Three Dimensional Incompressible Laminar Boundary Layer on a Spinning Cone," *Applied Scientific Research*, Sec. A, Vol. 8, pp. 140–146.

Zien, T. F., Ragsdale, W. C., and Spring, W. C., 1975, "III. Quantitative Determination of Three-Dimensional Density Field of a Circular Cone by a Holographic Interferometry," AIAA Paper No. 74-636, presented at the AIAA 8th Aerodynamic Testing Conference, Bethesda, Md., 8–10, July 1974.

Journal of Fluids Engineering
Technical Briefs

"Heavy" Particle Dispersion Measurements With Mono- and Polydisperse Particle Size Distributions

J. R. Ferguson[1] and D. E. Stock[1]

A method is presented to estimate the effects of a polydisperse particle size distribution on the measured turbulent dispersion of particles. In addition, the analysis provides a means to estimate the standard deviation of the size distribution for which a class of particles may be considered monodisperse. If monodisperse particles are unavailable because of practical considerations (e.g., the required standard deviation of particle size is too small to obtain a sufficient quantity) then the method provides a means to correct the data of near monodisperse size distributions to reflect the dispersion of monodisperse particles.

Nomenclature

a = particle diameter
C_D = drag coefficient
g = gravitational acceleration
K = coefficient of dispersion
P = probability density function
R = Reynolds number
t = time
U = mean gas velocity
U_p = particle velocity
v_d = particle drift velocity
v_o = seeding velocity
x, y, z = coordinate direction

Greek

μ = gas viscosity
μ_a = mean particle radius
μ_z = center of particle plume
ρ = particle density
ρ_f = fluid density
σ_a = standard deviation of particle diameter
σ_p = standard deviation of polydisperse particle plume in direction of drift
σ_z = standard deviation of monodisperse particle plume in direction of drift
τ = particle relaxation time

Introduction

The turbulent dispersion of heavy particles is known to be influenced by particle inertia, the "crossing trajectories" effect, and the continuity effect. An additional effect which can be significant, particularly when analyzing experimental particle dispersion data, is that of a polydisperse size distribution. Many theoretical treatments of particle dispersion and analysis of experimental data assume the use of a monodisperse size distribution. In reality, truly monodisperse distributions are seldom obtained. As a consequence, discrepancies may arise between experimental findings and dispersion models which may be resolved by accounting for the effects of polydisperse size distributions.

Inertia effects describe the particle's response to drag forces created by the turbulent velocity fluctuations of the surrounding fluid. Particles with large mass react sluggishly to fluid velocity variations but once put in motion they retain their velocity for a longer time. Since dispersion is a function of the product of these two attributes, it is not clear if particle inertia increases or decreases dispersion. Detailed analysis and experiment have indicated that inertia tends to increase particle dispersion slightly (Reeks, 1977; Nir and Pismen, 1979; Csanady, 1963; Meek and Jones, 1973).

The crossing trajectories effect is caused by the differing paths a fluid element and particle take when a body force is present. Under the influence of a body force, "heavy" particles attain finite drift velocities causing them to change their respective fluid neighborhoods more rapidly than corresponding fluid elements thus reducing the dispersion of particles as compared to the fluid elements. The crossing trajectories effect has been well studied analytically and experimentally (Reeks, 1977; Nir and Pismen, 1979; Csanady, 1963; Snyder and Lumley, 1971; Wells and Stock, 1983).

Inertia effects and the crossing trajectories effect influence the dispersion in each coordinate direction equally. The continuity effect, on the other hand, affects the dispersion only in coordinate directions perpendicular to the free fall direction. This effect describes the tendency of a particle to drift under the influence of a body force from a region of fluid moving as a coherent "packet" into fluid filling the vacated region left by the original packet of fluid. The dispersion in directions normal to the drift velocity can be reduced by a factor of one half in isotropic turbulence in the limit of large drift velocities. The effect causes contours of particle density to appear el-

---

[1] Department of Mechanical and Materials Engineering, Washington State University, Pullman, Washington 99164. Dr. Ferguson's current address is: ABB Power Generation Ltd., Baden, Switzerland.

Contributed by the Fluids Engineering Division of THE AMERICAN SOCIETY OF MECHANICAL ENGINEERS. Manuscript received by the Fluids Engineering Division February 28, 1992; revised manuscript received January 8, 1993. Associate Technical Editor: E. E. Michaelides.

liptical in planes containing the drift direction (Reeks, 1977; Nir and Pismen, 1979; Csanady, 1963; Meek and Jones, 1973).

Particles with a polydisperse size distribution can also appear to "disperse" unequally between the direction of drift and directions normal to the drift. For example, under the influence of gravity, larger particles of a polydisperse distribution fall faster than smaller ones producing an apparent increase of dispersion in the vertical direction over other directions. This is referred to here as the polydisperse sedimentation effect. To measure the dispersion in the free fall direction either a monodisperse particle size distribution must be used or the measured dispersion must be corrected to account for the effects of the polydisperse size distribution.

The following sections analyze the conditions for which a particle size distribution may be considered monodisperse and present a method by which dispersion measurements of a polydisperse particle size distribution can be corrected to reflect the dispersion of monodisperse particles. In addition, the influences of nonisokinetic seeding with polydisperse size distributions on measured dispersion is also examined. Illustrative examples are given to demonstrate the magnitude of the various effects.

Analysis

Consider the vertical spatial distribution of monodisperse particles emitted from a point source at some downstream location, x, from the source, in a horizontal flow. The probability of finding a particle at some vertical location, z, is given by

$$P(z)=\frac{1}{(2\pi)^{1/2}\sigma_z}\exp\left(\frac{-1}{2}\left(\frac{z-\mu_z}{\sigma_z}\right)^2\right) \tag{1}$$

assuming the plume possesses a Gaussian profile (Hinze, 1975). μ_z is the monodisperse plume center and σ_z is the standard deviation of the profile at x. To obtain the spatial probability distribution for a polydisperse size distribution, this distribution is modified by making the plume center a function of particle diameter and multiplying by the probability distribution of particle size. Assuming a Gaussian distribution for particle size, the resulting probability distribution for finding a particle of size "a" at location "z" of a polydisperse collection of particles is

$$P(z,a)=\frac{1}{2\pi\sigma_z\sigma_a}\exp\left(\frac{-1}{2}\left(\left(\frac{z-\mu_z(a)}{\sigma_z}\right)^2+\left(\frac{a-\mu_a}{\sigma_a}\right)^2\right)\right). \tag{2}$$

This assumes that the particle size distribution is sufficiently narrow that the turbulent dispersion process including inertia effects, crossing trajectories effects and continuity effects produces the same spread (σ_z) for each particle size. Otherwise, σ_z becomes a function of particle diameter as well. This bivariate probability distribution is the product of two Gaussian distributions. One describes the spatial distribution of monodisperse particles at a given streamwise location and the other describes the distribution of particle diameter. The two distributions can be combined this way since "z" and "a" are independent random variables (Hines and Montgomery, 1980).

Assuming the particles move horizontally with the same velocity as the conveying air, the averaged location of the plume center in this flow for "heavy" particles of size a settling vertically is determined by integrating (Michaelides, 1988)

$$\frac{d^2\mu_z}{dt^2}=\frac{dU_p}{dt}=-C_D\frac{\mathrm{Re}}{24}U_p/\tau-g \tag{3}$$

with

$$\mathrm{Re}=\rho_f a^2 |(\mathbf{U}-\mathbf{U}_p)|/\mu$$

$$C_D=\frac{24}{\mathrm{Re}}\quad \mathrm{Re}<1 \tag{4}$$

$$C_D=\frac{24}{\mathrm{Re}}(1+0.15\,\mathrm{Re}^{0.687})\quad 1<\mathrm{Re}<1000 \tag{5}$$

from the particles point of release to the point of interest. Due to the density difference between the particles and air, the terms involving the pressure gradient caused by particle acceleration, the added mass caused by accelerating displaced fluid and the Basset history term are not included in the equation of motion.

It is instructive to examine the importance of isokinetic seeding (the seeding of particles into the flow with the same velocity as the conveying fluid) by integrating Eq. (3) for particles which obey Stokes' drag law (Eq. (4)). This yields

$$\mu_z=z_{\mathrm{seed}}+\nu_o\tau(1-e^{-t/\tau})-\nu_d\tau(1+t/\tau-e^{-t/\tau}) \tag{6}$$

where $t = x/U$ the time elapsed to reach the downstream location x, $\tau = a^2\rho/18\mu$ the particle relaxation time, $\nu_d = \tau g$ the particle drift velocity and z_{seed} is the height of the seeding point. The results qualitatively apply to heavier particles which follow the nonlinear drag law of Eq. (5) originally given by Rowe (1961). Stokes' drag law begins to introduce notable error for Re ~ 1. In air, Re = 1.1 for 60μ particles (ρ = 2.6 gm/cm^3) whose drift velocity is estimated to be ~24.5 cm/s using the nonlinear drag law compared to 28.1 cm/s using Stokes' drag relationship (a 13 percent error). This would lead to a ~3.6 cm error in the location of the plume center for each second the particles are carried downstream. In regions close to the seeding point the errors are less (e.g., a ~2.4 percent error in drift velocity after the elapse of τ).

The second term in Eq. (6) represents the plume displacement resulting from the initial vertical velocity at the inlet ν_o while the third term represents the displacement caused by the gravitationally induced drift velocity ($\nu_d = \tau g$). The importance of isokinetic seeding becomes apparent here. If ν_o is comparable in magnitude to ν_d then the location of the plume center can be significantly altered from the expected center location assuming isokinetic seeding. Since drift velocities in air range from ~1 to ~65 cm/s (10 to 100 μm dia) this is a rather stringent requirement of particle seeding. For example, a small misalignment (~5 deg) of the seeding injection mechanism in a tunnel operating with a mean velocity of 10 m/s can produce non-isokinetic seeding of this magnitude (ν_o = 87 cm/s).

Nonisokinetic seeding further complicates the measurement of particle dispersion where the particle size distribution is not truly monodisperse. Suppose the particles have an initial upward velocity leaving the particle seeder. The larger particles of the distribution would, on average, travel higher and have a more pronounced parabolic arch in their trajectories due to their greater inertia than the smaller particles of the distribution. This effect is illustrated in Fig. 1. In regions relatively close to the particle seeder the effects of polydisperse sedimentation would be effectively reduced until the trajectories of the larger particles cross the trajectories of the smaller ones.

A further nonisokinetic seeding effect occurs if the particles have a streamwise velocity much greater (or smaller) than the main flow at the seeding point. This effectively reduces (or increases) the elapsed time "t" over which the sedimentation effect separates the large and small particles causing the apparent increase of dispersion in the gravitational direction. This can be accounted for by a suitable adjustment to the streamwise starting location in the computations.

If the particles are introduced to the main flow truly isokinetically then the plume center can be estimated using

$$\mu_z=z_{\mathrm{seed}}-\nu_d\tau(1+t/\tau-e^{-t/\tau}). \tag{7}$$

Substituting this approximation (or other appropriate solution to Eq. (3)) for μ_z into Eq. (2), the plume center, μ_p, and variance, σ_p^2, for a polydisperse particle size distribution can then be computed from the standard statistical definitions,

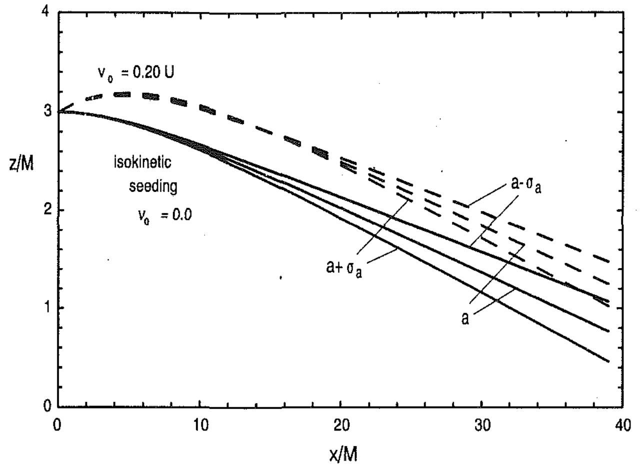

Fig. 1 Effects of particle size and nonisokinetic seeding on particle trajectories

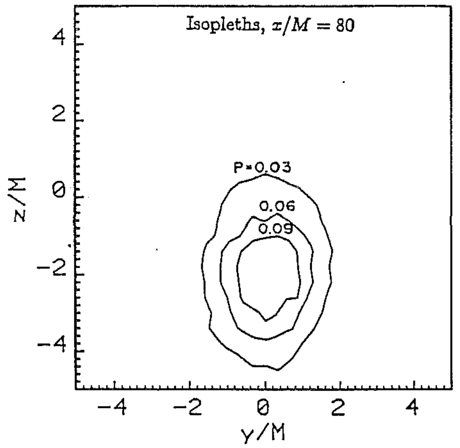

Fig. 3 Two-dimensional particle concentration profiles as measured in a horizontal wind tunnel. Flow direction is normal to the page.

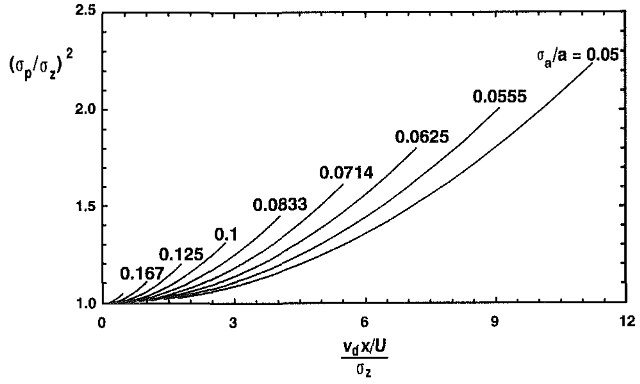

Fig. 2 Apparent increase in particle dispersion due to a polydisperse particle size distribution. Trajectories computed from Eq. (3) with a = 60 μ, σ_a = 5 μ and U = 4.5 m/s. Note the apparent reduction in dispersion for the polydisperse size distribution when ν_o = 20 percent of U around x/M = 15 and the apparent increase thereafter.

$$\mu_p = \int\int zP(z,a)dzda \tag{8}$$

$$\sigma_p^2 = \int\int (z-\mu_p)^2 P(z,a)dzda \tag{9}$$

remembering that ν_d and τ are functions of particle size.

Equations (2), (8), and (9) together with an appropriate solution for μ_z can be used to estimate (i) the effects of a polydisperse size distribution on measured dispersion, (ii) the allowable standard deviation of a particle size distribution for which it may be considered monodisperse, and (iii) the correction to measured dispersion data to obtain estimates of monodisperse particle dispersion.

"Monodisperse" Size Distributions

Evaluation of the integrals in Eqs. (8) and (9) using the probability distribution in Eq. (2) and the plume center given by Eq. (7) produces the curves shown in Fig. 2. This figure illustrates the apparent increase of dispersion in the direction of drift $(\sigma_p/\sigma_z)^2$ arising from a polydisperse particle size distribution plotted as a function of $(\nu_d x/U)/\sigma_z$. Holding particle properties and the standard deviation of the particle size distribution constant, the abscissa represents the ratio of the distance the average sized particle has gravitationally settled to the statistical size of the monodisperse particle plume, σ_z. As the elapsed time increases ($t = x/U$, time allowed for gravitational settling) the more pronounced become the effects of a polydisperse distribution on the apparent dispersion. This becomes more severe as the drift velocity of the average sized particle becomes larger. On the other hand, if the expected size of the plume is large then longer elapsed times or wider size distributions can be used.

The use of Fig. 2 is best illustrated with an example. In the design of an experiment to measure the vertical turbulence induced dispersion of particles with a 30 cm/s drift velocity (~60 μ diameter glass spheres, ρ = 2.6 g/cm^3) preliminary measurements estimate the size of the monodisperse plume at a location 200 cm downstream from the particle source to be σ_z = 3.5 cm. The velocity of the conveying air stream was 4.5 m/s. The apparent increase of dispersion from a polydisperse size distribution was to be limited to less than 15 percent of the monodisperse plume size. Then from Fig. 1, for $(\nu_d x/U)/\sigma_z = 3.8$ and $(\sigma_p/\sigma_z)^2 = (1.15)^2 = 1.32$ the acceptable σ_a/a = 0.076 or σ_a = 4.6 μ for the 60 μ particles. This is a rather narrow size distribution for particles of this size if a large quantity is required.

Correction of Dispersion Measurements

Once dispersion measurements have been obtained, Eqs.(2), (8), and (9) together with an appropriate expression for the plume center μ_z for each particle size, can be solved in an iterative manner to find the "monodisperse" dispersion for the mean particle size. The procedure is straightforward. First a guess is made for the monodisperse dispersion σ_z and then the polydisperse plume center, μ_p, and dispersion, σ_p, computed. The double integrals can be evaluated with some appropriate numerical procedure. The computed polydisperse dispersion is then compared with the measured value. The monodisperse dispersion σ_z is then adjusted in proportion to the error of the comparison. The polydisperse values are then recomputed and the process repeated until the error is reduced below some acceptable small value.

This procedure was used to compute σ_z for the measured dispersion data of Ferguson (1986) which is summarized in Table 1. The data were measured in a horizontal wind tunnel in the presence of grid generated turbulence. The two dimensional dispersion of 61.7 μ glass particles in the plane normal to the tunnel axis was measured at 5 downstream locations. An example of the measured particle concentration profiles is shown in Fig. 3. The purpose of the measurements was to show that the elliptical shape of the profiles was the result of unequal dispersion between the vertical and horizontal directions caused by the continuity effect. Analysis of the plume center showed that the particles were not seeded isokinetically. At the inlet, the particles were estimated to have an upward velocity of ~21.3 cm/s which is of the same order as the drift velocity

Table 1 "Heavy" particle dispersion measurements in grid generated turbulence. μ_p = measured plume center, σ_y = dispersion measured orthogonal to drift direction, σ_p = dispersion measured in drift direction, σ_z = corrected monodisperse dispersion in drift direction.

x/M	μ_p(cm)	σ_y^2(cm^2)	σ_p^2(cm^2)	σ_z^2(cm^2)
40	2.25 ± 0.014	3.83 ± 0.025	5.45 ± 0.035	5.41
50	0.87 ± 0.015	4.64 ± 0.030	6.08 ± 0.038	5.91
60	-1.16 ± 0.014	4.57 ± 0.028	6.94 ± 0.043	6.49
70	-1.73 ± 0.015	5.23 ± 0.033	7.87 ± 0.052	6.99
80	-4.88 ± 0.018	5.13 ± 0.034	9.37 ± 0.066	7.90
	$z_{\text{seed}} = 7.62$ cm		$U = 4.51$ m/s	
	$a = 61.7\ \mu$		$K_y = 2.83 \pm 0.40$ cm^2/s	
	$\sigma_a = 5.5\ \mu$		$K_z = 5.38 \pm 1.1$ cm^2/s	
			$K_y/K_z = 0.526 \pm 0.131$	

(29.9 cm/s) and an effective starting location of $x/M = 26$, where M is the bar spacing of the turbulence generating grid. As a consequence the computations were made using a numerical solution to Eq. 3 incorporating a nonlinear drag law (for these particles Re = 1.1). The results show (see Table 1) that relatively close to the particle seeder ($x/M = 40, 50$), the difference between σ_z and σ_p is small while further downstream the effects of the polydisperse particle size distribution and the associated sedimentation effect become more severe.

The coefficient of dispersion, K_i, can be determined for the particles in this tunnel from

$$K_i = \frac{1}{2} U \frac{d\sigma_i^2}{dx}. \tag{10}$$

Applying this formula to the data in Table 1 using a least squares straight line fit gives $K_y = 2.83$ cm^2/s, $K_z = 5.38$ cm^2/s and $K_y/K_z = 0.526$. This result supports the analysis of the continuity effect predicting the difference of dispersion between the horizontal and vertical directions to be 1/2.

Conclusions

Ideally, one would like to measure the dispersion of monodisperse particles directly but truly monodisperse size distributions are difficult to achieve. The criteria by which a polydisperse size distribution may be considered "monodisperse" is illustrated in Fig. 2. It depends significantly on individual experimental conditions such as mean flow velocity, location of measurements relative to seeding location, etc. If possible, "heavy" particle dispersion measurements should be restricted to directions which do not contain the particle's drift velocity to avoid the sedimentation effect.

Dispersion measurements of monodisperse heavy particles is difficult in practice due to the large change of mass for relatively small changes of particle diameter ($m \sim a^3$). This leads to very small allowable standard deviations of particle size. Generally the larger the particle,the smaller σ_a must be. The calculation of dispersion for monodisperse particles from data obtained with polydisperse particle size distributions, where small differences of particle size do not affect the dispersion mechanisms, is a straightforward procedure.

The effects of nonisokinetic seeding on measured dispersion have been shown to be significant for polydisperse particle size distributions. Depending on the nature of the seeding velocity relative to the main flow and particle drift direction, the influence may make the sedimentation effect more severe. Computations show the influence to be more sensitive the larger the particle's drift velocity is. Hence for large particles with size distributions which are marginally considered monodisperse, isokinetic seeding becomes very important. If isokinetic seeding is not possible then the methods presented here can be used to account for non-isokinetic effects as related to sedimentation effects of a polydisperse size distribution.

Although the manipulation of measured data to deduce a physical phenomenon is not desirable it is often the only recourse. The methods presented here can be used to determine the equivalent "monodisperse" dispersion for the averaged sized particle of the distribution for sufficiently narrow distributions.

References

Csanady, G. T., 1963, "Turbulent Diffusion of Heavy Particles in the Atmosphere," *Journal of the Atmospheric Sciences*, Vol. 20, pp. 201–208.

Ferguson, J. R., 1986, "The Effects of Fluid Continuity on the Turbulent Dispersion of Particles," Ph.D. dissertation, Washington State University.

Hines, W. H., and Montgomery, D. C., 1980, *Probability and Statistics in Engineering and Management*, Wiley, New York, NY

Hinze, J. O., 1975, *Turbulence*, McGraw-Hill, New York, NY.

Michaelides, E. E., 1988, "On the Drag Coefficient and the Correct Integration of the Equation of Motion of Particles in Gases,"ASME JOURNAL OF FLUIDS ENGINEERING, Vol. 110, pp. 339–341.

Meek, C. C., and Jones, B. G., 1973, "Studies of the Behavior of Heavy Particles in a Turbulent Flow," *Journal of the Atmospheric Sciences*, Vol. 30, pp. 239–251.

Nir, A., and Pismen, L. M., 1979, "The Effect of a Steady Drift Velocity on the Dispersion of a Particle in Turbulent Fluid," *Journal of Fluid Mechanics*, Vol. 94, No. 2, pp. 369–381.

Reeks, M. W., 1977, "On the Dispersion of Small Particles Suspended in an Isotropic Turbulent Field," *Journal of Fluid Mechanics*, Vol. 83, No. 3, pp. 529–546.

Rowe, P. N., 1961, "The Drag Coefficient of a Sphere," *Transactions of the Institute of Chemical Engineering*, Vol. 39, pp. 175–181.

Snyder, W. H., and Lumley, J. L., 1971, "Some Measurements of Particle Velocity Auto-Correlation Functions in a Turbulent Flow," *Journal of Fluid Mechanics*, Vol. 48, No. 1, pp. 41–71.

Wells, M. R., and Stock, D. E., 1983, "The Effects of Crossing Trajectories on the Dispersion of Particles in a Turbulent Flow," *Journal of Fluid Mechanics*, Vol. 136, pp. 31–62.

Pressure Measurements Around a Rotating Cylinder With and Without Crossflow

A. A. Tawfek,[1] B. V. S. S. S. Prasad,[2] and A. K. Mohanty[2]

Static pressure measurements around a cylinder rotating about an orthogonal axis with and without superimposed crossflow are carried out by using a capacitance type differential pressure transducer in conjunction with a slip-ring apparatus. A coefficient of pressure (C_p) is defined for the rotating cylinder and typical variations of C_p along its length and periphery are presented.

Nomenclature

$C_p(r, \theta)$ = pressure coefficient defined at Eq. (1)

p_0 = static pressure measured at the stagnation point, Pa

---

[1] Ship Engineering Dept., Port Said, Egypt.

[2] Mechanical Engineering Department, Indian Institute of Technology, Kharagpur.

Contributed by the Fluids Engineering Division of THE AMERICAN SOCIETY OF MECHANICAL ENGINEERS. Manuscript received by the Fluids Engineering Division October 22, 1991; revised manuscript received January 8, 1993. Associate Technical Editor: E. E. Michaelides.

Table 1 **"Heavy" particle dispersion measurements in grid generated turbulence. μ_p = measured plume center, σ_y = dispersion measured orthogonal to drift direction, σ_p = dispersion measured in drift direction, σ_z = corrected monodisperse dispersion in drift direction.**

x/M	μ_p(cm)	σ_y^2(cm^2)	σ_p^2(cm^2)	σ_z^2(cm^2)
40	2.25 ± 0.014	3.83 ± 0.025	5.45 ± 0.035	5.41
50	0.87 ± 0.015	4.64 ± 0.030	6.08 ± 0.038	5.91
60	-1.16 ± 0.014	4.57 ± 0.028	6.94 ± 0.043	6.49
70	-1.73 ± 0.015	5.23 ± 0.033	7.87 ± 0.052	6.99
80	-4.88 ± 0.018	5.13 ± 0.034	9.37 ± 0.066	7.90
	$z_{seed} = 7.62$ cm		$U = 4.51$ m/s	
	$a = 61.7\ \mu$		$K_y = 2.83 \pm 0.40$ cm^2/s	
	$\sigma_a = 5.5\ \mu$		$K_z = 5.38 \pm 1.1$ cm^2/s	
			$K_y/K_z = 0.526 \pm 0.131$	

(29.9 cm/s) and an effective starting location of $x/M = 26$, where M is the bar spacing of the turbulence generating grid. As a consequence the computations were made using a numerical solution to Eq. 3 incorporating a nonlinear drag law (for these particles Re = 1.1). The results show (see Table 1) that relatively close to the particle seeder ($x/M = 40, 50$), the difference between σ_z and σ_p is small while further downstream the effects of the polydisperse particle size distribution and the associated sedimentation effect become more severe.

The coefficient of dispersion, K_i, can be determined for the particles in this tunnel from

$$K_i = \frac{1}{2} U \frac{d\sigma_i^2}{dx}. \tag{10}$$

Applying this formula to the data in Table 1 using a least squares straight line fit gives $K_y = 2.83$ cm^2/s, $K_z = 5.38$ cm^2/s and $K_y/K_z = 0.526$. This result supports the analysis of the continuity effect predicting the difference of dispersion between the horizontal and vertical directions to be 1/2.

Conclusions

Ideally, one would like to measure the dispersion of monodisperse particles directly but truly monodisperse size distributions are difficult to achieve. The criteria by which a polydisperse size distribution may be considered "monodisperse" is illustrated in Fig. 2. It depends significantly on individual experimental conditions such as mean flow velocity, location of measurements relative to seeding location, etc. If possible, "heavy" particle dispersion measurements should be restricted to directions which do not contain the particle's drift velocity to avoid the sedimentation effect.

Dispersion measurements of monodisperse heavy particles is difficult in practice due to the large change of mass for relatively small changes of particle diameter ($m \sim a^3$). This leads to very small allowable standard deviations of particle size. Generally the larger the particle,the smaller σ_a must be. The calculation of dispersion for monodisperse particles from data obtained with polydisperse particle size distributions, where small differences of particle size do not affect the dispersion mechanisms, is a straightforward procedure.

The effects of nonisokinetic seeding on measured dispersion have been shown to be significant for polydisperse particle size distributions. Depending on the nature of the seeding velocity relative to the main flow and particle drift direction, the influence may make the sedimentation effect more severe. Computations show the influence to be more sensitive the larger the particle's drift velocity is. Hence for large particles with size distributions which are marginally considered monodisperse, isokinetic seeding becomes very important. If isokinetic seeding is not possible then the methods presented here can be used to account for non-isokinetic effects as related to sedimentation effects of a polydisperse size distribution.

Although the manipulation of measured data to deduce a physical phenomenon is not desirable it is often the only recourse. The methods presented here can be used to determine the equivalent "monodisperse" dispersion for the averaged sized particle of the distribution for sufficiently narrow distributions.

References

Csanady, G. T., 1963, "Turbulent Diffusion of Heavy Particles in the Atmosphere," *Journal of the Atmospheric Sciences*, Vol. 20, pp. 201–208.

Ferguson, J. R., 1986, "The Effects of Fluid Continuity on the Turbulent Dispersion of Particles," Ph.D. dissertation, Washington State University.

Hines, W. H., and Montgomery, D. C., 1980, *Probability and Statistics in Engineering and Management*, Wiley, New York, NY

Hinze, J. O., 1975, *Turbulence*, McGraw-Hill, New York, NY.

Michaelides, E. E., 1988, "On the Drag Coefficient and the Correct Integration of the Equation of Motion of Particles in Gases," ASME JOURNAL OF FLUIDS ENGINEERING, Vol. 110, pp. 339–341.

Meek, C. C., and Jones, B. G., 1973, "Studies of the Behavior of Heavy Particles in a Turbulent Flow," *Journal of the Atmospheric Sciences*, Vol. 30, pp. 239–251.

Nir, A., and Pismen, L. M., 1979, "The Effect of a Steady Drift Velocity on the Dispersion of a Particle in Turbulent Fluid," *Journal of Fluid Mechanics*, Vol. 94, No. 2, pp. 369–381.

Reeks, M. W., 1977, "On the Dispersion of Small Particles Suspended in an Isotropic Turbulent Field," *Journal of Fluid Mechanics*, Vol. 83, No. 3, pp. 529–546.

Rowe, P. N., 1961, "The Drag Coefficient of a Sphere," *Transactions of the Institute of Chemical Engineering*, Vol. 39, pp. 175–181.

Snyder, W. H., and Lumley, J. L., 1971, "Some Measurements of Particle Velocity Auto-Correlation Functions in a Turbulent Flow," *Journal of Fluid Mechanics*, Vol. 48, No. 1, pp. 41–71.

Wells, M. R., and Stock, D. E., 1983, "The Effects of Crossing Trajectories on the Dispersion of Particles in a Turbulent Flow," *Journal of Fluid Mechanics*, Vol. 136, pp. 31–62.

Pressure Measurements Around a Rotating Cylinder With and Without Crossflow

A. A. Tawfek,[1] B. V. S. S. S. Prasad,[2] and A. K. Mohanty[2]

Static pressure measurements around a cylinder rotating about an orthogonal axis with and without superimposed crossflow are carried out by using a capacitance type differential pressure transducer in conjunction with a slip-ring apparatus. A coefficient of pressure (C_p) is defined for the rotating cylinder and typical variations of C_p along its length and periphery are presented.

Nomenclature

$C_p(r, \theta)$ = pressure coefficient defined at Eq. (1)

p_0 = static pressure measured at the stagnation point, Pa

---

[1] Ship Engineering Dept., Port Said, Egypt.

[2] Mechanical Engineering Department, Indian Institute of Technology, Kharagpur.

Contributed by the Fluids Engineering Division of THE AMERICAN SOCIETY OF MECHANICAL ENGINEERS. Manuscript received by the Fluids Engineering Division October 22, 1991; revised manuscript received January 8, 1993. Associate Technical Editor: E. E. Michaelides.

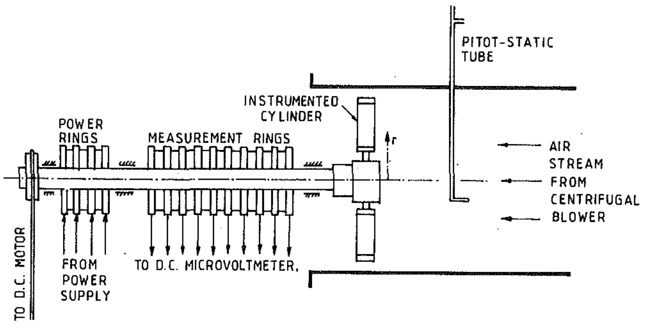

(a)

Fig. 1(*a*) Schematic of experimental setup

$p(r, \theta)$ = static pressure measured at any angle of θ, Pa
p = static pressure of surrounding fluid, Pa
r = radial position measured from the axis rotation, m
Re_c = cross-flow Reynolds number, $\mathrm{Re}_c = V_c D/\nu$
Re_r = rotational Reynolds number, $\mathrm{Re} = V_r D/\nu$
Re_R = resultant Reynolds number, $\mathrm{Re} = V_R D/\nu$
V_c = velocity of crossflow, m/s
V_r = rotational velocity, $V_r = \Omega r$, m/s
V_R = resultant velocity, $V_R = \sqrt{V_c^2 + V_r^2}$, m/s
α = angle of resultant velocity, measured w.r.t. the plane of rotation, rad.
ν = kinematic viscosity, m^2/s
θ = angular position on the cylinder, rad
ρ = density, $\mathrm{kg/m}^3$
Ω = angular velocity of the rotating body, 1/s

1 Introduction

Thermofluid-dynamic studies pertaining to rotating bodies are of particular importance to several engineering applications such as turbomachines. In turbine blade applications, it is customary to evaluate thermal transport rates on the basis of a relative velocity with the static wind tunnel tests as the base. This practice is open to scrutiny since the effects of centrifugal and Coriolis forces are neglected.

Indeed, significant differences in the values of lift coefficients between the stationary and rotating aerofoils were noted by Himmelskamp (see Schichting, 1987). Eisele et al. (1969), Mohanty et al. (1977), Cornet et al. (1980), and Sparrow and Kadle (1984) reported augmentation of average heat and mass transfer rates from flat plates and cylinders rotating about an orthogonal axis. While corroborating with these earlier results regarding the overall transport, Prasad et al. (1991) observed that the heat transfer values at the stagnation point of a circular cylinder decreased, whereas they registered an increase at the other angular locations. The present experimental study is undertaken with the objective that a knowledge of the pressure distribution around a rotating cylinder can lead to an understanding of the variations of local transport rates due to rotational effects. Rotating cylinders (Fig. 1) in both quiescent and in superimposed cross (air) flow environments are considered for the experiments.

2 Experiments

Figures 1(*a*) and (*b*) show a general arrangement of the experimental setup and the details of a pair of acrylic test cylinders of 45 mm OD, respectively. Two such pairs with $L/D = 4$ and 5 were used in the present experiments. The two cylinders were mounted 180 deg apart on the hub, which, in turn, was fastened to the rotating shaft. Each cylinder was provided with three miniature holes and an arrangement to vary their angular position with respect to the flow direction. The pressure variations were recorded by a capacitance type differential pressure transducer (Furnes Controls FC-040), whose metal membrane was oriented in the plane of rotation and found unaffected by the centrifugal force. The 15 volt d.c. excitation to the transducer and the milli-volt output from the same were connected through the power and instrumentation rings of the slip-ring apparatus respectively. While the above cylinder assembly was rotated freely in a large laboratory room for the quiescent environment, it was located inside a 500 mm ID wind tunnel for the measurements in crossflow.

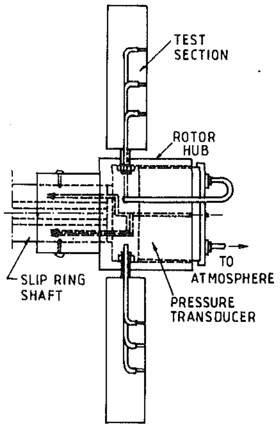

(b)

Fig. 1(*a*) Schematic of experimental setup

The pressure measuring arrangement was calibrated in two stages: independently, by using a pressure vessel and a micromanometer (Askania, 0.001 mm Wg resolution within ±1 percent accuracy), and in-situ, for pressure distribution on a cylinder in crossflow. Agreement within ±1 percent was noted between the transducer and the micromanometer outputs and the presence of slip-rings had little influence on the transducer read-out.

Measurements were carried out at three radii r = 137, 157, and 177 mm, and at different rotational speeds from 250 to 900 rpm, for pure rotation and with superimposed crossflow. The rotational speed was monitored continuously and was maintained within ±1 rpm by means of the d.c. drive control, during each set of experiments. For further details, refer to Tawfek (1990).

3 Results

Rotation to the cylinder introduces work input, and therefore, it would be prudent not to refer the pressure variation through a non-inertial application of Bernoulli's equation. The dual presence of rotation and cross-flow, additionally, causes a shift of the stagnation point from the plane of rotation. Experimentally, the stagnation point on the cylinder surface was identified by the angular position where the measured static pressure had the highest value. Measuring angular locations from the stagnation point, we define a pressure coefficient:

$$C_p = \frac{(p(r,\theta) - p(r,0))}{\left(\frac{1}{2}\rho V_R^2\right)} \tag{1}$$

It would be readily noted that the definition of $C_p(r, \theta)$ specializes to the practice in literature when $V_r = 0$ and $p(\theta) = p + 1/2\rho V_c^2$ in the presence of pure crossflow.

3.1 Rotation in Quiescent Air.

Measurements corresponding to a rotational Reynolds number range of 15,700 to

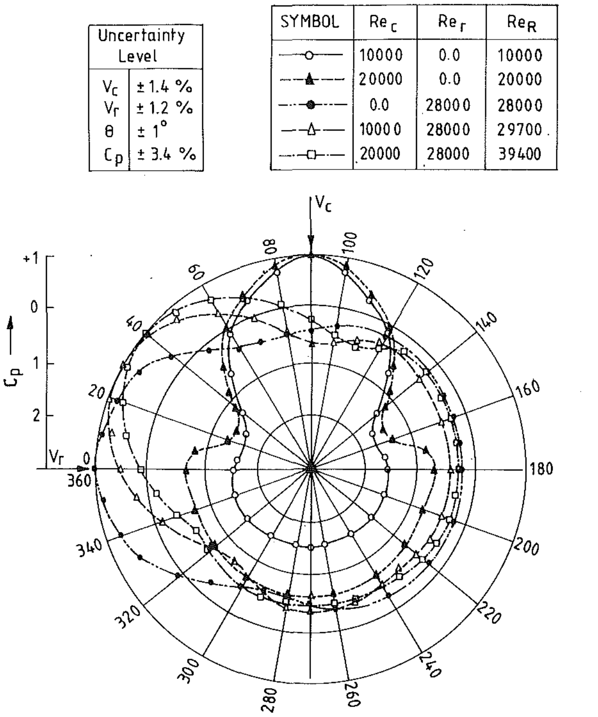

Uncertainty Level	
V_c	± 1.4 %
V_r	± 1.2 %
θ	± 1°
C_p	± 3.4 %

SYMBOL	Re_c	Re_r	Re_R
—○—	10000	0.0	10000
—▲—	20000	0.0	20000
---●---	0.0	28000	28000
—△—	10000	28000	29700
—□—	20000	28000	39400

Fig. 2 Pressure distribution of cylinder in pure crossflow, pure rotation, and both

40,300 were taken and a typical variation is presented in Fig. 2. The stagnation point lies in the plane of rotation, and C_p is a function of both r and θ. The zero value of C_p occurs around $\theta = 45$ deg, unlike the 30 deg condition for cylinder in pure crossflow. This was also predicted by Sears (1950) for an infinite cylinder under rotation.

The pressure coefficient, in general, decreases from 0 to 80 deg and remains fairly constant between 120 and 240 deg and could be summarized through Re_r, reminiscent to the behavior of stationary cylinder in crossflow (Schlichting, 1987). However, unlike the stationary cylinder case, C_p could not group the pressure variations at different Re into a single curve. The reason is attributable to the presence of longitudinal pressure gradient due to the centrifugal force. The difference in C_p values for various Re_r is, however, less pronounced in the front region. This signifies dominance of the circumferential pressure gradient over the centrifugal in the neighborhood of the stagnation point.

3.2 Superimposed Crossflow. While the experimental range covered simultaneous variation of Re_c from 0 to 26,000 and Re_r from 0 to 38,000, only typical variations are presented in Fig. 2, for the sake of brevity. Note the shift in stagnation point from the plane of rotation to the point of application of the resultant velocity, Fig. 2, as the crossflow velocity changes from zero. At a given speed of rotation and crossflow, the angular shift varies with the radius of measurement as

$$\frac{\tan \alpha_1}{\tan \alpha_2}=\frac{r_2}{r_1} \tag{2}$$

The difference between α_1 and α_2, between the two extreme points of our measurements, $r_1 = 137$ and $r_2 = 177$ mm, was of the order of 5 deg, nominally for $\mathrm{Re}_c/\mathrm{Re}_r = 0.5$. The measured location of the maximum pressure point is compared with the so estimated value of α in Fig. 3.

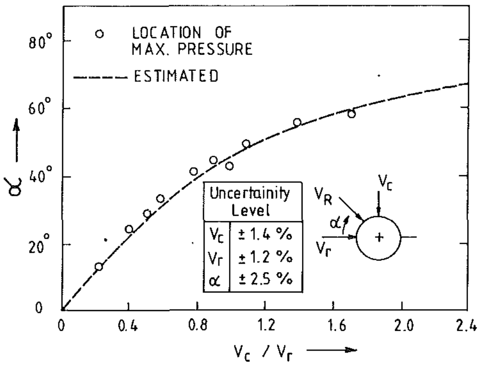

Fig. 3 Measured and estimated position of the stagnation condition for rotating cylinder in crossflow

The effects of centrifugal and Coriolis forces do not permit the C_p curves at different radii to merge into one, even when the rotational Reynolds number is the same. This can be a pointer for summarizing transport rate values where the effects of body forces may be accounted for the nondimensional parameters in addition to Re_R.

The overall experimental uncertainty of the pressure coefficient is estimated to be 3.4 percent at the lowest values of V_c and V_r and the value of uncertainty, in general, decreases with their increasing magnitude.

4 Conclusions

1. A coefficient of pressure has been defined at Eq. (1) for cylinders rotating about an orthogonal axis, with and without superimposed crossflow.
2. The point of zero C_p lies around $\theta = 45$ deg for cylinder rotating in quiescent air.
3. The position of maximum pressure or stagnation point is predictable by vectorially summing V_c and V_r.
4. The effects of centrifugal and Coriolis forces due not permit the C_p curves at different radii to merge into one, even when the rotational Re_r is same.
5. The variations in the relative magnitudes of longitudinal and circumferential pressure gradients could explain the transport rate behaviors.

Acknowledgment

This work was partially supported by the propulsion panel, AR & DB, Government of India.

References

Cornet, I., Grief, R., Teng, J. T., and Rochler, F., 1980, "Mass Transfer to Rotating Rods and Plates," *International Journal of Heat and Mass Transfer*, Vol. 23, p. 805.

Eisele, E. H., Leidenfrost, W., and Muthunayagam, A. E., 1969, "Studies of Heat Transfer from Rotating Heat Exchangers," *Progress in Heat and Mass Transfer*, Vol. 2, p. 483.

Mohanty, A. K., Raghavachar, T. S., and Nanda, R. S., 1977, "Heat Transfer from Rotating Short Radial Blades," *International Journal of Heat and Mass Transfer*, Vol. 20, p. 1417.

Prasad, B. V. S. S. S., Tawfek, A. A., and Mohanty, A. K., 1991, "Heat Transfer from a Circular Cylinder Rotating About an Orthogonal Axis in Quiescent Air," *Experiments in Fluids*, Vol. 4, p. 44.

Schlichting, H., 1987, *Boundary Layer Theory*, 7th ed., McGraw-Hill, New York, N.Y.

Sears, W. R., 1950, "Potential Flow Around a Rotating Cylindrical Blade," *Reader's Forum, Journal of Aeronautical Sciences*, Vol. 17, p. 183.

Sparrow, E. M., and Kadle, D. S., 1984, "Heat Transfer from Rods or Pins Which Extend Radially Outward from Rotating Shaft," ASME *Journal of Heat Transfer*, Vol. 106, p. 290.

Tawfek, A. A., 1990, "Heat Transfer from Rotating Cylinders and Blades," Ph.D. thesis, Indian Institute of Technology, Kharagpur, India.

Capillary Instability of a Jet of Liquid Metal

David B. Wallace[1]

A system based on ink-jet technology has been used to demonstrate the controlled generation of monodispersed 100 μm diameter molten solder droplets. Oxide formation on the surface of the molten solder jet was shown to have a drastic effect on the droplet formation process. If the oxygen is not removed from the environment, no jet break up occurs. The growth rate of a radial disturbance on a capillary jet of molten solder is similar in magnitude to that predicted by Rayleigh and Weber theory, but the agreement is not good enough to say that these theories are valid for the liquid metal jet.

Introduction

Recent advances in semiconductor manufacturing and electronics assembly have caused applied solder volumes in these processes to decrease drastically. At the same time, the positional control requirements have become more exacting. One potential solution to this problem is the use of ink-jet technology to create 50–150 μm diameter droplets of molten solder and direct them toward a substrate. Liquid metal jets have been investigated previously by Vasil'ev (1977), Hendricks (1981), Kendall (1981), and Artemyev and Kochetov (1990), but the details of the jet breakup process were not described, or the break-up mechanism was turbulence induced. This paper attempts to quantify the breakup of a capillary jet of liquid metal and compare the results with existing theory.

Droplet Formation Analysis

The phenomena of uniform drop formation from a stream of liquid issuing from an orifice were initially described mathematically by Lord Rayleigh (1878). His theory describes the growth of a radially symmetric initial diameter disturbance on an inviscid jet, and it is based on a small perturbation assumption (i.e., linear theory). Given a disturbance of the form shown in Eq. (1), the non-dimensional disturbance growth rate, according to Rayleigh theory, is given in Eq. (2).

Rayleigh (1892) extended his analysis to viscous jets, but the complexity of the relationships makes it of little utility. Weber (1931) used a similar approach as Rayleigh, but produced a much more practicable result by making several simplifying assumptions. His relationship for the normalized disturbance growth rate, given in Eq. (3), reduces to Rayleigh's equation if the viscosity is zero and Weber's approximation of the Bessel function term is employed. These relationships will be used to evaluate the experimentally observed solder jet breakup behavior described below.

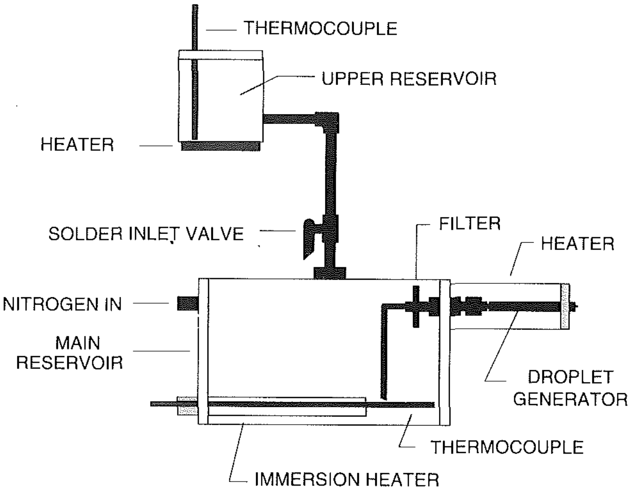

Fig. 1 Molten solder jetting hydraulic system configuration

Test System and Materials

Figure 1 illustrates the hydraulic system used in this study. The functional requirements of the system were to provide oxide and contaminant free molten solder at a controlled temperature to the droplet generator.

The upper reservoir is a temperature controlled, enclosed "solder pot." The solder is melted in the upper reservoir and the dross/impurities can rise to the surface while the molten solder is gravity fed to the main reservoir. The main reservoir is a temperature controlled (via a thermocouple mounted inside the reservoir), teflon coated, chamber to house the pure solder. By pressurizing the chamber with nitrogen, clean liquid solder is forced through the droplet generator.

The droplet generator is mounted to the reservoir. A separate thermocouple/heater combination is used to control the temperature of the solder in the droplet generator. This defines the temperature of the solder jet as it exits the droplet generator. For all of the results described in the following, the operating temperature of the droplet generator was 100°C. Details of the droplet generator design are given in Wallace (1989).

The droplet generator and the region several inches downstream from the droplet generator orifice were encased in a plexiglass box (not shown in the figure). The atmosphere in this box was controlled by inputting a constant flow on dry nitrogen.

$$r' = r_0' e^{at} \cos\left(\frac{x}{r_0}\xi\right) \qquad \xi \equiv \frac{2\pi r_0}{\lambda}$$

r_0 = jet radius
r_0' = initial radius perturbation
r' = radius perturbation
a = disturbance growth rate
t = time
x = axial distance
λ = disturbance wavelength (1)

$$\alpha \equiv a\left(\frac{\rho r_0^3}{\sigma}\right)^{0.5} \qquad \alpha^2 = \frac{(1-\xi^2) i\xi J_0'(i\xi)}{J_0(i\xi)}$$

ρ = density
σ = surface tension
J_0 = Bessel function (2)

---

[1] MicroFab Technologies, Inc., Plano, TX 75205.

Contributed by the Fluids Engineering Division of THE AMERICAN SOCIETY OF MECHANICAL ENGINEERS. Manuscript received by the Fluids Engineering Division April 28, 1992; revised manuscript received November 30, 1992. Associate Technical Editor: Ho, Chih Ming.

$$\alpha^2 = \frac{\xi^2(1-\xi^2)}{2} - 3\sqrt{2}\xi^2 Z\alpha$$

$$Z = \frac{\sqrt{\mathrm{We}_d}}{\mathrm{Re}_d}$$

$$\mathrm{We}_d = \text{Weber number} = \frac{Ud^2}{\sigma}$$

$$\mathrm{Re}_d = \text{Reynolds number} = \frac{Ud}{\nu}$$

U = jet velocity

d = jet diameter (3)

The solder selected for this study was Indalloy-158, a low melting temperature eutectic solder. A eutectic solder composition was selected because it directly transitions from solid to liquid with no phase containing a solid/liquid mixture. The melting point of Indalloy-158 is 70°C and the composition is 50 Bi, 26.7 Pb, 13.3 Sn, 10 Cd. Unlike tin-lead solder alloys (Jones and Davies, 1957-1958; Fisher and Phillips, 1954), published fluid properties of Indalloy-158 are not available. Specific heat, density, and surface tension were estimated by taking the weighted average of the properties of the pure metal constituents at 100°C. This method produced a reasonable estimate compared to the properties of similar materials given in Lea (1988). An estimate of 1.5-3.0 cp for the viscosity of Indalloy-158 was obtained from Mankamyer et al. (1985) and Holman (1981). Estimates of the viscosity derived from experimental data obtained in this study ranged from 8-37 cp. These estimates will be discussed in more detail below.

Droplet Formation Experimental Evaluation

At a given reservoir pressure, the molten solder was caught in a tared receptacle to determine the flow rate. After selecting the disturbance frequency (sinusoidal waveforms with frequencies of 10-25kHz were used for all test cases) to be applied to the droplet generator, the disturbance wavelength was obtained by measuring the drop-to-drop spacing optically from a stroboscopically frozen image of the drops. The combination of flow rate, frequency, and wavelength allows the droplet velocity (assumed to be the same as the jet velocity), drop diameter, and jet diameter to be calculated. Note that the jet diameter cannot be assumed to be the same as the orifice diameter (Goren and Wronski, 1966).

At each frequency, the breakoff length was measured for (peak-to-peak) voltages in the range 1-160V. Breakoff length is defined as the distance from the orifice to the location where the drops separate from the jet. To illustrate disturbance wavelength effects, break off length behavior was examined for several frequencies and a fixed jet velocity. Viscous effects (both nozzle flow and capillary instability) were examined by measuring the break off length for the same disturbance wavelength at a different jet velocity. Finally, the tests were repeated with a second device with a different orifice diameter.

Examination of Eq. (1) reveals that the disturbance growth is exponential in time and independent of jet velocity. Therefore, the breakoff length data was converted to breakoff time by dividing breakoff length by the jet velocity. The experimental uncertainty of the break off length measurement was ±20 μm and the velocity measurement uncertainty was 0.1-0.15m/s. Since these two errors are uncorrelated, the breakoff time uncertainty is the RMS of the combined errors, or 25-94 μs.

The breakoff time results for the 51 μm orifice diameter device are shown in Fig. 2. Since the data are approximately linear on semilog plot, the jet breakup behavior is qualitatively similar to the behavior assumed in Eq. (1). In reaching this conclusion, it is must be assumed that the initial disturbance

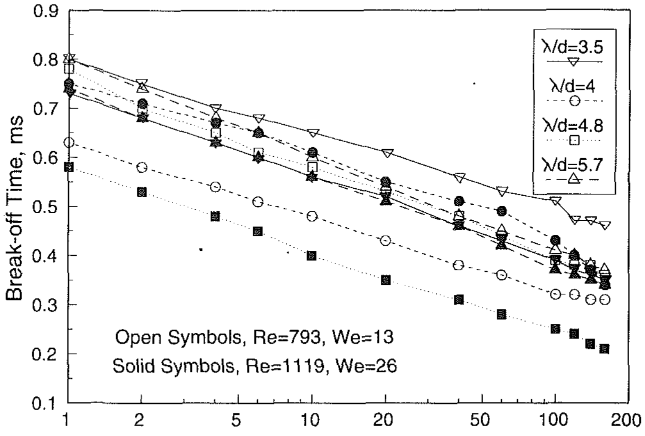

Fig. 2 Break-off time versus voltage applied, Indalloy-158 solder and a 51 μm orifice diameter device

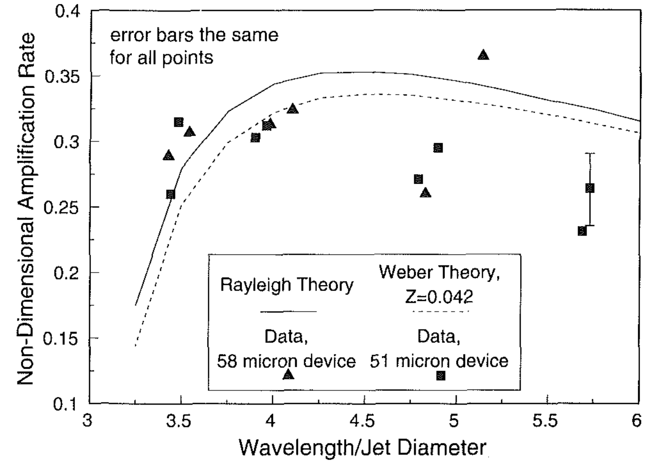

Fig. 3 Amplification rate as a function of λ/d, Indalloy-158

amplitude has a 1:1 relationship to the voltage applied to the droplet generator device, assuming all other parameters are held constant. Also note that, because the droplet generator device has acoustic resonances, the initial disturbance amplitude will be a function of frequency, and thus λ/d. Hence, this type of presentation cannot be used to evaluate the effects of nondimensional wavelength, Reynolds number, or Weber number.

To compare the experimental results to theory in a quantitative fashion, the slope of the breakoff time versus voltage curve was obtained from a regression fit to the data in the same manner as Pimbly and Lee (1977). The breakoff time is substituted into Eq. (1), and the disturbance amplitude at this time is set to r_0. Assuming that breakoff occurs at the same phase angle (i.e., cosine term is set equal to 1.0), a single equation in two unknowns (disturbance growth rate, a; and initial disturbance, r_0') is obtained. By assuming that the initial disturbance is directly proportional to the drive voltage (all other parameters being held constant), and by taking the logarithm of both sides of the equation, a linear equation in drive voltage and disturbance growth rate is obtained, as shown in Eq. (4).

From the slope of the regression fit, the nondimensional amplification rate defined in Eq. (2) was calculated and is plotted in Fig. 3 versus non-dimensional wavelength, along with Rayleigh and Weber theory curves. Note that the Weber theory results are very close to the Rayleigh theory results using the estimated solder fluid properties.

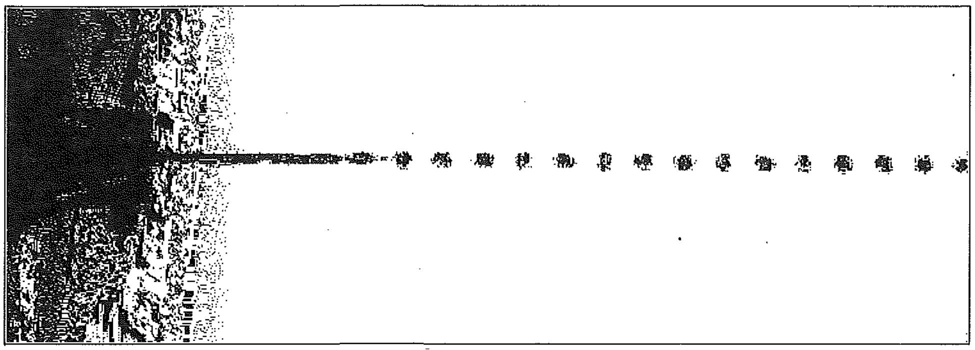

Fig. 4 50 μm Indalloy-158 solder jet and 100 μm droplets forming in a nitrogen atmosphere

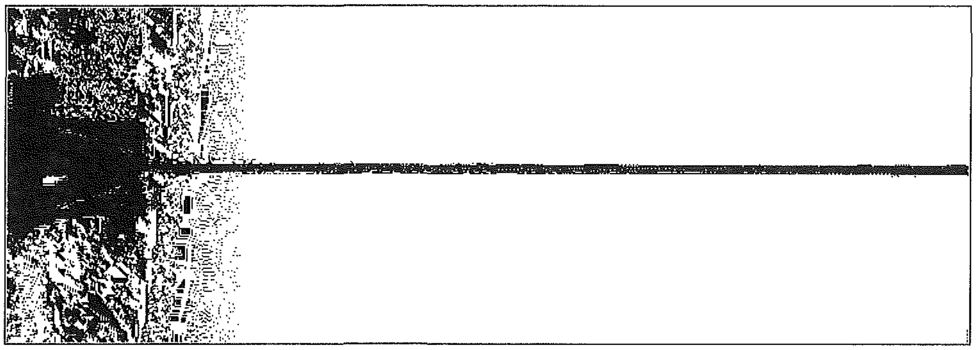

Fig. 5 50 μm Indalloy-158 solder jet in air

In comparing of the data and theory in Fig. 3, we can only conclude that the measured and predicted amplification rates are of similar in magnitude, and the shape of the amplification rate data versus normalized wavelength is qualitatively similar to theory. Whether the lack of comparison between the data and theory is due to a fundamental difference in behavior caused by an unidentified phenomenon, such as oxide formation on the surface of the jet (see below), or due to errors in the experimental system is not know at this time. This will be an area of further investigation in the future.

A great deal of emphasis in the system design was placed on controlling the gaseous materials that come into contact with the solder in a molten state. Control of oxide formation is potentially important to the quality of solder joint that can be achieved using this type of dispensing, and has previously been observed to degrade the breakup of liquid metal jets (Kochetov, 1990). During the current study of jet breakup behavior, an experiment was conducted that illustrates the drastic effect that oxide formation has on the surface tension of a liquid metal jet. Figure 4 shows the controlled breakup of a 50 μm jet of a Indalloy-158 solder jet into 100 μm droplets in a nitrogen atmosphere. For this case, the breakup occurs in less than 3 mm. Holding all operating conditions the same, Fig. 5 illustrates what happens when room air is allowed into the controlled atmosphere chamber. The change in behavior from that shown in Fig. 4 to that shown in Fig. 5 occurs in less than 5 seconds, representing the time it takes room air to migrate to the region of the jet.

$$at_{break\text{-}off} + \ln(V) + C = 0$$

V = drive voltage
C = constant (4)

In the electronics industry, oxide formation on metal is known to have a drastic effect on contact angle and surface tension. Unless oxides are prevented from forming, or are removed through the use of fluxes, the reflowed (i.e., molten) solder will not wet onto the leads of an electrical component, and a poor solder joint will result. The decrease in surface tension of molten solder that has an oxidized surface can easily be observed in the "slumping" of the solder. Measurement of liquid metal surface tension is a difficult procedure, but some data is available in the literature (Carroll and Warwick, 1987; Schaneke, et. al., 1978). Oxides are prevented from forming on the surface of the liquid metal during these measurements by use of inert gases (e.g., nitrogen or argon), and/or gasses that chemically reduce oxygen (hydrogen). The author knows of no surface tension data available for liquid metals with known levels of surface oxides. Since Eq. (2) dictates that the breakoff time is proportional to the square of the surface tension, the change in behavior shown between Fig. 4 and Fig. 5 indicates that oxide formation on the surface of a liquid metal decreases the surface tension by at least an order of magnitude. In addition, to prevent the jet from breaking up before oxides have formed on the liquid metal surface, the time scale for oxide formation must be <100 μs.

Due to the lack of viscosity data for the solder alloy used in this study, an estimate of the molten solder viscosity was obtained from the experimental data and a previously developed empirical model. The model, shown in Fig. 6, is a standard orifice flow model (Filmore, 1983) for the type of droplet generator used in the current study, and the data shown in Fig. 6 were obtained using glycerin and water solutions. Using this model, two estimates of the viscosity were obtained from the pressure and flow rate data for Indalloy-158: 8 cp for the 58 μm orifice diameter device tests and 37 cp for the 51 μm orifice diameter device tests. The large uncertainty in estimating the viscosity in this manner is due to the low slope of the discharge versus Reynolds number curve. The fact that these two estimates are large compared to the expected value, 1.5-3.0 cp, may be due to a change in the viscosity over time. The solder was recycled several times during these tests, and

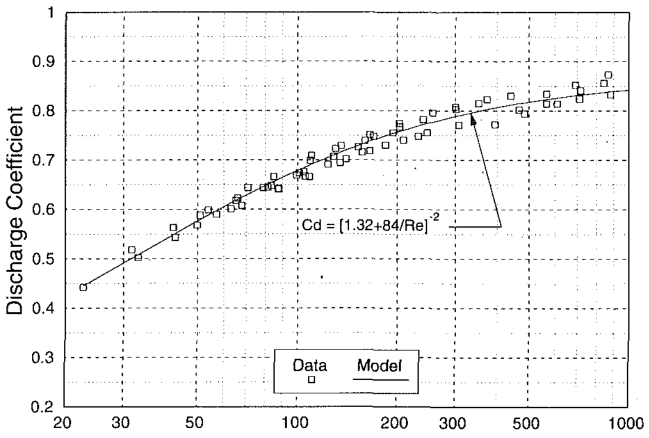

Fig. 6 Orifice flow model and data

the higher value was obtained from tests that occurred after the tests which produced the lower value. It is plausible that a build up of impurities in the solder caused the viscosity to increase over time. Future studies will include direct viscosity measurements before and after all tests.

Conclusions

Micro-solder droplets of uniform size, 100 μm in diameter, were produced using a low temperature solder in a continuous type ink-jet device. Oxide formation on the surface of the molten solder jet was shown to have a drastic effect on the droplet formation process. If the oxygen is not removed from the environment, no jet breakup occurs. The growth rate of a radial disturbance on a capillary jet of molten solder is similar in magnitude to that predicted by Rayleigh and Weber theory, but the agreement is not good enough to say that these theories are valid for the liquid metal jet.

Acknowledgment

This research has been funded in part by an SBIR grant from the National Science Foundation, grant number ISI-9060945.

References

Carroll, M. A., and Warwick, M. E., 1987, "Surface Tension of Sn-Pb Alloys: Part 1 - Effect of Bi, Sb, P, Ag, and Cu on 60-40 Solder," *Material Science and Technology*, Vol. 3, pp. 1040–1045.

Filmore, G. L., 1983, "Drop Velocity From an Ink-Jet Nozzle," *IEEE Transactions on Industry Applications*, Vol. 9, No. 6, p. 1098.

Fisher, H. J., and Phillips, A., 1954, "Viscosity and Density of Liquid Lead-Tin and Antimony-Cadmium Alloys," *Journal of Metals*, p. 1060.

Goren, S. L. and Wronski, S., 1966, "The Shape of Low-Speed Capillary Jets of Newtonian Liquids," *Journal of Fluid Mechanics*, Vol. 25, Part 1, pp. 185–198.

Hendricks, C. D., 1982, "Inertial Confinement Fusion Targets," *Proceedings of the 2nd International Colloquium on Drops and Bubbles*, D. H. LeCroissette, ed., NASA-CR-168848.

Holman, J. P., 1981, *Heat Transfer*, McGraw-Hill, New York, p. 545.

Jones, W. R. D., and Davies, J. B., 1957–1958, "The Viscosity of Lead, Tin, and Their Alloys," *Journal of the Institute of Metals*, Vol. 86, p. 164.

Kendall, J. M., 1982, "Hydrodynamic Performance of an Annular Liquid Jet: Production of Spherical Shells," *Proceedings of the 2nd International Colloquium on Drops and Bubbles*, D. H. LeCroissette, ed., NASA-CR-168848.

Kocheov, S. G., 1990, "Abnormal Capillary Breaking of the Liquid Metal Free Jet in Oxidizing Medium," *Advances in Gas-Liquid Flows - 1990*, ASME.

Lea, C., 1988, *A Scientific Guide to Surface Mount Technology*, Electrochemical Publication Limited, Ayr, Scotland, p. 316.

Mankamyer, M. M., Snyder, R. E., and Taussig, R. T., 1985, "Liquid Droplet Radiator Systems Investigation," AFRPL TR-85-808.

Pimbly, W. T., and Lee, H. C., 1977, "Satellite Droplet Formation in a Liquid Jet," *IBM Journal of Research and Developement*, pp. 22–23.

Rayleigh, Lord, 1878, "On the Instability of Jets," *Proceedings of the London Mathematical Society*, Vol. 10, No. 4.

Rayleigh, Lord, 1892, "On the Instability of a Cylinder of Viscous Liquid Under Capillary Force," *Philosophical Magazine*, Vol. 34, No. 145.

Schwaneke, A. E., Falke, W. L., and Miller, V. R., 1978, "Surface Tension and Density of Liquid Tin-Lead Solder Alloys," *Journal of Chemical and Engineering Data*, Vol. 23, No. 4, pp. 298–301.

Vasil'ev, M. N., 1977, "Decay of a Jet of Liquid Metal in a Magnetic Field," *Magnitnaya Gidrodinamika*, No. 1, pp. 137–140.

Wallace, D. B., 1989, "A Method of Characteristics Model of a Drop-On-Demand Ink-Jet Device Using an Integral Drop Formation Method," ASME publication 89-WA/FE-4.

Weber, C., 1931, "Zum Zerfall eines Flussigkeitsstrables," *Zeitschrift Angewandte Mathematik Fuer Mechanik*, Vol. 11, No. 136.

Analytic Expression for the Universal Logarithmic Velocity Law

A. Yakhot,[1,2] V. D. Khait,[3] and S. A. Orszag[1,4]

A new formulation of an algebraic eddy viscosity model based on a new length scale dependent on boundary layer flow characteristics (displacement thickness, momentum-loss thickness) has been recently developed by Yakhot et al. (1992). Using this new approach, they have calculated transitional flow in a flat plate boundary layer. The integral characteristics of the turbulent boundary layer including the location of transition, skin friction coefficient, and velocity distribution across the boundary layer, are in very good agreement with available experimental data.

The derivation of the model could be found in Yakhot et al. (1992). Here, we provide a completely self-consistent formulation of the model and emphasize the assumptions made in its derivation. The algebraic eddy viscosity model of Yakhot et al. (1992) is based on a form of the turbulent eddy viscosity suggested by renormalization group (RNG) approach to turbulence (Yakhot and Orszag, 1986). The RNG theory involves systematic elimination of small scales of motion from the Navier-Stokes equations. By eliminating the small-scale modes from the wave number interval $\Lambda_f < k < \Lambda_0$, the following expression for the turbulent viscosity has been derived by Yakhot and Orszag (1986):

$$\nu = \nu_0 \left[1 + H\left(a\,\frac{\bar{\epsilon}\Lambda_f^{-4}}{\nu_0^3} - C \right) \right]^{1/3}, \qquad (1)$$

where ν_0 is molecular viscosity, $a \approx 0.12$, $C = O(100)$ is the RNG constant, and $H(x)$ is the ramp function defined by $H(x) = \max(x, 0)$.

The RNG turbulent viscosity (1) is expressed in terms of the mean dissipation rate, $\bar{\epsilon}$, and the length scale, $\Delta = 2\pi\Lambda_f^{-1}$, corresponding to the smallest fluctuating scales retained in the system after the RNG procedure of scale elimination is completed. In transport models of turbulence *all* fluctuating modes are eliminated, so Δ must be expressed in terms of an integral length scale (l). In terms of $\bar{\epsilon}$ and l, the expression (1) may be written in the form:

---

[1] Cambridge Hydrodynamics, Inc., Princeton, NJ 08542.

[2] Department of Mechanical Engineering, Ben-Gurion University, Beersheva 84105, Israel.

[3] Cornell University Medical College, New York, NY 10021.

[4] Applied and Computational Mathematics, Princeton University, Princeton, NJ 08544.

Contributed by the Fluids Engineering Division of THE AMERICAN SOCIETY OF MECHANICAL ENGINEERS. Manuscript received by the Fluids Engineering Division October 16, 1992; revised manuscript received March 26, 1993. Associate Technical Editor: D. P. Telionis.

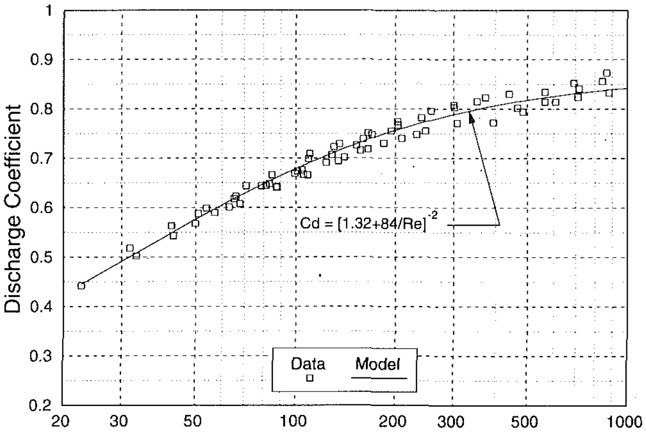

Fig. 6 Orifice flow model and data

the higher value was obtained from tests that occurred after the tests which produced the lower value. It is plausible that a build up of impurities in the solder caused the viscosity to increase over time. Future studies will include direct viscosity measurements before and after all tests.

Conclusions

Micro-solder droplets of uniform size, 100 μm in diameter, were produced using a low temperature solder in a continuous type ink-jet device. Oxide formation on the surface of the molten solder jet was shown to have a drastic effect on the droplet formation process. If the oxygen is not removed from the environment, no jet breakup occurs. The growth rate of a radial disturbance on a capillary jet of molten solder is similar in magnitude to that predicted by Rayleigh and Weber theory, but the agreement is not good enough to say that these theories are valid for the liquid metal jet.

Acknowledgment

This research has been funded in part by an SBIR grant from the National Science Foundation, grant number ISI-9060945.

References

Carroll, M. A., and Warwick, M. E., 1987, "Surface Tension of Sn-Pb Alloys: Part 1 - Effect of Bi, Sb, P, Ag, and Cu on 60-40 Solder," *Material Science and Technology*, Vol. 3, pp. 1040-1045.

Filmore, G. L., 1983, "Drop Velocity From an Ink-Jet Nozzle," *IEEE Transactions on Industry Applications*, Vol. 9, No. 6, p. 1098.

Fisher, H. J., and Phillips, A., 1954, "Viscosity and Density of Liquid Lead-Tin and Antimony-Cadmium Alloys," *Journal of Metals*, p. 1060.

Goren, S. L. and Wronski, S., 1966, "The Shape of Low-Speed Capillary Jets of Newtonian Liquids," *Journal of Fluid Mechanics*, Vol. 25, Part 1, pp. 185-198.

Hendricks, C. D., 1982, "Inertial Confinement Fusion Targets," *Proceedings of the 2nd International Colloquium on Drops and Bubbles*, D. H. LeCroissette, ed., NASA-CR-168848.

Holman, J. P., 1981, *Heat Transfer*, McGraw-Hill, New York, p. 545.

Jones, W. R. D., and Davies, J. B., 1957-1958, "The Viscosity of Lead, Tin, and Their Alloys," *Journal of the Institute of Metals*, Vol. 86, p. 164.

Kendall, J. M., 1982, "Hydrodynamic Performance of an Annular Liquid Jet: Production of Spherical Shells," *Proceedings of the 2nd International Colloquium on Drops and Bubbles*, D. H. LeCroissette, ed., NASA-CR-168848.

Kocheov, S. G., 1990, "Abnormal Capillary Breaking of the Liquid Metal Free Jet in Oxidizing Medium," *Advances in Gas-Liquid Flows - 1990*, ASME.

Lea, C., 1988, *A Scientific Guide to Surface Mount Technology*, Electrochemical Publication Limited, Ayr, Scotland, p. 316.

Mankamyer, M. M., Snyder, R. E., and Taussig, R. T., 1985, "Liquid Droplet Radiator Systems Investigation," AFRPL TR-85-808.

Pimbly, W. T., and Lee, H. C., 1977, "Satellite Droplet Formation in a Liquid Jet," *IBM Journal of Research and Developement*, pp. 22-23.

Rayleigh, Lord, 1878, "On the Instability of Jets," *Proceedings of the London Mathematical Society*, Vol. 10, No. 4.

Rayleigh, Lord, 1892, "On the Instability of a Cylinder of Viscous Liquid Under Capillary Force," *Philosophical Magazine*, Vol. 34, No. 145.

Schwaneke, A. E., Falke, W. L., and Miller, V. R., 1978, "Surface Tension and Density of Liquid Tin-Lead Solder Alloys," *Journal of Chemical and Engineering Data*, Vol. 23, No. 4, pp. 298-301.

Vasil'ev, M. N., 1977, "Decay of a Jet of Liquid Metal in a Magnetic Field," *Magnitnaya Gidrodinamika*, No. 1, pp. 137-140.

Wallace, D. B., 1989, "A Method of Characteristics Model of a Drop-On-Demand Ink-Jet Device Using an Integral Drop Formation Method," ASME publication 89-WA/FE-4.

Weber, C., 1931, "Zum Zerfall eines Flussigkeitsstrables," *Zeitschrift Angewandte Mathematik Fuer Mechanik*, Vol. 11, No. 136.

Analytic Expression for the Universal Logarithmic Velocity Law

A. Yakhot,[1,2] V. D. Khait,[3] and S. A. Orszag[1,4]

A new formulation of an algebraic eddy viscosity model based on a new length scale dependent on boundary layer flow characteristics (displacement thickness, momentum-loss thickness) has been recently developed by Yakhot et al. (1992). Using this new approach, they have calculated transitional flow in a flat plate boundary layer. The integral characteristics of the turbulent boundary layer including the location of transition, skin friction coefficient, and velocity distribution across the boundary layer, are in very good agreement with available experimental data.

The derivation of the model could be found in Yakhot et al. (1992). Here, we provide a completely self-consistent formulation of the model and emphasize the assumptions made in its derivation. The algebraic eddy viscosity model of Yakhot et al. (1992) is based on a form of the turbulent eddy viscosity suggested by renormalization group (RNG) approach to turbulence (Yakhot and Orszag, 1986). The RNG theory involves systematic elimination of small scales of motion from the Navier-Stokes equations. By eliminating the small-scale modes from the wave number interval $\Lambda_f < k < \Lambda_0$, the following expression for the turbulent viscosity has been derived by Yakhot and Orszag (1986):

$$\nu = \nu_0 \left[1 + H\left(a \frac{\bar{\epsilon}\Lambda_f^{-4}}{\nu_0^3} - C \right) \right]^{1/3}, \tag{1}$$

where ν_0 is molecular viscosity, $a \approx 0.12$, $C = O(100)$ is the RNG constant, and $H(x)$ is the ramp function defined by $H(x) = \max(x, 0)$.

The RNG turbulent viscosity (1) is expressed in terms of the mean dissipation rate, $\bar{\epsilon}$, and the length scale, $\Delta = 2\pi\Lambda_f^{-1}$, corresponding to the smallest fluctuating scales retained in the system after the RNG procedure of scale elimination is completed. In transport models of turbulence *all* fluctuating modes are eliminated, so Δ must be expressed in terms of an integral length scale (l). In terms of $\bar{\epsilon}$ and l, the expression (1) may be written in the form:

---

[1] Cambridge Hydrodynamics, Inc., Princeton, NJ 08542.

[2] Department of Mechanical Engineering, Ben-Gurion University, Beersheva 84105, Israel.

[3] Cornell University Medical College, New York, NY 10021.

[4] Applied and Computational Mathematics, Princeton University, Princeton, NJ 08544.

Contributed by the Fluids Engineering Division of THE AMERICAN SOCIETY OF MECHANICAL ENGINEERS. Manuscript received by the Fluids Engineering Division October 16, 1992; revised manuscript received March 26, 1993. Associate Technical Editor: D. P. Telionis.

$$\nu=\nu_0\left[1+H\left(\bar{a}\frac{\bar{\epsilon}l^4}{\nu_0^3}-C\right)\right]^{1/3}, \tag{2}$$

where $\bar{a}$ is a constant which is discussed below.

Yakhot et al. (1992) expressed the mean dissipation rate, $\bar{\epsilon}$, from the well-known expression for the eddy viscosity used in $k-\epsilon$ transport models of turbulence:

$$\bar{\epsilon}=C_\mu\frac{k^2}{\nu},\quad C_\mu\approx 0.09, \tag{3}$$

where k is the turbulent energy. Assuming equilibrium between production and dissipation, when $k\approx C_\mu^{-1/2}u_*^2$ and $u_*=(\tau_w/\rho)^{1/2}$ is a wall-shear velocity, and substituting (3) into (2), for the eddy viscosity we have:

$$\nu=\nu_0\left[1+H\left(\bar{a}\frac{u_*^4 l^4}{\nu\nu_0^3}-C\right)\right]^{1/3} \tag{4}$$

For wall-bounded turbulent flows one may expect that near the wall (within the logarithmic layer) the length scale, l, is equal to the distance from the wall: $l=y$. If we also require that $\nu=\kappa u_* y$ ($\kappa\approx 0.4$), as widely used in mixing length theory, we must choose the constant $\bar{a}$ in (4) to be equal to κ^4. Thus, we may rewrite (4) as:

$$\nu=\nu_0\left[1+H\left(\kappa^4\frac{u_*^4 l^4}{\nu\nu_0^3}-C\right)\right]^{1/3}, \tag{5}$$

where κ is the von Karman constant, $C=O(100)$, and $H(x)=\max(x,0)$.

Assuming that $H(x)=x$, the expression (5) may be written in the form of a quartic ($Q4$) equation:

$$Q4(\hat{\nu})=\hat{\nu}^4+(C-1)\hat{\nu}-\hat{\nu}_m^4=0 \tag{6}$$

where

$$\hat{\nu}=\frac{\nu}{\nu_0},\quad \hat{\nu}_m=\kappa l_+,\quad l_+=\frac{u_* l}{\nu_0}$$

As a result of the ramp function $H(x)$ used in the model, the quartic Eq. (6) must be solved for $\hat{\nu}$ under the constraint:

$$\hat{\nu}=\max(\hat{\nu},1) \tag{7}$$

The length scale, l, appearing in (6), is defined by:

$$l=\min(y,\gamma\delta_*), \tag{8}$$

where y, is the distance from the wall and δ_* is the displacement thickness. It has been shown by Yakhot et al. (1992) that, the length scale, l, *cannot* be defined assuming that γ is a constant in (8). Instead, they suggest the following expression for γ:

$$\gamma=\gamma_0(1-H^{-1})^{-1},\quad \gamma_0=0.3, \tag{9}$$

where $H=\delta_*/\theta$ is a shape factor, δ_* is the displacement thickness and θ is the momentum-loss thickness defined by:

$$\delta_*=\int_0^\infty\left(1-\frac{u}{U_0}\right)dy,\quad \theta=\int_0^\infty\frac{u}{U_0}\left(1-\frac{u}{U_0}\right)dy$$

The H-dependent γ has the same meaning as an empirical intermittency coefficient used in standard eddy-viscosity models to account for the transition region (Cebeci and Smith, 1974). The value of the constant $\gamma_0=0.3$ in (9) has been chosen by Yakhot et al. (1992) from the analysis of the fully turbulent boundary layer over a flat plate and in order to obtain that the laminar-turbulent transition ($\hat{\nu}>1$) occurs at the Reynolds number $\mathrm{Re}_x\approx 10^5$.

To conclude, algebraic-$Q4$ eddy viscosity model is defined by (6–9). The eddy viscosity is presented as a solution of a quartic ($Q4$) Eq. (6). The model accurately describes transitional boundary layer flow over a flat plate (Yakhot et al., 1992). The integral characteristics, such as the total skin friction coefficient and mean velocity across the boundary layer, are found to be in good agreement with experimental data, and, as an example, the mean velocity profiles at different downstream locations, Re_x, are plotted in Fig. 1.

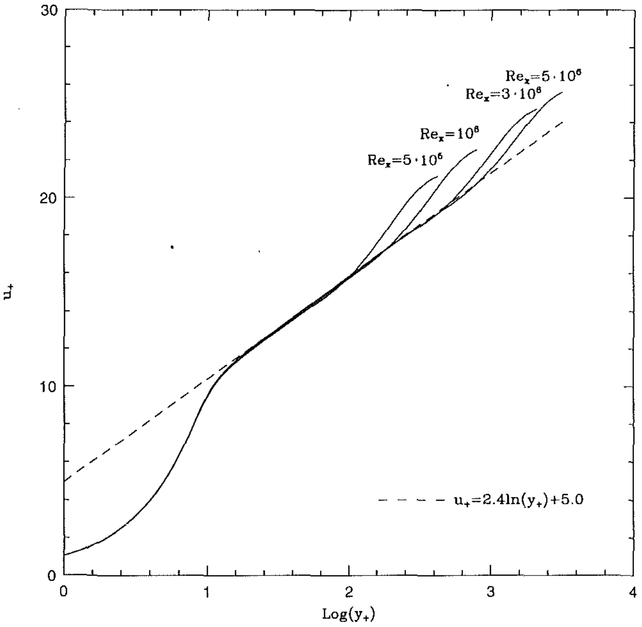

Fig. 1 Turbulent boundary layer flow over a flat plate: mean velocity profiles at different downstream locations

In this note, we shall use the algebraic-Q4 eddy viscosity model of Yakhot et al. (1992) to derive analytically the form of the logarithmic velocity-distribution law. For the purpose of this note, the algebraic model (6–9), being applied to the inner regions ($l=y$) of fully developed turbulent flow in boundary layer, channel or pipe, gives an eddy-viscosity, ν, that satisfies the quartic equation:

$$Q4(\hat{\nu})=\hat{\nu}^4+(C-1)\hat{\nu}-(\kappa y_+)^4=0, \tag{10}$$

where $\hat{\nu}=\nu/\nu_0$, ν_0 is molecular viscosity, $C=O(100)$ is a constant, κ is the von Karman constant, and y_+ is nondimensional distance to the wall measured in wall units. The quartic Eq. (10) is solved for $\hat{\nu}$ under the constraint $\hat{\nu}=\max(\hat{\nu},1)$, so the turbulent viscosity turns on ($\hat{\nu}>1$) at $y_+=y_*=C^{1/4}/\kappa$. Since $Q4(0)<0$ while $Q4'(\hat{\nu})>0$ for $\hat{\nu}\geq 0$, (10) has *only* one positive root which is a continuous function of y_+.

Within the inner region, the velocity is governed by:

$$\frac{du_+}{dy_+}=\frac{1}{\hat{\nu}}, \tag{11}$$

where $u_+=u/u_*$, and u_* is the wall-shear velocity. Integrating (11) from y_* to y_+, and assuming that $u_+(y_+)=y_+$ for $y_+\leq y_*$, gives:

$$u_+(y_+)=\frac{C^{1/4}}{\kappa}+\int_{y_*}^{y_+}\frac{d\eta}{\hat{\nu}(\eta)}, \tag{12}$$

Using (10), it follows that:

$$u_+(y_+)=\frac{C^{1/4}}{\kappa}+\frac{1}{4\kappa}\int_1^{\hat{\nu}}\frac{4\hat{\nu}^3-1+C}{\hat{\nu}^{3/4}(\hat{\nu}^3-1+C)^{3/4}}d\hat{\nu},$$

so that:

$$u_+(y_+)=\frac{1}{3\kappa}\left[4C^{1/4}-z+\ln\left(\frac{z+1}{z-1}\right)+2\arctan(z)-\ln\left(\frac{C^{1/4}+1}{C^{1/4}-1}\right)-2\arctan(C^{1/4})\right], \tag{13}$$

where $z=(\hat{\nu}^3-1+C)^{1/4}/\hat{\nu}^{3/4}$ and $\hat{\nu}=\hat{\nu}(y_+)$ is the solution of the quartic Eq. (10).

For $y_+ \gg 1$, it follows from (10) that $\hat{\nu} \approx \kappa y_+$, while (13) gives:

$$u_+(y_+) = \frac{1}{\kappa} \ln y_+ + B, \tag{14}$$

where

$$B = \frac{1}{3\kappa}\left[4C^{1/4} + \ln\left(\frac{8\kappa^3}{C-1}\right) + \frac{\pi}{2} - 1 - \ln\left(\frac{C^{1/4}+1}{C^{1/4}-1}\right) - 2\arctan(C^{1/4})\right] \tag{15}$$

Evaluating B at $\kappa = 0.4$ and $C = 160$, as was used by Yakhot et al. (1992), we obtain $B = 4.9$ which is in very good agreement with experimental fits. From (15), one can see that when $C \approx$ 130-220, the constant B is varied over the experimentally observed range 4.5-5.5. Thus, when $C = O(100)$ as given by the RNG theory of turbulence (Yakhot and Orszag, 1986), the value of B agrees with experiment.

In conclusion, we have given an elementary analytic expression of the shift constant B of the logarithmic velocity law based on the algebraic-$Q4$ eddy viscosity model.

Acknowledgments

This work was supported by NASA under Contract NAS3-25942, the Office of Naval Research under Contract N00014-82-C-0451, and The United States-Israel Binational Science Foundation under grant 87-00399.

References

Cebeci, T., and Smith, A. M. O., 1974, *Analysis of Turbulent Boundary Layers*, Academic Press.

Yakhot, A., Kedar, O., and Orszag, S. A., 1992, "Algebraic-$Q4$ Turbulent Eddy Viscosity Model: Boundary Layer Flow Over a Flat Plate and Flow in a Pipe," *Journal of Scientific Computing*, Vol. 7, pp. 229-239.

Yakhot, V., and Orszag, S. A., 1986, "Renormalization Group Analysis of Turbulence. 1. Basic Theory," *Journal of Scientific Computing*, Vol. 1, No. 1, pp. 3-57.

Mean Streamwise Velocity Measurements in a Triple Jet of Equilateral Triangular Configuration

G. H. Moustafa,[1] T. Sundararajan,[2] and E. Rathakrishnan[3]

Introduction

Multijet flows arise in several applications such as jet engine/rocket combustors, the thrust augmenting ejectors for VTOL/STOL aircraft, and industrial gas burners. In order to achieve proper combustion, thrust development, and reduction in the noise level, it is often desirable to control the inter-mixing between the jets and also the entrainment of the surrounding atmosphere. This, in turn, requires a detailed study of the behavior of high speed jets in multijet configuration. The situation of interest here is an array of three axisymmetric nozzles set in a common end wall with equal spacing in a triangular configuration (Fig. 1). The reason why this particular configuration has been chosen is that it promotes bending of the jet axes toward each other, thus leading to greater mixing.

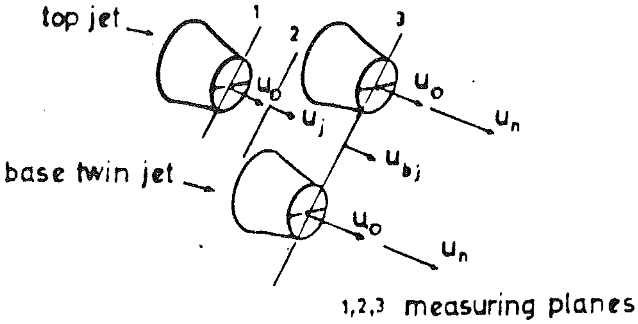

Fig. 1 Triple jet triangular configuration

Table 1

p_a/p_0	u/u_0	y/d_e	x/d_e	S	L_m/d_e
±0.022	±0.012	±0.0012	±0.006	±0.022	±0.006

The available literature on multijet flows mainly concerns the turbulence characteristics of incompressible jets and the acoustic behavior of compressible jets. Turbulent incompressible jet flows have been studied by Sforza et al. (1966), Krothapalli et al. (1983), and Quinn (1989). These authors have performed mean flow and turbulence measurements and have analyzed the effects of nonaxisymmetric nozzle geometries. The results obtained lead to the conclusion that low speed jets originating from nonaxisymmetric orifices decay to form axisymmetric jets far downstream. The noise generation mechanisms of high speed multiple jets have been studied by Raghunathan and Reid (1981) and Krothapalli et al. (1989), while supersonic jet-interactions have been considered by Wlezien (1989). No investigations have so far been reported regarding the behavior and development of compressible triple jet configurations. In the present study, experiments have been conducted to investigate the effect of stagnation pressure ratio and nozzle spacing upon the mean flow characteristics of compressible jets in triangular configuration. The individual flow features of the vertex jet and the base twin jet are analyzed and their contributions to the axis switching as well as the overall triple jet behavior are highlighted.

Experimental Apparatus and Procedure

Compressed dry air was passed through the gate valve and pressure regulating valve into the stagnation chamber. It was then accelerated through an array of convergent nozzles and released into the ambient atmosphere in the form of free jets. Mesh wire screens were inserted inside the stagnation chamber to produce a uniform velocity at the nozzle exit. Models containing nozzles of the following dimensions were used in this study; nozzle length = 25 mm, inlet diameter = 10 mm and exit diameter d_e = 4.2 mm. Four models with a nozzle spacing S of 12, 16, 18, and 22 mm were fabricated and tested. The distribution of the total pressure in the jet was measured by a three hole pitot tube. Time-averaged (mean) values of total pressure were measured at several X, Y, and Z locations. The distance between the nozzle axes and the floor was kept sufficiently large for ignoring the wall effects in the present

---

[1] Lecturer, College of Engineering, Menoufia University, Egypt.

[2] Associate Professor, Department of Mechanical Engineering, IIT Kanpur, India.

[3] Associate Professor, Department of Aerospace Engineering, IIT Kanpur, India.

Contributed by the Fluids Engineering Division of THE AMERICAN SOCIETY OF MECHANICAL ENGINEERS. Manuscript received by the Fluids Engineering Division August 20, 1991; revised manuscript received November 3, 1992. Associate Technical Editor: Ho, Chih Ming.

For $y_+ \gg 1$, it follows from (10) that $\hat{\nu} \approx \kappa y_+$, while (13) gives:

$$u_+(y_+) = \frac{1}{\kappa} \ln y_+ + B, \qquad (14)$$

where

$$B = \frac{1}{3\kappa}\left[4C^{1/4} + \ln\left(\frac{8\kappa^3}{C-1}\right) + \frac{\pi}{2} - 1 - \ln\left(\frac{C^{1/4}+1}{C^{1/4}-1}\right) - 2\arctan(C^{1/4})\right] \qquad (15)$$

Evaluating B at $\kappa = 0.4$ and $C = 160$, as was used by Yakhot et al. (1992), we obtain $B = 4.9$ which is in very good agreement with experimental fits. From (15), one can see that when $C \approx$ 130–220, the constant B is varied over the experimentally observed range 4.5–5.5. Thus, when $C = O(100)$ as given by the RNG theory of turbulence (Yakhot and Orszag, 1986), the value of B agrees with experiment.

In conclusion, we have given an elementary analytic expression of the shift constant B of the logarithmic velocity law based on the algebraic-$Q4$ eddy viscosity model.

Acknowledgments

This work was supported by NASA under Contract NAS3-25942, the Office of Naval Research under Contract N00014-82-C-0451, and The United States–Israel Binational Science Foundation under grant 87-00399.

References

Cebeci, T., and Smith, A. M. O., 1974, *Analysis of Turbulent Boundary Layers*, Academic Press.

Yakhot, A., Kedar, O., and Orszag, S. A., 1992, "Algebraic-$Q4$ Turbulent Eddy Viscosity Model: Boundary Layer Flow Over a Flat Plate and Flow in a Pipe," *Journal of Scientific Computing*, Vol. 7, pp. 229–239.

Yakhot, V., and Orszag, S. A., 1986, "Renormalization Group Analysis of Turbulence. 1. Basic Theory," *Journal of Scientific Computing*, Vol. 1, No. 1, pp. 3–57.

Mean Streamwise Velocity Measurements in a Triple Jet of Equilateral Triangular Configuration

G. H. Moustafa,[1] T. Sundararajan,[2] and E. Rathakrishnan[3]

Introduction

Multijet flows arise in several applications such as jet engine/rocket combustors, the thrust augmenting ejectors for VTOL/STOL aircraft, and industrial gas burners. In order to achieve proper combustion, thrust development, and reduction in the noise level, it is often desirable to control the inter-mixing between the jets and also the entrainment of the surrounding atmosphere. This, in turn, requires a detailed study of the behavior of high speed jets in multijet configuration. The situation of interest here is an array of three axisymmetric nozzles set in a common end wall with equal spacing in a triangular configuration (Fig. 1). The reason why this particular configuration has been chosen is that it promotes bending of the jet axes toward each other, thus leading to greater mixing.

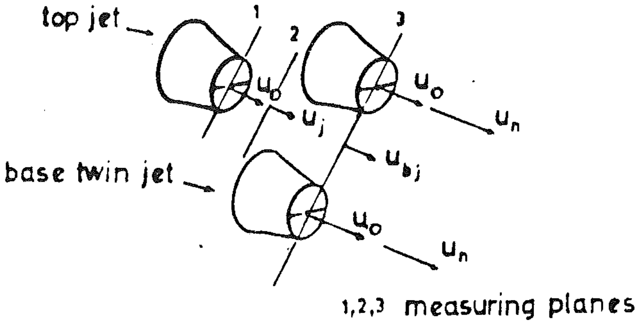

Fig. 1 Triple jet triangular configuration

Table 1

p_a/p_0	u/u_0	y/d_e	x/d_e	S	L_m/d_e
±0.022	±0.012	±0.0012	±0.006	±0.022	±0.006

The available literature on multijet flows mainly concerns the turbulence characteristics of incompressible jets and the acoustic behavior of compressible jets. Turbulent incompressible jet flows have been studied by Sforza et al. (1966), Krothapalli et al. (1983), and Quinn (1989). These authors have performed mean flow and turbulence measurements and have analyzed the effects of nonaxisymmetric nozzle geometries. The results obtained lead to the conclusion that low speed jets originating from nonaxisymmetric orifices decay to form axisymmetric jets far downstream. The noise generation mechanisms of high speed multiple jets have been studied by Raghunathan and Reid (1981) and Krothapalli et al. (1989), while supersonic jet-interactions have been considered by Wlezien (1989). No investigations have so far been reported regarding the behavior and development of compressible triple jet configurations. In the present study, experiments have been conducted to investigate the effect of stagnation pressure ratio and nozzle spacing upon the mean flow characteristics of compressible jets in triangular configuration. The individual flow features of the vertex jet and the base twin jet are analyzed and their contributions to the axis switching as well as the overall triple jet behavior are highlighted.

Experimental Apparatus and Procedure

Compressed dry air was passed through the gate valve and pressure regulating valve into the stagnation chamber. It was then accelerated through an array of convergent nozzles and released into the ambient atmosphere in the form of free jets. Mesh wire screens were inserted inside the stagnation chamber to produce a uniform velocity at the nozzle exit. Models containing nozzles of the following dimensions were used in this study; nozzle length = 25 mm, inlet diameter = 10 mm and exit diameter d_e = 4.2 mm. Four models with a nozzle spacing S of 12, 16, 18, and 22 mm were fabricated and tested. The distribution of the total pressure in the jet was measured by a three hole pitot tube. Time-averaged (mean) values of total pressure were measured at several X, Y, and Z locations. The distance between the nozzle axes and the floor was kept sufficiently large for ignoring the wall effects in the present

---

[1] Lecturer, College of Engineering, Menoufia University, Egypt.

[2] Associate Professor, Department of Mechanical Engineering, IIT Kanpur, India.

[3] Associate Professor, Department of Aerospace Engineering, IIT Kanpur, India.

Contributed by the Fluids Engineering Division of THE AMERICAN SOCIETY OF MECHANICAL ENGINEERS. Manuscript received by the Fluids Engineering Division August 20, 1991; revised manuscript received November 3, 1992. Associate Technical Editor: Ho, Chih Ming.

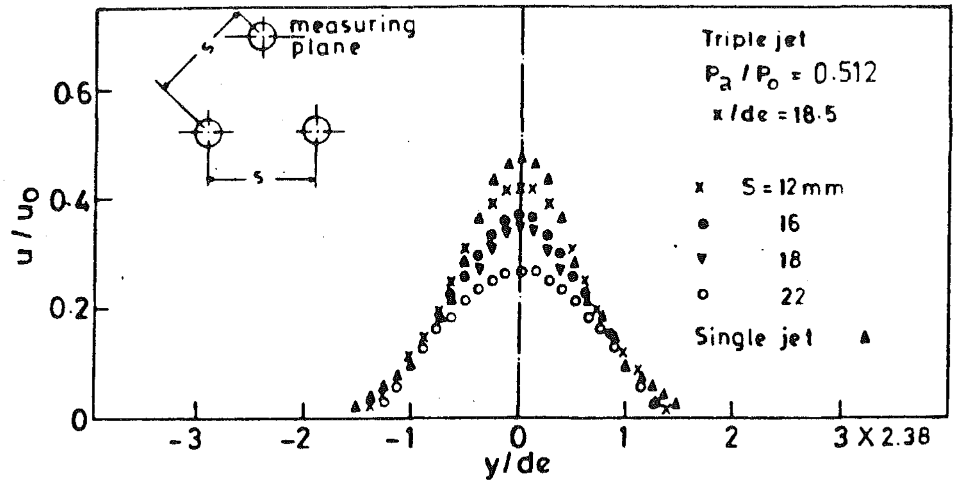

Fig. 2 Velocity distribution of the top-jet

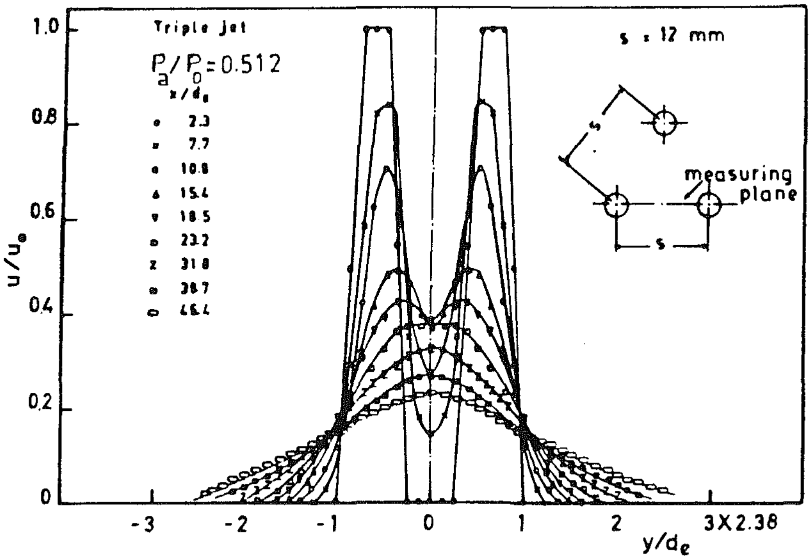

Fig. 3 Velocity profile of the base twin jet

experiment. The uncertainty involved in the measured (or calculated) values of various quantities are presented in Table 1.

Results and Discussion

In order to highlight the mutual interaction between the jets, the results are presented in the form of the vertex jet behavior and the twin jet behavior (see Fig. 1). Various aspects such as velocity profiles, decay rates, and spreading rates are examined for both the vertex and the twin jets. The trends observed in the overall triple jet behavior are explained with the help of the vertex and twin jet characteristics.

In Fig. 2, the mean velocity profiles of the vertex jet at a downstream location of $x/d = 18.5$ are shown for different nozzle spacings. The velocity u is normalized by the velocity at the nozzle exit u_0. All the length dimensions are normalized by the nozzle exit diameter. Also, the stagnation pressure p_0 is normalized by the ambient pressure p_a. The velocity profile for a single jet is also included for the sake of comparison. The velocity decay is more rapid in the case of the vertex jet than for the single jet. Also, it increases with an increase in the nozzle spacing. Expressing the mean velocity decay ratio as

$$MVDR = \frac{u/u_0|_{\text{single}} - u/u_0}{u/u_0|_{\text{single}}}$$

it is seen that MVDR for S = 12 mm is 13.5 percent and for S = 22 mm, it is equal to 44.5 percent. These trends can be explained as follows. In the triple jet configuration, entrainment of ambient fluid from inner region between the jets leads to a low pressure zone. Because of this low pressure zone, the jets attract each other and axis-shifting takes place. As a consequence of axis-shifting phenomenon, the decay rate observed for the vertex jet is greater than that for the single jet. As the nozzle spacing increases, the bending of the jet axes is more which explains the effect of nozzle spacing on the velocity profile. Thus, it can be concluded that the level of entrainment as well as the mixing between the jets are enhanced in a multijet configuration such as the triple jet.

The velocity distributions in the base twin jet are shown at several axial locations for $S = 12$ mm, in Fig. 3. Close to the nozzle exit, the velocity profiles indicate the presence of a potential core region surrounded by an axisymmetric shear layer, for each jet. After some distance, the jets merge and

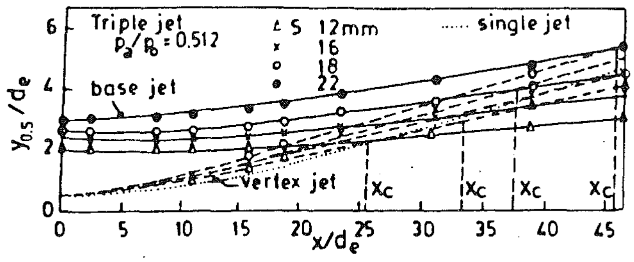

Fig. 4 The axis switching of the vertex and base jets

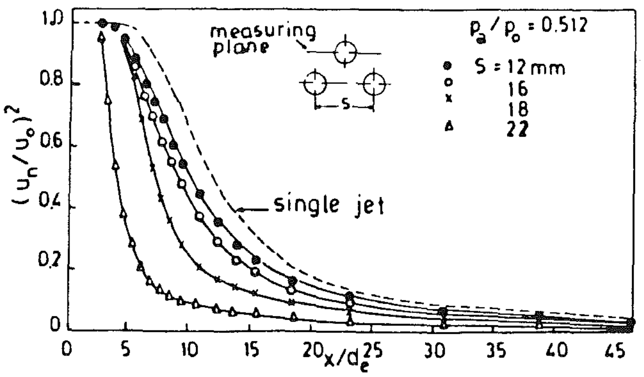

Fig. 5 Variation of axial velocity of the vertex jet with nozzle spacing

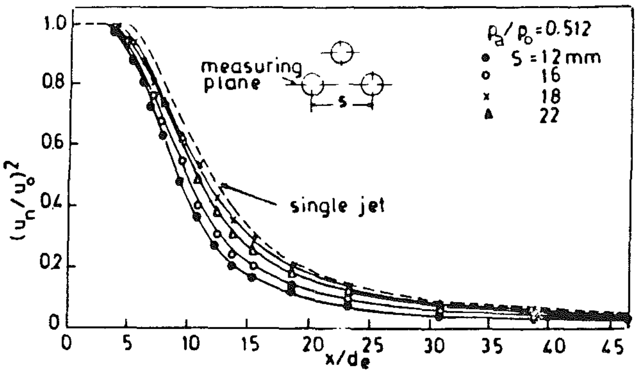

Fig. 6 Variation of axial velocity of the base jet with nozzle spacing

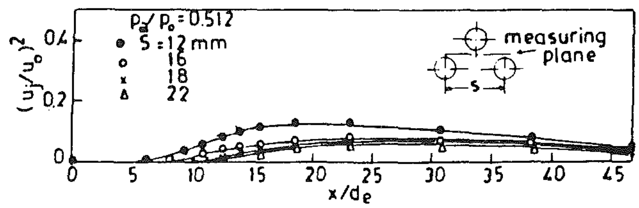

Fig. 7 Variation of the triple jet velocity u_j with nozzle spacing

the velocity in the symmetrical plane ($y = 0$) increases gradually. At a large downstream distance, the velocity becomes maximum at the mid-point between the jets and the base twin jet exhibits "fully developed" behavior. In this region, the combined jet behaves as a single incompressible jet. Experimental measurements indicate that the distance at which the jets completely merge increases with nozzle spacing.

Figure 4 shows the spreading rate of the vertex and the base twin jets. The spreading rate of the base twin jet is larger than that of the vertex jet. At some intermediate location, the half velocity widths ($y_{0.5}$) of the base jet and the vertex jet cross over. Beyond this location, the spread rates are more or less same for both the vertex and base jets, indicating a single jet behavior. The distance from the nozzle exit plane to the cross-point (X_c), increases with increasing nozzle spacing. The large difference in spreading rate at the base side and the vertex side leads to axis-switching, which is important in several chemical applications (Koshigoe et al., 1990).

In Figs. 5 and 6, the decay rates of the vertex and base twin jets are examined. The variation of the square of the normalized axial velocity $(u_n/u_0)^2$ with distance x/d_e is taken as a measure of the decay rate, since $(u_n/u_0)^2$ can be associated with the momentum of the flow. In Fig. 5, the decay rate of the vertex jet has been compared with that of the single jet, for pressure ratio $p_a/p_0 = 0.512$ and different nozzle spacings. The velocity decay increases with increase of nozzle spacing and the number of nozzles, implying greater entrainment. Significant decay occurs between $x/d_e = 5$ and 25 for the single jet. The corresponding values for the vertex jet with $S = 22$ mm are 2.5 and 10. On the other hand, the potential core length decreases with increase of nozzle spacing and the number of nozzles; its value for the single jet is around 5 and in the case of the vertex jet with $S = 22$ mm, it is equal to 2.5 d_e. Also far from the nozzle exit plane, in all the cases of nozzle spacings, the velocity decay profiles of the jet approach that of the single jet. A word of caution with regard to the trends seen in Fig. 5 concerning the influence of the nozzle spacing is that these correspond to moderately small spacings. When the value of S is very large ($S \Rightarrow \infty$), the single jet behavior will be recovered once again, for each of the jets in the multijet configuration. From Fig. 6, it is evident that the decay rate of the base twin jet is closer to that of the single jet, than was observed in the case of the vertex jet.

The variation of the triple jet velocity, u_j with axial distance is shown in Fig. 7. It is seen that after a distance L_m, the triple jet velocity gradually increases from zero. It attains a maximum value at a distance L_c from the nozzle exit. The distances L_m and L_c can be identified with the merging point and the combining point of the jet. Beyond L_c, the combined jet propagates as a single jet. Both the merging and combining point distances increases with nozzle spacing; however, the merging point location is more sensitive to variation in nozzle spacing.

Conclusion

From the above results, it can be summarized that: the velocity decay of the triple jet is more than that of the single jet. Also, the spread rate is greater on the base side than on the vertex side, leading to axis switching far downstream of the nozzle exit. This, in turn, promotes mixing which is necessary for many engineering applications.

References

Sforza, P. M., Steiger, M. H., and Trentacoste, N., 1966, "Studies on Three Dimensional Viscous Jets," *AIAA Journal*, Vol. 4, pp. 800–806.

Krothapalli, A., Baganoff, D., and Karamcheti, K., 1980, "Development and Structure of a Rectangular Jet in a Multiple Jet Configuration," *AIAA Journal*, Vol. 18, pp. 945–950.

Quinn, W. R., 1990, "Mean Flow and Turbulence Measurements in a Triangular Turbulent Free Jet," *Int. J. Heat and Fluid Flow*, Vol. 11, pp. 220–224.

Raghunathan, S., and Reid, I. M. 1981, " A Study of Multiple Jets," *AIAA Journal*, Vol. 19, pp. 124–127.

Krothapalli, A., Karamcheti, K., Hsia, Y., and Baganoff, D., 1983, "Edge Tones in High Speed Flow and Their Application to Multiple Jet Mixing," *AIAA Journal*, Vol. 21, pp. 937–938.

Wlezien, R. W., 1989, "Nozzle Geometry Effects on Supersonic Jet Interaction," *AIAA Journal*, Vol. 27, pp. 1361–1367.